THE JOURNAL OF DIAGNOSTIC AND INTERVENTIONAL NEURORADIOLOGY
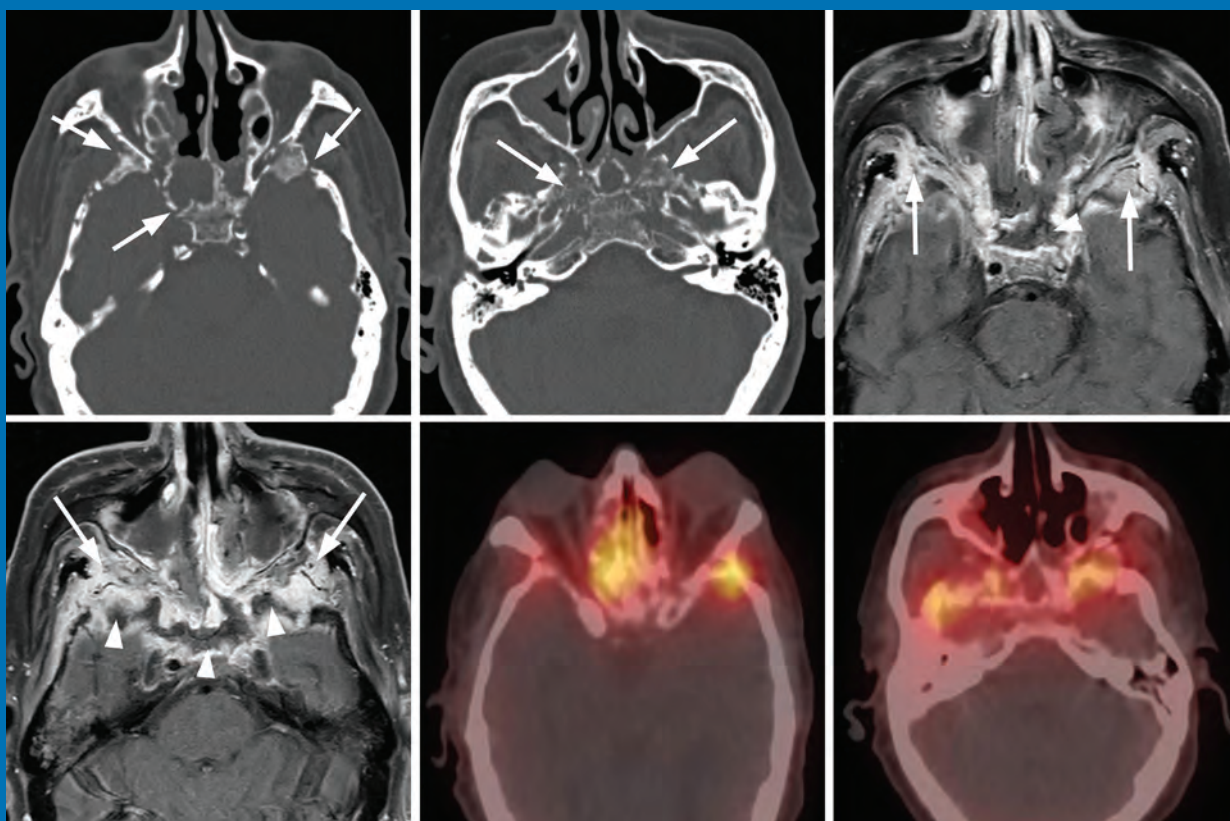
Skull base osteomyelitis

Synthetic MRI in the evaluation of multiple sclerosis lesions

Real-time ultrasound image fusion with FDG-PET/CT for node aspiration

Reliability of the diagnosis of cerebral vasospasm

ONLINE FEATURES

WHITE PAPER

BOOK REVIEWS *R.M. Quencer, Section Editor*

Please visit www.ajnrblog.org to read and comment on Book Reviews.

Extensive skull base osteomyelitis secondary to mucormycosis.

★ Indicates Editor's Choices selection

⚓ Indicates Fellows' Journal Club selection

⊙— Indicates open access to non-subscribers at www.ajnr.org

▤ Indicates article with supplemental online table

◧ Indicates article with supplemental online photo

▶ Indicates article with supplemental online video

EBM Evidence-Based Medicine Level 1

EBM Evidence-Based Medicine Level 2

Title: Lotus Pond. Acrylic on paper, 15″ × 12″.

Bejoy Thomas, MD, DNB, PDCC, Trivandrum, Kerala, India

Skull Base Osteomyelitis: A Comprehensive Imaging Review

P.R. Chapman, G. Choudhary, and A. Singhal

ABSTRACT

SUMMARY: Skull base osteomyelitis is a relatively rare condition, generally occurring as a complication of advanced otologic or sinus infection in immunocompromised patients. Skull base osteomyelitis is generally divided into 2 broad categories: typical and atypical. Typical skull base osteomyelitis occurs secondary to uncontrolled infection of the temporal bone region, most often from necrotizing external otitis caused by *Pseudomonas aeruginosa* in a patient with diabetes. Atypical skull base osteomyelitis occurs in the absence of obvious temporal bone infection or external auditory canal infection. It may be secondary to advanced sinusitis or deep face infection or might occur in the absence of a known local source of infection. Atypical skull base osteomyelitis preferentially affects the central skull base and can be caused by bacterial or fungal infections. Clinically, typical skull base osteomyelitis presents with signs and symptoms of otitis externa or other temporal bone infection. Both typical and atypical forms can produce nonspecific symptoms including headache and fever, and progress to cranial neuropathies and meningitis. Early diagnosis can be difficult both clinically and radiologically, and the diagnosis is often delayed. Radiologic evaluation plays a critical role in the diagnosis of skull base osteomyelitis, with CT and MR imaging serving complementary roles. CT best demonstrates cortical and trabecular destruction of bone. MR imaging is best for determining the overall extent of disease and best demonstrates involvement of marrow space and extraosseous soft tissue. Nuclear medicine studies can also be contributory to diagnosis and follow-up. The goal of this article was to review the basic pathophysiology, clinical findings, and key radiologic features of skull base osteomyelitis.

ABBREVIATIONS: ASBO = atypical skull base osteomyelitis; EAC = external auditory canal; Ga-67 = gallium-67 citrate; IgG4 = immunoglobulin G4; Tc99m MDP = technetium Tc99m methylene diphosphonate; NEO = necrotizing external otitis; SBO = skull base osteomyelitis; TSBO = typical skull base osteomyelitis

Skull base osteomyelitis (SBO) is a rare, potentially life-threatening infection that can present a diagnostic challenge clinically and radiologically.[1-4] While reports differ in terminology, there are generally 2 categories of SBO: typical and atypical. Typical SBO (TSBO) is the most common and classically occurs in elderly patients with diabetes as a result of necrotizing external otitis (NEO) caused by *Pseudomonas* species. (Fig 1).[1,3] Atypical SBO (ASBO), also called central SBO, predominantly involves the basisphenoid and basiocciput and occurs without preceding otologic infection (Fig 2).[2,5] Recognition of SBO is increasing, and it is clear that radiologic evaluation plays a critical role in diagnosis and management. The goal of this article was to review the

pathophysiology, clinical presentation, and detailed radiologic findings using multiple modalities including CT, MR imaging, and nuclear medicine.

TSBO

TSOB is considered a part of the NEO spectrum, and these terms are often used interchangeably.[1,2,6] TSBO can also occur secondary to other otologic infections, including complicated otomastoiditis or petrous apicitis.[4,7,8] It can also occur secondary to trauma or as a surgical complication.[7-10]

Disease may begin as localized otitis externa (Fig 3). Progressive, deeper infection leads to NEO, in which microorganisms invade local cartilage and bone, spreading through natural gaps in the cartilaginous framework of the external auditory canal (EAC) (fissures of Santorini).[1] Infection can extend from the EAC through the foramen of Huschke into the temporomandibular joint (Fig 4). Progression of NEO ultimately causes TSOB, with local osseous destruction and localized marrow infiltration. From the EAC, infection most often spreads anteromedially to the infratemporal and preclival soft tissues, petrous apex, and clivus (Fig 5).[1]

Patients with TSBO have otorrhea and severe otalgia, with pain often out of proportion to the physical findings. Local adenopathy may be present, but fever and leukocytosis are often absent.[1] The erythrocyte sedimentation rate is generally increased and can be used to monitor treatment. Trismus may occur with involvement of the masticator space. Infiltration of the EAC or nasopharyngeal soft tissues may produce mass effect and suggests underlying malignancy. Eustachian tube obstruction can cause further fluid accumulation and phlegmon in the middle ear. Cranial neuropathies can occur and may indicate a poor prognosis. Facial nerve palsy is seen in 25% of patients as the disease spreads medially to involve the stylomastoid foramen.[1,11] Extension to the petrous apex may result in Gradenigo syndrome (facial pain, cranial nerve VI palsy, and persistent otorrhea).[12]

Inferomedial spread of infection to the jugular foramen and carotid space can result in multiple lower cranial neuropathies (cranial nerves IX–XII).[1,2] Involvement of the sympathetic plexus along the internal carotid artery can also produce Horner syndrome. Rare cases of Villaret syndrome (neuropathies of cranial nerves IX–XII plus Horner syndrome) have been reported when SBO affects the jugular foramen.[13] Secondary thrombophlebitis of the jugular bulb and sigmoid sinus can also occur.[11] The internal carotid artery can be affected anywhere from the neck to the cavernous sinus, producing infectious arteritis, thrombosis, pseudoaneurysm, and stroke.

Intracranial spread can result in meningitis, epidural abscess, and cavernous sinus thrombosis. If the cavernous sinus is affected, multiple upper cranial nerves can be involved.[11] Cranial nerve involvement is typically unilateral but can be bilateral in advanced SBO crossing the midline.

Patients with diabetes are particularly prone to NEO/TSBO due to a combination of immune dysfunction and microvascular angiopathy. *Pseudomonas aeruginosa* is responsible for 98% of cases.[14] The virulence of this Gram-negative bacterium is related to angioinvasion and small-

FIG 1. Typical skull base osteomyelitis. A 55-year-old man with type 2 diabetes with low-grade fever, severe pain, and drainage from his left ear. Eight weeks before imaging, the patient had been diagnosed with left-sided otitis media and possible otitis externa. He had initially been treated with amoxicillin and ofloxacin drops, without improvement. Culture from left-ear drainage revealed methicillin-sensitive *S aureus*. The patient was treated with IV vancomycin and piperacillin/tazobactam for 2 weeks and then 14 weeks of amoxicillin/clavulanate. All clinical and laboratory parameters initially resolved during 4 months. However, a gallium scan continued to indicate abnormal activity of the skull base at both 8 and 16 weeks. Despite the gallium scan, antibiotics were discontinued. Within 2 weeks, the patient had recurrent symptoms and severe neck pain. Additional imaging (not shown) indicated new cervicocranial septic arthritis, requiring an additional 3 months of IV antibiotics that led to a cure. *A,* Axial CT demonstrates opacification of left-mastoid air cells. There is subtle erosion along the petro-occipital fissure (*arrow*) and loss of cortical bone along the left lateral margin of the clivus (*arrowhead*). *B,* Axial unenhanced T1-weighted MR image demonstrates abnormal signal in the marrow space of the basiocciput (*arrow*), ill-defined signal in the left carotid space, and masslike submucosal infiltration of the left nasopharynx (*arrowhead*). *C,* Axial T1-weighted fat-saturated contrast-enhanced image demonstrates abnormal enhancement involving the marrow space of the clivus (*arrow*) as well as heterogeneous enhancement of infiltrating soft tissue in the left nasopharynx (*arrowhead*).
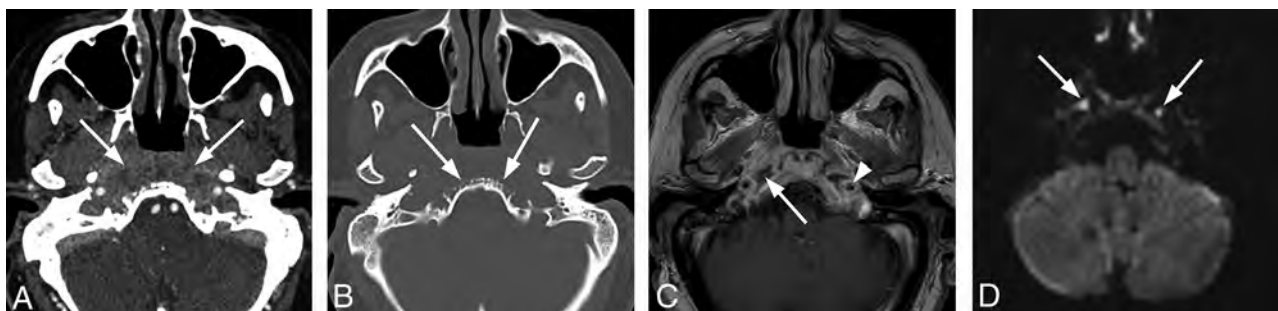
FIG 2. Atypical skull base osteomyelitis. A 72-year-old man with history of hypertension presented with a 9-week history of sinus congestion, rhinorrhea, and headache. The patient had been treated for severe sinusitis with several courses of oral antibiotics and steroid injections prescribed by his primary care physician as well as community ear, nose, and throat physicians. Just before admission, he developed left hearing loss and left-sided facial palsy. Swab culture of the nasopharynx revealed *P aeruginosa*. The patient was treated with amoxicillin-pot clavulanate (Augmentin) and Ceftazidime (Ceftaz) with clinical resolution after several weeks. Follow-up MR imaging at 4 months confirmed improvement. *A,* Axial contrast-enhanced CT scan demonstrates patchy heterogeneous density in the preclival soft tissues extending to involve the carotid spaces bilaterally (*arrows*). The inflammatory tissues in the preclival soft tissues could mimic an infiltrative neoplasm of the nasopharynx. *B,* Axial bone CT at the same level shows irregular erosions of the ventral clivus (*arrows*). *C,* Axial T1-weighted contrast-enhanced MRI. There is nodular enhancement involving the clivus at this level with focal areas of necrosis and abscess just inferior to the foramina lacerum (*arrow*). Note circumferential enhancement of the petrous internal carotid arteries (*arrowhead*). *D,* Axial DWI depicts small foci of fluid near the foramen lacerum bilaterally as diffusion-restricted, consistent with focal abscesses (*arrows*).
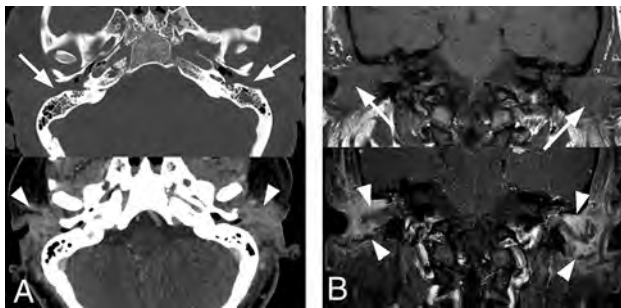
FIG 3. Bilateral external otitis. A 44-year-old woman presented with severe bilateral ear pain and drainage with conductive hearing loss. Clinically, there was marked inflammatory thickening of the EACs bilaterally. *Pseudomonas* species were cultured from the external auditory canals bilaterally. The patient was treated with IV vancomycin and piperacillin/tazobactam for 4 days followed by 2 weeks of oral ciprofloxacin. Symptoms resolved at 3 weeks without additional imaging work-up. *A*, Axial enhanced CT images are shown. Upper image with bone windows shows marked opacification of the EACs (*arrows*). The lower image with a soft-tissue filter shows marked inflammation of the EACs and periauricular tissues (*arrowheads*). *B*, The upper coronal T1 image shows marked opacification and thickening of the EACs (*arrows*) and associated opacification of the middle ear cavities. The lower image depicts postcontrast fat-saturated T1 images. A discrete mass is not identified. However, there is marked enhancement along the walls of the EACs (*arrowheads*), compatible with otitis externa.
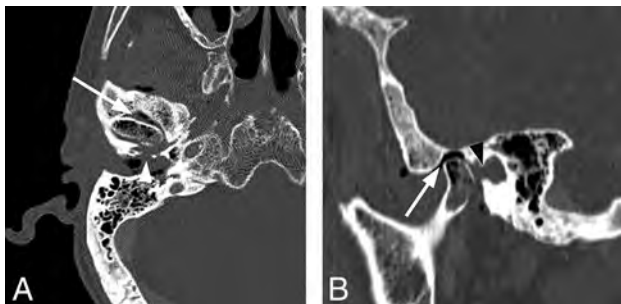
FIG 4. Necrotizing external otitis complicated by septic temporomandibular joint arthritis. An 88-year-old man with several months of right ear pain and drainage presented with progressive symptoms and right temporomandibular joint pain and trismus. In the prior weeks, he had been treated for NEO with oral and IV antibiotics at an outside facility. After initial evaluation, debridement and temporomandibular joint replacement were planned, but the patient was lost to follow-up. *A*, Axial contrast-enhanced CT with bone windows demonstrates abnormal opacification of the right EAC and inferior middle air cavity. There is erosion of the floor of the EAC, potentially involving the foramen of Huschke (*arrowhead*), and communication with the right temporomandibular joint. Air/gas density is identified within the temporomandibular joint (*arrow*) as well as within the mandibular condyle itself. *B*, Sagittal reformatted CT scan again demonstrates abnormal air density within the right temporomandibular joint and mandibular condyle (*arrow*). Note a defect in the anterior inferior margin of the EAC (*black arrowhead*).

vessel thrombosis.[1] Rarely, other bacteria including *Staphylococcus* species are reported. Otologic fungal infections, especially *Aspergillus* species, are increasingly reported in immunocompromised patients and can lead to fungal SBO.[4,15]

TSBO has been traditionally associated with high morbidity and mortality despite intensive antibiotic therapy, with reported survival rates of around 50%.[2,16] Although prognosis has improved, recent studies still report mortality of up to 30%, and it is still difficult to cure.[17-19]

ASBO

ASBO, or central SBO, for has a predilection for the clivus and occurs without precipitating otologic infection. It can be idiopathic or secondary to regional infections of the sinus, deep face, or oral cavity.[4,8,10,16,19] The distinction between typical and atypical is not always clear because patients may have occult or partially treated infection before diagnosis of SBO. Furthermore, infection of the temporal bone can spread medially to the central skull base and vice versa, making the true origin uncertain in some cases.[6,20]

The clinical features of ASBO are nonspecific. Patients are generally middle-aged to elderly with underlying diabetes or other immunocompromised states (HIV, chronic steroid use, and so forth).[2] Ridder et al[18] reported that 70% of patients with ASBO had a predisposing factor affecting bone vascularization, including diabetes (45%). Additional predisposing factors include previous radiation therapy, anemia, malnutrition, chronic cardiopulmonary disease, Paget disease, and osteoporosis. Rare patients have ASBO with no relevant pre-existing illness.

The most common symptoms of ASBO are headache and cranial neuropathies, with sinonasal symptoms reported in 25%.[2] Fever is uncommon, found in <20%.[2,3,5] The erythrocyte sedimentation rate can be elevated, but leukocytosis is absent more often than not.[3,5] ASBO can begin with persistent sinus or other local infections, with spread from pneumatized space or soft tissues to the osseous skull base. Involvement of preclival or nasopharyngeal soft tissues raises concern for nasopharyngeal neoplasm. Intracranial extension can lead to meningitis, multiple cranial neuropathies, and cavernous sinus thrombosis.[2,5,16]

Gram-positive bacteria, including *Staphylococcus* species, are more common than *Pseudomonas* species.[2,3] ASBO can be caused by fungal organisms, especially mucoraceal family in ketoacidosis and *Aspergillus* species in patients with neutropenia (Fig 6).[3,15,21] Nontuberculous *Mycobacteria* species are being increasingly recognized in the immunocompromised population. Some cases are polymicrobial.

In ASBO, a 90.5% survival rate has been reported with aggressive management at 18-month follow-up, though up to one-third of the patients experienced residual neurologic sequelae.[2]

A summary of the comparison of clinical characteristics of TSBO and ASBO is shown in the Table.

Pathology

Biopsy is often necessary in the clinical course to exclude neoplasm, examine features of non-neoplastic tissue, and obtain direct microbiologic specimens for Gram stain, culture, and antibiotic-sensitivity assessment. In cases of SBO, pathologic specimens show inflammatory changes that vary from edema to purulence, with varying degrees of tissue necrosis. Histology may not reveal microbes directly, and cultures are important for definitive diagnosis and specific treatment.[5] However, there have been
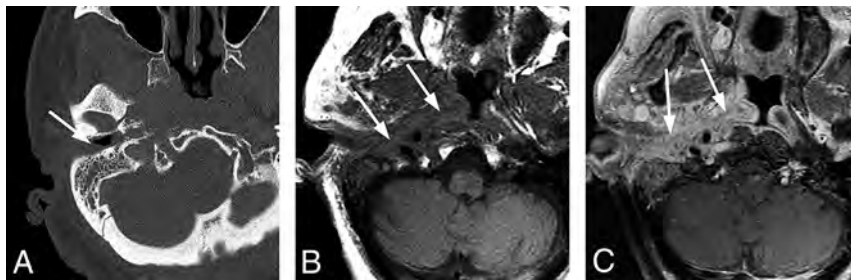
FIG 5. Typical SBO from NEO. An 82-year-old woman with insulin-dependent diabetes presented with a several-month history of pain and drainage from the right ear. The patient was recently treated as an outpatient with several rounds of antibiotics (including amoxicillin/clavulanate and ciprofloxacin) for otitis media and NEO, but symptoms had progressed. Following imaging and a diagnosis of SBO, the patient was treated with 4 weeks of IV vancomycin and piperacillin/tazobactam and additional 4 weeks of oral ciprofloxacin. The patient initially had clinical improvement, but a gallium scan at 8 weeks showed persistent uptake. The patient did not return for follow-up as instructed but returned 8 months after the original admission with progressive infection extending to the central skull base and left temporal bone, requiring an additional 6 weeks of IV antibiotic treatment. *A*, Axial CT scan through the right EAC demonstrates thickening and partial opacification of the external auditory canal (*arrow*). There is subtle erosion along the posterior wall of the external auditory canal and mild soft-tissue fullness of the right nasopharynx. *B*, Axial T1-weighted MR image demonstrates obliteration of normal fat planes in the submucosal and preclival tissues of the nasopharynx (*arrows*). This process extends posterolaterally to the tip of the mastoid on the right. *C*, Axial T1-weighted contrast-enhanced image demonstrates heterogeneous enhancement of abnormal tissue extending from the tip of the mastoid on the right to the nasopharynx (*arrows*) without discrete abscess formation.

emerging reports of culture-negative SBO, typically in patients with previous incomplete/partial treatment with topical or oral antibiotics.[22,23] There is a wide range of reported culture-negative cases in the literature.[24-26] In a systematic review by Mahdyoun et al,[26] culture-negative cases of NEO in the literature ranged from 0% to 36%. Djalilian et al,[22] in 2006, reported 8 cases of SBO, all of which were culture-negative. Some authors have reported 100% positive cultures in their studies of patients with SBO,[27] whereas some have reported up to 70% of patients with negative cultures, ultimately requiring empiric treatment.[28] These data are limited by the absence of prospective studies and small sample sizes; a systematic analysis of these data to assess differences between typical and atypical SBO in this regard is beyond the scope of this article.

Imaging. Radiologic evaluation is critical for prompt diagnosis of SBO. The imaging approach depends on presenting symptoms. However, in general, a combination of complementary studies using high-resolution bone CT and gadolinium-enhanced MR imaging is often necessary. In challenging cases, molecular imaging studies can provide functional and metabolic information.

CT. Unenhanced CT is often first-line for suspected head and neck infections and is adequate for identifying opacification, mucosal thickening, and air-fluid levels in the temporal bones and sinuses. High-resolution submillimeter-section CT using a bone algorithm can be reformatted in multiple planes and is the study of choice for identifying cortical bone erosion or trabecular demineralization that accompanies osteomyelitis.

In suspected TSBO, it is critical to assess cortical bone loss, which can be subtle. In areas without prominent marrow and trabecular bone, this may be the only clue to SBO. Several key areas should be evaluated, including the bony EAC, mastoid tip, temporomandibular joint, petrous apex, petro-occipital fissure, foramen lacerum, jugular foramen, and clivus. In cases of ASBO, there is often evidence of invasive sinusitis with cortical erosions of the paranasal sinuses, particularly the sphenoid or ethmoid sinuses and possibly along the anterior clivus and foramina of the central skull base.[5]

Contrast-enhanced CT with soft-tissue windows can also be useful. In TSBO, the anteromedial spread of cellulitis and phlegmon in the infratemporal soft tissues manifests as poorly defined enhancement and soft-tissue infiltration. Occasionally, a frank abscess can be identified in the preclival soft tissues. Asymmetric soft-tissue fullness of the nasopharynx is common and can mimic an infiltrating neoplasm, especially nasopharyngeal carcinoma (Fig 7*A*). The soft-tissue invasion and neurovascular complications can occur before or without frank bone destruction, especially in early or aggressive diseases such as fungal SBO. CTA or CTV can be of additional benefit for evaluation of vascular complications, including cavernous sinus thrombosis or stroke.

MR Imaging. MR imaging of the skull base is complementary to CT and is superior for evaluating soft-tissue extent, marrow involvement, and intracranial complications related to SBO.[3] A combination of MR images is necessary to fully evaluate the skull base and surrounding structures, including T1, T2, STIR, DWI, and T1-weighted fat-saturated contrast-enhanced images. Early TSBO may demonstrate abnormal signal and enhancement of the EAC, with marked edema and inflammation of the auricular soft tissues. With progression, there is anteromedial spread as described above.

On T1 images, the ill-defined soft-tissue process demonstrates hypo- or isointensity to muscle and causes obliteration of normal fat planes: retromandibular fat, parapharyngeal fat, and retropharyngeal fat in the preclival region. The infiltration consists of inflammation, edema, and phlegmon and produces T2 hyperintensity and heterogeneous enhancement on T1-weighted fat-saturated contrast-enhanced sequences. As noted, the soft-tissue abnormality in the nasopharynx may be the dominant feature and can be indistinguishable from an infiltrative neoplasm (Fig 7*B*, -*C*).

When osteomyelitis affects the bone marrow, there is loss of normal fat signal in the marrow space, causing T1 hypointensity and STIR hyperintensity. The affected marrow demonstrates heterogeneous gadolinium enhancement.[4,7,21] With advanced infection, bone marrow may become necrotic and evolve into an abscess, producing a region of peripherally enhancing tissue.
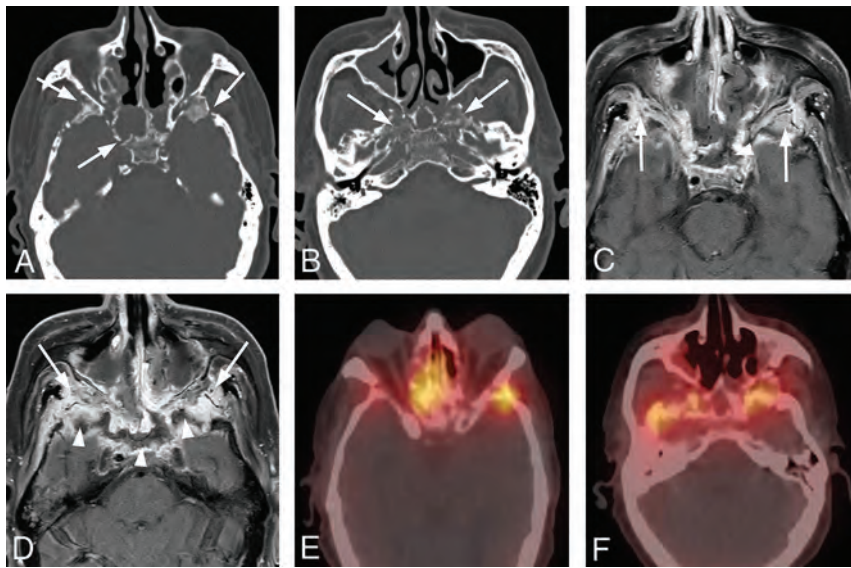
FIG 6. Extensive atypical skull base osteomyelitis secondary to invasive fungal sinusitis (mucormycosis). A 68-year-old man with insulin-dependent diabetes mellitus and a history of chronic sinusitis and previous sinus operations presented with a 6-month history of severe headache, nausea and vomiting, and weight loss. Endoscopic debridement and biopsies were performed. While cultures were negative for fungus, pathologic evaluation of sinus material yielded microscopic evidence of invasive fungal sinusitis consistent with mucormycosis. The patient was treated with micafungin and amphotericin B. A protracted course was complicated by persistent symptoms, and the patient had additional sinonasal debridement at 4 months. Endoscopic culture at that time yielded *P aeruginosa* as a new or potentially coexistent organism, and IV ceftazidime was added to treatment. The patient was followed clinically and with CT/MR imaging until resolution. *A*, Axial unenhanced CT image through the skull base demonstrates diffuse osteolysis and fragmentation of the sphenoid bone, including the walls of the sphenoid sinus and greater wing (*arrows*). There is marked mucosal thickening and opacification of the visualized sinuses. *B*, Axial CT image through the central skull base shows diffuse bone demineralization of the body of the sphenoid bone (*arrows*). *C*, Axial T1-weighted fat-saturated contrast-enhanced image shows abnormal enhancement in the greater wings of the sphenoid bone bilaterally (*arrows*) and confluent opacification of the sinuses. There is evidence of devitalization and necrosis in the upper clivus (*arrowhead*). *D*, Axial T1-weighted fat-saturated contrast-enhanced image shows marked infiltrative signal abnormality and enhancement in the greater wings of the sphenoid bone (*arrows*). There is marrow necrosis and devitalization of the body of the sphenoid bone centrally (*arrowheads*). *E*, Axial fused Tc99m MDP bone scan SPECT image shows marked radiotracer uptake in the greater wing of the sphenoid bone on the left and the anterior midline skull base, consistent with osteomyelitis. *F*, Axial fused Tc99m MDP bone scan SPECT image shows multifocal areas of radiotracer uptake in the sphenoid bone bilaterally.

Mucormycosis infection, in particular, can produce a combination of abnormal enhancement and nonenhancing areas of devitalized soft tissue and bone.[15,21]

Early in TSBO, the volume of marrow space abnormality may be small and attention to detail and use of fat-suppression are necessary to identify subtle involvement of mastoid bone, petrous apex, or occipital bone. Progression of disease can lead to more diffuse involvement of the marrow space and can include the clivus. While most cases will present as unilateral abnormalities, disease can progress to bilateral skull base involvement.

With ASBO, the MR signal abnormalities of the affected soft tissues and the bone marrow will be similar to those in TSBO. The primary difference is that the epicenter of disease will be the sphenoid bone. Paranasal sinus opacification may be conspicuous. The primary marrow signal abnormality will be in the clivus but may also involve the lesser and greater wings of the sphenoid

or petrous apices. The soft-tissue abnormalities will also involve the preclival soft tissues but may be more symmetric, producing diffuse fullness in the nasopharynx. Soft-tissue infiltration of the pterygopalatine fossa with obliteration of normal fat in these regions is typical of invasive sinusitis associated with SBO.

DWI, especially non-EPI DWI, may be of benefit in evaluating SBO. Diffusion restriction in nonenhancing fluid collections can help confirm an abscess. Additionally, ADC values may allow distinction between SBO and neoplasm, with bacterial SBO values shown to be higher than those in nasopharyngeal carcinoma or lymphoma.[17] On postcontrast imaging, focal abscesses could show a peripheral rim of enhancement, whereas a neoplasm would generally demonstrate enhancement within the diffusion-restricting tissue.[29]

CT or MR imaging is not necessarily helpful in long-term monitoring of the disease because radiologic findings lag behind clinical improvement.[1,11,30] Overall, improvement in soft-tissue findings is the best radiologic indicator of early improvement,[11,31] but abnormalities of bone may persist for weeks to months despite a clinical response to treatment.[1,3,5,31]

Nuclear Medicine. Before the advent of CT and MR imaging, nuclear imaging served as a cornerstone for evaluation of SBO.[32] The various radionuclide studies provide functional and metabolic information that can help confirm and localize infection of the skull base and can be complementary to clinical findings and anatomic imaging to monitor treatment response.

Technetium Tc99m methylene diphosphonate (Tc99m MDP) can demonstrate increased osteoblastic bone activity that occurs in response to infection. A 3-phase Tc99m MDP bone scan is more sensitive than CT for early detection of SBO, with sensitivity approaching 100%, including SPECT Tc99m MDP scans, which are reported to be more sensitive and a better prognosticator for patients with malignant external otitis.[33] It typically shows abnormal increased tracer uptake in bone on all 3 phases (ie, immediate blood flow, blood pool [5–10 minutes], and delayed phase [3–4 hours]), whereas isolated soft-tissue infection will be differentiated by a normal delayed phase. If available, delayed-phase SPECT improves anatomic localization. A bone scan, however, lacks specificity for infection because it can demonstrate abnormal bone

Comparison of clinical characteristics of typical versus atypical SBO

	Typical SBO	Atypical SBO
Age	Elderly	Middle-aged
Predisposing factors	DM more common than immunocompromised	DM, immunocompromised
Clinical features	Otorrhea, otalgia (severe, with pain out of proportion to the physical findings), hearing loss	Headache, atypical facial pain, cranial neuropathies, sinonasal symptoms in 25%
Cranial nerve involvement	VII most common	VI, IX, and X more common than VII
Pathogen	*P aeruginosa* in most cases; fungal more common in immunosuppressed patients without diabetes	*S aureus* slightly more common than *P aeruginosa* and fungal
Primary epicenter of disease process	EAC, petrous apex, and clivus	Central skull base, sphenoid bone, or clivus with or without evidence of regional infection of the sinuses, deep face, or oral cavity

Note:—DM indicates diabetes mellitus.

FIG 7. Typical SBO with atypical organisms. A 75-year-old man with diabetes presented with left-ear discharge, conductive hearing loss, and headache. Initial imaging suggested an infiltrative neoplasm of the nasopharynx, and multiple endoscopic biopsies of the nasopharynx were performed to exclude nasopharyngeal carcinoma. Ultimately, biopsies of the external auditory canal revealed an infectious organism, *Aspergillus* species. The patient was treated with amphotericin with gradual resolution of symptoms. *A*, Axial enhanced CT image through the level of the nasopharynx suggests an infiltrative soft-tissue abnormality involving the submucosa and preclival soft tissues of the nasopharynx (*arrow*). *B*, Axial T1-weighted MR image through the nasopharynx shows poorly defined infiltrative soft tissue (*arrowhead*) in the submucosa of the nasopharynx on the left, extending to involve the left carotid space. There is also replacement of normal marrow on the left side of the basiocciput (*arrow*). *C*, Axial enhanced fat-saturated T1 image through the nasopharynx demonstrates abnormal enhancement on the left side of the occipital bone (*arrow*) as well as abnormal enhancing infiltrative tissue (*arrowheads*) in the preclival soft-tissue left carotid space and left retromandibular region. Courtesy of Dr Christine Glastonbury, Professor of Clinical Radiology, Otolaryngology Head and Neck Surgery, and Radiation Oncology, University of California, San Francisco, California.
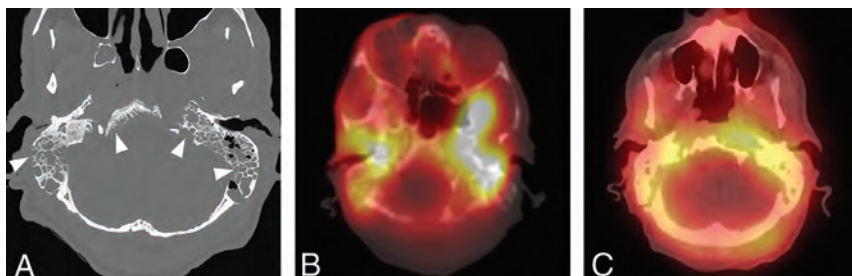
FIG 8. Extensive skull base osteomyelitis. A 70-year-old man with poorly controlled diabetes presented with symptoms of otomastoiditis with associated hearing loss, left facial nerve paralysis, and dysphagia. A culture of the left external auditory canal revealed *Pseudomonas* infection. The patient received aggressive treatment for several months, including IV vancomycin and piperacillin/tazobactam, but he ultimately died from meningitis and aspiration pneumonia. *A*, Axial CT demonstrates multiple focal areas of cortical dehiscence involving the temporal bones bilaterally as well as the clivus (*arrowheads*). The generalized erosion is compatible with diffuse osteomyelitis of the skull base. *B*, Axial fused Tc99m MDP bone scan SPECT image demonstrates significant accumulation of radiotracer in the skull base bilaterally, preferentially affecting the temporal bones. *C*, An axial fused gallium scan SPECT image shows bilateral accumulation of radiotracer in the temporal bones, with some extraosseous accumulation in the left preclival region.

activity in malignancies, trauma, recent surgery, or noninfectious inflammation. Furthermore, in the setting of osteomyelitis, a bone scan can remain abnormal even after satisfactory treatment due to bone healing and remodeling (Fig 8).[1,2,34,35]

A gallium-67 citrate (Ga-67) scan targets acute-phase reactants like lactoferrin and bacterial siderophores and can bind to white blood cells engaged in the immune response to infection. This feature provides high specificity for infection and is complementary to the bone scan (Fig 9). A normal Ga-67 scan, even with an abnormal bone scan, reliably excludes SBO, and increased uptake on a Ga-67 scan confirms infection. A Ga-67 scan plays an important role in monitoring of treatment response, converting to normal findings after successful treatment; persistent increased uptake suggests residual infection. The scan can be repeated to monitor antibiotic response until findings become normal.[6,34] This repetition can be reassuring for the consulting physician and the patient, especially in complicated cases in which the diagnosis was delayed or in doubt. The major limitation of a Ga-67 scan is the long scan time requiring delayed images up to 48–72 hours.

A technetium-labeled white blood cell scan is less commonly used but like Ga-67, it has a high specificity for SBO in the initial diagnosis. A tagged white blood cell study can be used for confirming healing at the end of antibiotic therapy.[1,11,36]

Overall, the literature has variable data regarding the overall diagnostic value of nuclear medicine
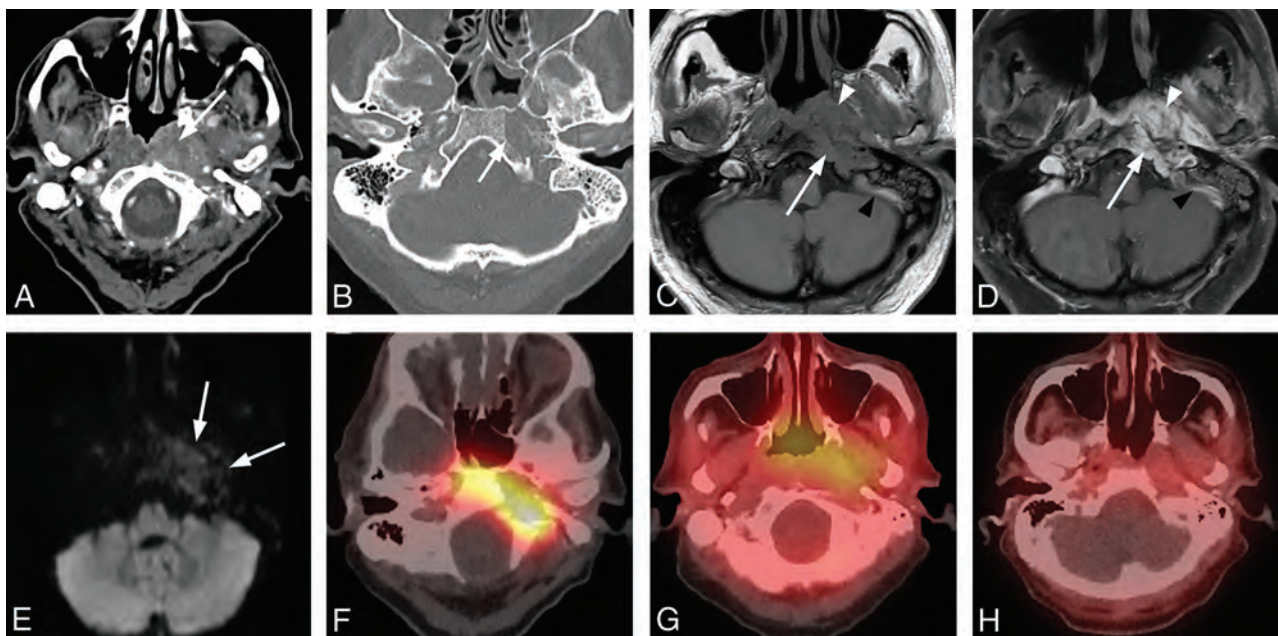
FIG 9. Typical skull base osteomyelitis. A 63-year-old man with diabetes presented to an outside hospital with a several-month history of left ear pain. He was initially diagnosed with otitis media and treated with several rounds of antibiotics. A recent evaluation at an outside hospital suggested the presence of a nasopharyngeal mass with skull base invasion. Two separate biopsies of the nasopharynx failed to demonstrate nasopharyngeal carcinoma. While a discrete organism was not cultured, the patient was presumptively treated with levofloxacin and clindamycin with gradual improvement and resolution of all symptoms. He was monitored using serial CT, MR imaging, and gallium scans. *A*, Axial postcontrast CT of the soft tissue of the neck at the level of the nasopharynx demonstrates a heterogeneously enhancing soft-tissue lesion involving the submucosal region of the left nasopharynx (*arrow*). The process extends laterally to the left carotid space, and there is occlusion or thrombosis of the left internal jugular vein. *B*, Axial postcontrast CT scan through the skull base with bone windows demonstrates focal cortical erosion along the margins of the foramen lacerum (*arrow*), consistent with osteomyelitis. *C*, Axial TI-weighted MR image through the skull base shows an infiltrative process involving the left side of the clivus (*arrow*) and adjacent preclival tissues of the left nasopharynx. The lesion appears masslike on the left (*arrowhead*). The infiltrative process extends posterolaterally on the left to the jugular foramen. Partial thrombosis of the jugular bulb and sigmoid sinus is identified (*black arrowhead*). *D*, Axial enhanced TI-weighted MR image through the skull base shows an enhancing infiltrative process involving the left side of the clivus (*arrow*) and adjacent preclival tissues of the left nasopharynx (*arrowhead*). The process extends posterolaterally on the left to the jugular foramen. Partial thrombosis of the jugular bulb and sigmoid sinus is identified (*black arrowhead*). *E*, Axial DWI shows no diffusion restriction in the nasopharyngeal soft tissue, favoring a non-neoplastic process over lymphoma or nasopharyngeal carcinoma. *F*, Axial fused Tc99m MDP bone scan SPECT image shows localized accumulation of radiotracer in the left skull base, compatible with osteomyelitis. *G*, An axial fused gallium scan SPECT image at the level of the nasopharynx shows mild uptake in the soft tissues of the nasopharynx. *H*, A follow-up fused gallium scan SPECT image at the level of the nasopharynx demonstrates resolution of previously seen uptake in the nasopharyngeal soft tissues, favoring a treatment response.

studies.[37] A recent review of malignant otitis externa literature revealed pooled sensitivities for technetium-99 and gallium-67 of 85.1% and 71.2%, respectively, with poor specificity; however, the data were deemed insufficient for a meta-analysis. The authors, therefore, advised against the routine use of these studies in SBO management in patients with a known diagnosis on conventional imaging. However, these examinations were considered to be reasonably sensitive tests in patients with an unclear diagnosis despite an otomicroscopic examination or other imaging studies.[37] The authors also concluded that there were insufficient data to determine the usefulness of these modalities during follow-up and that larger prospective studies would be necessary.

[18F] FDG- PET detects increased glucose metabolism. FDG is nonspecific and accumulates at sites of high glucose demand, including active infection, but also in postoperative, inflammatory, or neoplastic tissue. The advantages of FDG-PET/CT over other nuclear studies are wider clinical availability, shorter imaging time, and higher spatial resolution. It can be complementary to determine the extent of infection in confirmed cases of SBO and

for evaluation of treatment response. In a recent study comparing the diagnostic performance of [18F] FDG-PET/CT with MR imaging, both modalities had comparable sensitivities (87.5 versus 81.25%, respectively), but PET-CT had better specificity (71.0% versus 28.5%, respectively) in identifying infection. The sensitivity, specificity, positive predictive value, negative predictive value, and accuracy of FDG-PET/CT in detecting SBO were 96.7%, 93.3%, 98.3%, 87.5%, and 96.1%, respectively.[38] With wider availability of hybrid PET-MR imaging scanners with superior soft-tissue detail and metabolic information in a single imaging session, PET-MR can be used to follow patients with SBO.[6,38,39] PET-MR imaging with gadolinium in combination with high-resolution CT is an excellent approach for suspected new SBO, and a combination of FDG-PET with either MR imaging or CT may provide sufficient follow-up (Fig 10).[6]

Differential Considerations. The primary diagnostic dilemma for SBO arises from neoplastic processes because they can also infiltrate the skull base and the adjacent soft tissues. Carcinoma of the EAC can have similar clinical and radiologic features to
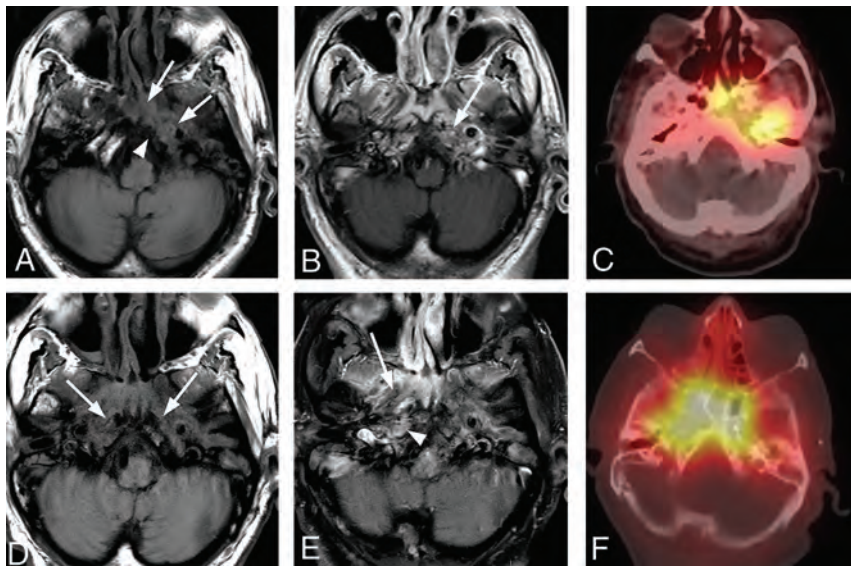
FIG 10. Progressive left-sided skull base osteomyelitis. A 65-year-old man with multiple comorbidities, including poorly controlled diabetes, presented with a relatively long-standing history of chronic sinusitis and bilateral otitis media. He was recently treated for otitis media of the left ear and presented with new headache and left-sided hearing loss. Culture from the left EAC was negative for a causative organism, and cultures from the sphenoid sinus demonstrated methicillin-resistant *S aureus*. The patient was treated with 4 weeks of IV vancomycin and piperacillin/tazobactam. The patient improved, and a gallium scan performed during follow-up showed significant improvement and only mild residual uptake in the skull base. Antibiotics were discontinued. The patient returned 4 weeks later with sepsis, and blood cultures were positive for *Klebsiella* species. In the next 3 months, the patient had a return of headaches and new right-sided symptoms. Imaging evaluation demonstrated progressive infection of the right skull base. Re-institution of IV antibiotics led to gradual resolution of clinical and imaging findings. *A*, Axial T1-weighted MRI through the skull base shows an infiltrative soft-tissue abnormality (*arrows*) involving the central skull base with abnormal marrow signal on the left side of the occipital bone (*arrowhead*). *B*, Axial enhanced T1-weighted MR image shows heterogeneous enhancement in the corresponding areas of the left petro-occipital fissure (*arrow*). *C*, Axial bone scan fused with CT shows radiotracer accumulation in the left central skull base, including the sphenoid bone and left petrous apex. *D*, Following initiation of empiric IV antibiotic treatment, the patient had improvement of symptoms on the left, but 4 months later, he developed severe headache, fever, and right-sided facial pain. Axial T1-weighted image shows an infiltrative process (*arrows*) of the central skull base that now extends to the right. *E*, Axial enhanced fat-saturated T1-weighted image demonstrates improved enhancement of the left central skull base and the adjacent soft tissues but interval worsening of enhancement of the right skull base (*arrowhead*) and soft tissues of the nasopharynx (*arrow*). *F*, Follow-up axial fused bone scan SPECT image demonstrates radiologic worsening with marked radiotracer uptake in the central skull base in the right petro-occipital region.

secondarily invades the bone. While the osseous skull base may have significant derangement due to invasion and destruction, the primary lesion presents on cross-sectional imaging as nodular or masslike enhancement in the extraosseous soft tissues. As opposed to SBO, malignant neoplasms typically displace or replace normal anatomy without preservation of tissue planes. Enhancement and fullness without destruction of fascial planes may support a diagnosis of SBO over tumor.[29,40] Additionally, at presentation, MR imaging has been reported to show greater disease involvement compared with CT in central SBO, whereas malignancy generally shows equal involvement; and combining the CT and MR imaging information can help differentiate between central SBO and malignancy.[40] With high-resolution imaging, especially T1-weighted contrast-enhanced fat-saturated MR imaging, the margins of the tumor can be reasonably mapped and measured. If a lesion involving the skull base has a dominant, solidly enhancing soft-tissue component that correlates with a clinically obvious mass involving the skin or mucosa, neoplasm is strongly favored over infection. In these cases, biopsy of the apparent lesion is indicated as initial management. In situations in which a primary lesion is not clinically apparent, imaging can help direct a potential biopsy of suspected viable tumor by identifying localized extraosseous soft-tissue enhancement.[29]

The dilemma is made more difficult in the setting of a small or occult

those of TSBO and, therefore, needs to be excluded. Other neoplasms to consider are metastatic disease, nasopharyngeal carcinoma, sinonasal neoplasm, and lymphoma.[3]

Neoplasms that affect the skull base may arise locally from various sources that are amenable to clinical evaluation. For example, a primary skin lesion such as EAC squamous cell carcinoma or a primary mucosal lesion such as nasopharyngeal carcinoma may have a dominant, clinically obvious primary soft-tissue mass that heavily influences image interpretation and preliminary management decisions. Other neoplasms of the skull base such as lymphoma, myeloma, or metastatic disease may be accompanied by pertinent clinical history and other extracranial findings to indicate underlying systemic metastatic or multifocal disease and would typically present with more bulky lesions than ill-defined skull base pathologies.

Most primary forms of local invasive neoplasms that affect the skull base have a dominant soft-tissue mass or nodule that

primary tumor, deep subcutaneous or submucosal invasion, or tumor with significant ulceration or necrosis. In these cases, a dominant soft-tissue nodule or mass may be lacking both clinically and radiologically. This situation occasionally occurs in the setting of nasopharyngeal carcinoma or adenoid cystic carcinoma that affects the central skull base. In such circumstances, the radiologic picture may be dominated by osseous demineralization on CT and abnormal marrow space signal and enhancement on MR imaging. In these cases, infiltrating tumor can be difficult to distinguish from SBO. In addition, focal soft-tissue infection associated with SBO can produce phlegmon, occasionally taking on masslike qualities of soft-tissue fullness, mass effect, and enhancement.

The decision to biopsy tissue is based on multidisciplinary consultation. Surface mucosal or submucosal disease can be biopsied through endoscopic approaches by ear, nose and throat surgeons, whereas more deep-seated disease may require image-

guided biopsies. Radiologic findings can provide specific clues in cases in which there have been repeat biopsies negative for malignancy. Alternate biopsy targets can be suggested on the basis of the imaging appearance to plan surgical approaches to the pterygopalatine fossa or orbital apex for biopsy and tissue analysis.[23] Often during the course of the disease, these cases will need a multidisciplinary approach, with consultations among the referring clinician, surgeons, infectious disease specialists, and radiologists at different steps.[23]

Neoplasms that are intrinsic to the skull base such as chordoma or chondrosarcoma can be considered invasive or infiltrative, but they tend to be slow-growing, focally expansile, and relatively well-circumscribed. Tumor grows beyond the margins of the bone into adjacent soft tissues, but there is not typically an inflammatory response.

Rare differential considerations would include non-neoplastic diseases, including granulomatosis with polyangiitis and other granulomatous diseases (eg, tuberculosis, sarcoidosis).[3] Idiopathic skull base inflammation (inflammatory pseudotumor), an idiopathic noninfectious inflammatory condition, may primarily involve the skull base or extend from the orbit and can appear identical to SBO.[41] Immunoglobulin G4 (IgG4)-related disease can affect almost any organ, most commonly the submandibular, lacrimal, or parotid glands, but it can also involve the skull base. IgG4-related disease typically shows increased IgG-4-positive plasma cells on tissue sampling, and elevated serum IgG4 concentrations are also seen.[42] An elevated IgG4/IgG ratio of >0.4 was detected in 40% of cases in a study of inflammatory pseudotumor and helped to distinguish them from SBO in some instances because none of the SBO cases had a ratio of >0.4.[43] Ultimately, radiologic findings alone are insufficient to differentiate these inflammatory entities from SBO and malignancy. These entities often are suspected in the absence of a mass or signs of infection, but endoscopic biopsy/tissue sampling will be needed for diagnosis.[23,43]

Primary bone conditions of the skull base, including fibrous dysplasia and Paget disease, can be in the differential for SBO on MR imaging; however, CT would show their typical appearances with bony expansion and no associated soft-tissue abnormality. Ground glass opacification with variable lytic foci would be seen in fibrous dysplasia and osseous expansion with a lytic lesion (osteoporosis circumscripta) or mixed lytic-sclerotic foci having a cotton wool appearance as seen in Paget disease.[3]

Management/Treatment. TSBO often has a classic presentation and is not difficult to diagnose, whereas ASBO is often a diagnostic dilemma due to the nonspecific initial presentation. For any infiltrative/destructive process of the central skull base, neoplastic processes including nasopharyngeal carcinoma, lymphoma, or leukemia need to be ruled out first with other aforementioned inflammatory or noninflammatory conditions also considered. Skull base or nasopharyngeal biopsies need to be performed in a timely manner to rule out these differential possibilities as well as to obtain tissue samples due to the potential for rapid progression of SBO.[11,18] Tissue samples should undergo microbial analysis with culture and flow cytometry for lymphoma in addition to pathologic analysis, especially if the clinical suspicion is high and no obvious soft-tissue lesions are seen.[1,5] Pathogen-specific

antibiotic therapy including IV antibiotics followed by long-term oral antibiotics would be the mainstay of treatment, currently recommended for 6–20 weeks,[2,18,44] with wide variations in the duration of treatment observed in a survey-based study of otolaryngologists in the United Kingdom.[45] Initially however, broad-spectrum antimicrobials, including coverage for *P aeruginosa* and methicillin-resistant *Staphylococcus aureus* particularly for non-otologic causes, are recommended to cover the possibility of polymicrobial infection in ASBO before culture and sensitivity information is available.[18] Antipseudomonal antibiotics, such as carbapenems and third-generation cephalosporins, with ciprofloxacin in the long term, are considered an alternative to single initial therapy with ciprofloxacin in view of growing ciprofloxacin resistance in the intensive care setting, including in culture-negative cases, in which the antibiotic choice can be difficult.[1,18,24] Surgical debridement of necrotic bone and soft tissue, especially for fungal disease, may be required in advanced cases with drainage of involved air cells or sinuses and of abscesses to also help improve antimicrobial penetration. However, an early and aggressive surgical approach has also been found to be beneficial and is recommended by some authors, especially in patients with prolonged ear infections and at the first signs of cranial neuropathy.[18] Hyperbaric oxygen therapy has also been suggested as an ancillary treatment but has not shown an impact on survival.[1,2]

Summary

Diagnosis of SBO, clinically and radiologically, requires a high index of suspicion, and a delay in diagnosis is common. It should be considered in the differential consideration for any infiltrative skull base process, particularly if biopsies are negative for malignancy. Thin section, high-resolution bone CT of the skull base would be necessary to identify early cortical erosion followed by multiplanar pre- and postcontrast MR imaging to identify marrow space involvement. Nuclear medicine imaging studies can play an important role in difficult-to-diagnose cases and in follow-up. Long-term antibiotics with surgical debridement in advanced cases are the mainstay of management.

REFERENCES

1. Carfrae MJ, Kesser BW. **Malignant otitis externa.** *Otolaryngol Clin North Am* 2008;41:537–49 CrossRef Medline
2. Johnson AK, Batra PS. **Central skull base osteomyelitis: an emerging clinical entity.** *Laryngoscope* 2014;124:1083–87 CrossRef Medline
3. Chang PC, Fischbein NJ, Holliday RA. **Central skull base osteomyelitis in patients without otitis externa: imaging findings.** *AJNR Am J Neuroradiol* 2003;24:1310–16 Medline
4. Borges A. **Imaging of the central skull base.** *Neuroimaging Clin N Am* 2009;19:669–96 CrossRef Medline

5. Clark MP, Pretorius PM, Byren I, et al. **Central or atypical skull base osteomyelitis: diagnosis and treatment.** *Skull Base* 2009;19:247–54 CrossRef Medline

6. van Kroonenburgh A, van der Meer WL, Bothof RJ, et al. **Advanced imaging techniques in skull base osteomyelitis due to malignant otitis externa.** *Curr Radiol Rep* 2018;6:3 CrossRef Medline

7. Bag AK, Chapman PR. **Neuroimaging: intrinsic lesions of the central skull base region.** *Semin Ultrasound CT MR* 2013;34:412–35 CrossRef Medline

8. Prasad SC, Prasad KC, Kumar A, et al. **Osteomyelitis of the temporal bone: terminology, diagnosis, and management.** *J Neurol Surg B Skull Base* 2014;75:324–31 CrossRef Medline

9. Chen JC, Yeh CF, Shiao AS, et al. **Temporal bone osteomyelitis: the relationship with malignant otitis externa, the diagnostic dilemma, and changing trends.** *ScientificWorldJournal* 2014;2014:591714 CrossRef Medline

10. Ducic Y. **Skull base osteomyelitis.** *South Med J* 2006;99:1051 CrossRef Medline

11. Adams A, Offiah C. **Central skull base osteomyelitis as a complication of necrotizing otitis externa: imaging findings, complications, and challenges of diagnosis.** *Clin Radiol* 2012;67:e7–16 CrossRef Medline

12. Holder CD, Gurucharri M, Bartels LJ, et al. **Malignant external otitis with optic neuritis.** *Laryngoscope* 1986;96:1021–23 Medline

13. Huang KL, Lu CS. **Skull base osteomyelitis presenting as Villaret's syndrome.** *Acta Neurol Taiwan* 2006;15:255–58 Medline

14. Rubin Grandis J, Branstetter BF, Yu VL. **The changing face of malignant (necrotising) external otitis: clinical, radiological, and anatomic correlations.** *Lancet Infect Dis* 2004;4:34–39 CrossRef Medline

15. Chan LL, Singh S, Jones D, et al. **Imaging of mucormycosis skull base osteomyelitis.** *AJNR Am J Neuroradiol* 2000;21:828–31 Medline

16. Chandler JR, Grobman L, Quencer R, et al. **Osteomyelitis of the base of the skull.** *Laryngoscope* 1986;96:245–51 CrossRef Medline

17. Ozgen B, Oguz KK, Cila A. **Diffusion MR imaging features of skull base osteomyelitis compared with skull base malignancy.** *AJNR Am J Neuroradiol* 2011;32:179–84 CrossRef Medline

18. Ridder GJ, Breunig C, Kaminsky J, et al. **Central skull base osteomyelitis: new insights and implications for diagnosis and treatment.** *Eur Arch Otorhinolaryngol* 2015;272:1269–76 CrossRef Medline

19. Singh A, Al Khabori M, Hyder MJ. **Skull base osteomyelitis: diagnostic and therapeutic challenges in atypical presentation.** *Otolaryngol Head Neck Surg* 2005;133:121–25 CrossRef Medline

20. Kwon BJ, Han MH, Oh SH, et al. **MRI findings and spreading patterns of necrotizing external otitis: is a poor outcome predictable?** *Clin Radiol* 2006;61:495–504 CrossRef Medline

21. Alleyne CH, Jr, Vishteh AG, Spetzler RF, et al. **Long-term survival of a patient with invasive cranial base rhinocerebral mucormycosis treated with combined endovascular, surgical, and medical therapies: case report.** *Neurosurgery* 1999;45:1461–63; discussion 1463–64 CrossRef Medline

22. Djalilian HR, Shamloo B, Thakkar KH, et al. **Treatment of culture-negative skull base osteomyelitis.** *Otol Neurotol* 2006;27:250–55 CrossRef Medline

23. See A, Tan TY, Gan EC. **Atypical culture-negative skull base osteomyelitis masquerading as advanced nasopharyngeal carcinoma.** *Am J Otolaryngol* 2016;37:236–39 CrossRef Medline

24. Loh S, Loh WS. **Malignant otitis externa: an Asian perspective on treatment outcomes and prognostic factors.** *Otolaryngol Head Neck Surg* 2013;148:991–96 CrossRef Medline

25. Spielmann PM, Yu R, Neeff M. **Skull base osteomyelitis: current microbiology and management.** *J Laryngol Otol* 2013;127(Suppl 1):S8–12 CrossRef Medline

26. Mahdyoun P, Pulcini C, Gahide I, et al. **Necrotizing otitis externa: a systematic review.** *Otol Neurotol* 2013;34:620–29 CrossRef Medline

27. Le Clerc N, Verillaud B, Duet M, et al. **Skull base osteomyelitis: incidence of resistance, morbidity, and treatment strategy.** *Laryngoscope* 2014;124:2013–16 CrossRef Medline

28. Sokołowski J, Lachowska M, Karchier E, et al. **Skull base osteomyelitis: factors implicating clinical outcome.** *Acta Neurol Belg* 2019;119:431–37 CrossRef Medline

29. Jain N, Jasper A, Vanjare HA, et al. **The role of imaging in skull base osteomyelitis: reviewed.** *Clin Imaging* 2020;67:62–67 CrossRef Medline

30. Rothholtz VS, Lee AD, Shamloo B, et al. **Skull base osteomyelitis: the effect of comorbid disease on hospitalization.** *Laryngoscope* 2008;118:1917–24 CrossRef Medline

31. Rubin J, Curtin HD, Yu VL, et al. **Malignant external otitis: utility of CT in diagnosis and follow-up.** *Radiology* 1990;174:391–94 CrossRef Medline

32. Mendelson DS, Som PM, Mendelson MH, et al. **Malignant external otitis: the role of computed tomography and radionuclides in evaluation.** *Radiology* 1983;149:745–49 CrossRef Medline

33. Balakrishnan R, Dalakoti P, Nayak DR, et al. **Efficacy of HRCT imaging vs SPECT/CT scans in the staging of malignant external otitis.** *Otolaryngol Head Neck Surg* 2019;161:336–42 CrossRef Medline

34. Chakraborty D, Bhattacharya A, Gupta AK, et al. **Skull base osteomyelitis in otitis externa: the utility of triphasic and single photon emission computed tomography/computed tomography bone scintigraphy.** *Indian J Nucl Med* 2013;28:65–69 CrossRef Medline

35. Strashun AM, Nejatheim M, Goldsmith SJ. **Malignant external otitis: early scintigraphic detection.** *Radiology* 1984;150:541–45 CrossRef Medline

36. Rozenblum-Beddok L, Verillaud B, Paycha F, et al. **(99m)Tc-HMPAO-leukocyte scintigraphy for diagnosis and therapy monitoring of skull base osteomyelitis.** *Laryngoscope Investig Otolaryngol* 2018;3:218–24 CrossRef Medline

37. Moss WJ, Finegersh A, Narayanan A, et al. **Meta-analysis does not support routine traditional nuclear medicine studies for malignant otitis.** *Laryngoscope* 2020;130:1812–16 CrossRef Medline

38. Kulkarni SC, Padma S, Shanmuga Sundaram P. **In the evaluation of patients with skull base osteomyelitis, does 18F-FDG PET CT have a role?** *Nucl Med Commun* 2020;41:550–59 CrossRef Medline

39. Louarn N, Alias Q, Aupin L, et al. **A rare presentation of skull-base osteomyelitis with neurovascular sheath extension following external otitis resolved by PET/MRI.** *Eur J Nucl Med Mol Imaging* 2018;45:2025 CrossRef Medline

40. Lesser FD, Derbyshire SG, Lewis-Jones H. **Can computed tomography and magnetic resonance imaging differentiate between malignant pathology and osteomyelitis in the central skull base?** *J Laryngol Otol* 2015;129:852–59 CrossRef Medline

41. Lee EJ, Jung SL, Kim BS, et al. **MR imaging of orbital inflammatory pseudotumors with extraorbital extension.** *Korean J Radiol* 2005;6:82–88 CrossRef Medline

42. Yim CD, An HJ, Ahn SK, et al. **IgG4-related disease presenting as otogenic skull base osteomyelitis.** *Auris Nasus Larynx* 2020 Feb 25. [Epub ahead of print] CrossRef Medline

43. Ryu G, Cho HJ, Lee KE, et al. **Clinical significance of IgG4 in sinonasal and skull base inflammatory pseudotumor.** *Eur Arch Otorhinolaryngol* 2019;276:2465–73 CrossRef Medline

44. Hsiao YC, Lee JC, Kang BH, et al. **Idiopathic osteomyelitis at the base of the skull.** *South Med J* 2006;99:1121–23 CrossRef Medline

45. Chawdhary G, Pankhania M, Douglas S, et al. **Current management of necrotising otitis externa in the UK: survey of 221 UK otolaryngologists.** *Acta Otolaryngol* 2017;137:818–22 CrossRef Medline

Anatomic and Embryologic Analysis of the Dural Branches of the Ophthalmic Artery

S. Bonasia, S. Smajda, G. Ciccio, and T. Robert

ABSTRACT

SUMMARY: The ophthalmic artery has one of the most fascinating embryologic developments among the craniofacial arteries. Most of the ophthalmic artery orbital branches develop from the formation and regression of the stapedial artery and share their origin with dural branches of the ophthalmic artery. The concomitant embryologic development of the ophthalmic artery and middle meningeal artery explains adequately the important varieties of anastomosis between these 2 arteries. It also explains the presence of many dural branches from the ophthalmic artery. In this review, we focused on dural branches of the ophthalmic artery with the description of rare variations possible, in particular the ophthalmic artery origin of the middle meningeal artery and the ophthalmic artery origin of the marginal tentorial artery.

ABBREVIATIONS: dAVF = dural arteriovenous fistula; ECA = external carotid artery; MMA = middle meningeal artery; MTA = marginal tentorial artery; OA = ophthalmic artery; PDOA = primitive dorsal ophthalmic artery; PVOA = primitive ventral ophthalmic artery; SA = stapedial artery

The ophthalmic artery (OA) is a very fascinating artery for its complex embryologic development and also for numerous vascular anastomoses developed with branches of the external carotid artery (ECA). The role of the OA in supplying the dura is not well-known, but the understanding of the dural function of the OA and also of its possible variations is a cornerstone for surgical and endovascular treatment of dural pathologies (dural arteriovenous fistulas (dAVFs), skull base meningiomas, chronic subdural hematoma embolization). In this review, we will focus on the dural branches of the OA with rare variations, in particular the OA origin of the middle meningeal artery (MMA) and the OA origin of the marginal tentorial artery (MTA). All procedures performed in the studies involving human participants were in accordance with the ethical standards of the institutional and/or national research committee and with the 1964 Helsinki Declaration and its later amendments or comparable ethical standards.

Informed consent was obtained from all individual participants included in the study.

History

Meyer,[1] in 1887, considered a pioneer in the orbital vascular anatomy, was the first to precisely describe all branches of the ophthalmic artery, including its dural territory. A few years before, Curnow,[2] in 1873, had already described 3 cadaveric cases of variations in the origin of the OA. One of these 3 cases was the first description of an OA origin of the MMA. With the advent of the DSA, Kuru,[3] in 1967, gave a detailed description of the OA meningeal branches, and after him, a few authors[4-10] focused on the variants of the OA and the MMA. Lasjaunias et al[8,9,11] gave their crucial contribution to the comprehension of the orbital and meningeal vascular supply, combining their knowledge of the embryology with an accurate angiographic analysis. The last author to give a comprehensive description of dural vascularization was Rhoton,[12] in 2002, based on a large cadaveric dissection experience.

Embryology. The OA starts its development when the embryo is about 4 mm and reaches its adult configuration at about 40 mm. Its development is strictly connected with the arterial embryology of the primitive ICA, the stapedial artery (SA), and the pharyngeal artery system. In the past, 2 authors were interested in the comprehension of the complex events of the OA formation: Padget,[13] who formulated her theory after the dissection of 22 embryos, and Lasjaunias et al,[11] who added to Padget's

FIG 1. Theories of Padget and Lasjauinias et al about OA origin migration. When the embryo is about 18 mm, the OA reaches its definitive origin on the supraclinoid ICA. This phenomenon is explained by Padget[13] by the cranial elongation of the ICA during this stage with the consequent movement of the PDOA origin (*black arrows* in *A*). On the other hand, Lasjaunias et al[11] hypothesized the presence of an intradural anastomosis between the PVOA and the primitive ICA (*black arrow* in *B*) in correspondence with the future origin with successive regression of the original stem. HA indicates hyaloid artery; M×M, maxillo-mandibulary artery; SOrbA, supraorbital artery.

knowledge an accurate angiographic evaluation. These authors agreed that the definitive features of the OA depend mostly on 2 embryonic arteries, the primitive dorsal ophthalmic artery (PDOA) and the primitive ventral ophthalmic artery (PVOA).

According to Padget's theory,[13] the embryologic development of the OA could be divided into 6 stages, which are summarized in the Online Supplemental Data. The PDOA appears when the embryo is about 4–5 mm (stage 1), originating from the bifurcation of the primitive internal carotid artery. In the following stage 2 (9-mm embryos), while the PDOA enlarges through the optic cup as plexiform channels, the PVOA arises from the cranial division of the primitive ICA. The PDOA and PVOA are then destined to elongate following the ventral shifting of the optic cup and the dorsal shifting of the cerebral hemispheres. In embryos of 14–17 mm, one can note the appearance of 2 branches from the PDOA artery: the primitive hyaloid artery and the common temporal ciliary artery (future lateral posterior ciliary artery). The PVOA gives off, at the same time, the common nasal ciliary artery (future medial posterior ciliary artery).

In the embryo of about 18 mm (stage 3), the OA undergoes a process that will cause migration of its origin on the supraclinoid ICA. This phenomenon is explained by Padget by the cranial elongation of the ICA during this stage with the consequent movement of the PDOA. On the other hand, Lasjaunias et al[9,11,14] explained this migration by the presence of an intradural anastomosis between the PVOA and the primitive carotid artery in correspondence of the future origin, with consequent regression of the original stem. The 2 theories of OA origin migration are illustrated in Fig 1.

From stage 1 to 4, another artery grows at the same time and contributes to the adult configuration of the orbital arteries: the SA. In the first stages, the optic cup is supplied on its ventral side by the primitive maxillary artery. However, it starts to regress at the end of stage 2, to be substituted by the SA in its orbital territory. This latter gives off 2 branches that follow the 3 divisions of the trigeminal nerve: the maxillomandibular artery and the

supraorbital artery. The supraorbital artery enters the orbit through the superior orbital fissure and gives off 2 branches: the ethmoid nasal and the lacrimal artery.

The relationship among the PDOA, the PVOA, and the SA is most important in the last 2 stages (stage 5: embryo of 20 mm; stage 6: embryo of 40 mm). During stage 5, an anastomotic ring appears around the optic nerve, formed by the anastomosis among the PVOA, the PDOA, and the supraorbital artery (through the ethmoid nasal artery). However, in stage 6, this ring is ventrally interrupted to give the definitive configuration of the OA. The part of the anastomotic ring that regresses is crucial to determine which of the 2 primitive OAs persists to form the adult OA. According to Padget,[13] it is the PDOA that persists, with consequent PVOA proximal regression. On the other hand, Lasjaunias et al[9,11,14] wrote that the distal portion of the PDOA regresses and its proximal part is destined to form the future inferolateral trunk. Thus, their opinion is that the PVOA mostly contributes to the formation of the definitive OA.

At the same time, the extraorbital part of the supraorbital artery regresses to let the lacrimal artery to be annexed by the OA.

Dural Branches of the OA
Different dural branches of the OA and their possible anastomoses with other dural arteries are listed in Table 1; their respective dural territories are illustrated in Fig 2.

Deep Recurrent Ophthalmic Artery. The deep recurrent ophthalmic artery arises from the first segment of the OA and has a recurrent course through the medial part of the superior orbital fissure. This artery supplies the dura of the lateral wall of the cavernous sinus. It consistently anastomoses with the anteromedial branch of the inferolateral trunk and often with the cavernous branch of the middle meningeal artery and with the accessory meningeal artery. It is considered as a remnant of the primitive dorsal ophthalmic artery.[9]

Superficial Recurrent Ophthalmic Artery. The superficial recurrent ophthalmic artery is a meningeal branch that takes its origin from the proximal part of the lacrimal artery or directly from the second segment of the OA.[9,11,15] This artery passes through the lateral part of the superior orbital fissure to reach the dura over the anterior clinoid process and the cavernous sinus roof.[3,16] The superficial recurrent ophthalmic artery also supplies the intradural part of the third and fourth cranial nerves. This artery is the orbital remnant of the supraorbital branch of the stapedial artery.[11]

Posterior Ethmoidal Artery. The posterior ethmoidal artery is a small meningeal branch that originates from the third segment of the OA, which exits the orbit through the posterior ethmoidal

Table 1: Different dural branches of the OA with their respective supply and anastomoses

OA Branches	Origin from the OA	Foramen	Dural Territory	Possible Anastomosis	Clinical Consequences in Case of Embolism
Deep recurrent OA	First segment	Superior orbital fissure	Superior orbital fissure (lateral part), sphenoid wing	Inferolateral trunk (ICA)	Cerebrovascular accident
Superficial recurrent OA	Second segment	Superior orbital fissure	Anterior clinoid process Lesser sphenoid wing Middle fossa (anteromedial portion)	Posterior ethmoidal artery MMA (anterior division) Medial tentorial artery (ICA)	Cerebrovascular accident, loss of vision
Anterior ethmoidal artery	Third segment	Anterior ethmoidal canal	Anterior convexity (anterior meningeal artery) Anterior cranial fossa (medial third) Anterior falx cerebri (anterior falcine artery)	Contralateral anterior ethmoidal artery Bilateral MMAs Posterior ethmoidal artery Olfactory branch (ACA)	
Posterior ethmoidal artery	Third segment	Posterior ethmoidal canal	Anterior cranial fossa (medial third) Anterior clinoid process Chiasmatic groove	Contralateral posterior ethmoidal artery Anterior ethmoidal artery MMA (anterior division)	

Note:—ACA indicates anterior cerebral artery.
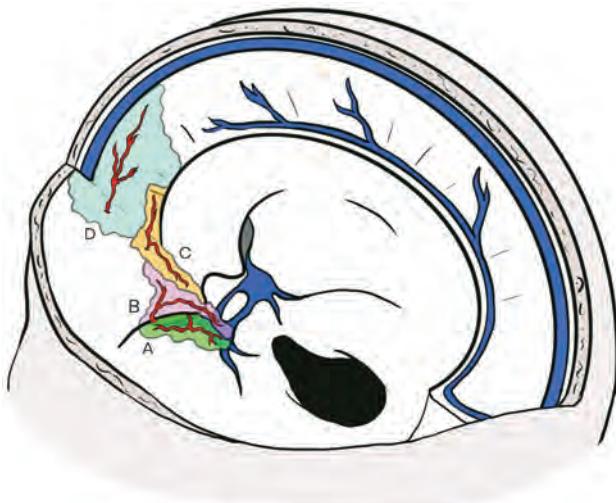
FIG 2. Dural territories of OA branches. *A*, Territory of the deep recurrent ophthalmic artery (green), which exits from the medial part of the superior orbital fissure and supplies the dura of the lateral wall of the cavernous sinus. *B*, Dural territory of the superficial recurrent ophthalmic artery (pink), which passes through the lateral part of the superior orbital fissure to reach the dura over the anterior clinoid process and the cavernous sinus roof. *C*, The posterior ethmoidal artery (orange) passes through the posterior ethmoidal canal to reach the dura of the planum sphenoidale, the posterior cribriform plate, and the anterior clinoid process. *D*, The anterior ethmoidal artery (light blue) passes through the anterior ethmoidal canal, and its meningeal territory consists of the anterior part of the cribriform plate, the medial part of the orbital roof, and the anterior third of the falx cerebri.

canal.[15] Its average diameter is 0.4 mm, and it is usually in balance with the diameter of the anterior ethmoidal artery.[17] This artery supplies the dura of the planum sphenoidale, the posterior cribriform plate, and the anterior clinoid process.[11] Martins et al,[16] in 2005, showed that the posterior ethmoidal artery often anastomoses with dural branches of the internal carotid artery, middle meningeal artery, and anterior ethmoidal artery. When absent (approximately 20%), its meningeal territory is taken over by these 3 other arteries.[16]

Anterior Ethmoidal Artery. The anterior ethmoidal artery is a more constant artery, which has been found in >90% of the orbits if the OA crosses over the optic nerve, and in 80% of cases when the OA crosses under the nerve. It originates from the distal part of the OA and could give off from 1 to 5 little branches that pass through the anterior ethmoidal canal. Other than the nasal septum and nasal fossa, its meningeal territory is limited to the anterior part of the cribriform plate, the medial part of the orbital roof, and the anterior third of the falx cerebri. The anterior ethmoidal artery gives off a branch, well-described angiographically by Kuru,[3] in 1967, along the falx cerebri, called the anterior falcine artery or the artery of the falx cerebri. This anterior falcine artery could be present bilaterally, but usually 1 side is predominant. If the anterior ethmoidal artery is well-developed, it can give off some branches called "anterior meningeal arteries," that differ from the anterior falcine artery because of their paramedial course and can supply the dura of the anterior convexity.
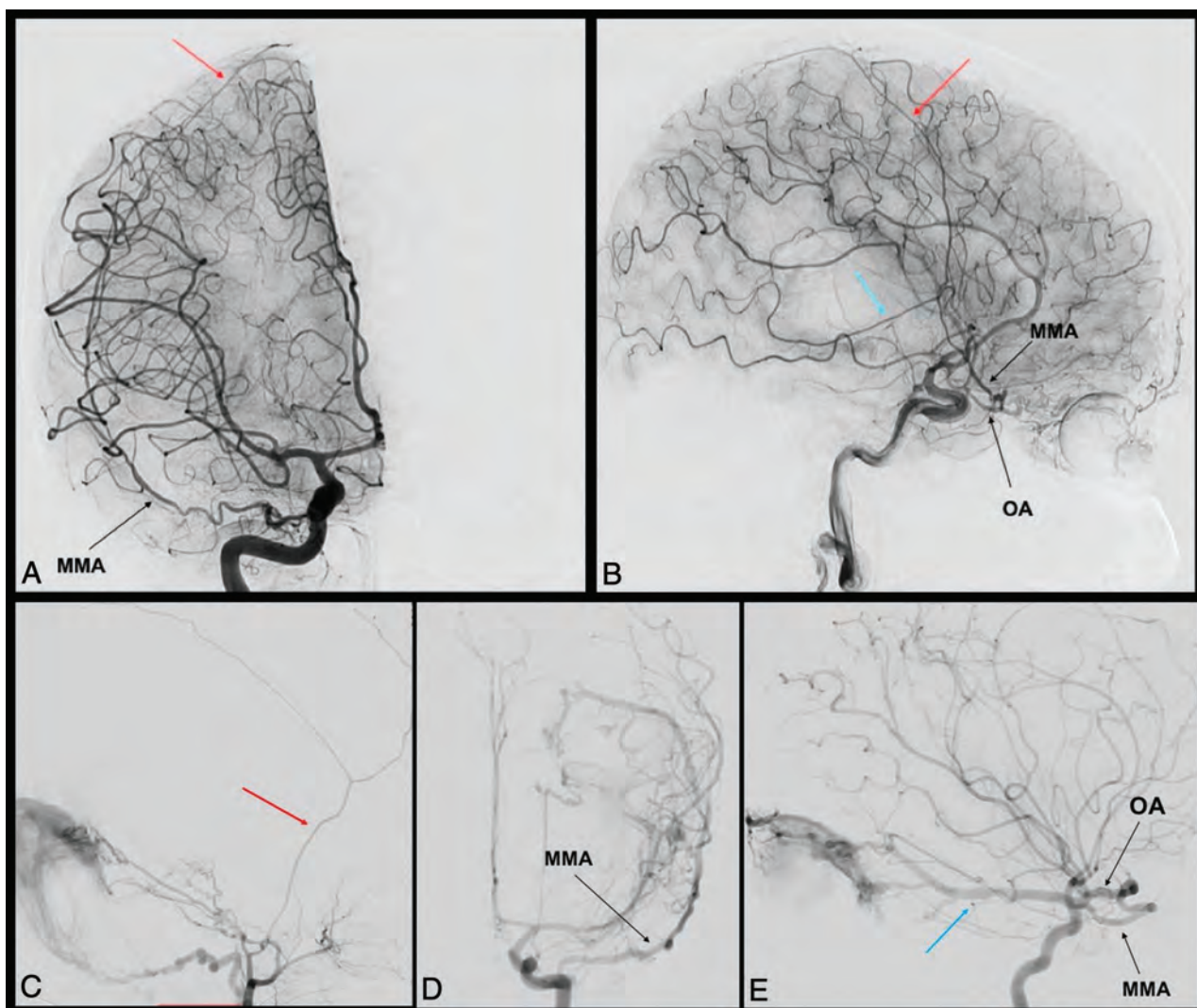
FIG 3. MMA origin from the OA. Anterior-posterior and lateral view angiograms (*A* and *B*) show a rare case of complete MMA origin from the OA. The OA, through the superficial recurrent OA, gives rise to the MMA, which passes through the lateral part of the superior orbital fissure and gives off its anterior (*red arrow*) and posterior divisions (*blue arrow*). In the angiograms *C, D,* and *E,* a rare case of partial origin of the MMA from the OA is shown. The angiograms *D* and *E* show a left ICA injection in frontal and lateral views, where the posterior branch of the MMA (*blue arrow*) originates from the OA and feeds a tentorial arteriovenous fistula. After the ECA injection (*C*), only the anterior branch of the MMA is enhanced (*red arrow*). Reproduced from Bonasia et al.[27]

Dural Supply of the OA

The 4 meningeal branches previously described supply the dura of the cribriform plate: the planum, the anterior clinoid process, the superior orbital region, the roof and the lateral part of the cavernous sinus, the medial part of the orbital roof, and the anterior part of the falx cerebri. This vascular territory is variable, and the OA is in balance with other meningeal arteries of this region like the middle meningeal artery (cavernous ramus), the accessory meningeal artery, and the inferolateral trunk.

Variations of Dural Branches of the Ophthalmic Artery

Ophthalmic Artery Origin of the Middle Meningeal Artery. In rare cases, the middle meningeal artery could originate from the OA instead of the internal maxillary artery. The incidence of this vascular variation was estimated to be 0.5% by Dilenge and Ascherl,[10] in 1980, based on a large angiographic series. A few cases of the middle meningeal artery arising from the OA have

been described in the literature. The first case was presented by Curnow,[2] in 1873, and in the same period, Meyer,[1] in 1887, also cited 4 cadaveric cases originally described by Zuckerkandl in 1876 during a congress presentation.[18] Two rare cases of this variation are shown in Fig 3. This vascular anomaly is considered the consequence of 2 different embryologic processes. The first is the failure of the supraorbital branch (stapedial artery) regression. The second is the absence of anastomosis between the maxillomandibular branch of the stapedial artery and the internal maxillary artery. Consequently, the MMA originates from the OA and passes through the lateral part of the superior orbital fissure; thus, the foramen spinosum is usually absent. Maiuri et al,[19] in 1998, proposed 3 different types of this vascular variation as highlighted in Table 2. The first type is the complete MMA territory taken over by the OA through the superficial recurrent OA. In the second type, only the anterior branch of the MMA origin from the OA and the posterior branch of the MMA retain their

origin from the internal maxillary artery. The third type is not really an OA origin of the MMA but an anastomosis between the OA and the accessory meningeal artery (through the deep recurrent OA). The consequence is that the anterior meningeal territory is supplied by both the MMA and the OA without any communication. It is still a matter of debate whether the MMA originates from the OA directly or from the proximal part of the lacrimal artery.

Ophthalmic Artery Origin of the Marginal Tentorial Artery. The marginal tentorial artery (or artery of the free margin of the tentorium cerebelli) normally arises from the meningohypophysary trunk, but its origin is variable, as illustrated in Fig 4. This artery supplies the medial third of the tentorium, partially the walls of the cavernous sinus, and also the transdural segment of the oculomotor and trochlear nerves.[16] An OA origin of this artery has been described by Lasjaunias et al,[11] in 2001, distinguishing 2 different types. The first is when the marginal tentorial artery originates from the lacrimal artery. The second when the marginal tentorial artery arises directly from the OA and the lacrimal artery originates from the MMA (meningolacrimal type). A marginal tentorial artery arising from the MMA,

Table 2: Different types of OA origin of the MMA by Maiuri et al[19]

Type	Vascular Anatomy	Foramen Spinosum
I	Complete OA origin of the MMA	Absent
II	Partial OA origin of the MMA	Reduced in size
	Anterior division from the OA	
	Posterior division from the IMA	
III	OA origin of the accessory meningeal artery	Normal

Note:—IMA indicates internal maxillary artery.

the accessory meningeal artery or the inferolateral trunk, has also been described.

Clinical Implications

The knowledge of the dural branches arising from the OA and their variations represents the cornerstone for interventional neuroradiologists and neurosurgeons who treat anterior and middle cranial fossa pathologies. Two critical examples are cribriform plate dAVFs and anterior and middle skull base meningiomas.

Cribriform Plate Dural Arteriovenous Fistulas. The cribriform plate dAVFs are usually mostly supplied by the anterior ethmoidal artery and the MMA. A bilateral supply of the dAVF, found in approximately 10% of cases, is well-explained by the anastomoses between the 2 anterior ethmoidal arteries within the dural or ethmoidal sinuses. Endovascular treatment of such pathologies consists of the embolization, usually through branches of the MMA. The neuroradiologist has to consider the presence of dural MMA-OA anastomoses during the injection of the liquid agent to avoid retrograde flow into ocular branches of the OA. In case of direct embolization of the dAVF through the ophthalmic artery, attention should be paid to the possibility of retrograde flow of the embolic agent into ocular branches. Because the central retinal artery usually arises from the second segment of the OA, the injection should be performed as distal as possible to limit the eventual damage caused by the reflux.

The surgical exclusion of a cribriform plate dAVF also necessitates a precise knowledge of dural branches of the OA. The aim of the treatment is to exclude the cortical venous drainage of the dAVF, clipping or coagulating the draining vein at its exit point from the dura. A case of a cribriform plate dAVF treated surgically is shown in Fig 5. The knowledge of the arterioarterial anastomoses among the anterior ethmoidal, posterior ethmoidal, and middle meningeal
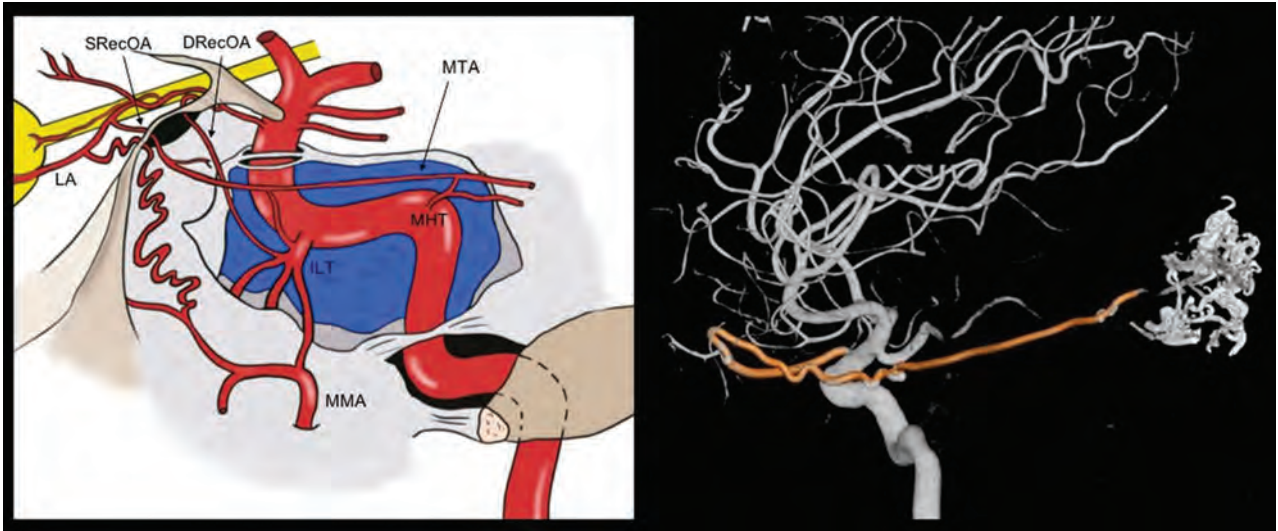
FIG 4. Marginal tentorial artery origin and course. The marginal tentorial artery, also called artery of the free margin of the tentorium or artery of Bernasconi and Cassinari, may have different origins, which are shown in the graphic representation. It can arise from the lacrimal artery (LA) within the orbit, through the superficial recurrent ophthalmic artery (SRecOA), from the inferolateral trunk (ILT), and from the meningohypophyseal trunk (MHT). The artery courses posterolaterally along the free margin of the tentorium. Note a 3D-DSA reconstruction of a rare case of MTA (highlighted in red) origin from the OA. The MTA exits the orbit through the superior orbital fissure (SOF) and is directed posteriorly to feed an arteriovenous malformation. DRecOA indicatesdeep recurrent ophthalmic artery .
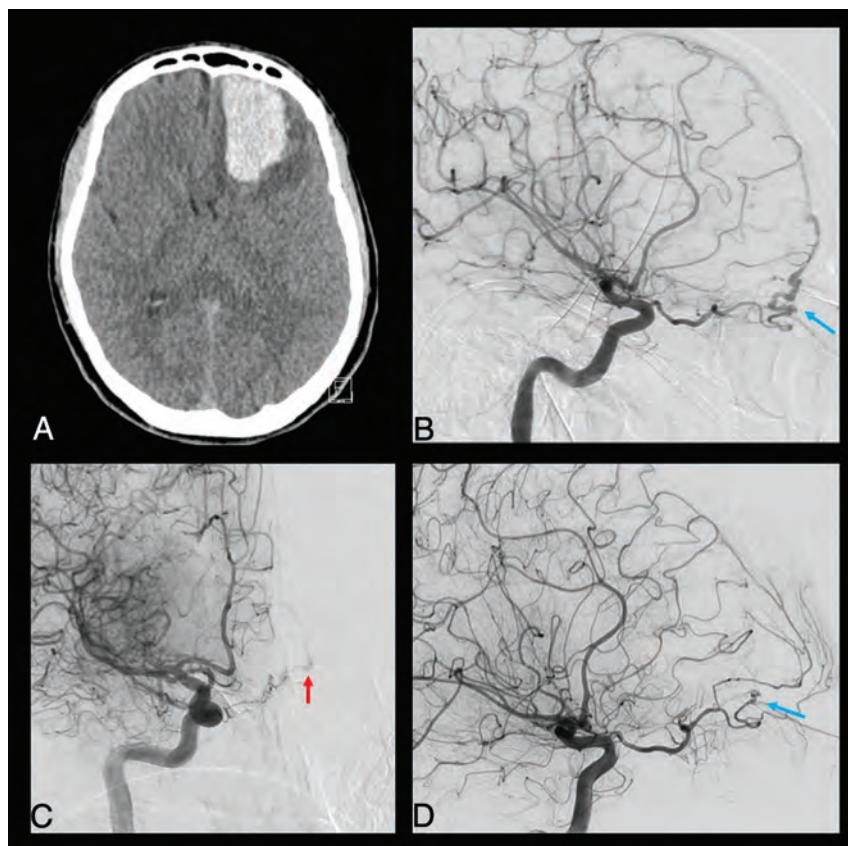
FIG 5. Clinical case of a ruptured cribriform plate dAVF. A 49-year-old man was admitted for sudden onset of unusual headache with nausea and vomiting. The CT scan performed in the emergency department (*A*) shows a left frontal basis intraparenchymal hematoma. The DSA highlighted a cribriform plate dAVF with major feeders represented by the left anterior ethmoidal artery from the left OA (*blue arrow* in *B*). The right ICA injection also showed a contribution from the contralateral OA through its ethmoidal branches (*red arrow* in *C*). The venous drainage was represented by a single cortical vein directed into the superior sagittal sinus (type III according to the Cognard-Lariboisière classification[26]). The patient successfully underwent left supraorbital craniotomy and clipping of the dAVF (*D*), with no enhancement of the dAVF on the postoperative DSA (*blue arrow*) and complete clinical recovery.

In case of an operation in a middle cranial fossa meningioma, the devascularization of the tumor as a first step could be helpful to better understand the arterial supply of the lesion and limit drastically blood loss.

Intra-arterial Injection of Chemotherapy for Retinoblastoma. The classic technique used to inject chemotherapeutic agents into the OA for the treatment of retinoblastoma requires the superselective catheterization of the OA.[20] However, the knowledge of OA dural branches acquires a more important role when the direct catheterization of the OA is not possible, as can happen in children due to its reduced size. In these cases, alternative ways to reach the OA indirectly have been described,[21] especially through catheterization of the MMA. Thus, the pharmacologic agents can be injected through the anterior division of the MMA, cannulating its meningolacrimal branch. The reflux into the OA could be from anastomoses between MMA orbital branches and the recurrent branches of the OA, from the lacrimal artery, or sometimes from the direct origin of the OA from the MMA.

arteries is necessary to understand the dAVF and the technical difficulties of the treatment. Another case of a dAVF fed by dural branches of the OA is shown in Fig 6, also with a contribution from the MTA.

The knowledge of the dural branches of the OA and MMA origin from the OA also adequately explains the possible participation of OA branches in the supply of carotid-cavernous fistulas or tentorial pathologies (Figs 3 and 4).

Anterior and Middle Cranial Fossa Meningiomas. The surgical removal of cribriform plate or sphenoid wing meningiomas requires a detailed knowledge of vascular normal anatomy and tumor vascular supply. Meningeal tumors of the anterior and middle skull base are usually supplied by dural branches of the MMA, internal carotid artery, and the ophthalmic artery. It is of paramount importance for interventional neuroradiologists who plan an embolization, usually performed through the MMA, to consider the possible variations in the supply of the skull base dura to avoid involuntary OA reflux of embolic liquid agent.

Surgical and Endovascular Treatment of Refractory Epistaxis. Re-fractory epistaxis may be caused by many clinical conditions and occurs in about 60% of the adult population, with most cases considered idiopathic. Among them, about 6% of the epistaxis is refractory to conservative management and requires surgical or interventional treatment.[22]

The best way to understand the source of bleeding in case of refractory epistaxis is to perform a diagnostic DSA including the ICA and ECA. The DSA allows identifying the so called "vascular blush," an anastomotic plexus located in the nasal septum, considered the source of 90% of epistaxis. The sphenopalatine artery represents its main blood supply, and it is most commonly responsible for refractory epistaxis, even if, in rare cases, the ethmoidal arteries could also be involved.[23] If these latter are involved in the bleeding, they can be ligated through a surgical approach. On the other hand, if the sphenopalatine artery is responsible for bleeding, it can be occluded through an endonasal approach or it can be embolized.[23]

FIG 6. Clinical case of a dAVF fed by multiple OA dural branches. An 89-year-old woman, previously having undergone an operation for a pituitary adenoma, was admitted for unusual headache associated with vomiting. The CT scan shows an intraventricular hemorrhage with mild hydrocephalus. The diagnostic DSA shows a complex dAVF (Cognard-Lariboisière grade IIa+b[26]) supplied by the OA through the anterior and posterior ethmoidal arteries (AEtA, PEtA), with both direct and indirect shunts with the superior sagittal sinus (SSS). Another point of shunt with the SSS is reached by the MTA and the posterior meningeal artery (PMA) and the MMA. Also, other branches from the ECA contribute to the shunt, like the occipital artery (OccA) and the superficial temporal artery (STA). Because of the patient's age, the complexity of the dAVF, the high risk associated with every option of treatment, and the absence of alteration of consciousness, we managed the dAVF conservatively.

The diagnostic DSA allows identifying possible dangerous anastomoses between branches of the ECA and the OA, which can result in postembolization visual or central deficits. The occurrence of cerebrovascular accidents and obstruction of the central retinal artery have been described to occur in about 0%–2% of cases.[24] The most important anastomoses to consider during such procedures are between the sphenopalatine and anterior ethmoidal arteries via the turbinate and infraorbital arteries[23] and between the lacrimal artery and the middle meningeal artery through the recurrent meningeal artery.[24] The relevance of these anastomoses and the periprocedural risk can be estimated by analyzing the "choroidal blush." This blush is commonly visualized after contrast injection into the ICA. However, if the anastomoses among the posterior ciliary arteries, the lacrimal artery, and the MMA are very consistent or if the lacrimal artery and the OA branch directly from the MMA, the choroidal blush can be seen after the ECA injection.[24]

Embolization of Facial Tumors. Even if epistaxes are mostly idiopathic, some cases can be due to neoplastic erosion of vascular structures or as result of tumor necrosis after treatment. In these cases, the symptoms can also cause hemoptysis due to the frequent nasopharyngeal localization of these tumors. Endovascular treatment should be considered in these cases to treat uncontrollable epistaxis or hemoptysis. Also benign tumors, like paragangliomas and nasopharyngeal angiofibromas, can benefit from endovascular embolization as a preoperative procedure to reduce the intraoperative blood loss. In these cases, the embolization of the sphenopalatine artery could be insufficient, and devascularization requires the embolization of the facial artery and ascending pharyngeal artery.[23] In these cases, neuroradiologists should pay attention to the known anastomoses between the facial artery and the dorsal nasal artery (through the angular artery).[25] For these pathologies, the neuroradiologists should observe the same rules as previously described to avoid complications due to ICA-ECA anastomoses.[23]

In conclusion, the knowledge of the embryology and anatomy of the dural branches of the OA is mandatory for treating pathology of the dura mater located in the anterior and middle cranial fossae. These arteries show high variability and supply territories

in competition with the middle meningeal artery and internal carotid artery branches.

REFERENCES

1. Meyer F. **Zur anatomie der Orbitalarteien.** *Morph Jahr* 1887;12:414–58

2. Curnow J. **Two instances of irregular ophthalmic and middle meningeal arteries.** *J Anat Physiol* 1873;8:155–56 Medline

3. Kuru Y. **Meningeal branches of the ophthalmic artery.** *Acta Radiol Diagn (Stockh)* 1967;6:241–51 CrossRef Medline

4. Gabriele OF, Bell D. **Ophthalmic origin of the middle meningeal artery.** *Radiology* 1967;89:841–44 CrossRef Medline

5. Royle G, Motson R. **An anomalous origin of the middle meningeal artery.** *J Neurol Neurosurg Psychiatry* 1973;36:874–76 CrossRef Medline

6. McLennan JE, Rosenbaum AE, Haughton VM. **Internal carotid origins of the middle meningeal artery: the ophthalmic-middle meningeal and stapedial-middle meningeal arteries.** *Neuroradiology* 1974;7:265–75 CrossRef Medline

7. Vignaud J, Hasso AN, Lasjaunias P, et al. **Orbital vascular anatomy and embryology.** *Radiology* 1974;111:617–26 CrossRef Medline

8. Lasjaunias P, Moret J, Manelfe C, et al. **Arterial anomalies at the base of the skull.** *Neuroradiology* 1977;13:267–72 CrossRef Medline

9. Lasjaunias P, Brismar J, Moret J, et al. **Recurrent cavernous branches of the ophthalmic artery.** *Acta Radiol Diagn (Stockh)* 1978;19:553–60 CrossRef Medline

10. Dilenge D, Ascherl GF Jr. **Variations of the ophthalmic and middle meningeal arteries: relation to the embryonic stapedial artery.** *AJNR Am J Neuroradiol* 1980;1:45–54 Medline

11. Lasjaunias P, Bereinstein A, Ter Brugge KG. *Surgical Neuroangiography.* Springer-Verlag; 2001

12. Rhoton AL Jr. **The orbit.** *Neurosurgery* 2002;51:S303–34 CrossRef Medline

13. Padget DH. **The development of cranial arteries in the human embryo.** In: Corner G, ed. *Contributions to Embryology.* Carnegie Institution; 1948:205–62

14. Lasjaunias P, Moret J, Mink J. **The anatomy of the inferolateral trunk (ILT) of the internal carotid artery.** *Neuroradiology* 1977;13:215–20 CrossRef Medline

15. Hayreh SS. **The ophthalmic artery, III: branches.** *Br J Ophthalmol* 1962;46:212–47 CrossRef Medline

16. Martins C, Yasuda A, Campero A, et al. **Microsurgical anatomy of the dural arteries.** *Neurosurgery* 2005;56:211–51; discussion 211–51 CrossRef Medline

17. Lang J, Kageyama I. **The ophthalmic artery and its branches, measurements and clinical importance.** *Surg Radiol Anat* 1990;12:83–90 CrossRef Medline

18. Zuckerkandl E. **Zur Anatomie der Orbita Arterien.** *Med Jahr* 1876:343

19. Maiuri F, Donzelli R, de Divitiis O, et al. **Anomalous meningeal branches of the ophthalmic artery feeding meningiomas of the brain convexity.** *Surg Radiol Anat* 1998;20:279–84 CrossRef Medline

20. Yamane T, Kaneko A, Mohri M. **The technique of ophthalmic arterial infusion therapy for patients with intraocular retinoblastoma.** *Int J Clin Oncol* 2004;9:69–73 CrossRef Medline

21. Klufas MA, Gobin YP, Marr B, et al. **Intra-arterial chemotherapy as a treatment for intraocular retinoblastoma: alternatives to direct ophthalmic artery catheterization.** *AJNR Am J Neuroradiol* 2012;33:1608–14 CrossRef Medline

22. Christensen NP, Smith DS, Barnwell SL, et al. **Arterial embolization in the management of posterior epistaxis.** *Otolaryngol Head Neck Surg* 2005;133:748–53 CrossRef Medline

23. Reyre A, Michel J, Santini L, et al. **Epistaxis: the role of arterial embolization.** *Diagn Interv Imaging* 2015;96:757–73 CrossRef Medline

24. Mames RN, Snady-McCoy L, Guy J. **Central retinal and posterior ciliary artery occlusion after particle embolization of the external carotid artery system.** *Ophthalmology* 1991;98:527–31 CrossRef Medline

25. Bertelli E, Regoli M, Bracco S. **An update on the variations of the orbital blood supply and hemodynamic.** *Surg Radiology Anat* 2017;39:485–96 CrossRef Medline

26. Cognard C, Gobin YP, Pierot L, et al. **Cerebral dural arteriovenous fistulas: clinical and angiographic correlation with a revised classification of venous drainage.** *Radiology* 1995;194:671–80 CrossRef Medline

27. Bonasia S, Smajda S, Ciccio G, et al. **Middle meningeal artery: anatomy and variations.** *AJNR Am J Neuroradiol* 2020;41:1777–85 CrossRef Medline

Correlation between ASPECTS and Core Volume on CT Perfusion: Impact of Time since Stroke Onset and Presence of Large-Vessel Occlusion

S. Nannoni, F. Ricciardi, D. Strambo, G. Sirimarco, M. Wintermark, V. Dunet, and P. Michel

ABSTRACT

BACKGROUND AND PURPOSE: Both ASPECTS and core volume on CTP are used to estimate infarct volume in acute ischemic stroke. To evaluate the potential role of ASPECTS for acute endovascular treatment decisions, we studied the correlation between ASPECTS and CTP core, depending on the timing and the presence of large-vessel occlusion.

MATERIALS AND METHODS: We retrospectively reviewed all MCA acute ischemic strokes with standardized reconstructions of CTP maps entered in the Acute STroke Registry and Analysis of Lausanne (ASTRAL) registry. Correlation between ASPECTS and CTP core was determined for early (<6 hours) versus late (6–24 hours) times from stroke onset and in the presence versus absence of large-vessel occlusion. We used correlation coefficients and adjusted multiple linear regression models.

RESULTS: We included 1046 patients with a median age of 71.4 years (interquartile range, IQR = 59.8–79.4 years), an NIHSS score of 12 (IQR, 6–18), an ASPECTS of 9 (IQR, 7–10), and a CTP core of 13.6 mL (IQR, 0.6–52.8 mL). The overall correlation between ASPECTS and CTP core was moderate ($\rho = -0.49$, $P < .01$) but significantly stronger in the late-versus-early window ($\rho = -0.56$ and $\rho = -0.48$, respectively; $P = .05$) and in the presence versus absence of large-vessel occlusion ($\rho = -0.40$ and $\rho = -0.20$, respectively; $P < .01$). In the regression model, the independent association between ASPECTS and CTP core was confirmed and was twice as strong in late-arriving patients with large-vessel occlusion ($\beta = -0.21$ per 10 mL; 95% CI, −0.27 to −0.15; $P < .01$) than in the overall population ($\beta = -0.10$; 95% CI, −0.14 to −0.07; $P < .01$).

CONCLUSIONS: In a large cohort of patients with acute ischemic stroke, we found a moderate correlation between ASPECTS and CTP core. However, this was stronger in patients with large-vessel occlusion and longer delay from stroke onset. Our results could support the use of ASPECTS as a surrogate marker of CTP core in late-arriving patients with acute ischemic stroke with large-vessel occlusion.

ABBREVIATIONS: AIS = acute ischemic stroke; ASTRAL = Acute STroke Registry and Analysis of Lausanne; CBS = clot burden score; CTP = Computed tomographic perfusion; EVT = endovascular treatment; LPGH = last proof of good health; LVO = large-vessel occlusion; MCA = middle cerebral artery; NCCT = non-contrast CT scan

Both the ASPECTS[1,2] and automated core volume on CTP[3,4] have been used to estimate infarct volume in the acute phase

of stroke. However, the level of agreement between the two modalities remains uncertain.

ASPECTS is a useful and easily applicable tool for standardized evaluation of the extent of early ischemic changes in anterior circulation strokes on non-contrast CT scan (NCCT). In the original report describing the ASPECTS[1] and in a subsequent observational study involving 1135 patients undergoing intravenous thrombolysis (IVT), the ASPECTS grading was shown to be an independent predictor of functional outcome.[5] For mechanical thrombectomy performed within 6 hours after onset, a clear benefit was found for patients with an NCCT ASPECTS of 6–10, while for ASPECTS values of 0–5, the treatment effect was not clear.[6]

Recently, the efficacy of endovascular treatment (EVT) beyond the 6-hour time window was demonstrated in 2 randomized trials using a tissue-based approach: An advanced neuroimaging protocol (with CTP or DWI) was used to identify

patients with acute ischemic stroke (AIS) with a low infarct core despite late presentation.[7,8]

The role of ASPECTS in selecting patients likely to benefit from EVT and for predicting clinical outcome has not been clearly established in the late time window.[9,10] Its use in the setting of late-presenting AIS could enlarge EVT eligibility in centers without the availability of advanced neuroimaging techniques or in patients who have contraindications to such imaging.

The main purposes of our study were the following: 1) to investigate the correlation between ASPECTS and automated core volume on CTP in a large cohort of patients with AIS with involvement of the middle cerebral artery (MCA territory), 2) to assess the influence of large-vessel occlusion (LVO) and time from stroke onset on this correlation, and 3) to evaluate the association of ASPECTS with clinical outcome at 3 months, with a special focus on late-arriving patients with AIS (ie, 6–24 hours after last proof of good health [LPGH]).

MATERIALS AND METHODS
Study Design and Patient Selection
We performed a retrospective analysis of all consecutive patients entered in the Acute STroke Registry and Analysis of Lausanne (ASTRAL) from January 2003 to December 2018. The ASTRAL registry includes all patients with AIS admitted to the stroke unit and/or intensive care unit of the Lausanne University Hospital (Centre Hospitalier Universitaire Vaudois) within 24 hours after LPGH. For each patient, >250 prespecified demographic, clinical, and laboratory variables and multimodal neuroimaging items were prospectively collected, as previously reported.[11]

For the current analysis, we selected patients according to the following criteria: acute CT-based multimodal imaging performed <24 hours after LPGH; stroke involving the MCA based on clinical findings such as new hemispheric deficits (aphasia, hemineglect, eye deviation toward the side of the hemiparesis); the simultaneous absence of neuroimaging findings showing posterior circulation stroke; and availability of good-quality CTP maps (ie, with the arterial input function returning to baseline before the end of the acquisition), reconstructed with a standardized method.[12]

Demographic data, medical history, and vascular risk factors were reviewed. We collected prestroke modified Rankin scale (mRS) and current medications at the time of the index event. We recorded neurologic symptoms and signs, stroke severity (NIHSS) on admission, and biochemical parameters at baseline. Acute recanalization treatments, including intravenous thrombolysis and/or EVT, were administered in accordance with Swiss and European Stroke Organization guidelines[13,14] and were updated with recent positive randomized trial data.[7,8] We calculated LPGH to arrival, to first imaging, and to treatment times. Stroke mechanism was classified according to the trial of ORG 10172 in acute stroke treatment classification,[15] with dissection, embolic stroke of undetermined source, and multiple causes added as categories.

Clinical outcome was measured at 3 months using the mRS, either at the outpatient stroke clinic or by standardized telephone interview by Rankin-certified medical staff. Favorable outcome was considered as a 3-month mRS of ≤2.

The Strengthening the Reporting of Observational Studies in Epidemiology (STROBE) method was applied, and the STROBE checklist for observational studies is available in the Online Supplemental Data. The local ethics commission of Canton de Vaud approved the scientific use of anonymized data from the ASTRAL registry.

Neuroimaging Protocol
During the study period, patients admitted to our institution with suspected AIS were examined with a multimodal, mostly CT-based neuroimaging protocol as a standard of care. In patients without contraindications for iodinated contrast, this protocol included NCCT, CTA, and CTP.

Cerebral CT was performed on a 16–detector row multidetector CT scanner (LightSpeed; GE Healthcare) up to November 2005 and on a 64–detector row multidetector CT scanner (LightSpeed VCT; GE Healthcare) thereafter. NCCT was acquired in the axial mode using the following parameters: 120-kV(peak) tube voltage; 320-mA tube current; section thickness, 5 mm; 32-cm scan FOV; and 512 × 512 matrix. Raw data were reconstructed in the axial plane using filtered back-projection until 2009 and adaptive statistical iterative reconstruction thereafter. Using NCCT, we searched for intracranial hemorrhage, the hyperdense MCA sign, chronic stroke lesions, the presence of leukoaraiosis, and the presence and extent of early ischemic changes in the MCA territory to calculate the ASPECTS.[2]

The cervical and cerebral CTAs were acquired in helical scan mode from the aortic arch to the top of the frontal sinuses, according to the following parameters: 120-kVp tube voltage, 1500- to 260-mA tube current, 0.9:1 pitch, 0.625-mm section thickness (1.25 mm before November 2005), and 512 × 512 matrix. Data acquisition was performed after intravenous injection of 50 mL of iodinated contrast material at a flow rate of 5 mL per second, with a delay according to the perfusion data. We defined LVO as an internal carotid artery, M1, or proximal M2 occlusion. We calculated clot burden score (CBS) for each patient as an indicator of clot extension.[16] We defined tandem occlusion as arterial occlusion affecting both the extra- and intracranial circulation in the same carotid axis. In patients with LVO, collaterals were graded according to Tan et al.[17] We considered collaterals as "good" if >50% of the ischemic territory distal to the occluded artery was filled.

CTP images were acquired for 50 seconds in a cine mode with a delay of 5–7 seconds after beginning the injection of 50 mL of iodinated contrast at a flow rate of 5 mL per second; four 10-mm slices (40-mm coverage) were imaged before November 2005, and 18 groups of sixteen 5-mm slices (80-mm coverage) thereafter. CTP data were transferred to a workstation and analyzed using the Brilliance Workspace Portal (Philips Healthcare). This team performed manual checks and adjustments and correction of artifacts. The locations of early signs of ischemia and infarct core on CTP were not checked for accordance. A deconvolution approach, based on the central volume principle, was used to create parametric maps of MTT. CBV was calculated from the area under the time-enhancement curves, and CBF was derived from

the formula CBF = CBV/MTT. Infarct core and ischemic penumbra volumes were calculated by applying appropriate MTT and CBV thresholds, which are MTT >145% of the contralateral side values and CBV >2.0 mL/100 g for the penumbra volume, and MTT >145% of the contralateral side values and CBV <2.0 mL/100 g for the core volume.[12]

NCCT images were reviewed for ASPECTS, retrospectively, by an experienced vascular neurologist (P.M.), who compared his value with the assessment established by the radiologist in the acute phase and appearing in the official (clinical) radiology report. In cases of disagreement between the 2 ASPECTS values, the case was discussed at the weekly joint neuroradiology meetings to reach a consensus. We had previously assessed interrater variability between the vascular neurologist and senior neuroradiologist using the Cohen κ on 100 consecutive acute CT scans with anterior circulation occlusive stroke for NCCT ASPECTS, CBS, and collateral status (poor versus good). The ASPECTS was scored by the Lausanne team, without considering results of the CTP, the latter being performed by a completely independent team in Stanford. Both ASPECTS and CTP were calculated in the acute phase, without knowledge of the long-term clinical outcome.

Statistical Analysis

Categoric and binary variables were summarized as frequencies and percentages, while continuous variables were summarized as median and interquartile range.

Statistical correlation between the ASPECTS and core volume on CTP was quantified using the Spearman ρ coefficient. To report the strength and direction of the correlation, we referred to a commonly used interpretation of the Spearman correlation coefficient in medical research.[18] We calculated the statistical significance of this association both in the overall study population and in several meaningful subpopulations defined by the following settings: 1) presence and absence of LVO, 2) early- and late-arriving patients, and 3) known and unknown stroke onset. Furthermore, we compared the correlation coefficients between groups defined by variable combinations of the above-mentioned scenarios (eg, late-arriving patients with LVO). Comparisons between the different groups of patients were based on z scores obtained using the Fisher r-to-z transformation of the ρ; this allows determining the statistical significance of the differences by means of tests based on the Student t distributions. We performed a complete case analysis, and no imputations of missing data were performed.

To check for independent factors associated with ASPECTS (used as a dependent variable), we developed a multivariate linear regression model. We included in the model variables likely to influence the ASPECTS based on pathophysiologic considerations (such as age, NIHSS, prestroke treatments, vascular risk factors, clot burden, leukoaraiosis, core, and penumbra volumes on CTP) and variables that were supposed to influence the relationship between ASPECTS and core volumes (such as the above variables and time from LPGH and LVO and onset type). The complete list of variables included in the model, along with the P values obtained using univariate analysis, is shown in the Online Supplemental Data. We used a stepwise backward elimination method based on the Akaike Information Criterion to select

relevant covariates for inclusion in the final model. Then, we checked the sensitivity of our findings by fitting the same model (except for LVO) into the subpopulation of late-presenting patients with LVO. Heteroscedasticity and normality of residuals were checked using graphic methods (QQ and residuals versus fitted plots).

To identify independent predictors of good clinical outcome at 3 months (mRS ≤2), we fitted a multivariate logistic regression model with the stepwise backward elimination method. This model included demographic, clinical, and radiologic variables at stroke onset that are known to be related to the functional long-term outcome (Online Supplemental Data).[19,20] Then, as before, we performed a separate logistic regression analysis on the subgroup of late-arriving patients with LVO, applying the same model (except for LVO).

Finally, to understand better the capability of NCCT and CTP to predict clinical outcome, we performed receiver operating characteristic (ROC) curve analyses for both imaging modalities in patients showing a concordant or discordant NCCT CTP profile. We defined favorable NCCT as ASPECTS ≥6, and favorable CTP if the core volume was ≤70 mL, as previously suggested.[7,21]

RESULTS

Study Population and Baseline Characteristics

Of 5049 patients with AIS entered in the ASTRAL registry during the study period, 1046 were included in the current analysis. The flow chart in the Online Supplemental Data describes the reasons for exclusion from the analysis and the main differences between the included and excluded patients.

The median age of the included patients was 71.4 years (interquartile range, IQR = 59.8–79.4 years), and the median NIHSS score was 12 (IQR, 6–18), as described in the Online Supplemental Data. The median time from LPGH to hospital arrival was 2.6 hours (IQR, 1.3–6.9 hours), and the median time from LPGH to imaging was 3.4 hours (IQR, 1.9–8.5 hours). Two hundred ninety-two patients (27.9%) were admitted in the late time window; their median LPGH to hospital arrival time was 10.2 hours (IQR, 7.9–13.4 hours), and their median LPGH to CT time was 11.5 hours (IQR, 8.7–15.3 hours).

We previously assessed interrater agreement measures for the following CT-based neuroimaging variables, finding almost perfect agreement for ASPECTS ($\kappa = 0.82$) and collaterals ($\kappa = 0.81$) and good agreement for the clot burden score ($\kappa = 0.77$).

In the study population, the median ASPECTS was 9 (IQR, 7–10), and median core volume on CTP was 13.6 mL (IQR, 0.6–52.8 mL). On CTA, an LVO was detected in 612 (58.5%) patients and in 151 (51.7%) late-arriving patients (Online Supplemental Data). Additional treatment details, stroke etiology, and clinical outcome measures are available in the Online Supplemental Data.

Correlation between ASPECTS and CTP Core, and Influence of Time and LVO

The overall correlation between ASPECTS and CTP core was moderate ($\rho = -0.49$, $P < .01$). The distribution of CTP core volumes across ASPECTS grades is depicted in Fig 1A, and it showed a definitive trend of increasing median baseline CTP cores as the ASPECTS decreased. The ASPECTS-CTP core
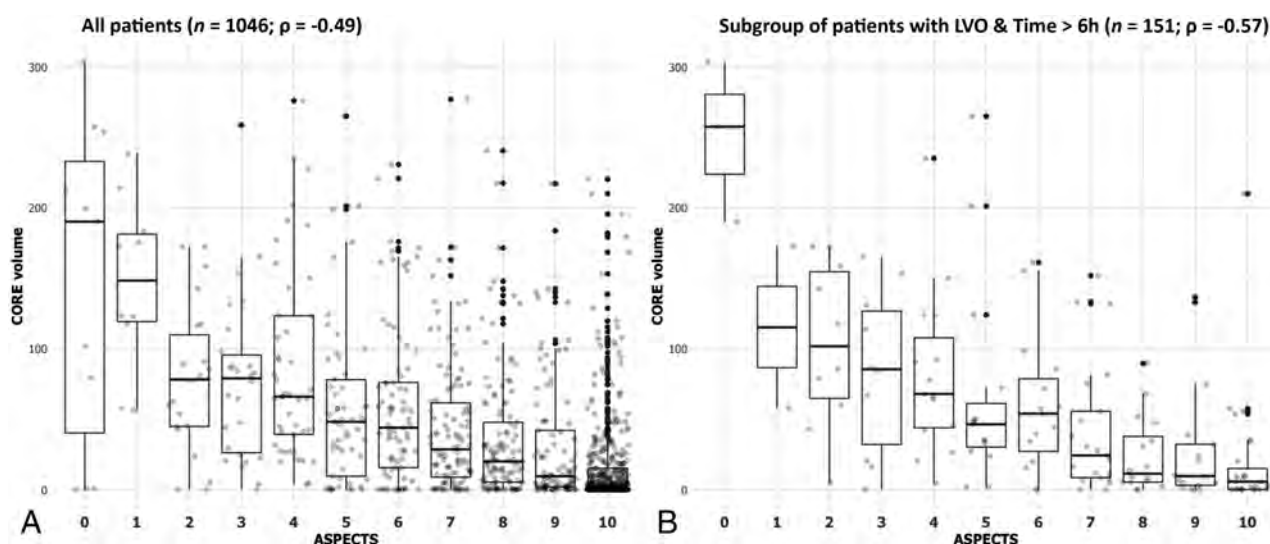
FIG 1. Boxplot of ASPECTS (x-axis) and baseline CTP core volumes (y-axis) in the overall population ($n = 1046$, A) and in subgroup of late-arriving patients with LVO ($n = 151$, B). We observe a moderate ASPECTS-CTP core correlation in our study cohort ($\rho = -0.49$) and a stronger correlation among late-arriving patients with LVO ($\rho = -0.57$).

Table 1: Significant results from the multiple regression model with NCCT ASPECTS as dependent variable in the overall population and in late-arriving (>6 hours from LPGH) patients with AIS with LVO[a]

Variables Associated with ASPECTS	Study Cohort ($n = 1046$)	Late AIS with LVO ($n = 151$)
Age (yr)	0.02 (0.01–0.03)	0.05 (0.02–0.07)
LPGH to arrival time (h)	−0.11 (−0.15 to −0.08)	−0.21 (−0.30 to −0.12)
Prestroke statin use	0.67 (0.13–1.21)	NS
Acute glucose (g/L)	−0.07 (−0.13 to −0.01)	NS
Hyperdense MCA sign	−0.56 (−0.98 to −0.14)	NS
LVO[b]	−0.73 (−1.26 to −0.20)	—
CBS	0.14 (0.06–0.21)	0.17 (0.03–0.31)
Good collaterals	0.87 (0.51–1.23)	NS
Core volume, per 10 mL	−0.10 (−0.14 to −0.07)	−0.21 (−0.27 to −0.15)

Note:—NS indicates nonsignificant; —, variable was non included in the model.
[a] Results are expressed as β coefficient and relative 95% CI.
[b] Included in the predictive model for the entire study cohort only.

correlation was significantly stronger in the subgroup of patients admitted in the late rather than in the early time window ($\rho = -0.56$ and $\rho = -0.48$, respectively; $P = .05$; Online Supplemental Data). In addition, this correlation was significantly better in the presence versus absence of an LVO ($\rho = -0.40$ and $\rho = -0.20$, respectively; $P < .01$; Online Supplemental Data). We did not find any significant difference in the ASPECTS-CTP core correlation in the subgroup of patients with known-versus-unknown stroke onset ($\rho = -0.55$ and $\rho = -0.44$, respectively; $P = .12$).

Testing the combined covariates LVO and time, we found that the correlation increased up to a moderately strong degree ($\rho = -0.57$, $P < .01$) in the subgroup of late-arriving patients with LVO (Fig 1B). On the other hand, it was poor in early patients with and without LVO ($\rho = -0.36$, $P < .01$; and $\rho = -0.23$, $P = .01$, respectively).

With the linear multiple regression model, we confirmed an independent association between ASPECTS and CTP core ($\beta = -0.10$ per 10 mL; 95% CI, −0.14 to −0.07; $P < .01$). Moreover, a

higher ASPECTS was independently associated with older age, shorter delay to arrival time, prestroke statin use, and lower admission glucose levels. Regarding radiologic variables, we found an independent association between a higher ASPECTS and the absence of a hyperdense MCA sign, absence of LVO, higher CBS, and the presence of good collaterals (Table 1). In the subpopulation of late-arriving patients with LVO, the association of ASPECTS and CTP core was twice as strong ($\beta = -0.21$ per 10 mL; 95% CI, 0.27 to −0.15; $P < .01$). Again, older age, shorter delay to arrival time, and higher CBS were independently associated with a higher ASPECTS (Table 1).

To check whether ASPECTS could reliably identify the CTP core volume thresholds, which have been used in recent clinical trials of the late time window, we performed a ROC analysis using a CTP core of 70 mL (as used in the Endovascular Therapy Following Imaging Evaluation for Ischemic Stroke [DEFUSE-3] trial)[22] investigating whether a higher ASPECTS was associated with a favorable CTP profile. We found an area under the curve of 0.76 in the overall population and an under the curve of 0.79 in the subpopulation of late-arriving stroke with LVO (Online Supplemental Data). In this latter group, a cutoff of ASPECTS of ≥ 7 (based on the Youden index) identified patients with a CTP core of <70 mL, with a sensitivity of 65.7% and a specificity of 76.7%.

Association of ASPECTS with Clinical Outcome

The overall percentage of good clinical outcome at 3 months was 51.9%. Fitting a logistic multiple regression model, ASPECTS emerged as an independent predictor of good outcome in both the overall population (OR = 1.10; 95% CI, 1.00–1.20; $P = .05$) and late-arriving patients with AIS (OR = 1.23; 95% CI, 1.02–

Table 2: Independent predictors of good clinical outcome at 3 months (mRS ≤2) in the overall population and in late-arriving (>6 hours from LPGH) patients with AIS with LVO[a]

Variables Associated with Good Outcome	Study Cohort (n = 1046)	Late AIS with LVO (n = 151)
Age (yr)	0.96 (0.94–0.97)	NS
NIHSS on admission	0.87 (0.84–0.91)	0.86 (0.80–0.93)
Decreased LOC on admission	0.45 (0.24–0.83)	NS
LPGH to arrival time (h)	0.95 (0.91–0.99)	NS
NCCT ASPECTS	1.10 (1.00–1.20)	1.23 (1.02–1.51)
CBS	1.17 (1.08–1.28)	NS
Tandem occlusion	0.54 (0.32–0.92)	0.23 (0.06–0.76)
	AIC = 694.76	AIC = 146.02

Note:—LOC indicates level of consciousness; AIC, Akaike Information Criteria.
[a] Results are adjusted for prestroke mRS and expressed as odds ratio and relative 95% CI.

1.51; $P = .03$; Table 2). Moreover, we found younger age, lower NIHSS score on admission, and lower frequency of a decreased level of consciousness as independently associated with a favorable outcome in our study cohort. Among radiologic variables, a smaller clot (ie, higher CBS) and the absence of tandem occlusion also predicted favorable outcome.

For a sensitivity analysis, we compared the predictive capabilities of the models for good clinical outcome at 3 months in which ASPECTS is replaced with the CTP core (Online Supplemental Data). These models showed very similar performances as indicated by the similar coefficients and the Akaike Information Criteria, in both the overall cohort and in the subpopulation of late-arriving patients with LVO; the Vuong tests for the difference in the Akaike Information Criteria were not significant ($P = .39$ for the overall cohort; $P = .14$ for the late-arriving patients with LVO).

Looking at the relationship between imaging concordance and clinical outcome, we identified the following subgroups of patients: patients with favorable NCCT/CTP ($n = 756/1046$, 72%), patients with poor NCCT/CTP ($n = 79$, 8%), and patients with discordant NCCT/CTP ($n = 211$, 20%). The percentages of good outcome across the subgroups were the following: 61% in patients with both images being favorable, 14% in patients with both unfavorable images, and 32% in patients with discordant images. The areas under the curve (AUC) for predicting good outcome for each imaging technique in the 3 subgroups of patients are reported in the Online Supplemental Data. We observed a similar but poor prognostic performance of NCCT and CTP in patients with favorable profiles on both modalities. The performance was higher in patients showing both unfavorable NCCT and CTP, without any statistical difference between the ASPECTS and CTP. In patients with discordant NCCT and CTP profiles, the performance of both modalities was again modest, without a higher accuracy for CTP core compared with ASPECTS.

DISCUSSION

In a large cohort of consecutive patients with AIS involving the MCA territory, we showed a moderate correlation between the ASPECTS and core volume on CTP in the acute phase of stroke. This correlation was significantly better in the presence of an LVO (ICA, M1, or proximal M2 occlusion) and was time-dependent, being stronger in the subgroup of patients potentially eligible for late endovascular treatment (ie, LVO-positive and arriving after 6 hours of last proof of good health). In the latter, we confirmed an independent role of ASPECTS in determining good clinical outcome at 3 months, which was similar to the CTP core.

Compared with previous studies reporting a weak[23]-to-moderate[24] ASPECTS-CTP core correlation, correlations in a larger study cohort were tested, applying multiple adjustments. We demonstrated that the ASPECTS-CTP core association was stronger in patients with LVO than without it. This finding was very robust, given that the association was present even after correction for several clinical and radiologic variables. We suppose that the presence of a proximal intracranial occlusion leads to higher ischemic core volume and, therefore, to a higher likelihood of detecting early ischemic changes on NCCT and, as a consequence, to a higher accuracy of ASPECTS on estimating core volume.[25] This was especially evident in patients assessed 6 hours after symptom onset, which probably reflects the progressive development of cytotoxic edema, the histologic equivalent of early ischemic changes on NCCT.

We also found that multiple other clinical and radiologic variables, in addition to time and presence of an LVO, influenced the ASPECTS. Patients with prestroke statin use presented with higher ASPECTS, which is in line with previous studies reporting that statin pretreatment enhances collateral perfusion and reduces final infarct volume.[26,27] We also demonstrated that admission hyperglycemia was associated with poorer ASPECTS; this finding is consistent with previous human and animal studies showing that hyperglycemia is associated with early infarct expansion in AIS.[28,29] Regarding radiologic variables, we found higher ASPECTS in patients without the hyperdense MCA sign (which is a marker of proximal MCA occlusion) and with higher CBS (which means smaller clots). Taken together, these results suggest a favorable NCCT profile in patients with a distal or small area of vascular occlusion. Moreover, we identified an independent association between higher ASPECTS and good collaterals, further supporting the role of collateral circulation in the early prevention of tissue loss.[25]

Our results confirm that in a mixed population of patients with AIS, some treated with intravenous thrombolysis and/or EVT, baseline ASPECTS is a major determinant of good clinical outcome at 3 months, after adjusting for known confounders (including age, prestroke disability, stroke severity, and admission glycemia). This finding has already been shown in the early time window for patients without revascularization treatment,[30] treated with intravenous thrombolysis[5] and with early EVT.[6,31,32] In our subgroup of patients admitted late and who had LVO (a minority of whom underwent EVT), we confirmed that a higher ASPECTS also remained independently associated with good clinical outcome, and we showed that the prognostic value of ASPECTS was similar to that of core volume on CTP.

Nevertheless, relying on imaging alone could lead to erroneous outcome prediction. Our results showed that a good and concordant NCCT/CTP imaging profile on admission was not a sufficient condition for sure translation to a positive clinical outcome, and the performance of both imaging modalities did not seem to contribute to prediction. We can probably explain this outcome by the other numerous variables that may have an impact on the outcome (as emerged from our multivariate model of prediction of good clinical outcome at 3 months). In addition, the small number of patients with LVO who underwent EVT in our cohort might have influenced this finding. We also showed that 20% of patients presented with a discordant NCCT/CTP profile, of whom 30% achieved a good outcome. These patients include patients with good ASPECTS despite a large infarct volume, in whom it was demonstrated that a quick and successful revascularization of the hypoperfused region was still associated with a high probability of good outcome. In fact, up to 20% of such patients might present with a final infarct volume lower than that of the admission volume, due to an overestimation of the latter by CTP in the early hours after stroke onset.[33,34] In the opposite situation of low ASPECTS associated with acceptable core volumes on CTP, a revision of early ischemic NCCT changes should be considered (eg, to exclude old infarctions or NCCT artifacts), especially for patients imaged in the extended time window and with good collateral circulation.

The clinical implications of our findings are that ASPECTS appears a quite reliable surrogate marker for the ischemic core in patients with LVO in the later time window. Such a finding supports the possible role of ASPECTS as a selection tool for late mechanical thrombectomy. We previously demonstrated that the strict application of trial criteria (DWI or CTP Assessment with Clinical Mismatch in the Triage of Wake-Up and Late Presenting Strokes Undergoing Neurointervention with Trevo [DAWN] and DEFUSE-3) translated into a low proportion of patients eligible for late EVT in the real-word scenario and that this treatment could be offered to a larger population of patients if more liberal criteria were adopted.[22] In this setting, the use of ASPECTS could help with the decision to proceed to thrombectomy in cases of absent, failed, or contraindicated advanced imaging or in situations of CT and CTP discordant profiles.[21] The success of late revascularization therapies according to trial criteria could be hopefully replicated by simpler selection criteria. This strategy is currently being evaluated in ongoing randomized clinical trials (Endovascular Treatment of Acute Stroke for Late arrivals, MR CLEAN-LATE;[35] Tenecteplase in Wake-up Ischaemia Trial [TWIST][36]).

Several limitations of our study need to be acknowledged. First, its single-center retrospective design and the exclusion of patients due to the absence of reconstructed CTP volumes could lead to a selection bias; furthermore, an external validation of the study results is lacking. Second, we did not assess the spatial agreement between the ASPECTS and CTP core; therefore, we could not assess whether unequal weighting of brain regions in the ASPECTS rating could hamper its correlation with core volumes. Third, the thresholds model used for core and penumbra volume reconstructions was different from those adopted in recent EVT trials;[37] however, it is a well-established model, based on a systematic evaluation of all PCT parameters and is the most suitable for the software used in the analysis.[12] Finally, given the small number of patients treated with late EVT in our cohort, we could not analyze the impact of ASPECTS on the response to revascularization treatments.

A future potential development of this study includes the comparison between visual ASPECTS and scoring with automated software applications able to detect and quantify early ischemic changes.[38]

CONCLUSIONS

In our series of 1046 patients with MCA stroke, ASPECTS showed a moderate correlation with CTP-based infarct core, which is stronger in late-arriving patients with large-vessel occlusion. This could support the use of ASPECTS as a surrogate marker for CTP core for selection of late endovascular treatment and for estimation of prognosis. Further studies on the effect of an ASPECTS-based selection for late revascularization therapies are strongly welcomed.

ACKNOWLEDGMENTS

REFERENCES

1. Barber PA, Demchuk AM, Zhang J, et al. **Validity and reliability of a quantitative computed tomography score in predicting outcome of hyperacute stroke before thrombolytic therapy: ASPECTS Study Group—Alberta Stroke Programme Early CT Score.** *Lancet* 2000;355:1670–74 CrossRef Medline

2. Puetz V, Dzialowski I, Hill MD, et al. **The Alberta Stroke Program Early CT Score in clinical practice: what have we learned?** *Int J Stroke* 2009;4:354–64 CrossRef Medline

3. Wintermark M, Reichhart M, Thiran JP, et al. **Prognostic accuracy of cerebral blood flow measurement by perfusion computed tomography, at the time of emergency room admission, in acute stroke patients.** *Ann Neurol* 2002;51:417–32 CrossRef Medline

4. Albers GW, Goyal M, Jahan R, et al. **Ischemic core and hypoperfusion volumes predict infarct size in SWIFT PRIME.** *Ann Neurol* 2016;79:76–89 CrossRef Medline

5. Hill MD, Buchan AM. Canadian Alteplase for Stroke Effectiveness Study (CASES) Investigators. **Thrombolysis for acute ischemic stroke: results of the Canadian Alteplase for Stroke Effectiveness Study.** *CMAJ* 2005;172:1307–12 CrossRef Medline

6. Goyal M, Menon BK, van Zwam WH, et al; HERMES Collaborators. **Endovascular thrombectomy after large-vessel ischaemic stroke: a meta-analysis of individual patient data from five randomised trials.** *Lancet* 2016;387:1723–31 CrossRef Medline

7. Albers GW, Marks MP, Kemp S, et al; DEFUSE 3 Investigators. **Thrombectomy for stroke at 6 to 16 hours with selection by perfusion imaging.** *N Engl J Med* 2018;378:708–18 CrossRef Medline

8. Nogueira RG, Jadhav AP, Haussen DC, et al; DAWN Trial Investigators. **Thrombectomy 6 to 24 hours after stroke with a mismatch between deficit and infarct.** *N Engl J Med* 2018;378:11–21 CrossRef Medline

9. Konstas AA, Minaeian A, Ross IB. **Mechanical thrombectomy in wake-up strokes: a case series using Alberta Stroke Program Early CT Score (ASPECTS) for patient selection.** *J Stroke Cerebrovasc Dis* 2017;26:1609–14 CrossRef Medline

10. Nagel S, Herweh C, Pfaff JA, et al. **Simplified selection criteria for patients with longer or unknown time to treatment predict good outcome after mechanical thrombectomy.** *J Neurointerv Surg* 2019;11:559–62 CrossRef Medline

11. Michel P, Odier C, Rutgers M, et al. **The Acute STroke Registry and Analysis of Lausanne (ASTRAL): design and baseline analysis of an ischemic stroke registry including acute multimodal imaging.** *Stroke* 2010;41:2491–98 CrossRef Medline

12. Wintermark M, Flanders AE, Velthuis B, et al. **Perfusion-CT assessment of infarct core and penumbra: receiver operating characteristic curve analysis in 130 patients suspected of acute hemispheric stroke.** *Stroke* 2006;37:979–85 CrossRef Medline

13. Michel P, Engelter S, Arnold M, et al. **Thrombolyse de l'attaque cérébrale ischémique: recommandations actualisées.** *Swiss Medical Forum* 2009;9:225–28 CrossRef

14. Turc G, Bhogal P, Fischer U, et al. **European Stroke Organisation (ESO): European Society for Minimally Invasive Neurological Therapy (ESMINT) Guidelines on Mechanical Thrombectomy in Acute Ischaemic Stroke Endorsed by Stroke Alliance for Europe (SAFE).** *Eur Stroke J* 2019;4:6–12 CrossRef Medline

15. Adams HP Jr, Bendixen BH, Kappelle LJ, et al. **Classification of subtype of acute ischemic stroke. Definitions for use in a multicenter clinical trial. TOAST. Trial of Org 10172 in Acute Stroke Treatment.** *Stroke J* 1993 Jan;24(1):35–41 CrossRef Medline

16. Puetz V, Dzialowski I, Hill MD, et al. **Intracranial thrombus extent predicts clinical outcome, final infarct size and hemorrhagic transformation in ischemic stroke: the clot burden score.** *Int J Stroke* 2008;3:230–36 CrossRef Medline

17. Tan JC, Dillon WP, Liu S, et al. **Systematic comparison of perfusion-CT and CT-angiography in acute stroke patients.** *Ann Neurol* 2007;61:533–43 CrossRef Medline

18. Fowler J, Cohen L, Jarvis P. **Practical Statistics for Field Biology 2nd ed.** Wiley; 2013:132–33

19. Quinn TJ, Singh S, Lees KR, et al; VISTA Collaborators. **Validating and comparing stroke prognosis scales.** *Neurology* 2017;89:997–1002 CrossRef Medline

20. Ntaios G, Faouzi M, Ferrari J, et al. **An integer-based score to predict functional outcome in acute ischemic stroke: the ASTRAL score.** *Neurology* 2012;78:1916–22 CrossRef Medline

21. Sarraj A, Hassan AE, Grotta J, et al. **Optimizing Patient Selection for Endovascular Treatment in Acute Ischemic Stroke (SELECT): a prospective, multicenter cohort study of imaging selection.** *Ann Neurol* 2020;87:419–33 CrossRef Medline

22. Nannoni S, Strambo D, Sirimarco G, et al. **Eligibility for late endovascular treatment using DAWN, DEFUSE-3, and more liberal selection criteria in a stroke center.** *J Neurointerv Surg* 2020;12:842–47 CrossRef Medline

23. Demeestere J, Scheldeman L, Cornelissen SA, et al. **Alberta Stroke Program Early CT Score versus computed tomographic perfusion to predict functional outcome after successful reperfusion in acute ischemic stroke.** *Stroke* 2018;49:2361–67 CrossRef Medline

24. Olive-Gadea M, Martins N, Boned S, et al. **Baseline ASPECTS and e-ASPECTS correlation with infarct volume and functional outcome in patients undergoing mechanical thrombectomy.** *J Neuroimaging* 2019;29:198–202 CrossRef Medline

25. Nannoni S, Cereda CW, Sirimarco G, et al. **Collaterals are a major determinant of the core but not the penumbra volume in acute ischemic stroke.** *Neuroradiology* 2019;61:971–78 CrossRef Medline

26. Shook SJ, Gupta R, Vora NA, et al. **Statin use is independently associated with smaller infarct volume in nonlacunar MCA territory stroke.** *J Neuroimaging* 2006;16:341–46 CrossRef Medline

27. Malhotra K, Safouris A, Goyal N, et al. **Association of statin pretreatment with collateral circulation and final infarct volume in acute ischemic stroke patients: a meta-analysis.** *Atherosclerosis* 2019;282:75–79 CrossRef Medline

28. MacDougall NJ, Muir KW. **Hyperglycaemia and infarct size in animal models of middle cerebral artery occlusion: systematic review and meta-analysis.** *J Cereb Blood Flow Metab* 2011;31:807–18 CrossRef Medline

29. Shimoyama T, Shibazaki K, Kimura K, et al. **Admission hyperglycemia causes infarct volume expansion in patients with ICA or MCA occlusion: association of collateral grade on conventional angiography.** *Eur J Neurol* 2013;20:109–16 CrossRef Medline

30. Demchuk AM, Hill MD, Barber PA, et al. **Importance of early ischemic computed tomography changes using ASPECTS in NINDS rtPA stroke study.** *Stroke* 2005;36:2110–15 CrossRef Medline

31. Pfaff J, Herweh C, Schieber S, et al. **e-ASPECTS correlates with and is predictive of outcome after mechanical thrombectomy.** *AJNR Am J Neuroradiol* 2017;38:1594–99 CrossRef Medline

32. Haussen DC, Dehkharghani S, Rangaraju S, et al. **Automated CT perfusion ischemic core volume and noncontrast CT ASPECTS (Alberta Stroke Program Early CT Score): correlation and clinical outcome prediction in large vessel stroke.** *Stroke* 2016;47:2318–22 CrossRef Medline

33. Martins N, Aires A, Mendez B, et al. **Ghost infarct core and admission computed tomography perfusion: redefining the role of neuroimaging in acute ischemic stroke.** *Interv Neurol* 2018;7:513–21 CrossRef Medline

34. Rotem SH, Mor S, Chen B, et al. **Infarct core reliability by CT perfusion is a time-dependent phenomenon.** *J Neuroimaging* 2020;30:240–45 CrossRef Medline

35. van Oostenbrugge R, van Zwam W. **MR CLEAN LATE Trial Protocol.** 2018. https://mrclean-late.nl/trial-protocol.html. Accessed September 11, 2019

36. Tenecteplase in Wake-up Ischaemic Stroke Trial (TWIST) study protocol. https://clinicaltrials.gov/ProvidedDocs/60/NCT03181360/Prot_SAP_000.pdf. Accessed September 11, 2019

37. Lansberg MG, Lee J, Christensen S, et al. **RAPID automated patient selection for reperfusion therapy: a pooled analysis of the Echoplanar Imaging Thrombolytic Evaluation Trial (EPITHET) and the Diffusion and Perfusion Imaging Evaluation for Understanding Stroke Evolution (DEFUSE) Study 3.** *Stroke* 2011;42:1608–14 CrossRef Medline

38. Hoelter P, Muehlen I, Goelitz P, et al. **Automated ASPECTS scoring in acute ischemic stroke: comparison of three software tools.** *Neuroradiology* 2020;62:1231–38 CrossRef Medline

Analysis of Stroke Detection during the COVID-19 Pandemic Using Natural Language Processing of Radiology Reports

M.D. Li, M. Lang, F. Deng, K. Chang, K. Buch, S. Rincon, W.A. Mehan, T.M. Leslie-Mazwi, and J. Kalpathy-Cramer

ABSTRACT

BACKGROUND AND PURPOSE: The coronavirus disease 2019 (COVID-19) pandemic has led to decreases in neuroimaging volume. Our aim was to quantify the change in acute or subacute ischemic strokes detected on CT or MR imaging during the pandemic using natural language processing of radiology reports.

MATERIALS AND METHODS: We retrospectively analyzed 32,555 radiology reports from brain CTs and MRIs from a comprehensive stroke center, performed from March 1 to April 30 each year from 2017 to 2020, involving 20,414 unique patients. To detect acute or subacute ischemic stroke in free-text reports, we trained a random forest natural language processing classifier using 1987 randomly sampled radiology reports with manual annotation. Natural language processing classifier generalizability was evaluated using 1974 imaging reports from an external dataset.

RESULTS: The natural language processing classifier achieved a 5-fold cross-validation classification accuracy of 0.97 and an F1 score of 0.74, with a slight underestimation (−5%) of actual numbers of acute or subacute ischemic strokes in cross-validation. Importantly, cross-validation performance stratified by year was similar. Applying the classifier to the complete study cohort, we found an estimated 24% decrease in patients with acute or subacute ischemic strokes reported on CT or MR imaging from March to April 2020 compared with the average from those months in 2017–2019. Among patients with stroke-related order indications, the estimated proportion who underwent neuroimaging with acute or subacute ischemic stroke detection significantly increased from 16% during 2017–2019 to 21% in 2020 ($P = .01$). The natural language processing classifier performed worse on external data.

CONCLUSIONS: Acute or subacute ischemic stroke cases detected by neuroimaging decreased during the COVID-19 pandemic, though a higher proportion of studies ordered for stroke were positive for acute or subacute ischemic strokes. Natural language processing approaches can help automatically track acute or subacute ischemic stroke numbers for epidemiologic studies, though local classifier training is important due to radiologist reporting style differences.

ABBREVIATIONS: ASIS = acute or subacute ischemic stroke; COVID-19 = coronavirus disease 2019; NLP = natural language processing

There is much concern regarding the impact of the coronavirus disease 2019 (COVID-19) pandemic on the quality of stroke care, including issues with hospital capacity, clinical resource re-allocation, and the safety of patients and clinicians.[1,2] Previous reports have shown that there have been substantial decreases in stroke neuroimaging volume during the pandemic.[3,4] In addition, acute ischemic infarcts have been found on neuroimaging studies in many hospitalized patients with COVID-19, though the causal relationship is unclear.[5,6] Studies like these and other epidemiologic analyses usually rely on the creation of manually curated databases, in which identification of cases can be time-consuming and difficult to update in real-time. One way to facilitate such research is to use natural language processing (NLP), which has shown utility for automated analysis of radiology report data.[7] NLP algorithms have been developed previously for the classification of neuroradiology reports for the presence of ischemic stroke findings and acute ischemic stroke subtypes.[8,9] Thus, NLP has the potential to facilitate COVID-19 research.

In this study, we developed an NLP machine learning model that classifies radiology reports for the presence or absence of acute or subacute ischemic stroke (ASIS), as opposed to chronic stroke. We used this model to quantify the change in ASIS detected on all CT or MR imaging studies performed at a large comprehensive stroke center during the COVID-19 pandemic in the United States. We also evaluated NLP model generalizability and different training strategies using a sample of radiology reports from a second stroke center.

MATERIALS AND METHODS

This retrospective study was exempted with waiver of informed consent by the institutional review board of Mass General Brigham (Boston, Massachusetts), the integrated health system that includes both Massachusetts General Hospital and Brigham and Women's Hospital.

Radiology Report Extraction

We used a custom hospital-based radiology report search tool to extract head CT and brain MR imaging study reports performed at Massachusetts General Hospital (hospital 1) and its affiliated imaging centers (a comprehensive stroke center) from March 1 to April 30 in each year from 2017 to 2020. At this hospital, head CT and brain MR imaging studies are routinely performed for patients with stroke. Head CTs included noncontrast and contrast-enhanced head CT and CT angiography studies. Brain MRIs included noncontrast and contrast-enhanced brain MRIs and MR angiography studies. After we removed outside imaging studies also stored in the data base, there were 15,627 head CT and 17,151 brain MR imaging reports (a total of 32,778 studies). Of these studies, 15,590 head CT and 16,965 brain MR imaging reports had study "Impressions", which restricted the analysis to 98.9% and 99.8% of the dataset, respectively. These studies formed the aggregate study cohort, which included a total of 32,555 brain MR imaging and head CT reports on 20,414 unique patients.

Of the original 32,778 study reports extracted, 1000 head CT and 1000 brain MR imaging studies were randomly sampled for manual annotation to serve as training and testing data for an NLP machine learning model. Of these studies, 1987 contained study Impressions (99.4%). The studies without study Impressions were predominantly pediatric brain MR imaging studies that involved a different structure for reporting.

Using a commercial radiology information system (Primordial/Nuance Communications), we also extracted an additional dataset of radiology reports from Brigham and Women's Hospital (hospital 2) and its affiliated imaging centers (also a comprehensive stroke center). We analyzed the overlap in radiologists and trainees involved in the dictation of these reports between hospitals 1 and 2. The first 500 consecutive head CTs and the first 500 brain MRIs performed in both April 2019 and April 2020 were obtained (a total of 1000 head CTs and 1000 brain MR imaging study reports), with the same inclusion criteria for noncontrast and contrast-enhanced studies, as well as angiographic studies. All of these reports had study Impressions. After removing duplicate study entries in this dataset (26, 1.3%), 1974 head CT and brain MR imaging reports remained for further analysis.

NLP Training Dataset Annotation

For NLP model training, the 1987 study reports sampled from hospital 1 and the 1974 study reports available from hospital 2 were manually annotated, each by a diagnostic radiology resident (F.D. for CT and M.L. for MR imaging from hospital 1 and M.D.L. for CT and MR imaging from hospital 2). The annotators classified each report for the presence of ASIS using the study "Impression." This finding could be explicitly or implicitly stated in the report, and reports that stated or suggested chronicity of an infarct were not considered to have this finding. For example, "old" or "chronic" infarct suggests chronicity, though more ambiguous terms like "age-indeterminate" or "unclear timeframe" were sometimes found. Reports with ambiguous terms were not considered to have ASIS, unless an expression of newness was conveyed in the report (eg, "new age-indeterminate infarct").

NLP Machine Learning Model Training and Testing

We trained a random forest machine learning model that takes the radiology report free-text Impression as input and classifies the report for the presence or absence of an ASIS. To train a machine learning model to automatically parse the radiology report text, we used the *re* (Version 2.2.1), *sklearn* (Version 0.20.3), and *nltk* (Version 3.4) packages in Python (Version 3.7.1). Before model training, we used regular expressions to extract sentences with words containing the stems "infarct" or "ischem" from each study Impression. This step helped to focus the algorithm on sentences containing content relevant to the classification task. The words in the extracted sentences were stemmed using the snowball.EnglishStemmer from the *nltk* package. The extracted and stemmed sentences were then represented as vectors using bag-of-words vectorization with N-grams ($n = 2–3$; minimum term frequency, 1%), an approach previously used for radiology report natural language processing.[10] Negation was dealt with using the *nltk* mark_negation function, which appends a "_NEG" suffix between words that appear between a negation term and a punctuation mark. These vector representations of the radiology report Impression served as inputs to the random forest NLP classifier.

The random forest NLP classifier was trained using default hyperparameters in *sklearn*, Version 0.20.3, including 100 trees in the forest using the Gini Impurity for measuring the quality of the data split. Using the manually annotated datasets from hospitals 1 and 2, we evaluated 2 training strategies. First, we trained a classifier using the hospital 1 annotated dataset and tested performance using 5-fold cross-validation, stratified on outcome (ASIS), given the class imbalance. We also tested this classifier on the external hospital 2 annotated dataset. Second, we trained a classifier using the combined hospital 1 and 2 annotated datasets and tested performance using 5-fold cross-validation, also stratified on outcome, but only including hospital 1 reports in the cross-validation to assess performance on hospital 1 data specifically. We repeated this testing using only hospital 2 reports in the cross-validation to assess the performance on the hospital 2 data specifically. When the combined hospital 1 and 2 datasets were used for classifier training, the N-gram minimum term frequency was halved to 0.5%; empirically, the number of N-gram terms

was then similar between this classifier and the classifier trained on hospital 1 data only. The Python code for training these random forest classifiers is available at github.com/QTIM-Lab/asis_nlp.

The metrics used to assess model performance included accuracy, precision, recall, and F1 score. Performance was evaluated for CT and MR imaging reports combined, CT reports alone, and MR imaging reports alone, with 5-fold cross-validation when appropriate.

NLP-Based Epidemiologic Analysis

On the basis of the results of the NLP model testing, an NLP classifier was then applied to the complete cohort of 32,555 brain MR imaging and head CT reports from hospital 1 to estimate the number of patients with ASIS. Patients with at least 1 neuroimaging study (CT or MR imaging) with an ASIS during the time period in question were considered to have had an infarct. Demographic information associated with these patients was extracted along with the radiology report text.

Statistics

Statistical testing was performed using the *scipy* Version 1.1.0 package in Python. The Pearson χ^2 test of independence and 1-way ANOVA were used when appropriate. Statistical significance was determined a priori to be $P < .05$. Performance metrics were reported as the bootstrap median estimate with 95% confidence intervals.[11]

RESULTS

Manually Annotated Radiology Report Dataset Characteristics

Among the randomly sampled 1987 neuroimaging reports from hospital 1 used for NLP model development, 67 head CT and 68 brain MR imaging reports were manually classified as positive for ASIS (positive in 129 patients from 1904 total unique patients). Among the 1974 neuroimaging reports from hospital 2, 84 head CT and 91 brain MR imaging reports were manually classified as positive for ASIS (positive in 101 patients from 1514 total unique patients). The remainder of studies were negative for ASIS. In the hospital 1 annotated report dataset, 126 unique radiologists and trainees (residents and fellows) were involved in the dictation of these reports. In the hospital 2 annotated report dataset, there were 94 unique radiologists and trainees involved. There was an overlap of 3 radiologists and trainees between these 2 datasets due to radiologists/trainees moving between institutions. The hospital 1 and hospital 2 reports were all free-text without a standardized structure. The manual annotators who read the report Impressions found that they differed stylistically between the hospitals.

NLP Model Performance

Random forest NLP classifier testing performance is summarized in the Online Supplemental Data. The stratified 5-fold cross-validation performance of the NLP classifier trained on the hospital 1 annotated dataset showed an average accuracy of 0.97 (95% CI, 0.96–0.97) and an F1 score of 0.74 (95% CI, 0.72–0.76). When this NLP classifier was tested on the hospital 2 annotated dataset,

the performance was lower, with an accuracy of 0.95 (95% CI, 0.94–0.96) and an F1 score of 0.66 (95% CI, 0.59–0.72). In both tests, when the performance results for CT and MR imaging were separately analyzed, we found that the model performed better for MR imaging reports compared with CT reports.

We also trained a random forest NLP classifier using the combined annotated reports from hospitals 1 and 2. In the stratified 5-fold cross-validation performance with testing of only hospital 1 data in the validation folds, the average accuracy was 0.96 (95% CI, 0.96-0.96) and the average F1 score was 0.74 (95% CI, 0.72–0.76). This performance on hospital 1 data was similar compared with the NLP classifier trained using only hospital 1 data. In the stratified 5-fold cross-validation performance with testing of only hospital 2 data in the validation folds, the average accuracy was 0.96 (95% CI, 0.96-0.97) and the average F1 score was 0.79 (95% CI, 0.77–0.80). This performance on hospital 2 data was substantially improved compared with the NLP classifier trained using only hospital 1 data. Because the performance on hospital 1 data was similar between the NLP classifier trained on hospital 1 reports and the NLP classifier trained on hospitals 1 and 2 reports, we used the former classifier for further analysis of the complete hospital 1 dataset.

For the NLP classifier trained on hospital 1 reports, in the 5 cross-validation folds for the combined CT and MR imaging analysis, there was an average of 19.4 (95% CI, 18.6–20.2) true-positive, 6.2 (95% CI, 5.6–6.8) false-positive, 7.6 (95% CI, 6.8–8.4) false-negative, and 364.2 (95% CI, 18.6–20.2) true-negative classifications. In misclassified cases, the reports typically contained uncertainty regarding the chronicity of the infarct (eg, age-indeterminate or not otherwise specified in the study Impression). For each of the 5 cross-validation folds, there was an average of 25.6 positive results predicted (95% CI, 24.6–26.8), compared with 27.0 actual positive results in each validation fold, due to the stratification on outcome. The NLP predicted that the number of cases slightly underestimated the actual number of studies positive for ASIS in the validation folds (average difference, −1.4; 95% CI, 0.2–2.4; expressed as percentages, −5.1%; 95% CI, 0–8.8%).

To ensure that variations in reporting styles within the hospital 1 reports did not systematically differ by year (because our epidemiologic analysis would compare reports from different years), we performed leave-one-year-out cross-validation on the hospital 1 dataset, in which NLP classifiers were trained on data from all years except the year of the excluded validation set (eg, trained on reports from 2018, 2019, and 2020, and then tested on reports from 2020). We found that there was no substantial difference in model performance in each of those validation folds (with overlap of 95% CI), which shows that the model performed similarly across time periods at hospital 1 (Online Supplemental Data). The F1 score was 0.72 in 2020 versus between 0.68 and 0.73 from 2017 to 2019.

While the NLP model systematically slightly underestimated ASIS case numbers, because the model performed similarly from year-to-year, we used this random forest classifier to estimate changes in the numbers of ASISs detected in the complete hospital 1 study cohort of 32,555 head CT and brain MR imaging reports.

Table 1: Natural language processing-based analysis of all radiology reports from hospital 1

Time Period	Total No. of Neuroimaging Studies Performed (CT/MRI)	Estimated No. of Neuroimaging Studies with ASIS Detected (% of Total)	Total No. of Patients Undergoing Neuroimaging	Estimated No. of Patients with ASIS Detected (% of Total)	No. of Neuroimaging Studies per Patient
March-April 2020 (COVID-19 pandemic)	5709	428 (7.4%)	3977	231 (5.8%)	1.4
March-April 2017–2019[a]	8949	541 (6.0%)	6312	304 (4.8%)	1.4
2019	9403	586 (6.2%)	6770	313 (4.6%)	1.4
2018	9086	523 (5.8%)	6417	302 (4.7%)	1.4
2017	8357	515 (6.2%)	5750	297 (5.1%)	1.5

[a] Three-year average.
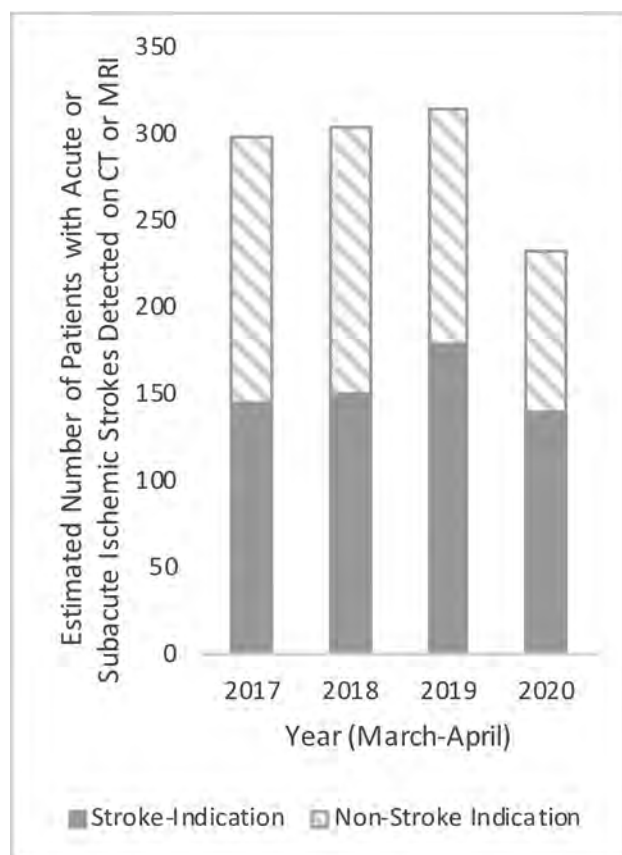
FIGURE. Estimated numbers of patients with acute or subacute ischemic strokes detected on CT or MR imaging in March and April from 2017 to 2020 at hospital 1.

ASIS during the COVID-19 Pandemic

Using this random forest NLP classifier, we estimated the number of neuroimaging studies performed and the number of patients with detected ASIS (Table 1). Patients with at least 1 neuroimaging study (CT or MR imaging) with an ASIS during the time period in question were considered to have had ASIS. There was an estimated 24% decrease in patients with ASIS reported on CT or MR imaging from March to April 2020 compared with the average of the same months from 2017 to 2019, after previous year-on-year growth from 2017 to 2019 (Figure). There was a concomitant decrease in the total number of neuroimaging studies performed and patients undergoing neuroimaging in March

and April 2020 compared with 2019 (−39% and −41%, respectively).

In the complete cohort of 32,555 study reports, 32,358 of the reports (99.4%) included structured and/or unstructured text in the study indication field, entered at the time of order entry. Of those cases, we filtered for indications including "stroke," "neuro deficit," and "TIA," which resulted in 5204 study reports (Table 2). In these patients, we found an estimated 21% decrease in ASIS reported from March to April 2020 compared with March to April 2019 (Figure). In the subset of patients who underwent imaging with stroke-related indications, the estimated proportion of patients with ASIS detected increased from 16% during 2017–2019 to 21% in 2020 ($P = .01$) (Table 2). The estimated proportion of neuroimaging studies with ASIS detected increased from 20% during 2017–2019 and 24% in 2020 ($P = .01$).

The average age of patients with ASIS detected was 66 [SD, 17] years, and there was no significant difference in age among any of the years ($P = .9$). There was also no significant difference in the sex ratio of March to April 2020 compared with the March to April 2017–2019 time periods ($P = .8$). In aggregate, 56% of patients with ASIS were men. See Online Supplemental Data for data by year.

Neuroimaging Studies Performed per Patient

If the number of neuroimaging studies performed per patient differed between the prepandemic and pandemic time periods, the number of opportunities to detect ASIS in a patient could vary. However, this variance did not appear to be a confounding factor in our analysis because we found no significant difference in the number of neuroimaging studies performed per patient between the March and April 2020 time period and each of the March to April 2017, 2018, or 2019 time periods ($P > .2$).

DISCUSSION

In this study, we developed a random forest NLP algorithm for automated classification of ASIS in radiology report Impressions and applied this algorithm to reports during and before the COVID-19 pandemic. We found a substantial decrease in the number of patients with ASIS detected on all CT and MR imaging studies performed at a comprehensive stroke center during the pandemic in the United States. This decrease could be related to avoidance of the hospital due to fear of contracting COVID-19, as previously speculated.[12,13] Previous studies have shown a 39% decrease in neuroimaging studies performed primarily for stroke thrombectomy evaluation using commercial software in

Table 2: NLP-based analysis of radiology reports from hospital 1 containing "stroke," "neuro deficit," or "TIA" in the order indication

Time Period	Total No. of Neuroimaging Studies Performed (CT/MRI)	Estimated No. of Neuroimaging Studies with ASIS Detected (% of Total)	Total No. of Patients Undergoing Neuroimaging	Estimated No. of Patients with ASIS Detected (% of Total)
March-April 2020 (COVID-19 pandemic)	1046	254 (24.3%)	660	140 (21.2%)
March-April 2017–2019[a]	1386	274 (19.8%)	970	157 (16.2%)
2019	1720	314 (18.3%)	1283	178 (13.9%)
2018	1234	253 (20.5%)	820	149 (18.2%)
2017	1204	256 (21.3%)	808	144 (17.8%)

[a] Three-year average.

the United States and a 59.7% decrease in stroke code CT-specific cases in New York.[3,4] Our study differs because we sought to quantify the decrease in actual ASISs detected on such studies and the rate of detection. Among patients with stroke-related image-order indication, we found a significant increase in the proportion of neuroimaging studies positive for ASIS. This finding could suggest that during the COVID-19 pandemic, imaged patients had, on average, more severe or clear-cut stroke syndromes (with a higher pretest probability of stroke), implying that patients with mild or equivocal symptoms presented to the hospital less often than in previous years.

The NLP machine learning approach that we used in this study can also be applied to additional data relatively easily, which will allow us to continue to monitor the detection of ASIS on neuroimaging at our institution in the future. NLP algorithms have been used to analyze neuroradiology reports for stroke findings, specifically for the presence of any ischemic stroke findings or ischemic stroke subtypes.[8,9] The task in our model, however, is relatively challenging in that we sought to identify acute or subacute strokes specifically and deliberately excluded chronic infarcts. There is often uncertainty or ambiguity in radiology reports related to the timeframe for strokes, which can make this task challenging for the NLP algorithm. Thus, it is not surprising that our NLP model performed better on MR imaging reports compared with CT reports, given the superiority of MR imaging for characterizing the age of an infarct.

The NLP classifier trained on only hospital 1 reports showed lower performance when tested on radiology reports from an external site, which was likely due to systematic differences in linguistic reporting styles between the radiology departments in hospitals 1 and 2. While combining training data from hospitals 1 and 2 helped to create a more generalizable classifier with improved performance on hospital 2 data, the test performance of this classifier on data from hospital 1 was not substantially different from the classifier trained on only hospital 1 data. These findings highlight the importance of localized testing of NLP algorithms before clinical deployment. Nevertheless, a locally trained and deployed model can still be useful, as long as its specific use case and limitations are understood.[14]

Instead of using the radiology report NLP approach presented in our study, we could have used the International Classification of Diseases codes from hospital administrative and billing data. However, the International Classification of Diseases coding is known to have variable sensitivity and specificity for acute stroke

in the literature[15] and may be particularly problematic for reliably differentiating stroke chronicity. Comparison of NLP analyses of radiology reports versus administrative data base International Classification of Diseases coding could be an avenue of future research.

There are important limitations to this study. First, we used an automated NLP approach for analysis, which systematically slightly underestimates the number of ASISs but may be scaled to analyze large numbers of reports. In the future, newer NLP technologies including deep learning–based algorithms may help improve the ability to perform studies like this one.[16] Second, the radiology report is an imperfect reference standard for assessment of ASIS, particularly for CT in which early infarcts may not be seen. In our epidemiologic analysis, patients with at least 1 neuroimaging study with ASIS during the time period of interest were counted as having ASIS. Thus, patients with early infarcts not reported on CT would still be counted as having ASIS if reported on the subsequent MR imaging, reducing the impact of false-negative CTs. However, false-positive head CTs would falsely elevate the count of ASIS. Third, identification of studies with stroke-related indications likely underestimates the total number of studies performed for suspicion of stroke because nonspecific indications like "altered mental status" were not included. This bias should be consistent across each year though; thus, it should not impact our comparison of the positive case rate between the time periods in question.

CONCLUSIONS

We developed an NLP machine learning model to characterize trends in stroke imaging at a comprehensive stroke center before and during the COVID-19 pandemic. The sequelae of decreased detection of strokes remains to be seen, but this algorithm and the shared code can help facilitate future research of these trends.

REFERENCES

1. Leira EC, Russman AN, Biller J, et al. **Preserving stroke care during the COVID-19 pandemic: potential issues and solutions.** *Neurology* 2020;95:124–33 CrossRef Medline

2. Markus HS, Brainin M. **COVID-19 and stroke: a global World Stroke Organization perspective.** *Int J Stroke* 2020;15:361–64 CrossRef Medline

3. Phillips CD, Shatzkes D, Moonis G, et al. **From the eye of the storm: multi-institutional practical perspectives on neuroradiology from the COVID-19 outbreak in New York City.** *AJNR Am J Neuroradiol* 2020;41:960–65 CrossRef Medline

4. Kansagra AP, Goyal MS, Hamilton S, et al. **Collateral effect of Covid-19 on stroke evaluation in the United States.** *N Engl J Med* 2020;383:400–01 CrossRef Medline

5. Mahammedi A, Saba L, Vagal A, et al. **Imaging in neurological disease of hospitalized COVID-19 patients: an Italian multicenter retrospective observational study.** *Radiology* 2020;297:E270–73 CrossRef Medline

6. Jain R, Young M, Dogra S, et al. **COVID-19 related neuroimaging findings: a signal of thromboembolic complications and a strong prognostic marker of poor patient outcome.** *J Neurol Sci* 2020;414:116923 CrossRef Medline

7. Pons E, Braun LM, Hunink MG, et al. **Natural language processing in radiology: a systematic review.** *Radiology* 2016;279:329–43 CrossRef Medline

8. Wheater E, Mair G, Sudlow C, et al. **A validated natural language processing algorithm for brain imaging phenotypes from radiology reports in UK electronic health records.** *BMC Med Inform Decis Mak* 2019;19:184 CrossRef Medline

9. Garg R, Oh E, Naidech A, et al. **Automating ischemic stroke subtype classification using machine learning and natural language processing.** *J Stroke Cerebrovasc Dis* 2019;28:2045–51 CrossRef Medline

10. Hassanpour S, Langlotz CP, Amrhein TJ, et al. **Performance of a machine learning classifier of knee MRI reports in two large academic radiology practices: a tool to estimate diagnostic yield.** *AJR Am J Roentgenol* 2017;208:750–73 CrossRef Medline

11. Efron B, Tibshirani RJ. *An Introduction to the Bootstrap*. Chapman & Hall/CRC; 1994

12. Oxley TJ, Mocco J, Majidi S, et al. **Large-vessel stroke as a presenting feature of Covid-19 in the young.** *N Engl J Med* 2020;382:e60 CrossRef Medline

13. Zhao J, Rudd A, Liu R. **Challenges and potential solutions of stroke care during the coronavirus disease 2019 (COVID-19) outbreak.** *Stroke* 2020;51:1356–57 CrossRef Medline

14. Futoma J, Simons M, Panch T, et al. **The myth of generalisability in clinical research and machine learning in health care.** *Lancet Digit Heal* 2020;2:e489–92 CrossRef Medline

15. McCormick N, Bhole V, Lacaille D, et al. **Validity of diagnostic codes for acute stroke in administrative databases: a systematic review.** *PLoS One* 2015;10:e0135834 CrossRef Medline

16. Wolf T, Debut L, Sanh V, et al. **HuggingFace's Transformers: State-of-the-art Natural Language Processing.** Oct 9, 2019. https://arxiv.org/abs/1910.03771. Accessed June 15, 2020.

CTA Protocols in a Telestroke Network Improve Efficiency for Both Spoke and Hub Hospitals

A.T. Yu, R.W. Regenhardt, C. Whitney, L.H. Schwamm, A.B. Patel, C.J. Stapleton, A. Viswanathan, J.A. Hirsch, M. Lev, and T.M. Leslie-Mazwi

ABSTRACT

BACKGROUND AND PURPOSE: Telestroke networks support screening for patients with emergent large-vessel occlusions who are eligible for endovascular thrombectomy. Ideal triage processes within telestroke networks remain uncertain. We characterize the impact of implementing a routine spoke hospital CTA protocol in our integrated telestroke network on transfer and thrombectomy patterns.

MATERIALS AND METHODS: A protocol-driven CTA process was introduced at 22 spoke hospitals in November 2017. We retrospectively identified prospectively collected patients who presented to a spoke hospital with National Institutes of Health Stroke Scale scores ≥6 between March 1, 2016 and March 1, 2017 (pre-CTA), and March 1, 2018 and March 1, 2019 (post-CTA). We describe the demographics, CTA utilization, spoke hospital retention rates, emergent large-vessel occlusion identification, and rates of endovascular thrombectomy.

RESULTS: There were 167 patients pre-CTA and 207 post-CTA. The rate of CTA at spoke hospitals increased from 15% to 70% ($P < .001$). Despite increased endovascular thrombectomy screening in the extended window, the overall rates of transfer out of spoke hospitals remained similar (56% versus 54%; $P = .83$). There was a nonsignificant increase in transfers to our hub hospital for endovascular thrombectomy (26% versus 35%; $P = .12$), but patients transferred >4.5 hours from last known well increased nearly 5-fold (7% versus 34%; $P < .001$). The rate of endovascular thrombectomy performed on patients transferred for possible endovascular thrombectomy more than doubled (22% versus 47%; $P = .011$).

CONCLUSIONS: Implementation of CTA at spoke hospitals in our telestroke network was feasible and improved the efficiency of stroke triage. Rates of patients retained at spoke hospitals remained stable despite higher numbers of patients screened. Emergent large-vessel occlusion confirmation at the spoke hospital lead to a more than 2-fold increase in thrombectomy rates among transferred patients at the hub.

ABBREVIATIONS: EVT = endovascular thrombectomy; LKW = last known well; SH = spoke hospital; ELVO = emergent large-vessel occlusion; LVO = large-vessel occlusion; NIHSS = National Institutes of Heath Stroke Scale

Telestroke supports thrombolytic use and screening for patients with emergent large-vessel occlusion (ELVO) across stroke systems of care.[1-3] ELVOs represent a minority of acute stroke presentations but produce most morbidity and

mortality in ischemic stroke and are therefore a critical area of focus within stroke care systems.[4-6] For patients with ELVO, the current target of acute stroke therapy is penumbral salvage, which relies on numerous factors, the most important of which is timely reperfusion.[7-9] The powerful therapeutic effect of early reperfusion (<6 hours from last known well [LKW]) through endovascular thrombectomy (EVT) for patients with ELVO is now well established.[10-12] The time window for treatment expanded with the demonstration of benefit of reperfusion in patients between 6 and 24 hours from LKW, a demographic for which previously no therapeutic intervention was available.[13-14] Selection for thrombectomy in both early and late treatment windows required identification of ELVO by noninvasive imaging in all recent trials.

The expansion of treatment with EVT up to 24 hours from LKW has dramatically increased the pool of patients to screen. Current telestroke care system approaches require the emergent

transfer of patients from spoke hospitals (SHs), which lack the ability to perform thrombectomy, to hub hospitals, which are thrombectomy capable. Ideal triage processes within telestroke networks remain uncertain and may vary based on geographic region. Here we describe the effects of the implementation of a routine SH CTA protocol within our integrated telestroke network on SH retention rates and hub hospital thrombectomy rates.

MATERIALS AND METHODS

We introduced a protocol-driven CTA process at 22 SHs within our telestroke network in the northeastern United States in November 2017. The CTA protocol specified CTA indications, acquisition parameters, and methods for image reconstruction (Supplemental Online Data) to provide a standardized imaging approach across the telestroke network. Before this CTA protocol, in the pre-CTA era, transfer for EVT consideration occurred mainly driven by stroke severity (NIHSS score ≥6 points), time from LKW (≤6 hours), ASPECTS score ≥6 on noncontrast CT, and mRS score 0–2, based primarily on the American Heart Association guidelines at that time.[15] After implementation of the protocol, the post-CTA era, all patients presenting to an SH with NIHSS score ≥6 points and <24 hours from LKW were required to undergo CTA imaging in addition to and immediately after their noncontrast head CT. Head and neck CTA with reconstruction of thick, overlapping axial MIPs was a requirement in the protocol. Additional imaging suggested by the protocol but at the discretion of the site included CTA delays of the head and neck and sagittal and/or coronal MIPs. After acquisition, this imaging was shared through a cloud-based platform between the SH and the hub. Additional criteria for transfer for EVT consideration in the post-CTA era were based on updated guidelines and included ASPECTS score ≥6 and mRS score 0–2.[16]

We retrospectively identified patients who presented to an SH with NIHSS scores ≥6 points between March 1, 2016 and March 1, 2017 (pre-CTA), and between March 1, 2018 and March 1, 2019 (post-CTA). A 1-year gap between our pre-CTA and post-CTA cohorts was used to allow enough time for uniform adoption of the CTA protocol across all SHs. Patients were identified through our telestroke consult log, which records consecutive telestroke consults placed within our network. Within each cohort, we analyzed baseline demographics, risk factors, CTA utilization, ELVO identification, and transfer to a hub hospital. We defined off-hour telestroke utilization as a consult start time between 7 PM and 7 AM regardless of the day of the week. We obtained patient demographic and risk factor data from our telestroke log and our hub hospital electronic medical record. CTA utilization was determined by telestroke consult log documentation because most SHs used a separate electronic medical record, which we did not have access to; for this reason, we were unable to include reliable door-in and door-out times. Patients with CTA recommended but not documented were defined as not undergoing CTA imaging. An ELVO was confirmed if vessel imaging performed at the SH showed an occlusion in the intracranial ICA, MCA M1 segment, proximal M2 segment, or basilar artery with NIHSS score ≥6 points and LKW <24 hours. Tandem lesions involving cervical ICA stenosis or occlusion with an intracranial occlusion were

Table 1: Patient demographics pre- and post-CTA protocol implementation[a]

	Pre-CTA, n = 167 (%)	Post-CTA, n = 207 (%)	P Value
Characteristics			
Age, median (IQR)	76 (63, 85)	71 (57, 82)	.066
Female sex	88 (53)	113 (55)	.755
White race	151 (90)	88 (84)	.127
Risk factors			
Atrial fibrillation	54 (32)	50 (24)	.083
Coronary artery disease	42 (25)	28 (14)	.005
Diabetes mellitus	26 (16)	46 (22)	.115
Dyslipidemia	43 (26)	53 (26)	1.000
Heart failure	12 (7)	15 (7)	1.000
Hypertension	85 (51)	100 (48)	.677
Previous stroke or TIA	41 (25)	59 (29)	.413
Smoking	8 (5)	18 (9)	.101

[a] Count and percent are reported. For age, median and IQR are reported.

included.[17] We defined late-window patients as >4.5 hours from LKW to consult start time at the SH; this equated to roughly >6 hours at the time of arrival to an EVT capable center, allowing 1.5 hours for time for the evaluation and transport of the patient. For patients transferred to our hub, we analyzed rates of additional imaging after arrival, EVT, and utilization of a direct-to-EVT protocol, which allowed transferred patients with confirmed ELVO to bypass both the emergency department and further imaging to proceed directly to the endovascular suite for thrombectomy. The overall rate of large-vessel occlusion (LVO) transferred was defined as the total number of LVOs identified at the SH in addition to LVOs identified at the hub that were not previously identified at the SH among patients transferred to the hub hospital.

This study was approved by the local institutional review board. Median and interquartile range were reported for continuous variables. Percent and count were reported for categoric variables. Differences were assessed by using nonparametric Wilcoxon rank-sum for continuous variables and Fisher exact tests for categoric variables. Two-tailed P values <.05 were interpreted as statistically significant. Analyses were performed with SPSS version 23.0 (IBM). The data that support the findings of this study are available from the corresponding author upon request.

RESULTS

There were 167 patients pre-CTA and 207 patients post-CTA from 22 SHs. These cohorts were broadly similar (Table 1). The median ages in the pre-CTA and post-CTA groups were 76 years and 71 years, respectively ($P = .066$). Most patients were white (88%). There were no differences in risk factors between the 2 groups, with the exception of coronary artery disease (25% pre-CTA versus 14% post-CTA; $P = .005$). The proportion of off-hour consults was similar at approximately 30%. The median NIHSS score was 12 points for both groups, and no significant differences in rates of tPA administration were present (Table 2). There were fewer than 5 posterior circulation LVOs in each cohort.

The rate of CTA utilization at SHs increased significantly from 25/167 (15%) to 144/207 (70%) ($P < .001$) (Table 2). Three

patients in the pre-CTA group had MRA rather than CTA. Reasons for not obtaining a CTA in the post-CTA cohort included known allergy to iodinated contrast (5 patients), renal dysfunction (4 patients), technical difficulties (3 patients; 1 unclear reasons, 1 lack of radiology technicians overnight, and 1 inability to obtain intravenous access), high suspicion for an alternative diagnosis (13 patients, including seizure, toxic-metabolic encephalopathy, or functional neurologic disorder), and determination of EVT ineligibility based on other factors (1 patient). Technical difficulties preventing CTA acquisition represented only 1.4% of cases after protocol implementation. The rates of late-window (>4.5 hours from LKW) consults also increased significantly from 14/167 (8%) to 42/207 (20%) (P = .001). Despite increased screening of patients in this late window, the rates of patient transfer out of SHs remained stable (93/167, 56% versus 112/207, 54%; P = .83). This rate of transfer encompasses patients with ELVO who were transferred to another thrombectomy-capable center, as well as patients transferred to our center for other reasons, including seeking a higher level of care, such as a neurologic intensive care unit, seeking care for a nonstroke diagnosis, or to complete a stroke work-up. The rate of transfer to our hub hospital specifically for EVT showed a nonsignificant increase (46/167, 26% versus 73/207, 35%; P = .119), but the proportion of patients transferred in the late window increased nearly 5-fold (3/46, 7% versus 25/73, 34%; P < .001). Of those transferred to our hub hospital as ELVO, the overall LVO identification rate, whether imaged at the SH or hub, increased (67% to 93%; P = .001) (Table 3). Furthermore,

there was a decrease in the need for repeat imaging at our hub hospital (43/46, 94% versus 48/73, 66%; P < .001). For the 48 patients in the post-CTA cohort who required repeat imaging, 34/48 (71%) required imaging to confirm mismatch before proceeding with late-window thrombectomy. A total of 24/34 (71%) were already considered late window by our criteria before transfer, and 10/34 (29%) were considered early window. Repeat imaging was required in 3/48 (6%) cases for worsening NIHSS score. The most common technique for repeat imaging was MR imaging with or without MRA in 42/48 (88%). In the pre-CTA cohort, 14/46 patients (30%) without a CTA at the SH were transferred to our center for EVT evaluation but were not found have an LVO on their hub hospital CTA or MRA imaging. The overall rate of EVT performed on patients transferred to our hub for possible EVT more than doubled (10/46, 22% to 34/73, 47%; P = .011). In the post-CTA cohort, 20/73 (27%) of transferred patients were processed via our direct-to-EVT protocol (this protocol was introduced in December 2017 and therefore did not exist in the pre-CTA era).

Our post-CTA cohort spanned a timeframe after which the late-window thrombectomy trials were published and the potential pool of EVT candidates was increased. Given these differences, to better compare our 2 cohorts, we performed sensitivity analyses based on the early-window patients. The transfer rate was nonsignificantly decreased after implementation of the CTA protocol (88/153, 57% to 84/164, 51%; P = .26). The decrease in repeat imaging after transfer was notably even greater for patients transferred in the early window (39/43, 91% versus 24/48, 50%; P < .001). The rate of EVT performed at our center for patients in the early window increased significantly (9/43, 21% to 25/48, 52%; P = .004).

DISCUSSION

These findings demonstrate the successful implementation of a systematic CTA protocol performed at SHs within our telestroke network and its impact on SH retention rates and hub hospital EVT rates. Implementation of a CTA protocol proved feasible. Provision to SHs of a standardized imaging protocol and the use of cloud-based image sharing proved useful in maintaining image quality across the network. The rate of CTA utilization at SHs increased from 15% to 70% during the study period, with multiple gains in system efficiency.

Most patients with acute ischemic strokes, including ELVOs, present to nonthrombectomy-capable hospitals.[11] Telestroke networks therefore have a crucial role in not only delivering care, including thrombolytics, but also quickly and cost-effectively triaging patients who may need EVT.[1] The ideal triage system is uncertain, and debate remains regarding different triage strategies, which likely depend on geographic region.[18] A persistent challenge is the low rates of ELVO among general stroke presentations.[19] Currently, randomized trials are evaluating the triage option of bypassing the SH for patients whom emergency first responders in the field suspect harbor an ELVO.[20-22] The possibility of SH bypass, though promising, has raised

Table 2: Clinical, imaging, and transfer variables pre- and post-CTA protocol implementation[a]

	Pre-CTA, n = 167 (%)	Post-CTA, n = 207 (%)	P Value
NIHSS score at SH (IQR)	12 (8–19)	12 (8–18)	.678
Late window	14 (8)	42 (20)	.001
Off hours (7 PM–7 AM)	53 (32)	61 (30)	.653
CTA performed at SH	25 (15)[b]	144 (70)	< .001
LVO identified at SH	13 (8)	81 (39)	< .001
tPA administered at SH	93 (60)	96 (68)	.185
Transferred to hub hospital	46 (26)	73 (35)	.119
Retained at SH	74 (44)	95 (46)	.834
Retained at SH, of those in early window	65 (43)	81 (49)	.260

[a] Count and percent are reported.
[b] Includes 3 patients who underwent MRA. Late window was defined as >4.5 hours from LKW at telestroke consult start time.

Table 3: Processing of transferred patients at the hub hospital[a]

	Pre-CTA, n = 46 (%)	Post-CTA, n = 73 (%)	P Value
Late window	3 (7)	25 (34)	< .001
Overall LVO transferred to hub	31 (67)	68 (93)	.001
Repeat imaging, overall	43 (94)	48 (66)	< .001
Repeat imaging, early window	39 (91)	24 (50)	< .001
Direct-to-EVT protocol utilization	0	20 (27)	< .001
Received EVT, overall	10 (22)	34 (47)	.011
Received EVT, early window	9 (21)	25 (52)	.004

[a] Repeat hub imaging, direct-to-EVT protocol utilization, and EVT for patients transferred to our institution from an SH with NIHSS scores ≥6 points for consideration of EVT.

concerns regarding care quality at both SHs (decreased patient volumes and local expertise) and hub hospitals (excessive patient volumes straining resources).[18,23] The expansion of the treatment window for thrombectomy to 24 hours raises further unique concerns with triage, given the expanded pool of patients to be evaluated for a progressively smaller number of treatment candidates.[24]

One potential system solution is to refine triage at the level of the SH by improved identification of patients with ELVO. This refinement and reinforcement of existing care models seeks to improve overall system efficiency. A primary reason patients transferred to a hub hospital for EVT do not ultimately undergo thrombectomy is that no ELVO is present despite a suggestive clinical presentation.[25-27] This was confirmed in our pre-CTA cohort in which one-third of patients transferred to our hub did not have an LVO. Identifying which patients do not require EVT while still at the SH represents, therefore, a potential intervention in the evolution of stroke care systems. Although several available imaging modalities exist, ELVO identification is most accurately accomplished by using CTA because of both rapid image acquisition and high sensitivity and specificity.[28] Triage with CTA at the level of the SH allows stroke care to remain local for patients without ELVO while transporting confirmed patients with ELVO to appropriately enabled care environments. The impact of CTA for all patients with stroke is being increasingly defined at thrombectomy capable centers. A health system in Detroit expanded CTA imaging to all patients with stroke after previously reserving it for patients with NIHSS scores ≥6 points.[29] CTA scanning for all suspected patients with stroke led to increased rates of ELVO detection, increased mechanical thrombectomy treatment, and a possible trend toward improved outcomes in that system (a single comprehensive stroke center hub and 8 associated hospitals). By comparison, this present study is novel in describing the effects of CTA triage in SHs within an entire, widely distributed telestroke network where CTA imaging had not been routinely performed previously.

The long-term effects of late-window EVT trials on telestroke networks remain unknown. Our findings indicate an expansion of the pool of candidates evaluated, driven predominantly by the large increase in late-window candidates. However, despite the additional patients screened in the post-CTA cohort, the overall rate of transfers from SHs was similar (56% versus 54%). This is noteworthy given the anticipated higher transfer numbers based on clinical grounds alone that are expected with the expansion of the thrombectomy window to 24 hours. In the pre-CTA era, patients >6 hours from onset would have been deemed nonthrombectomy candidates. With the expanded window, these patients would be expected to transfer for evaluation for thrombectomy if clinical criteria alone were used. The use of CTA at SHs allowed screening at the source to select appropriate candidates from this larger pool. CTA application demonstrated a trend toward decreasing transfers in the early window after the protocol was implemented (57% versus 51%), but concurrently, rates of patients transferred to our center >4.5 hours from LKW increased nearly 5-fold as extended-window evaluation was increasingly implemented across the SH network. The decrease in futile transfers therefore helped balance the expected rise in

transfers to keep the retention rate stable in the pre- and post-CTA periods. We anticipate the proportion of late-window transfers to continue to increase with increasing awareness regarding late-window therapy for patients with ELVO and with revisions to existing SH emergency protocols.

Patients with ELVO require specialized attention, which in addition to EVT may include support in a neurologic critical care unit or open surgical interventions (hemicraniectomy or suboccipital craniectomy). Comprehensive stroke centers, such as hub hospitals in telestroke networks, are best equipped to manage these patients.[30,31] The rates of EVT performed on transferred patients more than doubled from 22% pre-CTA to 47% in the post-CTA cohort. This finding was also observed when analyzing early-window patients alone (21% versus 52%), supporting the fact that this was not driven by the increase in late-window patients. Reduction in false activation of the EVT treatment team represents appreciable resource conservation for the hub hospital. In addition, the need for repeat imaging was decreased as ELVO status was established before hub hospital arrival, allowing the use of direct-to-EVT protocols that have been proved to save time in other practice settings.[32,33] This was true for 27% of our transferred population undergoing thrombectomy. For patients in the early window, CTA at the SH represents a task shifted from the hub hospital, often obviating the need for imaging at the hub if transfer occurs expeditiously. Accelerating transfer between SH and hub ensures that imaging performed at the SH is temporally relevant to hub hospital treatment decisions. For late-window patients, although CTA screens for the presence of ELVO, it does not provide the additional information necessary for guideline-based treatment decisions (core volume, perfusion deficit, mismatch volume, and so on).[16,34] These patients therefore require additional imaging on arrival at the hub.

The ability to shift imaging tasks from the hub to the SH has additional implications for future efforts in ELVO triage and EVT selection. Automation of stroke imaging, already established for CT perfusion, shows nascent promise for ELVO detection and other components of stroke imaging.[35-37] The role of this software in the SH environment may expand with time and remains to be explored as the software becomes more available, affordable, and refined. The implications for automation and coordination of triage in a stroke system of care may be large, with telestroke networks well poised to pioneer these approaches.

There are several limitations to our study, mostly related to its retrospective design. The late-window thrombectomy trials, which resulted in more patients being eligible for EVT and in an increasing awareness of ELVOs, were published before our post-CTA cohort. However, our sensitivity analyses included only patients in the early window, thereby making the cohorts more comparable, and did not change interpretation of the results. We relied on data that were available in clinical documentation. Furthermore, we selected an NIHSS score threshold of 6 points at the SH based on our clinical practice and guideline recommendations but recognize some patients with ELVOs may have had NIHSS scores <6 points and may not be captured in these data.[29] A limited number of patients with high NIHSS scores or ELVOs were transferred to other thrombectomy centers, and we do not

have details about what proportion of these patients later had confirmed ELVOs or underwent EVT. We focus on system processes and therefore do not detail patient outcomes because of limitations in data available in both the pre-CTA cohort and for patients with confirmed ELVOs transferred to other centers.

Finally, although we successfully implemented a CTA protocol at SHs, we are unable to compare time metrics at SHs, such as door-in-door-out and transport times, because SHs used a separate electronic medical record, and documentation of these metrics was not a requisite in our telestroke log or consistent in available documentation. Acquisition of the CTA immediately after the head CT without returning the patient to the emergency department is an important part of the CTA imaging protocol to ensure time savings, but implications for tPA delivery times remain to be explored. However, we present a practical and real-world experience that details the response to SH imaging triage in a telestroke network.

CONCLUSIONS

CTA application in a standardized fashion to the imaging protocols of SHs in a large telestroke network was feasible. Adoption was high within 1 year of protocol implementation and added important additional screening information for potential patients with ELVO at SHs. A standardized CTA protocol at SHs was associated with increased telestroke network efficiency by increasing the proportion of transferred patients who undergo EVT, thereby decreasing futile transfers. The retention rate for SHs remained relatively stable despite higher numbers of patients screened (partly caused by a 5-fold expansion of late-window candidates). For 27% of transferred patients undergoing thrombectomy, this shift in imaging confirmation to the SH enabled a direct-to-EVT protocol, eschewing emergency department evaluation and further imaging at the hub hospital. Future evaluation for such system evolutions will include analysis of transfer times and an economic analysis of the economic consequences. Continued research to identify optimized triage in stroke care systems is needed.

REFERENCES

1. Akbik F, Hirsch JA, Chandra RV, et al. **Telestroke—the promise and the challenge. Part one: growth and current practice.** *J Neurointerv Surg* 2017;9:357–60 CrossRef Medline

2. Akbik F, Hirsch JA, Chandra RV, et al. **Telestroke—the promise and the challenge. Part two—expansion and horizons.** *J Neurointerv Surg* 2017;9:361–65 CrossRef Medline

3. Leslie-Mazwi T, Chandra RV, Baxter BW, et al. **ELVO: an operational definition.** *J Neurointerv Surg* 2018;10:507–09 CrossRef Medline

4. Malhotra K, Gornbein J, Saver JL. **Ischemic strokes due to large-vessel occlusions contribute disproportionately to stroke-related dependence and death: a review.** *Front Neurol* 2017;8:651 CrossRef Medline

5. Regenhardt RW, Takase H, Lo EH, et al. **Translating concepts of neural repair after stroke: structural and functional targets for recovery.** *Restor Neurol Neurosci* 2020;38:67–92 CrossRef Medline

6. Regenhardt RW, Biseko MR, Shayo AF, et al. **Opportunities for intervention: stroke treatments, disability and mortality in urban Tanzania.** *Int J Qual Health Care* 2019;31:385–92 CrossRef Medline

7. Sheth SA, Jahan R, Gralla J, et al. **Time to endovascular reperfusion and degree of disability in acute stroke.** *Ann Neurol* 2015;78:584–93 CrossRef Medline

8. Jahan R, Saver JL, Schwamm LH, et al. **Association between time to treatment with endovascular reperfusion therapy and outcomes in patients with acute ischemic stroke treated in clinical practice.** *JAMA* 2019;322:252–63 CrossRef Medline

9. Regenhardt RW, Das AS, Stapleton CJ, et al. **Blood pressure and penumbral sustenance in stroke from large vessel occlusion.** *Front Neurol* 2017;8:317 CrossRef Medline

10. Seners P, Turc G, Naggara O, et al. **Post-thrombolysis recanalization in stroke referrals for thrombectomy: incidence, predictors, and prediction scores.** *Stroke* 2018;49:2975–82 CrossRef Medline

11. Katz BS, Adeoye O, Sucharew H, et al. **Estimated impact of emergency medical service triage of stroke patients on comprehensive stroke centers: an urban population-based study.** *Stroke* 2017;48:2164–70 CrossRef Medline

12. Goyal M, Menon BK, van Zwam WH, et al. **Endovascular thrombectomy after large-vessel ischaemic stroke: a meta-analysis of individual patient data from five randomised trials.** *Lancet* 2016;387:1723–31 CrossRef Medline

13. Albers GW, Marks MP, Kemp S, et al. **Thrombectomy for stroke at 6 to 16 hours with selection by perfusion imaging.** *N Engl J Med* 2018;378:708–18 CrossRef Medline

14. Nogueira RG, Jadhav AP, Haussen DC, et al. **Thrombectomy 6 to 24 hours after stroke with a mismatch between deficit and infarct.** *N Engl J Med* 2018;378:11–21 CrossRef Medline

15. Jauch EC, Saver JL, Adams HP Jr, et al. **Guidelines for the early management of patients with acute ischemic stroke: a guideline for healthcare professionals from the American Heart Association/American Stroke Association.** *Stroke* 2013;44:870–947 CrossRef Medline

16. Powers WJ, Rabinstein AA, Ackerson T, et al. **Guidelines for the Early Management of Patients With Acute Ischemic Stroke: 2019 Update to the 2018 Guidelines for the Early Management of Acute Ischemic Stroke: A Guideline for Healthcare Professionals From the American Heart Association/American Stroke Association.** *Stroke* 2019;50:e344–418 CrossRef Medline

17. Nolan NM, Regenhardt RW, Koch MJ, et al. **Treatment Approaches and Outcomes for Acute Anterior Circulation Stroke Patients with Tendem Lesions.** *J Stroke Cerebrovasc Dis* 2021;30:105478 CrossRef Medline

18. Southerland AM, Johnston KC, Molina CA, et al. **Suspected large vessel occlusion: should emergency medical services transport to the nearest primary stroke center or bypass to a comprehensive stroke center with endovascular capabilities?** *Stroke* 2016;47:1965–67 CrossRef Medline

19. Raychev RI, Stradling D, Patel N, et al. **Evolution of a US county system for acute comprehensive stroke care.** *Stroke* 2018;49:1217–22 CrossRef Medline

20. Froehler MT, Saver JL, Zaidat OO, et al. **Interhospital transfer before thrombectomy is associated with delayed treatment and worse outcome in the STRATIS Registry (Systematic Evaluation of Patients Treated With Neurothrombectomy Devices for Acute Ischemic Stroke).** *Circulation* 2017;136:2311–21 CrossRef Medline

21. Abilleira S, Perez de la Ossa N, Jimenez X, et al. **Transfer to the Local Stroke Center versus Direct Transfer to Endovascular Center of Acute Stroke Patients with Suspected Large Vessel Occlusion in the Catalan Territory (RACECAT): study protocol of a cluster randomized within a cohort trial.** *Int J Stroke* 2019;14:734–44 CrossRef Medline

22. Behrndtz A, Johnsen SP, Valentin JB, et al. **TRIAGE-STROKE: Treatment strategy In Acute larGE vessel occlusion: prioritize IV or endovascular treatment—a randomized trial.** *Int J Stroke* 2020;15:103–08 CrossRef Medline

23. Reznek MA, Murray E, Youngren MN, et al. **Door-to-imaging time for acute stroke patients is adversely affected by emergency department crowding.** *Stroke* 2017;48:49–54 CrossRef Medline

24. Adeoye O, Nystrom KV, Yavagal DR, et al. **Recommendations for the establishment of stroke systems of care: a 2019 update.** *Stroke* 2019;50:e187–210 CrossRef Medline

25. Leslie-Mazwi TM, Hirsch JA, Falcone GJ, et al. **Endovascular stroke treatment outcomes after patient selection based on magnetic resonance imaging and clinical criteria.** *JAMA Neurol* 2016;73:43–49 CrossRef Medline

26. Yi J, Zielinski D, Ouyang B, et al. **Predictors of false-positive stroke thrombectomy transfers.** *J NeuroIntervent Surg* 2017;9:834–36 CrossRef Medline

27. Regenhardt RW, Mecca AP, Flavin SA, et al. **Delays in the air or ground transfer of patients for endovascular thrombectomy.** *Stroke* 2018;49:1419–25 CrossRef Medline

28. Verro P, Tanenbaum LN, Borden NM, et al. **CT angiography in acute ischemic stroke: preliminary results.** *Stroke* 2002;33:276–78 CrossRef Medline

29. Mayer SA, Viarasilpa T, Panyavachiraporn N, et al. **CTA-for-all: impact of emergency computed tomographic angiography for all patients with stroke presenting within 24 hours of onset.** *Stroke* 2020;51:331–34 CrossRef Medline

30. Ali SF, Singhal AB, Viswanathan A, et al. **Characteristics and outcomes among patients transferred to a regional comprehensive stroke center for tertiary care.** *Stroke* 2013;44:3148–53 CrossRef Medline

31. Meretoja A, Roine RO, Kaste M, et al. **Effectiveness of primary and comprehensive stroke centers: PERFECT stroke: a nationwide observational study from Finland.** *Stroke* 2010;41:1102–07 CrossRef Medline

32. Jadhav AP, Kenmuir CL, Aghaebrahim A, et al. **Interfacility transfer directly to the neuroangiography suite in acute ischemic stroke patients undergoing thrombectomy.** *Stroke* 2017;48:1884–89 CrossRef Medline

33. Mendez B, Requena M, Aires A, et al. **Direct transfer to angio-suite to reduce workflow times and increase favorable clinical outcome.** *Stroke* 2018;49:2723–27 CrossRef Medline

34. Saposnik G, Menon BK, Kashani N, et al. **Factors associated with the decision-making on endovascular thrombectomy for the management of acute ischemic stroke.** *Stroke* 2019;50:2441–47 CrossRef Medline

35. Vagal A, Wintermark M, Nael K, et al. **Automated CT perfusion imaging for acute ischemic stroke: pearls and pitfalls for real-world use.** *Neurology* 2019;93:888–98 CrossRef Medline

36. Amukotuwa SA, Straka M, Dehkharghani S, et al. **Fast automatic detection of large vessel occlusions on CT angiography.** *Stroke* 2019;50:3431–38 CrossRef Medline

37. Feng R, Badgeley M, Mocco J, et al. **Deep learning guided stroke management: a review of clinical applications.** *J Neurointerv Surg* 2018;10:358–62 CrossRef Medline

Regional and Volumetric Parameters for Diffusion-Weighted WHO Grade II and III Glioma Genotyping: A Method Comparison

S.C. Thust, J.A. Maynard, M. Benenati, S.J. Wastling, L. Mancini, Z. Jaunmuktane, S. Brandner, and H.R. Jäger

ABSTRACT

BACKGROUND AND PURPOSE: Studies consistently report lower ADC values in *isocitrate dehydrogenase* (*IDH*) wild-type gliomas than in *IDH* mutant tumors, but their methods and thresholds vary. This research aimed to compare volumetric and regional ADC measurement techniques for glioma genotyping, with a focus on *IDH* status prediction.

MATERIALS AND METHODS: Treatment-naïve World Health Organization grade II and III gliomas were analyzed by 3 neuroradiologist readers blinded to tissue results. ADC minimum and mean ROIs were defined in tumor and in normal-appearing white matter to calculate normalized values. T2-weighted tumor VOIs were registered to ADC maps with histogram parameters (mean, 2nd and 5th percentiles) extracted. Nonparametric testing (eta^2 and ANOVA) was performed to identify associations between ADC metrics and glioma genotypes. Logistic regression was used to probe the ability of VOI and ROI metrics to predict *IDH* status.

RESULTS: The study included 283 patients with 79 *IDH* wild-type and 204 *IDH* mutant gliomas. Across the study population, *IDH* status was most accurately predicted by ROI mean normalized ADC and VOI mean normalized ADC, with areas under the curve of 0.83 and 0.82, respectively. The results for ROI-based genotyping of nonenhancing and solid-patchy enhancing gliomas were comparable with volumetric parameters (area under the curve = 0.81–0.84). In rim-enhancing, centrally necrotic tumors (*n* = 23), only volumetric measurements were predictive (0.90).

CONCLUSIONS: Regional normalized mean ADC measurements are noninferior to volumetric segmentation for defining solid glioma *IDH* status. Partially necrotic, rim-enhancing tumors are unsuitable for ROI assessment and may benefit from volumetric ADC quantification.

ABBREVIATIONS: AUC = area under the curve; NAWM = normal-appearing white matter; min = minimum; 1p19q^{codel} = codeletion of the short arm of chromosome 1 and the long arm of chromosome 19; rADC = normalized ADC; WHO = World Health Organization

D iffuse gliomas of World Health Organization (WHO) grades II and III comprise a diverse group of tumors characterized by distinct genetic profiles and varied median survival.[1] Three major types of diffuse gliomas are found in adults: *isocitrate*

dehydrogenase (*IDH*) wild-type gliomas with a molecular profile of *IDH* wild-type glioblastoma, *IDH* mutant astrocytoma (with p53 and *ATRX chromatin remodeler* [*ATRX*] mutations), and the *IDH* mutant oligodendroglioma with a codeletion of the short arm of chromosome 1p and the long arm of chromosome 19q (*IDH* mutant/1p19q^{codel}).[2] In addition to these major intrinsic neoplasms, multiple other tumor types exist, for example, with alterations in the map kinase pathway (*B-Raf proto-oncogene, serine/threonine kinase* [*BRAF*] mutations), histone mutations, and the distinct group of ependymal tumors.

IDH wild-type astrocytomas share glioblastoma-specific genetic mutations such as combined chromosome 7 gain and

chromosome 10 loss, *epidermal growth factor receptor* (*EGFR*) amplification, and/or *telomerase reverse transcriptase* (*TERT*) promoter mutations[3] and have a short life expectancy.[3,4] Henceforth, with the term "*IDH* wild-type diffuse glioma," we will refer to molecular glioblastoma, *IDH* wild-type.

Rapid glioma genotyping is of prognostic importance and influences therapeutic planning; for example, *IDH* mutant/ 1p19q^codel gliomas are responsive to chemotherapy,[5] whereas in 1p19q intact (*IDH* mutant/1p19q intact) tumors, maximum safe resection appears critical to improve outcomes.[6] It remains uncertain to what extent the strategy of maximal glioblastoma resection[7,8] could prolong survival for diffusely infiltrative *IDH* wild-type gliomas in the WHO grade II and III stages.

A number of imaging techniques have shown the potential for glioma genotype predictions. Of these, conventional MR imaging has the advantage of universal availability, but mostly provides visual-anatomic features, some of which have limited reproducibility.[9,10] Advanced MR imaging techniques such as perfusion and spectroscopy provide physiologic, quantifiable tumor data but can have threshold overlap and lack of technical standardization.[11]

DWI is widely integrated into clinical glioma MR imaging protocols with tissue properties measurable at the time of reporting. DWI exploits the inverse relationship between free water motion in tissues and cellularity.[12] Differences in diffusion-weighted image signals have been shown for glioma WHO grades and, more recently, between genetic subtypes.[13,14] The finding of lower ADC values in *IDH* wild-type diffuse glioma compared with *IDH* mutant tumors is consistently reported; however, the methods and accuracy vary among studies, whereby published techniques include mean and minimum ROI measurements and, in some cases, volumetric ADC quantification.[13-16] Hypothetically, "entire lesion" analysis might provide the most representative information on any individual tumor, whereas ROI placements have the advantage of being minimally time-consuming in clinical workflow.

There are few data comparing regional and volumetric diffusivity measurements for glioma genotyping, currently limited to nonenhancing glioma evaluation. The purpose of this study was to compare the performance of whole-tumor ADC measurements with different ROI parameters for glioma molecular typing, with a focus on *IDH* status prediction.

MATERIALS AND METHODS
Patients
Ethics review board approval (University College London Hospitals and Health Research Authority, United Kingdom) was obtained with informed consent waived for this retrospective imaging data study. Consecutive patients diagnosed at our national brain tumor referral institution from July 2008 to January 2018 were eligible for the research.

Inclusion criteria consisted of histologic confirmation of WHO grade II and III glioma, documented *IDH* and 1p19q genetic test results, and available pretreatment MR imaging. Exclusion criteria were previous glioma treatment; a diagnosis other than WHO grade II and III gliomas; incomplete, inconclusive, or ambiguous molecular results (eg, *IDH* wild-type/1p19q^codel); a

prolonged ($\geq$ year) interval from MR imaging to surgery; incomplete images; and failed volumetric image registration.

All tissue samples were analyzed at our neuropathology department, using the latest methodology according to the WHO 2016 Classification of CNS Tumors, as described previously.[17,18] Multiple gene Sanger sequencing was completed for *IDH* R132H-negative tumors to identify rarer *IDH* mutations, and the 1p/19q status was established through quantitative polymerase chain reaction–based copy number assay.

MR Imaging Acquisition and Postprocessing
All MR imaging examinations included T2-weighted, T2-FLAIR, and T1-weighted sequences; pre- and postadministration of a gadolinium-based contrast agent; and DWI sequences ($n = 211$ at 1.5T, $n = 79$ at 3T). Because our institution is a quaternary center, the imaging originated from 23 different MR imaging machines with no individual scanner contributing >14% of any glioma subtype. In the generation of an ADC map, the image acquired without diffusion gradients is divided by the image acquired with diffusion gradients, removing dependence on T1, T2, and TR.[19] Sufficient comparability of ADC among scanners has been demonstrated previously.[20] The range of MR imaging parameters used has been described in a prior component of the study.[21] ADC maps were calculated from 3-directional DWI acquired with 2 gradient values ($b = 0$ and $b = 1000$ s/mm^2) using proprietary software (Olea Sphere, Version 2.3; Olea Medical).

ROI Measurements
The ADC regional measurements were performed by 3 independent observers as detailed in Maynard et al,[21] blinded to tissue diagnosis. First, each observer sited small (30–40 mm^2) ROIs 3× into the visually perceived lowest ADC portions of each glioma (within $\geq$1 axial image slice), while remaining in the solid tumor component and avoiding apparent necrotic, hemorrhagic, or cystic areas or blood vessels, as identified on the relevant accompanying contrast-enhanced and other sequences. From these 3 ROIs, the mean value of the numerically lowest ADC measurement was designated minimum ADC (ADC$_{min}$) as described in Xing et al.[14]

Thereafter, 1 large ROI (ADC$_{mean}$) was placed to cover most of the largest axial tumor cross-section, excluding tumor margins, necrosis, macroscopic hemorrhage, and calcifications, as described in Thust et al.[22] Finally, a comparative ROI was positioned in the contralateral normal-appearing centrum semiovale white matter (ADC$_{NAWM}$), amounting to 5 ROI measurements per patient. Multifocal tumors were measured as 1 glioma.

Observer 1 analyzed all ($n = 290$) gliomas, observer 2 re-analyzed a subset of 75 gliomas, and observer 3 re-analyzed the remaining subset of 215 gliomas, totaling 2900 ADC measurements (ie, 5 ROIs by 2 observers per glioma, ie, 10×290 measurements). From these, the normalized minimum ADC (rADC$_{min}$, defined as ADC$_{min}$/ADC$_{NAWM}$ ratio) and the mean normalized ADC (rADC$_{mean}$) (defined as ADC$_{mean}$/ADC$_{NAWM}$ ratio) were calculated, resulting in 4 regional ADC parameters (ROI ADC$_{min}$, ROI rADC$_{min}$, ROI ADC$_{mean}$, and ROI
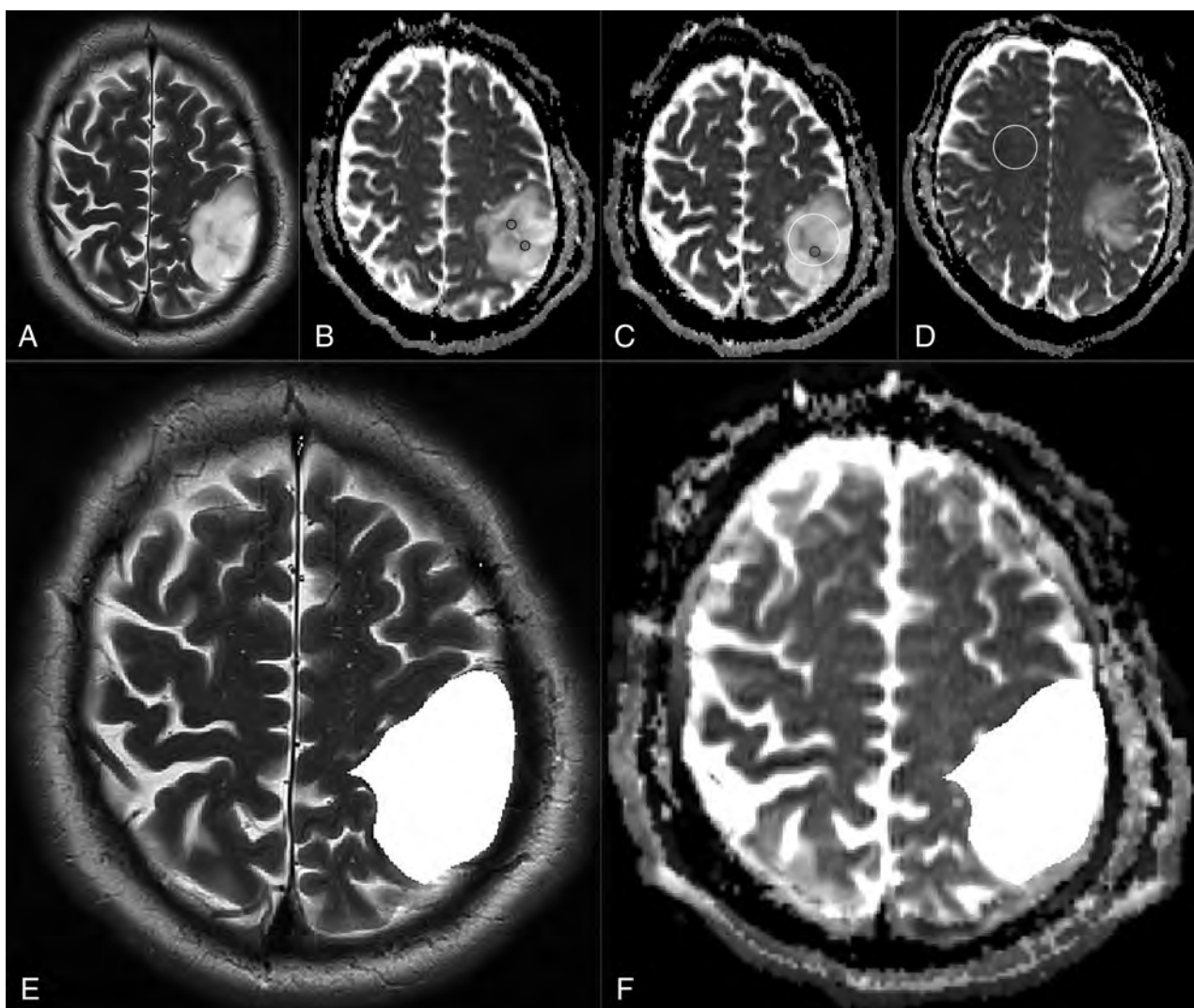
FIG 1. An example of regional and volumetric ADC measurements in a patient with *IDH* mutant 1p19q intact glioma. T2-weighted image (*A*) and ADC maps (*B–D*) show ADC_{min} (3×30–$40\,mm^2$ (black, *B* and *C*), ADC_{mean} (white, *C*), and ADC_{NAWM} (white, *D*) ROI measurements. T2-weighted image (*E*) and ADC map (*F*) in the same patient demonstrate the volumetric segmentation and image registration, respectively.

$rADC_{mean}$) per glioma. An example of the ROI placements is shown in Fig 1*A–D*.

Volumetric ADC Histogram Analysis

Whole-tumor VOIs were segmented by a general radiologist (M.B., 5 years' experience) using the ITK-Snap Toolbox, Version 3.6 (www.itksnap.org[23]) following training and under supervision of a neuroradiologist specialized in brain tumor imaging (S.C.T, 9 years' experience). Segmentations incorporated the entire T2-weighted signal abnormality. For multicentric gliomas, the total volume of signal abnormality was treated as 1 lesion. To assess interobserver reproducibility, a proportion (10%) of gliomas was randomly chosen to undergo a repeat unsupervised segmentation by a second neuroradiologist (J.A.M., 4 years' experience, including brain tumor research).

ADC maps were then co-registered to T2-weighted sequences using the FMRIB Linear Image Registration Tool (FLIRT; http://www.fmrib.ox.ac.uk/fsl/fslwiki/FLIRT),[24,25] according to an affine 12-parameter model with the correlation ratio as a cost function, except in 15 cases in which manual review favored optimization

of the registration by substitution of Normalized Mutual Information as the cost function. Subsequently, ADC histogram data were obtained for each tumor ROI, using an in-house script written in Python 2.7. For each tumor, the second and fifth ADC histogram percentiles, ADC mean, and the T2-weighted total lesion volume were extracted. Normalized histogram parameters were calculated using the same ROI ADC_{NAWM} value for the regional measurements to maximize direct comparability. An example of the volumetric segmentation is provided in Fig 1*E, -F*.

Enhancement Pattern Subgroup Analysis

Information on tumor enhancement, recorded as part of a preceding study,[21] was used for a subgroup analysis. Thus, the ability of ROI and VOI parameters to predict the *IDH* genotype was assessed separately for 3 morphologic groups: 1) nonenhancing, 2) solid-patchy enhancing, and 3) rim-enhancing, centrally necrotic gliomas. An example of the enhancement pattern distinction is provided in the Online Supplemental Data.

Patient demographics, *IDH*, and 1p19q genotypes of the study population

	All Glioma Subtypes	*IDH* Wild-Type	*IDH* Mutant/ 1p19q Intact	*IDH* Mutant/ 1p19q^{codel}
No. of patients = 283 (male/female = 164:119)	283	79	104	100
Median age (interquartile range) (yr)	40 (33–53)	59 (43–67)	35 (29–41)	40 (35–48)
Enhancement category[a]				
Nonenhancing	171	33	75	63
Solid-patchy enhancing	87	28	27	32
Rim-enhancing	23	18	0	5

Note:—1p19q^{codel} indicates codeletion of the short arm of chromosome 1 and the long arm of chromosome 19.
[a] In 2/283 patients, T1-weighted contrast-enhanced MR images were unavailable.

Statistical Analysis

All statistical testing was performed in SPSS 25 (IBM). The inter-observer agreement for the ROI-derived ADC measurements and for the volumetric segmentations was assessed by intraclass correlation coefficient analysis, using a 2-way random effects model. For each ADC ROI, the mean of the observers' measurements was adopted as the final value. For the proportion of tumors that were segmented by 2 observers, the average of the volumetric ADC results was designated as the final value.

To compare the mean ranks of the groups of ADC values and glioma subtypes, we used the nonparametric Kruskal-Wallis ANOVA test, including the Dunn pair-wise comparisons with Bonferroni correction. The strength of the association between glioma subtype and ADC metrics was tested using eta^2 (η^2), which quantifies the percentage of variance in the dependent variable (ADC value) that is explained by >1 independent variable (glioma genotype).

Univariable logistic regression was applied to test which ROI or VOI ADC parameter best predicted glioma *IDH* status (with $P < .05$ considered significant). The Youden index was used to identify diagnostic thresholds for the most predictive parameter, as determined by the area under the curve (AUC). Nonparametric (Wilcoxon signed rank) testing was performed to assess differences between the region-derived and volumetric ADC values.

RESULTS

Patient Demographics

Of 515 patients identified as potentially eligible for the study, 42 were duplicates, and 190 met the exclusion criteria as follows: previous glioma treatment ($n = 60$), tumor other than WHO grade II or III glioma ($n = 43$ and $n = 1$ spinal cord tumor), ambiguous or incomplete molecular results ($n = 29$), no preoperative DWI ($n = 24$ and $n = 15$ ADC maps not computable), unavailable histopathology report ($n = 2$), prolonged (≥ 1 year) interval from MR imaging to surgery ($n = 3$), MRI artefact ($n = 5$), incomplete images ($n = 1$), and failed volumetric image registration ($n = 7$). Finally, 283 patients (median, 40 years of age; interquartile range, 33–53 years; 164 men) were included in the analysis. The demographic details for the study population are listed in the Table.

Observer Comparison

The reproducibility of the ROI ADC parameters and contrast-enhancement patterns among 3 independent raters has been established in preceding research (intraclass correlation coefficient = 0.83–0.96 and Cohen κ = 0.69–0.72, respectively).[21] In the current study, the concordance between the 2 observers for the twice-segmented tumor volumes ($n = 28$) was near-complete (intraclass correlation coefficient = 0.97–0.98). This information is further detailed in the Online Supplemental Data.

Association between ADC Values and IDH Genotype

Box and whisker plots showing a comparison between *IDH* mutant and *IDH* wild-type gliomas for ADC$_{mean}$, rADC$_{mean}$, ADC$_{min}$, and rADC$_{min}$ are shown in the Online Supplemental Data (VOI and ROI methods). Detailed results from the statistical analysis with Kruskal-Wallis and η^2 tests are provided in the Online Supplemental Data. For all regional parameters (ROI ADC$_{min}$, ROI rADC$_{min}$, ROI ADC$_{mean}$, and ROI rADC$_{mean}$), the ADC values significantly differed among the *IDH* wild-type, *IDH* mutant, 1p19q intact, and *IDH* mutant 1p19q^{codel} glioma groups ($P < .001$). VOI ADC$_{mean}$ and VOI rADC$_{mean}$ also differed among the glioma molecular groups ($P < .001$).

VOI ADC$_{min}$ and VOI rADC$_{min}$ differed between *IDH* wild-type and *IDH* mutant 1p19q^{codel} genotypes ($P = .003$ and $P < .001$, respectively). However, no significant difference in VOI ADC$_{min}$ or VOI rADC$_{min}$ was shown between *IDH* mutant 1p19q intact and *IDH* mutant 1p19q^{codel} gliomas.

Wilcoxon signed rank testing confirmed statistically significant differences between the VOI and ROI results of the absolute and normalized ADC values ($P < .001$). The association between glioma genotype and diffusivity was strongest for ROI ADC$_{mean}$ and ROI rADC$_{mean}$ values ($\eta^2 = 0.38$) across the study population, while also being substantial for ROI ADC$_{min}$ and ROI rADC$_{min}$ ($\eta^2 = 0.28$–0.29).

The subgroup analysis according to the contrast-enhancement pattern revealed associations between ROI ADC$_{mean}$ and ROI rADC$_{mean}$ values and genotype for nonenhancing gliomas ($n = 170$, $\eta^2 = 0.39$–0.41) and solid-patchy enhancing gliomas ($n = 85$, $\eta^2 = 0.24$–0.28). No association was evident between ROI ADC parameters and the rim-enhancing, centrally necrotic glioma *IDH* genotype ($n = 23$, $\eta^2 = 0.0$–0.05). The strongest association for the rim-enhancing gliomas was with VOI rADC$_{mean}$ values ($\eta^2 = 0.36$).

No correlation among *IDH* status, VOI ADC$_{min}$, and VOI rADC$_{min}$ was identified for nonenhancing gliomas ($\eta^2 = 0.02$–0.03). Across all regional and volumetric parameters, smaller η^2 effect sizes were observed for minimum ADC values compared with mean ADC values. The VOI ADC$_{min}$ was tested as determined by either the 2nd or 5th percentile by histogram analysis, with consistently larger η^2 values observed between ADC$_{min}$ and genotype when the 5th percentile was used. Thereafter, VOI ADC$_{min}$ referred to the 5th percentile only.

ROC Curves for the prediction of *IDH* genotype in the study population (*n* = 283)

Area Under the ROC Curve (AUC)		
ADC metrics	Area Under the Curve	95% CI
VOI ADC$_{min}$	0.68	0.61 - 0.75
VOI rADC$_{min}$	0.72	0.66 - 0.79
VOI ADC$_{mean}$	0.78	0.72 - 0.84
VOI rADC$_{mean}$	0.82	0.76 - 0.88
ROI ADC$_{min}$	0.79	0.73 - 0.85
ROI rADC$_{min}$	0.81	0.76 - 0.86
ROI ADC$_{mean}$	0.81	0.75 - 0.86
ROI rADC$_{mean}$	0.83	0.78 - 0.89
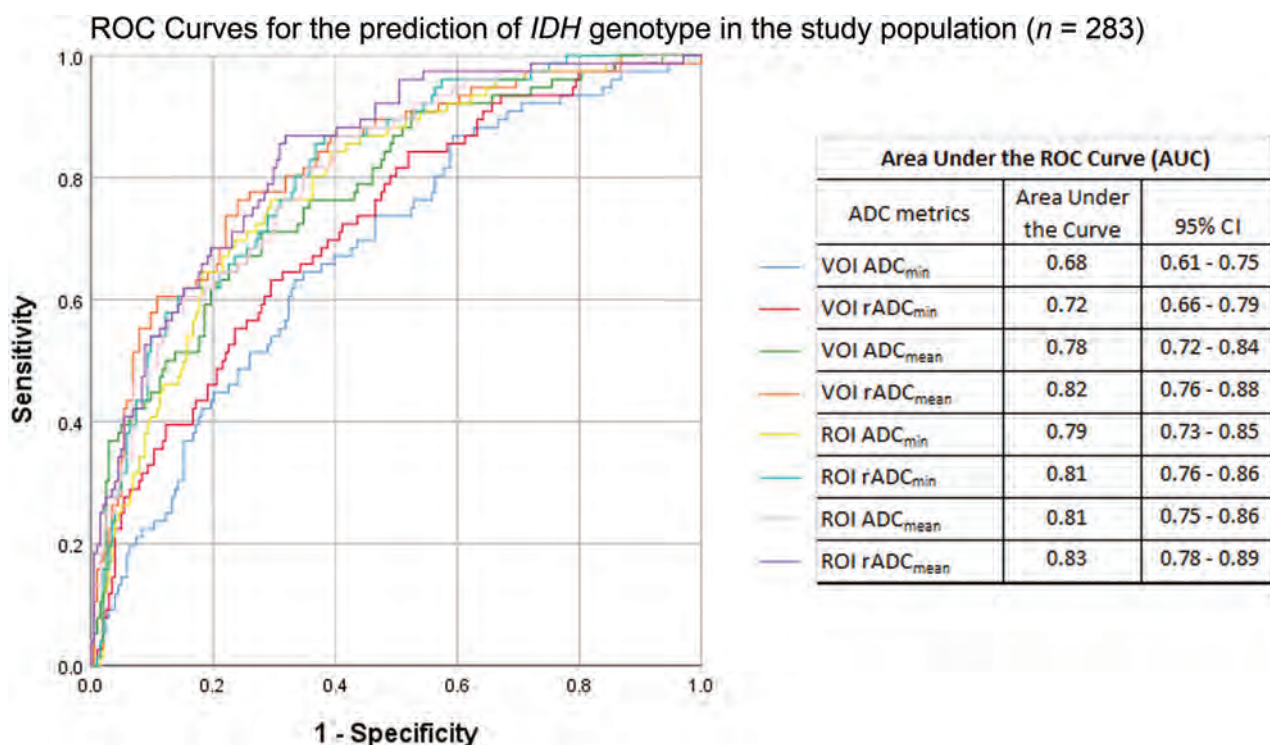
FIG 2. ROC curves for the prediction of *IDH* genotype in the study population (*n* = 283).

Univariable Analysis for Prediction of IDH Status

The univariable analysis of regional and volumetric ADC metrics, when compared across all (*n* = 283) gliomas, showed that the most accurate prediction of *IDH* status was achieved using ROI rADC$_{mean}$ or VOI rADC$_{mean}$ (AUC = 0.83 and 0.82, respectively). The least accurate predictions were observed for VOI ADC$_{min}$ (AUC = 0.68) and VOI rADC$_{min}$ (AUC = 0.72). The ROC curve analysis is presented in Fig 2, with additional results listed in the Online Supplemental Data.

When assessing nonenhancing gliomas alone, the ROI ADC$_{mean}$ (AUC = 0.82) and ROI rADC$_{mean}$ (AUC = 0.84) results were almost equal to the VOI ADC$_{mean}$ (AUC = 0.81) and VOI rADC$_{mean}$ (AUC = 0.84). For solid-patchy tumors, the ROI ADC$_{mean}$ (AUC = 0.79) and ROI rADC$_{mean}$ (AUC = 0.81) were almost equal to the VOI ADC$_{mean}$ (AUC = 0.78) and VOI rADC$_{mean}$ (AUC = 0.80), respectively.

Conversely, in rim-enhancing centrally necrotic lesions, only volumetric ADC results demonstrated a significant ability to predict *IDH* status (VOI ADC$_{mean}$ [AUC = 0.84], VOI rADC$_{mean}$ [AUC = 0.90]), but not the ROI ADC$_{mean}$ and ROI rADC$_{mean}$ values (AUC = 0.49–0.61). Given the lack of an association between the volumetric ADC$_{min}$ parameters and *IDH* status, these were not further subjected to a subgroup analysis according to enhancement patterns.

DISCUSSION

This study investigated the comparability of region-derived and volumetric ADC values for WHO grade II and III glioma genotyping, specifically their performance for predicting *IDH* status. Our results indicate that the accuracy of regional measurements

for solid glioma *IDH* typing is unimproved by performing whole-tumor segmentations (maximum AUC = 0.84 for VOI and ROI rADC$_{mean}$). However, for *IDH* status prediction in the small proportion of rim-enhancing, centrally necrotic tumors (*n* = 23), entire lesion ADC mean parameters were superior to solid-tumor ROI measurements. Throughout the study, mean ADC measurements appeared more accurate than ADC$_{min}$ metrics, particularly if performing a volumetric analysis.

Before the discovery of glioma molecular subgroups, research was focused on testing the ability of ADC to predict glioma histologic grades, showing an inverse correlation between cellularity and diffusion.[26-28] More recently, Leu et al[13] demonstrated a stronger association between glioma ADC values and genotype than WHO grade. Specifically for *IDH* wild-type glioblastoma, no difference in diffusivity may exist between grades II and IV.[29] Villaneuva-Meyer et al[30] previously assessed ROI-derived minimum, mean, and maximum in WHO grade II gliomas: A minimum ADC threshold of 0.9×10^{-3} seconds/mm^2 provided the greatest sensitivity (91%) and specificity (76%) for *IDH* typing, with an AUC of 0.901.[19] ROI-based minimum ADC analysis was also performed by Wasserman et al[15] with a proposed cutoff point of 0.95×10^{-3} seconds/mm^2 (sensitivity of 76.9%, specificity of 65.2%, and AUC = 0.711)[13] and by Xing et al[14] with a suggested minimum ADC threshold of 1.01×10^{-3} seconds/mm^2 (sensitivity of 76.9%, specificity of 82.6%, AUC = 0.87).[15]

By means of ROI measurements, ADC$_{min}$ and rADC$_{min}$ appeared valuable for *IDH* typing in our study, with optimal thresholds in the region of 1.07×10^{-3} seconds/mm^2 (sensitivity of 82.3%, specificity of 61.3%, AUC = 0.79) and 1.40 (sensitivity of 85.5%, specificity of 62.3%, AUC = 0.81), respectively. For an ROI ADC$_{mean}$ threshold of 1.34×10^{-3} seconds/mm^2, a similar

sensitivity of 84.8%, specificity of 60.3%, and AUC of 0.81 were observed. For an $rADC_{mean}$ threshold of 1.75, the results were marginally better (sensitivity of 86.8%, specificity of 62.3, AUC = 0.83).

Across the whole study population, the largest ROI AUC (0.83) was observed for $rADC_{mean}$ values in our research. Liu et al[16] previously assessed glioma mean and minimum ADC, but only the results for mean ADC reached statistical significance ($P = .028$). Recently, in a study of normalized mean measurements for *IDH* typing of non-gadolinium-enhancing WHO grades II and III gliomas, an $rADC_{mean}$ threshold in the region of 1.8 was proposed.[22]

Several studies reported lower ADC values in *IDH* mutant 1p19q^{codel} oligodendrogliomas compared with *IDH* mutant 1p19q intact astrocytomas, with 2 studies indicating an ADC_{mean} threshold in the region of $1.4–1.6 \times 10^{-3}$ ^{seconds}/mm^2 for 1p19q genotyping.[31,32] However, similar to the reduced specificity of elevated perfusion (blood volume), which may be observed in low-grade oligodendrogliomas, erroneously low ADC values can occur in this tumor type despite its relatively good prognosis. A potential influence from extracellular matrix components is probable.[33] It is also noteworthy that measurements in calcified tumor components may underestimate ADC values and should be avoided.

From our results, it appears that ROI ADC_{mean} and $rADC_{mean}$ are slightly superior to minimum ROI ADC measurements for *IDH* genotyping of WHO grade II and III gliomas. Similarly, Han et al[34] investigated the variability of ADC values according to the ROI technique for glioma grading, with the mean ADC value of single-round ROI showing the highest effect size (0.72) and the greatest AUC (0.872), being superior to minimum measurements for the identification of high-grade gliomas. Within the aforementioned study, minimum ADC values also differed significantly between whole-volume and single-round ROI placements ($P = .003$),[34] indicating that these are not interchangeable.

It has been shown that volumetric tumor diffusivity analysis is not necessarily superior to ROI placements, for example, for WHO grading.[35] In 2 recent studies using ADC for H3 K27M histone-mutant glioma characterization, only the study using ROI measurements was predictive of genotype.[36,37]

It could be hypothesized that the previously reported lower accuracy of ADC for WHO grade IV glioblastoma *IDH* typing[38] could be related to the foci of necrosis. However, in our current study, the best prediction of *IDH* status for such masses was achieved using VOI $rADC_{mean}$ values derived from segmentation inclusive of necrosis, as opposed to ROI measurement in solid lesion components. Indeed, our data suggest that partially necrotic tumors may benefit from a volumetric diffusivity (VOI $rADC_{mean}$) assessment, but the small patient number ($n = 23$) in this subgroup is a limitation of our research. Furthermore, it is possible that in some cases of necrotic tumors, limited tissue sampling resulted in a WHO grade II and III diagnosis instead of glioblastoma.

Imperfections in the volumetric image registration at glioma margins due to ADC map distortion from susceptibility gradients and eddy current effects, which are not visible in the T2-weighted image data, could have contributed to volumetric minimum ADC measurements performing less well in our research.

While the binary discrimination of *IDH* wild-type from *IDH* mutant gliomas is imperfect, noninvasive identification of early glioblastoma stages could help prioritize tissue sampling in such circumstances in which observational management is initially favored or when waiting times to surgery could result in a diagnostic delay.

CONCLUSIONS

Regional diffusivity measurements are noninferior and are possibly preferable to volumetric histogram analysis for *IDH* status prediction of macroscopically solid WHO grade II and III gliomas. ROI $rADC_{mean}$ calculation is rapid and scanner-independent, thus easily introduced into clinical reporting. Partially necrotic, rim-enhancing lesions are unsuitable for ROI assessment and may benefit from volumetric ADC quantification for genotyping.

REFERENCES

1. Brat DJ, Verhaak RG, Aldape KD, et al; Cancer Genome Atlas Research Network. **Comprehensive, integrative genomic analysis of diffuse lower-grade gliomas.** *N Engl J Med* 2015;372:2481–98 CrossRef Medline

2. Louis DN, Perry A, Reifenberger G, et al. **The 2016 World Health Organization Classification of Tumors of the Central Nervous System: a summary.** *Acta Neuropathol* 2016;131:803–20 CrossRef Medline

3. Stichel D, Ebrahimi A, Reuss D, et al. **Distribution of EGFR amplification, combined chromosome 7 gain and chromosome 10 loss, and TERT promoter mutation in brain tumors and their potential for the reclassification of *IDH* wild type astrocytoma to glioblastoma.** *Acta Neuropathol* 2018;136:793–803 CrossRef Medline

4. Tesileanu CM, Dirven L, Wijnenga MM, et al. Survival of diffuse astrocytic glioma, IDH1/2-wild type, with molecular features of glioblastoma, WHO grade IV: a confirmation of the cIMPACT-NOW criteria. *Neuro Oncol* 2020;22:515–23 CrossRef Medline

5. van den Bent MJ, Brandes AA, Taphoorn MJ, et al. **Adjuvant procarbazine, lomustine, and vincristine chemotherapy in newly diagnosed anaplastic oligodendroglioma: long-term follow-up of EORTC brain tumor group study 26951.** *J Clin Oncol* 2013;31:344–50 CrossRef Medline

6. Wijnenga MM, French PJ, Dubbink HJ, et al. **The impact of surgery in molecularly defined low-grade glioma: an integrated clinical, radiological, and molecular analysis.** *Neuro Oncol* 2018;20:103–12 CrossRef Medline

7. Kreth FW, Thon N, Simon M, et al. **Gross total but not incomplete resection of glioblastoma prolongs survival in the era of radiochemotherapy.** *Ann Oncol* 2013;24:3117–23 CrossRef Medline

8. Li YM, Suki D, Hess K, et al. **The influence of maximum safe resection of glioblastoma on survival in 1229 patients: can we do better than gross-total resection?** *J Neurosurg* 2016;124:977–88 CrossRef Medline

9. Mazurowski MA, Desjardins A, Malof JM. **Imaging descriptors improve the predictive power of survival models for glioblastoma patients.** *Neuro Oncol* 2013;15:1389–94 CrossRef Medline

10. Hyare H, Rice L, Thust S, et al. **Modelling MR and clinical features in grade II/III astrocytomas to predict *IDH* mutation status.** *Eur J Radiol* 2019;114:120–27 CrossRef Medline

11. Thust SC, Heiland S, Falini A, et al. **Glioma imaging in Europe: a survey of 220 centres and recommendations for best clinical practice.** *Eur Radiol* 2018;28:3306–17 CrossRef Medline

12. Patterson DM, Padhani AR, Collins DJ. **Technology insight: water diffusion MRI–a potential new biomarker of response to cancer therapy.** *Nat Clin Pract Oncol* 2008;5:220–33 CrossRef Medline

13. Leu K, Ott GA, Lai A, et al. **Perfusion and diffusion MRI signatures in histologic and genetic subtypes of WHO grade II-III diffuse gliomas.** *J Neurooncol* 2017;134:177–88 CrossRef Medline

14. Xing Z, Yang X, She D, et al. **Noninvasive assessment of *IDH* mutational status in World Health Organization grade II and III astrocytomas using DWI and DSC-PWI combined with conventional MR imaging.** *AJNR Am J Neuroradiol* 2017;38:1138–44 CrossRef Medline

15. Wasserman JK, Nicholas G, Yaworski R, et al. **Radiological and pathological features associated with IDH1-R132H mutation status and early mortality in newly diagnosed anaplastic astrocytic tumours.** *PLoS One* 2015;10:e0123890 CrossRef Medline

16. Liu T, Cheng G, Kang X, et al. **Noninvasively evaluating the grading and IDH1 mutation status of diffuse gliomas by three-dimensional pseudo-continuous arterial spin labeling and diffusion-weighted imaging.** *Neuroradiology* 2018;60:693–702 CrossRef Medline

17. Jaunmuktane Z, Capper D, Jones DTW, et al. **Methylation array profiling of adult brain tumours: diagnostic outcomes in a large, single centre.** *Acta Neuropathol Commun* 2019;7:24 CrossRef Medline

18. Reuss DE, Sahm F, Schrimpf D, et al. **ATRX and IDH1-R132H immunohistochemistry with subsequent copy number analysis and *IDH* sequencing as a basis for an "integrated" diagnostic approach for adult astrocytoma, oligodendroglioma and glioblastoma.** *Acta Neuropathol* 2015;129:133–46 CrossRef Medline

19. Pipe J. Pulse sequences for diffusion-weighted MRI. In: Johansen-Berg H, Behrens TE, eds. *Diffusion MRI.* Academic Press; 2009:11–35

20. Grech-Sollars M, Hales PW, Miyazaki K, et al. **Multi-centre reproducibility of diffusion MRI parameters for clinical sequences in the brain.** *NMR Biomed* 2015;28:468–85 CrossRef Medline

21. Maynard J, Okuchi S, Wastling S, et al. **World Health Organization grade II/III glioma molecular status: prediction by MRI morphologic features and apparent diffusion coefficient.** *Radiology* 2020;296:111–21 CrossRef Medline

22. Thust SC, Hassanein S, Bisdas S, et al. **Apparent diffusion coefficient for molecular subtyping of non-gadolinium-enhancing WHO grade II/III glioma: volumetric segmentation versus two-dimensional region of interest analysis.** *Eur Radiol* 2018;28:3779–88 CrossRef Medline

23. Yushkevich PA, Piven J, Hazlett HC, et al. **User-guided 3D active contour segmentation of anatomical structures: significantly improved efficiency and reliability.** *Neuroimage* 2006;31:1116–28 CrossRef Medline

24. Jenkinson M, Bannister P, Brady M, et al. **Improved optimization for the robust and accurate linear registration and motion correction of brain images.** *Neuroimage* 2002;17:825–41 CrossRef Medline

25. Jenkinson M, Smith S. **A global optimisation method for robust affine registration of brain images.** *Med Image Anal* 2001;5:143–56 CrossRef Medline

26. Louis DN, Ohgaki H, Wiestler OD, et al. **The 2007 WHO Classification of Tumours of the Central Nervous System.** *Acta Neuropathol* 2007;114:97–109 CrossRef Medline

27. Hilario A, Ramos A, Perez-Nuñez A, et al. **The added value of apparent diffusion coefficient to cerebral blood volume in the preoperative grading of diffuse gliomas.** *AJNR Am J Neuroradiol* 2012;33:701–07 CrossRef Medline

28. Sugahara T, Korogi Y, Kochi M, et al. **Usefulness of diffusion-weighted MRI with echo-planar technique in the evaluation of cellularity in gliomas.** *J Magn Reson Imaging* 1999;9:53–60 CrossRef Medline

29. Figini M, Riva M, Graham M, et al. **Prediction of isocitrate dehydrogenase genotype in brain gliomas with MRI: single-shell versus multishell diffusion models.** *Radiology* 2018;289:788–96 CrossRef Medline

30. Villanueva-Meyer JE, Wood MD, Choi BS, et al. **MRI Features and *IDH* Mutational Status of Grade II Diffuse Gliomas: Impact on Diagnosis and Prognosis.** *American Journal of Roentgenology* 2018;210:621–28 CrossRef Medline

31. Johnson DR, Diehn FE, Giannini C, et al. **Genetically defined oligodendroglioma is characterized by indistinct tumor borders at MRI.** *AJNR Am J Neuroradiol* 2017;38:678–84 CrossRef Medline

32. Cui Y, Ma L, Chen X, et al. **Lower apparent diffusion coefficients indicate distinct prognosis in low-grade and high-grade glioma.** *J Neurooncol* 2014;119:377–85 CrossRef Medline

33. Sadeghi N, Camby I, Goldman S, et al. **Effect of hydrophilic components of the extracellular matrix on quantifiable diffusion-weighted imaging of human gliomas: preliminary results of correlating apparent diffusion coefficient values and hyaluronan expression level.** *AJR Am J Roentgenol* 2003;181:235–41 CrossRef Medline

34. Han X, Suo S, Sun Y, et al. **Apparent diffusion coefficient measurement in glioma: Influence of region-of-interest determination methods on apparent diffusion coefficient values, interobserver variability, time efficiency, and diagnostic ability.** *J Magn Reson Imaging* 2017;45:722–30 CrossRef Medline

35. Takano K, Kinoshita M, Arita H, et al. **Influence of region-of-interest designs on quantitative measurement of multimodal imaging of MR non-enhancing gliomas.** *Oncol Lett* 2018;15:7934–40 CrossRef Medline

36. Aboian MS, Tong E, Solomon DA, et al. **Diffusion characteristics of pediatric diffuse midline gliomas with histone H3-K27M mutation using apparent diffusion coefficient histogram analysis.** *AJNR Am J Neuroradiol* 2019;40:1804–10 CrossRef Medline

37. Chen H, Hu W, He H, et al. **Noninvasive assessment of H3 K27M mutational status in diffuse midline gliomas using apparent diffusion coefficient measurements.** *Eur J Radiol* 2019;114:152–59 CrossRef Medline

38. Tan WL, Huang WY, Yin B, et al. **Can diffusion tensor imaging noninvasively detect IDH1 gene mutations in astrogliomas? A retrospective study of 112 cases.** *AJNR Am J Neuroradiol* 2014;35:920–97 CrossRef Medline

MRI Features May Predict Molecular Features of Glioblastoma in *Isocitrate Dehydrogenase* Wild-Type Lower-Grade Gliomas

C.J. Park, K. Han, H. Kim, S.S. Ahn, D. Choi, Y.W. Park, J.H. Chang, S.H. Kim, S. Cha, and S.-K. Lee

ABSTRACT

BACKGROUND AND PURPOSE: *Isocitrate dehydrogenase* (*IDH*) wild-type lower-grade gliomas (histologic grades II and III) with *epidermal growth factor receptor* (*EGFR*) amplification or *telomerase reverse transcriptase* (*TERT*) promoter mutation are reported to behave similar to glioblastoma. We aimed to evaluate whether MR imaging features could identify a subset of *IDH* wild-type lower-grade gliomas that carry molecular features of glioblastoma.

MATERIALS AND METHODS: In this multi-institutional retrospective study, pathologically confirmed *IDH* wild-type lower-grade gliomas from 2 tertiary institutions and The Cancer Genome Atlas constituted the training set (institution 1 and The Cancer Genome Atlas, 64 patients) and the independent test set (institution 2, 57 patients). Preoperative MRIs were analyzed using the Visually AcceSAble Rembrandt Images and radiomics. The molecular glioblastoma status was determined on the basis of the presence of *EGFR* amplification and *TERT* promoter mutation. Molecular glioblastoma was present in 73.4% and 56.1% in the training and test sets, respectively. Models using clinical, Visually AcceSAble Rembrandt Images, and radiomic features were built to predict the molecular glioblastoma status in the training set; then they were validated in the test set.

RESULTS: In the test set, a model using both Visually AcceSAble Rembrandt Images and radiomic features showed superior predictive performance (area under the curve = 0.854) than that with only clinical features or Visually AcceSAble Rembrandt Images (areas under the curve = 0.514 and 0.648, respectively; $P < .001$, both). When both Visually AcceSAble Rembrandt Images and radiomics were added to clinical features, the predictive performance significantly increased (areas under the curve = 0.514 versus 0.863, $P < .001$).

CONCLUSIONS: MR imaging features integrated with machine learning classifiers may predict a subset of *IDH* wild-type lower-grade gliomas that carry molecular features of glioblastoma.

ABBREVIATIONS: AUC = area under the receiver operating characteristic curve; cIMPACT-NOW = Consortium to Inform Molecular and Practical Approaches to CNS Tumor Taxonomy; GBM = glioblastoma; LASSO = least absolute shrinkage and selection operator; RFE = recursive feature elimination; SVM = support vector machine; TCGA = The Cancer Genome Atlas; VASARI = Visually AcceSAble Rembrandt Images; WHO = World Health Organization

A mutation in the *isocitrate dehydrogenase* (*IDH*) gene is a major classifier that leads to the stratification of gliomas with significantly different survival rates among the lower-grade gliomas (World Health Organization [WHO] grades II and III) as well as glioblastomas (GBMs).[1-4] *IDH* wild-type tumors, which account for <30% of the histologic grade II and III gliomas, show worse prognoses than those with the *IDH* mutation.[1,5,6]

Previous studies have reported heterogeneous clinical outcomes among the *IDH* wild-type lower-grade gliomas according to a variable combination of genetic profiles.[7-9] Recently, the Consortium to Inform Molecular and Practical Approaches to CNS Tumor Taxonomy (cIMPACT-NOW) provided a new designation for gliomas, namely, "diffuse astrocytic glioma, *IDH*-

wildtype, with molecular features of GBM, WHO grade IV," which corresponds to histologic grades II and III *IDH* wild-type gliomas showing high-level *epidermal growth factor receptor* (*EGFR*) amplification, the combination of a whole chromosome 7 gain and a whole chromosome 10 loss (+7/−10), or *telomerase reverse transcriptase* (*TERT*) promotor mutations.[10] These specifications emphasize that the *IDH* wild-type lower-grade gliomas that fulfill these molecular criteria will follow an aggressive clinical course closely resembling that of an *IDH* wild-type GBM. Therefore, it is highly desirable that MR imaging predict the tumors with specific molecular features that would have a worse prognosis than the others. Especially, this characteristic will be clinically relevant in cases in which detailed genetic profiling cannot be performed.

The Visually AcceSAble Rembrandt Images (VASARI; https://wiki.nci.nih.gov/display/CIP/VASARI) are a standardized feature set that was developed to describe MR imaging features of gliomas using a standardized vocabulary. It provides 26 distinct imaging lexicons that allow accurate, reproducible, and comprehensive assessment of the gliomas. Previous studies have reported that the VASARI assessment was highly reproducible, clinically meaningful, and biologically relevant in glioblastomas.[11-13]

Radiomics extracts high-dimensional quantitative imaging features, such as intensity distributions, spatial relationships, textural heterogeneity, and shape descriptors;[14] hidden information can be revealed using radiomics.[15] In particular, a strength of radiomics is that it reflects intratumoral heterogeneity by a variety of mathematic methods used to quantify the gray-level spatial variations within an image to derive textural features.[16] Several previous studies have applied radiomics to predict specific genetic mutations in patients with lower-grade gliomas, including *EGFR* expression.[17-19] The predictive role of radiomics for *EGFR* amplification or *TERT* promotor mutation in patients with *IDH* wild-type lower-grade gliomas is clinically relevant in the light of cIMPACT-NOW recommendations; however, it has not been studied to date.

Our study aimed to evaluate whether comprehensive analysis of MR imaging features using the VASARI set and radiomics can identify a subset of *IDH* wild-type lower-grade gliomas with molecular features that may also follow a clinical course similar to that of GBM.

MATERIALS AND METHODS

This retrospective study was approved by the institutional review boards of the 2 academic institutions, Yonsei University Health System (Seoul, Korea) (institution 1) and University of California, San Francisco Medical Center (California, United States) (institution 2). The requirement for obtaining informed patient consent was waived. For another dataset, the publicly available National Institutes of Health/National Cancer Institute–approved Cancer Genome Atlas (TCGA) and The Cancer Imaging Archive data bases in which all data are anonymized were used.[20] Thus, individual institutional approval was not required for using the TCGA dataset.

Patients

Patients with pathologically confirmed lower-grade gliomas were identified in each institution and in the TCGA dataset. The

inclusion criteria were as follows: 1) *IDH* wild-type; 2) with preoperative MR imaging; 3) with known specific molecular features of GBM. According to cIMPACT-NOW, *EGFR* amplification, chromosome +7/–10, and *TERT* promotor mutation determine whether *IDH* wild-type lower-grade gliomas have the molecular features of GBM. However, because the chromosome +7/–10 status was not available in the test set, this feature was excluded from our analysis.

The patients were divided into 2 subsets according to their *EGFR* amplification and *TERT* promotor mutation status: If either the *EGFR* amplification or the *TERT* promotor mutation status was positive, the tumor was considered an *IDH* wild-type lower-grade glioma with the molecular features of GBM. If both the *EGFR* amplification and *TERT* promotor mutation status were negative, the tumor was considered an *IDH* wild-type lower-grade glioma without the molecular features of GBM. The primary outcome was the status of molecular features of GBM. The patients' ages and WHO grades were retrieved from the electronic medical records.

Training Set: Institution 1 + TCGA

Institution 1 and TCGA data constituted the training set. We identified 166 patients with pathologically confirmed lower-grade gliomas from January 2012 to December 2018 at the University of California, San Francisco. The exclusion criteria were as follows: 1) *IDH*-mutant tumors ($n = 47$); 2) unknown *IDH* mutation status ($n = 3$); 3) history of brain surgery ($n = 59$); 4) younger than 18 years of age ($n = 7$); 5) without preoperative MR imaging ($n = 3$); and 6) unknown status of molecular features of GBM ($n = 15$). Thirty-two patients with *IDH* wild-type lower-grade gliomas were enrolled (Fig 1). Among the 32 patients, 21 patients (65.6%) had *IDH* wild-type lower-grade gliomas with molecular features of GBM.

The TCGA (http://cancergenome.nih.gov) provided the clinical and MR imaging data of 199 lower-grade gliomas in patients older than 18 years of age. The exclusion criteria were as follows: 1) *IDH*-mutant tumors ($n = 151$); 2) unknown *IDH* mutation status ($n = 2$); and 3) unknown status of molecular features of GBM ($n = 14$). Thirty-two patients with *IDH* wild-type lower-grade gliomas were enrolled (Fig 1). Among 32 patients, 26 patients (81.3%) had *IDH* wild-type lower-grade gliomas with molecular features of GBM.

In the training set, 25 and 39 patients had WHO grade II and III gliomas, respectively. Among 47 patients with molecular features of GBM, 32 patients had WHO grade III gliomas (32/47, 68.1%) and 15 patients had WHO grade II gliomas (15/47, 31.9%).

Test Set: Institution 2

From January 2007 to October 2018, four hundred eighty-six patients with pathologically confirmed lower-grade gliomas were identified. The exclusion criteria were as follows: 1) *IDH*-mutant tumors ($n = 210$); 2) unknown *IDH* mutation status ($n = 85$); 3) history of brain surgery ($n = 10$); 4) younger than 18 years of age ($n = 13$); 5) without preoperative MR imaging ($n = 11$); and 6) unknown status of molecular features of GBM ($n = 100$). Finally, 57 patients constituted an independent test set (Fig 1). Among

Institution 1

TCGA

Institution 2
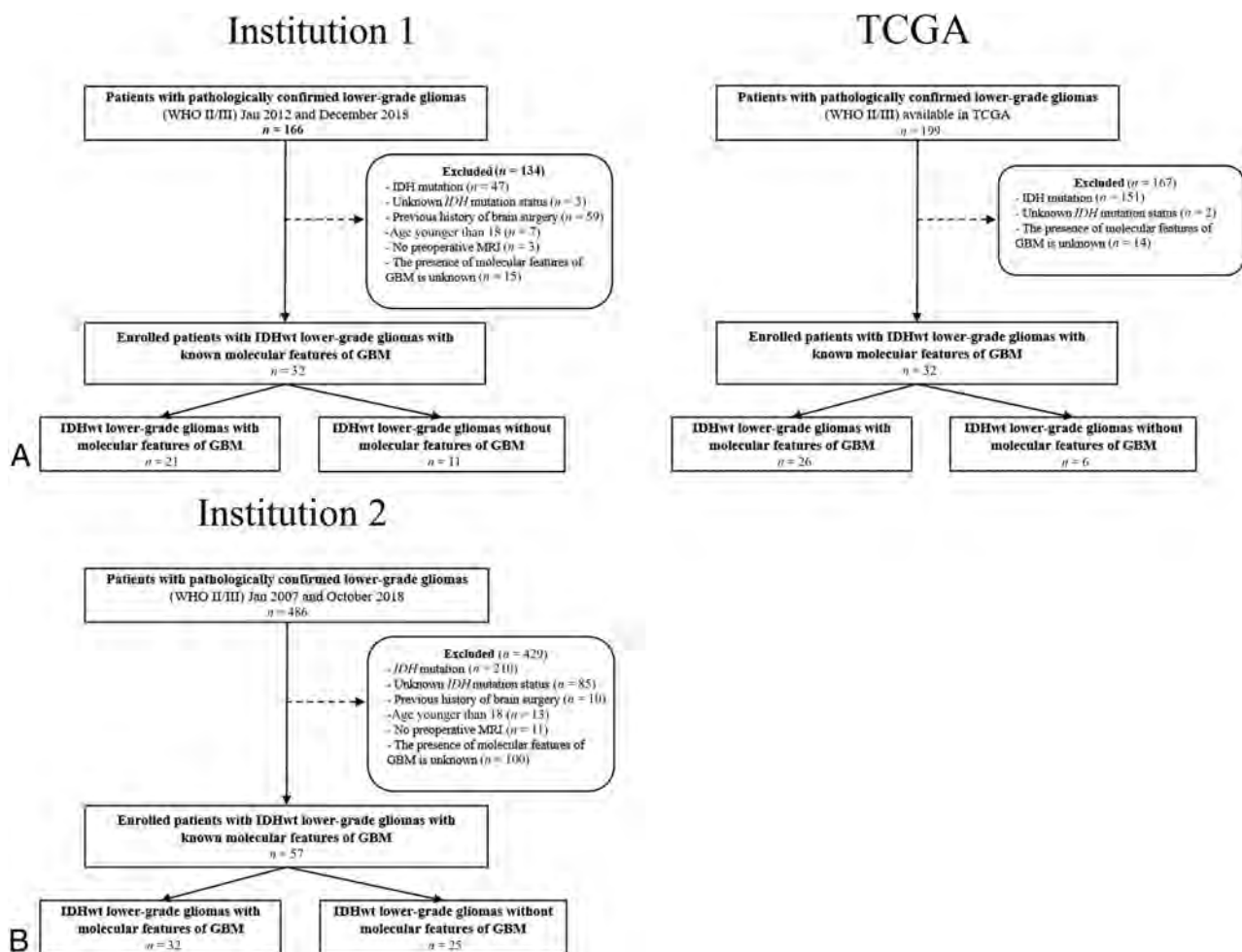
FIG 1. Flow chart showing the distribution of the patient population in the training (*A*) and the test (*B*) sets. IDHwt indicates *isocitrate dehydrogenase* wild-type.

the 57 patients, 32 patients (56.1%) had *IDH* wild-type lower-grade gliomas with molecular features of GBM.

In the test set, 23 and 34 patients had WHO grade II and III gliomas, respectively. Among 32 patients with molecular features of GBM, 15 patients had WHO grade III gliomas (15/32, 46.9%) and 17 patients had WHO grade II gliomas (17/32, 53.1%).

MR Image Acquisition
Patients from institutions 1 and 2 both underwent brain MRI with a 3T system (institution 1, Discovery, GE Healthcare; institution 2, Achieva or Ingenia, Philips Healthcare). The detailed parameters of MR imaging sequences from each institution are illustrated in the Online Supplement Data.

Image Analysis
Two board-certified neuroradiologists (12 and 3 years' experience, respectively) independently reviewed the MR images of all patients according to the VASARI feature set, blinded to patients' clinical information. Discrepancies between them were settled by consensus. The VASARI lexicon provides 26 imaging descriptors based on T1, T2, FLAIR, and DWI. Diffusion features were not evaluated because many patients lacked preoperative DWI in TCGA cohorts. We analyzed the following MR

imaging features: location (lobar/nonlobar), side of lesion center (midline or not), eloquent brain involvement, presence of enhancement, proportion of enhancing tumor, nonenhancing tumor, edema and necrosis, presence of cysts, multifocality, expansile or infiltrative growth, margin of nonenhancing tumor (well-defined or poorly-defined), hemorrhage, pial invasion, ependymal extension, cortical involvement, deep white matter involvement, midline cross, and satellites. Detailed descriptions of all features are available at the National Cancer Institute's Cancer Imaging Archive (https://wiki.cancerimagingarchive.net/display/Public/VASARI+Research+Project).[21]

Image Preprocessing and Radiomic Feature Extraction
First, T2WI and postcontrast T1 images were resampled to an identical spatial resolution of $1 \times 1 \times 1$ mm using Nilearn (https://nilearn.github.io). These images were subjected to N4 bias correction to remove low-frequency intensity and nonuniformity.[22,23] After resampling and N4 bias correction, postcontrast T1 images were registered to identical spatial coordinates using T2WI as a template with SimpleITK (http://www.simpleitk.org). Signal intensity was normalized using the WhiteStripe R package,[24] which is implemented in R software (Version 3.5.1; www.R-project.org). The ROI was drawn by a neuroradiologist and

Table 1: Patient clinical characteristics[a]

Clinical Characteristics	Training Set		Test Set, Institution 2	P Value[b]
	Institution 1	TCGA		
No. of patients	32	32	57	
Age (yr)	49.0 [SD, 19.1]	51.1 [SD, 14.7]	53.4 [SD, 16.2]	.291
Sex (male/female)	19:13	17:15	27:30	.901
WHO grade				.800
Grade II	16 (50.0%)	9 (28.1%)	23 (40.4%)	
Grade III	16 (50.0%)	23 (71.9%)	34 (59.6%)	
Molecular GBM status				.053
With molecular features of GBM	21 (65.6%)	26 (81.3%)	32 (56.1%)	
Without molecular features of GBM	11 (34.4%)	6 (18.7%)	25 (43.9%)	

[a] Data are expressed as a mean [SD] or as a number with percentage in parentheses.
[b] Comparisons between the training and the test sets using the Student t test for continuous variables and the χ^2 test for categoric variables.

confirmed by another neuroradiologist (3 and 12 years' experience, respectively) to segment the infiltrative tumor and edema—defined with high signal intensity on T2WI—using a semiautomatic method of signal intensity threshold with the Medical Image Processing, Analysis, and Visualization software, Version 7.0 (National Institutes of Health; mipav.cit.nih.gov). The radiomic features were extracted from the ROIs on T2WI and postcontrast T1 images using PY RADIOMICS 1.2.0 (http://www.radiomics.io/pyradiomics.html).[25]

Twelve shapes, 18 first-orders, 23 gray-level co-occurrence matrices, gray-level run length matrices, 16 gray-level size zone matrices, and 5 neighborhood gray tone difference matrices were extracted from the ROIs on T2WI and postcontrast T1 images, constituting a total of 180 radiomic features.

Pathologic Evaluation and Molecular Subtyping
In the 2 academic institutions (institution 1 and 2), all surgical specimens were histopathologically diagnosed according to the 2016 WHO classification. Both peptide nucleic acid–mediated clamping polymerase chain reaction and immunohistochemical analysis were performed to detect the IDH1-R132H mutation.[1] Monoclonal antibody H09 was used for immunohistochemical analysis. The degree of IDH1-R132H staining was considered positive if stained cells were observed, while specimens without stained cells were deemed negative.[26,27] In *IDH1*-negative cases, the *IDH1/2* status was confirmed by the peptide nucleic acid–mediated clamping polymerase chain reaction. Targeted next-generation sequencing was performed using the TruSight Tumor 170 panel (Illumina; https://www.illumina.com/products/by-type/clinical-research-products/trusight-tumor-170.html).[28,29] For copy number analysis, *EGFR* genes with greater than a 2-fold change relative to the average level were considered to have undergone amplification. The *TERT* promotor mutation was determined using a pyrosequencing assay, and the C228T and C250T mutations were analyzed, as described previously.[29]

In the TCGA dataset, the detailed information of molecular subtyping is provided in the Genomic Data Commons Data Portal of The Cancer Genome Atlas Low Grade Glioma (TCGA-LGG) data collection (https://www.cancer.gov/about-nci/organization/ccg/research/structural-genomics/tcga/studied-cancers/glioma).[20]

Feature Selection and Classification Methods
Feature selection and classification methods were performed using R software (Version 3.5.1). To avoid collinearity and minimize the potential risk of overfitting while handling high-dimensional radiomic features,[30,31] we used the least absolute shrinkage and selection operator (LASSO) and recursive feature elimination (RFE) to select the important features using the caret R package.[32] Feature selection was performed before model construction using either LASSO, RFE, or RFE + LASSO, when LASSO was performed after RFE to further minimize the redundant features. Three subsets of selected features were combined with 4 different machine learning classifiers: XGboost (https://xgboost.ai), support vector machine (SVM), linear discriminant analysis, and adaptive boosting. The performance of the feature-selection methods + classifiers was tested using 5-fold cross-validation with 3 repetitions to enhance the generalizability of our results.

Statistical Analysis
Statistical analysis was performed using R software (Version 3.5.1).

Interobserver agreement for assessing VASARI features was expressed with the weighted κ coefficients as follows: < 0.20, poor; 0.21–0.40, fair; 0.41–0.60, moderate; 0.61–0.80, good; 0.81–1.00, excellent.[33]

In the training set, there were 4 different models: model 1, clinical features, only age and WHO grade; model 2, VASARI features only; model 3, VASARI + radiomic features; and model 4, clinical + VASARI + radiomic features. Multivariable logistic regression was used to develop models 1 and 2: model 1 with 2 clinical features, patient age and WHO grade; model 2 with VASARI features. In models 3 and 4, twelve combinations of the aforementioned feature-selection methods and machine learning classifiers were used. These 4 models were validated in the test set. Receiver operating characteristic curves were obtained, and the area under the curve (AUC) was calculated to measure the predictive performance. The AUCs from different models were compared by mean of the Delong method, and multiple comparisons were corrected using the Benjamini-Hochberg procedure.[34]

RESULTS
The characteristics of enrolled patients from all 3 datasets are summarized in Table 1. The proportions of *IDH* wild-type lower-grade gliomas with molecular features of GBM were 73.4% (47/64) and 56.1% (32/57) in the training and test sets, respectively.
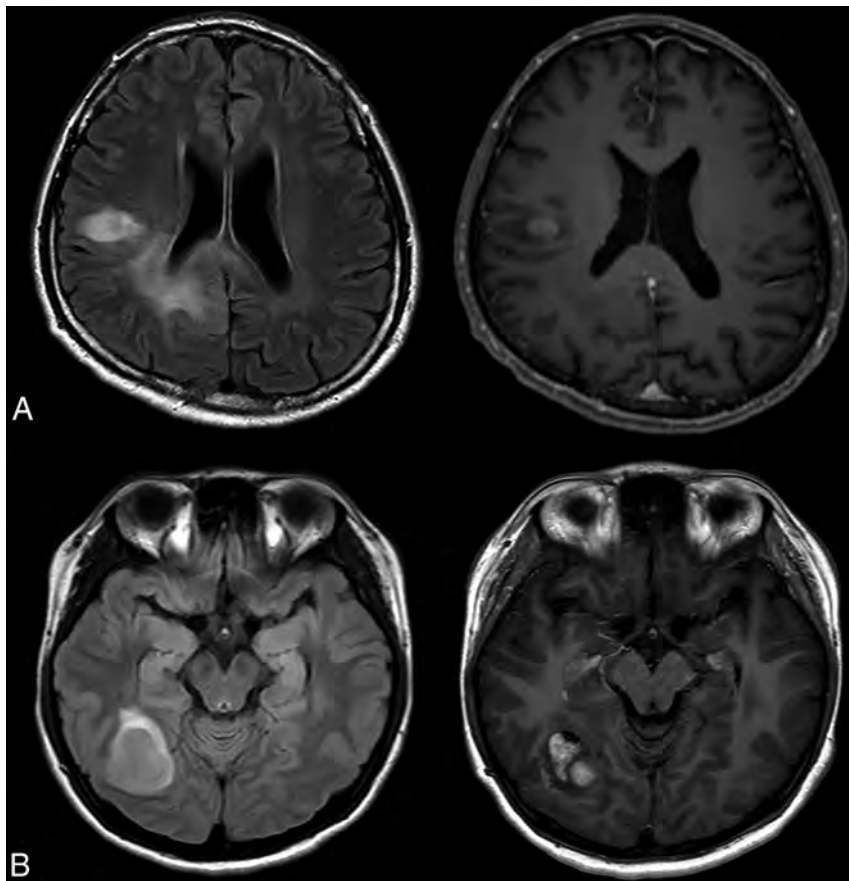
FIG 2. Representative cases of *IDH* wild-type lower-grade gliomas with (*A*) and without (*B*) molecular features of GBM. *A*, Initial MR imaging of a 49-year-old man with *IDH* wild-type lower-grade glioma with molecular features of GBM, WHO grade III. MRIs reveal infiltrative T2-hyperintense tumor in the right frontal and parietal lobes extending into the corpus callosum with cortical involvement (*left*). Focal contrast enhancement is noted in the right frontal lobe (*right*). *B*, Initial MRIs of a 26-year-old woman without molecular features of GBM, WHO grade III. MRIs reveal a relatively well-defined enhancing mass with peritumoral edema in the right temporo-occipital lobe without cortical involvement.

Representative figures of *IDH* wild-type diffuse gliomas with and without molecular features of GBM are presented in Fig 2.

Model 1 (Clinical Features Only)
The predictive performances of model 1 were 0.863 (95% confidence interval, 0.753–0.972) and 0.514 (95% CI, 0.356–0.672) in the training and the test sets, respectively.

Model 2 (VASARI Features Only)
The predictive performances of model 2 with only VASARI features were 0.988 (95% CI, 0.969–1) and 0.648 (95% CI, 0.511–0.784) in the training and the test sets, respectively.

Model 3 (VASARI + Radiomic Features)
In the training set, model 3 accurately predicted the status of molecular features of GBM in *IDH* wild-type lower-grade gliomas with high AUCs, ranging from 0.872 to 1. In the test set, all the AUCs of models 3 with different combinations of feature-selection methods and classifiers are presented in Fig 3. Model 3 predicted the status of molecular GBM with AUCs ranging from 0.567 to 0.854. The combination of SVM and RFE showed the highest predictive performance with an AUC of 0.854 (95% CI, 0.766–0.941), with a sensitivity and specificity of 71.9% and 88.0%, respectively.

Interobserver agreement for VASARI features was good-to-excellent (range, 0.774–1.000) (Online Supplemental Data). The imaging features with the highest interobserver agreement were tumor location, side of lesion center, presence of enhancement, and multifocality ($\kappa = 1$); the lowest interobserver agreement was found in the proportion of necrosis ($\kappa = 0.774$).

The differences of VASARI features between the *IDH* wild-type lower-grade gliomas with and without molecular features of GBM in the training and the test sets are provided in the Online Supplemental Data. In both the training and test sets, cortical involvement was the only feature that was significantly different between the 2 groups.

In the training set, a total of 5, 174, and 9 features were selected through LASSO, RFE, and RFE + LASSO, respectively. Five consistently selected features among all 3 methods were 2 texture features, 1 first-order feature, and 2 VASARI features: short run emphasis (T2), gray-level nonuniformity normalized (postcontrast T1), minimum (T2), infiltrative tumor growth, and cortical involvement.

Model 4 (Clinical + VASARI + Radiomic Features)
In the training set, model 4 accurately predicted the status of molecular features of GBM in *IDH* wild-type lower-grade gliomas with high AUCs, ranging from 0.943 to 1. In the test set, model 4 predicted the status of molecular GBMs with AUCs ranging from 0.524 to 0.863. The combination of SVM and RFE provided the highest predictive performance with an AUC of 0.863 (95% CI, 0.778–0.947), with a sensitivity and specificity of 81.3% and 88.0%, respectively.

Model Comparisons
The best-performing models in the test set from models 3 and 4 were compared with each other and with models 1 and 2 (Table 2 and Fig 4). Model 3 (AUC = 0.854) and model 4 (AUC = 0.863) yielded significantly superior performances for molecular GBM-status prediction compared with model 1 (AUC = 0.514; $P <$ .001, both) and model 2 (AUC = 0.648; $P =$ .023 and .02, respectively). There was no significant difference between models 3 and 4 ($P =$ .476).

DISCUSSION

In this study, we integrated MR imaging features with machine learning techniques to establish accurate models to identify the specific subset of *IDH* wild-type lower-grade gliomas that had molecular features of GBM. Our models were subsequently tested using an independent test set, which proved their generalizability and robustness (AUC = 0.854).

Several studies have reported that *EGFR* amplification and *TERT* promotor mutations are significantly associated with aggressive tumor behavior and worse prognosis in patients with lower-grade gliomas[35-38] and GBMs.[39-41] Particularly, because the alterations in the *EGFR* gene are the potential therapeutic targets, several previous studies attempted to capture the imaging signature of *EGFR* mutations and to detect them noninvasively in an in vivo setting using complex multiparametric MR imaging or perfusion MR imaging in patients with GBM.[42,43] Also in *IDH* wild-type lower-grade gliomas, tumors having *EGFR* amplification or *TERT* promotor mutations can be classified into "molecularly" high-grade tumors with a significantly shorter survival rate than gliomas with no mutations.[7] Subsequently, the recent cIMPACT-NOW defined *IDH* wild-type lower-grade gliomas with 1 of 3 characteristics (*EGFR* amplification, +7/–10 loss, or *TERT* promotor mutations) as "diffuse astrocytic glioma, *IDH*-wild-type, with molecular features of GBM, WHO grade IV."[10]

Therefore, in our study, we investigated whether the subset of *IDH* wild-type lower-grade gliomas with molecular features of GBM could be predicted noninvasively using comprehensive MR imaging analysis. Rather than considering individual *EGFR* amplification or *TERT* promotor mutation, we focused on predicting the molecular features of GBM. This focus was because the molecular features of GBM incorporate both of these genetic mutations, which enable the identification of more patients with unfavorable prognoses who might need more aggressive treatment. In addition, we included only the *IDH* wild-type subgroup of lower-grade gliomas in our study because predicting the molecular GBM status in this subgroup might be more clinically relevant according to the cIMPACT-NOW recommendations.

The patients' age and WHO grades served as our clinical parameters, according to previous studies that reported that *IDH* wild-type grade II and III gliomas with genetic alterations characteristic of GBM were diagnosed at a significantly older age.[35,38] WHO grade III, together with high-risk genetic alterations, was also a significant prognostic factor in patients with *IDH* wild-type lower-grade gliomas.[7,38] However, our model with only clinical features showed a poor predictive performance (AUC = 0.514). Furthermore, comprehensive MR imaging analysis using VASARI allowed slightly better prediction for the molecular GBM status than the clinical features; however, it still showed unsatisfactory performance (AUC = 0.648). A recent study revealed that radiomics allowed the prediction of *EGFR* expression in patients with diffuse lower-grade gliomas.[17] Our study results proved that radiomics functions equally well in the *IDH* wild-type subgroup of lower-grade gliomas because it can accurately stratify patients according to the molecular GBM status when added to the VASARI features (AUC = 0.854). It is important to identify the molecular features of GBM beyond *IDH* mutation status noninvasively because they convey prognostic information that could help clinicians decide different treatment schemes for their patients.

Among 5 consistently selected features, 2 features were texture-based. Texture analysis refers to a variety of
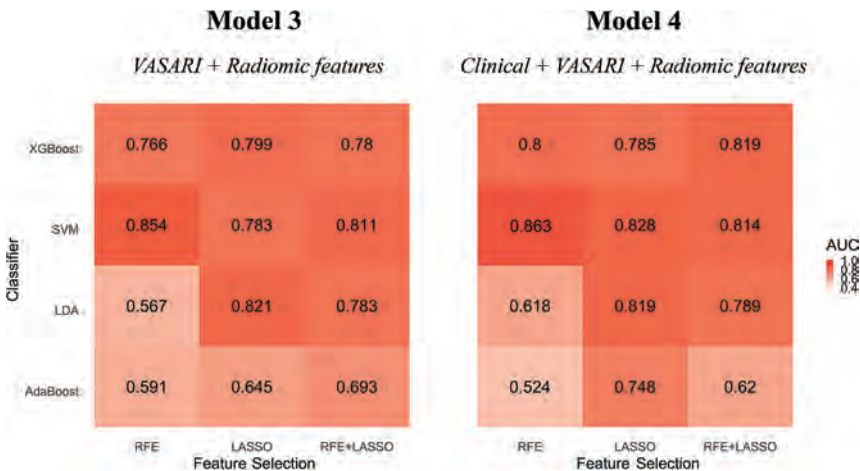
FIG 3. Heat maps illustrating the predictive performance (AUCs) of the different combinations of feature selection methods (*rows*) and classifiers (*columns*) from models 3 and 4 in the test set. LDA indicates linear discriminant analysis; AdaBoost, adaptive boosting.

Table 2: Highest predictive performances of different models in identifying the molecular features of glioblastomas in *IDH* wild-type lower-grade gliomas in the test set

Model	Feature Selection + Classifier	AUC	P Values for Model Comparisons		
Model 1 (clinical features)	NA	0.514 (0.356–0.672)			
Model 2 (VASARI features)	NA	0.648 (0.511–0.784)			
Model 3 (VASARI + radiomics features)	RFE + SVM	0.854 (0.766–0.941)	<.001[a]	.023[b]	
Model 4 (clinical + VASARI + radiomics features)	RFE + SVM	0.863 (0.778–0.947)	<.001[a]	.02[b]	.476[c]

Note:—NA indicates not applicable.
[a] Compared with model 1.
[b] Compared with model 2.
[c] Compared with model 3.
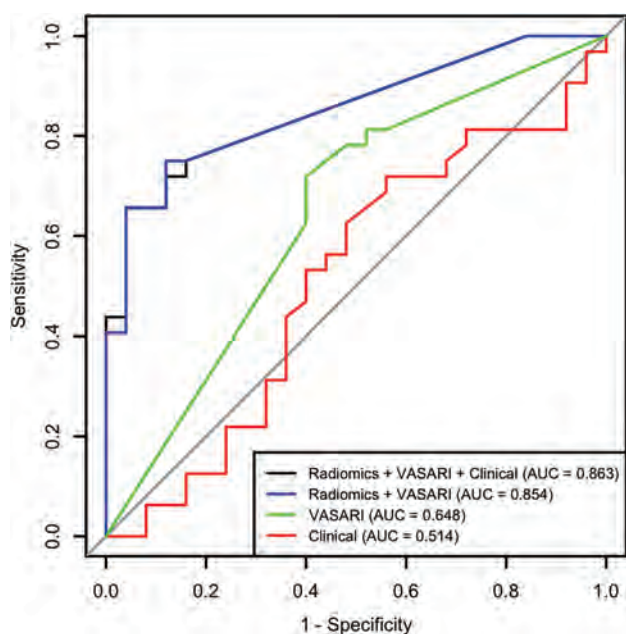
FIG 4. Receiver operating characteristic curves of models 1, 2, 3, and 4 with the highest predictive performance. The combination of SVM and RFE shows the highest predictive performance in both models 3 and 4.

mathematic methods used to quantify the gray-level spatial variations within an image to derive textural features, which reflect intratumoral heterogeneity.[16] These textural features reflecting intratumoral heterogeneity have shown potential in predicting specific genetic mutations[17-19] and survival rates[44] in patients with lower-grade gliomas. Specifically, one of the gray-level run length matrix features called short run emphasis derived from T2WI was significantly associated with *EGFR* expression in patients with lower-grade gliomas in a recent study,[17] which was also selected as a potential predictor in our study. Another selected gray-level run length matrix feature called gray-level nonuniformity normalized derived from postcontrast T1 has also been reported to have a significant association with *TERT* promotor mutation status in lower-grade gliomas.[45] Because the gray-level run length matrix is a measurement of regional heterogeneity,[16] tumors with higher values of those features are more likely to carry molecular features of GBM.

The proportions of tumors with molecular features of GBM were different across the 3 datasets. In the TCGA dataset, tumors with molecular features of GBM were approximately 80%, which was the highest. In the test set, approximately half of the tumors had molecular features of GBM. We believe that these differences reflect the differences in patient characteristics at each institution. The innate heterogeneity within the TCGA dataset might have also contributed to the differences. However, MR imaging features showed superior predictive performances when tested in the new external validation set, regardless of the difference in proportions of the tumors with features of molecular GBM, which proved their robustness.

There are several limitations of this study. First, this was a retrospective study with a small number of patients available from each dataset. Information on *EGFR* amplification or *TERT*

promotor mutation was not available in many cases, and only a small number of tumors with known genetic alterations were studied. It would be highly desirable if we could compare the performances of different combinations of feature-selection methods and classifiers on a separate validation set and then test the final model on a test set, to obtain more reliable results. However, because the number of enrolled patients was low, we were not able to have another separate validation set. Instead, we performed 5-fold cross-validation with 3 repetitions in the training set. Future studies with larger numbers of patients are required to validate our study results.

Second, the combination of whole chromosome 7 gain and 10 loss is also one of the key genetic alterations that determine the status of molecular GBM; however, this could not be evaluated because the relevant information was not available in the test set. Further studies using a larger number of patients with available +7/−10 information are required to validate our study results. Third, although there have been some issues of interobserver variability in the grading of gliomas,[46-48] we could not calculate the interrater reliability of the WHO grade in this study because 1 senior neuropathologist reviewed the pathologic reports of enrolled subjects. In addition, the molecular subtyping of gliomas was performed by senior pathologists in each academic institution according to 2016 WHO classification; however, whether there were any discrepancies between the pathologists was not evaluated. Fourth, we did not perform the skull-stripping before the signal intensity normalization in the preprocessing for the radiomics feature extraction. However, because all patients' MR images were processed without skull-stripping uniformly, the final results of our study might not have been affected profoundly. Furthermore, we believe that it is noteworthy to investigate the predictive potential of radiomics in future studies with various research topics: whether radiomics could accurately classify *IDH* wild-type lower-grade gliomas with molecular features of GBM and grade IV GBM or could predict the WHO grade in gliomas with specific genetic mutations such as *EGFR* amplification or *TERT* promotor mutation.

CONCLUSIONS

MR imaging features combined with machine learning classifiers can noninvasively predict the molecular features of GBM in *IDH* wild-type lower-grade gliomas with high accuracy.

REFERENCES

1. Yan H, Parsons DW, Jin G, et al. **IDH1 and IDH2 mutations in gliomas.** *N Engl J Med* 2009;360:765–73 CrossRef Medline
2. Louis DN, Perry A, Reifenberger G, et al. **The 2016 World Health Organization Classification of Tumors of the Central Nervous System: a summary.** *Acta Neuropathol* 2016;131:803–20 CrossRef Medline
3. Jiao Y, Killela PJ, Reitman ZJ, et al. **Frequent ATRX, CIC, FUBP1 and IDH1 mutations refine the classification of malignant gliomas.** *Oncotarget* 2012;3:709–22 CrossRef Medline
4. Brat DJ, Verhaak RG, Aldape KD, et al; Cancer Genome Atlas Research Network. **Comprehensive, integrative genomic analysis of**

diffuse lower-grade gliomas. *N Engl J Med* 2015;372:2481–98 CrossRef Medline

5. Metellus P, Coulibaly B, Colin C, et al. **Absence of *IDH* mutation identifies a novel radiologic and molecular subtype of WHO grade II gliomas with dismal prognosis.** *Acta Neuropathol* 2010;120:719–29 CrossRef Medline

6. Eckel-Passow JE, Lachance DH, Molinaro AM, et al. **Glioma groups based on 1p/19q, *IDH*, and *TERT* promoter mutations in tumors.** *N Engl J Med* 2015;372:2499–508 CrossRef Medline

7. Aibaidula A, Chan AK, Shi Z, et al. **Adult *IDH* wild-type lower-grade gliomas should be further stratified.** *Neuro Oncol* 2017;19:1327–37 CrossRef Medline

8. Chan AK, Yao Y, Zhang Z, et al. ***TERT* promoter mutations contribute to subset prognostication of lower-grade gliomas.** *Mod Pathol* 2015;28:177–86 CrossRef Medline

9. Chan AK, Yao Y, Zhang Z, et al. **Combination genetic signature stratifies lower-grade gliomas better than histological grade.** *Oncotarget* 2015;6:20885–901 CrossRef Medline

10. Brat DJ, Aldape K, Colman H, et al. **cIMPACT-NOW update 3: recommended diagnostic criteria for "Diffuse astrocytic glioma, *IDH*-wildtype, with molecular features of glioblastoma, WHO grade IV."** *Acta Neuropathol* 2018;136:805–10 CrossRef Medline

11. Gutman DA, Cooper LA, Hwang SN, et al. **MR imaging predictors of molecular profile and survival: multi-institutional study of the TCGA glioblastoma data set.** *Radiology* 2013;267:560–69 CrossRef Medline

12. Gutman DA, Dunn WD, Grossmann P, et al. **Somatic mutations associated with MRI-derived volumetric features in glioblastoma.** *Neuroradiology* 2015;57:1227–37 CrossRef Medline

13. Park YW, Han K, Ahn SS, et al. **Prediction of IDH1-mutation and 1p/19q-codeletion status using preoperative MR imaging phenotypes in lower grade gliomas.** *AJNR Am J Neuroradiol* 2018;39:37–42 CrossRef Medline

14. Gillies RJ, Kinahan PE, Hricak H. **Radiomics: images are more than pictures, they are data.** *Radiology* 2016;278:563–77 CrossRef Medline

15. Aerts HJ, Velazquez ER, Leijenaar RT, et al. **Decoding tumour phenotype by noninvasive imaging using a quantitative radiomics approach.** *Nat Commun* 2014;5:4006 CrossRef Medline

16. Molina D, Pérez-Beteta J, Martínez-González A, et al. **Influence of gray level and space discretization on brain tumor heterogeneity measures obtained from magnetic resonance images.** *Comput Biol Med* 2016;78:49–57 CrossRef Medline

17. Li Y, Liu X, Xu K, et al. **MRI features can predict *EGFR* expression in lower grade gliomas: a voxel-based radiomic analysis.** *Eur Radiol* 2018;28:356–62 CrossRef Medline

18. Li Y, Qian Z, Xu K, et al. **MRI features predict p53 status in lower-grade gliomas via a machine-learning approach.** *Neuroimage Clin* 2018;17:306–11 CrossRef Medline

19. Li Y, Qian Z, Xu K, et al. **Radiomic features predict Ki-67 expression level and survival in lower grade gliomas.** *J Neurooncol* 2017;135:317–24 CrossRef Medline

20. Pedano N, Flanders A, Scarpace L, et al. **Radiology data from the Cancer Genome Atlas low grade glioma [TCGA-LGG] collection.** *The Cancer Imaging Archive* 2016 CrossRef

21. **Wiki for the VASARI feature set.** The National Cancer Institute Website. https://wiki.cancerimagingarchive.net/display/Public/VASARI +Research+Project. Updated March 30, 2020. Accessed September 17, 2019

22. Tustison NJ, Avants BB, Cook PA, et al. **N4ITK: improved N3 bias correction.** *IEEE Trans Med Imaging* 2010;29:1310–20 CrossRef Medline

23. Sled JG, Zijdenbos AP, Evans AC. **A nonparametric method for automatic correction of intensity nonuniformity in MRI data.** *IEEE Trans Med Imaging* 1998;17:87–97 CrossRef Medline

24. Shinohara RT, Sweeney EM, Goldsmith J, et al. **Statistical normalization techniques for magnetic resonance imaging.** *Neuroimage Clin* 2014;6:9–19 CrossRef Medline

25. van Griethuysen JJ, Fedorov A, Parmar C, et al. **Computational radiomics system to decode the radiographic phenotype.** *Cancer Res* 2017;77:e104–07 CrossRef Medline

26. Takano S, Tian W, Matsuda M, et al. **Detection of IDH1 mutation in human gliomas: comparison of immunohistochemistry and sequencing.** *Brain Tumor Pathol* 2011;28:115–23 CrossRef Medline

27. Choi J, Lee EY, Shin KJ, et al. **IDH1 mutation analysis in low cellularity specimen: a limitation of diagnostic accuracy and a proposal for the diagnostic procedure.** *Pathol Res Pract* 2013;209:284–90 CrossRef Medline

28. Sahm F, Schrimpf D, Jones DTW, et al. **Next-generation sequencing in routine brain tumor diagnostics enables an integrated diagnosis and identifies actionable targets.** *Acta Neuropathol* 2016;131:903–10 CrossRef Medline

29. Na K, Kim HS, Shim HS, et al. **Targeted next-generation sequencing panel (TruSight Tumor 170) in diffuse glioma: a single institutional experience of 135 cases.** *J Neurooncol* 2019;142:445–54 CrossRef Medline

30. Friedman J, Hastie T, Tibshirani R. **Regularization paths for generalized linear models via coordinate descent.** *J Stat Softw* 2010;33:1–22 Medline

31. Dormann CF, Elith J, Bacher S, et al. **Collinearity: a review of methods to deal with it and a simulation study evaluating their performance.** *Ecography* 2013;36:27–46 CrossRef

32. Kuhn M. **Building predictive models in R using the caret package.** *J Stat Soft* 2008;28 CrossRef

33. Landis JR, Koch GG. **The measurement of observer agreement for categorical data.** *Biometrics* 1977;33:159–74 Medline

34. DeLong ER, DeLong DM, Clarke-Pearson DL. **Comparing the areas under two or more correlated receiver operating characteristic curves: a nonparametric approach.** *Biometrics* 1988;44:837–45 Medline

35. Bale TA, Jordan JT, Rapalino O, et al. **Financially effective test algorithm to identify an aggressive, *EGFR*-amplified variant of *IDH*-wildtype, lower-grade diffuse glioma.** *Neuro Oncol* 2019;21:596–605 CrossRef Medline

36. Weller M, Weber RG, Willscher E, et al. **Molecular classification of diffuse cerebral WHO grade II/III gliomas using genome- and transcriptome-wide profiling improves stratification of prognostically distinct patient groups.** *Acta Neuropathol* 2015;129:679–93 CrossRef Medline

37. Wijnenga MM, Dubbink HJ, French PJ, et al. **Molecular and clinical heterogeneity of adult diffuse low-grade *IDH* wild-type gliomas: assessment of *TERT* promoter mutation and chromosome 7 and 10 copy number status allows superior prognostic stratification.** *Acta Neuropathol* 2017;134:957–59 CrossRef Medline

38. Aoki K, Nakamura H, Suzuki H, et al. **Prognostic relevance of genetic alterations in diffuse lower-grade gliomas.** *Neuro Oncol* 2018;20:66–77 CrossRef Medline

39. Stichel D, Ebrahimi A, Reuss D, et al. **Distribution of *EGFR* amplification, combined chromosome 7 gain and chromosome 10 loss, and *TERT* promoter mutation in brain tumors and their potential for the reclassification of *IDH* wild type astrocytoma to glioblastoma.** *Acta Neuropathol* 2018;136:793–803 CrossRef Medline

40. Gupta A, Young RJ, Shah AD, et al. **Pretreatment dynamic susceptibility contrast MRI perfusion in glioblastoma: prediction of *EGFR* gene amplification.** *Clin Neuroradiol* 2015;25:143–50 CrossRef Medline

41. Ivanidze J, Lum M, Pisapia D, et al. **MRI features associated with *TERT* promoter mutation status in glioblastoma.** *J Neuroimaging* 2019;29:357–63 CrossRef Medline

42. Akbari H, Bakas S, Pisapia JM, et al. **In vivo evaluation of *EGFR*vIII mutation in primary glioblastoma patients via complex multiparametric MRI signature.** *Neuro Oncol* 2018;20:1068–79 CrossRef Medline

43. Bakas S, Akbari H, Pisapia J, et al. **In vivo detection of *EGFR*vIII in glioblastoma via perfusion magnetic resonance imaging signature**

consistent with deep peritumoral infiltration: the φ-Index. *Clin Cancer Res* 2017;23:4724–34 CrossRef Medline

44. Liu X, Li Y, Qian Z, et al. **A radiomic signature as a non-invasive predictor of progression-free survival in patients with lower-grade gliomas.** *Neuroimage Clin* 2018;20:1070–77 CrossRef Medline

45. Jiang C, Kong Z, Zhang Y, et al. **Conventional magnetic resonance imaging-based radiomic signature predicts telomerase reverse transcriptase promoter mutation status in grade II and III gliomas.** *Neuroradiology* 2020;62:803–13 CrossRef Medline

46. Kros JM. **Grading of gliomas: the road from eminence to evidence.** *J Neuropathol Exp Neurol* 2011;70:101–09 CrossRef Medline

47. Prayson RA, Agamanolis DP, Cohen ML, et al. **Interobserver reproducibility among neuropathologists and surgical pathologists in fibrillary astrocytoma grading.** *J Neurol Sci* 2000;175:33–39 CrossRef Medline

48. Vigneswaran K, Neill S, Hadjipanayis CG. **Beyond the World Health Organization grading of infiltrating gliomas: advances in the molecular genetics of glioma classification.** *Ann Transl Med* 2015;3:95 CrossRef Medline

Utility of Contrast-Enhanced T2 FLAIR for Imaging Brain Metastases Using a Half-dose High-Relaxivity Contrast Agent

T. Jin, M. Ge, R. Huang, Y. Yang, T. Liu, Q. Zhan, Z. Yao, and H. Zhang

ABSTRACT

BACKGROUND AND PURPOSE: Efficient detection of metastases is important for patient' treatment. This prospective study was to explore the clinical value of contrast-enhanced T2 FLAIR in imaging brain metastases using half-dose gadobenate dimeglumine.

MATERIALS AND METHODS: In vitro signal intensity of various gadolinium concentrations was explored by spin-echo T1-weighted imaging and T2 FLAIR. Then, 46 patients with lung cancer underwent nonenhanced T2 FLAIR before administration of half-dose gadobenate dimeglumine and 3 consecutive contrast-enhanced T2 FLAIR sequences followed by 1 spin-echo T1WI after administration of half-dose gadobenate dimeglumine. After an additional dose of 0.05 mmol/kg, 3D brain volume imaging was performed. All brain metastases were classified as follows: solid-enhancing, $\geq$ 5 mm (group A); ring-enhancing, $\geq$ 5 mm (group B); and lesion diameter of $<$5 mm (group C). The contrast ratio of the lesions on 3 consecutive phases of contrast-enhanced T2 FLAIR was measured, and the percentage increase of contrast-enhanced T2 FLAIR among the 3 groups was compared.

RESULTS: In vitro, the maximal signal intensity was achieved in T2 FLAIR at one-eighth to one-half of the contrast concentration needed for maximal signal intensity in T1WI. In vivo, the mean contrast ratio values of metastases on contrast-enhanced T2 FLAIR for the 3 consecutive phases ranged from 63.64% to 83.05%. The percentage increase (PI) values of contrast-enhanced T2 FLAIR were as follows: $PI_A < PI_B$ ($P = .001$) and $PI_A < PI_C$ ($P < .001$). The degree of enhancement of brain metastases on contrast-enhanced T2 FLAIR was lower than on 3D brain volume imaging ($P < .001$) in group A, and higher than on 3D brain volume imaging ($P < .001$) in group C.

CONCLUSIONS: Small or ring-enhancing metastases can be better visualized on delayed contrast-enhanced T2 FLAIR using a half-dose high-relaxivity contrast agent.

ABBREVIATIONS: BRAVO = brain volume imaging; CE = contrast-enhanced; CR = contrast ratio; GBCA = gadolinium-based contrast agents; PI = percentage increase

B rain metastases occur in approximately 25% of patients with cancer and account for 40% of adult brain tumors.[1] The incidence of brain metastases in patients with lung cancer is highest (19.9%),[2] resulting in high morbidity and mortality.[3] Small metastases, not combined with vasogenic edema or mass effects, are often missed.[1] Improvement of the early detection of small brain

metastases will contribute to developing treatment protocols and will affect the outcomes[4] because small lesions effectively respond to therapies and can be controlled at a substantially higher rate compared with larger lesions.[5,6] For patients with metastases, contrast-enhanced T1WI (CE-T1WI) should be repeatedly performed to assess the progress of brain metastases[7,8] or the efficacy of treatment.[9,10] The conspicuity and detection rate of brain metastases can be improved with a higher dose of gadolinium-based contrast agents (GBCA).[11] However, multiple enhanced examinations or use of higher contrast doses may increase the potential adverse effects, such as nephrogenic systemic fibrosis,[12,13] and may lead to higher gadolinium deposition in the brain[14] or other tissues.[15,16]

Therefore, reducing the gadolinium-based contrast agent dose may decrease the adverse effects produced by gadolinium accumulation, which is crucial to the patient's health. T2 FLAIR is an inversion recovery pulse sequence that is sensitive to low concentrations of GBCA in the tissue.[17] It is reported that only one-

quarter of the routine dose of GBCA is needed for CE-T2 FLAIR to achieve a signal enhancement comparable with that of CE-T1WI; moreover, CE-T2 FLAIR may offer additional morphologic information compared with CE-T1WI alone.[17,18] Due to the suppression of intravascular and CSF signal,[19] CE-T2 FLAIR imaging has been used in the detection of various intra- and extra-axial brain lesions, eg, the delineation of meningeal lesions including meningoencephalitis and leptomeningeal metastases.[20-22]

Previous studies mostly focused on the use of CE-T2 FLAIR after use of the normal GBCA dose; no studies were performed to assess the utility of low-dose CE-T2 FLAIR in the detection of brain metastases. Additionally, an increased delay of CE-T2 FLAIR scanning can improve the diagnosis of leptomeningeal infectious or tumoral diseases,[23] which means CE-T2 FLAIR has a relationship with scanning time. The purpose of the present study was to investigate the value of delayed low-dose CE-T2 FLAIR compared with routine-dose CE brain volume imaging (BRAVO; GE Healthcare) for contrast enhancement in brain metastases.

MATERIALS AND METHODS

Phantom Study
Eleven 2-mL tubes filled with gadobenate dimeglumine (Gd-BOPTA, MultiHance; Bracco) at different concentration (0.015, 0.03, 0.06, 0,12, 0.24, 0.48, 0.96, 1.92, 3.84, 7.68, and 15.36 mmol/L) were tested by T2 FLAIR and T1WI, with the following parameters—T2 FLAIR: TR = 8000 ms, TE = 150 ms, TI = 2250 ms; T1WI: TR = 1800 ms, TE = 24 ms. ROI measurements of the signal intensity were made in axial slices of the test tube in the homogeneous-appearing area.

Clinical Study
Patients. Our study was conducted under the supervision of the institutional review board of Huashan Hospital, Fudan University, and informed consent was obtained from each patient before the examination. From February 2018 to July 2019, ninety patients were consecutively enrolled into our study; 7 patients had MR imaging contraindications, and 37 patients were excluded because they had undergone radiation therapy, chemotherapy, or gamma knife radiosurgery within the preceding 2 months. The predefined criteria for brain metastasis were as follows:[8] 1) a new enhancing lesion or size change of a pre-existing lesion detected on 2-month follow-up MR imaging; and 2) the lesion must be located in the brain parenchyma and show enhancement either on CE-BRAVO or CE-T2 FLAIR.

Clinical MR Imaging Protocol. MR imaging of the patients was performed on a 3T MR imaging system (Signa HDxt; GE Healthcare) with an 8-channel phased array coil. Data and information on the patients for this study are presented in the flow chart (Fig 1). All patients underwent precontrast conventional MR imaging, including an axial T1WI (TR/TE = 2050/24 ms), axial T2WI (TR/TE = 3340/120 ms), and axial T2 FLAIR sequences (TR/TE/TI = 8000/150/2250 ms); all sequences had excitations = 1, thickness = 2 mm, and interstitial gap = 1 mm.

After intravenous bolus injection of half-dose (0.05 mmol/kg) Gd-BOPTA, CE-T2 FLAIR was acquired 3 consecutive times
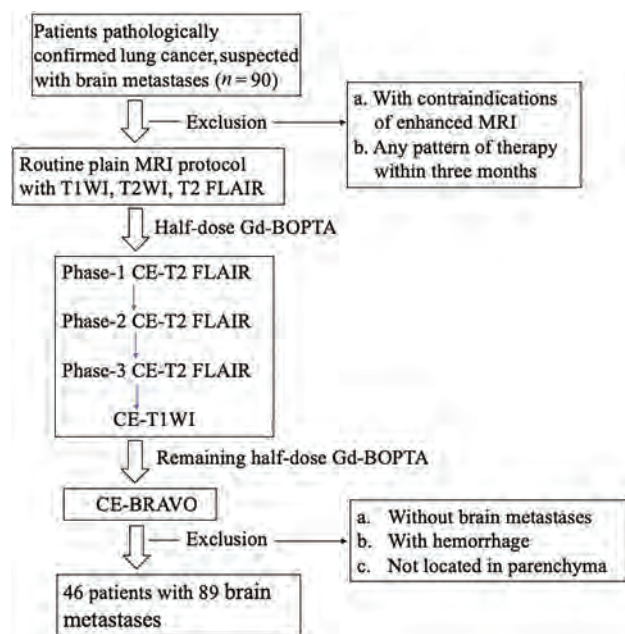
FIG 1. Flow chart of the study population.

(Phase 1 to Phase 3: immediate scanning, 2 minutes 49 seconds, and 5 minutes 38 seconds after contrast application) to observe the optimal delay time; then, half-dose CE-T1WI was performed. Following application of the remaining dose of 0.05 mmol/kg, a 3D contrast-enhanced CE-BRAVO sequence (TR = 7.7 ms, TE = 12 ms, flip angle = 15°, section thickness = 2 mm, section gap = 0 mm) was acquired. The scan time points for each sequence after enhancement were as follows—precontrast T1WI, T2WI, T2 FLAIR, 0.05 mmol/kg of Gd-BOPTA; CE-T2 FLAIR (Phase1: immediate scanning); CE-T2 FLAIR (Phase two: 2 minutes 49 seconds); CE-T2 FLAIR (Phase three: 5 minutes 38 seconds); CE-T1WI (7 minutes 14 seconds), 0.05 mmol/kg of Gd-BOPTA; and CE-BRAVO (9 minutes 7 seconds).

MR Imaging Analysis
The MR imaging data were evaluated and analyzed on an AW4.6 workstation (GE Healthcare).

Lesion Grouping. The enhancement pattern of brain metastases was assessed and classified into solid- and ring-enhancing lesions. The longest diameter of the lesion was measured on both axial CE-BRAVO and axial CE-T2 FLAIR. The lesions were grouped according to their size (max diameter < or ≥5 mm), and the enhancement pattern (solid or rim enhancement) was divided into the following groups:

Group A: solid-enhancing lesions with ≥5-mm diameter
Group B: ring-enhancing lesions with ≥5-mm diameter
Group C: lesions with <5-mm diameter.

Subjective Scoring of Enhancement Degree. The degree of enhancement on CE-T2 FLAIR, CE-T1WI, and CE-BRAVO was qualitatively assessed using a 3-point scale by 2 experienced radiologists (each with >6 years of experience in neuroradiology). If the scoring was different, both radiologists would reach an agreement after discussion. The scoring criteria were as follows—1
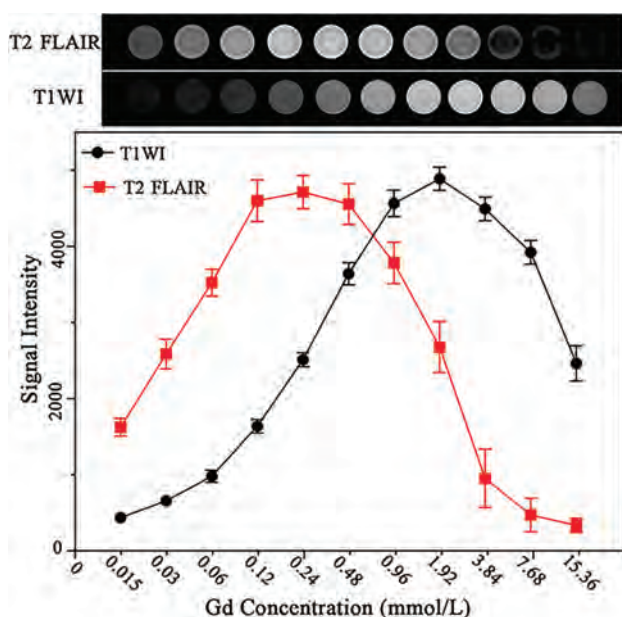
FIG 2. Images of phantom tubes containing increasing concentrations of gadobenate dimeglumine (0.015–15.36 mmol/L) acquired by T2 FLAIR and CE-T1WI. Gd indicates gadolinium.

point: poor enhancement (the signal intensity of the lesions was almost equal to that of the adjacent white matter and hardly identifiable; missed lesions were also included in this group); 2 points: moderate enhancement (the signal intensity was moderately higher than that of the adjacent white matter, but reliably identifiable); and 3 points: good enhancement (the signal intensity was significantly higher than that of the adjacent white matter and easily identifiable).

Quantitative Index Measurement. Contrast ratio (CR) was calculated for the 3 consecutive CE-T2 FLAIR sequences as follows:

$$CR = [(SI_{CE\text{-}T2FLAIR} - SI_{NWM})/SI_{NWM}] \times 100\%.$$

$SI_{CE\text{-}T2FLAIR}$ represents the signal intensity of the lesion after enhancement, and SI_{NWM} represents the signal intensity of ROI-based normal-appearing white matter (NWM) adjacent to the tumor.

Percentage increase (PI) was used to observe the real enhancement degree between the nonenhanced T2 FLAIR and CE-T2 FLAIR[1] to avoid an inherent high signal on nonenhanced T2 FLAIR.

$$PI = [(SI_{CE\text{-}T2\ FLAIR} - SI_{nonenhanced\ T2\ FLAIR})/SI_{nonenhanced\ T2\ FLAIR}] \times 100\%.$$

$SI_{CE\text{-}T2\ FLAIR}$ represents the signal intensity after enhancement, and $SI_{nonenhanced\ T2\ FLAIR}$ represents the signal intensity before enhancement.

ROI. Two radiologists independently drew the ROIs guided by an experienced neuroradiologist. Each radiologist drew 3 ROIs, and the mean value was recorded as the final value measured by each radiologist. The mean value of the measurements by 2 radiologists was used as the final value of the patient. "Function tool" (AW 4.6 workstation, GE Healthcare) was used to fuse all sequences (including nonenhanced CE-T2 FLAIR and 3

consecutive CE-T2 FLAIR, CE-T1WI, and CE-BRAVO sequences; then, ROIs were drawn on CE-T2 FLAIR images and propagated to all other sequences to make certain that all ROIs were in the same position. If the ROIs were not in the same position in different sequences after propagation, ROIs were independently drawn to keep them in the same position as much as possible. An ROI was drawn to cover the entire lesion and was placed within a homogeneously enhanced area if all lesions had enhancement. If the lesion was ring-enhancing, the ROI was placed on a homogeneous-appearing part of the ring. Hemorrhagic, necrotic, and vascular areas were carefully spared.

Statistical Analysis
Statistical analysis was performed using the SPSS 21.0 software package (IBM). The measured data were presented as mean [SD].

CR and PI values of 3 consecutive CE-T2 FLAIR sequences from all brain metastases were compared among groups A, B, and C using a paired t test for CR values and a Kruskal–Wallis test for PI values. A χ^2 test was used to compare the qualitative enhancement degree of the 3 sequences. $P < .05$ was statistically significant. In pair-wise comparisons, the corrected significance level was set at .017.

RESULTS
Phantom Study
In vitro experiments demonstrated that the concentration of Gd-BOPTA required to generate reliable signal intensities on CE-T2 FLAIR images was approximately 0.12–0.48 mmol/L, corresponding to one-eighth to one-half lower than the concentration needed to achieve comparable signal intensity on CE-T1WI (Fig 2).

Clinical Study
Forty-six patients (22 men and 24 women; age range, 35–73 years; mean age, 61.7 years) with a total of 89 brain metastatic lesions were included. Twenty-seven lesions were assigned to group A; 23, to group B; and 39, to group C.

The CR measured on consecutive CE-T2 FLAIR sequences was $CR_{Phase1} = 63.64\%$ [SD, 32.19%], $CR_{Phase2} = 77.34\%$ [SD, 40.19%], and $CR_{Phase3} = 83.05\%$ [SD, 46.65%]. CR_{phase1} was significantly lower than CR_{phase2} ($P < .001$); and CR_{phase2} was lower than CR_{phase3} ($P = .01$); thus, an increasing delay between contrast administration and image acquisition led to a significant CR increase in brain metastases (Fig 3). The mean values of PI on the third phase on CE-T2 FLAIR of groups A, B, and C were $PI_A = 31.42\%$ [SD, 11.65%], $PI_B = 58.60\%$ [SD, 27.79%], and $PI_C = 61.05\%$ [SD, 29.55%], respectively. PI_A was significantly lower than PI_B ($P = .001$) and PI_C ($P < .001$). There was no significant difference between PI_B and PI_C ($P = .759$).

Group A. The enhancement degree on half-dose CE-T2 FLAIR was lower than that with half-dose CE-T1WI ($P = .001$) and routine-dose CE-BRAVO ($P < .001$). No significant difference was found between half-dose CE-T1WI and routine-dose CE-BRAVO ($P = .046$) (Fig 4).

Group B. The enhancement degree on half-dose CE-T2 FLAIR was higher than that of half-dose CE-T1WI ($P = .003$) (Fig 5). No
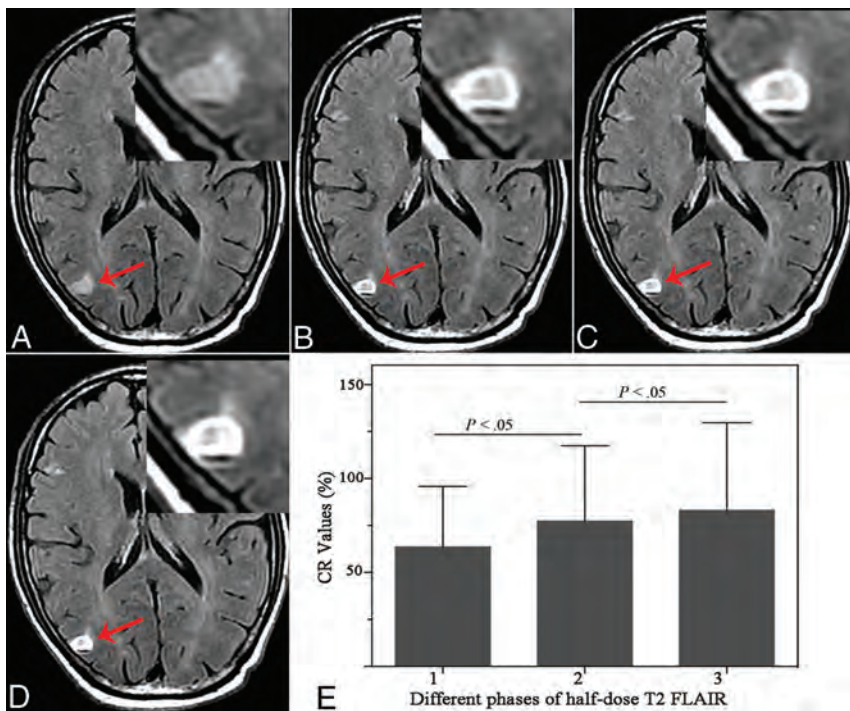
FIG 3. A 64-year-old man with brain metastases in the right parietal cortex (*arrow*). *A*, Nonenhanced T2 FLAIR. *B*, Phase 1: half-dose CE-T2 FLAIR shows a ring-enhancing lesion. *C*, Phase 2: half-dose CE-T2 FLAIR at 2 minutes 49 seconds. *D*, Phase 3: half-dose CE-T2 FLAIR at 5 minutes 38 seconds. *E*, The CR value of the ring wall on T2 FLAIR shows a tendency toward an increase with delayed scanning time.

significant difference was found between half-dose CE-T2 FLAIR and routine-dose CE-BRAVO ($P = .122$), or between half-dose CE-T1WI and routine-dose CE-BRAVO ($P = .113$).

Group C. The enhancement degree on half-dose CE-T2 FLAIR was significantly higher than that of half-dose CE-T1WI ($P < .001$) and routine-dose CE-BRAVO ($P < .001$) (Fig 6). The enhancement degree on routine-dose CE-BRAVO was higher than that on half-dose CE-T1WI ($P < .001$).

Of these brain metastases, 1 of 27 was missed in group A with half-dose CE-T2 FLAIR, while 1 of 23 was missed in group B with half-dose CE-T1WI as shown in Tables 1 and 2. Especially for small lesions in group C, 16 of 39 lesions were missed with half-dose CE-T1WI and 9 of 39 with routine-dose CE-BRAVO as shown in Table 3.

DISCUSSION

Accurate diagnosis of brain metastases before treatment is important because therapeutic planning is dependent on the presence and number of metastatic lesions;[24] however, different imaging methods have different detection efficiencies. In this study, we compared the enhancement degree among half-dose CE-T2 FLAIR, half-dose CE-T1WI, and routine-dose CE-BRAVO in brain metastases and concluded that large and solid-enhancing brain metastases are better visualized on CE-T1WI or CE-BRAVO, while small and ring-enhancing brain metastases are

better shown on CE-T2 FLAIR using a half dose of the high-relaxivity contrast agent gadobenate dimeglumine.

A previous study found that when the GBCA concentration was set between 0.1 and 0.3 mmol/L, the difference in signal intensity between T2 FLAIR and T1WI was obvious;[25] this concentration was almost the same as that in our in vitro study (0.12–0.48 mmol/L). According to our results from the in vitro measurements, CE-T2 FLAIR was more sensitive to lower GBCA concentrations than CE-T1WI and low-dose CE-T2 FLAIR could provide satisfactory signal intensity. Considering that gadolinium cannot penetrate completely from plasma into the lesion, we speculated that half-dose gadolinium might overlap with the optimum concentration range required for CE-T2 FLAIR. We performed 2 different contrast-enhanced T1-weighted sequences, including spin-echo T1WI and 3D-BRAVO as reference standards to assess the enhancement degree of CE-T2 FLAIR. 3D-BRAVO is a gradient-echo sequence that uses thin-layer and no interlayer spacing scans, combined with variable flip angle spin-echo acquisition technology, which can observe lesions from multiple orientations and angles. Previous studies also demonstrated the higher detectability of small metastases using 3D-BRAVO sequences compared with conventional spin-echo sequences.[26] Therefore, in our study, low-dose CE-T2 FLAIR was used to evaluate the conspicuity of cerebral brain metastases with different sizes in comparison with CE-BRAVO after administration of a normal dose (0.1 mmol/kg) of GBCA.

Scanning time is an important factor that affects the signal intensity of lesions, because the infiltration of gadolinium from blood vessels into the extracellular space is a dynamic process. A delay in imaging time may be effective in increasing the signal intensity because it prolongs the perfusion of contrast agent by the leaky neovasculature within the metastases.[27] Keremer et al[23] studied the role of delayed CE-T2 FLAIR in meningeal diseases. They pointed out that delayed CE-T2 FLAIR could achieve more accurate information compared with delayed CE-T1WI or early CE-T2 FLAIR, but optimal imaging time for CE-T2 FLAIR was not studied in their work. In our study, we performed 3 consecutive phases of CE-T2 FLAIR to observe the effect of scanning time on T2 FLAIR, and we found that the later time points (2 minutes 49 seconds to 5 minutes 38 seconds) of CE-T2 FLAIR acquisitions showed a higher enhancement degree compared with the first acquisition. Thus, a delay of at least 3–5 minutes is suggested for the postcontrast CE-T2 FLAIR imaging. As for spin-echo T1WI, Akeson et al[28] suggested that the scan should not be started within 5 minutes after injection; the tumor showed better enhancement when delayed for 5–25 minutes. Thus, we
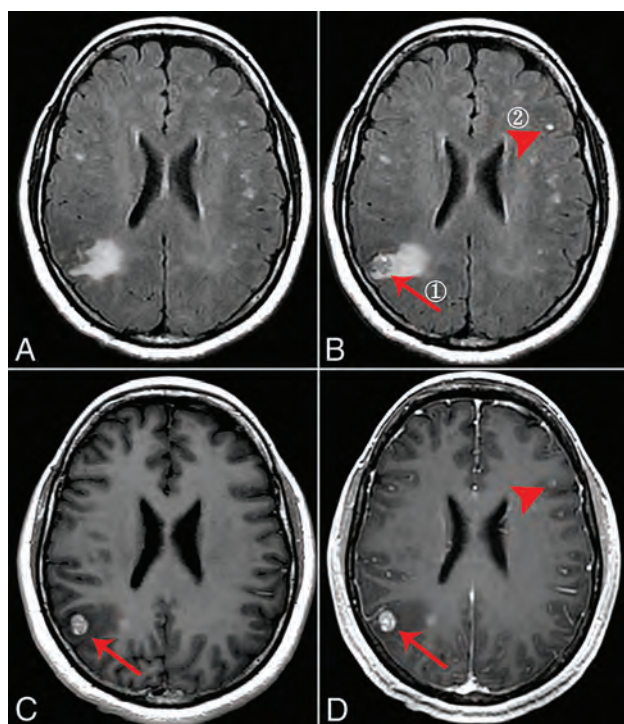
FIG 4. A 48-year-old man with solid brain metastases in the right parietal cortex (①, ≥5 mm, *arrow*) and left frontal cortex (②, <5 mm, *arrowhead*). *A*, Nonenhanced T2 FLAIR. *B*, Phase 3 half-dose CE-T2 FLAIR (①, 1 point; ②, 3 points). *C*, Half-dose CE-T1WI (①, 3 points; ②, missed diagnosis). *D*, Routine-dose CE-BRAVO (①, 3 points; ②, missed diagnosis).

FIG 5. A 62-year-old woman with ring (①, ≥5 mm, *arrow*) and solid (②, ≥5 mm, *arrowhead*) enhancing brain metastases. *A*, Nonenhanced T2 FLAIR. *B*, Phase 3 half-dose CE-T2 FLAIR (①, 3 points; ②, missed diagnosis). *C*, Half-dose CE-T1WI (①, 1 point; ②, 3 points). *D*, Routine-dose CE-BRAVO (①, 2 points; ②, 3 points).

performed CE-T1WI after 3 phases of CE-T2 FLAIR to ensure that all sequences were at their optimum scanning time.

Up to 50% of patients with brain metastasis have 1 lesion.[1,29] For these patients, the detection of metastases is extremely important for treatment. Small metastases are not combined with vasogenic edema, and they usually show slight enhancement.[1] Therefore, they are often missed using nonenhanced T2 FLAIR or enhanced T1-weighted sequences. As for the small metastases (<5 mm) in our study, we found that half-dose CE-T2 FLAIR showed a better enhancement degree and higher a detection rate than CE-T1WI or CE-BRAVO. Our in vitro experiments suggested that T2 FLAIR may show better enhancement at a lower concentration of gadolinium-based contrast agent. This phenomenon is explained by the unique T1-weighting of the T2 FLAIR sequence. Because of the mild T1-weighting induced by the long TI and T1-shortening caused by gadolinium, the T2 FLAIR sequence is more sensitive to low concentrations than a conventional contrast-enhanced T1 sequence.[17,19,25]

When the diameter of the lesion is <5 mm, the damage of the blood-brain barrier is mild and the vascular permeability is relatively low,[30] leading to a low contrast agent concentration in the extracellular space in tumor tissue. The concentration satisfies the enhancement level of CE-T2 FLAIR but does not satisfy that of CE-BRAVO; hence the enhancement degree on CE-T2 FLAIR was higher than that on CE-BRAVO. The capillary permeability varies with the size of metastases,[31,32] and large solid metastases usually have immature vessels with high permeability.[33,34] When

the metastases become larger, the concentration largely accumulates in the extracellular space due to the severe damage to the blood-brain barrier and progression of angiogenesis,[4] dramatically shortening the T2 effect and obscuring the signal-enhanced T1 effect on CE-T2 FLAIR.[35]

Thus, the high concentration of gadolinium "inverts" the T2 FLAIR signal intensity and makes the lesions invisible, but it fulfills the requirement for CE-BRAVO, consistent with our in vitro findings of signal reduction in higher contrast concentrations. In our in vivo experiments, we also found that low-dose CE-T2 FLAIR could clearly show meningeal metastases because the gadolinium concentration is diluted when it leaks into the adjacent CSF through mildly damaged vessels, corresponding to the low-concentration setting used in an in vitro study.[36]

In a previous study, it was demonstrated that the peripheral margin of an invasive tumor has a lower vascular permeability,[30] leading to a higher sensitivity of CE-T2 FLAIR in the delineation of brain metastases boundaries.[22] This effect was found in our study in which brain metastases with rim enhancement showed higher signal enhancement on T2 FLAIR, probably due to a decreased capillary permeability in this part of the tumor.

Although using high-dose contrast on CE-T1WI can increase the detection rate of metastases,[37] it may also increase the adverse effects on patients with cancer. Half-dose CE-T2 FLAIR would not only reduce the contrast agent dose but could also improve the detection rate of small cerebral metastases. However, hyperintense signal of the lesion on nonenhanced T2 FLAIR images caused by prolonged T2 signal could mask the real margin of

Table 2: Group B, comparison of the enhancement degree of 3 sequences of ring-enhancing lesions with diameters of ≥ 5 mm

	Half-Dose CE-T2 FLAIR	Half-Dose CE-T1WI	Routine-Dose CE-BRAVO
Three points	17	6	11
Two points	4	12	10
One point	2 (0[a])	5 (1[a])	2 (0[a])
Total	23	23	23

[a] Missed brain metastases.

Table 3: Group C, comparison of the enhancement degree of 3 sequences of lesions with diameters of < 5 mm

	Half-Dose CE-T2 FLAIR	Half-Dose CE-T1WI	Routine-Dose CE-BRAVO
Three points	32	1	7
Two points	6	9	20
One point	1 (0[a])	29 (16[a])	12 (9[a])
Total	39	39	39

[a] Missed brain metastases.

FIG 6. A 56-year-old woman with small brain metastases (① and ②, <5 mm, *arrow*). *A*, Nonenhanced T2 FLAIR. *B*, Phase 3 half-dose CE-T2 FLAIR (①, 3 points; ②, 3 points). *C*, Half-dose CE-T1WI completely missed the lesions. *D*, Routine-dose CE-BRAVO (①, 1 point; ②, missed diagnosis).

Table 1: Group A, comparison of the enhancement degree of 3 sequences of solid-enhancing lesions with diameters of ≥ 5 mm

	Half-Dose CE-T2 FLAIR	Half-Dose CE-T1WI	Routine-Dose CE-BRAVO
Three points	5	11	20
Two points	7	14	6
One point	15 (1[a])	2 (0[a])	1 (0[a])
Total	27	27	27

[a] Missed brain metastases.

tissue showing contrast enhancement and is not as intuitive as CE-T1WI. This feature might, to some extent, limit the clinical application of CE-T2 FLAIR in central nervous system imaging. Therefore, at least a half-dose CE-T1WI should be acquired after CE-T2 FLAIR to identify the lesion margin or demonstrate metastases with a high concentration of gadolinium. In general, half-dose CE-T2 FLAIR and CE-T1-weighted sequences can provide complementary information.

This study has certain limitations. First, the sample size of each group is relatively small, which may have some negative impact on the statistical results. Second, it would be better to study the signal enhancement of brain metastases on half-dose CE-T2 FLAIR images during a longer time period; however, for ethical reasons, this was not feasible because patients with cancer and brain metastases can undergo MR imaging with only a limited examination time. Third, there is a potential bias in the evaluation of different sequences because the raters were not blinded to the sequence type. Additionally, half-dose CE-T1WI was performed in our study because we intended to ensure that the total dose was halved when our protocol was applied to the clinical practice, but the dosages used for CE-T1WI and CE-BRAVO were different, possibly causing a certain bias in the comparison of the enhancement degree between the 2 sequences.

CONCLUSIONS

CE-T1-weighted sequences and CE-T2 FLAIR are mutually complementary for evaluating brain metastases. Large and solid-enhancing brain metastases are better visualized on CE-T1-weighted sequences, while small and ring-enhancing metastases are better visualized on delayed (3–5 minute) CE-T2 FLAIR sequences using a half-dose of the high-relaxivity contrast agent gadobenate dimeglumine.

REFERENCES

1. Essig M, Knopp MV, Schoenberg SO, et al. **Cerebral gliomas and metastases: assessment with contrast-enhanced fast fluid-attenuated inversion-recovery MR imaging.** *Radiology* 1999;210:551–57 CrossRef Medline
2. Aizer AA, Lee EQ. **Brain metastases.** *Neurol Clin* 2018;36:557–77 CrossRef Medline
3. Sorensen JB, Hansen HH, Hansen M, et al. **Brain metastases in adenocarcinoma of the lung: frequency, risk groups, and prognosis.** *J Clin Oncol* 1988;6:1474–80 CrossRef Medline
4. Ahn SJ, Chung TS, Chang JH, et al. **The added value of double dose gadolinium enhanced 3D T2 fluid-attenuated inversion recovery for evaluating small brain metastases.** *Yonsei Med J* 2014;55:1231–37 CrossRef Medline
5. Park J, Kim J, Yoo E, et al. **Detection of small metastatic brain tumors: comparison of 3D contrast-enhanced whole-brain black-blood imaging and MP-RAGE imaging.** *Invest Radiol* 2012;47:136–41 CrossRef Medline

6. Chang EL, Hassenbusch SJ 3rd, Shiu AS, et al. **The role of tumor size in the radiosurgical management of patients with ambiguous brain metastases.** *Neurosurgery* 2003;53:272–72 CrossRef Medline

7. Park J, Kim EY. **Contrast-enhanced, three-dimensional, whole-brain, black-blood imaging: application to small brain metastases.** *Magn Reson Med* 2010;63:553–61 CrossRef Medline

8. Kim D, Heo YJ, Jeong HW, et al. **Usefulness of the delay alternating with nutation for tailored excitation pulse with T1-weighted sampling perfection with application-optimized contrasts using different flip angle evolution in the detection of cerebral metastases: comparison with MPRAGE.** *AJNR Am J Neuroradiol* 2019;40:1469–75 CrossRef Medline

9. Fahlstrom M, Fransson S, Blomquist E, et al. **Dynamic contrast-enhanced magnetic resonance imaging may act as a biomarker for vascular damage in normal appearing brain tissue after radiotherapy in patients with glioblastoma.** *Acta Radiol Open* 2018;7:2058460118808811 CrossRef Medline

10. Ozturk K, Soylu E, Tolunay S, et al. **Dynamic contrast-enhanced T1-weighted perfusion magnetic resonance imaging identifies glioblastoma immunohistochemical biomarkers via tumoral and peritumoral approach: a pilot study.** *World Neurosurg* 2019;128: e195–208 CrossRef Medline

11. Mathews VP, King JC, Elster AD, et al. **Cerebral infarction: effects of dose and magnetization transfer saturation at gadolinium-enhanced MR imaging.** *Radiology* 1994;190:547–52 CrossRef Medline

12. Rogosnitzky M, Branch S. **Gadolinium-based contrast agent toxicity: a review of known and proposed mechanisms.** *Biometals* 2016;29:365–76 CrossRef Medline

13. Endrikat J, Dohanish S, Schleyer N, et al. **10 years of nephrogenic systemic fibrosis: a comprehensive analysis of nephrogenic systemic fibrosis reports received by a pharmaceutical company from 2006 to 2016.** *Invest Radiology* 2018;53:541–50 CrossRef Medline

14. Tedeschi E, Caranci F, Giordano F, et al. **Gadolinium retention in the body: what we know and what we can do.** *Radiol Med* 2017; 122:589–600 CrossRef Medline

15. Semelka RC, Ramalho J, Vakharia A, et al. **Gadolinium deposition disease: initial description of a disease that has been around for a while.** *Magn Reson Imaging* 2016;34:1383–90 CrossRef Medline

16. Lord ML, Chettle DR, Grafe JL, et al. **Observed deposition of gadolinium in bone using a new noninvasive in vivo biomedical device: results of a small pilot feasibility study.** *Radiology* 2018;287:96–103 CrossRef Medline

17. Mathews VP, Caldemeyer KS, Lowe MJ, et al. **Brain: gadolinium-enhanced fast fluid-attenuated inversion-recovery MR imaging.** *Radiology* 1999;211:257–63 CrossRef Medline

18. Oguz KK, Cila A. **Rim enhancement of meningiomas on fast FLAIR imaging.** *Neuroradiology* 2003;45:78–81 CrossRef Medline

19. Terae S, Yoshida D, Kudo K, et al. **Contrast-enhanced FLAIR imaging in combination with pre- and postcontrast magnetization transfer T1-weighted imaging: usefulness in the evaluation of brain metastases.** *J Magn Reson Imaging* 2007;25:479–87 CrossRef Medline

20. Rumpel H, Chan LL. **Serial FLAIR imaging after Gd-DTPA contrast: pitfalls in stroke trial magnetic resonance imaging.** *Stroke* 2003;34:797–98 CrossRef Medline

21. Mathews VP. **Show me the gadolinium!** *AJNR Am J Neuroradiol* 2005;26:440–41 Medline

22. Ercan N, Gultekin S, Celik H, et al. **Diagnostic value of contrast-enhanced fluid-attenuated inversion recovery MR imaging of intracranial metastases.** *AJNR Am J Neuroradiol* 2004;25:761–65 Medline

23. Kremer S, Abu Eid M, Bierry G, et al. **Accuracy of delayed post-contrast FLAIR MR imaging for the diagnosis of leptomeningeal infectious or tumoral diseases.** *J Neuroradiol* 2006;33:285–91 CrossRef Medline

24. Vecht CJ, Haaxma-Reiche H, Noordijk EM, et al. **Treatment of single brain metastasis: radiotherapy alone or combined with neurosurgery?** *Ann Neurol* 1993;33:583–90 CrossRef Medline

25. Jackson EF, Hayman LA. **Meningeal enhancement on fast FLAIR images.** *Radiology* 2000;215:922–94 CrossRef Medline

26. Furutani K, Harada M, Mawlan M, et al. **Difference in enhancement between spin echo and 3-dimensional fast spoiled gradient recalled acquisition in steady state magnetic resonance imaging of brain metastasis at 3-T magnetic resonance imaging.** *J Comput Assist Tomogr* 2008;32:313–19 CrossRef Medline

27. Lüdemann L, Grieger W, Wurm R, et al. **Quantitative measurement of leakage volume and permeability in gliomas, meningiomas and brain metastases with dynamic contrast-enhanced MRI.** *Magn Reson Imaging* 2005;23:833–41 CrossRef Medline

28. Akeson P, Nordstrom CH, Holtas S. **Time-dependency in brain lesion enhancement with gadodiamide injection.** *Acta Radiol* 1997;38:19–24 CrossRef Medline

29. Delattre JY, Krol G, Thaler HT, et al. **Distribution of brain metastases.** *Arch Neurol* 1988;45:741–44 CrossRef Medline

30. Hasegawa H, Ushio Y, Hayakawa T, et al. **Changes of the blood-brain barrier in experimental metastatic brain tumors.** *J Neurosurg* 1983;59:304–10 CrossRef Medline

31. Yamada K, Ushio Y, Hayakawa T, et al. **Quantitative autoradiographic measurements of blood-brain barrier permeability in the rat glioma model.** *J Neurosurg* 1982;57:394–98 CrossRef Medline

32. Blasberg RG, Kobayashi T, Patlak CS, et al. **Regional blood flow, capillary permeability, and glucose utilization in two brain tumor models: preliminary observations and pharmacokinetic implications.** *Cancer Treat Rep* 1981;65(Suppl 2)3–12 Medline

33. Zagzag D, Hooper A, Friedlander DR, et al. **In situ expression of angiopoietins in astrocytomas identifies angiopoietin-2 as an early marker of tumor angiogenesis.** *Exp Neurol* 1999;159:391–400 CrossRef Medline

34. Fukumura D, Xu L, Chen Y, et al. **Hypoxia and acidosis independently up-regulate vascular endothelial growth factor transcription in brain tumors in vivo.** *Cancer Res* 2001;61:6020–24 Medline

35. Davis PL, Parker DL, Nelson JA, et al. **Interactions of paramagnetic contrast agents and the spin echo pulse sequence.** *Invest Radiol* 1988;23:381–88 CrossRef Medline

36. Park YW, Ahn SJ. **Comparison of contrast-enhanced T2 FLAIR and 3D T1 black-blood fast spin-echo for detection of leptomeningeal metastases.** *Investig Magn Reson Imaging* 2018;22:86 CrossRef

37. Akeson P, Larsson EM, Kristoffersen DT, et al. **Brain metastases–comparison of gadodiamide injection-enhanced MR imaging at standard and high dose, contrast-enhanced CT and non-contrast-enhanced MR imaging.** *Acta Radiol* 1995;36:300–06 CrossRef Medline

Regional Aneurysm Wall Enhancement is Affected by Local Hemodynamics: A 7T MRI Study

S. Hadad, F. Mut, B.J. Chung, J.A. Roa, A.M. Robertson, D.M. Hasan, E.A. Samaniego, and J.R. Cebral

ABSTRACT

BACKGROUND AND PURPOSE: Aneurysm wall enhancement has been proposed as a biomarker for inflammation and instability. However, the mechanisms of aneurysm wall enhancement remain unclear. We used 7T MR imaging to determine the effect of flow in different regions of the wall.

MATERIALS AND METHODS: Twenty-three intracranial aneurysms imaged with 7T MR imaging and 3D angiography were studied with computational fluid dynamics. Local flow conditions were compared between aneurysm wall enhancement and nonenhanced regions. Aneurysm wall enhancement regions were subdivided according to their location on the aneurysm and relative to the inflow and were further compared.

RESULTS: On average, wall shear stress was lower in enhanced than in nonenhanced regions ($P = .05$). Aneurysm wall enhancement regions at the neck had higher wall shear stress gradients ($P = .05$) with lower oscillations ($P = .05$) than nonenhanced regions. In contrast, aneurysm wall enhancement regions at the aneurysm body had lower wall shear stress ($P = .01$) and wall shear stress gradients ($P = .008$) than nonenhanced regions. Aneurysm wall enhancement regions far from the inflow had lower wall shear stress ($P = .006$) than nonenhanced regions, while aneurysm wall enhancement regions close to the inflow tended to have higher wall shear stress than the nonenhanced regions, but this association was not significant.

CONCLUSIONS: Aneurysm wall enhancement regions tend to have lower wall shear stress than nonenhanced regions of the same aneurysm. Moreover, the association between flow conditions and aneurysm wall enhancement seems to depend on the location of the region on the aneurysm sac. Regions at the neck and close to the inflow tend to be exposed to higher wall shear stress and wall shear stress gradients. Regions at the body, dome, or far from the inflow tend to be exposed to uniformly low wall shear stress and have more aneurysm wall enhancement.

ABBREVIATIONS: AWE = aneurysm wall enhancement; CFD = computational fluid dynamics; 3DRA = 3D rotational conventional angiography; Gd = gadolinium; HR-VWI = high-resolution vessel wall imaging; mWSS = mean (time-averaged) wall shear stress magnitude; pWSS = peak systole WSS magnitude; WSS = wall shear stress

High-resolution vessel wall imaging (HR-VWI) and aneurysm wall enhancement (AWE) are increasingly used to identify intracranial aneurysms with a higher risk of growth[1-3] and

rupture.[4] Aneurysms deemed "stable" on the basis of AWE may be managed conservatively and followed across time,[5] whereas unstable aneurysms are treated to prevent rupture.

However, the clinical significance and exact mechanisms leading to AWE remain unclear.[6] One early study of patients with SAH with multiple intracranial aneurysms showed enhancement in thick-walled regions of ruptured aneurysms, while unruptured aneurysms did not enhance.[7] This finding suggested that the presence of AWE on HR-VWI may identify the culprit aneurysm

in patients with multiple aneurysms and SAH. Another study observed focal AWE in association with intramural thrombus of ruptured aneurysms and suggested that AWE may be useful in identifying rupture points.[8] Histopathologic analyses of specimens of intracranial aneurysms treated with microsurgical clipping have shown associations between AWE and wall thickening accompanied by atherosclerotic remodeling,[9] neovascularization,[10] macrophage infiltration,[11] and inflammation.[12,13] Several other studies have demonstrated associations between AWE and known clinical rupture risk factors: size of >7 mm,[14] anterior and posterior communicating artery location,[15] irregular shape,[16] and PHASES score >3 (https://qxmd.com/calculate/calculator_464/phases-score).[17]

The subjective characterization of AWE has described patterns of enhancement as focal and circumferential. However, it is unknow why AWE does not distribute evenly within the aneurysm sac and whether this heterogeneous AWE is the result of different flow conditions within the aneurysm that ultimately translate into histologic changes.[18] It is believed that flow-induced inflammation may lead to AWE. One study found lower wall shear stress (WSS) and oscillatory shear index in AWE regions compared with nonenhanced regions.[19] Similarly, another study found that aneurysms with AWE were larger and had lower WSS and velocities than aneurysms without enhancement, and the AWE signal intensity was inversely correlated with WSS magnitude.[20] A recent study showed that the presence of AWE was associated with low normalized WSS, size, and size ratio.[21] However, several factors other than inflammation have been proposed as potential causes of increased AWE signals, in particular low-flow patterns that lead to pseudoenhancement signals in vivo.[22]

Our purpose was to further investigate possible associations between local flow characteristics and focal AWE with the hope of shedding light on the mechanisms responsible for wall enhancement. We used high-resolution 7T MR imaging in determining AWE and studied the local flow patterns in different areas of the aneurysm.

MATERIALS AND METHODS

Image Data

Twenty patients with 23 unruptured intracranial aneurysms were prospectively enrolled in our study of aneurysm characterization with 7T MR imaging. The MR imaging studies included a TOF-MRA and 3D T1-weighted MR imaging sequences acquired before and after intravenous injection of gadolinium (Gd) (Online Supplemental Data). Additionally, 13 patients were imaged with 3D rotational conventional angiography (3DRA) and another 4 with CTA as the standard of care and as part of their presurgical assessment if they were scheduled for an intervention. Otherwise, 3DRA or CTA or both were performed during their clinic visit if the aneurysm was not going to be treated. 3DRA, CTA, and 7T MR imaging were performed within 2 weeks as patients were recruited into the study during presurgical planning. For patients who were not treated, imaging was also completed within 2 weeks for consistency. Patient and aneurysm characteristics are summarized in the Online Supplemental Data.

Hemodynamics Modeling

Using previously described methods,[23] patient-specific aneurysm models were reconstructed from the available 3D images (in

order of preference, 13 from 3DRA, 4 from CTA, and 6 from 7T TOF-MRA), and computational fluid dynamics (CFD) simulations were performed by numerically solving the Navier-Stokes equations. Pulsatile inflow conditions were prescribed using waveforms measured in the internal carotid and vertebral arteries of older patients scaled with an empirical power law of the vessel area.[24] Outflow boundary conditions were specified consistently with the Murray's law. Vessel walls were approximated as rigid. Simulations were performed for 2 cardiac cycles with a time-step of 0.01 seconds, and results from the second cycle were used to characterize the local hemodynamics of the aneurysm and AWE regions.

Mapping AWE Regions

The methodology to map AWE regions to CFD models is illustrated in Fig 1. Step 1 is the construction of a vascular model from the available 3D images, as described above. Bilateral 3DRA images (Fig 1A, -B) are used to construct a model of an anterior communicating artery aneurysm (Fig 1C).[25] Step 2 consists of performing a rough segmentation of the vasculature from the TOF-MRA (Fig 1D) and aligning it with the 3D model (Fig 1E, segmentation = red, model = transparent) using the image-processing software Amira Software (Thermo Fisher Scientific). In step 3, pre- and post-Gd T1-weighted images (Fig 1F, -G) are first subtracted (Fig 1H); then, AWE regions are manually segmented Fig 1I). Areas of AWE were subjectively determined by 2 teams of experienced investigators (E.A.S. and J.A.R., and S.H. and J.R.C.) and fused together by overlapping the regions. The high spatial resolution of 7T imaging allows visual determination of areas of enhancement (Fig 1F, -I) within the aneurysmal wall. In step four, 3D surfaces are recovered by extracting isosurfaces in Amira. These AWE region surfaces were thus already aligned with the 3D vascular model (Fig 1J) and were then projected onto the vascular model and used to label its surface elements as "enhanced" or "nonenhanced". Finally, AWE regions are split into connected components and assigned different labels (colors) (Fig 1K). Note that in cases in which the vascular model was constructed from the TOF-MRA images, the AWE regions are automatically aligned and step 2 is skipped.

AWE Region Characterization

The local hemodynamic environment in the aneurysm regions with and without enhancement were then quantitatively characterized by computing the region average of a number of hemodynamic variables,[26] including the following: peak systole and mean (time-averaged) wall shear stress magnitude (pWSS, mWSS, respectively), oscillatory shear index, relative residence time, mean gradient oscillatory number, mean WSS divergence, and mean WSS gradient.

The location of the AWE regions on the aneurysm sac as well as with respect to the inflow stream were characterized as described below and illustrated in the Online Supplemental Data.

As in previous studies,[26] the aneurysm neck was delineated by interactively selecting points on the neck and connecting them along geodesic lines (lines of minimum distance on the surface) (Online Supplemental Data). The geodesic distance to the neck was then computed for all points in the aneurysm. The aneurysm
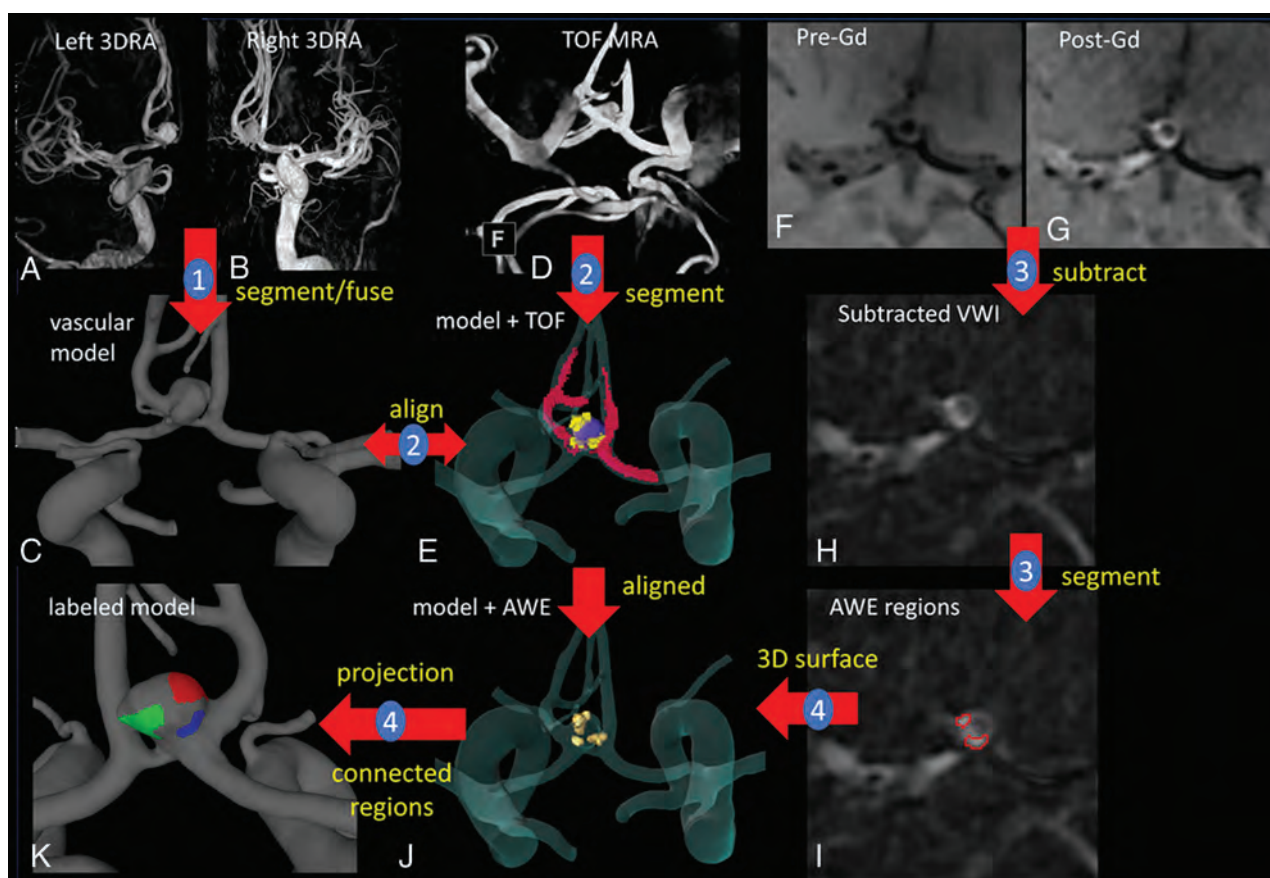
FIG 1. Illustration of methodology with the anterior communicating artery aneurysm. Step 1: model construction from 3DRAs (*A–C*). Step 2: rough segmentation of TOF-MRA and alignment with the vascular model (*D* and *E*). Step 3: pre- and post-Gd MR image subtraction and AWE region segmentation (*F–I*). Step 4: 3D-AWE region isosurface extraction, alignment, projection to the vascular model, and splitting into connected components (*J* and *K*). Models constructed from CTAs follow a similar approach, while models from TOF-MRA are automatically aligned to the Gd MR imaging series. VWI indicates vessel wall imaging.

was then subdivided into 3 subregions (Online Supplemental Data) corresponding to the neck (pink), body (red), and dome (yellow).[26] Then, the location of each single-connected AWE region was defined as in the neck, body, or dome, depending on the maximum percentage of overlap of the area of the AWE region and each aneurysm region. The example in the Online Supplemental Data shows 3 regions of wall enhancement (white contours) superimposed with the aneurysm regions. In this case, 1 region is located at the neck, and the other 2, at the aneurysm body.

The location of AWE regions was also characterized according to their distance to the inflow. On the basis the labels defining each region (Online Supplemental Data), close tetrahedral elements of the CFD grid were identified (Online Supplemental Data). These elements were then used to seed streamlines that pass near the AWE region. Starting at one of these seed elements, we constructed and concatenated 2 randomly selected streamlines, one in the negative velocity direction (ie, toward the inflow) and another in the positive velocity direction (ie, toward the outflow) (Online Supplemental Data). The time that it takes a particle to flow from the inflow to the seed and from the seed to the outflow was calculated. This time is given as a percentage (ie, the time from inflow to outflow is 100%). The process was repeated for 10 different seeds, and the average "time-to-inflow" was

assigned to the region. AWE regions were then classified as "close" or "far" from the inflow, depending on whether their time-to-inflow was smaller or larger than the median of this variable over all AWE regions in our sample.

Data Analysis
Paired 2-sample nonparametric Wilcoxon (Mann-Whitney) tests were used to compare the means of hemodynamic variables between aneurysm regions with and without enhancement. In this case, variables were normalized with the value corresponding to the entire aneurysm, and the AWE region of each aneurysm was considered a single region (union of all connected components).

Next, single-connected AWE regions located at the neck, body, or dome were compared with the nonenhancement regions of the same aneurysm. Thus, the ratio of hemodynamic variables in each AWE region over the nonenhanced region of the same aneurysm was computed, and single-sample Wilcoxon tests were performed to test whether the ratios were significantly different from 1. Similar comparisons were also made between AWE regions located near and far from the inflow and the nonenhanced regions of the same aneurysm.

Finally, hemodynamic characteristics of AWE regions at different locations on the aneurysm (neck, body, or dome) and relative to the inflow (close, far) were compared. Thus, the ratio of

Hemodynamic characteristics (normalized with aneurysm-averaged values) of AWE and nonenhanced regions[a]

Variable	AWE	NoE	P	95% CI (Diff)[b]
pWSS	0.95 [SD, 0.52]	1.02 [SD, 0.07]	.18	(−0.051, 0.254)
mWSS	0.87 [SD, 0.21]	1.03 [SD, 0.07]	.05[c]	(0.001, 0.273)
OSI	1.96 [SD, 3.67]	0.98 [SD, 0.14]	.3	(−0.350, 0.074)
RRT	1.46 [SD, 1.57]	0.98 [SD, 2.10]	.15	(−0.324, 0.066)
GON	1.12 [SD, 0.53]	0.99 [SD, 0.07]	.81	(−0.173, 0.162)
WSSDIV	−2.85 [SD, 6.92]	0.45 [SD, 2.10]	.03[c]	(0.170, 5.457)
WSSGRAD	0.95 [SD, 0.48]	1.03 [SD, 0.08]	.18	(−0.030, 0.194)

Note:—NoE indicates nonenhanced; OSI, oscillatory shear index; RTT, relative residence time; GON, mean gradient oscillatory number; WSSDIV, mean WSS divergence; WSSGRAD, mean WSS gradient.
[a] Values are given as mean [SD] unless otherwise noted.
[b] 95% confidence intervals of the differences. Mathematic definitions of the variables are provided in Mut et al.[26]
[c] Significant differences ($P < .05$).

variables computed in AWE regions divided by the nonenhanced region of the same aneurysm were compared using 2-sample Wilcoxon tests.

All statistical tests were performed in R statistical and computing software (http://www.r-project.org/). Differences were considered significant with $P < .05$ for 2-sided tests, while trends were considered marginally significant at $P < .05$ in corresponding 1-sided tests.

RESULTS

All 23 aneurysms studied had AWE regions. A total of 72 single-connected regions were identified in these aneurysms. Most AWE regions were located in the aneurysm body ($n = 40$, 56%); the remaining regions were roughly equally distributed at the dome ($n = 18$, 25%) and neck ($n = 14$, 19%). The median time-to-inflow of AWE regions was 48% with an SD of 28%.

Results of comparisons of hemodynamic characteristics of the entire AWE region against the nonenhanced region of the same aneurysm are presented in the Table. On average, the mean WSS was lower in AWE regions than in nonenhanced regions ($P = .05$). Additionally, the WSS divergence was negative (indicating convergence of WSS vectors) and of larger magnitude in AWE regions than in nonenhanced regions where it was positive (indicating divergence of WSS vectors) and of smaller magnitude ($P = .03$).

Average ratios of hemodynamic variables between AWE regions at different locations over the corresponding nonenhanced region of the same aneurysm are presented in the Online Supplemental Data along with their SDs. This table includes data for regions at the neck, body, and dome, as well as regions close and far from the inflow. The P values corresponding to the comparisons of these ratios against 1 are also listed in this table where statistically significant differences are indicated with an asterisk.

AWE regions at the neck had smaller mean gradient oscillatory numbers ($P = .05$), higher (and negative) WSS divergence ($P = .05$), and higher WSS gradients ($P = .05$) than nonenhanced regions. In contrast, AWE regions at the body had lower peak ($P = .02$) and mean ($P = .01$) WSS and lower WSS gradients ($P = .008$) than nonenhanced regions. Compared with the nonenhanced regions, AWE regions at the dome also had lower WSS gradients ($P = .09$), but this trend only reached marginal significance. Most interesting, AWE regions far from the inflow had lower WSS (pWSS, $P = .004$; mWSS, $P = .006$) than nonenhanced

regions, while AWE regions near the inflow tended to have higher WSS than nonenhanced regions, but this latter association did not reach statistical significance.

Comparisons of AWE regions at different locations on the aneurysm are presented in the Online Supplemental Data. Regions at the neck had larger WSS gradient than regions at the body ($P = .002$) or dome ($P = .007$), while the WSS gradient was not significantly different between regions in the body and dome. Additionally, AWE regions near the inflow had larger WSS (pWSS, $P = .01$; mWSS, $P = .08$) than AWE regions far from the inflow.

DISCUSSION

Previous studies have reported possible associations between AWE and low WSS.[19,20] In our study, the normalized mean WSS computed over the entire AWE region was lower than that in the nonenhanced region. This result is consistent with previous reports. However, it was noticed that in most of our aneurysms, the AWE region was not single-connected. Separating them into connected components revealed that most AWE regions (56%) were located in the body of the aneurysm, with fewer regions at the neck (19%) and the dome (25%). Visualizations of the AWE regions and aneurysm flow dynamics then suggested that AWE regions at different locations could be exposed to different local flow conditions. These observations suggest that the aneurysm sac is composed of different microenvironments with different stages of histologic response to flow stressors. Wall enhancement within the aneurysm is not uniform and translates different stages of aneurysm biology on the basis of location and flow conditions.

As examples, AWE regions and flow visualizations in 4 representative aneurysms are presented in Fig 2. Aneurysm 1 has a region aligned with the inflow jet with higher WSS than the 2 other regions in the flow-recirculation regions. Note that this anterior communicating artery aneurysm has 2 daughter sacs (arrows) that colocalize with regions of AWE and low WSS. Daughter sacs or "blebs" are known sites of rupture. Aneurysm 2 has a region at the neck near the inflow, another at the neck but near the outflow, and a third at the dome. Flow conditions at these locations look qualitatively different. Aneurysm 3 has 2 regions at the neck, one near the inflow and the other near the outflow; again, WSS and flow conditions look different in these 2 regions. Aneurysm 4 has 1 region at the dome where the inflow jet impacts the wall and another near the outflow where WSS is
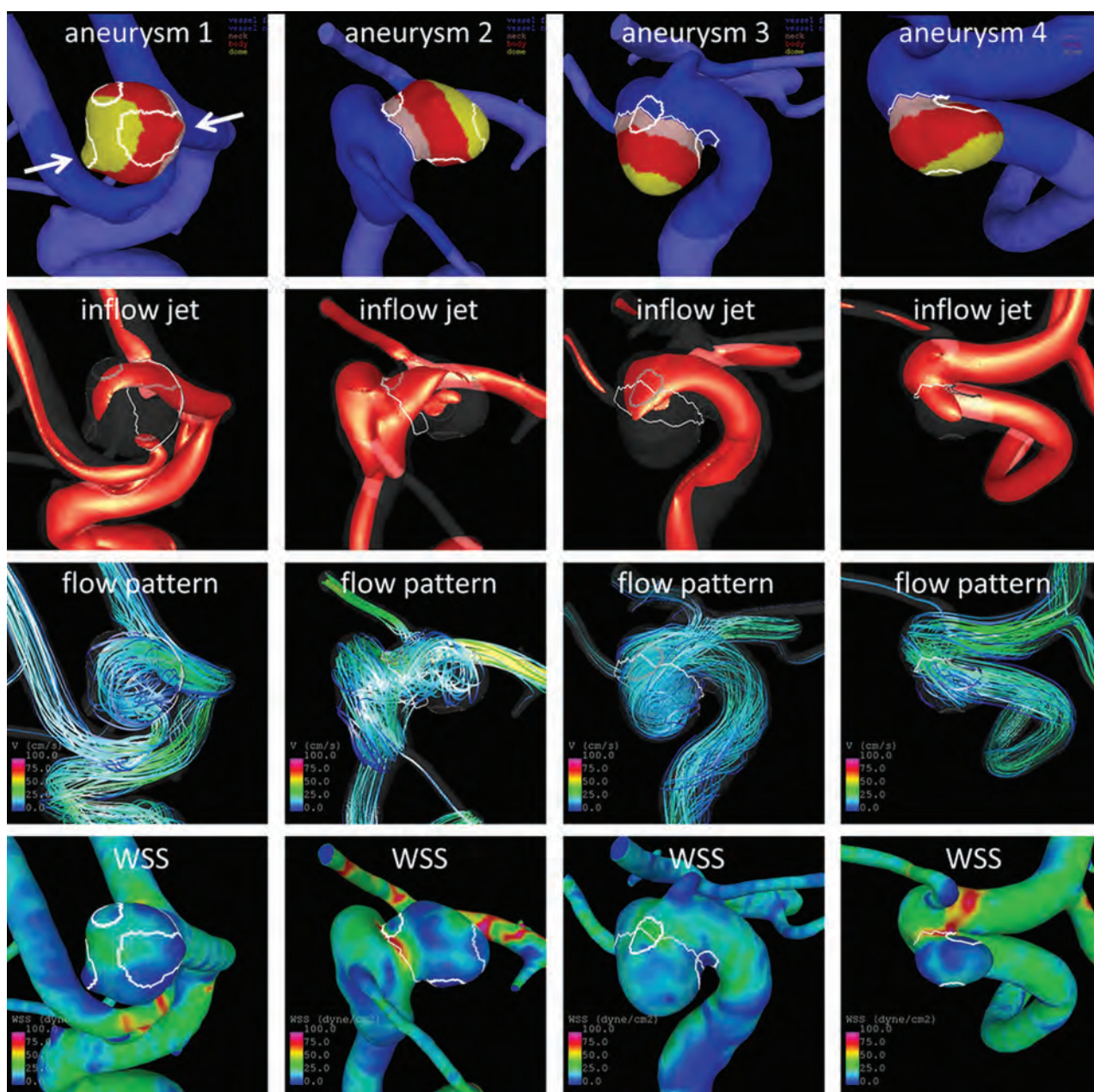
FIG 2. Sample aneurysms with multiple AWE regions at different locations on the aneurysm (row 1: AWE regions = white contours, neck = pink, body = red, dome = yellow) and relative to the inflow (rows 2 and 3), which could be exposed to different WSS (row 4).

low. These examples illustrate the complex flow conditions that shape morphologic changes and AWE regions within the aneurysm.

On the basis of these observations, AWE regions were subdivided depending on their location on the aneurysm and their "time-distance" to the inflow along streamlines, to test the hypothesis that they may be exposed to different hemodynamic conditions. Our findings indicate that AWE regions at the neck near the inflow tend to be exposed to higher WSS, higher and less oscillatory WSS gradient, and higher but negative WSS divergence (indicating convergence of WSS vectors) compared with nonenhanced regions. In contrast, AWE regions at the body or dome or farther from the inflow tend to have lower WSS and lower WSS gradients (ie, more uniformly lower WSS

distribution) and were more common. These opposite trends suggest that perhaps different mechanisms are involved in the processes responsible for the enhancement of regions at these different locations.

The mechanism responsible for AWE remains poorly understood. One possible mechanism is related to infiltration of Gd into the wall at locations where the endothelium became permeable. Increased endothelial permeability could also favor wall inflammation. Thus, it has been suggested that AWE is a marker of wall inflammation.[10,11,18] In analyzing 25 unruptured intracranial aneurysms with 7T HR-VWI, we demonstrated a significant correlation between circumferential AWE and contrast enhancement in the parent artery.[27] This suggests an underlying inflammatory/vasculopathic process in the

wall of the parent vessel that ultimately may lead to aneurysm formation and growth. Endothelial dysfunction in the aneurysm and parent vessel could be the result of abnormally low WSS or oscillatory WSS conditions. The pattern of avid AWE seen in large aneurysms could be explained by the transport of Gd through the rich network of the vasa vasorum usually seen in these aneurysms.[10] Finally, regions of the aneurysm wall exposed to high WSS and high WSS gradients could also result in local damage to the endothelium[28] (perhaps even denudation of the endothelial layer), which may lead to wall inflammation[29] and perhaps intake of Gd. Further studies will focus on better understanding of these possible mechanisms of AWE and their potential as biomarkers for aneurysm instability.

This study is limited by the small sample size and lack of follow-up data because most aneurysms were treated. Further studies with larger samples should be conducted to confirm the associations identified here. The ultra-high resolution of 7T MR imaging allowed identification of AWE in all aneurysms. This may not be feasible with lower-strength magnets, especially for aneurysms close to enhancing structures such as the cavernous sinus or in small aneurysms (≤ 3 mm). In these aneurysms, it may be challenging to isolate the aneurysm boundaries with 3T MR imaging. Another limitation of the study is that AWE was not objectively quantified. However, due to the small sample size, it would have been difficult to identify a specific threshold of enhancement.

CONCLUSIONS

On average, AWE regions have lower WSS than nonenhanced regions of the same aneurysm. The association between local flow conditions and AWE seems to be different for regions located at the neck and near the inflow than for regions in the aneurysm body and dome and far from the inflow. Regions in the neck and near the inflow tend to be exposed to higher WSS and WSS gradients, while regions in the body, dome, or far from the inflow tend to be exposed to uniformly low WSS. This finding suggests different mechanisms of AWE for these different regions.

REFERENCES

1. Texakalidis P, Hilditch CA, Lehman V, et al. **Vessel wall imaging of intracranial aneurysms: systematic review and meta-analysis.** *World Neurosurg* 2018;117:453–58.e1 CrossRef Medline

2. Vergouwen MDI, Backes D, van der Schaaf IC, et al. **Gadolinium enhancement of the aneurysm wall in unruptured intracranial aneurysms is associated with an increased risk of aneurysm instability: a follow-up study.** *AJNR Am J Neuroradiol* 2019;40:1112–16 CrossRef Medline

3. Gariel F, Ben Hassen W, Boulouis G, et al. **Increased wall enhancement during follow-up as a predictor of subsequent aneurysmal growth.** *Stroke* 2020;51:1868–72 CrossRef Medline

4. Wang X, Zhu C, Leng Y, et al. **Intracranial aneurysm wall enhancement associated with aneurysm rupture: a systematic review and meta-analysis.** *Acad Radiol* 2019;26:664–73 CrossRef Medline

5. Roa JA, Zanaty M, Ishii D, et al. **Decreased contrast enhancement on high-resolution vessel wall imaging of unruptured intracranial aneurysms in patients taking aspirin.** *J Neurosurg* 2020 Mar 6. [Epub ahead of print] CrossRef Medline

6. Samaniego EA, Roa JA, Hasan D. **Vessel wall imaging in intracranial aneurysms.** *J Neurointerv Surg* 2019;11:1105–12 CrossRef Medline

7. Matouk CC, Mandell DM, Günel M, et al. **Vessel wall magnetic resonance imaging identifies the site of rupture in patients with multiple intracranial aneurysms: proof of principle.** *Neurosurgery* 2013;72:492–96; discussion 496 CrossRef Medline

8. Matsushige T, Shimonaga K, Mizoue T, et al. **Focal aneurysm wall enhancement on magnetic resonance imaging indicates intraluminal thrombus and the rupture point.** *World Neurosurg* 2019;127: e578–84 CrossRef Medline

9. Hashimoto Y, Matsushige T, Shimonaga K, et al. **Vessel wall imaging predicts the presence of atherosclerotic lesions in unruptured intracranial aneurysms.** *World Neurosurg* 2019;132:e775–82 Medline

10. Larsen N, von der Brelie C, Trick D, et al. **Vessel wall enhancement in unruptured intracranial aneurysms: an indicator for higher risk of rupture? High-resolution MR imaging and correlated histologic findings.** *AJNR Am J Neuroradiol* 2018;39:1617–21 CrossRef Medline

11. Shimonaga K, Matsushige T, Ishii D, et al. **Clinicopathological insights from vessel wall imaging of unruptured intracranial aneurysms.** *Stroke* 2018;49:2516–19 CrossRef Medline

12. Hu P, Yang Q, Wang DD, et al. **Wall enhancement on high-resolution magnetic resonance imaging may predict an unsteady state of an intracranial saccular aneurysm.** *Neuroradiology* 2016;58:979–85 CrossRef Medline

13. Quan K, Song J, Yang Z, et al. **Validation of wall enhancement as a new imaging biomarker of unruptured cerebral aneurysm.** *Stroke* 2019;50:1570–73 CrossRef Medline

14. Liu P, Qi H, Liu A, et al. **Relationship between aneurysm wall enhancement and conventional risk factors in patients with unruptured intracranial aneurysms: a black-blood MRI study.** *Interv Neuroradiol* 2016;22:501–05 CrossRef Medline

15. Lv N, Karmonik C, Chen S, et al. **Relationship between aneurysm wall enhancement in vessel wall magnetic resonance imaging and rupture risk of unruptured intracranial aneurysms.** *Neurosurgery* 2019;84:E385–91 CrossRef Medline

16. Wang GX, Li W, Lei S, et al. **Relationships between aneurysmal wall enhancement and conventional risk factors in patients with intracranial aneurysm: a high-resolution MRI study.** *J Neuroradiol* 2019;46:25–28 CrossRef Medline

17. Hartman JB, Watase H, Sun J, et al. **Intracranial aneurysms at higher clinical risk for rupture demonstrate increased wall enhancement and thinning on multicontrast 3D vessel wall MRI.** *Br J Radiol* 2019;92:20180950 CrossRef Medline

18. Matsushige T, Shimonaga K, Mizoue T, et al. **Lessons from vessel wall imaging of intracranial aneurysms: new era of aneurysm evaluation beyond morphology.** *Neurol Med Chir (Tokyo)* 2019;59:407–14 CrossRef Medline

19. Xiao W, Qi T, He S, et al. **Low wall shear stress is associated with local aneurysm wall enhancement on high-resolution MR vessel wall imaging.** *AJNR Am J Neuroradiol* 2018;39:2082–87 CrossRef Medline

20. Khan MO, Toro Arana V, Rubbert C, et al. **Association between aneurysm hemodynamics and wall enhancement on 3D vessel wall MRI.** *J Neurosurg* 2020 Jan 10. [Epub ahead of print] CrossRef Medline

21. Lv N, Karmonik C, Chen S, et al. **Wall enhancement, hemodynamics, and morphology in unruptured intracranial aneurysms with high rupture risk.** *Transl Stroke Res* 2020;11:882–89 CrossRef Medline

22. Cornelissen BM, Leemans EL, Slump CH, et al. **Vessel wall enhancement of intracranial aneurysms: fact or artifact?** *Neurosurg Focus* 2019;47:E18 CrossRef Medline

23. Cebral JR, Castro MA, Appanaboyina S, et al. **Efficient pipeline for image-based patient-specific analysis of cerebral aneurysm hemodynamics: technique and sensitivity.** *IEEE Trans Med Imaging* 2005;24:457–67 CrossRef Medline

24. Durka MJ, Wong IH, Kallmes DF, et al. **A data-driven approach for addressing the lack of flow waveform data in studies of cerebral arterial flow in older adults.** *Physiol Meas* 2018;39:015006 CrossRef Medline

25. Castro MA, Putman CM, Cebral JR. **Patient-specific computational modeling of cerebral aneurysms with multiple avenues of flow from 3D rotational angiography images.** *Acad Radiol* 2006;13:811–21 CrossRef Medline

26. Mut F, Löhner R, Chien A, et al. **Computational hemodynamics framework for the analysis of cerebral aneurysms.** *Int J Numer Method Biomed Eng* 2011;27:822–39 CrossRef Medline

27. Samaniego EA, Roa JA, Zhang H, et al. **Increased contrast enhancement of the parent vessel of unruptured intracranial aneurysms in 7T MR imaging.** *J Neurointerv Surg* 2020;12:1018–22 CrossRef Medline

28. Metaxa E, Tremmel M, Xiang J, et al. **High wall shear stress and positive wall shear stress gradient trigger the initiation of intracranial aneurysms.** In: Proceedings of the American Society of Mechanical Engineers Summer Bioengineering Conference, SBC2009-206395: 523–24, Lake Tahoe, California. June 17–21, 2009 CrossRef

29. Frösen J, Cebral J, Robertson AM, et al. **Flow-induced, inflammation-mediated arterial wall remodeling in the formation and progression of intracranial aneurysms.** *Neurosurg Focus* 2019;47:E21 CrossRef Medline

3D Quantitative Synthetic MRI in the Evaluation of Multiple Sclerosis Lesions

S. Fujita, K. Yokoyama, A. Hagiwara, S. Kato, C. Andica, K. Kamagata, N. Hattori, O. Abe, and S. Aoki

ABSTRACT

BACKGROUND AND PURPOSE: Synthetic MR imaging creates multiple contrast-weighted images based on a single time-efficient quantitative scan, which has been mostly performed for 2D acquisition. We assessed the utility of 3D synthetic MR imaging in patients with MS by comparing its diagnostic image quality and lesion volumetry with conventional MR imaging.

MATERIALS AND METHODS: Twenty-four patients with MS prospectively underwent 3D quantitative synthetic MR imaging and conventional T1-weighted, T2-weighted, FLAIR, and double inversion recovery imaging, with acquisition times of 9 minutes 3 seconds and 18 minutes 27 seconds for the synthetic MR imaging and conventional MR imaging sequences, respectively. Synthetic phase-sensitive inversion recovery images and those corresponding to conventional MR imaging contrasts were created for synthetic MR imaging. Two neuroradiologists independently assessed the image quality on a 5-point Likert scale. The numbers of cortical lesions and lesion volumes were quantified using both synthetic and conventional image sets.

RESULTS: The overall diagnostic image quality of synthetic T1WI and double inversion recovery images was noninferior to that of conventional images ($P = .23$ and $.20$, respectively), whereas that of synthetic T2WI and FLAIR was inferior to that of conventional images (both $Ps < .001$). There were no significant differences in the number of cortical lesions ($P = .17$ and $.53$ for each rater) or segmented lesion volumes ($P = .61$) between the synthetic and conventional image sets.

CONCLUSIONS: Three-dimensional synthetic MR imaging could serve as an alternative to conventional MR imaging in evaluating MS with a reduced scan time.

ABBREVIATIONS: DIR = double inversion recovery; PSIR = phase-sensitive inversion recovery; QALAS = quantification using an interleaved Look-Locker acquisition sequence with a T2 preparation pulse

M S is a chronic, immune-mediated, demyelinating disorder of the CNS that usually affects young adults and leads to chronic disability.[1,2] The diagnostic criteria for MS are based on

the lesion number, size, and location.[3] Although diffuse periventricular lesions are most commonly observed, previous studies have shown that the cortical and juxtacortical lesion load is associated with cognitive impairment.[4,5] Additionally, the detection of cortical and juxtacortical lesions may contribute to early diagnosis because these lesions are characteristic of MS. MR imaging plays an integral role in the diagnosis and management of patients with MS through the in vivo detection and characterization of lesions. Although MR imaging is highly sensitive in detecting periventricular lesions and is considered as a standard biomarker in the monitoring of treatment response,[6] conventional MR imaging techniques have a relatively low sensitivity for detecting (juxta)cortical lesions. Phase-sensitive inversion recovery (PSIR) and double inversion recovery (DIR) are recently developed imaging techniques useful for detecting MS lesions, especially (juxta)cortical ones.[7,8] The PSIR preserves the positive and negative polarities of tissues as they recover from the inversion pulse, thus providing a T1-weighted contrast with higher

Table 1: Acquisition parameters for 3D-QALAS and conventional MR imaging sequences

Parameters	3D-QALAS	3D T1WI	3D FLAIR	3D DIR	TSE T2WI
Acquisition plane	3D axial	3D sagittal	3D sagittal	3D sagittal	2D axial
Image matrix	192 × 192	256 × 256	208 × 208	176 × 174	368 × 230
FOV (mm)	256	256	256	250	230
Section thickness (mm)	1.3	1	1.2	1.5	5
Voxel size (mm)	1.3 × 1.3 × 1.3	1.0 × 1.0 × 1.0	1.2 × 1.2 × 1.2	1.4 × 1.4 × 1.5	0.6 × 1.0
TR (ms)	6.2	8.2	4800	5500	4082
TE (ms)	2.8	3.8	371	306	90
TI (ms)	[a]	−	1660	2510/480	−
Flip angle (degree)	4	10	90	90	90
Bandwidth (Hz/pixel)	249	191	910	1076	167
Averages	1	1	1	2	3
Scanning time	9:06	6:20	5:22	5:03	1:42

Note: — − indicates no value.
[a] Inversion delay times, 100 ms, 1000 ms, 1900 ms, and 2800 ms; T2 prep echo time, 100 ms.

SNR and GM-WM contrast. DIR is an imaging technique that suppresses both WM and CSF signals, thus significantly increasing lesion conspicuity in both GM and WM compared with FLAIR or T2-weighted images. PSIR and DIR have been shown to improve sensitivity compared with FLAIR or T2-weighted images in the detection of cortical lesions. However, the additional scanning time associated with PSIR and DIR has hindered the use of these techniques in clinical practice. Thus, a rapid imaging technique that can acquire these contrast-weighted images with high spatial resolution is desired.

Quantitative synthetic MR imaging is a time-efficient MR imaging technique that enables simultaneous quantification of T1 and T2 relaxation times and proton attenuation and allows the creation of any contrast-weighted image, including DIR and PSIR, without additional scanning time.[9–13] Previous studies have shown that synthetic MR imaging is useful for detecting and characterizing MS lesions.[10,11,14] However, these studies were based on a multisection 2D acquisition, providing a relatively low resolution in the section direction. 3D quantitative synthetic MR imaging, enabling the simultaneous quantification of T1, T2, and proton attenuation of the whole brain in 3D,[15–17] with smaller section thickness, should allow for more detailed delineation of MS lesions. With the combination of high spatial resolution 3D acquisition and DIR as well as PSIR contrasts, 3D quantitative synthetic MR imaging could serve as a clinically useful technique for monitoring MS lesions.

Here, we assessed the utility of the recently developed 3D quantitative synthetic MR imaging for evaluating MS lesions by comparing the synthetic and conventional MR image sets. We hypothesized that 3D synthetic MR imaging would have a comparable diagnostic quality with that of a conventional image set (including 3D FLAIR and DIR) while shortening the total acquisition time.

MATERIALS AND METHODS
Study Participants
This study complied with the Declaration of Helsinki and the Health Insurance Portability and Accountability Act and was approved by the local institutional review board. Written informed consent was obtained from all participants. In this single-center prospective study, 24 patients with MS diagnosed by the McDonald

criteria[18] were recruited between May 2018 and September 2018. The exclusion criteria comprised contraindications to MR imaging, such as metallic implants, claustrophobia, or tattoos.

MR Imaging Settings
All participants were scanned on a 1.5-T scanner (A patched R5.3.0 Ingenia; Philips Healthcare) with a 12-channel head coil. 3D quantitative imaging was performed with 3D-quantification using an interleaved Look-Locker acquisition sequence with a T2 preparation pulse (3D-QALAS) sequence.[16,17] The 3D-QALAS sequence produces 5 raw images that are used to fit relaxation curves based on a least-squares approach. From these quantitative maps, synthetic MR images could be generated by setting arbitrary TRs, TEs, and TIs. 3D-QALAS and conventional imaging (3D T1WI, 2D axial T2WI, 3D FLAIR, and 3D DIR) were performed in the same session on all participants. The acquisition parameters of the sequences are shown in Table 1. Synthetic 3D T1WI, 3D T2WI, 3D FLAIR, 3D PSIR, and 3D DIR images were generated on synthetic MR imaging software (SyMRI version 0.45.14; SyntheticMR) by virtually setting TR, TE, and TI as follows: T1WI, 650/10/- ms; T2WI, 4500/100/- ms; FLAIR, 15,000/75/3000 ms; DIR, 15,000/100/3600 ms; and PSIR, 6000/10/500 ms. All images were visually inspected by a radiologic technologist for gross movement artifacts.

Qualitative Assessments
All images were independently reviewed on a standard DICOM viewer, capable of window level and width adjustment and multiplanar reformation, by 2 neuroradiologists (C.A. and S.K.) with 10 and 6 years of experience, respectively. The readers were blinded to all clinical information to minimize bias. For each participant, conventional and synthetic images were assessed during 2 separate reading sessions with a 5-week memory-washout interval. Patients with MS were randomly assigned to 1 of the following groups: for the first group, a set of synthetic images (eg, 3D T1WI, 3D T2WI, 3D FLAIR, 3D DIR, and 3D PSIR) was presented in the first session and a set of conventional images (eg, 3D T1WI, 2D T2WI, 3D FLAIR, and 3D DIR) in the second session and vice versa for the second group. Each session included either all synthetic or all conventional contrast-weighted images from a case. In each reading session, the raters evaluated 3

metrics, which were overall image quality, structural delineation, and (juxta)cortical lesion count.

Overall Image Quality

The overall image quality was scored for each contrast-weighted image on a 5-point Likert scale, as follows: 1, unacceptable; 2, poor; 3, acceptable (acceptable for diagnostic use but with minor issues); 4, good; and 5, excellent. For each contrast-weighted image, readers recorded whether any of the following artifacts were present: truncation and ringing artifacts, aliasing artifacts, chemical shift artifacts, and any other artifacts (eg, spike noise, banding, and blurring).[19]

Structural Delineation

The structure delineation scoring was performed in addition to overall image quality scoring, intending to provide specific information about detailed visualization of anatomic regions. Each target structure was rated on a 5-point Likert scale as follows: 1, not visible; 2, not easily detectable (not easily differentiable from neighboring structures); 3, detectable (subtle differentiation from the neighboring structure); 4, easily delineated (easily differentiated from the neighboring structure); and 5, excellent delineation. The target structures included MS lesions, central sulcus, head of the caudate nucleus, posterior limb of the internal capsule, cerebral peduncle, and middle cerebellar peduncle. This approach was a modified version of the method used by Tanenbaum et al.[20]

Cortical Lesion Count

We did not distinguish between cortical and juxtacortical lesions as per current imaging criteria for MS.[18] For simplicity, we therefore referred to both types of lesions as cortical lesions. Cortical lesions larger than 3 mm in diameter were counted by 2 neuroradiologists using all contrast-weighted images of either the synthetic or conventional image sets. Each detected lesion was retrospectively validated on all available imaging data by the other 2 neuroradiologists (S.F. and A.H., with 6 and 11 years of experience, respectively) in consensus to exclude false-positive lesions.

Quantitative Assessment

Lesion Volume Segmentation. Because periventricular lesions were often diffuse or confluent, they were not manually counted and were assessed with semiautomated lesion segmentation. Lesions were segmented on 3D conventional and synthetic FLAIR images using the lesion probability algorithm implemented in the Lesion Segmentation Toolbox 2.0.12 (Technische Universitat Munchen) running under Statistical Parametric Mapping (https://www.fil.ion.ucl.ac.uk/spm).[21] A neuroradiologist (S.F.) performed manual corrections of the automatically segmented lesions. The total volume of the lesions was calculated by each of the synthetic and conventional FLAIR imagings. The Dice similarity coefficient of lesion maps was calculated between the segmentation results of synthetic images and those of conventional images. The Dice similarity coefficient represents the percentage of spatial overlap between 2 binary segmentation results, which is defined as

Table 2: Demographics of patients with MS (n = 23)

Characteristics	Findings
Participants (n)	23
Sex (male/female)	6/17
Age (years)	41.3 ± 9.8 (range, 19–59)
Disease duration (years)	10.1 ± 5.2
Subtype (RR/SP/PP)	20/1/2
EDSS score (range)	[0, 8.5] (median 1.5)

Note—EDSS indicates Expanded Disability Status Scale; PP, primary-progressive; RR, relapsing-remitting; SP, secondary-progressive.
Data are shown as mean ± SD unless otherwise specified.

$$\text{Dice similarity coefficient } (A, \ B) = \frac{2(A \cap B)}{(A + B)}$$

in which A and B are target segmentations and $\cap$ is the intersection.[22] The value of the Dice similarity coefficient ranges from 0 to 1, with higher values indicating more overlap between the 2 segmentations.

Statistical Analysis

All statistical analyses were performed on the R program version 3.3.0 (http://www.r-project.org/). The nonparametric Wilcoxon signed rank test was used to compare qualitative (overall image quality, structural delineation, and lesion count) and quantitative scores (lesion volume) between synthetic and conventional images. Interrater reliability for categoric data between readers were assessed by the Kendall coefficient of concordance.[23] Agreement between lesion volumes obtained with synthetic and conventional imaging were also assessed by interclass correlation coefficient. A P value of <.05 was considered statistically significant.

RESULTS

Among the 24 patients with MS, 1 patient showed severe movement artifacts on both 3D-QALAS and conventional imaging and was excluded from the study. The demographic details of the patients in this study are listed in Table 2. Fig 1 shows representative examples of 3D synthetic and conventional images of a patient with MS.

Qualitative Assessment

Overall Image Quality. Because the interclass correlation coefficient of overall image quality between the 2 readers was high (0.883), the results were pooled for analysis. Fig 2 shows a comparison of overall image quality between synthetic and conventional MR imaging. Considering all contrast views, 97.8% (225/230) of the synthetic contrast-weighted images and 100% (184/184) of the conventional images were rated as ≥3 on the 5-point Likert scale. The overall diagnostic image quality of synthetic T1WI and DIR images was statistically noninferior to that of conventional images (P = .23 and .20, respectively). The image quality of synthetic T2WI and FLAIR was statistically inferior to that of conventional images (both Ps < .001). Of the synthetic PSIR images, 95.6% (44/46) were rated 4 (good) or 5 (excellent). High-signal artifact on the brain surface on synthetic FLAIR images (Online Supplemental Data) and DIR images (Online Supplemental Data) were observed in 13.0% (3/23) and 17.4% (4/23) of the cases,
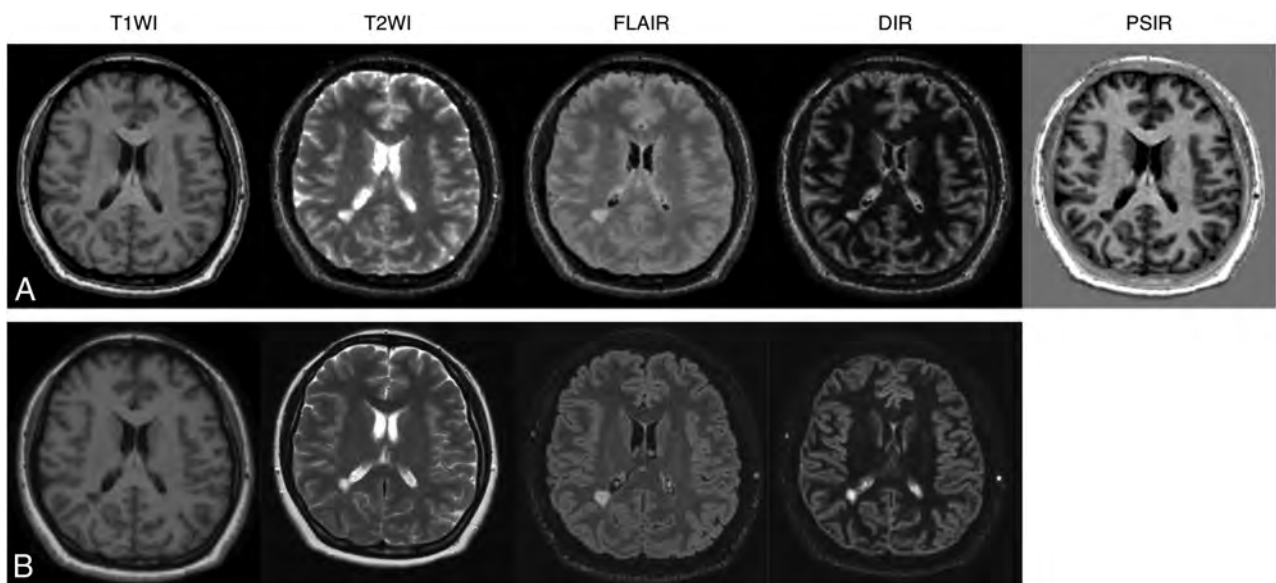
FIG 1. Representative examples of quantitative synthetic (*A*) and conventional (*B*) MR imaging in a 35-year-old woman with MS. The overall image quality of synthetic T1WI, T2WI, FLAIR, DIR, and PSIR were scored as 5, 3, 3, 5, and 5 by reader 1 and 5, 3, 4, 5, and 5 by reader 2. All of the conventional contrast-weighted images were scored as 5 by both readers.
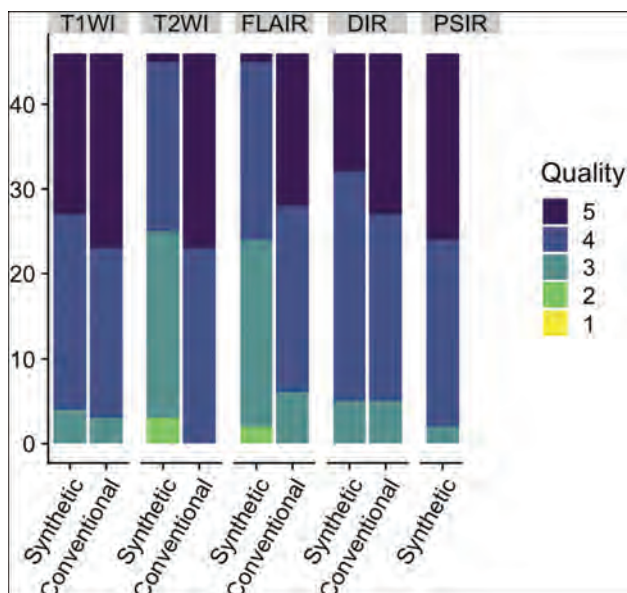
FIG 2. Comparison of overall image quality for conventional and synthetic MR imaging in patients with MS. Each contrast-weighted image in 23 patients was rated on a 5-point Likert scale by 2 readers.

respectively. A ring-shaped artifact was observed on the brain surface in 8.7% (2/23) of cases in synthetic MR imaging (Online Supplemental Data).

Structural Delineation. Regarding lesion delineation, 98.7% (227/230) of the synthetic contrast-weighted images and 98.9% (182/184) of the conventional images were rated as ≥3 on the 5-point Likert scale, considering all contrast views (Fig 3). All images rated 2 were either synthetic T2WI (2/46) or synthetic FLAIR (1/46); no images were rated as 1. The lesion delineation

of synthetic T2WI and FLAIR was statistically inferior to that of conventional images (both *P*s < .001), whereas no significant difference was found for T1WI and DIR between synthetic and conventional images.

Considering all evaluated brain structures (ie, the central sulcus, head of the caudate nucleus, posterior limb of the internal capsule, cerebral peduncle, and middle cerebellar peduncle) across all contrast views, 98.1% (1128/1150) of the synthetic contrast-weighted images and 98.8% (909/920) of the conventional images were rated as ≥3 on the 5-point Likert scale (Fig 3). The contrast views that were rated 2 for any of the structures were either synthetic T2WI (14/230), synthetic FLAIR (8/230), or conventional DIR (11/230); no images were rated as 1.

Cortical Lesion Counts. The interobserver reproducibility between the 2 readers for the number of detected cortical lesions was assessed. The interclass correlation coefficient of synthetic MR imaging was 0.90 (95% CI, 0.76–0.96); that of conventional MR imaging was 0.87 (95% CI, 0.69–0.94). Fig 4 shows a representative cortical lesion depicted by conventional and synthetic imaging. The cortical lesion counts with synthetic and conventional image sets were 2.9 ± 3.3 (range, 0–11) and 3.4 ± 3.7 (range, 0–11) by reader 1 and 2.3 ± 2.7 (range, 0–8) and 2.2 ± 3.1 (range, 0–11) by reader 2. Three false-positives were found in both the synthetic and conventional image sets. There was no significant difference in the number of cortical lesion counts between the synthetic and conventional image sets (*P* = .17 and .53 for each rater).

Quantitative Assessment

Lesion Volume Assessment. Fig 5 illustrates a representative MS lesion segmentation map on conventional and synthetic images. There was no significant difference in the segmented lesion volumes between synthetic and conventional images: 12.0 ± 10.9
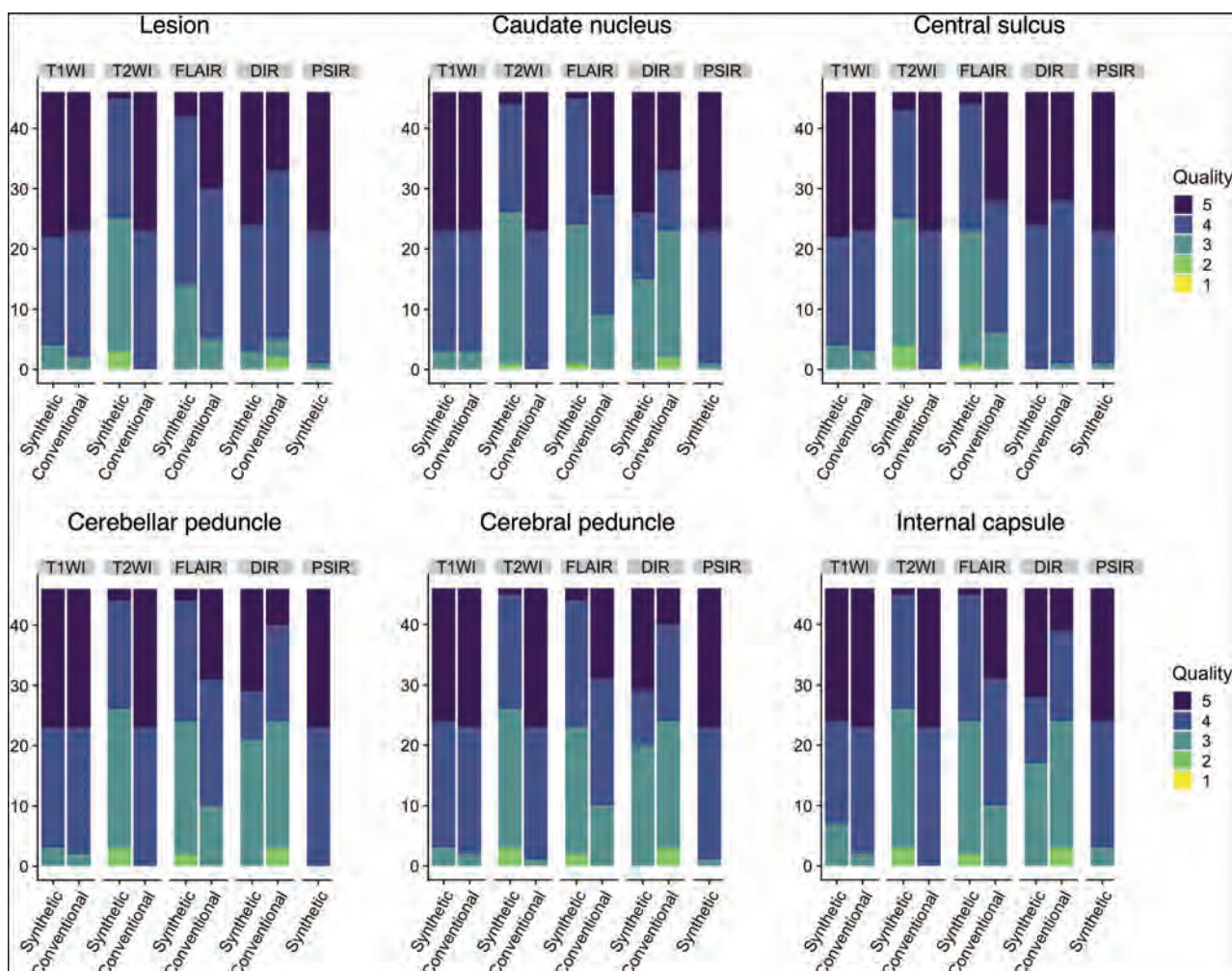
FIG 3. Comparison of structural delineations between conventional and synthetic MR imaging in patients with MS. Each target structure in 23 patients was rated for each contrast-weighted image on a 5-point Likert scale by 2 readers.
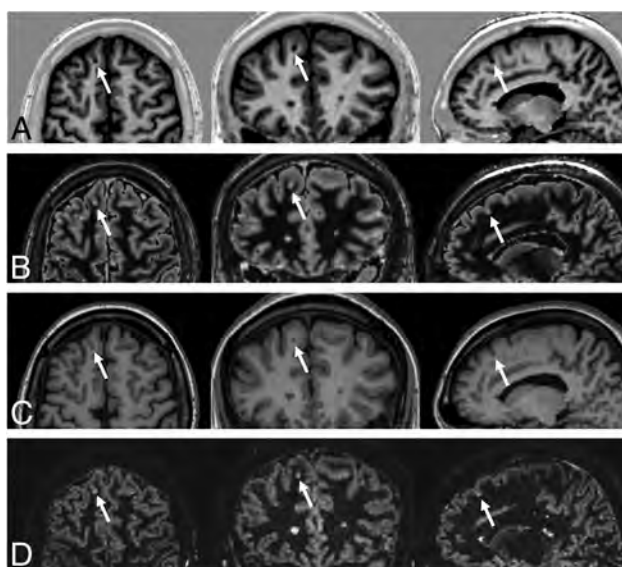
FIG 4. Example of an MS cortical lesion (*arrows*) in synthetic PSIR (*A*) and DIR (*B*) images. Conventional T1WI (*C*) and DIR (*D*) images are shown for reference. (*Left*) axial, (*middle*) coronal, and (*right*) sagittal views.

(range, 1.4–35.7) and 12.2 $\pm$ 11.9 (range, 0.8–41.0) mL, respectively ($P = .61$). The interclass correlation coefficient of the segmented lesion volumes was 0.98 (95% CI, 0.97–0.99), indicating excellent agreement. The Dice similarity coefficient of lesion maps between the synthetic and conventional MR imaging among all patients was 0.72 $\pm$ 0.07.

DISCUSSION

In this study, we evaluated the image quality and utility of 3D synthetic MR imaging in the assessment of MS lesions in both qualitative and quantitative approaches. To the best of our knowledge, this article is the first report of a clinical evaluation of 3D synthetic MR imaging. The time-efficient acquisition of synthetic imaging enabled the shortening of total acquisition time by 51% (9 minutes, 3 seconds and 18 minutes, 27 seconds for 3D-QALAS and conventional sequences, respectively) while maintaining enough image quality for both cortical lesion counts and quantitative lesion volumetric analysis. The acquisition time of 3D-QALAS is even shorter than that of the combination of T1-weighted, T2-weighted, and FLAIR images, which were recently reported to be used for creating 3D DIR images with deep learning.[24]
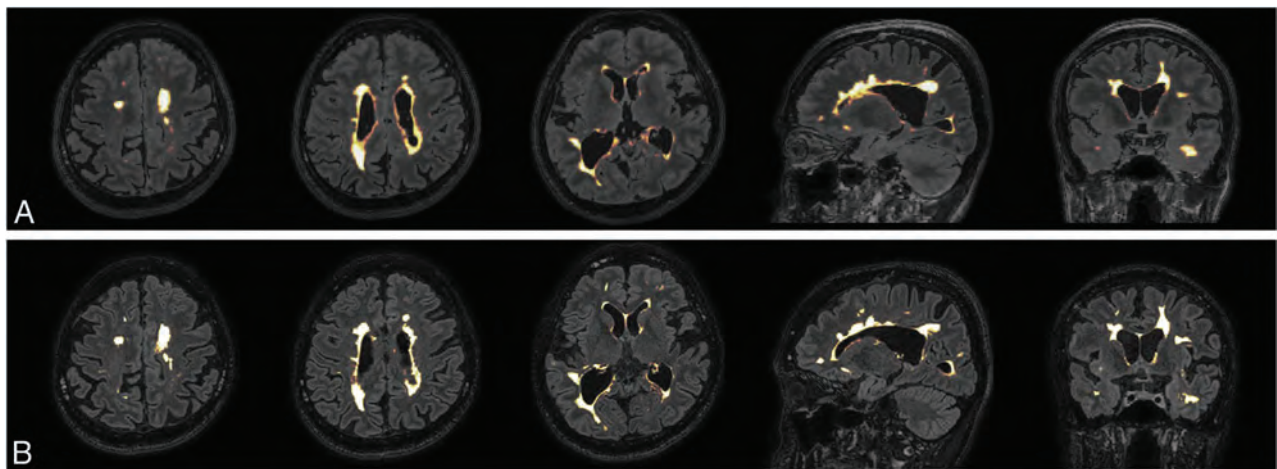
FIG 5. Representative examples of lesion segmentation in a 35-year-old woman with MS. Lesions were automatically segmented on synthetic and conventional FLAIR images. The segmented lesions are overlaid on the images used for segmentation. *A*, Lesions overlaid on 3D synthetic FLAIR images. *B*, Lesions overlaid on conventional 3D FLAIR images. Minimal differences are observed between segmented lesions of 3D synthetic and conventional FLAIR images.

Although the image quality of synthetic T2WI and FLAIR images was inferior to that of the conventional contrast-weighted images, there was no significant difference in the number of detected cortical lesions and automatically segmented lesion volumes. These findings support the notion that 3D synthetic imaging could provide essential information for clinical evaluation of MS lesions. Despite the inevitable trade-off between imaging time and image quality, 3D synthetic MR imaging is a promising method for achieving accelerated acquisition while retaining clinical utility.

Several artifacts were reported in the reading session. The high-signal artifact on the brain surface on synthetic FLAIR images is consistent with that reported in 2D imaging and seems to be caused by a partial volume effect.[12] This artifact may mimic subpial lesions located at the cortex–CSF interface or make it difficult to identify them. Because no subpial lesion was observed in this study both on synthetic and conventional images, the sensitivity and specificity of synthetic MR imaging to subpial lesions remain unclear. The relatively inferior image quality of synthetic T2WI and FLAIR images is desired to be solved for synthetic MR imaging to be used in routine clinical imaging protocols.[12] For 2D synthetic FLAIR, deep learning has been reported to be useful for improving the image quality of synthetic FLAIR while reducing artifacts.[25] In this study, a ringing artifact was observed on the brain surface, which was also seen in the original 3D-QALAS images. These findings indicate that this artifact was not caused by the process of image synthesis but rather propagated from the artifacts presenting in the original images to all the contrast-weighted images that were synthesized from the original images. Although readers rated conventional DIR superior to synthetic DIR for overall image quality, they preferred synthetic DIR for structural delineation. One possible reason for this discrepancy is that the readers were accustomed to the appearance of conventional contrast-weighted images, and hence they may have rated familiar conventional DIR images high in terms of overall image quality.

3D acquisition can provide thin continuous sections, which reduces the effects of partial volume averaging. Datasets of isotropic voxel size permit multiplanar reformations, allowing lesions to be viewed in any conventional axial, sagittal, and coronal plane and an oblique reformatted plane after a single acquisition. Furthermore, image synthesis is not limited to 3D-QALAS and could be applied to other multiparametric approaches, such as MR fingerprinting. In addition to the quantitative values, this produces contrast-weighted images that allow radiologists to fully use their knowledge and abilities for diagnosis. The synthesis of MRA from 3D-QALAS data is also feasible.[26]

One of the strengths of synthetic MR imaging that remains to be studied is the possibility of adjusting the synthetic TR, TE, and TI parameters to optimize them for each pathology, which has been shown in 2D synthetic MR imaging.[11] Although we have used preset parameters for creating synthetic images in this study, optimization of the contrast may improve the detection and delineation of lesions over conventional imaging. This could potentially lead to an early and accurate diagnosis of MS based on MR imaging. Another strength of 3D-QALAS is that it obtains not only multiple contrast images for visual assessment but also quantitative maps that could be useful for personalized or precision medicine.[27] Blystad et al[28] reported that contrast-enhancing MS lesions have significantly lower T1, T2, and proton density than nonenhancing lesions. This raises the possibility of predicting active lesions without gadolinium-based contrast agents.

The study limitations include the relatively small sample size and single-center design. Future multicenter studies evaluating the diagnostic accuracy of synthetic MR imaging in a large cohort are desired before its introduction into clinical practice. Another limitation is that the in-plane resolution of 1.30 mm in this study was lower than the recommended in-plane resolution of 1.0 mm described in the MAGNIMS guidelines.[29] A 3T scanner could increase signal-to-noise ratio, enabling improved in-plane resolution. Combining with techniques such as compressed sensing[30] may further increase the resolution with comparable or shorter scanning times.

CONCLUSIONS

3D synthetic MR imaging of the brain enables the creation of useful contrast-weighted images, including DIR and PSIR, in a single acquisition, thus reducing scanning time compared with conventional MR imaging. The synthetic contrast-weighted images were inferior in image quality but comparable in diagnostic power to those acquired by conventional MR imaging in patients with MS. 3D synthetic MR imaging may be considered an alternative to conventional MR imaging for generating diagnostic T1-weighted, DIR, and PSIR images, but synthetic T2-weighted and FLAIR images are currently unsatisfactory.

ACKNOWLEDGMENTS

REFERENCES

1. Brownlee WJ, Hardy TA, Fazekas F, et al. **Diagnosis of multiple sclerosis: progress and challenges.** *Lancet* 2017;389:1336–46 CrossRef Medline

2. Reich DS, Lucchinetti CF, Calabresi PA. **Multiple sclerosis.** *N Engl J Med* 2018;378:169–80 CrossRef Medline

3. Filippi M, Preziosa P, Banwell BL, et al. **Assessment of lesions on magnetic resonance imaging in multiple sclerosis: practical guidelines.** *Brain* 2019;142:1858–75 CrossRef Medline

4. Calabrese M, Filippi M, Gallo P. **Cortical lesions in multiple sclerosis.** *Nat Rev Neurol* 2010;6:438–44 CrossRef Medline

5. Harrison DM, Roy S, Oh J, et al. **Association of cortical lesion burden on 7-T magnetic resonance imaging with cognition and disability in multiple sclerosis.** *JAMA Neurol* 2015;72:1004–12 CrossRef Medline

6. Traboulsee A, Simon JH, Stone L, et al. **Revised Recommendations of the Consortium of MS Centers Task Force for a Standardized MRI Protocol and Clinical Guidelines for the Diagnosis and Follow-Up of Multiple Sclerosis.** *AJNR Am J Neuroradiol* 2016;37:394–401 CrossRef Medline

7. Sethi V, Yousry TA, Muhlert N, et al. **Improved detection of cortical MS lesions with phase-sensitive inversion recovery MRI.** *J Neurol Neurosurg Psychiatry* 2012;83:877–82 CrossRef Medline

8. Geurts JJ, Pouwels PJW, Uitdehaag BM, et al. **Intracortical lesions in multiple sclerosis: improved detection with 3D double inversion-recovery MR imaging.** *Radiology* 2005;236:254–60 CrossRef Medline

9. Wallaert L, Hagiwara A, Andica C, et al. **The advantage of synthetic MRI for the visualization of anterior temporal pole lesions on double inversion recovery (DIR), phase-sensitive inversion recovery (PSIR), and myelin images in a patient with CADASIL.** *Magn Reson Med Sci* 2018;17:275–76 CrossRef Medline

10. Forslin Y, Bergendal A, Hashim F, et al. **Detection of leukocortical lesions in multiple sclerosis and their association with physical and cognitive impairment: a comparison of conventional and synthetic phase-sensitive inversion recovery MRI.** *AJNR Am J Neuroradiol* 2018;39:1995–2000 CrossRef Medline

11. Hagiwara A, Hori M, Yokoyama K, et al. **Synthetic MRI in the detection of multiple sclerosis plaques.** *AJNR Am J Neuroradiol* 2017;38:257–63 CrossRef Medline

12. Hagiwara A, Warntjes M, Hori M, et al. **SyMRI of the brain: rapid quantification of relaxation rates and proton density, with synthetic MRI, automatic brain segmentation, and myelin measurement.** *Invest Radiol* 2017;52:647–57 CrossRef Medline

13. Warntjes JBM, Leinhard OD, West J, et al. **Rapid magnetic resonance quantification on the brain: optimization for clinical usage.** *Magn Reson Med* 2008;60:320–29 CrossRef Medline

14. Krauss W, Gunnarsson M, Nilsson M, et al. **Conventional and synthetic MRI in multiple sclerosis: a comparative study.** *Eur Radiol* 2018;28:1692–700 CrossRef Medline

15. Fujita S, Hagiwara A, Hori M, et al. **3D quantitative synthetic MRI-derived cortical thickness and subcortical brain volumes: scan-rescan repeatability and comparison with conventional T$_1$-weighted images.** *J Magn Reson Imaging* 2019;50:1834–42 CrossRef Medline

16. Fujita S, Hagiwara A, Hori M, et al. **Three-dimensional high-resolution simultaneous quantitative mapping of the whole brain with 3D-QALAS: an accuracy and repeatability study.** *Magn Reson Imaging* 2019;63:235–43 CrossRef Medline

17. Kvernby S, Warntjes MJB, Haraldsson H, et al. **Simultaneous three-dimensional myocardial T1 and T2 mapping in one breath hold with 3D-QALAS.** *J Cardiovasc Magn Reson* 2014;16:102 CrossRef Medline

18. Thompson AJ, Banwell BL, Barkhof F, et al. **Diagnosis of multiple sclerosis: 2017 revisions of the McDonald criteria.** *Lancet Neurol* 2018;17:162–73 CrossRef Medline

19. Krupa K, Bekiesińska-Figatowska M. **Artifacts in magnetic resonance imaging.** *Pol J Radiol* 2015;80:93–106 CrossRef Medline

20. Tanenbaum LN, Tsiouris AJ, Johnson AN, et al. **Synthetic MRI for clinical neuroimaging: results of the magnetic resonance image compilation (MAGiC) prospective, multicenter, multireader trial.** *AJNR Am J Neuroradiol* 2017;38:1103–10 CrossRef Medline

21. Schmidt P, Gaser C, Arsic M, et al. **An automated tool for detection of FLAIR-hyperintense white-matter lesions in multiple sclerosis.** *Neuroimage* 2012;59:3774–83 CrossRef Medline

22. Fenster A, Chiu B. **Evaluation of segmentation algorithms for medical imaging.** *Conf Proc IEEE Eng Med Biol Soc* 2005;2005:7186–89 CrossRef Medline

23. Landis JR, Koch GG. **The measurement of observer agreement for categorical data.** *Biometrics* 1977;33:159–74 CrossRef Medline

24. Finck T, Li H, Grundl L, et al. **Deep-learning generated synthetic double inversion recovery images improve multiple sclerosis lesion detection.** *Invest Radiol* 2020;55:318–23 CrossRef Medline

25. Hagiwara A, Otsuka Y, Hori M, et al. **Improving the quality of synthetic FLAIR images with deep learning using a conditional generative adversarial network for pixel-by-pixel image translation.** *AJNR Am J Neuroradiol* 2019;40:224–30 CrossRef Medline

26. Fujita S, Hagiwara A, Otsuka Y, et al. **Deep learning approach for generating MRA images from 3D quantitative synthetic MRI without additional scans.** *Invest Radiol* 2020;55:249–56 CrossRef Medline

27. Hagiwara A, Fujita S, Ohno Y, et al. **Variability and standardization of quantitative imaging: monoparametric to multiparametric quantification, radiomics, and artificial intelligence.** *Invest Radiol* 2020;55:601–16 CrossRef Medline

28. Blystad I, Hakansson I, Tisell A, et al. **Quantitative MRI for analysis of active multiple sclerosis lesions without gadolinium-based contrast agent.** *AJNR Am J Neuroradiol* 2016;37:94–100 CrossRef Medline

29. Rovira A, Wattjes MP, Tintore M, MAGNIMS study group, et al. **Evidence-based guidelines: MAGNIMS consensus guidelines on the use of MRI in multiple sclerosis-clinical implementation in the diagnostic process.** *Nat Rev Neurol* 2015;11:471–82 CrossRef Medline

30. Lustig M, Donoho D, Pauly JM. **Sparse MRI: the application of compressed sensing for rapid MR imaging.** *Magn Reson Med* 2007;58:1182–95 CrossRef Medline

Quantification of Oscillatory Shear Stress from Reciprocating CSF Motion on 4D Flow Imaging

S. Yamada, H. Ito, M. Ishikawa, K. Yamamoto, M. Yamaguchi, M. Oshima, and K. Nozaki

ABSTRACT

BACKGROUND AND PURPOSE: Oscillatory shear stress could not be directly measured in consideration of direction, although cerebrospinal fluid has repetitive movements synchronized with heartbeat. Our aim was to evaluate the important of oscillatory shear stress in the cerebral aqueduct and foramen magnum in idiopathic normal pressure hydrocephalus by comparing it with wall shear stress and the oscillatory shear index in patients with idiopathic normal pressure hydrocephalus.

MATERIALS AND METHODS: By means of the 4D flow application, oscillatory shear stress, wall shear stress, and the oscillatory shear index were measured in 41 patients with idiopathic normal pressure hydrocephalus, 23 with co-occurrence of idiopathic normal pressure hydrocephalus and Alzheimer-type dementia, and 9 age-matched controls. These shear stress parameters at the cerebral aqueduct were compared with apertures and stroke volumes at the foramen of Magendie and cerebral aqueduct.

RESULTS: Two wall shear stress magnitude peaks during a heartbeat were changed to periodic oscillation by converting oscillatory shear stress. The mean oscillatory shear stress amplitude and time-averaged wall shear stress values at the dorsal and ventral regions of the cerebral aqueduct in the idiopathic normal pressure hydrocephalus groups were significantly higher than those in controls. Furthermore, those at the ventral region of the cerebral aqueduct in the idiopathic normal pressure hydrocephalus group were also significantly higher than those in the co-occurrence of idiopathic normal pressure hydrocephalus with Alzheimer-type dementia group. The oscillatory shear stress amplitude at the dorsal region of the cerebral aqueduct was significantly associated with foramen of Magendie diameters, whereas it was strongly associated with the stroke volume at the upper end of the cerebral aqueduct rather than that at the foramen of Magendie.

CONCLUSIONS: Oscillatory shear stress, which reflects wall shear stress vector changes better than the conventional wall shear stress magnitude and the oscillatory shear index, can be directly measured on 4D flow MR imaging. Oscillatory shear stress at the cerebral aqueduct was considerably higher in patients with idiopathic normal pressure hydrocephalus.

ABBREVIATIONS: AD = Alzheimer-type dementia; iNPH = idiopathic normal pressure hydrocephalus; OSI = oscillatory shear index; OSS = oscillatory shear stress; TAWSS = time-averaged wall shear stress; WSS = wall shear stress

Impaired CSF absorption might be caused by increased CSF volume in idiopathic normal pressure hydrocephalus (iNPH); however, its etiology has not been elucidated. Stroke volume at the cerebral aqueduct has been reported to be considerably increased in most patients with iNPH.[1-9] Our previous study on 4D flow MR imaging revealed that patients with iNPH had significantly increased reciprocating bidirectional CSF movements and flow-related bimodal high wall shear stress (WSS), a force vector produced by the fluid flow acting tangentially on the wall surfaces at the cerebral aqueduct in 1 cardiac cycle.[10] Moreover, high time-averaged wall shear stress (TAWSS) due to bidirectional CSF movements at the cerebral aqueduct was significantly associated with z-axial expansion of the frontal horn of the lateral ventricles in iNPH. WSS is known to regulate vessel caliber and influences the development of vascular pathologies.[11-20] Oscillating flow dynamics, specifically turbulent or disturbed flow, has been noticed

in the pathogenesis of flow-mediated arterial dilation or atherosclerosis.[11-20] Oscillating low WSS due to turbulent flow at the arterial bifurcation is associated with atherosclerotic plaque,[11,16-18] whereas chronic high WSS contributes to expansive or outward remodeling of vessels in response to a sustained increase in flow.[19,20]

In the CSF dynamics, the normal CSF movements generated by the directional beating of motile cilia on the ependymal cells lining the ventricular surface maintain a calm environment in the ventricles; however, increased reciprocating bidirectional CSF movements might induce the disruption of motile cilia and ependymal gliosis, which has been shown to be directly associated with ventriculomegaly.[21-26] Therefore, we hypothesized whether oscillatory shear stress (OSS) due to bidirectional CSF movements at the cerebral aqueduct may also be associated with the size of the cerebral aqueduct and ventricles in iNPH. However, OSS could not be directly measured, which was different from the conventional WSS magnitude without direction information or the oscillatory shear index (OSI), indicating direction changes. Therefore, a novel method to directly measure OSS using 4D flow MR imaging was successfully developed. This study aimed to evaluate the significance of OSS at the cerebral aqueduct and foramen of Magendie in iNPH by comparing it with the conventional WSS magnitude and OSI. Furthermore, shear stress parameters were compared with apertures and stroke volumes at the foramen of Magendie and cerebral aqueduct among patients with iNPH only, patients with co-occurrence of iNPH and Alzheimer-type dementia (AD), and age-matched controls.

MATERIALS AND METHODS

The ethics committees for human research of Rakuwakai Otowa Hospital approved the study design and protocol (Nos. Rakuoto-Rin-17–041 and R2019-227). After obtaining written informed consent from patients or their relatives, the private information was anonymized in a linkable manner. Data collection, anonymization, image acquisition, and data-processing methods of 4D flow MR imaging were described in our previous study.[10] In brief, 64 patients diagnosed with iNPH and 9 age-matched controls who underwent MR imaging examinations from January 28, 2017, to August 30, 2019, using a 3T MR imaging system (Magnetom Skyra; Siemens) were included in this study. All patients with iNPH had gait disturbance, cognitive impairment, and/or urinary incontinence, which improved after the CSF tap test, and ventricular dilation, an enlarged Sylvian fissure, and narrow sulci at the high convexity on conventional CT or MR imaging. A total of 23 patients with iNPH also had clinical AD based on the comprehensive assessment of their symptoms and findings on MR imaging and SPECT. Furthermore, 9 participants 60 years of age or older were recruited as controls because they had no symptoms of a short-stepped gait and/or cognitive impairment.

The time-resolved 3D velocity-encoding data were obtained from the 4D flow MR imaging sequence with 5 cm/s of velocity encoding and synchronizing the peripheral pulse rate measured from the finger (TR, 100 ms; TE, 9 ms; flip angle, 8°; FOV, 200 mm; matrix, 192 × 192; and voxel size, 1.0 × 1.0 × 1.3 mm). The image range was obtained in the midsagittal plane with a width of 30 mm (1.26 mm × 24 slices) from the bilateral foramina
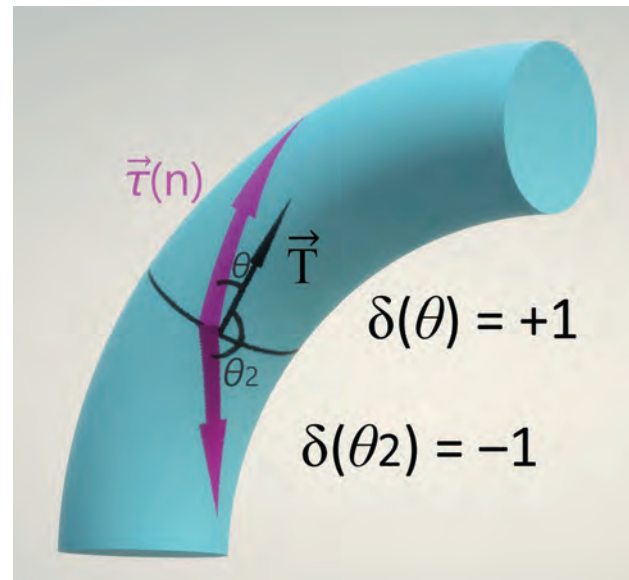
FIG 1. Schema explaining OSS: $\theta(n)$ is the angle between $\vec{T}$ and $\vec{\tau}(n)$ in the nth phase $\vec{\tau}(n)$

$$\delta[\theta(n)] : \begin{cases} +1(-90° < \theta(n) < 90°) \\ -1(90° < \theta(n) < 270°) \end{cases},$$

Where $\vec{T} : \dfrac{\sum_{n=1}^{N} \vec{\tau}(n)}{N}$ indicates a vector of TAWSS, and $\vec{\tau}(n) : \mu\dfrac{\Delta\vec{v}(n)}{\Delta z}$ indicates a vector of WSS.

of Monro to the upper cervical subarachnoid spaces. All 4D flow analyses were conducted using the 4D flow application in an independent 3D volume analyzer workstation (Synapse 3D; Fujifillm Healthcare). To increase the accuracy of fine anatomic information of <1 mm, we used volumetric data on a T2-weighted 3D spin-echo sequence with sampling perfection with application-optimized contrasts by using different flip angle evolution (SPACE sequence; Siemens). Sequence parameters (TR, 2800 ms; TE, 286 ms; FOV, 230 mm; matrix, 192 × 192; and voxel size, 0.6 × 0.6 × 0.9 mm) were superimposed on 3D phase images using a trilinear interpolation algorithm, and a 3D polygon mesh of ventricles and subarachnoid spaces was created from this high-resolution volumetric data using a marching cubes algorithm (Online Supplemental Data). In all 4D flow analyses, stress parameters were measured after confirming the absence of phase aliasing or motion artifacts. The anterior-posterior diameters of the foramen of Magendie, the lower and upper ends of the cerebral aqueduct, and the midbrain were measured on the midsagittal plane of T2-weighted 3D SPACE MR imaging (Online Supplemental Data).

The 3D flow velocities (centimeters/second) and volumes (milliliters/second) of the reciprocating CSF movements through 12 ROIs were measured from the bilateral foramina of Monro to the lower end of the second cervical vertebra. The stroke volume was calculated by adding the absolute forward and backward CSF flow volumes, and reversed flow rate (%) by the absolute backward flow volume divided by the absolute forward flow volume. The surface mesh of CSF spaces was generated by increasing the image resolution and applying maximum smoothing, with an
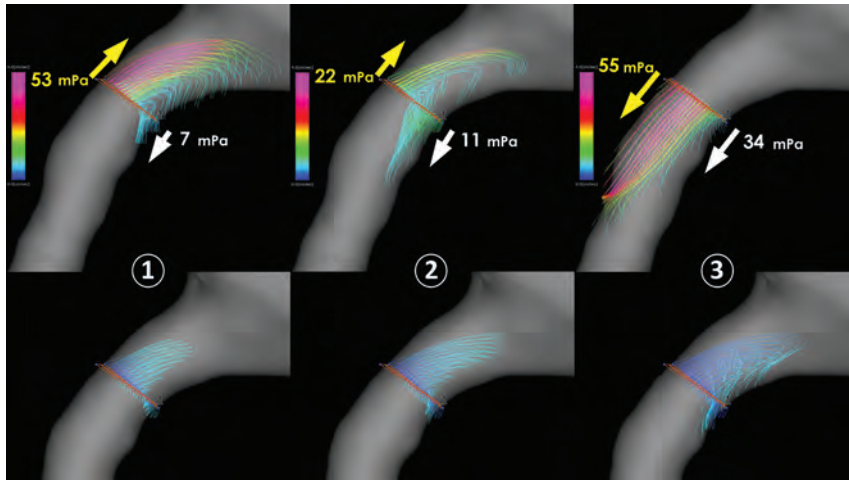
FIG 2. Oscillation of WSS due to bidirectional CSF flow through the cerebral aqueduct. The numbers 1, 2, and 3 demonstrate temporal changes of the reciprocating CSF motion during 1 cardiac cycle in a 77-year-old man diagnosed with iNPH. The *colored path lines* (*lower figures*) show the flow as a moving trajectory of the virtual particle through the middle part of the cerebral aqueduct in 1 heartbeat. The color and length of 3D streamlines (*upper figures*) indicate the flow velocity as pink for fast and blue for slow. The sampling interval of streamlines and *path lines* was set at 0.2 mm after the trilinear interpolation. The *arrows* indicate the WSS vector produced by the flow parallel to the wall surface. The size and direction of the *arrows* indicate the magnitude and direction of the WSS vector. Temporal changes of the WSS vector at the dorsal region (*yellow arrows*) were larger than those at the ventral region (*white arrows*).

interpolation of a one-fourth interval and a decimation rate of 50%.

Shear Stress Parameters

The conventional WSS vector in the nth phase $\vec{\tau}(n)$ (N/m^2) was calculated as

$$\vec{\tau}(n) = \mu \frac{\Delta \vec{v}(n)}{\Delta z},$$

where Δz was the distance perpendicular to the wall, $\Delta \vec{v}(n)$ was the flow velocity vector in the nth phase parallel to the wall separate from Δz, and μ was the dynamic viscosity. In this study, Δz was set at 0.8 mm considering the resolution and average diameter of the cerebral aqueduct, and μ was set 1.0 · $\times$ 0.001 (pascal $\times$ second) based on the CSF modeled as an incompressible Newtonian fluid with hydrodynamic characteristics of water.

The WSS magnitude $|\vec{\tau}(n)|$ was defined as an absolute value without direction information.

To evaluate the cumulative effect of WSS vector during 1 heartbeat, we calculated the TAWSS vector $\vec{T}$ as

$$\vec{T} = \frac{\sum_{n=1}^{N} \vec{\tau}(n)}{N},$$

where N was the total number of phases during 1 cardiac cycle and TAWSS magnitude $|\vec{T}|$ was defined as a scalar quantity of the TAWSS vector.

The angle between the nth phase direction of the WSS vector and the TAWSS vector as the principal axis was defined as $\theta(n)$,

and the scale for converting $\theta(n)$ into a binary value of $+1$ or -1 was defined as $\delta\ [\theta(n)]$, calculated as

$$\delta[\theta(n)] = \begin{cases} +1 (-90° < \theta(n) < 90°) \\ -1 (90° < \theta(n) < 270°) \end{cases},$$

where $\delta(\theta) = +1$ indicates the same direction as $\vec{T}$ and $\delta(\theta) = -1$ indicates a 180° opposite direction. As shown in Fig 1, the WSS magnitude multiplied by $+1$ or -1 was defined as OSS calculated as

$$\text{OSS} = |\vec{\tau}(n)| \ \times \ \delta[\theta(n)].$$

The OSS amplitude was calculated as the maximum minus the minimum OSS value.

OSI that monitors the direction changes of the WSS vector during 1 cardiac cycle was calculated as

$$\text{OSI} = \frac{1}{2} \left\{ 1 - \frac{\left| \sum_{n=1}^{N} \vec{\tau}(n) \right|}{\sum_{n=1}^{N} |\vec{\tau}(n)|} \right\}.$$

The OSI ranges from 0 to 0.5, where 0 indicates a complete unidirectional flow and 0.5 indicates oscillatory flow only.

The WSS magnitude and OSI were automatically calculated per pixel and displayed on the 3D surface display using a scalable color map of the 4D flow application on Synapse 3D.

Data and codes used in this study are not available within the public domain because of the commercially available workstation.

The WSS magnitude, OSS, and OSI were automatically measured using 5 dotlike ROIs with the highest WSS magnitude at the ventral (ROI 1) and dorsal (ROI 2) regions of the foramen magnum and dorsal (ROI 3) and ventral (ROI 4) regions of the cerebral aqueduct and interpeduncular cistern (ROI 5).

Statistical Analysis

The Kruskal-Wallis rank sum test was used to compare the mean values [SD] for age and several MR imaging measurements among the 3 groups. In addition, the Wilcoxon rank sum test was used to compare continuous variables between patients with iNPH with co-occurrence of iNPH and AD or controls. The Fisher exact test was used to compare the 3 proportions. The Pearson correlation coefficient (r) and 95% CI were used to determine relationships between shear stress and morphologic parameters or stroke volume. Statistical significance was assumed at a P value < .05. All missing data points were treated as deficit data that did not affect other variables. Statistical analyses were performed using R statistical and computing software (Version 3.6.2; http://www.R-project.org).

RESULTS

During 1 cardiac cycle, the CSF moved in the craniocaudal and caudocranial directions periodically through the cerebral
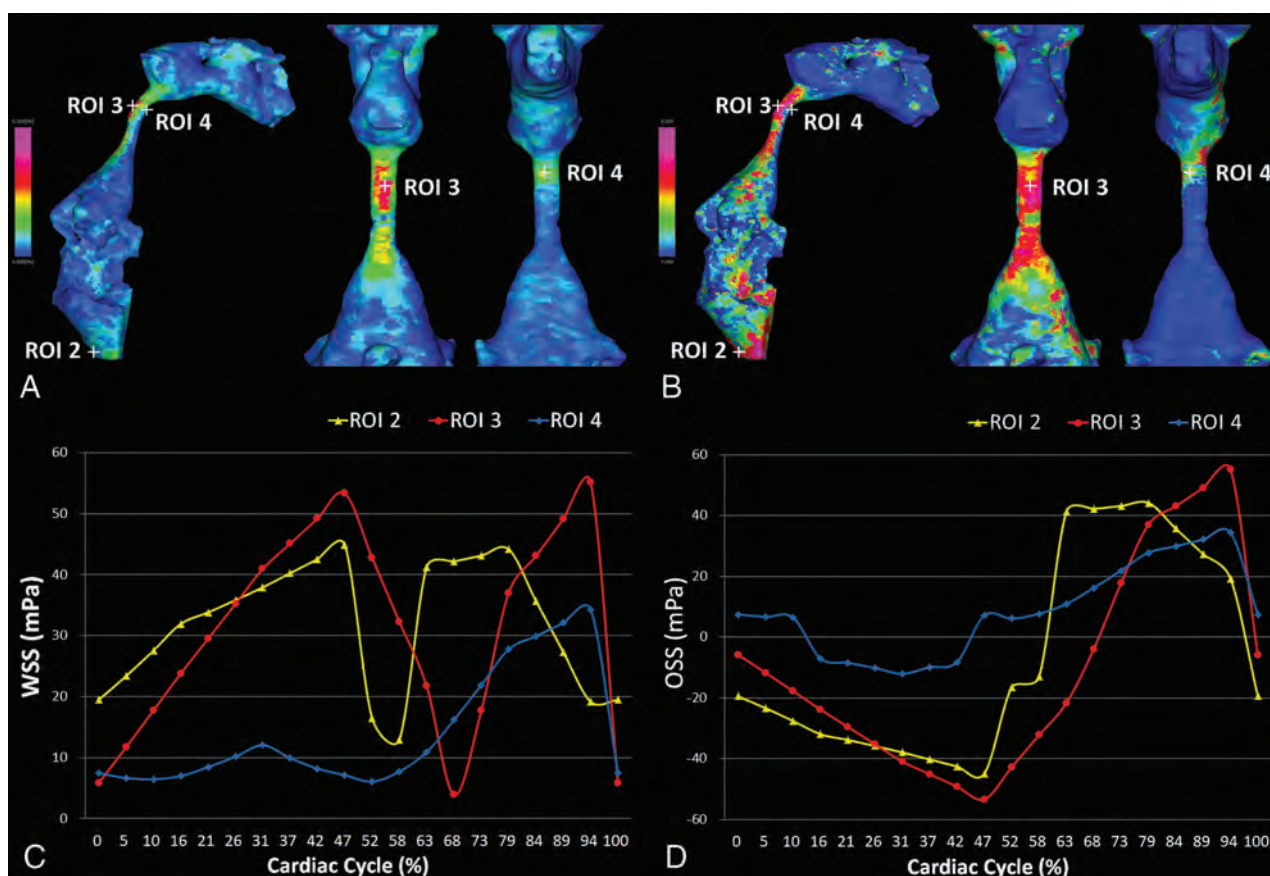
FIG 3. Distributions and fluctuations of shear stress parameters per heartbeat in iNPH. The *colored surfaces* in the ventricles show the distribution of WSS magnitude (*A*) and OSI (*B*) in the same patient with iNPH, as shown in Fig 2. Red indicates high and blue indicates low. *Line-graphs C* and *D* show chronologic changes of WSS magnitude and OSS at the dorsal region of the foramen magnum (ROI 2, yellow) and dorsal (ROI 3, red) and ventral (ROI 4, blue) regions of the cerebral aqueduct in 1 cardiac cycle. Considering the shear stress direction, these changes were completely different.

Table 1: Clinical and morphologic characteristics of the study population[a]

	iNPH Only	iNPH with AD	Control	*P* Value
Total number	41	23	9	
Male/female	28:13	13:10	4:5	.332
Age (yr)	78.2 [SD, 6.62]	79.8 [SD, 5.83]	75.7 [SD, 5.70]	.207
Anteroposterior diameter (mm)				
Foramen of Magendie	5.72 [SD, 1.77]	5.88 [SD, 2.04]	2.02 [SD, 0.44]	<.001
Lower end of cerebral aqueduct	4.44 [SD, 0.87]	4.25 [SD, 1.41]	2.23 [SD, 0.70]	<.001
Upper end of cerebral aqueduct	3.65 [SD, 0.66]	3.45 [SD, 0.73]	2.30 [SD, 0.54]	<.001
Midbrain	8.56 [SD, 0.88]	8.43 [SD, 0.92]	9.32 [SD, 1.57]	.230
Stroke volume (μL/heartbeat)				
Foramen of Magendie	32.9 [SD, 22.6]	37.4 [SD, 37.6]	21.1 [SD, 11.7]	.448
Lower end of cerebral aqueduct	37.6 [SD, 28.9]	39.6 [SD, 43.7]	17.8 [SD, 13.0]	.083
Upper end of cerebral aqueduct	49.0 [SD, 33.3]	52.6 [SD, 32.5]	18.9 [SD, 10.5]	.002
Foramina of Monro	96.5 [SD, 41.0]	97.8 [SD, 39.1]	62.8 [SD, 44.6]	.042

[a] Data are means. *P* value is from the Kruskal-Wallis rank sum test.

aqueduct (Fig 2 and Online Supplemental Data). Bidirectional CSF movements at the dorsal region of the cerebral aqueduct were larger than those in the ventral region in patients with iNPH. Chronologic WSS magnitude changes in the dorsal region of the cerebral aqueduct were also larger than those in the ventral region due to bidirectional CSF movements (Fig 3 and Online Supplemental Data). The distribution of WSS magnitude (Fig 3*A*) was somewhat different from that of the OSI (Fig 3*B*). The bimodal high WSS magnitude in Fig 3*C* at the dorsal region of the foramen magnum (ROI 2) and cerebral aqueduct (ROI 3) was changed to the periodic oscillation by converting OSS (Fig 3*D*). In other words, 1 of the 2 WSS magnitude peaks during a heartbeat was converted to the negative OSS.

A total of 73 participants comprising 41 patients diagnosed with iNPH only, 23 with co-occurrence of iNPH and AD, and 9 age-matched controls were included in this study (Table 1).

The difference in mean OSS amplitude, TAWSS, and OSI at the ventral (ROI 1) and dorsal (ROI 2) regions of the foramen magnum and interpeduncular cistern (ROI 5) was not significant among the 3 groups. Therefore, the amplitude, maximum, and

Table 2: Mean value [SD] of parameters at the cerebral aqueduct in the study population[a]

	All (n = 73)	iNPH Only (n = 41)	iNPH with AD (n = 23)	Control (n = 9)	P1	P2	P3
Dorsal region of the cerebral aqueduct							
OSS amplitude	52.5 [SD, 33.9]	59.7 [SD, 34.1]	52.9 [SD, 32.2]	19.8 [SD, 13.3]	.483	<.001	.004
Maximum OSS	35.9 [SD, 16.0]	38.7 [SD, 15.5]	37.3 [SD, 16.1]	19.7 [SD, 6.3]	.566	<.001	.002
Minimum OSS	−16.7 [SD, 19.8]	−21.0 [SD, 20.2]	−15.6 [SD, 18.9]	−0.1 [SD, 9.6]	.277	.001	.043
TAWSS	18.2 [SD, 8.9]	19.7 [SD, 8.7]	18.8 [SD, 9.3]	9.9 [SD, 2.2]	.678	<.001	.008
OSI	0.21 [SD, 0.13]	0.24 [SD, 0.12]	0.19 [SD, 0.14]	0.16 [SD, 0.11]	.234	.077	.614
Ventral region of the cerebral aqueduct							
OSS amplitude	27.2 [SD, 28.4]	36.0 [SD, 32.2]	18.1 [SD, 19.8]	11.9 [SD, 11.1]	.022	.020	.363
Maximum OSS	23.6 [SD, 15.9]	28.8 [SD, 17.9]	18.2 [SD, 10.9]	14.2 [SD, 6.4]	.017	.011	.246
Minimum OSS	−3.6 [SD, 13.9]	−7.1 [SD, 15.9]	0.14 [SD, 10.1]	2.3 [SD, 7.5]	.080	.091	.592
TAWSS	12.2 [SD, 7.1]	14.3 [SD, 8.1]	10.1 [SD, 4.9]	8.1 [SD, 2.7]	.038	.020	.458
OSI	0.13 [SD, 0.15]	0.15 [SD, 0.15]	0.10 [SD, 0.14]	0.11 [SD, 0.15]	.114	.355	.910

[a] P1 indicates probability value of iNPH only versus iNPH with AD by the Wilcoxon rank sum test; P2, probability value of iNPH only versus controls by the Wilcoxon rank sum test; and P3, probability value of iNPH with AD versus controls by the Wilcoxon rank sum test.

minimum OSS values; TAWSS; and OSI at the dorsal (ROI 3) and ventral (ROI 4) regions of the cerebral aqueduct are shown in Table 2. The mean OSS amplitude at the dorsal and ventral regions of the cerebral aqueduct in the iNPH groups was approximately 3 times higher than that in the controls because the maximum OSS in the iNPH groups was twice as high and the minimum OSS was considerably lower. Remarkably, the mean amplitude and maximum OSS values at the ventral region of the cerebral aqueduct in the iNPH-only group were twice as high as those in the iNPH with AD group. The mean TAWSS magnitude at the dorsal region of the cerebral aqueduct in the iNPH-only group was also significantly higher than that in the controls. Furthermore, patients with iNPH-only had a significantly higher mean TAWSS magnitude at the ventral region of the cerebral aqueduct compared with those with iNPH with AD. The median and distribution of the OSS amplitude and TAWSS magnitude at the dorsal and ventral regions of the cerebral aqueduct among the 3 groups are shown as boxplots in Fig 4. Both the OSS amplitude and TAWSS magnitude at the dorsal region of the cerebral aqueduct in the iNPH groups were significantly higher than those in the controls, whereas the OSS amplitude at the ventral region of the cerebral aqueduct in the iNPH-only group was significantly higher than that in the iNPH with AD group and controls. The difference in OSI was not significant among the 3 groups.

The TAWSS magnitude was strongly associated with the amplitude and maximum and minimum OSS values at the dorsal (r = 0.89, 0.93, and −0.77) and ventral (r = 0.88, 0.93, and −0.73) regions of the cerebral aqueduct (Online Supplemental Data).

Relationships between Shear Stress Parameters and Anterior-Posterior Diameter or Stroke Volume

The amplitude and maximum and minimum OSS values and TAWSS magnitude at the dorsal region of the cerebral aqueduct were significantly associated with the anterior-posterior diameters of the foramen of Magendie and the lower end of the cerebral aqueduct (Table 3) and were strongly associated with stroke volume at the upper and lower ends of the cerebral aqueduct and foramen of Magendie, respectively (Table 4). The amplitude and maximum and minimum OSS values and TAWSS magnitude at the ventral region of the cerebral aqueduct were significantly-but-weakly

associated with stroke volumes at the lower and upper ends of the cerebral aqueduct. However, OSI was not significantly associated with anterior-posterior diameters or stroke volumes at any locations.

DISCUSSION

The reciprocating bidirectional CSF movements increase the bimodal WSS magnitude at the cerebral aqueduct during a cardiac cycle in iNPH. The conventional WSS magnitude was calculated as an absolute value of the WSS vector without the direction information by converting to a scalar quantity. However, the actual shear stress was produced by the bidirectional CSF flows from positive to negative values, not in a bimodal waveform. Therefore, a novel parameter, OSS with plus/minus directional information in addition to the WSS magnitude, was developed. On the basis of our literature review, this study is the first report that directly measures the OSS on 4D flow MR imaging. The maximum value of positive OSS drastically fluctuated to the minimum value of negative OSS during a heartbeat due to the reciprocating CSF movements in iNPH. Conversely, the maximum WSS magnitude value was either of the 2 peaks, whereas the minimum value was nearly zero consistently. However, the TAWSS magnitude was significantly associated with the OSS amplitude.

The distribution and magnitude of OSI were different from those of OSS or WSS magnitude. In contrast to steady flow conditions, pulsatile bidirectional flows cause large OSS fluctuations.

In this study, the OSS amplitude at the dorsal region of the cerebral aqueduct was significantly associated with both the foramen of Magendie diameters and stroke volumes at the upper and lower ends of the cerebral aqueduct and foramen of Magendie, respectively. Our previous study demonstrated that the stroke volume at the cerebral aqueduct had the strongest association with the foramen of Magendie diameter.[10] These findings indicate that the dilation of the foramen of Magendie may be the first trigger for increased OSS amplitude at the dorsal region of the cerebral aqueduct due to increased aqueductal stroke volume. On the basis of study on oscillating flow dynamics,[11-20] chronic high OSS at the cerebral aqueduct may be involved in the expansive remodeling of the aqueductal lumen diameter and may
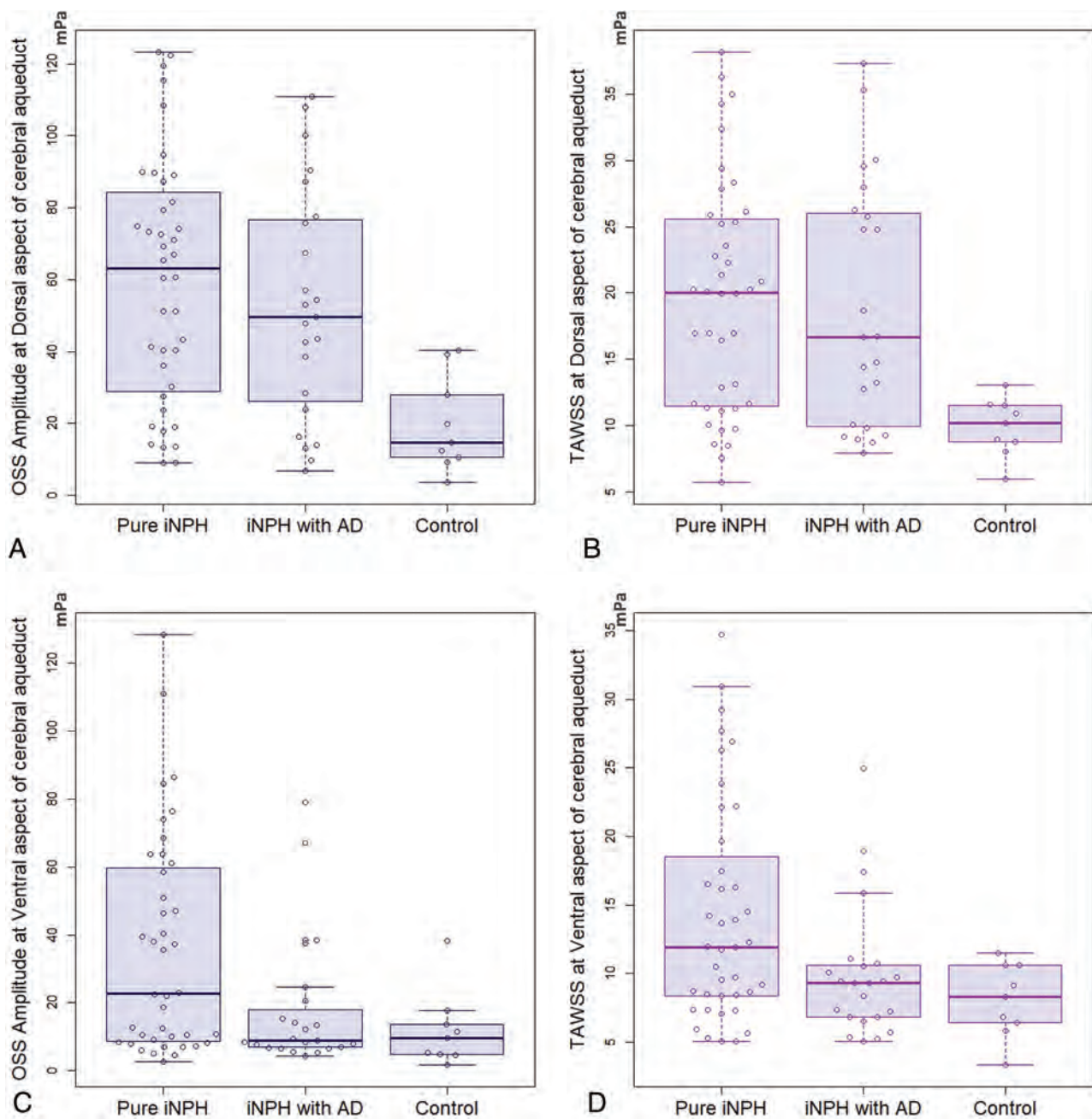
FIG 4. Boxplots for the amplitude of OSS and TAWSS at the dorsal and ventral regions of the cerebral aqueduct among 3 groups. *A*, Distribution of the OSS amplitude at the dorsal region of the cerebral aqueduct. *B*, Distribution of the TAWSS at the dorsal region of the cerebral aqueduct. *C*, Distribution of the OSS amplitude at the ventral region of the cerebral aqueduct. *D*, Distribution of the TAWSS at the ventral region of the cerebral aqueduct.

subsequently increase the pulsatile CSF inflow. However, this study has not yet proved this evidence.

Increased OSS amplitude may be associated with symptoms or pathologies of iNPH. We found that patients with iNPH-only had significantly higher OSS amplitude only at the ventral region of the cerebral aqueduct compared with those with co-occurrence of iNPH and AD. This finding was consistent with our previous result that patients with iNPH-only had not only smaller ventricular volume but also larger basal cistern and Sylvian fissure volumes than those with co-occurrence of iNPH and AD.[27] AD is known as the most common comorbidity with iNPH due to CSF stagnation,[28-32] hindering the clearance of neurotoxic molecules such as amyloid-β or τ.[33,34] Recently, pulsatile CSF inflow to the ventricular

systems during sleep was reportedly associated with large, coupled low-frequency oscillations in the neuronal activity and hemodynamic oscillations.[35] Decreased CSF pulsation may be associated with AD onset through the pathway in suppressed electrophysiologic slow waves that impair amyloid-β and τ excretion into the brain interstitial fluid and CSF during sleep.[36-39] Therefore, direct OSS measurement in future studies will help determine whether CSF oscillations are associated with the AD onset.

This study had some limitations as described in our previous study.[10] In particular, influences of respiration, wall motion, eddy currents, and background noise on the 4D flow MR imaging sequence were not assessed. Second, OSS and WSS magnitudes calculated by 4D flow MR imaging may be underestimated compared

Table 3: Relationships with anterior-posterior diameter by the Pearson correlation coefficient (95% confidence intervals)

	Foramen of Magendie	Lower End of Cerebral Aqueduct	Upper End of Cerebral Aqueduct	Midbrain
Dorsal region of the cerebral aqueduct				
OSS amplitude	0.55 (0.36–0.69)	0.47 (0.26–0.63)	0.28 (0.05–0.48)	NS
Maximum OSS	0.53 (0.34–0.68)	0.41 (0.20–0.59)	NS	NS
Minimum OSS	−0.51 (−0.66 to −0.31)	−0.46 (−0.63 to −0.26)	−0.32 (−0.51 to −0.10)	NS
TAWSS	0.56 (0.37–0.70)	0.40 (0.18–0.58)	NS	NS
OSI	NS	NS	NS	NS
Ventral region of the cerebral aqueduct				
OSS amplitude	NS	0.27 (0.04–0.47)	NS	NS
Maximum OSS	NS	0.31 (0.08–0.50)	NS	NS
Minimum OSS	NS	NS	NS	NS
TAWSS	0.26 (0.04–0.47)	0.33 (0.10–0.52)	NS	NS
OSI	NS	NS	NS	NS

Note:—NS indicates not significant ($P \geq .05$) by the Pearson correlation analysis.

Table 4: Relationships with stroke volume by the Pearson correlation coefficient (95% confidence intervals)

	Foramen of Magendie	Lower End of Cerebral Aqueduct	Upper End of Cerebral Aqueduct	Foramina of Monro
Dorsal region of the cerebral aqueduct				
OSS amplitude	0.48 (0.28–0.64)	0.53 (0.34–0.68)	0.63 (0.47–0.76)	NS
Maximum OSS	0.50 (0.31–0.66)	0.56 (0.37–0.70)	0.66 (0.50–0.77)	NS
Minimum OSS	−0.41 (−0.59 to −0.20)	−0.46 (−0.63 to −0.26)	−0.55 (−0.70 to −0.37)	NS
TAWSS	0.43 (0.22–0.60)	0.53 (0.34–0.68)	0.73 (0.60–0.82)	NS
OSI	NS	NS	NS	NS
Ventral region of the cerebral aqueduct				
OSS amplitude	NS	0.30 (0.07–0.50)	0.25 (0.02–0.46)	NS
Maximum OSS	NS	0.32 (0.10–0.52)	0.29 (0.07–0.49)	NS
Minimum OSS	NS	−0.24 (−0.45 to −0.01)	NS	NS
TAWSS	NS	0.37 (0.15–0.55)	0.34 (0.12–0.53)	NS
OSI	NS	NS	NS	NS

Note:—NS indicates not significant ($P \geq .05$) by the Pearson correlation analysis.

with the true values, though their distribution is considered reasonably accurate.[40] Third, the AD comorbidity was not pathologically confirmed through brain biopsy, CSF biomarkers, or amyloid imaging in this study. Finally, we were unable to determine a causal relationship between the dilated cerebral aqueduct and increased OSS amplitude because this study had a cross-sectional design. Therefore, a causal relationship should be investigated in a prospective cohort study or basic research.

CONCLUSIONS

OSS as a novel parameter combining the conventional WSS magnitude with a positive or negative sign indicating the WSS direction can be quantitatively measured at any point on 4D flow MR imaging. Therefore, the OSS amplitude produced by reciprocating bidirectional CSF movements reflects WSS vector changes better than the conventional scalar quantities of the WSS magnitude and OSI. Quantitative OSS measurement may help elucidate the pathophysiologic mechanism of ventricular dilation in iNPH or symptom progression. OSS brings a new perspective to the study of slowly and intricately moving CSF in the complex shapes of the ventricles and the subarachnoid space.

REFERENCES

1. Blitz AM, Shin J, Baledent O, et al. **Does phase-contrast imaging through the cerebral aqueduct predict the outcome of lumbar CSF drainage or shunt surgery in patients with suspected adult hydrocephalus?** *AJNR Am J Neuroradiol* 2018;39:2224–30 CrossRef Medline
2. Bradley WG Jr, Whittemore AR, Kortman KE, et al. **Marked cerebrospinal fluid void: indicator of successful shunt in patients with suspected normal-pressure hydrocephalus.** *Radiology* 1991;178:459–66 CrossRef Medline

3. Bradley WG Jr, Scalzo D, Queralt J, et al. **Normal-pressure hydrocephalus: evaluation with cerebrospinal fluid flow measurements at MR imaging.** *Radiology* 1996;198:523–29 CrossRef Medline

4. Bunck AC, Kroger JR, Juttner A, et al. **Magnetic resonance 4D flow characteristics of cerebrospinal fluid at the craniocervical junction and the cervical spinal canal.** *Eur Radiol* 2011;21:1788–96 CrossRef Medline

5. El Sankari S, Gondry-Jouet C, Fichten A, et al. **Cerebrospinal fluid and blood flow in mild cognitive impairment and Alzheimer's disease: a differential diagnosis from idiopathic normal pressure hydrocephalus.** *Fluids Barriers CNS* 2011;8:12 CrossRef Medline

6. Gupta S, Soellinger M, Grzybowski DM, et al. **Cerebrospinal fluid dynamics in the human cranial subarachnoid space: an overlooked mediator of cerebral disease, I: computational model.** *J R Soc Interface* 2010;7:1195–1204 CrossRef Medline

7. Krauss JK, Regel JP, Vach W, et al. **Flow void of cerebrospinal fluid in idiopathic normal pressure hydrocephalus of the elderly: can it predict outcome after shunting?** *Neurosurgery* 1997;40:67–74 CrossRef Medline

8. Lindstrom EK, Ringstad G, Mardal KA, et al. **Cerebrospinal fluid volumetric net flow rate and direction in idiopathic normal pressure hydrocephalus.** *Neuroimage Clin* 2018;20:731–41 CrossRef Medline

9. Stoquart-ElSankari S, Baledent O, Gondry-Jouet C, et al. **Aging effects on cerebral blood and cerebrospinal fluid flows.** *J Cereb Blood Flow Metab* 2007;27:1563–72 CrossRef Medline

10. Yamada S, Ishikawa M, Ito H, et al. **Cerebrospinal fluid dynamics in idiopathic normal pressure hydrocephalus on four-dimensional flow imaging.** *Eur Radiol* 2020;30:4454–65 CrossRef Medline

11. Caro CG, Fitz-Gerald JM, Schroter RC. **Arterial wall shear and distribution of early atheroma in man.** *Nature* 1969;223:1159–60 CrossRef Medline

12. Dolan JM, Kolega J, Meng H. **High wall shear stress and spatial gradients in vascular pathology: a review.** *Ann Biomed Eng* 2013;41:1411–27 CrossRef Medline

13. Gibbons GH, Dzau VJ. **The emerging concept of vascular remodeling.** *N Engl J Med* 1994;330:1431–38 CrossRef Medline

14. Hahn C, Schwartz MA. **Mechanotransduction in vascular physiology and atherogenesis.** *Nat Rev Mol Cell Biol* 2009;10:53–62 CrossRef Medline

15. Kouzbari K, Hossan MR, Arrizabalaga JH, et al. **Oscillatory shear potentiates latent TGF-beta1 activation more than steady shear as demonstrated by a novel force generator.** *Sci Rep* 2019;9:6065 CrossRef Medline

16. Ku DN, Giddens DP, Zarins CK, et al. **Pulsatile flow and atherosclerosis in the human carotid bifurcation: positive correlation between plaque location and low oscillating shear stress.** *Arteriosclerosis* 1985;5:293–302 CrossRef Medline

17. Malek AM, Alper SL, Izumo S. **Hemodynamic shear stress and its role in atherosclerosis.** *JAMA* 1999;282:2035–42 CrossRef Medline

18. Meng H, Tutino VM, Xiang J, et al. **High WSS or low WSS? Complex interactions of hemodynamics with intracranial aneurysm initiation, growth, and rupture: toward a unifying hypothesis.** *AJNR Am J Neuroradiol* 2014;35:1254–62 CrossRef Medline

19. Tremblay JC, Thom SR, Yang M, et al. **Oscillatory shear stress, flow-mediated dilatation, and circulating microparticles at sea level and high altitude.** *Atherosclerosis* 2017;256:115–22 CrossRef Medline

20. Zarins CK, Zatina MA, Giddens DP, et al. **Shear stress regulation of artery lumen diameter in experimental atherogenesis.** *J Vasc Surg* 1987;5:413–20 CrossRef Medline

21. Hickman TT, Shuman ME, Johnson TA, et al. **Association between shunt-responsive idiopathic normal pressure hydrocephalus and alcohol.** *J Neurosurg* 2017;127:240–48 CrossRef Medline

22. Kageyama H, Miyajima M, Ogino I, et al. **Panventriculomegaly with a wide foramen of Magendie and large cisterna magna.** *J Neurosurg* 2016;124:1858–66 CrossRef Medline

23. Morimoto Y, Yoshida S, Kinoshita A, et al. **Nonsense mutation in CFAP43 causes normal-pressure hydrocephalus with ciliary abnormalities.** *Neurology* 2019;92:e2364–74 CrossRef Medline

24. Mahuzier A, Shihavuddin A, Fournier C, et al. **Ependymal cilia beating induces an actin network to protect centrioles against shear stress.** *Nat Commun* 2018;9:2279 CrossRef Medline

25. Omran AJA, Saternos HC, Althobaiti YS, et al. **Alcohol consumption impairs the ependymal cilia motility in the brain ventricles.** *Sci Rep* 2017;7:13652 CrossRef Medline

26. Shook BA, Lennington JB, Acabchuk RL, et al. **Ventriculomegaly associated with ependymal gliosis and declines in barrier integrity in the aging human and mouse brain.** *Aging Cell* 2014;13:340–50 CrossRef Medline

27. Yamada S, Ishikawa M, Yamamoto K. **Comparison of CSF distribution between idiopathic normal pressure hydrocephalus and Alzheimer disease.** *AJNR Am J Neuroradiol* 2016;37:1249–55 CrossRef Medline

28. Cabral D, Beach TG, Vedders L, et al. **Frequency of Alzheimer's disease pathology at autopsy in patients with clinical normal pressure hydrocephalus.** *Alzheimers Dement* 2011;7:509–13 CrossRef Medline

29. Golomb J, Wisoff J, Miller DC, et al. **Alzheimer's disease comorbidity in normal pressure hydrocephalus: prevalence and shunt response.** *J Neurol Neurosurg Psychiatry* 2000;68:778–81 CrossRef Medline

30. Malm J, Graff-Radford NR, Ishikawa M, et al. **Influence of comorbidities in idiopathic normal pressure hydrocephalus: research and clinical care—a report of the ISHCSF task force on comorbidities in INPH.** *Fluids Barriers CNS* 2013;10:22 CrossRef Medline

31. Silverberg GD, Mayo M, Saul T, et al. **Alzheimer's disease, normal-pressure hydrocephalus, and senescent changes in CSF circulatory physiology: a hypothesis.** *Lancet Neurol* 2003;2:506–11 CrossRef Medline

32. Williams MA, Relkin NR. **Diagnosis and management of idiopathic normal-pressure hydrocephalus.** *Neurol Clin Pract* 2013;3:375–85 CrossRef Medline

33. Jingami N, Uemura K, Asada-Utsugi M, et al. **Two-point dynamic observation of Alzheimer's disease cerebrospinal fluid biomarkers in idiopathic normal pressure hydrocephalus.** *JAD* 2019;72:271–77 CrossRef Medline

34. Miyajima M, Nakajima M, Ogino I, et al. **Soluble amyloid precursor protein alpha in the cerebrospinal fluid as a diagnostic and prognostic biomarker for idiopathic normal pressure hydrocephalus.** *Eur J Neurol* 2013;20:236–42 CrossRef Medline

35. Fultz NE, Bonmassar G, Setsompop K, et al. **Coupled electrophysiological, hemodynamic, and cerebrospinal fluid oscillations in human sleep.** *Science* 2019;366:628–31 CrossRef Medline

36. Diekelmann S, Born J. **The memory function of sleep.** *Nat Rev Neurosci* 2010;11:114–26 CrossRef Medline

37. Holth JK, Fritschi SK, Wang C, et al. **The sleep-wake cycle regulates brain interstitial fluid tau in mice and CSF tau in humans.** *Science* 2019;363:880–84 CrossRef Medline

38. Kang JE, Lim MM, Bateman RJ, et al. **Amyloid-beta dynamics are regulated by orexin and the sleep-wake cycle.** *Science* 2009;326:1005–07 CrossRef Medline

39. Xie L, Kang H, Xu Q, et al. **Sleep drives metabolite clearance from the adult brain.** *Science* 2013;342:373–77 CrossRef Medline

40. Szajer J, Ho-Shon K. **A comparison of 4D flow MRI-derived wall shear stress with computational fluid dynamics methods for intracranial aneurysms and carotid bifurcations: a review.** *Magn Reson Imaging* 2018;48:62–69 CrossRef Medline

Anatomic Snuffbox (Distal Radial Artery) and Radial Artery Access for Treatment of Intracranial Aneurysms with FDA-Approved Flow Diverters

A.L. Kühn, S.R. Satti, T. Eden, K. de Macedo Rodrigues, J. Singh, F. Massari, M.J. Gounis, and A.S Puri

ABSTRACT

BACKGROUND AND PURPOSE: Transradial access for neurointerventional procedures has been proved a safer and more comfortable alternative to femoral artery access. We present our experience with transradial (distal radial/anatomic snuffbox and radial artery) access for treatment of intracranial aneurysms using all 3 FDA-approved flow diverters.

MATERIALS AND METHODS: This was a high-volume, dual-center, retrospective analysis of each institution's data base between June 2018 and June 2020 and a collection of all patients treated with flow diversion via transradial access. Patient demographic information and procedural and radiographic data were obtained.

RESULTS: Seventy-four patients were identified (64 female patients) with a mean age of 57.5 years with a total of 86 aneurysms. Most aneurysms were located in the anterior circulation (93%) and within the intracranial ICA (67.4%). The mean aneurysm size was 5.5 mm. Flow diverters placed included the Pipeline Embolization Device (Flex) (PED, $n = 65$), the Surpass Streamline Flow Diverter ($n = 8$), and the Flow-Redirection Endoluminal Device (FRED, $n = 1$). Transradial access was successful in all cases, but femoral crossover was required in 3 cases (4.1%) due to tortuous anatomy and inadequate support of the catheters in 2 cases and an inability to navigate to the target vessel in a patient with an aberrant right subclavian artery. All 71 other interventions were successfully performed via the transradial approach (95.9%). No access site complications were encountered. Asymptomatic radial artery occlusion was encountered in 1 case (3.7%).

CONCLUSIONS: Flow diverters can be successfully placed via the transradial approach with high technical success, low access site complications, and a low femoral crossover rate.

ABBREVIATIONS: CCA = common carotid artery; dRA = distal radial artery; FD = flow diverter; RA = radial artery; TRA = transradial access

The transradial access (TRA), including distal radial artery (dRA) access in the anatomic snuffbox and radial artery (RA) access at the palmar surface of the wrist, is being increasingly used as primary vascular access for neurointerventional procedures. In prior years, large randomized trials in the field of interventional cardiology and more recent articles in neurointerventional surgery have shown higher patient preference for the TRA, cost reduction, as well as lower morbidity and mortality compared with the traditional transfemoral access (TFA).[1-11]

Reduction in access site complications has been a particular advantage of wrist over femoral access and is an important consideration for vascular access choice in the treatment of intracranial aneurysms using flow diversion. Patients undergoing flow diversion are required to take dual-antiplatelet agents and receive heparin during the procedure, all of which increase the risk of bleeding from the access site.[12] Also, flow diverters (FDs) may require large-bore catheter assemblies for delivery and deployment, which may increase the risk of radial artery occlusion, access site bleeding, or vascular injury.[13,14]

To date, only a limited number of case reports and case series have described the safety and feasibility of TRA for the treatment of intracranial aneurysms using flow diverters.[15-22]

Recently, a large, retrospective multicenter study reported the safety of TRA for flow diversion, showing a lower access site ($P = .039$) and overall complication rate ($P = .035$).[12] This study, however, did not cover catheter systems, patient functional outcome, and aneurysm occlusion. Here, we report our experience with TRA (dRA [anatomic snuffbox] and RA) for the treatment

of intracranial aneurysms using all 3 FDA-approved flow diverters, including technical feasibility, procedural safety, patient outcome, and aneurysm occlusion on follow-up. Additionally, we reviewed the current literature on use of flow diverters via TRA.

MATERIALS AND METHODS
Study Design
Between June 2018 and June 2020, we retrospectively reviewed the data bases from 2 high-volume neurointerventional centers that routinely perform radial access in the United States and collected all patients treated with flow diversion via TRA. Patient demographic information and procedural and radiographic data were also obtained. The institutional review boards at the University of Massachusetts (H00001860_10) and Christiana Health System (CCC number: 34154 and DDD number: 602798) have approved the study.

Procedural Protocol and Technique
All patients received dual-antiplatelet therapy for at least 5 days before the elective procedure. The therapeutic antiplatelet effect was ensured by the VerifyNow P2Y12 assay (Accumetrics) (defined per our practice as showing at least 50% platelet inhibition or a P2Y12 reaction unit of <200 with the platelet aggregation assay) before each procedure. Dual-antiplatelet therapy was continued for a minimum of 6 months, and aspirin will be continued for life.

With the exception of 1 left RA access for treatment of a left vertebral artery dissecting aneurysm, all interventions were performed either via the right dRA in the anatomic snuffbox or right RA at the palmar surface of the wrist. After local subcutaneous anesthesia and vasodilation of the local periarterial tissue using 1 mL of lidocaine and 200–400 μg of nitroglycerine, the dRA or RA was accessed using a micropuncture needle under sonographic guidance. A 6F radial sheath was placed, and a radial cocktail consisting of verapamil, 2.5–5 mg; nitroglycerine, 100–200 μg; and heparin, 5000 IU, was slowly administered intra-arterially. In sheathless access cases, the guide catheter was directly inserted over its dilator. In patients with taut skin, a small incision with a scalpel at the access site was occasionally needed. Another dose of spasmolytic agents was administered through the radial sheath before catheter exchanges to prevent vasospasm. Activated clotting time was measured at baseline and throughout the procedure with activated clotting time goals of 250–300 seconds. Additional IV doses of heparin were administered as needed. A radial artery roadmap was obtained in all cases.

In most cases, the flow diverters were delivered and deployed via a triaxial catheter system. Most Pipeline Embolization Devices (PED; Medtronic) were deployed using a Benchmark guide catheter (Penumbra) or a Phenom Plus intermediate catheter or Phenom 27 microcatheter (Medtronic). The Surpass Streamline Flow Diverter (Stryker) was placed using either an AXS Infinity (Stryker) or Fubuki (Asahi Intecc) guide catheter and a AXS Catalyst 5 intermediate catheter (Stryker) as well as an AXS Offset Delivery Assist catheter (Stryker). The Flow-Redirection Endoluminal Device (FRED; MicroVention) was implanted using a Cerebase DA Guide Sheath (Cerenovus), a Sofia EX Intracranial Support Catheter (MicroVention), and a Headway 27 microcatheter (MicroVention). On completion of the procedure, a radial compression device was used to achieve patent hemostasis at the vascular access site.

RESULTS
Between June 2018 and June 2020, a total of 144 flow-diverter procedures were performed. We identified a total of 74 flow-diverter interventions performed via the anatomic snuffbox or radial artery access (51.4%). Sixty-four patients were women (86.5%). The mean patient age was 57.5 years. Mean distal radial and radial artery diameters were 2.1 and 2.6 mm, respectively.

Transradial access was achieved in all cases with anatomic snuffbox access in 42 cases (56.8%) and radial artery access in 32 cases (43.2%). However, 3 cases (4.1%) required conversion to femoral access due to tortuous anatomy and limited support of the catheters in 2 cases and an inability to navigate the catheters to the target vessel in a patient with an aberrant right subclavian artery. All of the other 71 interventions were successfully performed via a transradial approach. We did not observe any access-related complications, and no patients required a transfusion or vascular surgical repair for an access site injury. Figure 1 shows arches amenable to transradial intervention, and Fig 2 shows arch types that are difficult to navigate via transradial access.

A total of 86 aneurysms were treated, with most aneurysms located within the intracranial ICA (67.4%). One aneurysm was ruptured, and 4 were previously coiled but showed neck residual/recanalization. The mean aneurysm size was 5.5 mm. A summary of patient demographics and aneurysm characteristics is presented in the Table.

A PED was used in 65 cases, a Surpass Streamline Flow Diverter was placed in 8 patients, and 1 FRED was implanted. Additional coiling and placement of a Neuroform EZ stent (Stryker) for proper FD wall apposition were performed in 1 case for treatment of a large, 16-mm ICA aneurysm.

We experienced 3 intraprocedural complications (4.2%). Two patients showed a small amount of SAH on postprocedural head CT (2.8%). One of these patients had mild headache but was neurologically intact. The other patient showed new right-arm weakness on awakening from anesthesia and was brought back to the angiography suite where hyperacute platelet aggregation within the stent was identified and successfully treated with intra-arterial eptifibatide. The patient fully recovered within 6 months with an mRS of 0. In another case, we encountered acute clot formation during placement of the flow diverter, which was immediately treated with intra-arterial eptifibatide.

Of our 71 patients with transradial access, 1 patient died due to an unrelated cause, 3 patients moved out of state, and 1 patient requested follow-up at an outside institution. Ten patients were supposed to have follow-up, but this has been delayed due to institutional restrictions during the coronavirus disease 2019 (COVID-19) pandemic, and 14 patients have not yet reached their follow-up time point. Six patients were lost to follow-up.

Two- to 6-month follow-up angiograms and CTAs were available in 29 and 7 patients, respectively. Twenty-seven of the 29 angiogram follow-ups were performed transradially. Follow-up diagnostic angiograms were performed via a 5F radial sheath.
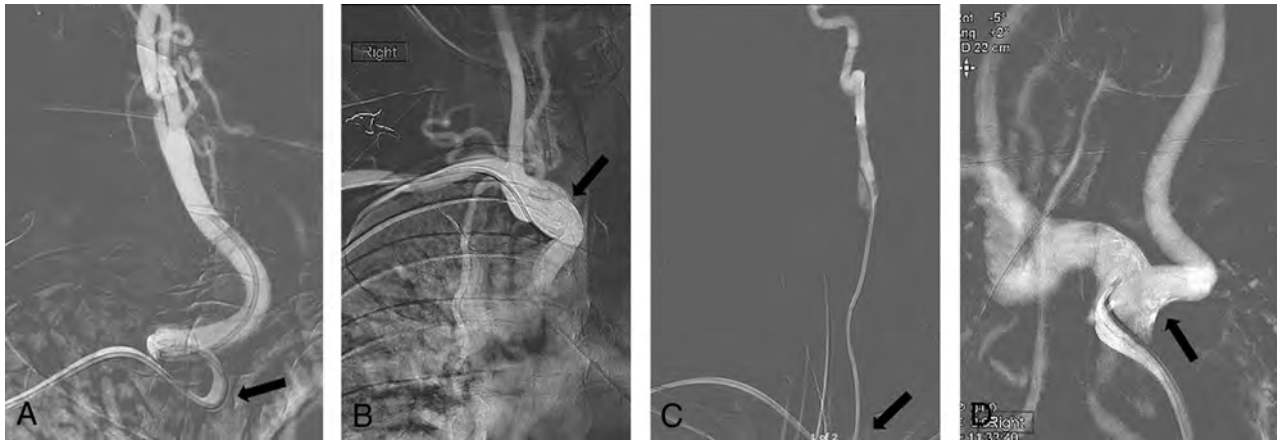
FIG 1. Frontal roadmap images show a curved origin of the right CCA at the junction of the innominate artery and right subclavian artery origin (*arrows*, *A* and *B*). This anatomy offers a "shelf" for right transradial catheters, which provides good stability, even with a tortuous course of the right CCA (*A*). Frontal roadmap image demonstrates a straight origin of the left CCA from the aortic arch (*C, arrow*), which allows good navigation of a right transradial catheter. The transverse portion of the aortic arch may act as a shelf for transradial catheters during intervention, providing good stability for an intervention. Frontal roadmap image shows a bovine-type aortic arch with horizontal origin of the left CCA (*D, arrow*). Access of the left CCA would be easy from a right transradial approach because the catheter can easily move across midline and into the vessel. There would be no risk of catheter herniation.
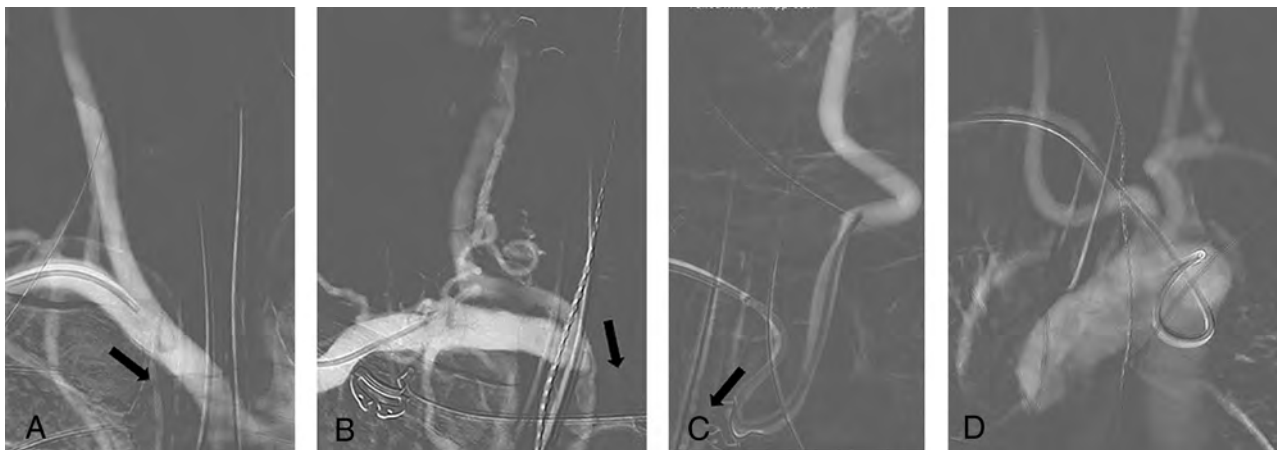
FIG 2. Frontal roadmap image reveals very straight anatomy of the innominate, right subclavian, and common carotid arteries (*A*). Catheter navigation from a right transradial access is not easy, given that the vector force will push the catheter into the right innominate artery (*A, arrow*). Frontal roadmap image shows a fairly horizontal course of the right subclavian artery and a straight continuation of the right innominate artery into the right CCA (*B*). Here, the vector force will push a right transradially navigated catheter into the innominate artery (*B, arrow*), making catheterization of the right intracranial vasculature difficult. Frontal roadmap image demonstrates a medially directed origin of the left CCA from the aortic arch. This makes access from a right radial approach difficult because the catheter will be pushed into the ascending aorta (*C, arrow*). Additional tortuosity along the course of the left CCA increases the difficulty of the approach. Frontal roadmap image shows an aberrant origin of the right subclavian artery (*D*). Navigation of a right transradial catheter is difficult, given that the catheter is directed toward the descending aorta. Larger catheter systems will not have sufficient stability, and catheter herniation into the descending aorta is to be expected.

Spasmolytic cocktails used for transradial access were the same as for the procedure. There were no conversions from initial anatomic snuffbox access to volar radial artery access for follow-up. In 3 cases, radial (volar) access was used for the intervention, but the follow-up angiogram was performed via anatomic snuffbox access. Asymptomatic radial artery occlusion was encountered in 1 case (3.7%). The initial procedure in this patient was performed via the radial artery (volar access) with a spasmolytic cocktail consisting of 2.5 mg of verapamil and nitroglycerin, 100 mcg.

Follow-up angiography in this patient was performed via the ulnar artery. One patient requested femoral access for the follow-up angiography. There was otherwise no contraindication to wrist access in this patient.

Complete and near-complete occlusion was seen in 27 of 43 aneurysms (62.8%). One-year follow-up (*n* = 5) showed progression to complete occlusion in 2 cases. Additional procedural information and follow-up data are summarized in the Online Supplemental Data.

Summary of patient demographics and aneurysm characteristics

Demographics and Characteristics	
No. of patients	$n = 74$
Sex	
Male	10 (13.5%)
Female	64 (86.5%)
Age (mean) (range) (yr)	57.5 (32–80)
No. of aneurysms	$n = 86$
Unruptured	85 (98.8%)
Ruptured	1 (1.2%)
Previous treatment	
None	82 (95.3%)
Coil embolization	4 (4.7%)
Aneurysm location	
Anterior circulation	80 (93%)
ICA	58 (67.4%)
Posterior communicating artery	13 (15.1%)
Anterior choroidal artery	2 (2.3%)
MCA	4 (4.7%)
Anterior cerebral artery	2 (2.3%)
Anterior communicating artery	1 (1.2%)
Posterior circulation	6 (7%)
Vertebral artery	2 (2.3%)
Basilar artery	3 (3.5%)
Posterior cerebral artery	1 (1.2%)
Aneurysm size (mean) (range) (mm)	5.5 (1.2–16)

DISCUSSION

The TRA approach for interventional cardiology procedures has been used since 1989.[23,24] Several large cardiology studies provided strong evidence in favor of wrist over femoral access, including decreased morbidity and mortality, reduced cost, better control of access site hemostasis, reduction in vascular complications, as well as higher patient satisfaction due to less postprocedural discomfort and faster recovery.[6,25-30] In the neurointerventional field, TRA is now beginning to gain popularity, and some reports on the feasibility and safety of this approach for diagnostic angiographies[31-33] and a variety of neurointerventions are available.[10,11,21,34-37] The first case reports on the use of TRA for flow diversion published between 2013 and 2017 were mostly on patients with difficult arch anatomy.[15-17] In 2019, the first case series on treatment of consecutive patients with aneurysms exclusively evaluated the use of the PED via TRA.[18,19,22] With a total of 71 successful interventions, our study is currently the largest series to evaluate TRA for intracranial aneurysm treatment with all FDA-approved flow diverters and also includes information on catheter systems, patient outcome, and aneurysm occlusion. In addition, our access conversion rate of only 4.1% is the lowest reported in the literature of transradial access for flow diversion to date. Previously reported conversion rates ranged between 5.7% and 20.4%.[12,18,19,22]

A stable catheter assembly is crucial to successfully deliver and deploy the flow diverters because their braided configuration and stiffness require a substantial forward-loading force. Lack of catheter support and radial artery vasospasm are the most commonly described reasons for TRA failure. Prior case series primarily reported failed TRA interventions for left-sided interventions,[18,19,22] but we experienced an inability to achieve a stable catheter position during catheterization of the right common carotid artery (CCA) and ICA in a patient with a type III arch. Left-sided interventions are generally regarded as more challenging; however, we believe that with certain anatomic configurations, right-sided interventions may be just as challenging. The course of the right subclavian artery, its angle of origin from the innominate artery, and the angle of origin of the innominate artery itself from the aortic arch are important for catheter navigation and steerability. The more tortuosity and steep angles that are present, the less one-to-one motion and catheter control are experienced.

Aortic arch configuration, great vessel takeoff angles, and proximal CCA tortuosity influence catheter stability. For left-sided interventions, we agree with Waqas et al,[22] who stated that a parallel configuration of the innominate artery and left CCA is challenging. However, we would argue that the distance between the origins of the innominate artery and the left CCA, their relationship to the ascending and descending aorta, the arch configuration, and its capaciousness are also important factors to consider. For right-sided interventions, a steep origin of the innominate artery from the arch, which continues into a straight right CCA, as well as a straight, wide-angle origin of the right subclavian artery represent a challenging anatomic configuration. We are presently still trying to understand what anatomy or combination of anatomic configurations can truly be considered unfavorable and what catheter systems are going to be successful in which kind of situations.

Chen et al[19] reported 2 cases of radial artery vasospasm in their study, which used biaxial, triaxial, and even quadriaxial catheter systems. Biaxial and triaxial systems were used in the studies reported by Sweid et al[18] and Waqas et al,[22] who did not encounter any case of radial artery vasospasm. In our large case series, we also did not encounter any radial artery vasospasm requiring access conversion despite using triaxial systems, even with large-bore catheters. We strongly believe that additional doses of antispasmolytic agents during catheter exchanges are crucial to minimize the occurrence of radial artery vasospasm. We did not observe any access site complications, persistent neurologic deficits, or procedure-related deaths. Two patients developed SAH (2.8%), with one of these patients also experiencing stroke symptoms, which completely resolved within 6 months postprocedure. Waqas et al[22] reported 1 death (3%) in their study. Major ipsilateral stroke or neurologic death was reported in 5.6% of patients undergoing PED deployment via traditional femoral artery access in the Pipeline Embolization Device for Uncoilable or Failed Aneurysms (PUFS) trial.[38] Headache or intracerebral hemorrhage was seen in 4.7% each, and ischemic stroke, in 3.7%.[38]

Routine sonographic follow-up evaluation of the RA was not performed, but there was no symptomatic RA occlusion. On follow-up, 1 of 27 patients was found to have an asymptomatic RA occlusion (3.7%). RA occlusion can be seen in 0.04%–10% of cases after radial access.[13,19,39-46] Most RA occlusions are asymptomatic due to collateral circulation from the ulnar artery. Another very rare complication of TRA is forearm compartment syndrome, which was reported in 1 of 9681 cases in an interventional cardiology study.[45] This complication can be avoided by accessing the radial artery more proximally, not deep to the brachioradialis muscle, or by puncturing the dRA, which lies beyond the forearm compartment.[46]

Limitations of a 6F Benchmark triaxial system include limited ability to obtain angiograms and roadmaps after the

microcatheter is advanced secondary to being able to inject only the intermediate catheter. Using a 5F Sofia 115-cm Intermediate Catheter (MicroVention) allows slightly larger inner diameter and better angiograms than a Phenom Plus. Additionally, jailing and coil-assisted flow-diverting stent placement preclude the use of an intermediate catheter, which can greatly affect column strength during stent delivery.

This study has limitations. Given its dual-center nature, different clinical settings, patient-selection bias, and technical/procedural variations were inevitable. However, patients benefited from TRA for flow diversion despite this heterogeneity. The study is further limited by the retrospective review of each center's prospective data base, and although our sample size is relatively large, more data (specifically long-term follow-up) are needed.

Nevertheless, our experience is promising and shows that TRA is a feasible and safe approach to treat a wide range of intracranial aneurysms with flow diversion. The improved TRA safety profile is undeniable and will benefit a large variety of patients, especially those with a large body habitus, previous iliofemoral artery stent placement or bypass, aortic dissections, heavily calcified pelvic vasculature, and femoral artery occlusions.

CONCLUSIONS

This study demonstrates the feasibility and safety of TRA for flow diversion to treat a broad range of anterior and posterior circulation intracranial aneurysms. Currently available catheters were originally designed for traditional femoral artery access interventions, but dedicated catheter systems for TRA are being developed. Catheters specifically tailored to traditional femoral artery access will facilitate vascular access and permit navigation of standard as well as challenging anatomy. Future technical advances, including dedicated guide catheters and smaller stent delivery systems, will inevitably decrease femoral conversion rates. Future research focusing on favorable and unfavorable anatomy will also be important to further aid in patient selection and decrease the need for access conversion.

REFERENCES

1. Mann JT 3rd, Cubeddu MG, Schneider JE, et al. **Right radial access for PTCA: a prospective study demonstrates reduced complications and hospital charges.** *J Invasive Cardiol* 1996;8(Suppl D): 40D–44D Medline

2. Kiemeneij F, Laarman GJ, Odekerken D, et al. **A randomized comparison of percutaneous transluminal coronary angioplasty by the radial, brachial and femoral approaches: the access study.** *J Am Coll Cardiol* 1997;29:1269–75 CrossRef Medline

3. Agostoni P, Biondi-Zoccai GG, de Benedictis ML, et al. **Radial versus femoral approach for percutaneous coronary diagnostic and interventional procedures; systematic overview and meta-analysis of randomized trials.** *J Am Coll Cardiol* 2004;44:349–56 CrossRef Medline

4. Jolly SS, Amlani S, Hamon M, et al. **Radial versus femoral access for coronary angiography or intervention and the impact on major bleeding and ischemic events: a systematic review and meta-analysis of randomized trials.** *Am Heart J* 2009;157:132–40 CrossRef Medline

5. Sciahbasi A, Pristipino C, Ambrosio G, et al. **Arterial access-site-related outcomes of patients undergoing invasive coronary procedures for acute coronary syndromes (from the ComPaRison of Early Invasive and Conservative Treatment in Patients With Non-ST-ElevatiOn Acute Coronary Syndromes [PRESTO-ACS] Vascular Substudy).** *Am J Cardiol* 2009;103:796–800 CrossRef Medline

6. Valgimigli M, Gagnor A, Calabró P, et al; MATRIX Investigators. **Radial versus femoral access in patients with acute coronary syndromes undergoing invasive management: a randomised multicentre trial.** *Lancet* 2015;385:2465–76 CrossRef Medline

7. Mamas MA, Tosh J, Hulme W, et al. **Health economic analysis of access site practice in England during changes in practice: insights from the British Cardiovascular Interventional Society.** *Circ Cardiovasc Qual Outcomes* 2018;11:e004482 CrossRef Medline

8. Valgimigli M, Frigoli E, Leonardi S, et al; MATRIX Investigators. **Radial versus femoral access and bivalirudin versus unfractionated heparin in invasively managed patients with acute coronary syndrome (MATRIX): final 1-year results of a multicentre, randomised controlled trial.** *Lancet* 2018;392:835–48 CrossRef Medline

9. Kok MM, Weernink MG, von Birgelen C, et al. **Patient preference for radial versus femoral vascular access for elective coronary procedures: the PREVAS study.** *Catheter Cardiovasc Interv* 2018;91:17–24 CrossRefMedline

10. Satti SR, Vance AZ, Golwala SN, et al. **Patient preference for transradial access over transfemoral access for cerebrovascular procedures.** *J Vasc Interv Neurol* 2017;9:1–5 Medline

11. Khanna O, Sweid A, Mouchtouris N, et al. **Radial artery catheterization for neuroendovascular procedures.** *Stroke* 2019;50:2587–90 CrossRef Medline

12. Li Y, Chen SH, Spiotta Am, et al. **Lower complication rates associated with transradial versus transfemoral flow diverting stent placement.** *J Neurointerv Surg* 2020 June 2. [Epub ahead of print] CrossRef Medline

13. Horie K, Tada N, Isawa T, et al. **A randomised comparison of incidence of radial artery occlusion and symptomatic radial artery spasm associated with elective transradial coronary intervention using 6.5 Fr SheathLess Eaucath guiding catheter vs. 6.0 Fr Glidesheath slender.** *Eurointervention* 2018;13:2018–25 CrossRef Medline

14. Starke RM, Snelling B, Al-Mufti F, et al; Society of Neuro-Interventional Surgery. **Transarterial and transvenous access for neurointerventional surgery: report of the SNIS standards and guidelines committee.** *J Neurointerv Surg* 2020;12:733–41 CrossRef Medline

15. Dietrich C, Hauck GH, Valvassori L, et al. **Transradial access or Simmons shaped 8F guide enables delivery of flow diverters in patients with large intracranial aneurysm and type III aortic arch: technical case report.** *Neurosurgery* 2013;73:onsE111–15 CrossRef Medline

16. Daou B, Chalouhi N, Tjoumakaris S, et al. **Alternative access for endovascular treatment of cerebrovascular diseases.** *Clin Neurol Neurosurg* 2016;145:89–95 CrossRef Medline

17. Peitz GW, Kura B, Johnson JN, et al. **Transradial approach for deployment of a flow diverter for an intracranial aneurysm in a patient with a type-3 aortic arch.** *J Vasc Interv Neurol* 2017;9:42–44 Medline

18. Sweid A, Starke RM, Herial N, et al. **Transradial approach for the treatment of brain aneurysms using flow diversion: feasibility, safety, and outcomes.** *J Neurosurg Sci* 2019;63:509–17 CrossRef Medline

19. Chen SH, Snelling BM, Shah SS, et al. **Transradial approach for flow diversion treatment of cerebral aneurysms: a multicenter study.** *J Neurointerv Surg* 2019;11:796–800 CrossRef Medline

20. Raz E, Shapiro M, Buciuc R, et al. **Radial artery access for treatment of posterior circulation aneurysms using the Pipeline embolization device: case series.** *Oper Neurosurg (Hagerstown)* 2019;17:340–47 CrossRef Medline

21. Kühn AL, de Macedo Rodrigues K, Singh J, et al. **Distal radial access in the anatomical snuffbox for neurointerventions: a feasibility, safety, and proof-of-concept study.** *J NeuroInterv Surg* 2020;12:798–801 CrossRef Medline

22. Waqas M, Vakharia K, Dossani RH, et al. **Transradial access for flow diversion of intracranial aneurysms: case series.** *Interv Neuroradiol* 2020 July 5. [Epub ahead of print] CrossRef Medline

23. Campeau L. **Entry sites for coronary angiography and therapeutic interventions: from the proximal to the distal radial artery.** *Can J Cardiol* 2001;17:319–25 Medline

24. Campeau L. **Percutaneous radial artery approach for coronary angiography.** *Cathet Cardiovasc Diagn* 1989;16:3–7 CrossRef Medline

25. Chase AJ, Fretz EB, Warburton WP, et al. **Association of the arterial access site at angioplasty with transfusion and mortality: the M.O.R.T.A.L. study (Mortality benefit Of Reduced Transfusion after percutaneous coronary intervention via the Arm or Leg).** *Heart* 2008;94:1019–25 CrossRef Medline

26. Jolly SS, Yusuf S, Cairns J, et al; RIVAL trial group. **Radial versus femoral access for coronary angiography and intervention in patients with acute coronary syndromes (RIVAL): a randomised, parallel group, multicentre trial.** *Lancet* 2011;377:1409–20 CrossRef Medline

27. Alnasser SM, Bagai A, Jolly SS, et al. **Transradial approach for coronary angiography and intervention in the elderly: a meta-analysis of 777,841 patients.** *Int J Cardiol* 2017;228:45–51 CrossRef Medline

28. Wang YB, Fu XH, Wang XC, et al. **Randomized comparison of radial versus femoral approach for patients with STEMI undergoing early PCI following intravenous thrombolysis.** *J Invasive Cardiol* 2012;24:412–16 Medline

29. Mitchell MD, Hong JA, Lee BY, et al. **Systematic review and cost-benefit analysis of radial artery access for coronary angiography and intervention.** *Circ Cardiovasc Qual Outcomes* 2012;5:454–62 CrossRef Medline

30. Pristipino C, Pelliccia F, Granatelli A, et al. **Comparison of access-related bleeding complications in women versus men undergoing percutaneous coronary catheterization using the radial versus femoral artery.** *Am J Cardiol* 2007;99:1216–21 CrossRef Medline

31. Snelling BM, Sur S, Shah SS, et al. **Transradial cerebral angiography: techniques and outcomes.** *J Neurointerv Surg* 2018;10:874–81 CrossRef Medline

32. Zussman BM, Tonetti DA, Stone J, et al. **A prospective study of the transradial approach for diagnostic cerebral arteriography.** *J Neurointerv Surg* 2019;11:1045–49 CrossRef Medline

33. Patel P, Majmundar N, Bach I, et al. **Distal transradial access in the anatomic snuffbox for diagnostic cerebral angiography.** *AJNR Am J Neuroradiol* 2019;40:1526–28 CrossRef Medline

34. Haussen DC, Nogueira RG, DeSousa KG, et al. **Transradial access in acute ischemic stroke intervention.** *J Neurointerv Surg* 2016;8:247–50 CrossRef Medline

35. Sur S, Snelling B, Khandelwal P, et al. **Transradial approach for mechanical thrombectomy in anterior circulation large-vessel occlusion.** *Neurosurg Focus* 2017;42:E13 CrossRef Medline

36. Snelling BM, Sur S, Shah SS, et al. **Transradial approach for complex anterior and posterior circulation interventions: technical nuances and feasibility of using current devices.** *Oper Neurosurg (Hagerstown)* 2019;17:293–302 CrossRef Medline

37. Almallouhi E, Leary J, Wessell J, et al. **Fast-track incorporation of the transradial approach in endovascular neurointervention.** *J Neurointerv Surg* 2020;12:176–80 CrossRef Medline

38. Becske T, Kallmes DF, Saatci I, et al. **Pipeline for uncoilable or failed aneurysms: results from a multicenter clinical trial.** *Radiology* 2013;267:858–68 CrossRef Medline

39. Stella PR, Kiemeneij F, Laarman GJ, et al. **Incidence and outcome of radial artery occlusion following transradial artery coronary angioplasty.** *Cathet Cardiovasc Diagn* 1997;40:156–58 CrossRef Medline

40. Nagai S, Abe S, Sato T, et al. **Ultrasonic assessment of vascular complications in coronary angiography and angioplasty after transradial approach.** *Am J Cardiol* 1999;83:180–86 CrossRef Medline

41. Dahm JB, Vogelgesang D, Hummel A, et al. **A randomized trial of 5 vs. 6 French transradial percutaneous coronary interventions.** *Catheter Cardiovasc Interv* 2002;57:172–6 CrossRef Medline

42. Takeshita S, Asano H, Hata T, et al; NAUSICA Trial Investigators. **Comparison of frequency of radial artery occlusion after 4Fr versus 6Fr transradial coronary intervention (from the Novel Angioplasty USing Coronary Accessor Trial).** *Am J Cardiol* 2014;113:1986–89 CrossRef Medline

43. Rashid M, Kwok CS, Pancholy S, et al. **Radial artery occlusion after transradial interventions: a systematic review and meta-analysis.** *J Am Heart Assoc* 2016;5:e002686 CrossRef Medline

44. Sinha SK, Jha MJ, Mishra V, et al. **Radial artery occlusion: incidence, predictors and long-term outcome after transradial catheterization—clinico-Doppler ultrasound-based study (RAIL-TRAC study.** *Acta Cardiol* 2017;72:318–27 CrossRef Medline

45. Cauley R, Wu WW, Doval A, et al. **Identifying complications and optimizing consultations following transradial arterial access for cardiac procedures.** *Ann Vasc Surg* 2019;56:87–96 CrossRef Medline

46. Brunet MC, Chen SH, Peterson EC. **Transradial access for neurointerventions: management of access challenges and complications.** *J Neurointerv Surg* 2020;12:82–86 CrossRef Medline

Is Transradial Access a Replacement Technique for Transfemoral Access in Neurointervention?

Transradial access for neurointervention has experienced an explosion in interest over the past few years because of patient preferences, extrapolated cardiology data, and early studies supporting its use in the neurointerventional setting. As with any innovation, although there may be advantages, in the enthusiasm to include more tools in the armamentarium, the utility of the "tried and true" should not be forgotten.

As a backdrop, transradial access is newer than transfemoral, but it is not novel. The first cases on transradial intracranial neurointervention were published in 2003 and 2004,[1,2] including aneurysm treatments in both anterior and posterior circulations, as well as spinal and dural fistula embolizations. This was preceded by a number of case series between 2000 and 2003,[2-5] which, together, demonstrated the use of transradial cerebral angiography since 1997 with an aggregated patient cohort in the hundreds. Techniques described then were similar to those used today, and the same difficulties were identified, including radial spasm, proximal vascular tortuosity[3] and stenoses,[4] limitations related to aortic arch branch morphology with resultant instability,[5] some branches are clearly easier to access via one route,[1] and learning curves.[4] So, what has changed?

In the article published in this issue of the *AJNR*, we glean factors that may have pushed us toward this different technique. First, neurointerventions themselves are becoming more commonplace. This encourages attention to all aspects of neurointervention, including vascular access. Second, procedures requiring stronger antithrombotic regimens are increasingly performed, of which one is flow diversion. Hemorrhagic complications are known to be more common with transfemoral access, and this advantage of transradial access can be directly translated from the cardiology literature.

However, it is important to note in this study's recruitment period that only 51% (74/144) of cases were performed transradially. The reasons are not clearly stated, but one can imagine such variability may be because of a different pace of individual operators at the study centers adopting the transradial approach, or alternatively, case selection. Unless we know the rationale for the breakdown of transradial versus transfemoral access, the transradial complication and access conversion rates noted cannot be applied for a blanket "radial-first" strategy; these may only apply to the "radial appears preferable in this patient" strategy.

The influence of patient selection on complication rates may be more widespread in our literature. In the largest study comparing transradial versus transfemoral flow diversion to date, comprising 2285 patients, cases were drawn from preradial (2010–2015) and postradial (2016–2019) eras. Regarding the postradial era, the authors note ". . . access approach was determined by the attending neurointerventionalist . . . based on operator expertise and patient-specific considerations."[6] Comparing 2151 transfemoral versus 134 transradial interventions recruited between 2010 and 2019 necessitates inclusion of cases (performed transfemorally) that would have been more optimally performed transradially. Against not having options other than transfemoral access, subsequent selection of suitable patients for transradial access should render better outcomes in both groups because these cases would have been more appropriate for transradial access in the first place. The relatively low numbers of transradial access cases (versus transfemoral) also suggest that patients were very highly selected for suitability.

Li et al's[6] argument against this is the lack of change in the transfemoral overall complication rates between their preradial (2010–2015) and postradial (2016–2019) eras, but this raises a bigger question: Why were transfemoral complication rates not falling, especially when predominantly 1 device (99.2%) was used, experience was growing, and presumably in the postradial era, cases less suitable for transfemoral access were being taken away for a transradial approach? Were cases with more challenging intracranial anatomy being attempted predominantly transfemorally? Unfortunately, the provided demographics pertaining to aneurysm location do not provide adequate information.

There are too many potential biases here to make a definite answer possible, and perhaps the only way to comprehensively prove this would be to randomize. This may prove that radial access is truly preferable, at least in most nonselected cases, for the average operator. Alternatively, it may be useful to retrospectively analyze aortic arch and branch characteristics in a semi-quantitative fashion between the 2 access techniques. Until then,

utter adherence to always attempting a radial-first strategy may, similar to only performing transfemoral access, render overall higher complication and access conversion rates. The difficulty here is we do not know how much more exactly, but an earlier study by Chen et al[7] suggests it may be as high as 20.4%.

As an analogy, there would presumably be little argument that transfemorally accessing a bovine left carotid using a Simmons catheter renders a somewhat higher difficulty and risk than using a right transradial approach (or transfemorally accessing a left carotid in a young, nonbovine patient). How much more is the question, and it may be that in the hands of an experienced operator, the difference in risk is negligible. It is thus fair to say that as individual experience with transradial approach increases, anatomic access-related risk may decrease, making the hemorrhagic risks of transfemoral access more prominent in the risk–benefit calculation. But this equipoise calculation may remain very individual.

Thus, the emphasis here is on the value of individualization, and the authors have commendably added to the important conversation regarding what constitutes favorable anatomy for transradial access. Previous papers have identified factors that favor radial access, such as anticoagulation, obesity, femoral artery atheroma, type 3 and bovine arch,[8] and narrow-angle[7] or parallel morphology of the brachiocephalic and left common carotid artery,[9] perhaps especially if they angulate toward the ascending or the descending aorta. However, the current article usefully takes these further, including specifics of aortic branch anatomy, with imaging. Such factors play into the safety of transradial versus transfemoral access, and these cannot be translated from the cardiology literature, as the arch, and obviously the carotid and vertebral arteries, are not accessed in the same fashion in coronary intervention compared with neurointervention.

It is also important to note that the current generation of guide catheters used in transradial neurointervention was not designed for this usage. Although they have performed well, it is conceivable that complication rates and specific difficulties experienced with the current generation of devices may not be applicable in the future. There needs to be ongoing review of the balance of safety between transradial and transfemoral intervention, especially as experience in transradial intervention and the scope of its utilization grows.

Lastly, although the need for flow diverter deployment systems to use larger bore guide catheters and larger loading forces was raised as a reason for making specific comparison between transradial and transfemoral access, 6F systems can perhaps be considered the standard in many centers for a multitude of more complex neurointerventional operations, such as stent-assisted coil embolization and endosaccular flow disruption. In tortuous vascular systems, a transradial approach for these cases would raise similar concerns. It is perhaps the aggregate stiffness and bulk of the device systems delivered, after arch anatomy and appropriateness of catheter systems, that poses the next most important factor to suitability. One such procedure is transradial

carotid stent placement. Although sometimes older systems have been repurposed satisfactorily for use in some cases (eg, Preformed Simmons Envoy XB catheters, Codman Neuro), it may be in this literature that we will glean the newest information regarding the actual, coal face applicability of improvements in catheter technology.

Perhaps the advent of mainstream transradial neurointervention can be thought of not as the succession of transfemoral access but as the opening of a door to more options resulting in better care of the patient, similar to the advent of flow diversion itself. There will always be practitioners who will prefer flow diverter techniques because of training or practice patterns. Transradial access is similar, and it is likely that transradial access will play a growing role in neurointervention. However, it is important that continued practice and training of future neurointerventionists maintain the ability for practitioners to use multiple alternatives so that patients who are at increased risk of transfemoral complications can be offered "radial first," and those with unfavorable arch profiles can be offered "femoral first"—that is, a patient-tailored strategy.

REFERENCES

1. Nohara AM, Kallmes DF. **Transradial cerebral angiography: technique and outcomes.** *AJNR Am J Neuroradiol* 2003;24:1247–50 Medline

2. Schönholz C, Nanda A, Rodríguez J, et al. **Transradial approach to coil embolization of an intracranial aneurysm.** *J Endovasc Ther* 2004;11:411–13 CrossRef Medline

3. Matsumoto Y, Hokama M, Nagashima H, et al. **Transradial approach for selective cerebral angiography: technical note.** *Neurol Res* 2000;22:605–08 CrossRef Medline

4. Matsumoto Y, Hongo K, Toriyama T, et al. **Transradial approach for diagnostic selective cerebral angiography: results of a consecutive series of 166 cases.** *AJNR Am J Neuroradiol* 2001;22:704–08 Medline

5. Levy EI, Boulos AS, Fessler RD, et al. **Transradial cerebral angiography: an alternative route.** *Neurosurgery* 2002;51:335–42 CrossRef Medline

6. Li Y, Chen SH, Spiotta AM, et al. **Lower complication rates associated with transradial versus transfemoral flow diverting stent placement.** *J Neurointervent Surg* 2020 Jun 2. [Epub ahead of print] CrossRef Medline

7. Chen SH, Snelling BM, Shah SS, et al. **Transradial approach for flow diversion treatment of cerebral aneurysms: a multicenter study.** *J Neurointervent Surg* 2019;11:796–800 CrossRef Medline

8. Snelling BM, Sur S, Shah SS, et al. **Transradial cerebral angiography: techniques and outcomes.** *J NeuroIntervent Surg* 2018;10:874–81 CrossRef Medline

9. Waqas M, Vakharia K, Dossani RH, et al. **Transradial access for flow diversion of intracranial aneurysms: case series.** *Interv Neuroradiol* 2020 Jul 5. [Epub ahead of print] CrossRef Medline

ⓘ A.H. Chiu
Neurological Intervention & Imaging Service of Western Australia, Sir Charles Gairdner, Royal Perth and Fiona Stanley Hospitals, WA Health; Internal Medicine, University of Western Australia; and UWA Centre for Medical Research, University of Western Australia, Perth, Australia

CTA-Based Patient-Tailored Femoral or Radial Frontline Access Reduces the Rate of Catheterization Failure in Chronic Subdural Hematoma Embolization

E. Shotar, G. Pouliquen, K. Premat, A. Pouvelle, S. Mouyal, L. Meyblum, S. Lenck, V. Degos, S. Abi Jaoude, N. Sourour, B. Mathon, and F. Clarençon

ABSTRACT

BACKGROUND AND PURPOSE: Chronic subdural hematoma embolization, an apparently simple procedure, can prove to be challenging because of the advanced age of the target population. The aim of this study was to compare 2 arterial-access strategies, femoral versus patient-tailored CTA-based frontline access selection, in chronic subdural hematoma embolization procedures.

MATERIALS AND METHODS: This was a monocentric retrospective study. From the March 15, 2018, to the February 14, 2019 (period 1), frontline femoral access was used. Between February 15, 2019, and March 30, 2020 (period 2), the choice of the frontline access, femoral or radial, was based on the CTA recommended as part of the preoperative work-up during both above-mentioned periods. The primary end point was the rate of catheterization failure. The secondary end points were the rate of access site conversion and fluoroscopy duration.

RESULTS: During the study period, 124 patients (with 143 chronic subdural hematomas) underwent an embolization procedure (mean age, 74 [SD, 13] years). Forty-eight chronic subdural hematomas (43 patients) were included during period 1 and were compared with 95 chronic subdural hematomas (81 patients) during period 2. During the first period, 5/48 (10%) chronic subdural hematoma embolizations were aborted due to failed catheterization, significantly more than during period 2 (1/95, 1%; $P = .009$). The rates of femoral-to-radial ($P = .55$) and total conversion ($P = .86$) did not differ between the 2 periods. No significant difference was found regarding the duration of fluoroscopy ($P = .62$).

CONCLUSIONS: A CTA-based patient-tailored choice of frontline arterial access reduces the rate of catheterization failure in chronic subdural hematoma embolization procedures.

ABBREVIATIONS: CSDH = chronic subdural hematoma; MMA = middle meningeal artery

The annual incidence of chronic subdural hematomas (CSDHs), 14 to 20 per 100,000 individuals, means that the condition is one of the most frequently managed by neurosurgery departments.[1,2] CSDHs are thought to be sentinel health events, akin to hip fractures, with important reduction in life expectancy for patients compared with age-matched controls.[3] The condition is, moreover, associated with far-from-negligible rates of morbidity and mortality, around 11% and 4%, respectively.[4]

Standard management of symptomatic CSDHs includes surgical evacuation, mostly through twist drill or burr-hole craniostomy with closed-system drainage.[4-6] Recently, middle meningeal artery (MMA) embolization has emerged as a possible treatment of CSDHs.[7,8] The procedure is simple in appearance but can prove to be challenging in a subset of patients because of tortuous vasculature. Indeed, CSDH is mostly a disease of the elderly with two-thirds of cases accounted for in patients older than 65 years of age.[1] In the elderly, several factors, including peripheral vascular disease and vascular anatomy, can complicate or even preclude cervical vessel navigation by a traditional transfemoral approach.[9,10]

The transradial approach has recently emerged as an alternative to transfemoral access in interventional neuroradiology, with the stated aim of reducing access-related complications and patient discomfort.[11] It has also been envisioned that radial access may facilitate anterior circulation navigation in some patients.[10,11] The aim of this study was to compare 2 arterial-

access strategies, frontline femoral versus patient-tailored frontline access selection (femoral or radial), based on a preoperative CTA, in CSDH embolization procedures.

MATERIALS AND METHODS

Study Design

This was a monocentric retrospective study performed in a tertiary care and teaching hospital. Starting from March 15, 2018, CSDH has been proposed as a treatment of CSDH, initially as an adjunct to surgery and more recently as a possible sole treatment in a minority of patients. The most common indication for CSDH embolization at our institution is a CSDH recurrence or a CSDH with an independent recurrence risk factor, including antiplatelet therapy, anticoagulation therapy, hepatopathy, or alcohol abuse, for instance.[12] Eligible patients were excluded if they refused the embolization procedure or were denied embolization by the attending physician because they presented in a moribund state, had a contraindication to the embolization procedure like severe renal dysfunction, or had a life expectancy of <6 months. A pre-embolization aortic arch and supra-aortic trunk CTA was recommended to rule out anatomic contraindications. The choice of the MMA embolization technique was left to the discretion of the attending interventional neuroradiologist.

From March 15, 2018, to February 14, 2019 (period 1), a femoral access was systematically used as a frontline strategy for CSDH embolization, in line with wider institutional habits. On the basis of this initial experience, from February 15, 2019, to March 30, 2020 (period 2), the choice of the arterial frontline access, femoral or radial, was patient-tailored and based on the available CTA. The choice of frontline access was left to the discretion of the attending interventional neuroradiologist. Radial frontline access was, nevertheless, strongly recommended for right carotid catheterization in case of a type III aortic arch with proximal common carotid artery tortuosity and for left carotid navigation in case of a bovine arch configuration.[10,11] For radial access (up to 6F sheaths), micropuncture under sonographic guidance was preferred, without prior testing of collateral circulation. Intra-arterial injection of verapamil (3 mg) through the sheath was performed. Given the context of intracranial hemorrhage, radial access in this specific setting was usually performed without anticoagulation. Postprocedure, patent hemostasis for 2 hours was recommended. No left radial or distal radial access was used in this series.

Demographic and clinical data were retrieved by retrospective review of patient medical records. Imaging data were analyzed on the local PACS.

End Points

The primary end point was the rate of catheterization failure leading to procedure abortion. The secondary end points were rate of access site conversion and fluoroscopy duration. Because some procedures were performed in a biplane angiosuite while others were performed in a monoplane angiosuite, only the fluoroscopy duration of the anterior-posterior plane was considered for biplane procedures.
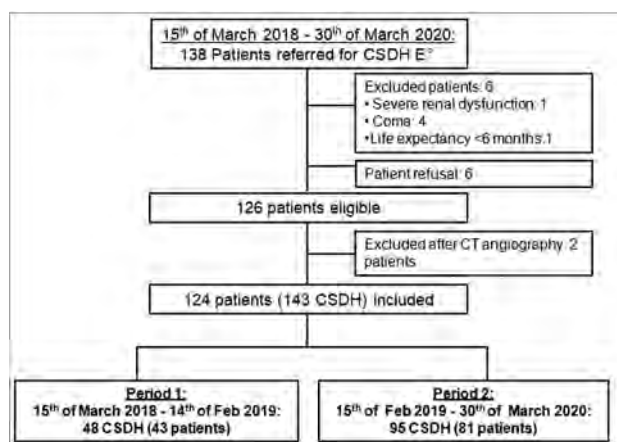
FIG 1. Flow chart. E° indicates embolization.

Statistical Analysis

Data are expressed as a percentage for binary variables and as mean [SD] for continuous variables. Probability values are provided uncorrected. Probability values < .05 were considered significant. A χ^2 test was used to compare frequencies, and comparison of means was performed using a Student t test. Statistical analyses were performed using MedCalc, Version 19.2 (MedCalc Software).

Ethical Statement

The institutional review board approved this study (Comité d'Ethique pour la Recherche en Imagerie Médicale CRM-2003–063) and the need for signed patient consent was waived.

Data-Sharing Statement

Raw data are available on reasonable request from the corresponding author.

RESULTS

Population Characteristics

One hundred thirty-eight patients were referred for MMA embolization during the study period (Fig 1). Six patients were deemed unfit to undergo embolization, and another 6 patients refused to undergo the procedure. Two patients were excluded on the basis of the result of the CTA because of extensive supra-aortic trunk atheroma precluding safe endovascular navigation. A total of 124 patients underwent embolization procedures of 143 target MMAs (105 unilateral and 19 bilateral CSDHs). The mean age of the study population was 74 [SD, 13] years, and most of the patients (94; 76%) were men. There was no difference in terms of demographics, clinical and radiologic presentation of the CSDHs, management strategy, and choice of anesthesia technique between patients managed during periods 1 and 2 (Table 1).

Embolization Procedures

During period 1, all 48 CSDH embolizations were performed via a frontline femoral access. In 1 instance (2%), a femoral-to-radial conversion was deemed necessary during the procedure (Fig 2, illustrative example C). During period 2, a frontline femoral access was chosen for 57/95 (60%) CSDH embolizations. Of these, a femoral-to-radial conversion was deemed necessary during the

Table 1: Patient characteristics[a]

	Total Study Population (143 CSDH; 124 Patients)	Period 1: Frontline Femoral Access (48 CSDH; 43 Patients)	Period 2: Patient-Tailored Arterial Access (95 CSDH; 81 Patients)	P Value
Demographics (patients)				
Mean age (yr)	74 [SD, 13]	73 [SD, 15]	75 [SD, 12]	.32
Male sex	94 (76)	34 (79)	60 (74)	.54
Anticoagulant medication	39 (31)	13 (30)	26 (32)	.83
Antiplatelet medication	55 (44)	18 (42)	37 (46)	.69
Coagulopathy	4 (3)	3 (7)	1 (1)	.09
Alcohol abuse	18 (15)	6 (14)	12 (15)	.9
Past CSDH recurrence	25 (20)	11 (26)	14 (17)	.28
Clinical presentation (patients)				
GCS score, <15	42 (34)	15 (35)	27 (33)	.86
Neurologic deficit	86 (69)	29 (67)	57(70)	.88
Cephalalgia	50 (40)	15 (35)	35 (43)	.42
Radiologic presentation (CSDHs)				
Maximal thickness (mean) (mm)	22 [SD, 7]	21 [SD, 8]	22 [SD, 7]	.65
CSDH management (CSDH)				
Unoperated CSDH	5 (3)	2 (4)	3 (3)	.76
Combined management (operation and embolization within 7 days)	132 (92)	42 (88)	90 (95)	.13
Delayed CSDH embolization (>7 days following the operation)	6 (4)	4 (8)	2 (2)	.08
Embolization procedures (patients)				
Local anesthesia	116 (94)	41 (95)	75 (93)	.55
Conscious sedation or general anesthesia	8 (6)	2 (5)	6 (7)	.55

Note:—GCS indicates Glasgow Coma Scale.
[a] Values are mean [SD] for quantitative variables or numbers and percentages for qualitative variables.

procedure in 1/57 (2%) instances (Fig 2, illustrative example D). Conversely, a frontline radial access was chosen for 38/95 (40%) cases with 3/38 (8%) radial-to-femoral per-procedure conversions. Figure 2 shows a series of anatomic configurations having led to difficult endovascular navigation or catheterization failure.

The CSDH embolization procedure was aborted in 15/143 (10%) cases, in 6 instances because of agitation, in 6 cases because of failed catheterization, and in 3 cases because of a so-called "dangerous anastomosis," including 2 cases in which the MMA originated from the ophthalmic artery. Notably, once the guiding catheter was successfully placed, microcatheter navigation in the external carotid artery and MMA was always achieved. A total of 128/143 (90%) MMAs were embolized. Embolization was performed with calibrated tris-acryl microspheres (300–500 μm in diameter) in 111/128 (87%) instances, with associated proximal MMA coiling in 33/111 (30%) cases; using an *n*-BCA liquid embolic agent in 6/128 (5%) cases; by proximal MMA coiling alone in 10/128 (8%) cases; and by a gelatin-based embolic agent in the remaining patient (1%). We registered 7 minor complications in 124 patients (6%): 1 partial seizure during the procedure, 1 reversible headache, 2 transient diplopias, 2 asymptomatic iatrogenic meningomeningeal fistulas treated by MMA coiling during the procedure, and 1 asymptomatic external carotid artery occlusion. The only major complication (1%) was a femoral artery occlusion at the access site, treated surgically. The patient died 6 weeks after the CSDH embolization procedure.

Outcome
During period one, 5/48 (10%) CSDH embolization procedures were aborted due to failed catheterization. In all cases of failed catheterization, only a femoral access was attempted (Fig 2,

illustrative cases A and B). In comparison, during period 2, only 1/95 (1%) procedures was interrupted after a failed attempt to catheterize a left carotid artery by a femoral access (Fig 2, illustrative case F), significantly less than during period 1 (P = .009). During periods 1 and 2, all 5 femoral-to-radial and radial-to-femoral conversions led to successful CSDH embolizations (Fig 2, illustrative cases C, D, and E). In none of the 6 failed catheterizations was an access site conversion attempted. The mean age of patients with failed catheterization was 81 [SD, 9] years and tended to be higher than that in the general study population, but the difference did not reach statistical significance (P = .21).

The rates of femoral-to-radial (P = .55) and total conversion (P = .86) did not differ significantly between the 2 periods. No significant difference was found regarding the duration of fluoroscopy between the 2 periods (P = .62) (Table 2).

DISCUSSION
Main Results
This nonrandomized study shows that a CTA-based patient-tailored choice of frontline arterial femoral or radial access reduces the rate of catheterization failure in CSDH embolization procedures. Moreover, femoral-to-radial and radial-to-femoral per-procedure conversion should be considered when faced with challenging endovascular navigation because versatility appears to improve procedure outcomes.

MMA Embolization in the Treatment of CSDH
MMA embolization has been proposed as a potential treatment for CSDH.[7,8] Enhanced understanding of CSDH physiopathology underlies the rationale for CSDH embolization.[13]
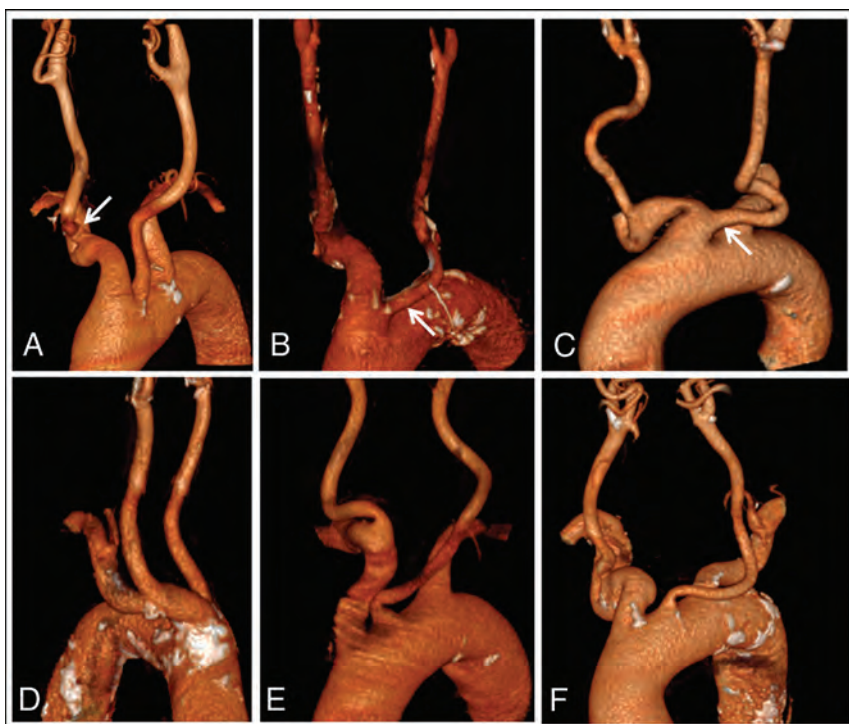
FIG 2. Illustrative examples of challenging and failed catheterization cases. Manually-segmented surface-rendering 3D reconstructions of CTAs of aortic arches of patients included during periods 1 (*A–C*) and 2 (*D–F*). *A*, Anterior view of a case of failed right carotid catheterization by femoral access due to a proximal kinking of the right common carotid artery (*right arrow*) in a type III aortic arch. *B*, Anterior view in a case of failed left carotid catheterization by femoral access due to a bovine arch configuration (*right arrow*), which, in retrospect, would have been an ideal candidate for radial access. *C*, Anterior view in a case of failed left carotid catheterization by femoral access converted secondarily to transradial catheterization in relation to a bovine arch (*right arrow*). *D*, Posterior view of a case of failed right carotid catheterization by a frontline femoral access most probably due to the angulation between the brachiocephalic trunk and the aortic arch, with subsequent successful radial access conversion. *E*, Anterior view of a bilateral CSDH in which a frontline radial access was chosen. Following right CSDH embolization by the transradial approach, failure to navigate the left carotid artery led to radial-to-femoral access conversion and left-sided successful embolization. *F*, Anterior view in a case of failed catheterization of the left carotid artery from a frontline femoral access after which the procedure was aborted.

significantly reduced (1%) compared with historical controls (27.5%).

Challenging Catheterization and Radial Access

As stated above, CSDH is mostly a disease of the elderly.[1] Indeed, the mean age of the study population described herein is >5 years higher than in patients included in real-life mechanical thrombectomy registries.[24,25] Advanced age is associated with peripheral vascular disease, aortic arch elongation, and increased carotid artery tortuosity, all of which can increase technical difficulty or even preclude endovascular navigation by femoral access.[9,10,26,27] The 2 largest CSDH embolization series to date have reported populations with an average age younger than 70 years,[7,8] closer to the ages of patients undergoing mechanical thrombectomy than those reported herein. This may explain why technical difficulties related to CSDH embolization have not been highlighted before.

Radial access was described >3 decades ago.[28] It has since become the access route of choice in percutaneous cardiac interventions, mainly due to demonstrated superiority in terms of patient satisfaction, cost effectiveness, and, more important, reduced local complication rates and even cardiac mortality.[29,30] Transfemoral access exposes patients to a risk of retroperitoneal hematoma with potentially catastrophic consequences, especially in the setting of antiplatelet or anticoagulant medication. Alternatively, hand ischemia is a potentially devastating complication of radial access, but in practice, radial artery occlusion remains essentially clinically silent.[31] In the Minimizing Adverse Haemorrhagic Events by Transradial Access Site and Systemic Implementation of AngioX (MATRIX) trial, >4000 patients were randomized to transradial access and none presented with symptomatic hand ischemia.[31,32]

Interventional neuroradiology has lagged behind in adopting radial access, and several factors have been proposed to explain this hesitancy: Interventional neuroradiology training is dominated by femoral access, and there is a perceived difficulty in navigating the cerebrovasculature from the radial artery.[11] Despite these potential impediments, several centers have successfully implemented radial-access strategies for diagnostic cerebral angiographies and neurointerventional therapeutic procedures.[11,33–35] Although definite evidence of the potential benefit of radial access in neurointerventional procedures is still lacking, several studies have pointed out reduced patient

Morphologically, microvasculature alterations of the outer membrane of the CSDH include increased vessel density, capillary diameter, and the occurrence of large intercellular gaps between the endothelial cells.[14,15] MMA embolization aims to occlude the so-called sinusoid neovessels of the CSDH outer membrane and subsequently reduce repeated microhemorrhage. Both curative embolization as a sole treatment[7,16-18] or combined management with embolization as an adjunct to surgical treatment have been proposed.[7,19,20] A variety of embolic agents have been described in this context, mostly calibrated particles but also coils, *n*-BCA, or ethylene-vinyl alcohol copolymer liquid embolic agents.[7,17,21-23] Ban et al,[7] in a relatively large study, compared 72 consecutive patients treated by CSDH embolization, either curative (27 patients) or as an adjunct to surgery (45 patients), with a historical control group of 469 patients managed conventionally either by an operation alone or conservatively. The treatment failure rate in the embolization group was found to be

Table 2: Comparison of outcomes[a]

	Period 1: Frontline Femoral Access (48 CSDH; 43 Patients)	Period 2: Patient-Tailored Arterial Access (95 CSDH; 81 Patients)	P Value
Embolization procedure (CSDHs)			
Middle meningeal artery occlusion	40 (83)	88 (93)	.09
Anatomic finding prohibiting embolization	2 (4)	1 (1)	.22
Procedural abortion related to patient agitation	1 (2)	5 (5)	.37
Primary outcome (CSDHs)			
Failed catheterization	5 (10)	1 (1)	.009
Secondary outcomes			
Femoral-to-radial access conversion	1 (2)	1/57 (2)	.55
Total rate of access conversion	1 (2)	4/95 (4)	.86
Mean fluoroscopy duration (patients) (min)	22 [SD, 16]	21 [SD, 10]	.62

[a] Values are mean [SD] for quantitative variables, or numbers and percentage for qualitative variables.

discomfort, reduced complication rates, and even enhanced technical feasibility in a subset of patients.[10,11,33,34] The critical importance of both safety and technical feasibility in the specific context of CSDH embolization is underlined by the results of this study.

Both radial and femoral access strategies have specific complications and drawbacks, further highlighting the potential benefit of a tailored-access strategy. For instance, considering alternative access sites to transfemoral access has been recommended in patients with known prior surgery, stent placement, or occlusion of the femoral or iliac arteries or descending aorta.[31] Alternatively, tortuosity and acute angulation of the left common carotid artery and internal carotid artery have been associated with radial approach failure.[36]

Study Limitations

The retrospective, monocentric, and nonrandomized design of this study are all potential sources of bias. In particular, it cannot be excluded that later-stage reduced rates of failure to catheterize are related to more aggressive endovascular navigation. Indeed, CSDH embolization is an emerging procedure for which the perceived utility may have increased across time during the study, therefore reducing the acceptability of procedural failure. However, the stability of fluoroscopy durations between the study periods contradicts this notion. Fluoroscopy duration as an outcome is, in itself, also subject to bias given that it does not distinguish the duration of endovascular navigation as opposed to embolization time. Also, criteria leading to the choice of a frontline radial or femoral access were largely based on operator preferences and eluded this study. Moreover, it could be that increased recourse to the radial route in itself, rather than the patient-tailored strategy of frontline access, reduced catheterization failure. Indeed, an increased choice of radial access as a frontline option and the propensity to switch from femoral to radial access in case of challenging anatomies may be thought of as mutually reinforcing. As stated earlier, in none of the 6 failed catheterizations was an access site conversion attempted, stressing the fact that improved catheterization rates may be a marker of increased versatility. This may be especially true in the general context of the modification of access strategies in interventional neuroradiology underway.

Also, the learning curve effect cannot be excluded to explain reduced later-stage catheterization failure. Experience gained during period 1 could have led to better operator performance during period 2. This is unlikely, however, for femoral access, given that challenging anatomies have become common with the advent of mechanical thrombectomy, and catheterization failure is now exceptional in this context, albeit with dedicated catheters with enhanced navigability. Also, given the potentially debilitating consequences of stroke, physicians may be less reluctant to perform more aggressive endovascular maneuvers to reach the target vessel in this setting. Finally, as illustrated in this study population, agitation is also a frequent cause of procedural abortion with the patient under local anesthesia or even conscious sedation. General anesthesia should be considered in a subset of patients to increase procedural success rates.

CONCLUSIONS

A CTA-based patient-tailored choice of frontline arterial access reduces the rate of catheterization failure in CSDH embolization procedures.

REFERENCES

1. Kudo H, Kuwamura K, Izawa I, et al. **Chronic subdural hematoma in elderly people: present status on Awaji Island and epidemiological prospect.** *Neurol Med Chir (Tokyo)* 1992;32:207–09 CrossRef Medline
2. Iorio-Morin C, Touchette C, Lévesque M, et al. **Chronic subdural hematoma: toward a new management paradigm for an increasingly complex population.** *J Neurotrauma* 2018;35:1882–85 CrossRef Medline
3. Dumont TM, Rughani AI, Goeckes T, et al. **Chronic subdural hematoma: a sentinel health event.** *World Neurosurg* 2013;80:889–92 CrossRef Medline
4. Almenawer SA, Farrokhyar F, Hong C, et al. **Chronic subdural hematoma management: a systematic review and meta-analysis of 34,829 patients.** *Ann Surg* 2014;259:449–57 CrossRef Medline
5. Liu W, Bakker NA, Groen RJ. **Chronic subdural hematoma: a systematic review and meta-analysis of surgical procedures.** *J Neurosurg* 2014;121:665–73 CrossRef Medline
6. Santarius T, Kirkpatrick PJ, Ganesan D, et al. **Use of drains versus no drains after burr-hole evacuation of chronic subdural haematoma: a randomised controlled trial.** *Lancet* 2009;374:1067–73 CrossRef Medline

7. Ban SP, Hwang G, Byoun HS, et al. **Middle meningeal artery embolization for chronic subdural hematoma.** *Radiology* 2018;286:992–99 CrossRef Medline

8. Link TW, Boddu S, Paine SM, et al. **Middle meningeal artery embolization for chronic subdural hematoma: a series of 60 cases.** *Neurosurgery* 2019;85:801–07 CrossRef Medline

9. Lam RC, Lin SC, DeRubertis B, et al. **The impact of increasing age on anatomic factors affecting carotid angioplasty and stenting.** *J Vasc Surg* 2007;45:875–80 CrossRef Medline

10. Sur S, Snelling B, Khandelwal P, et al. **Transradial approach for mechanical thrombectomy in anterior circulation large-vessel occlusion.** *Neurosurg Focus* 2017;42:E13 CrossRef Medline

11. Snelling BM, Sur S, Shah SS, et al. **Transradial cerebral angiography: techniques and outcomes.** *J Neurointerv Surg* 2018;10:874–81 CrossRef Medline

12. Shotar E, Meyblum L, Premat K, et al. **Middle meningeal artery embolization reduces the post-operative recurrence rate of at-risk chronic subdural hematoma.** *J Neurointerv Surg* 2020;12:1209–13 CrossRef Medline

13. Pouvelle A, Pouliquen G, Premat K, et al. **Larger middle meningeal arteries on computed tomography angiography in patients with chronic subdural hematomas as compared to matched controls.** *J Neurotrauma* 2020 Jul 10. [Epub ahead of print]]CrossRef Medline

14. Friede RL, Schachenmayr W. **The origin of subdural neomembranes, II: fine structural of neomembranes.** *Am J Pathol* 1978;92:69–84 Medline

15. Yamashima T, Yamamoto S, Friede RL. **The role of endothelial gap junctions in the enlargement of chronic subdural hematomas.** *J Neurosurg* 1983;59:298–303 CrossRef Medline

16. Mandai S, Sakurai M, Matsumoto Y. **Middle meningeal artery embolization for refractory chronic subdural hematoma: case report.** *J Neurosurg* 2000;93:686–88 CrossRef Medline

17. Ishihara H, Ishihara S, Kohyama S, et al. **Experience in endovascular treatment of recurrent chronic subdural hematoma.** *Interv Neuroradiol* 2007;13(Suppl 1):141–44 CrossRef Medline

18. Tempaku A, Yamauchi S, Ikeda H, et al. **Usefulness of interventional embolization of the middle meningeal artery for recurrent chronic subdural hematoma: five cases and a review of the literature.** *Interv Neuroradiol* 2015;21:366–71 CrossRef Medline

19. Nakagawa I, Park HS, Kotsugi M, et al. **Enhanced hematoma membrane on DynaCT images during middle meningeal artery embolization for persistently recurrent chronic subdural hematoma.** *World Neurosurg* 2019;126:e473–79 CrossRef Medline

20. Hashimoto T, Ohashi T, Watanabe D, et al. **Usefulness of embolization of the middle meningeal artery for refractory chronic subdural hematomas.** *Surg Neurol Int* 2013;4:104 CrossRef Medline

21. Fiorella D, Arthur AS. **Middle meningeal artery embolization for the management of chronic subdural hematoma.** *J Neurointerv Surg* 2019;11:912–15 CrossRef Medline

22. Kang J, Whang K, Hong SK, et al. **Middle meningeal artery embolization in recurrent chronic subdural hematoma combined with arachnoid cyst.** *Korean J Neurotrauma* 2015;11:187–90 CrossRef Medline

23. Matsumoto H, Hanayama H, Okada T, et al. **Which surgical procedure is effective for refractory chronic subdural hematoma? Analysis of our surgical procedures and literature review.** *J Clin Neurosci* 2018;49:40–47 CrossRef Medline

24. Boisseau W, Fahed R, Lapergue B, et al; ETIS Investigators. **Predictors of parenchymal hematoma after mechanical thrombectomy: a multicenter study.** *Stroke* 2019;50:2364–70 CrossRef Medline

25. Zaidat OO, Castonguay AC, Nogueira RG, et al. **TREVO stent-retriever mechanical thrombectomy for acute ischemic stroke secondary to large vessel occlusion registry.** *J Neurointerv Surg* 2018;10:516–24 CrossRef Medline

26. Faggioli G, Ferri M, Gargiulo M, et al. **Measurement and impact of proximal and distal tortuosity in carotid stenting procedures.** *J Vasc Surg* 2007;46:1119–24 CrossRef Medline

27. Mendiz OA, Sampaolesi AH, Londero HF, et al. **Initial experience with transradial access for carotid artery stenting.** *Vasc Endovascular Surg* 2011;45:499–503 CrossRef Medline

28. Campeau L. **Percutaneous radial artery approach for coronary angiography.** *Cathet Cardiovasc Diagn* 1989;16:3–7 CrossRef Medline

29. Romagnoli E, Biondi-Zoccai G, Sciahbasi A, et al. **Radial versus femoral randomized investigation in ST-segment elevation acute coronary syndrome: the RIFLE-STEACS (Radial Versus Femoral Randomized Investigation in ST-Elevation Acute Coronary Syndrome) study.** *J Am Coll Cardiol* 2012;60:2481–89 CrossRef Medline

30. Jolly SS, Yusuf S, Cairns J, et al. **Radial versus femoral access for coronary angiography and intervention in patients with acute coronary syndromes (RIVAL): a randomised, parallel group, multicentre trial.** *Lancet* 2011;377:1409–20 CrossRef Medline

31. Starke RM, Snelling B, Al-Mufti F, et al; Society of NeuroInterventional Surgery. **Transarterial and transvenous access for neurointerventional surgery: report of the SNIS Standards and Guidelines Committee.** *J Neurointerv Surg* 2020;12:733–41 CrossRef Medline

32. Valgimigli M, Frigoli E, Leonardi S, et al; MATRIX Investigators. **Radial versus femoral access and bivalirudin versus unfractionated heparin in invasively managed patients with acute coronary syndrome (MATRIX): final 1-year results of a multicentre, randomised controlled trial.** *Lancet* 2018;392:835–48 CrossRef Medline

33. Stone JG, Zussman BM, Tonetti DA, et al. **Transradial versus transfemoral approaches for diagnostic cerebral angiography: a prospective, single-center, non-inferiority comparative effectiveness study.** *J Neurointerv Surg* 2020;12:993–98 CrossRef Medline

34. Catapano JS, Fredrickson VL, Fujii T, et al. **Complications of femoral versus radial access in neuroendovascular procedures with propensity adjustment.** *J Neurointerv Surg* 2020;12:611–15 CrossRef Medline

35. Khanna O, Sweid A, Mouchtouris N, et al. **Radial artery catheterization for neuroendovascular procedures.** *Stroke* 2019;50:2587–90 CrossRef Medline

36. Waqas M, Vakharia K, Dossani RH, et al. **Transradial access for flow diversion of intracranial aneurysms: case series.** *Interv Neuroradiol* 2000 July 5. [Epub ahead of print] CrossRef Medline

Reliability of the Diagnosis of Cerebral Vasospasm Using Catheter Cerebral Angiography: A Systematic Review and Inter- and Intraobserver Study

T.E. Darsaut, C. Derksen, B. Farzin, M.B. Keough, R. Fahed, W. Boisseau, L. Letourneau-Guillon, A.-C. Januel, A. Weill, D. Roy, T.N. Nguyen, S. Finitsis, J.-C. Gentric, D. Volders, A. Carlson, M.M. Chow, C. O'Kelly, J.L. Rempel, R.A. Ashforth, M. Chagnon, J. Zehr, J.M. Findlay, G. Gevry, and J. Raymond

ABSTRACT

BACKGROUND AND PURPOSE: Conventional angiography is the benchmark examination to diagnose cerebral vasospasm, but there is limited evidence regarding its reliability. Our goals were the following: 1) to systematically review the literature on the reliability of the diagnosis of cerebral vasospasm using conventional angiography, and 2) to perform an agreement study among clinicians who perform endovascular treatment.

MATERIALS AND METHODS: Articles reporting a classification system on the degree of cerebral vasospasm on conventional angiography were systematically searched, and agreement studies were identified. We assembled a portfolio of 221 cases of patients with subarachnoid hemorrhage and asked 17 raters with different backgrounds (radiology, neurosurgery, or neurology) and experience (junior ≤10 and senior >10 years) to independently evaluate cerebral vasospasm in 7 vessel segments using a 3-point scale and to evaluate, for each case, whether findings would justify endovascular treatment. Nine raters took part in the intraobserver reliability study.

RESULTS: The systematic review showed a very heterogeneous literature, with 140 studies using 60 different nomenclatures and 21 different thresholds to define cerebral vasospasm, and 5 interobserver studies reporting a wide range of reliability ($\kappa = 0.14$–0.87). In our study, only senior raters reached substantial agreement ($\kappa \geq 0.6$) on vasospasm of the supraclinoid ICA, M1, and basilar segments and only when assessments were dichotomized (presence or absence of ≥50% narrowing). Agreement on whether to proceed with endovascular management of vasospasm was only fair ($\kappa \leq 0.4$).

CONCLUSIONS: Research on cerebral vasospasm would benefit from standardization of definitions and thresholds. Dichotomized decisions by experienced readers are required for the reliable angiographic diagnosis of cerebral vasospasm.

Cerebral vasospasm remains a major cause of poor outcome after aneurysmal SAH.[1] Timely identification of vascular constriction to avoid delayed cerebral ischemia can result in escalation of therapy and avoiding vasospasm-related strokes, disability, and death.[2] Endovascular rescue procedures such as intra-arterial infusion of calcium channel blockers and balloon angioplasty can be used to dilate constricted vessels and prevent strokes[3-5] but these treatments carry a risk.[6,7] The appropriate timing and indications for endovascular treatment in this setting remain unclear.[1,8]

Even though various noninvasive imaging methods have been proposed, conventional angiography remains the gold standard for evaluating whether a vessel is sufficiently narrowed to qualify as significant vasospasm and whether to proceed with endovascular treatment. However, the reliability of the diagnosis of vasospasm by conventional angiography has, in fact, rarely been studied.[9] There are few reported reliability studies to date and usually in the context of comparing a novel, non- or less-invasive

test with conventional angiography, with a small number of patients and a limited number of raters.[9-13]

Here, we first systematically reviewed the literature on classification systems used to describe vasospasm after aneurysmal SAH using conventional angiography, with particular attention paid to classifications tested for interobserver reliability. We then sought to rigorously evaluate the reliability of the assessments made by a substantial number of interventionists of various backgrounds and years of experience regarding the degree of vasospasm and the perceived need for endovascular treatment in a substantial number of clinical cases.

MATERIALS AND METHODS
A detailed protocol for the literature search strategy (Online Supplemental Data) was designed and implemented according to the Preferred Reporting Items for Systematic Reviews and Meta-Analysis statement.[14] The article was prepared in accordance with the Guidelines for Reporting Reliability and Agreement Studies.[15] The research ethics board at the University of Alberta provided consent to access patient clinical and angiographic data.

The electronic search was performed using the Cumulative Index of Nursing and Allied Health Literature, EMBASE, EBM, Cochrane Database of Systematic Reviews, and MEDLINE data bases with no start date specification, capturing English and French publications up to August 28, 2019. One author tested the ability of the search strategy to recover pertinent articles. The data were collected and reviewed in detail independently by 2 authors (B.F., T.E.D.), with 6 and 12 years' experience, respectively, and discrepancies were resolved by consensus.

Patients
We assembled an anonymized portfolio of 221 patients with SAH hospitalized at the University of Alberta from January 2007 to December 2017, identified through a prospectively maintained transcranial Doppler case log. The case log excluded patients with high-grade aneurysmal SAH who were considered moribund. Patients who had undergone catheter cerebral angiography during the vasospasm risk period (3–17 days post-SAH) with injections of the left and right ICAs and at least 1 vertebral artery injection were included (257 patients). Thirty-six cases were subsequently excluded because ≥1 of the angiographic images was judged too poor to evaluate, leaving 221 cases for assessment of the degree of vasospasm. Demographic and aneurysm characteristics of the patients included in the portfolio, including the proportion actually treated with hypertensive therapy or balloon angioplasty for vasospasm, are presented in Table 1.

Clinician Responders
The angiographic portfolio was sent to selected clinicians from different training backgrounds, working in different countries, with differing levels of experience. Responders provided some demographic information but were assured of anonymity. Senior raters were those with >10 years' experience in treating vasospasm. Raters were not provided with any clinical information regarding the case and were blinded to: i) the official radiology report, ii) whether the patient was receiving hypertensive therapy, iii) the scores given by the other responders.

Table 1: Characteristics of patients and aneurysms included in the portfolio

Characteristics	
No. of cases	221
Age (mean) (range)	51.4, 16–77
Female sex	144 (65.2%)
Aneurysm location	
Anterior circulation	183 (82.8%)
Posterior circulation	32 (14.5%)
No aneurysm identified	6 (2.7%)
Aneurysm location	
Left	58 (26.2%)
Right	96 (43.4%)
Midline	61 (27.6%)
None found	6 (2.7%)
WFNS grade	
I	78 (35.3%)
II	51 (23.1%)
III	16 (7.2%)
IV	33 (14.9%)
V	43 (19.5%)
Modified Fisher grade	
1	44 (20.0%)
2	29 (13.1%)
3	65 (29.4%)
4	83 (37.6%)
Treatment details	
Surgical clipping	123 (55.7%)
Endovascular treatment	91 (41.2%)
Spontaneous occlusion before treatment	1 (0.5%)
No treatment	6 (2.7%)
Received hypertensive therapy for vasospasm	52 (23.5%)
Received balloon angioplasty for vasospasm	26 (11.8%)

Note:—WFNS indicates World Federation of Neurosurgical Societies.

For each of the 221 cases, clinicians were provided with anterior-posterior projections for 3 injections (left ICA, right ICA, and 1 vertebral artery) and were asked to provide their visual judgment on the degree of vessel narrowing at the level of the supraclinoid ICA, M1, A1, and basilar segments, for a total of 7 assessments per case (1547 assessments per responder per reading session). Caliper measurements were not required. Baseline angiographic images were available for comparison in 342/663 (51.6%) injections. The categories and thresholds were the following—none/mild vasospasm: <33% vessel narrowing; moderate vasospasm: 33%–50% narrowing; or severe vasospasm: >50% narrowing, according to a modified scheme used at our institution.[13] Clinicians were then asked, for each case, if the patient is symptomatic without another cause, would you proceed with endovascular treatment of vasospasm? For the intrarater evaluation, raters were asked to independently evaluate the same-but-permutated portfolio twice, >4 weeks apart.

Finally, to assess whether a different defining threshold for severe vasospasm influenced agreement, we asked 4 clinicians to evaluate the same 221 cases 2 more times, at least 4 weeks apart using a different dichotomized threshold (not severe vasospasm: less than two-thirds narrowing; or severe vasospasm: equal or more than two-thirds vessel narrowing) and to consider only the ICA, M1, and basilar segments (1105 assessments per responder per reading session). An illustrative case from the portfolio is presented in Fig 1, and the questionnaire is available in the Online Supplemental Data.

Case 99

Right

ICA Mild _____ Moderate _____ Severe _____

M1 Mild _____ Moderate _____ Severe _____

A1 Mild _____ Moderate _____ Severe _____

Left

ICA Mild _____ Moderate _____ Severe _____

M1 Mild _____ Moderate _____ Severe _____

A1 Mild _____ Moderate _____ Severe _____

Basilar

Mild _____ Moderate _____ Severe _____

If the patient is symptomatic without another cause, would you proceed with endovascular treatment of vasospasm? YES _____ NO _____
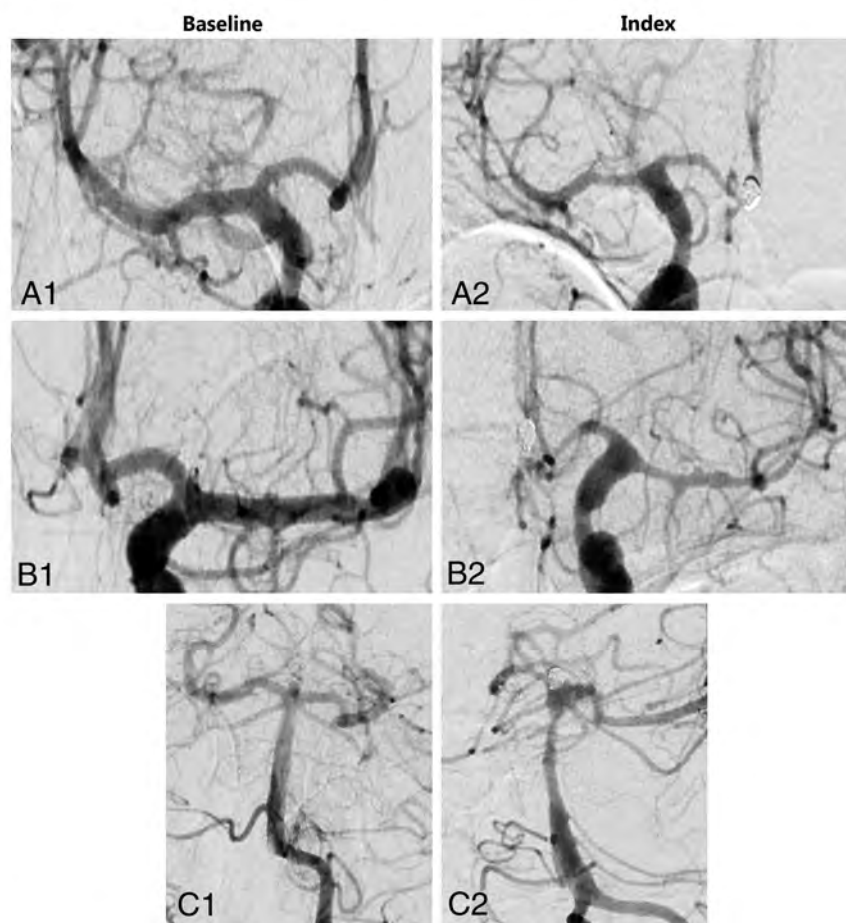
FIG 1. Illustrative case from the portfolio. The degree of vessel narrowing was assessed on the right-sided Index images (*A2, B2, C2*).

Statistical Analysis

Results were analyzed for all raters according to the arterial segment, first using all 3 categories and then dichotomized into nonsevere/severe using 50% vessel narrowing as the threshold. This analysis was then repeated for the raters who responded to the portfolio with the dichotomized higher (two-thirds) narrowing threshold. An overall per-patient assessment of severe vasospasm was considered to have been made when the rater assessed narrowing to be "severe" for at least one of the ICA, M1, or basilar segments. Isolated A1 segment vasospasm was not included in this definition to avoid the uncertainty regarding pre-existent A1 hypoplasia. Responses were then stratified according to training background and years of experience.

Interrater and intrarater agreement regarding the degree of vasospasm for each arterial segment was assessed using Fleiss κ statistics for dichotomized data using 95% bias-corrected confidence intervals obtained with 1000 bootstrap resampling. For nondichotomized data, agreement was determined using the Krippendorff α. The strength of agreement was interpreted according to Landis and Koch (0–0.2, slight; 0.21–0.4, fair; 0.41–0.6, moderate; 0.61–0.8, substantial; 0.81–1.0 almost perfect). Differences between point estimates or between κ values were considered to exist when confidence intervals did not overlap. All analyses were performed by statisticians (M.C., J.Z.) using

STATA, Version 16.0 (StataCorp) and SPSS Version 25 (IBM), with a significance level set at .05.

RESULTS

Systematic Review

A total of 1892 titles were reviewed, 683 abstracts were examined, 328 full-text articles were read in detail, and 140 eligible articles that used classification systems to evaluate cerebral vasospasm were included (flow chart, Online Supplemental Data). Articles described percentage luminal narrowing (91 articles), measured millimetric narrowing (11 articles), categorized the degree of vasospasm without quantification (9 articles), or did not categorize or quantify the degree of vasospasm (simple yes/no presence) (29 articles). Articles used a different number of tiers to grade the degree of vasospasm: 2 tiers (27 studies), 3 tiers (16 studies), 4 tiers (42 studies), 5 tiers (5 studies), and 6 tiers (1 study); no tiers were specified in 37 studies (Online Supplemental Data). Sixty different nomenclatures were used to define the degree of vasospasm. Measurement calipers (37 studies) or simple visual judgment (ie, eyeballing) (104 studies) were used to evaluate vessel diameter. Most (126/140, 89%) of the articles were diagnostic accuracy studies comparing how a second (noninvasive) imaging technique compared with conventional angiography. None of the

Table 2: Interrater agreement for the per-patient diagnosis of severe vasospasm on DSA using 50% vessel narrowing threshold (dichotomized)

	κ (95% CI)	Interventional				
	All Raters (n=17)	Neuroradiologists (n = 10)	Neurosurgeons (n = 4)	Neurologists (n = 3)	Junior (n = 9)	Senior (n = 8)
Supraclinoid ICA	0.568 (0.489–0.646)	0.535 (0.457–0.626)	0.549 (0.450–0.642)	0.625 (0.509–0.725)	0.484 (0.400–0.567)	0.652 (0.562–0.735)
M1 segment	0.576 (0.517–0.629)	0.579 (0.515–0.633)	0.514 (0.433–0.593)	0.554 (0.461–0.643)	0.512 (0.444–0.574)	0.638 (0.575–0.693)
A1 segment	0.511 (0.460–0.562)	0.511 (0.457–0.563)	0.452 (0.376–0.527)	0.512 (0.444–0.588)	0.512 (0.453–0.571)	0.495 (0.444–0.550)
Basilar	0.533 (0.413–0.646)	0.488 (0.364–0.604)	0.538 (0.364–0.697)	0.551 (0.391–0.699)	0.475 (0.348–0.604)	0.617 (0.493–0.737)
Per-patient assessment[a]	0.556 (0.498–0.611)	0.558 (0.494–0.616)	0.495 (0.412–0.583)	0.546 (0.452–0.638)	0.483 (0.414–0.552)	0.629 (0.566–0.686)
Decision to proceed with EVT	0.393 (0.344–0.444)	0.393 (0.336–0.445)	0.414 (0.344–0.490)	0.319 (0.229–0.415)	0.382 (0.328–0.445)	0.410 (0.351–0.469)

Note:—EVT indicates endovascular treatment.
[a] Severe vasospasm affecting at least 1 arterial segment (not a single A1).

published articles examined the same cases twice, with different thresholds to evaluate the consequence of changing thresholds on agreement.

The systematic review identified 5 interobserver variability studies, all of which had been published before the publication of the Guidelines for Reporting Reliability and Agreement Studies recommendations (2011).[15] The 5 articles each used a different classification system to evaluate the degree of vasospasm (with 2–4 tiers) using various arbitrary thresholds (Online Supplemental Data). All included an assessment of interobserver agreement on cerebral vasospasm using conventional angiography, but this was the main focus of only one of the articles.[11] The number of patients ranged from 22 to 101, and the number of raters, from 2–4. The degree of blinding of the raters was not reliably reported. The paucity of data and the heterogeneity of methods and end points precluded meta-analysis.

Agreement Study

The 221-patient portfolio included 52 patients (23.5%; 95% CI, 18.4%–29.5%) actually treated for vasospasm with vasopressor medications and 26 patients (11.8%; 95% CI, 8.1%–16.7%) who received balloon angioplasty for vasospasm. Six patients with high-volume subarachnoid hemorrhages were never found to have an aneurysm but were included in this series because they were considered at risk of developing symptomatic vasospasm.

The portfolio was sent to 20 clinicians, and 17 (85%) responded. All respondents (17/17) currently perform balloon angioplasty for cerebral vasospasm as part of their practice. Their training backgrounds were the following: interventional neuroradiology (n = 10), endovascular-trained cerebrovascular surgery (n = 4), and interventional neurology (n = 3). Raters were from Canada (n = 9), the United States (n = 5), or Europe (n = 3). Junior raters had ≤5 years' (n = 3) or 6–10 years' (n = 6) experience, while the senior raters had 11–20 years' (n = 4) or >20 years' experience (n = 4). Nine raters (53%) completed the survey twice (cases were permuted between the 2 reading sessions) >4 weeks apart for the intrarater evaluation. Four raters (24%) completed

the survey 2 more times using the two-thirds vessel narrowing threshold for severe vasospasm, again >4 weeks apart.

The prevalence of severe vasospasm in the portfolio, as assessed by the 17 readers, ranged from 7.4% to 40.3% (mean, 26.3% [SD, 9.7%]). The nondichotomized interrater agreement for the diagnosis of severe vasospasm using conventional angiography is available in the Online Supplemental Data, while the dichotomized agreement results are presented in Table 2. Interpretation of the dichotomized (nonsevere/severe) data, according to Landis and Koch, showed moderate agreement for the supraclinoid ICA (κ = 0.568; 95% CI, 0.489–0.646), M1 (κ = 0.576; 95% CI, 0.517–0.629), A1 (κ = 0.511; 95% CI, 0.460–0.562), and basilar (κ = 0.533; 95% CI, 0.413–0.646) arterial segments. Having a training background in radiology, neurosurgery, or neurology did not significantly influence agreement, but responders with >10 years' experience had significantly better agreement than junior readers when considering the presence of severe vasospasm in the M1 segment (κ = 0.638; 95% CI, 0.575–0.693 versus κ = 0.512 (95% CI, 0.444–0.574) and also agreed more on the per-patient assessment of severe vasospasm (κ = 0.629; 95% CI, 0.566–0.686) compared with junior readers (κ = 0.483; 95% CI, 0.414–0.552).

Perfect agreement (17/17 raters) on the presence of severe vasospasm in at least 1 arterial segment existed for 9 cases (4.0%). For 30/221 (14%) cases, 14/17 (80%) respondents considered the degree of vasospasm to be severe using a 50% narrowing threshold. Illustrative cases of maximal and minimal agreement for the diagnosis of severe vasospasm are presented in Fig 2.

The interobserver agreement for all raters on whether to proceed with endovascular treatment if the patient were symptomatic without another cause was fair (κ = 0.39) and was not significantly better when considering years of experience or training background. There was a strong association between the determination of severe vasospasm and the choice to proceed with endovascular treatment (OR = 20.57; 95% CI, 16.3–25.89; P < .001). Patients who actually underwent angioplasty in real life obtained "yes" votes for endovascular treatment 348 of 406 (86%) times, while patients who did not undergo angioplasty

obtained 1450/3326 (44%) yes votes ($P < .000$). The assessments of the 17 readers on the 221 cases are ordered and presented in Fig 3.

Nine clinicians answered the survey twice to obtain intraobserver agreement (Online Supplemental Data). Intraobserver agreement for the dichotomized evaluation of whether the patient had severe vasospasm was at least substantial for all raters ($\kappa = 0.639$–0.802). The range of intraobserver agreement on the decision of whether to proceed with endovascular management was at least substantial for 7 of 9 raters, varying from moderate ($\kappa = 0.464$) to almost perfect ($\kappa = 0.828$).

To test the impact of changing the threshold definition of severe vasospasm from 50% to 66.6% vessel narrowing, 4 readers completed the survey 4 times each, twice with the 50% threshold

FIG 2. Illustrative cases of maximal agreement and maximal disagreement. Two cases showing *A*) maximal agreement (17/17 readers rated vasospasm to be "severe" with 50% narrowing threshold), *B*) maximal disagreement (only 8/17 readers rated vasospasm to be "severe").

FIG 3. Total number of dichotomized assessments of severe vasospasm and choice for endovascular treatment. Along the x-axis, the graph shows patients primarily ordered according to increasing proportion of severe vasospasm votes. Patients are secondarily ordered within each bracket according to number of votes for endovascular treatment. *Circles* show patients who received angioplasty in real life. Note that perfect agreement occurs only at the tails of the distribution: cases 1–92 (all no) and 212–221 (all yes).

and twice with the two-thirds threshold. For these 4 readers, altering the threshold definition did not significantly change the agreement; interobserver agreement was substantial using 50% and remained at a substantial level using the two-thirds narrowing threshold for carotid and M1 segments and for per-patient assessments as well (Online Supplemental Data). The range of intrarater agreement was also substantial ($\kappa = 0.723$–0.784) at 50% and from moderate-to-almost-perfect agreement at two-thirds (range, $\kappa = 0.596$–0.834) (Online Supplemental Data).

DISCUSSION

The present work specifically addresses the angiographic diagnosis of vasospasm, which is only 1 aspect of the physiologic derangements that occur after aneurysmal SAH and which are collectively referred to as delayed cerebral ischemia/vasospasm.[1,2] The pathophysiologic association between the caliber of cerebral vessels and delayed cerebral ischemia was historically made with conventional angiography, a method that remains the gold standard, even if angiography is currently increasingly replaced by various noninvasive diagnostic alternatives.[9,10,16] The diagnosis of vasospasm on conventional angiography is, nevertheless, beset by a number of unresolved problems. There is no consensus in the literature on the diagnostic criteria for angiographic vasospasm, and our systematic review showed such heterogeneity in the way cerebral vasospasm is defined and evaluated that the comparison of results from 1 article to the next is difficult or impossible.

One major difficulty is that there is no way to verify whether the results of conventional angiography are accurate: There is no additional gold standard with which angiography can be verified, unlike appendicitis, for example, for which the accuracy of a sonographic diagnosis can be verified by surgical exploration. The best that can be done is to evaluate the reliability of the evaluations obtained with conventional angiography. However, because angiography often serves as the gold standard to evaluate other noninvasive tests, this evaluation becomes crucial. It is, thus, somewhat surprising that reliability has been so infrequently assessed, and never with the benefit of modern computing power and statistical techniques.[11] One explanation could be that in a study dedicated to the diagnostic accuracy of a new technique, there is little incentive to put the gold standard conventional angiography to a severe test.

We thus endeavored to address this gap by assembling a large number of cases and recruiting a large number of clinicians, hoping to establish that the best test of vessel narrowing was actually reliable. However, the reliability of the diagnosis of severe vasospasm remains borderline for a number of methodologic and practical clinical reasons. Variability in intracranial vessel diameters is inevitably present across individuals, and baseline catheter angiograms in the same patient are not always available for comparison (ie, for clipped aneurysms which are treated on

the basis of CT angiography). The determination of spasm can sometimes be made only by comparison with a noninvasive test or through a comparison with ipsilateral or contralateral presumably uninvolved arteries. Well-defined, precise measurement protocols, including which vessels should be measured (and how), remain elusive.

Second, whether readers can reliably differentiate 25% or 30% vessel narrowing is questionable, and even if precise and reliable measures were possible, there is no consensus on what baseline reference values should be used on which or how many vessels. The reasons for the various grading scales and the exact procedural methodology are frequently not clearly stated or validated, with some authors choosing to measure vessel diameter with calipers, while others use simple visual assessment.

Our findings have a number of important implications for vasospasm research. Correlative research on alternative (noninvasive) diagnostic tests such as transcranial Doppler,[13] CTA,[10,17,18] or MRA[18] that commonly use conventional angiography as the comparative benchmark examination should bear in mind the suboptimal reliability of the gold standard diagnostic test. All by itself, the lack of reliability of the diagnoses may explain how pharmacologic treatments such as nimodipine could be shown to be clinically effective despite the lack of a measurable effect on angiographic vessel narrowing;[19] this explanation further reinforces the notion that hard clinical outcomes should be selected for clinical trials on vasospasm.[19-23]

The most important questions following conventional angiography pertain to the clinical relevance of the interpretation. The clinical decision of whether to proceed with endovascular management of vasospasm is based primarily on the clinical and neurologic status, but it is also closely related to the judged degree of angiographic vasospasm, particularly for sedated or comatose patients. Currently, the use of conventional angiography is often restricted to patients already identified by noninvasive tests, and interpretation is often biased toward intervening. We attempted, in this survey, to eliminate any decisional variability due to differences in clinical status by not mentioning when the patients were already being treated with vasoactive drugs and by asking responders to consider, for each case, that the patient was symptomatic without another cause. This word choice may have influenced readers to proceed with endovascular treatment even when the degree of vasospasm was judged not severe. The wording of the questions may also have influenced results because the choice of whether to proceed with endovascular management could have been variously interpreted as including infusion of vasoactive medications or balloon angioplasty, which may have different thresholds for decisions to treat.

Limitations of this work include the artificially constructed portfolio and the self-selected readers. Different cases and readers could have produced different results. The choice of 50% and two-thirds thresholds for severe vasospasm were arbitrarily determined after a review of the literature. We did not ask readers to differentiate focal from diffuse vasospasm or to fastidiously evaluate spasm in more distal vessels such as the M2, A2, or P2 segments because we were mostly interested in an evaluation of vessel segments that are more reliably examined by noninvasive methods such as transcranial Doppler and CTA and are safely

treatable with balloon angioplasty. The representative images evaluated by the raters were only 3 still images; rating the entire dynamic angiographic study on a PACS system may have led to different results. Finally, evaluating a portfolio of images and making a case-by-case evaluation of real patients are different contexts, and we can only hope that readers took the same amount of time and care to respond as they would in a normal clinical setting.

To improve the ability to make meaningful comparisons regarding the degree of vessel narrowing in future research, standardization of thresholds and nomenclatures is desirable. We propose that core labs using angiographic vasospasm as an end point measure should use senior raters using a dichotomized assessment (presence or absence of severe vasospasm defined as >50% luminal narrowing) limited to the supraclinoid ICA and M1 segments.

CONCLUSIONS

Cerebral vasospasm research would benefit from standardization of definitions and thresholds. Dichotomized decisions by experienced readers are required for the reliable angiographic diagnosis of cerebral vasospasm.

REFERENCES

1. Macdonald RL. **Delayed neurological deterioration after subarachnoid haemorrhage.** Nat Rev Neurol 2014;10:44–58 CrossRef Medline
2. Vergouwen MD, Ilodigwe D, Macdonald RL. **Cerebral infarction after subarachnoid hemorrhage contributes to poor outcome by vasospasm-dependent and -independent effects.** Stroke 2011;42:924–29 CrossRef Medline
3. Anderegg L, Beck J, Z'Graggen WJ, et al. **Feasibility and safety of repeat instant endovascular interventions in patients with refractory cerebral vasospasms.** AJNR Am J Neuroradiol 2017;38:561–67 CrossRef Medline
4. Beck J, Raabe A, Lanfermann H, et al. **Effects of balloon angioplasty on perfusion- and diffusion-weighted magnetic resonance imaging results and outcome in patients with cerebral vasospasm.** J Neurosurg 2006;105:220–27 CrossRef Medline
5. Turowski B, Du Mesnil de Rochemont R, Beck J, et al. **Assessment of changes in cerebral circulation time due to vasospasm in a specific arterial territory: effect of angioplasty.** Neuroradiol 2005;47:134–43 CrossRef Medline
6. Muizelaar JP, Zwienenberg M, Rudisill NA, et al. **The prophylactic use of transluminal balloon angioplasty in patients with Fisher grade 3 subarachnoid hemorrhage: a pilot study.** J Neurosurg 1999;91:51–58 CrossRef Medline
7. Zwienenberg-Lee M, Hartman J, Rudisill N, et al; Balloon Prophylaxis for Aneurysmal Vasospasm (BPAV) Study Group. **Effect of prophylactic transluminal balloon angioplasty on cerebral vasospasm and outcome in patients with Fisher grade III subarachnoid hemorrhage: results of a phase II multicenter, randomized, clinical trial.** Stroke 2008;39:1759–65 CrossRef Medline
8. Li K, Barras CD, Chandra RV, et al. **A review of the management of cerebral vasospasm after aneurysmal subarachnoid hemorrhage.** World Neurosurg 2019;126:513–27 CrossRef Medline
9. Lindegaard KF, Nornes H, Bakke SJ, et al. **Cerebral vasospasm diagnosis by means of angiography and blood velocity measurements.** Acta Neurochir (Wien) 1989;100:12–24 CrossRef Medline

10. Binaghi S, Colleoni ML, Maeder P, et al. **CT angiography and perfusion CT in cerebral vasospasm after subarachnoid hemorrhage.** *AJNR Am J Neuroradiol* 2007;28:750–58 Medline

11. Eskesen V, Karle A, Kruse A, et al. **Observer variability in assessment of angiographic vasospasm after aneurysmal subarachnoid haemorrhage.** *Acta Neurochir (Wien)* 1987;87:54–57 CrossRef Medline

12. Krejza J, Kochanowicz J, Mariak Z, et al. **Middle cerebral artery spasm after subarachnoid hemorrhage: detection with transcranial color-coded duplex US.** *Radiology* 2005;236:621–29 CrossRef Medline

13. Vora YY, Suarez-Almazor M, Steinke DE, et al. **Role of transcranial Doppler monitoring in the diagnosis of cerebral vasospasm after subarachnoid hemorrhage.** *Neurosurgery* 1999;44:1237–47; discussion 1247–48 Medline

14. Liberati A, Altman DG, Tetzlaff J, et al. **The PRISMA statement for reporting systematic reviews and meta-analyses of studies that evaluate health care interventions: explanation and elaboration.** *J Clin Epidemiol* 2009;62:e1–34 CrossRef Medline

15. Kottner J, Audigé L, Brorson S, et al. **Guidelines for Reporting Reliability and Agreement Studies (GRRAS) were proposed.** *J Clin Epidemiol* 2011;64:96–106 CrossRef Medline

16. Sanelli PC, Ugorec I, Johnson CE, et al. **Using quantitative CT perfusion for evaluation of delayed cerebral ischemia following aneurysmal subarachnoid hemorrhage.** *AJNR Am J Neuroradiol* 2011;32:2047–53 CrossRef Medline

17. Letourneau-Guillon L, Farzin B, Darsaut TE, et al. **Reliability of CT angiography in cerebral vasospasm: a systematic review of the literature and an inter- and intraobserver study.** *AJNR Am J Neuroradiol* 2020;41:612–18 CrossRef Medline

18. Takano K, Hida K, Iwaasa M, et al. **Three-dimensional spin-echo-based black-blood MRA in the detection of vasospasm following subarachnoid hemorrhage.** *J Magn Reson Imaging* 2019;49:800–07 CrossRef Medline

19. Petruk KC, West M, Mohr G, et al. **Nimodipine treatment in poor-grade aneurysm patients. Results of a multicenter double-blind placebo-controlled trial.** *J Neurosurg* 1988;68:505–17 CrossRef Medline

20. Pickard JD, Murray GD, Illingworth R, et al. **Effect of oral nimodipine on cerebral infarction and outcome after subarachnoid haemorrhage: British Aneurysm Nimodipine Trial.** *BMJ* 1989;298:636–42 CrossRef Medline

21. Macdonald RL, Higashida RT, Keller E, et al. **Clazosentan, an endothelin receptor antagonist, in patients with aneurysmal subarachnoid haemorrhage undergoing surgical clipping: a randomised, double-blind, placebo-controlled phase 3 trial (CONSCIOUS-2).** *Lancet Neurol* 2011;10:618–25 CrossRef Medline

22. Macdonald RL, Higashida RT, Keller E, et al. **Preventing vasospasm improves outcome after aneurysmal subarachnoid hemorrhage: rationale and design of CONSCIOUS-2 and CONSCIOUS-3 trials.** *Neurocrit Care* 2010;13:416–24 CrossRef Medline

23. Carlson AP, Hanggi D, Wong GK, et al; NEWTON Investigators. **Single-dose intraventricular nimodipine microparticles versus oral nimodipine for aneurysmal subarachnoid hemorrhage.** *Stroke* 2020;51:1142–49 CrossRef Medline

Aneurysm Treatment in Acute SAH with Hydrophilic-Coated Flow Diverters under Single-Antiplatelet Therapy: A 3-Center Experience

D. Lobsien, C. Clajus, D. Behme, M. Ernst, C.H. Riedel, O. Abu-Fares, F.G. Götz, D. Fiorella, and J. Klisch

ABSTRACT

BACKGROUND AND PURPOSE: In certain clinical circumstances, dual-antiplatelet therapy can be problematic in patients with acute SAH. In some aneurysms, however, flow-diverting stents are the ideal therapeutic option. We report our experience with ruptured intracranial aneurysms treated with flow diverters with hydrophilic coating (p48 MW HPC and p64 MW HPC) under single-antiplatelet therapy.

MATERIALS AND METHODS: Patients were treated with either flow-diverter placement alone or a flow diverter and additional coiling. Due to the severity of the hemorrhage, the potential for periprocedural rehemorrhage, and the potential for additional surgical interventions, a single-antiplatelet regimen was used in all patients.

RESULTS: Thirteen aneurysms were treated in 10 patients. The median age was 62 years; 5 patients were male. All had acute SAH due to aneurysm rupture. Four blood-blister, 2 dissecting, and 7 berrylike aneurysms were treated. Seven aneurysms were adjunctively coiled. Eight of the 10 patients received a single-antiplatelet protocol of aspirin, 1 patient was treated with prasugrel only, and 1 patient was treated with tirofiban first and then switched to the aspirin single-antiplatelet protocol. One device-related complication occurred, a thrombosis of an overstented branch. All stents, however, remained open at DSA, CTA, or MRA follow-up.

CONCLUSIONS: The implantation of flow diverters with reduced thrombogenicity due to hydrophilic surface coating under single-antiplatelet therapy seems to be an option in carefully selected cases of SAH due to aneurysm rupture.

ABBREVIATION: PO = orally

The endovascular treatment of unruptured intracranial aneurysms with flow diverters has become a routine procedure.[1-4] The use of flow diverters for the treatment of ruptured aneurysms is considerably more complex due to the requirement for dual-antiplatelet therapy.[5] However, for selected ruptured aneurysms, flow diverters might still be considered the treatment of choice when other strategies are too risky or simply not possible. This scenario can occur in wide-neck sidewall, fusiform, or blister

aneurysms. Therefore, a modified flow diverter that could be safely implanted with single-antiplatelet therapy would represent a major advance.[6,7]

Three flow diverters with coatings or surface modifications designed to reduce thrombogenicity, the Pipeline Embolization Device with SHIELD technology (PED Shield, Medtronic) and the p48 MW HPC or p64 MW HPC with hydrophilic coating (phenox), currently have Conformitè Europëenne mark clearance. Although instructions for use recommend standard dual-antiplatelet therapy after the implantation of these devices, for the latter 2, the instructions for use indicate that single-antiplatelet therapy is on-label if justified by the clinical circumstances.[6,8]

In the present study, we report our experience using the p48 MW HPC and the p64 MW HPC with single-antiplatelet therapy for the treatment of ruptured intracranial aneurysms in the setting of acute SAH.

MATERIALS AND METHODS

We retrospectively included patients from prospectively collected data bases from 3 different centers (Institute for diagnostic and interventional Neuroradiology, Helios Klinikum Erfurt, Erfurt

Germany; Institute for diagnostic and interventional Neuroradiology, Hanover Medical School, Hanover, Germany; and Institute for diagnostic and interventional Neuroradiology, University Medical Center Göttingen, Göttingen, Germany) from August 2018 to June 2020 because the devices were unavailable before that time period. Patients had to have an acute SAH and had to be treated in the acute phase (<48 hours) after diagnosis of the SAH with a HPC coated flow diverter. The flow-diversion treatment could be accompanied by additional coiling or intrasaccular flow disruption but not by other stents, flow diverters, or bifurcation stents. Patients had to be kept on single-antiplatelet therapy. Patency of the stent had to be documented by either DSA, MR imaging, or CT. All therapeutic decisions had to be made in interdisciplinary teams consisting of interventional neuroradiologists and neurosurgeons experienced in endovascular therapy using careful evaluation of the available therapeutic options in the individual situations. Full informed consent was obtained from the patient or legal representative in each case.

Implanted Devices
The devices used in this study were the p48 MW HPC and the p64 MW HPC flow diverters. These stents consist of braided drawn nitinol tubing, platinum-filled and coated with the recently developed hydrophilic coating polymer (pHPC; phenox). The p48 MW HPC consists of 48 wires; the p64 MW HPC, 64 wires. Both stents can be inserted over a standard 0.021-inch microcatheter. They do not require a specific detachment system but are deployed by pushing the device out of the microcatheter under fluoroscopic control. A distinct marker indicates the point at which the device can be fully retrieved.

Procedures
All procedures were performed with the patient under general anesthesia in the setting of acute SAH on 3 different dedicated biplane angiography machines (Axiom Artis and Artis Q; Siemens). Arterial access was usually established via a standard 6F or 8F sheath in the right groin and a standard 6F or 8F guiding catheter in the individual target vessel, internal carotid artery or a vertebral artery. The aneurysm was identified on conventional angiograms, procedures were planned on 3D angiograms, and the p48 MW HPC or p64 MW HPC was chosen according to the sizing recommendations provided by the manufacturer. All flow diverters were deployed over a Rebar 18 microcatheter (Medtronic) as recommended by the manufacturer, which was brought into place over various microguidewires. In 7 aneurysms, additional coils were placed, as detailed in the Online Supplemental Data and below.

Medical Regimen during Procedure and Postprocedure
Four different medical regimens were chosen at the discretion of the operators.

Regimen 1. Six patients received 5000 IU of heparin IV and 250 or 500 mg of aspirin IV during the procedure after microcatheter positioning. After the procedure, the patients were given enoxaparin, 40 mg twice daily, and 250 mg of aspirin IV twice daily for the duration of the stay in the intensive care unit. Afterward, they were switched to 100 mg of aspirin orally (PO) per day, and the enoxaparin was withdrawn. SAH leads to an activated platelet

aggregation, which explains the increased dosage of aspirin and IV application.[9]

Regimen 2. One of the patients received 5000 IU of heparin IV after microcatheter positioning and before flow-diverter placement. A body weight–adapted continuous IV infusion of tirofiban was started after stent deployment. The patient was kept on tirofiban for 24 hours and was then switched to prasugrel 10 mg PO per day after a loading dose of 60 mg PO with an overlap of 4 hours accompanied by enoxaparin, 40 mg twice a day, for the duration of the stay in the intensive care unit.

Regimen 3. One patient who received 2 flow diverters in 2 different locations received 5000 IU of heparin IV and 250 mg of aspirin IV before placement of the flow diverter. During the procedure, a body weight–adapted bolus of tirofiban was given due to suspected thrombus formation. Another 250 mg of aspirin IV and 2500 IU of heparin IV were given before placement of the second flow diverter.

Regimen 4. In 2 patients, the interventions were performed with aspirin, 250 mg IV, and 5000 IU of heparin IV before stent placement. After stent placement, a continuous body weight–adapted IV infusion of eptifibatide was started for 8 hours. This was changed to prasugrel starting with a loading dose of 60 mg orally with an overlap of 2 hours. In 1 patient, the prasugrel was switched to ticagrelor after 2 days.

Response testing was not performed and, therefore, not included in the analysis. Details of the medical regimen for each patient included in the study are listed in the Online Supplemental Data.

Follow-up
All patients were followed with CT with CTA or, alternatively, MR imaging with MRA or DSA to prove the patency of the flow diverters. The methods chosen depended on the condition of each patient and the clinical situation.

RESULTS
From August 2018 to June 2020, ten patients were included of 260 screened patients treated endovascularly in the setting of acute SAH due to rupture of an intracranial aneurysm at the 3 different centers. All patients were treated within 24 hours of diagnosis of acute hemorrhage and within 48 hours of the onset of acute SAH-like headache. The median age of patients was 62 years (range, 50–76 years); 5 patients were men. The median Hunt and Hess grade was 2 (range, 1–4). Two patients were treated with 1 p64 MW HPC each; 8 patients were treated with 9 p48 MW HPCs. In 1 patient, 2 p48 MW HPCs were placed in 2 different aneurysms. In 7 aneurysms, additional coiling was used. Altogether, 13 aneurysms were treated. Of these aneurysms, 2 were classified as dissecting aneurysms; 7, as berry aneurysms; and 4, as blood-blister aneurysms. Eight patients were treated with the aspirin regimen (regimen 1), 1 patient was treated with the prasugrel regime, 1 patient was treated with the tirofiban/aspirin regimen (regimens 2 and 3, as described above under Materials and Methods).
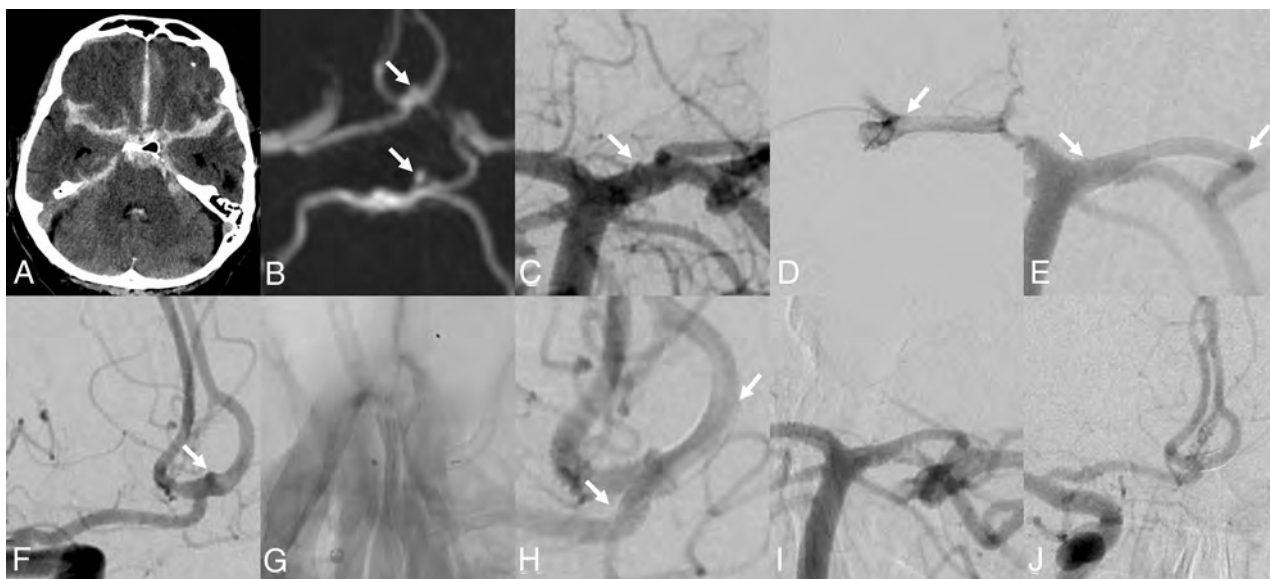
FIG 1. *A*, Initial NCCT showing the SAH. *B*, Axial MIP of the MRA. The suspected intracranial aneurysm of the anterior communicating artery (AcomA) and the posterior communicating artery (PcomA)/P1 can be seen (*white arrows*). *C*, DSA from the treatment. Left vertebral artery injection; a detailed view of the basilar artery head is shown. The blood-blister-like aneurysm of the P1 segment of the left posterior cerebral artery with the PcomA is demonstrated (*white arrow*), corresponding to the MRA, though smaller-appearing. *D*, Microcatheter injection. The tip of the microcatheter is in the distal left ICA, coming from the posterior via the PcomA. The left carotid-bifurcation is demonstrated (*arrow*). *E*, DSA after flow-diverter placement, reaching from the beginning of the P1 segment of the left posterior cerebral artery to the left PcomA, covering the left P1/PcomA angle (*arrows* pointing to the ends of the flow diverter). The aneurysm is no longer seen. *F*, Right ICA injection. The blood-blister-like aneurysm on the AcomA is identified, corresponding to the MRA. *G*, Unsubtracted view right after the deployment of the flow diverter from the A2 segment of the left anterior cerebral artery into the A1 segment of the right anterior cerebral artery. The delivering wire and the microcatheter are still in place. *H*, DSA after flow-diverter detachment. The aneurysm is covered but still filling with contrast (*arrows* indicate the ends of the flow diverter). *I*, Control angiogram left vertebral artery injection. The P1/PcomA aneurysm is occluded; the flow diverter is patent. *J*, Control angiogram of the right common carotid artery injection. The AcomA aneurysm is closed. The flow diverter is patent but shows a proximal shortening into the left A2 segment, just covering the site of the aneurysm (this is patient 1, Online Supplemental Data).

The median time on single-antiplatelet therapy until last available follow-up was 13.5 days (range, 3–194 days). Four patients were controlled with MR imaging/MRA, 1 patient was controlled with CT/CTA, and 5 patients were controlled with DSA. One device-related complication occurred (explained in detail below). There were 2 intraprocedural but not flow-diverter-related complications: 1 aneurysm rupture due to attempted placement of a Woven EndoBridge endosaccular flow disruptor (MicroVention), which was then coiled and secured with a p48 MW HPC flow diverter afterward to cover an adjacent blood-blister-like aneurysm as well. This patient died 3 days later due to the sequelae of the SAH (patient 2, Online Supplemental Data). In 1 aneurysm, which was treated with a p48 MW HPC and adjunctive coiling, a coil dislocation occurred, which led to a superior cerebellar artery infarction. In both cases, the flow diverter remained open on control (patient 4, Online Supplemental Data). Further detailed results and patient characteristics are given in the Online Supplemental Data. Four sample patients are detailed in Figs 1–4.

Device-Related Complications

One patient (patient 9, Online Supplemental Data) with a broad-based berry-type aneurysm sitting asymmetrically on the inferior trunk of the left MCA right after the bifurcation was treated with a p48 MW HPC, applying regimen 1 (mentioned above under Materials and Methods). The patient initially was Hunt and Hess grade 1 and therefore clinically well, other than a significant headache, with no neurologic deficits. The procedure was performed successfully, and the patient awoke from anesthesia with still no neurologic deficits. A scheduled angiogram 24 hours after the procedure showed the flow diverter perfectly patent. However, after removal of the arterial sheath, groin compression and application of the pressure dressing, the patient suddenly developed an aphasia and a right hemiparesis up to an NIHSS of about 15 during about 10 minutes. In an immediately performed angiogram of the left internal carotid artery, a thrombosis of the overstented superior branch of the left MCA was noted, with the flow-diverting device being perfectly patent. A body weight–adapted bolus of tirofiban with consecutive body weight–adapted continuous infusion of tirofiban accompanied by an elevation of the mean arterial blood pressure was initiated; and the thrombus was resolved, and the hemiparesis and aphasia recovered completely. The patient was then switched to a dual-antiplatelet therapy with aspirin, 100 mg PO, and prasugrel, 10 mg PO. The patient remained stable under this therapy for about 10 days when he began to develop severe vasospasm in the left MCA territory, which was treated noninvasively as well as by an intra-arterial medical vasodilation treatment, but which finally led to significant infarction in the left MCA and anterior cerebral artery territory. The flow diverter remained patent throughout all of the controls. The reason for the initial acute thrombosis of the over-stented superior trunk is not clear, but it was presumably due to a vaso-vagal reaction during the groin compression and a
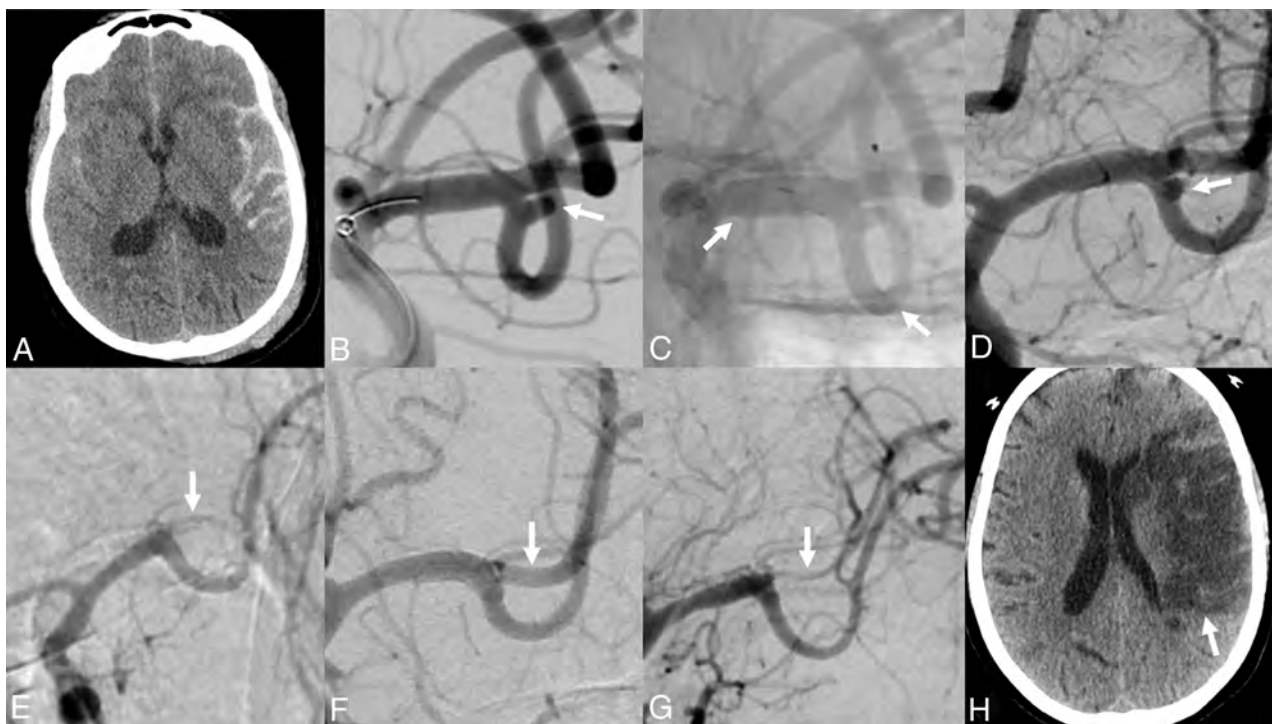
FIG 2. *A*, SAH primarily in the left Sylvian fissure on NCCT. The patient was Hunt and Hess 1 at that time, *B*, Aneurysm on the inferior trunk of the MCA, broad-based (*white arrow*). *C*, Implantation of a p48-MW-HPC flow-diverting stent from M1 into M2 (*white arrows pointing to stent endings*). *D*, DSA control 24 hours later. The flow diverter is patent; some stasis in the aneurysm is seen (*white arrow*). *E*, DSA control about 15 minutes later. Acute thrombosis developed on the superior trunk (*white arrow*). The flow diverter is patent. The patient had acute aphasia and hemiparesis after application of a pressure dressing in the groin. *F*, After therapy with IV tirofiban, the thrombosis disappeared (*white arrow*). The neurologic deficits resolved completely. *G*, After approximately 10 days, severe vasospam developed (*white arrow*). *H*, The vasospam, unfortunately, despite intense therapy, led to severe infarction of the left MCA and anterior cerebral artery territory (*white arrow*) (this is patient 9, Online Supplemental Data).

subsequent drop of blood pressure, which led to an overshoot of flow diversion and an initiation of the thrombosis in the superior trunk (Fig 2).

DISCUSSION

In our retrospective 3-center study, we present 10 patients with acute aneurysmal SAH treated with novel hydrophilic-coated flow diverters and a postprocedural single-antiplatelet therapy. The main observation is that all flow diverters remained patent with no ischemic events attributable to in-stent thrombosis of the flow diverters. However, 1 patient had a thrombotic complication in an overstented branch attributable to a blood pressure drop and overshoot of the flow-diverting effect of the flow diverter.

The rationale for the above-mentioned treatments is that the treatment of patients with acute aneurysmal SAH with flow diverters is complicated. Dual-antiplatelet therapy can result in hemorrhagic complications, elevating the risk of any subsequent surgical procedures and potentially increasing the risk and severity of aneurysm rerupture.[5,10,11]

Several publications, however, have evaluated the safety of flow-diverter treatment for ruptured intracranial aneurysms (Table). Recently, Ten Brinck et al[12] reported a series of 44 patients with acute SAH treated with standard flow diverters. The mean time from SAH to treatment was 3 days. In 9 cases,

additional coiling was used. Dual-antiplatelet therapy was used in all cases. Twenty-five (44%) periprocedural complications occurred in 20 different patients, 5 of which were intraprocedural, including 6 ischemic strokes (not related to vasospasm), 10 intracranial hemorrhages (2 ventricular shunt hematomas, 1 subdural hematoma), and 4 other non-CNS hemorrhages (gastrointestinal bleeds and retroperitoneal hematomas). Periprocedural stroke resulted in permanent neurologic deficits in 12 patients (27%). They concluded that flow-diverter treatment of ruptured intracranial aneurysms is associated with a high rate of periprocedural complications.[12]

A review by Cagnazzo et al,[13] in 2018, evaluated the topic in a meta-analysis that systemically reviewed studies from 2006 to 2018 addressing occlusion rates, complications, rebleeding, and factors influencing the outcome. They included 223 patients from 20 studies in their analysis. The mean interval between SAH and treatment was 6.7 days. Most patients were treated with a single flow diverter (75%) and some without additional coiling (81%). Most of the treatment targets were either blister, dissecting, or fusiform aneurysms; only 18% were saccular. A complete occlusion rate of 88.9% was reported, with immediate angiographic occlusion in 32%. The overall complication rate was 17.8%, with the highest rate of complications observed with saccular (23%) and posterior circulation aneurysms (27%). Ischemic complications occurred in 8%, and hemorrhagic events, in 7%. The rate of
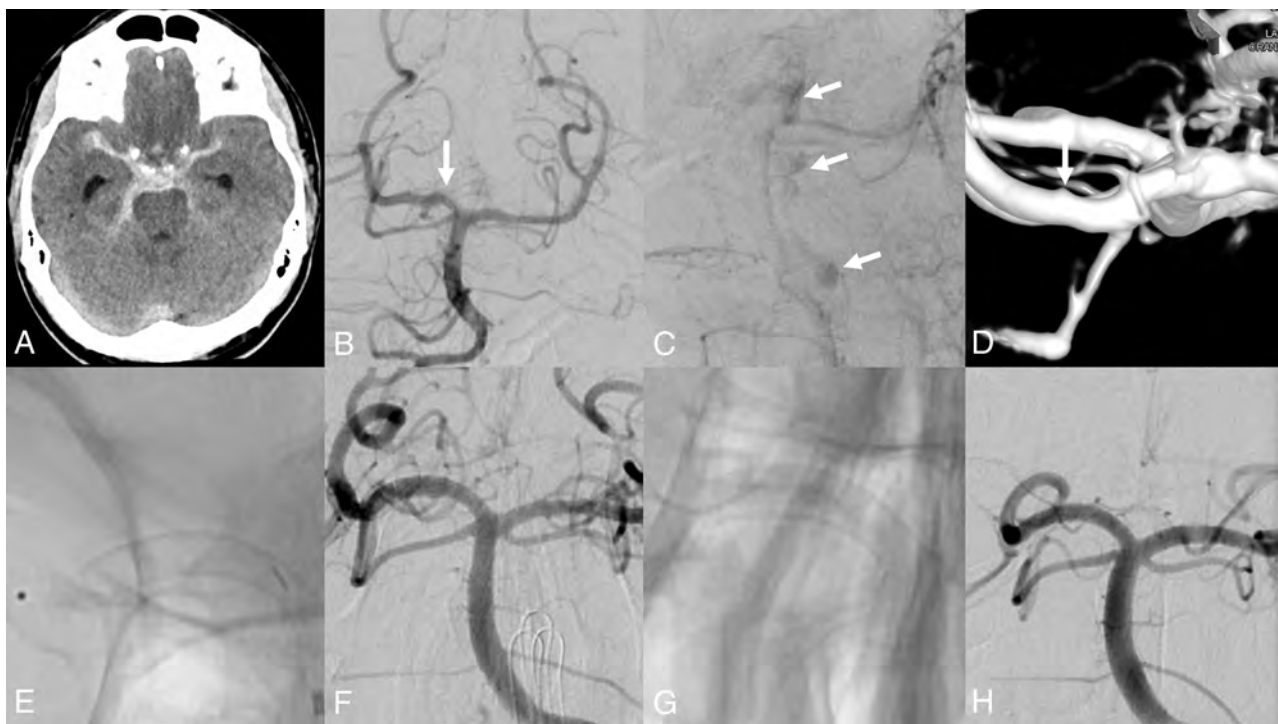
FIG 3. *A*, NCCT showing the SAH. *B*, Right vertebral artery injection. A faint extravasation around the P1/P2 segment of the right posterior cerebral artery is noted (*arrow*). *C*, Late-phase right vertebral artery injection, oblique view. The extravasation is demonstrated on the late phase (*arrows*). *D*, 3D DSA. A small outpouching at the proximal P2 segment is noted, consistent with a blood-blister-like aneurysm (*arrow*). *E*, Unsubtracted view from the treatment. The flow diverter and delivery wire are still in place. *F*, Final DSA run of the treatment. The flow diverter remains patent. *G*, Control angiography at 6 months. The flow diverter is unchanged and patent (*H*) (this is patient 3, Online Supplemental Data).

acute in-stent thrombosis was 4%. They reported a treatment-related mortality of 4.5% and a good neurologic outcome in 83%. Aspirin and clopidogrel were used in most cases (67.7%), with tirofiban, prasugrel, and abciximab used less frequently. The aneurysm rebleeding rate was 3%. They concluded that in their study, flow-diversion treatment led to a high complete occlusion rate; however, with a relatively high complication rate, especially in the posterior circulation.

Overall, the existing literature demonstrates that the treatment of acutely ruptured intracranial aneurysms with flow diverters is feasible and effective in achieving aneurysm occlusion but carries a substantial risk of periprocedural hemorrhagic and thrombotic complications. Fewer thrombogenic devices may obviate the requirement for dual-antiplatelet therapy and reduce the risk of periprocedural ischemic events. To this end, several surface modifications have been proposed to reduce the thrombogenicity of flow diverters.[6]

The PED Shield is covered with a 3-nm-thick layer of covalently bonded phosphorylcholine to reduce contact platelet activation.[10,14,15] In a study by Girdhar et al,[15] the PED Shield showed a lower thrombogenicity compared with other flow diverters. However, the PED Shield is supposed to be used under dual-antiplatelet therapy. The use of the PED Shield for recently ruptured aneurysms is off-label.[8,9] To date, there are 1 case report and 1 case series that reported the use of the PED Shield under single-antiplatelet therapy. Hanel et al,[10] in 2017, treated a patient with an acute SAH due to a fusiform aneurysm of the dominant

vertebral artery with 2 overlapping flow diverters and additional coiling of the aneurysm. The patient was preloaded with 325 mg of aspirin 2 hours before treatment. After the treatment, the patient was maintained on 81 mg of aspirin per day. For 24 hours after the procedure, the flow-diverter construct remained open, as proved by angiography. A third angiography after 10 days, however, demonstrated an occlusion of the flow diverter. It can be argued that the aspirin dose was way too low; therefore, an insufficient effect was achieved.[6]

In the retrospective multicenter study by Manning et al,[16] in 2019, fourteen patients were treated with the PED with Shield Technology for intracranial aneurysms with acute SAH. In all patients a single antiplatelet therapy with aspirin was used, with dosage at the discretion of the operator as well as a single dose of glycoprotein IIb/IIIa inhibitors. The time to treatment was 1 day. PED Shield placement was successful in all patients. Twelve patients received additional coiling. Complete aneurysm occlusion was achieved in 86%. Three symptomatic complications (4 in total) occurred; treatment mortality and morbidity were 7.1% and 7.1%. All of the symptomatic complications (2 hemorrhagic) were associated with postinterventional heparin use. In the last 5 patients with a twice-daily aspirin dosing regimen (twice, 100–150 mg daily), no complications occurred.

The p48 MW HPC is coated with a 10-nm thick glycan-based pHPC.[15] The pHPC aims to replicate the properties of carbohydrates on the endothelial surface ("surface coat"), thereby
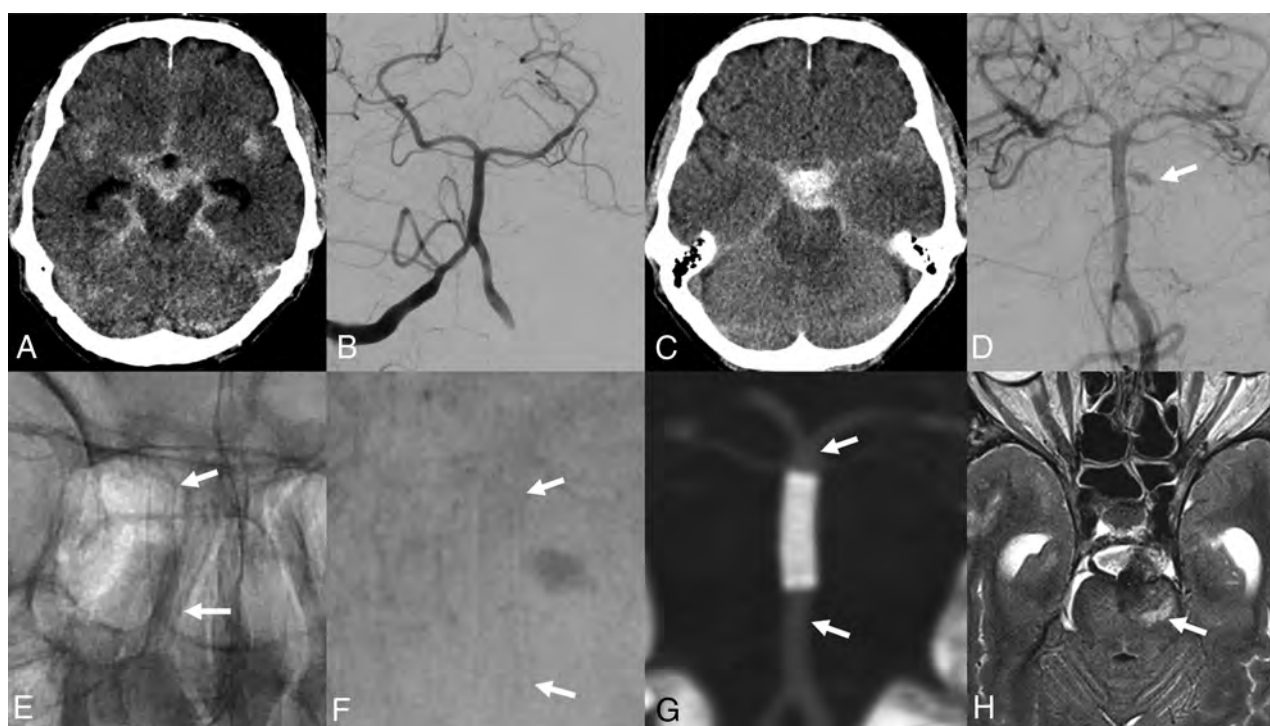
FIG 4. *A*, NCCT depicts an acute basal SAH. *B*, DSA on the day of the SAH shows no aneurysm. *C*, SAH rebleeding on day 5 after the initial bleed. *D*, NCCT now demonstrates an unusual aneurysm interpreted as a dissecting aneurysm of a basilar artery perforator (*arrow*). *E*, Treatment of the aneurysm with a hydrophilic-coated flow diverter; unsubtracted image right after deployment (*arrows* indicate the ends of the flow diverter). *F*, Subtracted image from the treatment. Slow filling of the aneurysm can be still seen (late arterial phase, *arrows* at the ends of the flow diverter). *G*, Five days after the treatment, CTA demonstrates that the flow diverter is patent (*arrows*). *H*, T2-weighted axial MR imaging 11 days after treatment. A small infarction in the territory of the aneurysm carrying the perforator can be seen (*arrow*). No infarcts due to the flow diverter are noted (this is patient 5, Online Supplemental Data).

Recent studies of FD treatment in acute SAH in specific conditions

Authors	Publication Date	Aneurysm Type	No. of Patients/ Mean Age	Treatments	Results/ Occlusion Rates	Complications
Maus et al[24]	2018	Dissecting vertebrobasilar	1556 yr	15 IAs, 22 FDSs, treatment within 12 h of SAH onset	36% Directly occluded; 100% occluded on FU	3 (Ischemia, vessel perforation, ongoing active bleeding)
Bhogal et al[22]	2018	Small IA (1–4 mm)	760 yr	7 IAs, 8 FDSs, treatment within 6.3 days from SAH (median)	100% Occluded on FU	None
Lozupone et al[23]	2018	8 BBAs, 9 dissecting IAs	174 yr	17 IAs, 21 FDs, treatment within 4.2 days (median)	12 of 15 Patients followed-up	12% Mortality; 12% morbidity
AlMatter et al[21]	2019	Saccular (18), fusiform (5), BBA (7), dissecting (15)	4558. 8 yr	45 IAs, FDSs as sole or adjunct device, treatment within 30 days after SAH	94.6% Complete occlusion on follow-up among survivors	13.3%; 2.2% Morbidity; 4.4% mortality

Note:—IA indicates intracranial aneurysm; FDS, flow-diverting stent; FU, follow-up; BBA, blood-blister-like aneurysm; FD, flow diverter.

reducing the thrombogenicity of the device.[6,17] To date, there are 2 case reports on single-antiplatelet regimens in pHPC-coated neuoroendovascular devices, 1 in the setting of acute SAH.[6,18] Henkes et al,[6] in 2019, reported a ruptured MCA bifurcation aneurysm treated endovascularly with a pHPC-coated bifurcation stent (pCONUS; phenox) and subsequent coiling. Before treatment, the patient was preloaded with 500 mg of aspirin IV. For a postprocedural regimen, they

chose to administer 500 mg of aspirin IV twice daily for the following days. On DSA after 13 days, the stent remained patent and the aneurysm was occluded. Clinically the condition of the patient improved to mild headaches and impaired short-term memory at a 3-month control.[6]

Schüngel et al[18] treated a patient with recurrent astrocytoma and an incidental broad-based anterior cerebral artery aneurysm. Because the aneurysm was increasing in size, it was treated electively with a p48 MW HPC flow diverter with planned dual-antiplatelet therapy for 6 months. However, after discharge, the patient stopped taking the dual-antiplatelet medication and switched to a phytopharmaceutical medication he designed on his own (primarily consisting of garlic oil). On DSA 3 months after the intervention, the stent was open, with only a mild in stent stenosis.

Very recently Bhogal et al,[19] in 2020, published a small retrospective series in which they reported their experience in aneurysm treatment with the p48 MW HPC and single-antiplatelet therapy. They treated 5 patients with 4 saccular aneurysms and 1 dissecting aneurysm. All patients were premedicated with 10 mg of prasugrel per day at least 5 days before the treatment and were kept on this medication afterward. One patient switched to 75 mg of aspirin per day after 2 weeks on her own volition. Angiographic follow-up was available in 4 patients at 8.5 months (range, 6–12 months). Three aneurysms were completely occluded. No thromboembolic complications occurred. One patient developed a localized hematoma from the treated dissecting aneurysm that was managed conservatively without any clinical sequelae.[19]

Also, very recently, Aguilar-Perez et al,[20] in 2020, reported their experience with the p48 MW HPC flow diverter in 8 patients with SAH due to ruptured intracranial aneurysms on single-antiplatelet therapy. They included patients up to 6 days after acute SAH. Mainly dissecting aneurysms were included. All stents could be successfully placed. They identified transient thrombus formation in 50% of their patients. In the follow-up period, 1 patient developed an in-stent thrombosis after 3 days, which resolved after a switch to dual-antiplatelet therapy. They recorded no rebleeding. Two of their patients died due to vasospasm. They used 2 single-antiplatelet regimens. They started with either 100 mg of aspirin or 10 mg of prasugrel PO 3 days before the procedure or with a loading dose of 500 mg of aspirin IV or 30 mg of prasugrel PO 3 hours before the procedure. They heparinized the patients during the procedure. After the procedure, they kept the patients on either 500 mg of aspirin IV or 10 mg of prasugrel PO. They concluded that their above-mentioned treatment is an option in selected cases but has to be applied with great caution because thromboembolic complications can be a problem.[20]

CONCLUSIONS

Hydrophilic-coated devices (like p48 MW HPC or the p46 MW HPC) may be used with single-antiplatelet therapy in selected clinical situations in which dual-antiplatelet therapy might be hazardous. This strategy is primarily relevant in the setting of ruptured aneurysms, which are unsuitable for standard endovascular or surgical treatments. Which drug

should be used for single-antiplatelet therapy, however, remains to be determined. Aspirin is a possible option, but other drugs like prasugrel might have advantages. In any case, the proper dosage in the acute phase after SAH also remains an issue. Prospective studies are underway to define the safety and effectiveness of this strategy.

REFERENCES

1. Pierot L, Biondi A. **Endovascular techniques for the management of wide-neck intracranial bifurcation aneurysms: a critical review of the literature.** J Neuroradiol 2016;43:167–75 CrossRef Medline

2. Bhatia KD, Kortman H, Orru E, et al. **Periprocedural complications of second-generation flow diverter treatment using Pipeline Flex for unruptured intracranial aneurysms: a systematic review and meta-analysis.** J NeuroIntervent Surg 2019;11:817–24 CrossRef Medline

3. Rajah G, Narayanan S, Rangel-Castilla L. **Update on flow diverters for the endovascular management of cerebral aneurysms.** Neurosurg Focus 2017;42:E2 CrossRef Medline

4. Texakalidis P, Bekelis K, Atallah E, et al. **Flow diversion with the Pipeline embolization device for patients with intracranial aneurysms and antiplatelet therapy: a systematic literature review.** Clin Neurol Neurosurg 2017;161:78–87 CrossRef Medline

5. Kung DK, Policeni BA, Capuano AW, et al. **Risk of ventriculostomy-related hemorrhage in patients with acutely ruptured aneurysms treated using stent-assisted coiling.** J Neurosurg 2011;114:1021–27 CrossRef Medline

6. Henkes H, Bhogal P, Aguilar Pérez M, et al. **Anti-thrombogenic coatings for devices in neurointerventional surgery: case report and review of the literature.** Interv Neuroradiol 2019;25:619–27 CrossRef Medline

7. Hellstern V, Aguilar-Pérez M, AlMatter M, et al. **Microsurgical clipping and endovascular flow diversion of ruptured anterior circulation blood blister-like aneurysms.** Interv Neuroradiol 2018;24:615–23 CrossRef Medline

8. Martínez-Galdámez M, Lamin SM, Lagios KG, et al. **Periprocedural outcomes and early safety with the use of the Pipeline Flex Embolization Device with Shield Technology for unruptured intracranial aneurysms: preliminary results from a prospective clinical study.** J NeuroInterv Surg 2017;9:772–76 CrossRef Medline

9. Perez P, Lukaszewicz AC, Lenck S, et al. **Platelet activation and aggregation after aneurysmal suarachnoid hemorrhage.** BMC Neurol 2018;18:57 CrossRef Medline

10. Hanel RA, Aguilar-Salinas P, Brasiliense LB, et al. **First US experience with Pipeline Flex with Shield Technology using aspirin as antiplatelet monotherapy.** BMJ Case Rep 2017;2017:bcr2017219406 CrossRef Medline

11. Bodily KD, Cloft HJ, Lanzino G, et al. **Stent-assisted coiling in acutely ruptured intracranial aneurysms: a qualitative, systematic review of the literature.** AJNR Am J Neuroradiol 2011;32:1232–36 CrossRef Medline

12. Ten Brinck MF, Jäger M, de Vries J, et al. **Flow diversion treatment for acutely ruptured aneurysms.** *J Neurointerv Surg* 2020;12:283–88 CrossRef Medline

13. Cagnazzo F, di Carlo DT, Cappucci M, et al. **Acutely ruptured intracranial aneurysms treated with flow-diverter stents: a systematic review and meta-analysis.** *AJNR Am J Neuroradiol* 2018;39:1669–75 CrossRef Medline

14. Cumberland DC, Gunn J, Malik N, et al. **Biomimicry, 1: PC.** *Semin Interv Cardiol* 1998;3:149–50 Medline

15. Girdhar G, Li J, Kostousov L, et al. **In-vitro thrombogenicity assessment of flow diversion and aneurysm bridging devices.** *J Thromb Thrombolysis* 2015;40:437–43 CrossRef Medline

16. Manning NW, Cheung A, Phillips TJ, et al. **Pipeline shield with single antiplatelet therapy in aneurysmal subarachnoid haemorrhage: multicentre experience.** *J Neurointerv Surg* 2019;11:694–8 CrossRef Medline

17. Lenz-Habijan T, Bhogal P, Peters M, et al. **Hydrophilic stent coating inhibits platelet adhesion on stent surfaces: initial results in vitro.** *Cardiovasc Intervent Radiol* 2018;41:1779–85 CrossRef Medline

18. Schüngel MS, Hoffmann KT, Quäschling U, et al. Anterior cerebral artery (A1 segment) aneurysm: abandoned dual platelet inhibition shortly after endovascular treatment with a hydrophilic polymer-coated flow diverter p48_HPC; good clinical outcome and early aneurysm occlusion. In: Henkes H, Lylyk P, Ganslandt O, eds. *The Aneurysm Casebook*. Springer; 2019:1–8 CrossRef

19. Bhogal P, Bleise C, Chudyk J, et al. **The p48_HPC antithrombogenic flow diverter: initial human experience using single antiplatelet therapy.** *J Int Med Res* 2020;48:300060519879580 CrossRef Medline

20. Aguilar-Perez M, Hellstern V, AlMatter M, et al. **The p48 flow modulation device with hydrophilic polymer coating (HPC) for the treatment of acutely ruptured aneurysms: early clinical experience using single antiplatelet therapy.** *Cardiovasc Intervent Radiol* 2020;43:740–48 CrossRef Medline

21. AlMatter M, Aguilar Pérez M, Hellstern V, et al. **Flow diversion for treatment of acutely ruptured intracranial aneurysms: a single center experience from 45 consecutive cases.** *Clin Neuroradiol* 2019 November 4. [Epub ahead of print] CrossRef Medline

22. Bhogal P, Henkes E, Schob S, et al. **The use of flow diverters to treat small (≤5 mm) ruptured, saccular aneurysms.** *Surg Neurol Int* 2018;9:216 CrossRef Medline

23. Lozupone E, Piano M, Valvassori L, et al. **Flow diverter devices in ruptured intracranial aneurysms: a single-center experience.** *J Neurosurg* 2018;128:1037–43 CrossRef Medline

24. Maus V, Mpotsaris A, Dorn F, et al. **The use of flow diverter in ruptured, dissecting intracranial aneurysms of the posterior circulation.** *World Neurosurg* 2018;111:e424–33 CrossRef Medline

Postinterventional Assessment after Stent and Flow-Diverter Implantation Using CT: Influence of Spectral Image Reconstructions and Different Device Types

C. Zaeske, T. Hickethier, J. Borggrefe, L. Goertz, R. Dettmeyer, M. Schlamann, N. Abdullayev, and C. Kabbasch

ABSTRACT

BACKGROUND AND PURPOSE: CTA provides a noninvasive alternative technique to DSA in the follow-up after endovascular aneurysm treatment to evaluate aneurysm occlusion and exclude intraluminal narrowing after stent or flow-diverter implantation; however, assessability may be impeded by stent material artifacts. The objective of this in vitro study was to compare the visual assessability of different conventional stents and flow diverters as well as different reconstructions of dual-layer CT images.

MATERIALS AND METHODS: Four conventional intracranial stents and 4 flow diverters were implanted in identical aneurysm phantoms. Conventional and monoenergetic images (40, 50, 60, 90, 120, 180 keV) were acquired to evaluate attenuation alteration, visible lumen diameter, and SNR. Image quality was rated subjectively by 2 independent radiologists using a 4-point Likert scale.

RESULTS: Low kiloelectron volt (40–60 keV) monoenergetic reconstructions showed an improved SNR and an improved lumen density ratio compared with high kiloelectron volt reconstructions (90–180 keV) and conventional reconstructions, however without reaching significance compared with the latter. Assessment of the adjacent aneurysm and subjective evaluation was not affected by the imaging technique and stent type. Artifact susceptibility varied with the device used and increased among flow diverters.

CONCLUSIONS: Low kiloelectron volt reconstructions improved the assessment of the stent lumen in comparison with high kiloelectron volt reconstructions. No significant improvement in image quality could be shown compared with conventional images. For some devices, iodine-specific reconstructions led to severe artifacts and are therefore not recommended. There was no relevant improvement in the assessability of the adjacent aneurysm.

ABBREVIATIONS: ID = iodine density; INW = iodine no water

Intracranial stent implantation is a well-established technique for endovascular treatment of intracranial aneurysms, stenoses, and dissections. In the context of stent-assisted coiling, the stent serves as a scaffold that creates a physical barrier between the aneurysm neck and parent vessel to prevent coil migration or protrusion, which can lead to thromboembolic complications.[1] Moreover, the stent can preserve vessel patency and provides more stable aneurysm occlusion, requiring retreatment less frequently than coiling alone.[1,2] Flow diverters are stents with special architectural properties that were developed to facilitate the

treatment of complex sidewall aneurysms and reduce the rate of associated complications.[3] In contrast to the merely supportive use of the stent in the context of stent-assisted coiling, the flow diverter functions as a stand-alone device that leads to consecutive aneurysm closure by flow diversion in the parent vessel and consecutive aneurysm thrombosis across time.[3]

Despite relevant technical improvements across the years, complications can occur after stent-assisted coiling and flow-diverter implantation, the most important of which are aneurysm remnants, aneurysm recanalization, and in-stent constriction.[4,5]

DSA represents the criterion standard to evaluate vessel patency and aneurysm occlusion.[5] However, DSA is an invasive procedure with a low-but-not-negligible complication rate.[5] A noninvasive and time-saving option for follow-up imaging with lower radiation exposure would therefore be desirable. In contrast, CTA is noninvasive and less time-consuming and has a lower radiation exposure; however, stent-associated artifacts hamper the assessment of the adjacent vessel and aneurysm sac, resulting in a lower diagnostic sensitivity for in-stent stenosis and aneurysm remnants.[5] These artifacts result from various

mechanisms, including beam-hardening, scatter effects, and Poisson noise, with beam-hardening being considered the main factor.[6] In this context, the extent of the artifacts depends, in particular, on the individual stent type, stent material, and the corresponding x-ray attenuation. By implication, reduction of stent-associated artifacts would presumably increase the diagnostic sensitivity of CTA so that it could be ultimately used as an alternative diagnostic tool to DSA. Previous studies on various medical implants have shown that monoenergetic reconstructions of modern dual-layer CT systems can reduce artifacts significantly.[6,7]

In contrast to conventional CT, in which the characterization of tissues is based on the respective attenuation of the x-ray spectrum of a certain energy level, dual-energy CT determines the attenuation properties of each tissue at 2 different energy levels, allowing a variety of additional image analyses. One of these additional images is monoenergetic reconstruction, for which many different energy levels can be used. This allows the calculation of the optimal contrasted image data for a particular diagnostic need. The, dual-layer CT is a special variant of the dual-energy CT, in which the spectral separation takes place at the level of the detectors so that the dual-energy information is available for each examination, and it shows a high degree of temporal and spatial correlation.[8] Although a large number of clinical applications have already been described, scientific data on the influence of dual-layer CT on different neuroradiologic stents and its potential to improve image quality of the CTA by artifact reduction are not yet available.
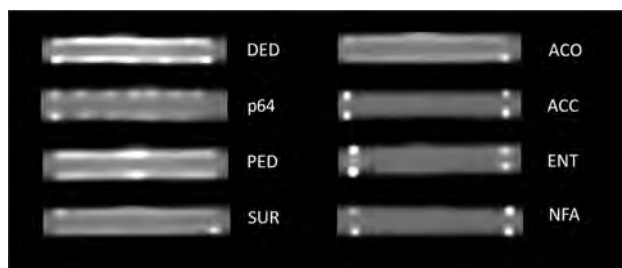
FIG 1. CT of the examined devices. *Left column*: flow diverters. *Right column*: conventional stents. The windowing was adjusted according to the lowest artifact interference of all stents (same settings for all devices).

The objective of this in vitro study was to compare the visual assessability of the aneurysm and stent lumen after implantation of different conventional stents and flow diverters using dual-layer CT image reconstructions.

MATERIALS AND METHODS

Evaluated Devices and Experimental Setup
In preparation for the study, 8 devices (4 flow diverters, 4 conventional stents) were implanted in 8 identical aneurysm phantoms (Fig 1), allowing a comparative analysis of the stent types.

The aneurysm phantoms consisted of a parent vessel with a seated, unilobular, saccular aneurysm with a wall thickness of 0.3 mm. They were manufactured from synthetic resin (Elastic 50A; Formlabs) using a 3D printer, which resulted in density values comparable with those of human vessels in native cranial CT (approximately 30 HU).[9] The diameter of the parent vessel of the aneurysm phantom was 4 mm with a length of 40 mm, and the aneurysm measured 15 × 10 × 10 mm. The characteristics of the stent types used are shown in Tables 1 and 2 and depicted in Fig 1.

After we manually implanted the devices, the aneurysm phantoms were filled with contrast medium (300 mg iohexol/mL, Accupaque 300; GE Healthcare Buchler GmbH & Co.KG), which was titrated with saline solution to a density value of 280 HU at 120 kV(peak), according to the typically expected vessel density values of an intracranial CTA,[10] and they were sealed at both ends. The models were then positioned in a human skull specimen in a stable position in the area of the sella turcica to simulate artifacts of the skull. This setup was positioned on the CT scanner table in the gantry orthogonal to the z-axis and centered in the middle of the isocenter of the scanner (Online Supplemental Data).

The term "stented" vessel is used to refer to the vessel area in which the device was positioned, regardless of whether a flow diverter or stent was inserted. The term "native" vessel refers to an unstented and artifact-free vessel section.

CT Acquisition Parameters
CT data were acquired on a 64–detector row spectral detector CT scanner (IQon Spectral CT; Philips Healthcare). The same institutional CT protocol used for craniocervical angiography in patients was used for data acquisition (section collimation, 64 ×

Table 1: Details of the flow diverters used in this study

Flow Diverter	Abbreviation	Diameter × Length [mm]	Manufacturer	Main Material	Metal Coverage
Derivo	DED	4 × 24	Acandis	Nitinol, platinum	35%–38%
p64	p64	4 × 40	Phenox	Nitinol	34%
Pipeline Flex with Shield technology	PED	4 × 20	Medtronic	Cobalt chromium, platinum	30%–35%
Surpass Streamline	SUR	4 × 40	Stryker	Cobalt chromium	30%

Table 2: Details of the stents used in this study

Stent	Abbreviation	Diameter × Length [mm]	Manufacturer	Main Material	Metal Coverage
Accero	ACO	4 × 20	Acandis	Nitinol platinum	15%–19%
Acclino Flex Plus	ACC	4 × 35	Acandis	Nitinol	6%–9%
Enterprise 2	ENT	4 × 30	Codman	Nitinol	10%
Neuroform Atlas	NFA	4 × 24	Stryker	Nitinol	6%–9%
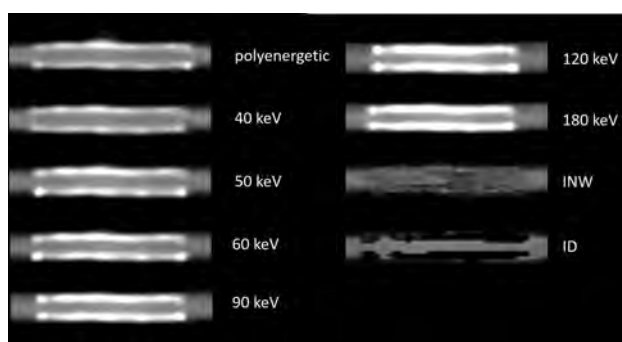
FIG 2. Composition of different reconstructions of the DED. The windowing was adjusted according to the lowest artifact interference and the most comparable vessel appearance (adjusted settings depending on the type of reconstruction; see Materials and Methods, CT Acquisition Parameters).

0.625 mm; rotation time, 0.27 seconds; voltage, 120 kV; tube current–time product, 180 mAs; and resulting CT dose index volume, 16.3 mGy). From the acquired raw data, images were reconstructed using a section thickness of 0.67 mm and an increment of 0.35 mm with a (statistical) hybrid iterative reconstruction algorithm (iDose4; Philips Healthcare) using the iteration level 3, kernel B. Conventional polyenergetic images (120 kVp), virtual monoenergetic images with different energy levels (40, 50, 60, 90, 120, 180 keV), as well as iodine no water (INW) and iodine density (ID) reconstructions were calculated (Fig 2).

Because contrast conditions vary considerably among the different monoenergetic images, individually adjusted window settings for each reconstruction were necessary. Window level and window width were chosen in a joint evaluation session by the 2 readers for an optimized assessment of the stent lumen. With this method, the reviewers jointly determined the most suitable window settings for each type of reconstruction and used them for all similar reconstructions of the different devices. Both subjective and objective evaluations were performed using the specific a priori-determined window settings.

CT Data Analysis
The quantitative data analysis was performed on a separate offline workstation (IntelliSpace Portal; Philips Healthcare).

In the objective analysis, we evaluated the following parameters:

- Lumen width ratio: defined as the visible lumen width of the stented vessel divided by the visible lumen width of the native vessel and measuring the extent of artifact-related restrictions of the assessable vessel lumen
- Lumen density ratio: defined as the density of the stented vessel divided by the density of the native vessel and measuring the extent of artifact-related distortions of the vessel density values. In the case of iodine-specific reconstructions, this parameter is referred to as the lumen iodine content ratio because no density is measured in iodine-specific reconstructions (see below)
- Aneurysm density ratio: defined as the density of the aneurysm divided by the density of the native vessel and measuring

the extent of artifact-related distortions of the aneurysm density values
- Aneurysm neck density ratio: defined as the density of the aneurysm neck adjacent to the stented vessel divided by the density of the native vessel and measuring the extent of artifact-related distortions of the aneurysm neck density values
- SNR: defined as the ratio of the density of the native vessel divided by the image noise (see below for definition of image noise) and measuring the general contrast conditions of the respective reconstruction.

The diameters of the native vessel and the stented vessel were determined for each reconstruction with the previously defined window settings by 2 independent readers and then averaged. The measurements were performed in standardized positions in longitudinal reformations along the centerline of the vessel.

Density measurements with the largest possible ROI (which, however, did not include artifacts or other interfering factors) were performed for all reconstructions and devices at predefined positions as follows: 1) inside the lumen of the aneurysm, 2) in the region of the aneurysm neck (immediately adjacent to the device), 3) within the native vessel lumen, and 4) within the stented vessel lumen (Online Supplemental Data). The corresponding ratios were used to achieve results as comparable as possible with the native vessel as a reference.

With regard to the density ratios, a separate evaluation of the iodine-specific reconstructions was performed because these reconstructions do not measure the density in Hounsfield units, but the iodine content. In INW reconstructions on the one hand, all waterlike substances are suppressed and the measured values are expressed as iodine concentration in milligrams/milliliter. In iodine density reconstructions on the other hand, all pixels that do not contain iodine are suppressed and the iodine concentration is also given in milligrams/milliliter.[11]

To define image noise, we performed standardized density measurements in an area without any content adjacent to the stent. The obtained SD in this ROI was then defined as image noise.

To allow a first comparison with clinical results, we compared image data from clinical examinations of 2 patients, one with an implanted flow diverter (Derivo embolization device [DED]; Acandis) and one with an implanted conventional stent (Neurform Atlas Stent System [NFA]; Stryker), with the in vitro results of our study with respect to the lumen density ratio and SNR (in both cases the adjacent aneurysm was additionally treated so that it could not be included in the evaluation).

Subjective Analysis
The subjective assessability of the vessel lumen and the aneurysm neck was performed independently by 2 blinded readers. A 4-point Likert scale was used to assess the aneurysm neck: 1) aneurysm neck not definable due to artifacts, no assessment possible; 2) aneurysm neck, in principle, definable, but density appears distorted, limited assessment possible; 3) aneurysm neck definable, residual artifacts, contrast medium intake assessable; 4) aneurysm neck definable, no artifacts, unrestricted assessment. We also assessed the vessel lumen: 1) vessel lumen not definable due to

Lumen density ratio
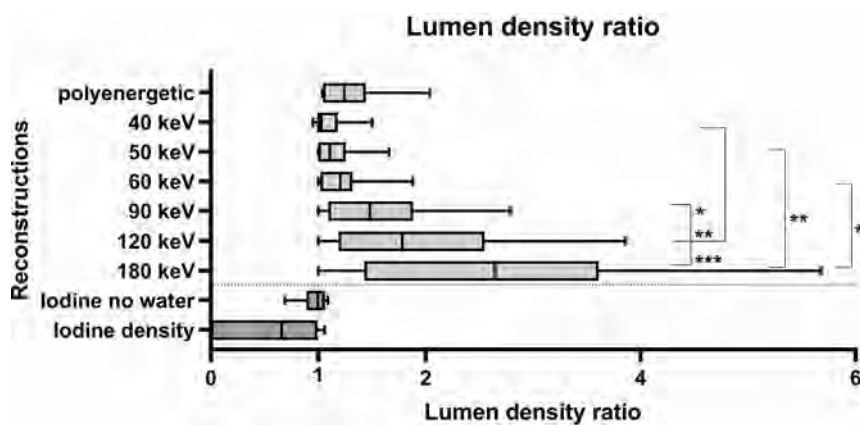
FIG 3. Graphic illustration of the different lumen density ratios/lumen iodine content ratios. *Asterisks* mark statistical significance (*P < .05, **P < .01, ***P < .001).

artifacts; 2) vessel lumen, in principle, definable, but density appears to be clearly falsified/not assessable; 3) vessel lumen definable, contrast assessable, residual artifacts; and 4) vessel lumen definable, contrast assessable, no artifacts.

Statistical Analysis

Statistical analysis was performed using GraphPad Prism, Version 8.0.0 for Windows (GraphPad Software). A 2-tailed P value < .05 was considered statistically significant. Parametric results are presented as mean [SD].

Normal distribution was tested using the Shapiro-Wilk test. Variances between the devices concerning the continuous data were compared using an ANOVA for matched parametric data with the Greenhouse-Geisser correction to compensate the variability of differences and then using post hoc testing for multiple comparisons by means of the Tukey test. For matched, nonparametric data, we used the Friedman test, with subsequent post hoc testing for multiple comparisons by means of the Dunn test. In the comparison of the iodine-specific reconstructions, we used the Wilcoxon matched-pairs signed rank test.

With regard to the subjective reading, the corresponding weighted Cohen κ was calculated to assess the interobserver agreement. The Cohen κ was rated on the following scale: $\kappa <$ 0, no agreement; $\kappa = 0.0–0.2$, slight agreement; $\kappa = 0.21–0.40$, fair agreement; $\kappa = 0.41–0.60$, moderate agreement; $\kappa = 0.61–0.80$, substantial agreement; $\kappa = 0.81–1.00$, almost perfect agreement.[12]

RESULTS
Reconstructions: Objective Reading

Lumen Width Ratio. Reconstructions with 40 and 50 keV had the highest lumen width ratio, with an assessable proportion of about 70% (mean lumen width ratio: 40 keV, 0.73 [SD, 0.21] keV; 50 keV, 0.73 [SD, 0.18] keV); however, the significance was not reached in the comparison with other monoenergetic reconstructions and the conventional polyenergetic images. Significant differences were found between the 40–60 keV reconstructions and the INW and ID reconstructions (40 keV versus INW, $P = .001$; 50 keV versus INW, $P = .006$; 60 keV versus INW, $P = .003$; 40 keV versus ID, $P = .01$; 50 keV versus ID, $P = .04$; 60 keV

versus ID, $P = .02$). For a more detailed description of the results, see the Online Supplemental Data.

Lumen Density Ratio. Low kiloelectron volt monoenergetic reconstructions (40–60 keV) had a lumen density ratio of almost 1.0, which corresponds to an almost undistorted representation of the vessel lumen. Increasing kiloelectron volt values correlated with a higher lumen density ratio, which indicates an increasing distortion of the density of the vessel lumen (Fig 3 and Online Supplemental Data). There were no statistically significant differences in comparison with the conventional polyenergetic images.

Significant differences were found with regard to the monoenergetic reconstructions when comparing the 40-keV reconstructions with the 90-keV ($P = .03$), 120-keV ($P = .001$), and 180-keV reconstructions ($P < .001$); the 50-keV reconstructions with the 180-keV reconstructions ($P = .006$); and the 60-keV reconstructions with the 180-keV reconstructions ($P = .02$). The conventional, polyenergetic images showed results comparable with the monoenergetic reconstructions in a range between 60 and 90 keV.

Aneurysm and Aneurysm Neck Density Ratio. There were no significant differences regarding the aneurysm and aneurysm neck density ratios. Monoenergetic and polyenergetic reconstructions both resulted in values around 1.0 (exemplarily for 40 keV; mean aneurysm density ratio, 1.07 [SD, 0.09]; mean aneurysm neck density ratio, 1.09 [SD, 0.09]). For a more detailed description of the results, see the Online Supplemental Data.

SNR. Low-energy monoenergetic reconstructions were associated with higher signal-to-noise ratios with a continuous decrease of the values at higher kiloelectron volt levels and the lowest value at 180 keV. The SNRs of the polyenergetic conventional images were within the range of the 50- and 60-keV monoenergetic reconstructions. Because the image noise in the INW and ID reconstructions each resulted in values of zero, no reasonable SNR could be calculated here. Results are graphically illustrated in Fig 4. All of the results can be found in the Online Supplemental Data.

The differences reached a significance level in comparison with the following reconstructions: 40 keV versus 90 keV ($P = .004$), 40 keV versus 120 keV ($P < .001$), 40 keV versus 180 keV ($P < .001$), 50 keV versus 120 keV ($P = .005$), and 50 keV versus 180 keV ($P = .003$).

Iodine-Specific Reconstructions. With regard to the lumen iodine content ratio, the INW reconstructions showed a mean value of 0.96 [SD, 0.13]; and the ID reconstructions, a mean value of 0.54 [SD, 0.50] without reaching a statistically significant level.

The values of the aneurysm iodine content ratio and the aneurysm neck iodine content ratio showed similar mean values of
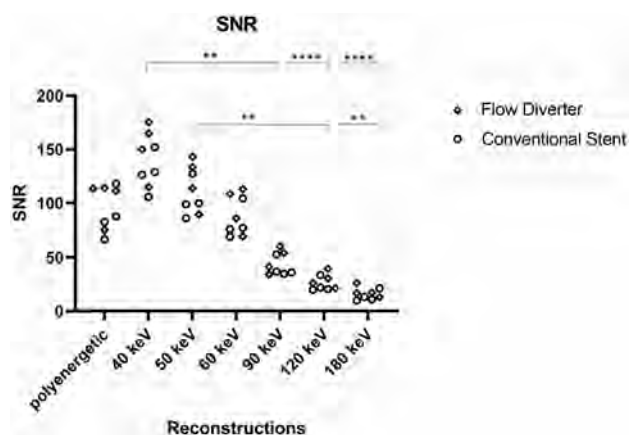
FIG 4. Graphic illustration of the SNR. *Asterisks* mark statistical significance (*$P < .05$, **$P < .01$, ***$P < .001$, ****$P < .0001$).

INW and ID reconstructions, respectively (aneurysm iodine content ratio: INW, 1.07 [SD, 0.07]; ID, 1.08 [SD, 0.09]; aneurysm neck iodine content ratio: INW, 1.08 [SD, 0.07]; ID, 1.09 [SD, 0.09], without significant differences between the reconstructions, either.

Reconstructions: Subjective Reading

The interobserver agreement yielded a weighted Cohen κ of 0.97 for the assessment of the stented vessel and a weighted Cohen κ of 0.97 for the assessment of the aneurysm neck.

Subjective assessability of the vessel lumen and the aneurysm neck was best at 40 keV (vessel lumen, 3.5 [SD, 0.53]; aneurysm neck, 3.69 [SD, 0.46]), and decreased with increasing kiloelectron volt (180 keV: vessel lumen, 3.13 [SD, 0.99]; aneurysm neck, 3.00 [SD, 0.93]). The worst results were obtained for the iodine-specific reconstructions (INW: vessel lumen, 2.38 [SD, 1.51]; aneurysm neck, 2.5 [SD, 1.41]; ID: vessel lumen, 2.50 [SD, 1.41]; aneurysm neck, 2.6 [SD, 1.41]). For a more detailed description of the results, see the Online Supplemental Data.

However, no statistical significance was reached when comparing the subjective assessability of the vessel lumen in the different image reconstructions. With regard to the assessability of the aneurysm neck, a significance level was achieved with the initial Friedman test ($P < .001$) but could then no longer be demonstrated for a specific comparison in the post hoc multiple comparisons.

Devices: Objective Reading

Lumen Width Ratio. A comparison of the different devices in the 40-keV reconstructions, for which vessels and aneurysms showed the best assessability in the previously performed analysis of different reconstructions, revealed that the different devices lead to artifacts of a varying extent. The lowest artifacts with a subsequently high lumen width ratio were found for the Acclino Flex Plus stent (ACC; Acandis), Enterprise stent (ENT; Codman), and NFA (ACC, 0.98; ENT, 0.95; NFA, 0.97). In contrast, the highest amount of artifacts with a consecutively low lumen-width ratio found for the devices DED and Pipeline Embolization Device (PED; Medtronic) were DED at 0.50 and PED at 0.50. The other devices ranged between the above-mentioned results (Accero stent [ACO], Acandis), 0.68; p64, Phenox, 0.60; and Surpass Streamline flow diverter [SUR], Stryker, 0.62).

Lumen Density Ratio. When comparing the devices at 40 keV, most lumen density ratios were close to 1.0 without relevant differences and only minor deviations for the PED (1.20) and SUR (1.50) devices.

However, the lumen density ratios for the other kiloelectron volt levels showed significant deviations, with a strong increase in kiloelectron volt values, especially for the SUR device (40 keV: 2.04/180 keV: 5.68) and a moderate increase for the ACO (40 keV: 0.95/180 keV: 3.61), DED (40 keV: 1.36/180 keV: 3.61), p64 (40 keV: 1.26/180 keV: 2.30), and PED (40 keV: 1.47/180 keV: 2.99). For the other devices, there was no or only a very small increase (ACC, 40 keV: 0.99/180 keV: 1.49; ENT, 40 keV: 1.00/180 keV: 1.00; NFA, 40 keV: 0.99/180 keV: 1.41). A graphic illustration of the different devices regarding the lumen density ratio in the 40-keV reconstruction can be found in the Online Supplemental Data.

Aneurysm and Aneurysm Neck Density Ratios. Aneurysm and aneurysm neck density ratios were comparable among the reconstructions and individual stent types with values around 1.0, respectively.

Iodine-Specific Reconstructions. With regard to the lumen iodine content ratio, there were strong fluctuations depending on the device. For the INW reconstructions, these were slightly less pronounced, with fluctuations between 0.69 (ACO) and 1.09 (SUR). For the ID reconstructions, these were more evident, with fluctuations between 0.00 (ACO, DED, SUR) and 1.06 (p64). The devices previously described as less susceptible to artifacts were again showing values close to 1.0 in both iodine-specific reconstructions (INW: ACC, 0.9; ENT, 1.00; NFA, 0.98; ID: ACC, 0.97; ENT, 1.00; NFA, 0.97). Regarding aneurysm and aneurysm neck iodine content, INW as well as ID reconstructions showed values around 1.0 for each of the devices without considerable deviation.

Devices: Subjective Reading

The assessability of the vessel lumen in the 40-keV reconstruction was rated as good or very good (4 points: ACC, ACO, ENT, NFA, p64; 3 points: DED, PED, SUR). Corresponding to the results of the objective evaluation, the INW and ID reconstructions in combination with certain devices showed significant limitations in the subjective image quality (ACO, PED, SUR [INW only]), while with other devices (ACC, ENT, NFA), the lumen and aneurysm could be assessed well. The comparison of the different devices with regard to the assessability of the aneurysm neck has led to comparable results and was, therefore, not analyzed separately.

Clinical Findings. A preliminary analysis of clinical data from routine imaging for a flow diverter (DED) and a conventional stent (NFA) showed a course of the lumen density ratio for the flow diverter comparable with that of the in vitro data, with the lowest lumen density ratio at 40 keV and an increase with increasing kiloelectron volt values (Online Supplemental Data).

When we compared the flow diverter and conventional stent, the values obtained for the conventional stent showed significantly less variation among the different reconstructions, which corresponds to the in vitro results of the comparison among the different devices. Regarding a preliminary analysis of the SNR, a comparable course of the clinical and in vitro data was also observed (Online Supplemental Data) with the best SNR at 40 keV and a decrease of SNR with increasing kiloelectron volt values.

DISCUSSION

The results of this study provide, so far, unavailable information of dual-layer CT imaging of vessels after implantation of intracranial stents and flow diverters. On the one hand, novel data on the benefit of spectral reconstructions of a dual-layer CT could be obtained, and on the other hand, new insights into the influence of different implanted devices on the assessment of the parent vessels and adjacent aneurysms were achieved.

Reconstructions

Our results indicated that monoenergetic reconstructions (without iodine-specific reconstructions) provide better image quality and consequently superior assessment of the stent lumen in the low kiloelectron volt range. This finding was demonstrated by a significantly higher lumen density ratio of low kiloelectron volt reconstructions (40–60 keV) compared with high kiloelectron volt reconstructions (90–180 keV). Likewise, the low kiloelectron volt reconstructions (40–50 keV) had a significantly better SNR compared with the higher kiloelectron volt reconstructions (90–180 keV). An analysis of the lumen width ratio and the subjective assessment of the vessel lumen did not reach the defined significance level; however, it showed a similar trend. In the comparison of monoenergetic and conventional polyenergetic images, significance could not be reached. However, there were pronounced differences among the different devices and their potential for artifact reduction, so further subgroup analyses with larger case numbers and a classification depending on the artifact susceptibility should verify the potential for artifact reduction for particularly artifact-susceptible devices. This point is discussed in more detail in the paragraph "Devices."

A preliminary analysis of clinical data supports the results regarding the comparison of different reconstructions in terms of lumen density ratio and SNR. Again, the analyzed flow diverters showed the best lumen density ratio and SNR at 40 keV, with a consecutive increase of the lumen density ratio and a decrease of the SNR with rising kiloelectron volt values. It could also be shown that regarding the lumen density ratio, different devices have a different potential for improvement of image quality, shown by considerably less variation in the comparison with different monoenergetic reconstructions in the case of the conventional stent. This is also compatible with the in vitro findings, which are discussed in more detail in the section "Devices."

The findings of a better image quality at lower kiloelectron volt reconstructions seem to contradict the results of a previous study,[11] which described better artifact reduction and less image noise at higher kiloelectron volt reconstructions; however, the clinical context must be considered here. Because higher

kiloelectron volt reconstructions are associated with not only fewer artifacts but a higher distance to the iodine k-edge at 33 keV, this finding leads to a decreased SNR as well as a decreased contrast of the vessel lumen, resulting in a reduced assessability of possible in-stent stenosis in comparison with low kiloelectron volt reconstructions. In accordance with these findings, Hickethier et al[6] already described a reduced contrast-to-noise ratio between nonstenosed and stenosed stent sections and an associated reduced assessability with increasing kiloelectron volt numbers.

Regarding the evaluation of the adjacent aneurysm, both the objective and the subjective reading showed no significant differences between the different reconstructions, so an additional benefit in the clinical evaluation of the aneurysm perfusions or reperfusion seems unlikely.

The iodine-specific reconstructions of some devices allowed an assessment of similar quality as the best monoenergetic and conventional reconstructions and could thus increase the diagnostic certainty as supplementary image information.[13] With other devices, however, they proved to be more susceptible to artifacts than the monoenergetic images, so they cannot be generally recommended. If more artifacts occurred, this increase led to significantly worse lumen width ratios and distortions of the lumen-iodine content ratio compared with the low kiloelectron volt reconstructions. This scenario could indicate that the corresponding algorithm cannot reliably distinguish iodine and other molecules of higher density in small structures.[14] Overall, the ID reconstruction, in particular, proved to be less reliable than the INW reconstruction, explaining why the latter should be preferred for this purpose.

Devices

On the basis of the results of the different devices that were evaluated here, they can be divided into 3 categories: devices that hardly cause artifacts (ACC, ENT, NFA), devices that lead to moderate artifacts (ACO, p64, SUR), and devices with strongly associated artifacts (DED, PED). Among other things, this finding can be explained by the fact, that most of the artifact prone devices are flow diverters (with the exception of ACO). For the purpose of flow diversion, these must have special architectural properties and be more tightly woven than conventional stents, probably having the disadvantage of inducing stronger artifacts.

The specific architectural properties of flow diverters are defined by the porosity (ratio of open, metal-free area to total stent area) and metal coverage (ratio of metal covered area to total stent area).[15] In accordance with our results, the less artifact-prone devices are laser-cut stents with low metal coverage (ACC, 6%–9%; ENT, 10%; NFA, 6%–9%),[16] while the more artifact-prone devices showed a higher metal coverage, with slightly increased values for the remaining conventional stent (ACO, 15%–19%) and considerably increased values of approximately 30% in the case of the examined flow diverters (DED, 35%–38%; p64, 34%; PED, 30%–35%; SUR, 30%).[15,17-19]

The material could further contribute to artifact generation. The less artifact-susceptible devices (ACC, NFA, ENT) and the p64, ACO, and DED devices mainly consist of nitinol, which is known to be associated with low radiopacity.[20] In contrast, SUR

and PED contain mainly cobalt chromium with a higher radio-pacity. In the case of the more artifact-prone devices (DED, PED) as well as the ACO with medium artifact susceptibility, however, an additional use of platinum is said to enhance the fluoroscopic visibility. This characteristic could further contribute to an increased susceptibility to artifacts.

As already suggested by the comparison of the reconstructions, the monoenergetic 40-keV reconstruction proved to be the most suitable for all evaluated devices. For the higher energy reconstructions, the decrease in image quality varied, depending on the individual device. This decrease was particularly pronounced for the SUR device. However, this could also indicate that there is a special potential for artifact reduction or improvement of image quality in this device through the use of particularly suitable reconstructions.

As with the poly- and monoenergetic images, the iodine-specific reconstructions produced artifacts of varying intensity depending on the respective device. Good results were obtained with the devices ACC, NFA, ENT, and p64, while the PED has already shown considerable limitations; for the other devices (ACO, DED, SUR), the iodine content ratio could not be determined at all. This result is also consistent with the artifact susceptibility of the different devices, depending on the respective monoenergetic energy level described above.

Overall, there were more pronounced differences when comparing the devices than when comparing different reconstructions. However, 50% of the devices investigated were conventional stents, which had a low susceptibility to artifacts and a correspondingly low potential for artifact reduction, which may have led to a reduced overall effect of monoenergetic reconstructions on the improvement of image quality and artifact reduction. Further subgroup analyses with larger numbers of cases should, therefore, be conducted in the future.

Limitations

The limitations of the study include the in vitro setting, so potential influences of the surrounding brain parenchyma on the imaging of the aneurysm and the device cannot be addressed. Because there are no recommendations for the windowing of monoenergetic reconstructions in cranial CTAs, these were determined for each reconstruction in a standardized process. In doing so, an attempt was made to do this determination in as standardized and objective a manner as possible, but a certain influence on the results of the lumen width ratio and the subjective results cannot be excluded with certainty. However, this influence is definitely smaller than if unadjusted window settings had been used.

Although preliminary clinical data are included in the study, a larger and more detailed clinical analysis should follow to evaluate the clinical translation. In addition, our model included an untreated aneurysm, so possible differences in the sensitivity of detecting an aneurysm remnant or reperfusion, eg, after aneurysm coiling, cannot be evaluated. Also, with regard to the detection of possible in-stent stenoses, only indirect conclusions can be drawn because a comparison with stenosed vascular phantoms has not been performed. Although our study

already shows promising results, a clinical trial to validate our results is warranted.

CONCLUSIONS

This study provides the first structured data on postinterventional noninvasive imaging of neurointerventional stent devices by CTA using spectral image results of a dual-layer CT. Low-energy monoenergetic reconstructions offer better image quality in comparison with high-energy monoenergetic reconstructions. However, in comparison with conventional images, no significant improvements in image quality could be shown for monoenergetic reconstructions, at least if the individual artifact susceptibility of the devices is not factored in. In this respect, the comparison of the different devices identified ones with low (ACC, ENT, NFA), medium (ACO, p64, SUR), and high (DED, PED) artifact susceptibility. The flow diverters generally proved to be more susceptible to artifacts than conventional stents. The first in vivo data from clinical examination, which were assessed analogous to the study evaluations, seem to support our achieved in vitro results.

REFERENCES

1. Mine B, Bonnet T, Vazquez-Suarez JC, et al. **Comparison of stents used for endovascular treatment of intracranial aneurysms.** *Expert Rev Med Devices* 2018;15:793–805 CrossRef Medline
2. Zhang X, Zuo Q, Tang H, et al. **Stent assisted coiling versus non-stent assisted coiling for the management of ruptured intracranial aneurysms: a meta-analysis and systematic review.** *J Neurointerv Surg* 2019;11:489–96 CrossRef Medline
3. Briganti F, Leone G, Marseglia M, et al. **Endovascular treatment of cerebral aneurysms using flow-diverter devices: a systematic review.** *Neuroradiol J* 2015;28:365–75 CrossRef Medline
4. Feng X, Qian Z, Liu P, et al. **Comparison of recanalization and in-stent stenosis between the low-profile visualized intraluminal support stent and Enterprise stent-assisted coiling for 254 intracranial aneurysms.** *World Neurosurg* 2018;109:e99–104 CrossRef Medline
5. Duarte Conde MP, de Korte AM, Meijer FJ, et al. **Subtraction CTA: an alternative imaging option for the follow-up of flow-diverter-treated aneurysms?** *AJNR Am J Neuroradiol* 2018;39:2051–56 CrossRef Medline
6. Hickethier T, Wenning J, Bratke G, et al. **Evaluation of soft-plaque stenoses in coronary artery stents using conventional and monoenergetic images: first in-vitro experience and comparison of two different dual-energy techniques.** *Quant Imaging Med Surg* 2020;10:612–23 CrossRef Medline
7. Hickethier T, Wenning J, Doerner J, et al. **Fourth update on CTA of coronary stents: in vitro evaluation of 24 novel stent types.** *Acta Radiol* 2018;59:1060–65 CrossRef Medline
8. Rassouli N, Etesami M, Dhanantwari A, et al. **Detector-based spectral CT with a novel dual-layer technology: principles and applications.** *Insights Imaging* 2017;8:589–98 CrossRef Medline
9. Kamalian S, Lev MH, Gupta R. **Computed tomography imaging and angiography-principles.** *Handb Clin Neurol* 2016;135:3–20 CrossRef Medline
10. Thust SC, Chong WK, Gunny R, et al. **Paediatric cerebrovascular CTA-towards better image quality.** *Quant Imaging Med Surg* 2014;4:469–44 CrossRef Medline
11. Romman Z, Yagil Y, Finzi D, et al. **Philips Healthcare: Using spectral results in CT imaging—Philips Iqon Spectral CT.** https://www.

philips.co.uk/c-dam/b2bhc/gb/resource-catalog/landing/brightontender/ct-iqon-white-paper-spectral-results-in-ct-imaging-hr.pdf. Accessed March 6, 2020

12. Landis JR, Koch GG. **The measurement of observer agreement for categorical data.** *Biometrics* 1977;33:159 CrossRef Medline

13. Weng CL, Tseng YC, Chen DY, et al. **Spectral imaging for intracranial stents and stent lumen.** *PLoS One* 2016;11:e0145999 CrossRef Medline

14. Knöß N, Hoffmann B, Krauss B, et al. **Dual energy computed tomography of lung nodules: differentiation of iodine and calcium in artificial pulmonary nodules in vitro.** *Eur J Radiol* 2011;80:e516–19 CrossRef Medline

15. Maragkos GA, Dmytriw AA, Salem MM, et al. **Overview of different flow diverters and flow dynamics.** *Neurosurgery* 2020;86:S21–34 CrossRef Medline

16. Spiotta AM, Turner RD, Chaudry MI, eds. *Management of Cerebrovascular Disorders*. Springer-Verlag; 2019

17. Sirakov S, Sirakov A, Bhogal P, et al. **The p64 flow diverter-midterm and long-term results from a single center.** *Clin Neuroradiol* 2020;30:471–80 CrossRef Medline

18. De Vries J, Boogaarts J, Van Norden A, et al. **New generation of flow diverter (Surpass) for unruptured intracranial aneurysms: a prospective single-center study in 37 patients.** *Stroke* 2013;44:1567–77 CrossRef Medline

19. Beuing O, Lenz A, Donitza A, et al. **Stent-assisted coiling of broad-necked intracranial aneurysms with a new braided microstent (ACCERO): procedural results and long-term follow-up.** *Sci Rep* 2020;10:412 CrossRef Medline

20. Boese A, Rose G, Friebe M, et al. **Increasing the visibility of thin NITINOL vascular implants.** *Current Directions in Biomedical Engineering* 2015;1:503–06 CrossRef

Widening the Indications for Intrasaccular Flow Disruption: WEB 17 in the Treatment of Aneurysm Locations Different from Those in the Good Clinical Practice Trials

S. Zimmer, V. Maus, C. Maurer, A. Berlis, W. Weber, and S. Fischer

ABSTRACT

BACKGROUND AND PURPOSE: The safety and efficacy of the Woven EndoBridge (WEB) device has been shown in multiple good clinical practice trials, whereas aneurysm locations in these trials were restricted to bifurcation aneurysms located at the circle of Willis (MCA bifurcation, ICA bifurcation, anterior communicating artery, basilar artery tip). Our aim was to evaluate angiographic and clinical results with the WEB 17 in aneurysm locations that were excluded from the good clinical practice trials, assuming that the angiographic and clinical results are similar to those of the good clinical practice trials for aneurysms in traditional locations.

MATERIALS AND METHODS: We performed retrospective analysis of immediate and follow-up results of aneurysms in locations outside the good clinical practice trials in which the WEB 17 was used on an intention-to-treat approach.

RESULTS: Between June 2017 and May 2020, forty-seven aneurysms in 44 patients met the inclusion criteria. Aneurysm locations were the ICA posterior communicating artery in 19 (40.3%), the ICA paraophthalmic or choroidal locations in 4 (8.6%), anterior cerebral artery A2 segment in 13 (27.7%), MCA M1 segment in 2 (4.3%), posterior cerebral artery P2 segment in 2 (4.3%), PICA in 3 (6.4%), and the superior cerebellar artery in 4 (8.4%) cases. The procedure-related morbidity and mortality rates in the entire series were 0.0%. The early and late (<12 and >12 months) complete occlusion rates were 63.9% (23/36) and 77.8% (14/18), respectively.

CONCLUSIONS: The WEB 17 is safe and effective in aneurysm locations different from the traditional bifurcation aneurysms included in the good clinical practice trials. Further studies will help to define the entire spectrum of aneurysm morphologies and locations suitable for the WEB 17.

ABBREVIATIONS: ACA = anterior cerebral artery; bif = bifurcation; BOSS = Bicêtre Occlusion Scale Score; GCP = good clinical practice; PcomA = posterior communicating artery; RROC = Raymond-Roy Occlusion Classification

I ntrasaccular flow disruption has emerged as an effective and safe endovascular treatment option for complex intracranial aneurysms that may be otherwise difficult to treat. Positive results from numerous retrospective and prospective studies involving the Woven EndoBridge (WEB; MicroVention) have contributed to the growing popularity of the WEB for intrasaccular flow disruption. The WEB device was initially intended for the treatment of broad-based bifurcation aneurysms because these aneurysms are difficult to treat without additional neck-bridging devices or stents. Therefore, in most studies using the WEB, bifurcation

aneurysms were analyzed.[1-5] Experience with the WEB is increasing with a rapidly growing number of cases since its introduction in 2011, while the device simultaneously underwent several revisions and innovations with the addition of smaller sizes of both the device and the delivery microcatheter. The visibility of the device was enhanced, and the number of wires making up the device was reduced without affecting of the hemodynamic efficacy. While the first-generation systems required comparatively large and difficult-to-navigate microcatheters for delivery (0.033 and 0.027 inch), the latest systems are compatible with 0.017-inch microcatheters. Recent studies regarding the WEB 17 supported an expansion of indications toward smaller and more distal aneurysms.[6-9] In addition, the use of the WEB in aneurysm locations distinct from the traditional bifurcation locations is becoming more recognized in clinical practice.

In this retrospective study, we sought to evaluate the angiographic and clinical results in the endovascular treatment of aneurysms in locations that were excluded from previous studies with the WEB device. We hypothesized that the angiographic and

clinical results in this specific subgroup of aneurysms are comparable with those of traditional bifurcation-type aneurysms, possibly widening the applications for intrasaccular flow disruption.

MATERIALS AND METHODS

Study Design and Data Analysis

We retrospectively reviewed the institutional data bases of 2 neuroendovascular centers regarding the endovascular treatment of ruptured and unruptured intracranial aneurysms treated with the WEB 17 device between June 2017 and May 2020. Aneurysm locations that met the inclusion criteria of good clinical practice (GCP) studies of the WEB device were excluded.[1-3,10] The excluded locations were the MCA bifurcation (bif), the anterior communicating artery, the ICA bif, and the tip of the basilar artery. The remaining aneurysm locations treated with the WEB 17 system were the following: the ICA at the paraophthalmic segment, the posterior communicating artery (PcomA) or the origin of the anterior choroidal artery (ICA choroid), the MCA M1, the A2 segment of the anterior cerebral artery (ACA A2), the P2 segment of the posterior cerebral artery (P2), the PICA, and the superior cerebellar artery. The aneurysms meeting the location criteria were included in further analysis according to the study design presented by Pierot et al,[11] who, with this approach, analyzed predecessor versions of the WEB device in 2017. Minor subsets of our study population were previously included in an overall analysis of the WEB 17 system.[8]

The decision for endovascular treatment of unruptured aneurysms was reached by consensus in a weekly interdisciplinary board meeting at each participating center, while the final treatment strategy was determined by the operator. In patients with rupture, the treatment decision was made by the responsible neuroradiologist and neurosurgeon. Only cases in which the WEB 17 was considered on an intention-to-treat approach without adjunctive devices were included. Because this was a retrospective observational analysis, inclusion or exclusion criteria were not prospectively defined. A dome-to-neck ratio of <2 indicated a broad-based anatomy as an indication for treatment, but morphologies with a defined neck were not excluded if the configuration of the aneurysm appeared suitable for treatment with the WEB device. Alternative treatment strategies included standard coiling, remodeling, stent-assisted coiling, or flow diversion. Treatment with the WEB is increasingly considered as a first-line approach in broad-based aneurysms whenever possible to avoid long-term dual-antiplatelet therapy as needed for stent-assisted coiling or flow diversion. Absolute criteria against treatment with the WEB 17 were an aneurysm morphology or size unsuitable for the given range of WEB 17 devices (maximum diameter, <2.0 or >6.5 mm) according to the manufacturer's sizing guide, an incorporation of branches into the aneurysmal sac, or a neck diameter larger than the maximum fundus diameter.[7,8]

We included the following clinical and angiographic data: demographic patient data; clinical status on admission, at discharge, and at each follow-up visit measured by the mRS; aneurysm location; rupture status; fundus and neck size; dome-to-neck ratio; type and size of the WEB 17 device deployed; technical success (navigation and deployment of the WEB); rate of unplanned additional devices applied for "bail out" adjunctive treatments (eg, stents, coils); occlusion rates at each follow-up visit (scheduled 3–6 and 12 months after treatment); and complications.

Occlusion rates were initially evaluated according to the Bicêtre Occlusion Scale Score (BOSS), which is scaled as follows: $0 =$ no residual flow inside the aneurysm or the WEB; $0' =$ opacification of the proximal recess of WEB; $1 =$ residual flow inside the WEB; $2 =$ neck remnant; $3 =$ aneurysm remnant; and $1 + 3 =$ contrast media depicted inside and around the device.[12] In the final descriptive analysis, these results were "translated" to the 3-point Raymond-Roy Occlusion Classification (RROC). BOSS grades 0 and $0'$ were classified as complete occlusion (RROC grade I), whereas BOSS grades 1 and 2 were recorded as neck remnants (RROC grade II). Correspondingly, BOSS grades 3 and $1 + 3$ describe an aneurysm remnant (RROC grade III).[11-13]

Angiographic results were independently analyzed and classified in a blinded fashion by 2 experienced neurointerventionalists. In cases of inconsistency concerning the final result, a decision was made by consensus.

Procedure-related complications that resulted in a clinical sequelae of at least 1 point on the mRS scale defined the procedure-related morbidity and mortality.

WEB Treatment

The technical specifications of the WEB 17 device were previously described.[7,8] Sizing of the WEB 17 device resulted from calibrated measurements of the aneurysm height and width in 2 orthogonal projections assisted by the manufacturer's sizing calculator based on the principle of slightly oversizing the device width with compensatory undersizing of its height.[7,8]

Procedures were exclusively performed on a biplane angiographic system with the patient under general anesthesia via transfemoral access. All devices were implanted using a VIA 17 microcatheter (MicroVention). In elective cases, patients were placed on a dual-antiplatelet therapy in preparation for the procedure according to the standards at the 2 centers. Ruptured aneurysms were treated without dual-antiplatelet therapy. All procedures were performed with 5000 IU of heparin given intravenously at the beginning of the procedure.

Statistical Analysis

The statistical analysis of all variables was performed independently using Excel (Microsoft). Continuous variables are given as the median and range, and independent variables are described as percentages.

Ethics Statement

The study has been performed in accordance with the ethical standards laid down in the 1964 Declaration of Helsinki and its later amendments. The study received approval from the local ethics committee. A separate informed consent from each patient before inclusion in this retrospective study was not required according to the guidelines of the responsible ethics committee.

RESULTS

Patient and Aneurysm Population

Between June 2017 and May 2020, a total of 198 intracranial aneurysms were treated with the WEB 17 device. Of those, 47

Table 1: Angiographic characteristics of the WEB 17-treated aneurysms

	No.		Neck (Median) (mm)	Dome (Median) (mm)	DN-Ratio
Total	47	100%	2.0	3.0	1.5
Anterior circulation	38	80.9%	2.0	3.0	1.5
ICA PcomA	19	40.3%	2.0	4.0	1.5
ACA A2	13	27.7%	2.0	3.0	1.0
MCA M1	2	4.3%	2.5	2.0	0.8
ICA o	2	4.3%	2.5	3.5	1.3
ICA choroid	2	4.3%	2.5	4.5	1.8
Posterior circulation	9	19.1%	3.0	3.0	1.0
PCA P2	2	4.3%	2.0	4.0	1.3
PICA	3	6.4%	2.0	3.0	1.0
SUCA	4	8.4%	2.5	3.5	1.2

Note:—PCA indicates posterior cerebral artery; ICA o, paraophthalmic segment of the ICA; SUCA, superior cerebellar artery; DN-Ratio, dome-to-neck ratio.

aneurysms in 44 patients (median age, 55 years; range, 39–78 years; 32 women) met the defined inclusion criteria of aneurysm locations treated with the WEB 17 device. Of the 47 aneurysms, 32 (68.1%) were found incidentally, 13 (27.7%) were treated in the acute (within 48 hours) phase of SAH from the target aneurysm, and 2 (4.3%) were remnants of previously coiled aneurysms. Thirty-eight (80.9%) aneurysms were located in the anterior circulation, and 9/47 (19.1%) were posterior circulation aneurysms. The median aneurysm fundus diameter was 3.0 mm (range, 2.0–6.5 mm), and the median neck width was 2.0 mm (range, 2.0–6.0 mm). Most aneurysms (41/47, 87.2%) had a dome-to-neck ratio of <2.

Table 1 summarizes the locations and morphologic features of the treated aneurysms.

Procedural Details and Complications

Treatment was successfully performed with the WEB 17 in all cases, meaning that a switch to an alternative treatment strategy due to a failed attempt to implant the WEB 17 did not occur. In 1 case, coils were used in addition to the WEB as part of the treatment strategy. This was an incidental ICA PcomA aneurysm with an upper lobule that was occluded with coils using a previously placed microcatheter after implantation of a WEB (WEB Single-Layer [SL] 7 × 3) into the aneurysm fundus.

The overall rate of complications in the entire series was 6.4% (3/47) to date. In 2 cases, a Neuroform Atlas Stent (Stryker) was placed as a bailout treatment to stabilize the WEB device and preserve the parent artery. One was a ruptured ICA choroidal aneurysm that was catheterized with the VIA 17 microcatheter, and a WEB device (WEB SL 5 × 3) was positioned within the aneurysm without problems, even though the angle between the longitudinal axis of the aneurysm and the parent artery was comparatively high (about 90°). Once the device was detached, it partly dislocated into the ICA. The operator performed a mild percutaneous transarterial angioplasty with a compliant balloon followed by implantation of a Neuroform Atlas stent to secure the WEB device and preserve the ICA. The postinterventional CT did not show any ischemic lesions, and the patient was discharged with an mRS score of 1 that was most likely related to the SAH.

In the second case, a ruptured ACA A2 aneurysm was treated with a WEB (WEB SL 3.5 × 2) with the base of the device slightly protruding into the parent artery. There was no evidence of flow disturbance or formation of thrombus; however, the operator decided to deploy the Neuroform Atlas stent to stabilize the WEB device. The third complication was a ruptured ACA A2 aneurysm treated with a WEB (WEB SL 3.5 × 2) initially without problems. Following detachment of the device, the angiographic run showed a thrombotic occlusion of a small branch originating in close vicinity of the aneurysm. The occlusion resolved within 30 minutes after 500 mg of acetylsalicylic acid was given intravenously and the systolic blood pressure was moderately elevated.

All 3 patients remained without clinical sequelae, resulting in procedure-related morbidity and mortality of 0.0% in the entire series. Of the 13 patients who presented with an SAH from the target aneurysm, one died during hospitalization.

Immediate and Follow-up Angiographic Results

Of the 47 aneurysms treated, 15 (31.9%) showed an immediate complete occlusion (RROC I) directly after implantation of the WEB 17 device, while the remaining 32 aneurysms (68.1%) showed a beginning stagnation of contrast media within the aneurysm (RROC II and III).

To date, a single follow-up angiography performed within the first 12 months after treatment is available for 36 aneurysms in 34 patients, obtained after a median of 4 months (range, 1–10 months). Of those, 23/36 (63.9%) aneurysms showed complete occlusion (RROC I) and 13/36 (36.1%) had a neck remnant (RROC II). Of the 13 aneurysms with a neck remnant, 9 were ICA PcomA aneurysms, while the median fundus size was 4.0 mm (range, 2.0 −6.5 mm). There were 2 cases in which a "crushing" of the WEB was observed.

A second follow-up angiography performed after the first 12 months was completed for 18 aneurysms in 17 patients after a median of 15.5 months (range, 12–24 months). The rate of complete occlusion (RROC I) was 77.8% (14/18 aneurysms) with 22.2% (4/18) showing a neck remnant (RROC II).

A summary of the follow-up results is given in Table 2.

Two cases of a ruptured MCA M1 and an incidental ICA PcomA aneurysm treated with the WEB 17 device alone and in combination with coils are presented in Figs 1 and 2.

DISCUSSION

Intrasaccular flow disruption is currently a well-established treatment option for broad-based intracranial aneurysms. The effectiveness of the WEB device as the most widely used flow

Table 2: Immediate and follow-up results of the treated aneurysms according to the BOSS classification[12]

BOSS Classification	RROC Grades	Immediate (n)	Ratio BOSS (%)	Ratio RROC (%)	FU1 (n)	Ratio BOSS (%)	Ratio RROC (%)	FU2 (n)	Ratio BOSS (%)	Ratio RROC (%)
		47			36			18		
0	I	14	29.8	31.9	20	55.6	63.9	13	72.2	77.8
0′		1	2.1		3	8.3		1	5.6	
1	II	28	59.6	59.6	4	11.1	36.1	1	5.6	22.2
2		0	0.0		9	25.0		3	16.6	
3	III	1	2.1	8.5	0	0.0	0.0	0	0.0	0.0
1 + 3		3	6.4		0	0		0	0.0	

Note:—FU1 indicates first follow-up angiography; FU2, second follow-up angiography.
BOSS classification[12]: 0, No residual flow inside the aneurysm or the WEB; 0′, opacification of the proximal recess of the WEB; 1, residual flow inside the WEB; 2, neck remnant; 3, aneurysm remnant; 1 + 3, contrast media depicted inside and around the device. BOSS results were transferred into the RROC.[13] RROC classification: RROC I, complete occlusion (BOSS 0 and 0′); RROC II, neck remnant (BOSS 1 and 2); RROC III, aneurysm remnant (BOSS 3 and 1 + 3).
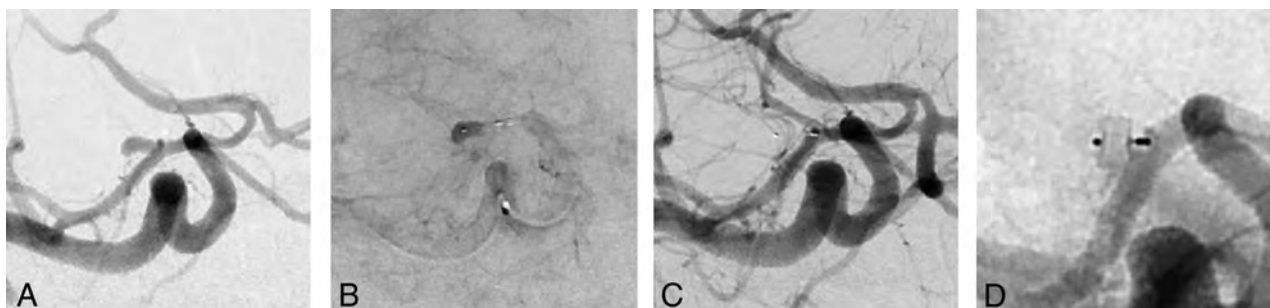
FIG 1. *A*, Acutely ruptured aneurysm of the MCA M1 segment in a 40-year-old female patient, right anterior oblique view, cranial angulation. *B*, Stasis of contrast media within the aneurysm after placement of a 3.5 × 2 mm WEB SL device, right anterior oblique view, cranial angulation. *C*, Prompt occlusion of the aneurysm after detachment of the WEB device, right anterior oblique view, cranial angulation. *D*, Twelve-month follow-up angiography reveals a stable and complete occlusion of the MCA M1 aneurysm.

disruptor was demonstrated in several prospective GCP studies. The inclusion criteria of the WEBCAST, WEBCAST 2, French Observatory, and WEB-IT studies for aneurysm location were restricted to bifurcation aneurysms of the MCA, anterior communicating artery, ICA bif, and basilar artery tip, and most aneurysms treated in those studies were broad-based. The complete aneurysm occlusion rate of aneurysms treated with WEB at 1 year in the WEBCAST, WEBCAST 2, and French Observatory studies was 52.9%, with similar results reported for the WEB-IT study (58.3%).[1-3] Following these results, the WEB device received FDA approval for broad-based, saccular aneurysms in the aforementioned locations.

The introduction of the WEB 17 system, not yet available for the mentioned studies, was a further step toward a lower device profile with an enhanced controllability, mainly due to the compatibility with a 0.017-inch microcatheter. Initial results with the WEB 17 device support an expansion of indications toward more distally located, smaller aneurysms.[7,8] This trend is evident in the inclusion criteria of an ongoing GCP study on the WEB 17 device, with no defined location excluded in contrast to the previous GCP studies.[14]

We sought to evaluate the safety and efficacy of the WEB 17 system in the specific subgroup of aneurysm locations that were excluded from prior GCP studies. Our hypothesis was that the angiographic success and safety profile would be comparable with those of bifurcation-type aneurysms in the "traditional" locations. Our short- and long-term complete occlusion rates of 63.9% and 77.8% with a procedure-related

morbidity and mortality of 0.0% are in line with the results of prior GCP studies.

The restriction to bifurcation aneurysms in the initial GCP trials conducted with the predecessor versions of the WEB device is mainly explained by the smaller angle between the parent artery and the aneurysm in bifurcation anatomies compared with sidewall aneurysms, where the angle is usually higher. Correct positioning of the WEB device with good apposition to the aneurysmal wall, including an exact reconstruction of the neck area, results from a controlled forward pushing of the partially unfolded device.[15] This maneuver as well as the initial catheterization becomes more challenging in anatomies with a higher angle between the aneurysm and the parent artery because the forward force applied to the microcatheter is vectored along the parent artery. The possibility of using a 0.017-inch microcatheter facilitates the catheterization in highly curved anatomies. Furthermore, the deviation of the (preshaped) microcatheter induced by the application of the WEB device is lower with the WEB 17 system due to the lower profile compared with the predecessor version. Thus, the transmission of force along a higher angle might be more efficient due to the softer structure of the WEB 17 system.

To date, there are only limited data on the WEB device in aneurysm locations outside the traditional study indications, and the existing literature is restricted to the predicate versions of the WEB. Pierot et al,[11] in 2017, were the first to present 20 patients with 20 aneurysms in "atypical locations" treated with the WEB device. Five of those were ruptured, and most were aneurysms of

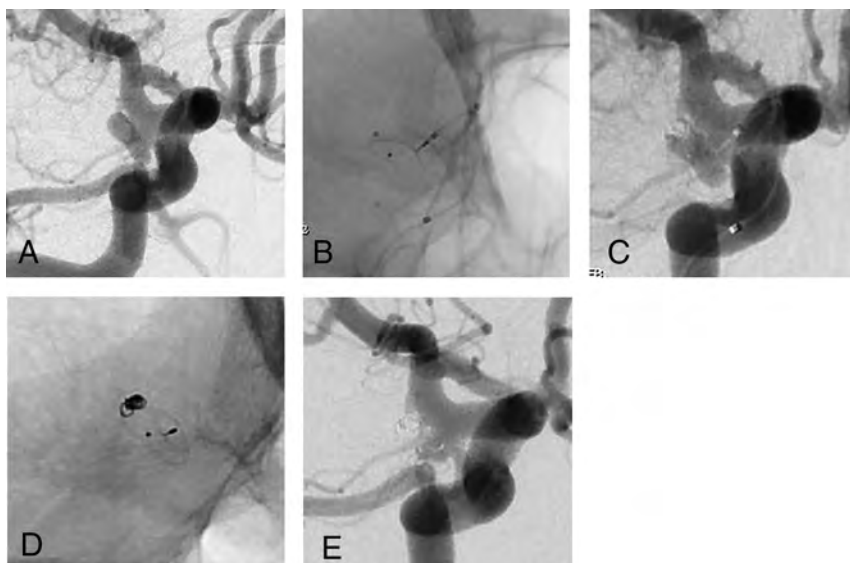FIG 2. *A*, Incidental finding of a "bean-shaped" ICA PcomA aneurysm in a 44-year-old male patient, right anterior oblique view, caudal angulation. *B*, Placement of an Excelsior SL 10 microcatheter (Stryker) inside the upper lobe of the aneurysm followed by a WEB SL 7 × 3 placed within the aneurysm fundus, fluoroscopy, right anterior oblique view, caudal angulation. *C*, Coil occlusion of the upper lobe of the aneurysm not completely covered by the WEB device, right anterior oblique view, caudal angulation. *D*, Three-month follow-up angiography demonstrates a crushing of the WEB device, fluoroscopy, right anterior oblique view, caudal angulation. *E*, Evidence of a neck remnant due to the crushing of the WEB device on the 3-month follow-up angiography, right anterior oblique view, caudal angulation.

the anterior circulation (9 paraophthalmic segments of the ICA, 4 ICA PcomAs; 5 of ACA A2). The mean aneurysm width was 5.4 mm, while 50.0% were broad-based (neck diameter, ≥4.0 mm). Implantation of the WEB using VIA 0.021-, 0.027-, or 0.033-inch microcatheters was successful in all aneurysms without adjunctive devices needed. The treatment-related morbidity and mortality at discharge were 0.0%. The complete occlusion rate after the mean follow-up period of 7.4 months in 17 aneurysms was 82.4%. Most interesting, this rate is superior to the 52.2% and 58.3% complete occlusion rates achieved in aneurysms in typical locations within the above-mentioned GCP studies. Furthermore, these results are slightly superior to the rate of complete occlusion found in our series, even though a direct comparison is generally difficult due to the heterogeneity of the populations treated with different versions of the WEB device.

In another series of 20 ICA aneurysms (10 paraophthalmic segments of the ICA, 9 ICA PcomAs, 1 ICA choroid) treated with the WEB device, implantation of the WEB failed in 2 aneurysms (both paraophthalmic ICAs), likely due to the sharp angle between the aneurysm and the ICA. In 7 cases, additional devices (coils/stents) were used, while 60% of the aneurysms were wide-neck (neck diameter, ≥4.0 mm, or dome-to-neck ratio, <2), and the aneurysms were larger (mean aneurysm width, 8.1 mm) compared with our cohort, which is explained by the different versions of the WEB devices used. The procedure-related morbidity and mortality rates in this series were 0.0%, with a complete occlusion rate of 76.5% after a mean follow-up period of 9.6 months.[16]

The most recent series of the WEB device in off-label locations was presented by Zanaty et al,[17] in 2020. Eleven patients with 12 aneurysms were treated using predecessor WEB devices without the VIA 0.017-inch microcatheter. Again, most were ICA aneurysms, and aneurysms were larger compared with those in our series (mean width, 8.0 mm; mean neck, 5.0 mm). Adjunctive devices were necessary in 3 cases (additional coiling in 2; stent in 1). They observed no procedure-related clinical sequelae, and the early complete and adequate occlusion rates were 33.3% and 66.7%, respectively.

Of the 13 cases with a neck remnant at the early follow-up angiography in our series, most (*n* = 9) were ICA PcomA aneurysms that were slightly larger than the aneurysms in the entire group. Besides the plausible factor of size, another possible explanation for the higher rate of ICA PcomA aneurysms might be found in the tight angle between the aneurysm and the parent artery in those aneurysms, which might impede an ideal position of the WEB with its hemodynamically active bottom vectored toward the parent artery. This theory might furthermore explain the 2 cases of crushing of the WEB device. However, these explanations remain hypothetic because factors determining recurrence or incomplete occlusion at the early follow-up examination were not analyzed in detail in our study due to the small sample size.

The aneurysms treated in our series were mainly small (fundus range, 2.0–6.5 mm; median, 3.0 mm). This feature is explained by the miniaturization of the device compared with predecessor systems as analyzed by different authors. König et al,[18] in their comparative analysis of aneurysms treated with the WEB 17 versus the WEB 21 system, found that the WEB 17 expands the treatment indications toward smaller and more distally located aneurysms with a similar and, to some extent, lower complication rate. These findings are in line with those of Goertz et al,[19] who found a potentially lower thromboembolic event rate without compromising the initial occlusion rate with the WEB 17.

Endovascular coiling of small and very small (≤3.0 mm) aneurysms is challenging compared with larger aneurysms. This issue is mainly related to the higher risk of rupture caused by an unexpected movement of the microcatheter.[20,21] Endovascular coiling of aneurysms of ≤3.0 mm is more prone to failure compared with larger aneurysms following a study of Pierot et al.[22] Compliant balloons or stents are helpful tools to increase the packing density in smaller aneurysms, while balloons are further useful devices in cases of an acute aneurysm rupture.[20,23,24] However additional devices are associated with a higher periprocedural complication rate in small aneurysms, and recanalization rates were

found to be higher in the group of stent-assisted coiling of small aneurysms according to the meta-analysis of Yamaki et al.[21]

The results of ours and previous studies underline the effectiveness of the WEB 17 in the treatment of small (atypically located) broad-based aneurysms, which is primarily related to the softness of the device, which might reduce the incidence of intraprocedural ruptures. Furthermore, does the "single device concept" compared with remodeling or stent-assisted coiling potentially reduce procedure time and with this the probability of adverse events.

Limitations

Our study has limitations that are mainly the consequence of the retrospective nature, without a stringent definition of inclusion and exclusion criteria. Furthermore, the angiographic results were graded without an independent assessment, and only midterm follow-up data are available to date. However, to the best of our knowledge, this is the largest series of aneurysms in alternative locations treated with the WEB 17 device.

CONCLUSIONS

Treatment of aneurysms with the WEB 17 in locations different from those included in the GCP trials is safe and effective. Our results represent a further step toward an expansion of indications for intrasaccular flow disruption. Additional studies are needed to define the ideal indication for the WEB 17 system in alternative locations among the existing potential treatment options.

REFERENCES

1. Pierot L, Moret J, Barreau X, et al. **Safety and efficacy of aneurysm treatment with WEB in the cumulative population of three prospective, multicenter series.** J Neurointerv Surg 2018;10:553–62 CrossRef Medline

2. Arthur AS, Molyneux A, Coon AL, et al; WEB-IT Study investigators. **The safety and effectiveness of the Woven EndoBridge (WEB) system for the treatment of wide necked bifurcation aneurysms: final 12-month results in the pivotal WEB Intrasaccular Therapy (WEB-IT) Study.** J Neurointerv Surg 2019;11:924–30 CrossRef Medline

3. Pierot L, Spelle L, Molyneux A, et al; WEBCAST and French Observatory Investigators. **Clinical and anatomical follow-up in patients with aneurysms treated with the WEB device: 1-year follow-up report in the cumulated population of 2 prospective, multicenter series (WEBCAST and French Observatory).** Neurosurgery 2016;78:133–41 CrossRef Medline

4. Lv X, Zhang Y, Jiang W, et al. **Systematic review of Woven EndoBridge for wide-necked bifurcation aneurysms: complications, adequate occlusion rate, morbidity, and mortality.** World Neurosurg 2018;110:20–25 CrossRef Medline

5. van Rooij S, Sprengers ME, Peluso JP, et al. **A systematic review and meta-analysis of Woven EndoBridge single layer for treatment of intracranial aneurysms.** Interv Neuroradiol 2020 Feb 6 [Epub ahead of print] CrossRef Medline

6. Ding YH, Lewis DA, Kadirvel R, et al. **The Woven EndoBridge: a new aneurysm occlusion device.** AJNR Am J Neuroradiol 2011;32:607–11 CrossRef Medline

7. van Rooij S, Peluso JP, Sluzewski M, et al. **The new low-profile WEB 17 system for treatment of intracranial aneurysms: first clinical experiences.** AJNR Am J Neuroradiol 2018;39:859–63 CrossRef Medline

8. Maurer C, König I, Berlis A, et al. **Two-center experience in the endovascular treatment of intracranial aneurysms using the Woven EndoBridge 17 device including midterm follow-up results: a retrospective analysis.** AJNR Am J Neuroradiol 2019;40:517–22 CrossRef Medline

9. Mihalea C, Caroff J, Pagiola I, et al. **Safety and efficacy of the fifth generation Woven EndoBridge device: technical note.** J Neurointerv Surg 2019;0:1–5 CrossRef Medline

10. Fiorella D, Molyneux A, Coon A, et al; WEB-IT Study Investigators. **Demographic, procedural and 30-day safety results from the WEB Intra-saccular Therapy Study (WEB-IT).** J Neurointerv Surg 2017;9:1191–96 CrossRef Medline

11. Pierot L, Biondi A, Narata AP, et al. **Should indications for WEB aneurysm treatment be enlarged? Report of a series of 20 patients in "atypical" locations for WEB treatment.** J Neuroradiol 2017;44:203–09 CrossRef Medline

12. Caroff J, Mihalea C, Tuilier T, et al. **Occlusion assessment of intracranial aneurysms treated with the WEB device.** Neuroradiology 2016;58:887–91 CrossRef Medline

13. Roy D, Milot G, Raymond J. **Endovascular treatment of unruptured aneurysms.** Stroke 2001;32:1998–2004 CrossRef Medline

14. CLEVER. https://clinicaltrials.gov/ct2/show/NCT03844334. Accessed May 15, 2020

15. Popielski J, Berlis A, Weber W, et al. **Two-center experience in the endovascular treatment of ruptured and unruptured intracranial aneurysms using the WEB device: a retrospective analysis.** AJNR Am J Neuroradiol 2018;39:111–17 CrossRef Medline

16. Goertz L, Liebig T, Siebert E, et al. **Extending the indication of Woven EndoBridge (WEB) embolization to internal carotid artery aneurysms: a multicenter safety and feasibility study.** World Neurosurg 2019;126:e965–74 CrossRef Medline

17. Zanaty M, Roa JA, Tjoumakaris SI, et al. **Off label use of the WEB device.** World Neurosurg 2020;134:e1047–52 CrossRef Medline

18. König I, Maurer C, Berlis A, et al. **Treatment of ruptured and unruptured intracranial aneurysms with WEB 17 versus WEB 21 systems: comparison of indications and early angiographic outcomes.** Clin Neuroradiol 2020 Sep 3 [Epub ahead of print] CrossRef Medline

19. Goertz L, Liebig T, Siebert E, et al. **Low-profile intra-aneurysmal flow disruptor WEB 17 versus WEB predecessor systems for treatment of small intracranial aneurysms: comparative analysis of procedural safety and feasibility.** AJNR Am J Neuroradiol 2019;40:1766–72 CrossRef Medline

20. Van Rooij WJ, Keeren GI, Peluso JP, et al. **Clinical and angiographic results of coiling of 196 very small (< or = 3 mm) intracranial aneurysms.** AJNR Am J Neuroradiol 2009;30:835–39 CrossRef Medline

21. Yamaki VN, Brinjikji W, Murad MH, et al. **Endovascular treatment of very small intracaranial aneurysms: meta-analysis.** AJNR Am J Neuroradiol 2016;37:862–67 CrossRef Medline

22. Pierot L, Barbe C, Spelle L; ATENA investigators. **Endovascular treatment of very small unruptured aneurysms: rate of procedural complications, clinical outcome, and anatomical results.** Stroke 2010;41:2855–59 CrossRef Medline

23. Nguyen TN, Raymond I, Guilbert F, et al. **Association of endovascular therapy of very small ruptured aneurysms with higher rates of procedure-related rupture.** J Neurosurg 2008;108:1088–92 CrossRef Medline

24. Lanzino G, Kallmes DF. **Endovascular treatment of very small ruptured intracranial aneurysms.** J Neurosurg 2008;108:1087 CrossRef Medline

Mechanical Thrombectomy in Nighttime Hours: Is There a Difference in 90-Day Clinical Outcome for Patients with Ischemic Stroke?

A. Benali, M. Moynier, C. Dargazanli, J. Deverdun, F. Cagnazzo, I. Mourand, A. Bonafe, C. Arquizan, I. Derraz, N. Menjot de Champfleur, F. Molino, A. Ducros, E. Le Bars, and V. Costalat

ABSTRACT

BACKGROUND AND PURPOSE: Few data are available regarding the influence of the timing of ischemic stroke management, such as daytime and nighttime hours, on the delay of mechanical thrombectomy, the effectiveness of revascularization, and clinical outcomes. We aimed to investigate whether admission during nighttime hours could impact the clinical outcome (mRS at 90 days) of patients with acute ischemic stroke treated by mechanical thrombectomy.

MATERIALS AND METHODS: We retrospectively analyzed 169 patients (112 treated during daytime hours and 57 treated during nighttime hours) with acute ischemic stroke in the anterior cerebral circulation. The main outcome was the rate of patients achieving functional independence at 90 days (mRS $\leq$2), depending on admission time.

RESULTS: In patients admitted during nighttime hours, the rate of mRS $\leq$ 2 at 90 days was significantly higher (51% versus 35%, $P = .05$) compared with those admitted in daytime hours. Patients in daytime and nighttime hours were comparable regarding admission and treatment characteristics. However, patients in nighttime hours tended to have a higher median NIHSS score at admission ($P = .08$) and to be younger ($P = .08$), especially among the mothership group ($P = .09$). The multivariate logistic regression analysis confirmed that patients in nighttime hours had better functional outcomes at 90 days than those in daytime hours ($P = .018$; 95% CI, 0.064–0.770; OR = 0.221).

CONCLUSIONS: In a highly organized stroke care network, mechanical thrombectomy is quite effective in the nighttime hours among acute ischemic stroke presentations. Unexpectedly, we found that those patients achieved favorable clinical outcomes more frequently than those treated during daytime hours. Larger series are needed to confirm these results.

ABBREVIATIONS: AIS = acute ischemic stroke; CSC = comprehensive stroke center; END = early neurologic deterioration; ENI = early neurologic improvement; IQR = interquartile range; MT = mechanical thrombectomy; mTICI = modified TICI; sICH = symptomatic intracranial hemorrhage

Blood flow restoration is the principal therapeutic goal in acute ischemic stroke (AIS). IV rtPA is recommended for all eligible patients within 4.5 hours of of symptoms onset. For patients with AIS with acute large-vessel occlusion, mechanical thrombectomy (MT) is highly beneficial and recommended as a standard of care.[1] Functional outcomes are better when the MT is performed early after stroke onset.[2]

The impact of admission hours on short-term prognosis of patients with AIS is still controversial. Some series investigated whether patients with AIS admitted during off-hours (Monday to Friday between 6 PM and 8 AM and weekends) had different outcomes compared with patients admitted during on-hours. One study reported that patients in off-hours had higher short-term mortality, greater disability at discharge, and worse outcomes at 90 days than patients admitted during working hours.[3] Conversely, another study suggested that rates of poor 90-day outcomes (mRS >2) were similar between off- and on-hours admissions.[4]

Furthermore, in a recent large cohort of Dutch patients, the overall outcome was not influenced by time of admission.[5] Results of these studies may be influenced by local stroke center organization and may not be generalized to other centers with different organizations.

The only study focusing on the outcomes after MT performed during on-versus-off hours was a recent analysis of the Multicenter Randomized CLinical trial of Endovascular treatment for Acute ischemic stroke in the Netherlands (MR CLEAN) registry group
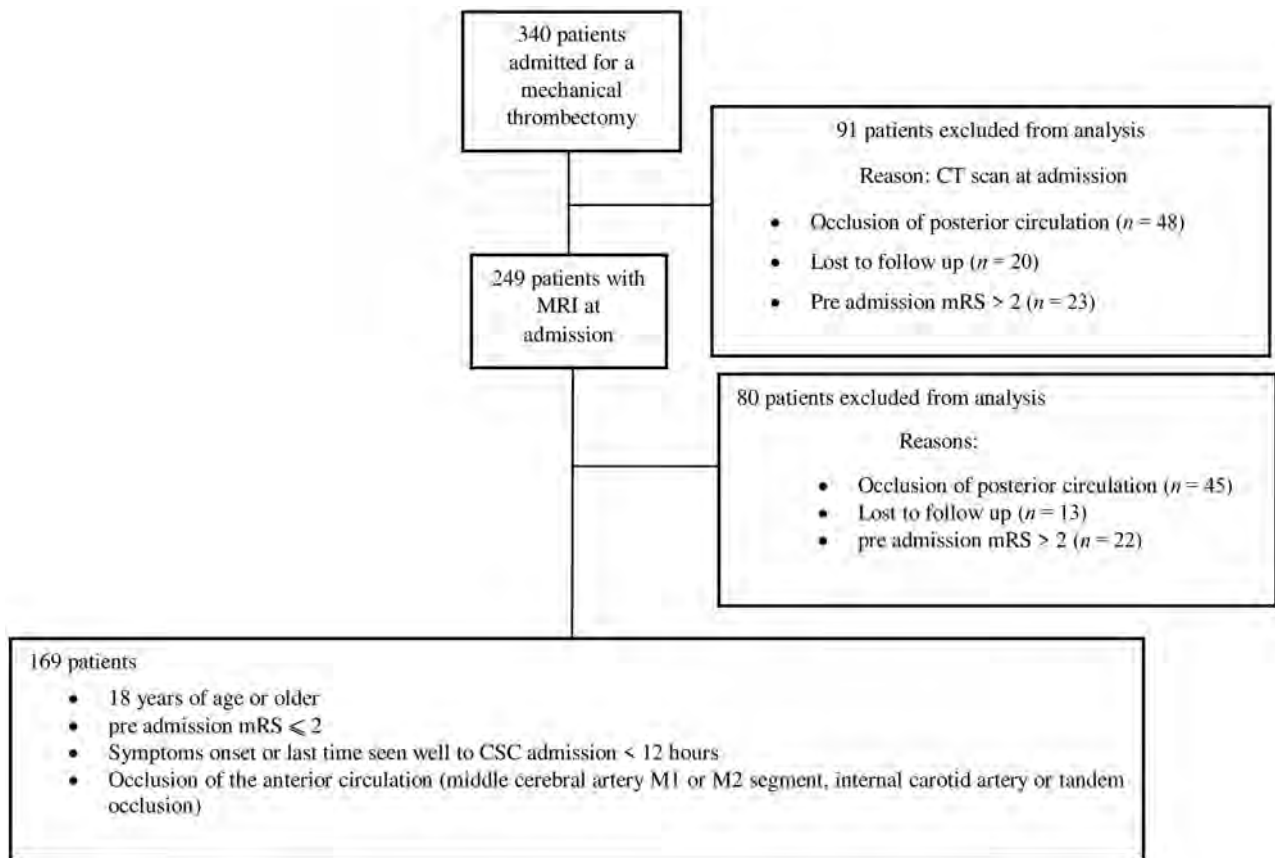
FIG 1. Flow chart: exclusion and inclusion criteria.

(https://mrclean-trial.org/), which showed comparable functional outcomes and complication rates among the 2 groups.[6]

Accordingly, outcomes after MT performed during working hours versus off-hours have not been accurately examined and require further research.

Night presentation and sleep deprivation have been reported as potential risk factors for patients presenting with unplanned critical illness and requiring rapid diagnostics and interventions.[7] This can cause worse outcome in these patients, that can be attributed to increased complications, fatigue, and differential staffing.[8] Accordingly, our hypothesis was that performance of the workflow and operators could be impacted during the night, reflecting worse outcomes after MT performed during nighttime hours. In addition, our institution (Millau hospital, Mende hospital and Perpignan hospital) receives patients with stroke from a 200-km perimeter; therefore, delay in transportation may negatively influence outcomes. We hypothesized that transport delays could be higher during nighttime hours compared with daytime hours due to less availability of helicopter transport at night. We aimed to investigate whether admission during nighttime hours could impact the clinical outcomes (in-hospital mortality and mRS at 90 days) of patients with AIS treated by MT.

MATERIALS AND METHODS
Population
Since 2015, a neuroradiologic data base (Commission Nationale de l'Informatique et des Libertés 1724786; https://www.cnil.fr/en/

home) includes, prospectively, all patients admitted to our comprehensive stroke center (CSC). The patients were managed directly in the CSC (mothership patients) or first admitted to 1 of the 4 primary stroke centers with or without IV rtPA before transfer for MT (patients experiencing drip and ship). These primary stroke centers are a distant 50–200 km from our CSC.

Three hundred forty patients admitted to our stroke unit from January 2017 to December 2018 were studied. In this retrospective cohort study, patients were included if they fulfilled the 4 following inclusion criteria: 1) 18 years of age or older, 2) preadmission mRS of ≤2, 3) symptom onset or last time seen well to CSC admission of <12 hours, and 4) anterior circulation occlusion (middle cerebral artery M1 or M2 segment, internal carotid artery, or tandem occlusion) visible on MR imaging at admission. As shown in Fig 1, our inclusion criteria were observed in 169 patients. We excluded from this study patients with a CT scan at admission ($n = 91$) to keep 1 imaging technique and compare infarct volume on the basis of only MR imaging.[9] Patients presenting with posterior occlusion, a preadmission mRS >2, or lost to follow-up ($n = 80$) were also excluded from the study.

All patients admitted in the CSC between 6:00 PM and 8:00 AM the next morning were grouped as the patients in nighttime hours. All patients admitted to the CSC between 8:00 AM and 6:00 PM were grouped as the patients in daytime hours. The whole medical staff was present during the daytime. During the nighttime hours, medical staff was reduced and composed of 1
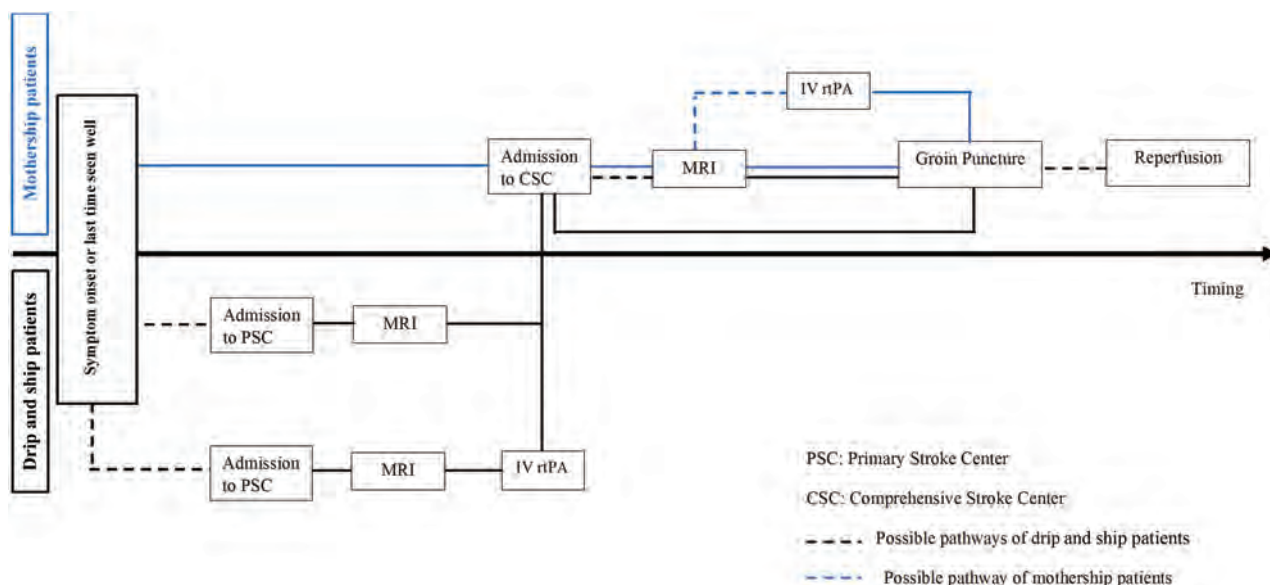
FIG 2. Pathways for management of patients with acute ischemic stroke from symptom onset to mechanical thrombectomy.

neuroradiologist resident, 1 senior stroke neurologist, a neurology resident on duty, and 2 technicians.

Scores and Parameters Evaluation

Clinical and Imaging Evaluation. Stroke severity was assessed by the NIHSS on CSC admission by a stroke neurologist. The following data were collected prospectively with a structured questionnaire: age, sex, cardiovascular risk factors (hypertension, dyslipidemia, diabetes mellitus, and smoking), time of symptom onset, NIHSS at CSC admission and at 24 hours, vital signs before treatment, imaging findings, use of IV rtPA, and clinical outcomes.

All patients underwent multimodal 1.5T (Aera; Siemens) or 3T (Skyra; Siemens) MR imaging before treatment, with a standardized protocol. Infarct volume was estimated in milliliters on DWI using RApid processing of PerfusIon and Diffusion (RAPID; iSchemaView).[10]

The ASPECTS on DWI was calculated by a neuroradiologist blinded to the results of the MT.

Timing. Delays were calculated in minutes. For all the calculated delays, admission was defined by the CSC admission except for admission to imaging. For mothership patients, admission was defined by CSC admission to imaging. Otherwise, for patients experiencing drip and ship, this delay was defined by primary stroke center admission to imaging except if a second imaging was performed in the CSC. In this case, the CSC admission to imaging was used. The other studied delays were the following: symptom to CSC admission, imaging to reperfusion, CSC admission to groin puncture, CSC admission to reperfusion, groin puncture to reperfusion, and symptom to reperfusion. All the crucial points for calculating these delays are shown in Fig 2.

IV rtPA and Endovascular Therapy. IV rtPA was administered according to the current guidelines.[11]

MT was performed via a femoral artery approach with the patient under general anesthesia or local anesthesia with sedation. Reperfusion was graded using the modified TICI (mTICI) score.[12] Successful reperfusion was defined as mTICI2b, 3; and first-pass success was defined as a good reperfusion (TICI 2b or 3) after a 1-pass device was used for MT.

Stroke subtypes were classified according to the Trial of Org 10172 in Acute Stroke Treatment (TOAST) classification.[13]

Measures and Main Outcome. Follow-up imaging was performed between 16 and 30 hours after MT to assess intracranial hemorrhage. Symptomatic intracranial hemorrhage (sICH) was defined as any hemorrhage occurring within 24 hours associated with an increase of ≥4 points in the NIHSS score or that caused death.[11] Early neurologic improvement (ENI) was defined as an improvement of at least 8 points between the NIHSS score at CSC admission and the NIHSS score at 24 hours (compared with baseline) after MT.[14] Early neurologic deterioration (END) was defined as a loss of 4 points in the NIHSS score between NIHSS at CSC admission and NIHSS at 24 hours.[15] Finally, in-hospital mortality was defined as the rate of patient death during hospitalization.

Functional outcome was assessed by a neurologist using the mRS at 90 days, during the clinical visit, or by a study nurse using a standardized telephone interview. Favorable functional outcome was defined as a mRS ≤ 2.

Statistical Analysis

Continuous variables were reported as median (interquartile range [IQR]). Univariate statistical analysis was performed using the Mann-Whitney U test for continuous variables and the Fisher exact test for categoric variables.

All statistical analyses were performed using MedCalc, Version 18.10 (MedCalc Software). Patients in daytime- and nighttime-hour groups were used in a logistic regression as independent predictors of the follow-up outcome, defined as good

(mRS ≤ 2) or bad (mRS > 2) outcome. Variables either known to be potential confounding factors or identified as the most significantly different in the univariate analysis were included in the logistic regression. Regarding our sample size, we chose to limit the number of covariables to 8. A stepwise method was used with an α-to-enter and α-to-exit set at .2 and .001, respectively. Eight variables, age, sex, NIHSS score at CSC admission, IV rtPA, dyslipidemia, atrial fibrillation, hypertension, and CSC admission to groin puncture were thus included in the model.

Finally, specificities of mothership patients and those in the drip and ship group were investigated using a subgroup analysis. For an optimal comparability, a backward method was used to compare patients in daytime and nighttime hours among mothership patients as well as those in the drip and ship group on the basis of the 8 previous variables. Data were adjusted by the NIHSS score at CSC admission, atrial fibrillation, IV rtPA, and CSC admission-to-groin puncture delay for mothership group and by the NIHSS score at CSC admission, dyslipidemia, and hypertension for patients in the drip and ship group.

The statistical threshold was set to $P < .05$ for all analyses.

RESULTS

Altogether, 169 patients (50% of men; mean age, 75 years; IQR, 63–83 years), of whom 44% (74/169) were transferred from another center, were included. Patient characteristics are reported in the Online Supplemental Data. The median NIHSS score at CSC admission was 17 (IQR = 11–20), and the median ASPECTS was 7 (IQR = 5–8). MT was performed within a median delay of 355 minutes (IQR = 248–544 minutes) from symptom onset. General anesthesia was used in 55% of patients (93/169). Good reperfusion (TICI 2b, 3) was achieved in 74% (125/169). Overall, at 90 days, 40% (68/169) of patients had an mRS ≤ 2.

Daytime-versus-Nighttime Hours

Patient Characteristics. Of 169 patients, 112 (66%) were treated during daytime hours, and 57 (34%), during nighttime hours. No significant difference was found between the nighttime- and daytime-hour groups regarding demographics and cardiovascular risks factors, though patients in daytime hours were slightly older (77 versus 74 years, $P = .08$) and tended to have more dyslipidemia (41% versus 28%, $P = .09$) (Online Supplemental Data).

The daytime- and nighttime-hour groups were comparable in terms of pre-MT (biologic parameters, occlusion site, ASPECTS, and infarct volume) and treatment characteristics (general anesthesia; successful first-pass recanalization; rate of TICI 2b, 3; rate of complications). Patients in nighttime hours tended to have a higher median NIHSS score at CSC admission, 18 (IQR = 14–22), than those in daytime hours, 16 (IQR = 10–20) ($P = .08$).

Procedural Timing and Reperfusion. All timing variables were comparable among daytime- and nighttime-hour groups, except the delay from CSC admission to groin puncture, which was significantly longer in the nighttime-hour group compared with the daytime-hour group (94 minutes; range, 78–123 minutes) versus (82 minutes; range, 61–105.25 minutes) ($P = .009$) (Online Supplemental Data).

Outcomes: Comparison between Patients in Nighttime and Daytime Hours. The in-hospital mortality rate was higher in the daytime-hour group (19/112 = 17%) than in the nighttime-hour group (3/57 = 5%, $P = .05$; OR = 3.6544; 95% CI, 1.007–20.1601). ENI and END were similar between the 2 groups ($P = .34$). At 90 days, patients in nighttime hours had significantly higher rates of favorable outcome (29/57 = 51%) compared with those in daytime hours (39/112 = 35%) (2-sided Wilcoxon test, $P = .05$; OR = 1.9308; 95% CI, 0.9619–3.9002) (Online Supplemental Data). After we adjusted for age, sex, NIHSS at CSC admission, dyslipidemia, atrial fibrillation, hypertension, IV rtPA, CSC admission to groin puncture, and delay in a logistic regression model, the nighttime-hour MT appeared to have an even higher significant impact on the 90-day outcome (logistic regression, $P = .018$; OR = 0.221; 95% CI, 0.064–0.770; Online Supplemental Data).

Subgroup Analysis: Mothership—Daytime-Versus-Nighttime Hours. In the subgroup of 95 mothership patients (Table 1), among those in nighttime hours, there was a trend toward a lower median age (69 versus 78 years, $P = .09$) and higher rates of successful first-pass recanalization (45% versus 26%, $P = .09$), whereas the median NIHSS score (20; IQR = 6–22) versus 15 (IQR = 10–20; $P = .03$) and CSC admission-to-groin puncture delay (115 versus 86 minutes, $P = .001$) were higher. In-hospital mortality was lower among patients in nighttime hours (3% versus 26%, $P = .01$), while 45% of patients in nighttime hours gained independence at 90 days compared with 36% in daytime hours. In logistic regression using the backward method, a model adjusted by atrial fibrillation, IV rtPA, and CSC admission-to-groin puncture delay showed that nighttime-hour MT appeared to have a higher significant impact on the 90-day outcome ($P = .018$; OR = 0.221; 95% CI, 0.064–0.770; Online Supplemental Data).

Drip and Ship: Daytime-versus-Nighttime Hours. In the subgroup of 74 patients experiencing drip and ship (Table 2), the rate of favorable outcome at 90 days was significantly higher in those in nighttime-versus-daytime hours (57% versus 33%, $P = .05$; OR = 2.716; 95% CI, 0.9401–8.1342). In a logistic regression using the backward method, a model adjusted by NIHSS at CSC admission, dyslipidemia, and hypertension showed that nighttime-hour MT appeared to have a higher significant impact on the 90-day outcome ($P = .024$; OR = 0.246; 95% CI, 0.073–0.831; Online Supplemental Data). None of the other parameters differed between the daytime-and nighttime-hour groups.

Nighttime-Hour Group: Characteristics of Patients with mRS ≤ 2 and mRS >2. In the subgroup of 57 patients with nighttime hours, among the patients with an mRS ≤ 2 at 90 days, there was a younger median age (69 versus 79 years, $P = .05$) with a lower median NIHSS score at CSC admission (16 [IQR, 9–20] versus 19 [IQR = 17–23], $P = .01$). Also, the rate of first-pass success was significantly higher (52% versus 21%, $P = .03$). The rate of favorable revascularization mTICI ≥ 2b was significantly higher in patients with mRS ≤2 (97% versus 57%, $P < .001$, Table 3).

There was a trend toward a lower median CSC admission-to-reperfusion delay among patient with mRS ≤ 2 (147 minutes

Table 1: Mothership patients—characteristics and comparison between patients in nighttime and daytime hours—univariate analysis[a]

	All (N = 95)	Nighttime Hours (n = 29)	Daytime Hours (n = 66)	P Value
Age (yr)	76 (62–84)	69 (59–83)	78 (71–84)	.09
Men	46 (48)	15 (52)	31 (47)	.82
Hypertension	60 (63)	17 (59)	43 (65)	.64
Diabetes mellitus	14 (15)	5 (17)	9 (14)	.75
Dyslipidemia	38 (40)	10 (34)	28 (42)	.50
Atrial fibrillation	29 (31)	12 (41)	17 (26)	.20
Smoking	21 (22)	9 (31)	12 (18)	.20
Tandem occlusion	14 (15)	4 (14)	10 (15)	1.00
NIHSS at admission	18 (11–21.5)	20 (6–22)	15 (10–20)	.03
IV rtPA	57 (60)	10 (34)	28 (42)	.50
ASPECTS	7 (5–7)	7 (5–7)	7 (5–8)	1.00
Infarct volume (mL)	18.8 (8.4–41)	29.8 (12–45.5)	18.3 (6.3–34)	.20
General anesthesia	41 (43)	14 (48)	27 (41)	.51
First-pass success	30 (32)	13 (45)	17 (26)	.09
mTICI > 2b	63 (66)	21 (72)	42 (64)	.50
Symptom onset to CSC admission (min)	170 (89.5–404)	170 (98–406)	170 (82–392)	.61
CSC admission to groin puncture (min)	93 (72–118)	115 (88–132.5)	86 (66–111)	.001
CSC admission to reperfusion (min)	168 (129–202)	176 (144–203)	168 (128–199)	.55
Groin puncture to reperfusion (min)	60 (43–90)	49 (33–81)	64 (43–95)	.11
ENI	28 (29)	10 (33)	18 (28)	.48
END	42 (44)	12 (41)	30 (46)	.82
sICH	8 (8)	1 (3)	7 (11)	.43
In-hospital mortality	18 (19)	1 (3)	17 (26)	.01
mRS ≤2 at 90 days	37 (39)	13 (45)	24 (36)	.50

[a] Categoric variables are expressed as number (%), and continuous variables, as median (IQR).

Table 2: Patients subject to drip and ship—characteristics and comparison between patients in nighttime and daytime hours—univariate analysis[a]

	All (N = 74)	Nighttime Hours (n = 28)	Daytime Hours (n = 46)	P Value
Age (yr)	73 (64.3–82)	71 (63–82)	75 (64.5–82)	.60
Men	39 (53)	15 (54)	24 (52)	1.00
Hypertension	53 (72)	17 (61)	36 (78)	.12
Diabetes mellitus	14 (19)	4 (14)	10 (22)	.55
Dyslipidemia	24 (32)	6 (21)	18 (39)	.13
Atrial fibrillation	25 (34)	11 (39)	14 (30)	.46
Smoking	23 (31)	6 (21)	17 (37)	.20
Tandem occlusion	16 (22)	6 (21)	10 (22)	1.00
NIHSS at admission	16 (11–19.8)	16 (9–19)	16 (11.5–20)	.90
IV rtPA	39 (53)	17 (61)	22 (48)	.34
ASPECTS	7 (6–8)	7 (6–8)	7 (6–8)	.70
Infarct volume (mL)	24.9 (10.7–6.8)	15.4 (9.7–36.7)	26.2 (11.3–4.1)	.20
General anesthesia	39 (53)	13 (46)	26 (57)	.47
First-pass success	24 (32)	8 (29)	16 (35)	.62
mTICI > 2b	61 (82)	23 (82)	38 (82)	1.00
Symptom onset to CSC admission (min)	298 (256–481)	277 (228–374)	302 (271–531)	.20
CSC admission to groin puncture (min)	71 (55–99)	85 (66–105)	67 (54–92)	.11
CSC admission to reperfusion (min)	152 (101–200)	164 (101–189)	147 (107–210)	.90
Groin puncture to reperfusion (min)	70 (47–106)	68 (47–78)	75.5 (49–125)	.21
ENI	28 (38)	12 (43)	16 (35)	.62
END	14 (19)	4 (14)	10 (22)	.55
sICH	8 (11)	2 (7)	6 (13)	.70
In-hospital mortality	5 (7)	2 (7)	3 (7)	1.00
mRS ≤2 at 90 days	31 (42)	16 (57)	15 (33)	.05

[a] Categoric variables are expressed as numbers (%), and continuous variables, as median (IQR).

[IQR = 123–188 minutes] versus 178 minutes [IQR = 153–207 minutes], $P = .09$).

DISCUSSION

Our study investigated outcomes after MT between patients with AIS admitted during nighttime hours compared with those admitted during daytime hours. These results are important because 30% of patients with strokes are admitted during nighttime hours, and both performance of the operators and efficiency of the workflow can be comparable with daytime hours. On the basis of our results, it seems that the nighttime-hour period is not an obstacle to the best treatment-management of patients with AIS and should not be regarded as a dangerous time for patients

Table 3: Characteristics and comparison between good outcome (mRS 0–2) and bad outcome (mRS 3–6) among patients in night-time hours—predictive factors of favorable outcome[a]

	All (N = 57)	mRS (0–2) (n = 29)	mRS (3–6) (n = 28)	P Value
Age (yr)	70 (60–83)	69 (58–73)	79 (62–85.5)	.05
Men	30 (53)	17 (59)	13 (46)	.43
Hypertension	34 (60)	16 (55)	18 (64)	.60
Diabetes mellitus	9 (16)	4 (14)	5 (18)	.73
Dyslipidemia	16 (28)	8 (28)	8 (29)	1.00
Atrial fibrillation	23 (40)	10 (34)	13 (46)	.42
Smoking	20 (35)	11 (38)	9 (32)	.78
Tandem occlusion	10 (18)	4 (14)	6 (21)	.50
NIHSS at admission	18 (14–22)	16 (9–20)	19 (17–23)	.01
IV rtPA	27 (47)	15 (52)	12 (43)	.60
ASPECTS	7 (5–8)	7 (5–7)	7 (5.75–8)	.43
Infarct volume	23 (11–45)	23 (11–47)	25 (10.5–37.3)	.73
General anesthesia	29 (51)	13 (45)	16 (57)	.43
First-pass success	21(37)	15 (52)	6 (21)	.03
mTICI >2	44 (77)	28 (97)	16 (57)	.0004
CSC admission to groin puncture (min)	94 (78–123)	87 (77–110)	108 (84−135.5)	.11
Symptom to groin puncture (min)	361 (272–487)	360 (272–485)	261 (273–494)	.82
Groin puncture to reperfusion (min)	56.5 (39–76)	51 (38–69)	64 (42–80)	.43
CSC admission to reperfusion (min)	168 (128–195)	147 (123–188)	178 (153–207)	.09
ENI	22 (39)	13 (45)	9 (32)	.42
END	12 (25)	3 (10)	9 (32)	.06
sICH	3	0 (0)	3 (11)	.11
In-hospital mortality	3	0 (0)	3 (11)	.11

[a] Categoric variables are expressed as numbers (%), and continuous variables, as median (IQR).

treated with MT in a highly organized stroke care network. Most interesting, patients treated during nighttime hours had a better outcome at 90 days than those treated during daytime hours. The topic is still controversial; a recent analysis from the MR CLEAN Registry of the workflow intervals of MT for patients presenting during off-hours (including weekends) and on-hours (8 AM–6 PM during weeks) showed no significant difference in functional outcome among these 2 groups, as well as similar reperfusion and complication rates.[6] On the contrary, a systematic review and meta-analysis of 21 studies performed by Sorita et al,[3] in 2014, in the pre-MT era showed that patients with AIS in off-hours had both higher short-term mortality and greater disability at discharge. Putative explanations included a less experienced staff, less available diagnostic procedures, variations in the processes of care, and a decreased likelihood of delivering IV rtPA or intra-arterial thrombolysis.

In our population, increased CSC admission-to-groin puncture delay during nighttime hours has been observed, possibly relying on the time required for the neuroradiologist on call to get to the hospital. However, this increased delay does not have a pejorative impact on patient outcome at 90 days. Besides CSC admission-to-groin puncture delay, patients in nighttime and daytime hours experienced similar stroke management, with similar symptom onset-to-groin puncture and groin puncture-to-reperfusion delays. The organization of stroke management appears equally as efficient whether during daytime or nighttime hours.

Not considering stroke management, a plausible explanation for the better neurologic outcome after nighttime MT would be the intrinsic variability of our patients between the samples in terms of stroke characteristics and clinical variables. The former does not differ between patients in nighttime and daytime hours regarding neither the ASPECTS, the infarct volume, nor the technical characteristic–related complications. However, the latter

shows some slight age (P = .08) differences. Patients in nighttime hours are slightly younger than those in daytime hours (3 years), especially among the mothership group (9 years). Age is an important factor influencing the probability of achieving a good outcome among patients with AIS. In a recent study, Jayaraman et al[16] quantified the interaction between age and outcomes after MT. The authors found a deleterious influence of age: With each 1-year advance in age, the increase in the mRS change worsened among recanalized patients (TICI 2b, 3) and approached the value of mRS change in the TICI 0-2a group.[16] Age could then explain, at least partially, the better outcome among the patients in nighttime hours.

However, adjusting statistical analysis by age is not sufficient to remove the observed outcome differences between groups. This issue suggests a more complex, multifactorial explanation. For more insight, we conducted a subgroup analysis, comparing characteristics of patients in nighttime hours between good (mRS ≤ 2) and poor (mRS > 2) outcome groups. First-pass success, favorable recanalization (mTICI ≥ 2), and a low NIHSS score at CSC admission appear to be predictors of good outcome. The NIHSS score at admission is known to be strongly associated with outcome.[17] Most interesting, except for age, patients do not clearly differ in terms of history characteristics, supporting our hypothesis that age is an important variable.

Impact of Drip and Ship versus Mothership Patients

The drip and ship scenario implies additional delays before performing MT, which might reduce the chance of success.[2] We, thus, investigated mothership patients and those experiencing drip and ship, independently. Mourand et al[18] reported no significant difference in 90-day outcomes when comparing mothership patients with those in the drip and ship group independent of admission time.

In our series, the proportion of patients having functional independence at 90 days was higher among patients in nighttime compared with daytime hours, both with the mothership and the drip and ship strategy. However, the latter was associated with a significantly higher rate of mRS ≤ 2 among patients in nighttime hours. Although it is difficult to explain why patients in nighttime hours treated in a drip and ship strategy had a good outcome more frequently compared with the mothership strategy, we can underline some differences between the 2 groups: The NIHSS score was lower (20 versus 16) among patients in nighttime hours treated in the drip and ship group; the rate of IV rtPA was lower among mothership patients (34% versus 61%); and the rate of ENI was higher in the drip and ship group (43% versus 33%). All these differences may, in part, explain why patients in nighttime compared with daytime hours gained independence more frequently at 90 days after the drip and ship strategy compared with the mothership strategy. However, bias related to the small sample size of the subgroups should be evaluated. In conclusion, we can demonstrate with this analysis that although potential confounders related to selection bias should be considered, workflow is quite efficient in the nighttime, leading to good treatment results among patients with AIS.

Limitations

Our study has some limitations. Although prospectively collected, our results were retrospectively analyzed. It is a single-center cohort study, a representation of the 2017–2018 clinical practices of our CSC. As in similar works, generalization to other centers can be difficult and highly depends on the management of each local patient.

Our work was focused on patients who underwent MT; thus, we have no access to information on patients not retained for it. We cannot exclude the hypothesis that during nighttime hours, patients are more carefully selected for MT due to reduced medical team availability. Such observations could explain a part of the nighttime-hour/daytime-hour differences but should be obvious when comparing characteristics of patients in daytime and nighttime hours, which is not clearly the case, except for age.

CONCLUSIONS

In a highly organized stroke care network, MT is effective both in nighttime- and daytime-hour AIS presentations. Nighttime-hour management does not lead to deleterious effects on outcome at 90 days, and treatment times are similar between daytime hours and nighttime hours. Unexpectedly, we found that patients treated during nighttime hours achieved a favorable clinical outcome more frequently at 90 days and had less in-hospital mortality than those treated during daytime hours. There was a difference in age between the groups. It might partially explain this observation and introduce a potential sample bias. Our results provide an important insight for later studies aiming to improve clinical practices in AIS care organization.

REFERENCES

1. Powers WJ, Derdeyn CP, Biller J, et al; American Heart Association Stroke Council. **2015 American Heart Association/American Stroke Association Focused Update of the 2013 Guidelines for the Early Management of Patients with Acute Ischemic Stroke Regarding Endovascular Treatment: A Guideline for Healthcare Professionals From the American Heart Association/American Stroke Association.** *Stroke* 2015;46:3020–35 CrossRef Medline

2. Ota T, Nishiyama Y, Koizumi S, et al. **Impact of onset-to-groin puncture time within three hours on functional outcomes in mechanical thrombectomy for acute large-vessel occlusion.** *Interv Neuroradiol* 2018;24:162–67 CrossRef Medline

3. Sorita A, Ahmed A, Starr SR, et al. **Off-hour presentation and outcomes in patients with acute ischemic stroke: a systematic review and meta-analysis.** *Eur J Intern Med* 2014;25:394–400 CrossRef Medline

4. Streifler JY, Benderly M, Molshatzki N, et al. **Off-hours admission for acute stroke is not associated with worse outcome: a nationwide Israeli stroke project: outcome of stroke off-hours admissions.** *Eur J Neurol* 2012;19:643–47 CrossRef Medline

5. Tuinman MP, van Golde EG, Portier RP, et al. **Comparison of outcome in stroke patients admitted during working hours vs. off-hours; a single-center cohort study.** *J Neurol* 2019;266:782–89 CrossRef Medline

6. Hinsenveld WH, de Ridder IR, van Oostenbrugge RJ, et al; MR CLEAN Registry Investigators. **Workflow intervals of endovascular acute stroke therapy during on-versus off-hours.** *Stroke* 2019;50:2842–50 CrossRef Medline

7. Carr BG, Reilly PM, Schwab CW, et al. **Weekend and night outcomes in a statewide trauma system.** *Arch Surg* 2011;146:810–17 CrossRef Medline

8. Shulkin DJ. **Like night and day: shedding light on off-hours care.** *N Engl J Med* 2008;358:2091–93 CrossRef Medline

9. Sotoudeh H, Shafaat O, Sotoudeh E. **Misleading CT perfusion in subacute ischemic stroke.** *Emerg Radiol* 2019;26:581–86 CrossRef Medline

10. Lansberg MG, Lee J, Christensen S, et al. **RAPID automated patient selection for reperfusion therapy: a pooled analysis of the Echoplanar Imaging Thrombolytic Evaluation Trial (EPITHET) and the Diffusion and Perfusion Imaging Evaluation for Understanding Stroke Evolution (DEFUSE) Study.** *Stroke* 2011;42:1608–14 CrossRef Medline

11. Hacke W, Kaste M, Bluhmki E, et al; ECASS Investigators. **Thrombolysis with alteplase 3 to 4.5 hours after acute ischemic stroke.** *N Engl J Med* 2008;359:1317–29 CrossRef Medline

12. Fugate JE, Klunder AM, Kallmes DF. **What is meant by "TICI"?** *AJNR Am J Neuroradiol* 2013;34:1792–97 CrossRef Medline

13. Adams HP, Bendixen BH, Kappelle LJ, et al. **Classification of subtype of acute ischemic stroke; definitions for use in a multicenter clinical trial; TOAST—Trial of Org 10172 in Acute Stroke Treatment.** *Stroke* 1993;24:35–41 CrossRef Medline

14. Ong CT, Sung SF, Wu CS, et al. **Early neurological improvement after intravenous tissue plasminogen activator infusion in patients with ischemic stroke aged 80 years or older.** *J Chin Medi Assoc* 2014;77:179–83 CrossRef Medline

15. Seners P, Turc G, Oppenheim C, et al. **Incidence, causes and predictors of neurological deterioration occurring within 24 h following acute ischaemic stroke: a systematic review with pathophysiological implications.** *J Neurol Neurosurg Psychiatry* 2015;86:87–94 CrossRef Medline

16. Jayaraman MV, Kishkovich T, Baird GL, et al. **Association between age and outcomes following thrombectomy for anterior circulation emergent large vessel occlusion is determined by degree of recanalisation.** *J Neurointerv Surg* 2019;11:114–18 CrossRef Medline

17. Wouters A, Nysten C, Thijs V, et al. **Prediction of outcome in patients with acute ischemic stroke based on initial severity and improvement in the first 24 h.** *Front Neurol* 2018;9:308 CrossRef Medline

18. Mourand I, Malissart P, Dargazanli C, et al. **A regional network organization for thrombectomy for acute ischemic stroke in the anterior circulation; timing, safety, and effectiveness.** *J Stroke Cerebrovasc Dis* 2019;28:259–66 CrossRef Medline

Endovascular Treatment of Ruptured Intracranial Blister Aneurysms: A Systematic Review and Meta-analysis

A. Scerrati, J. Visani, M.E. Flacco, L. Ricciardi, S. Trungu, A. Raco, F. Dones, P. De Bonis, and C.L. Sturiale

ABSTRACT

BACKGROUND: Endovascular treatment of blister aneurysms is a promising approach, even though they are vascular lesions challenging to treat due to their angioarchitectural characteristics.

PURPOSE: Our aim was to investigate clinical and radiologic outcomes after endovascular treatment of ruptured blister aneurysms.

DATA SOURCES: PubMed, Ovid MEDLINE, Ovid EMBASE, Scopus, and the Web of Science were screened.

STUDY SELECTION: We performed a comprehensive review of the literature from 2010 to 2019 reporting series of patients with blister aneurysms treated with an endovascular approach.

DATA ANALYSIS: Event rates were pooled across studies using a random effects meta-analysis.

DATA SYNTHESIS: A total of 32 studies reporting on 684 patients (707 aneurysms) were included. Stent placement, stent-assisted coiling, and flow diversion were the most commonly described treatments (282, 256, and 155 patients, respectively). The long-term complete occlusion rate was 76.9% (95% CI, 69.2%–83.9%). The perioperative complication rate was 8.9%, and clinical outcome at final follow-up was mRS <2 in 76.6% (95% CI, 68.2%–84.2%) of patients. The mortality rate was 4.7% (95% CI, 2.30%–7.80%). Among the different techniques, stent-assisted coiling is the one that had the higher rate of immediate occlusion (63.4%); however, the occlusion rate at the final follow-up was comparable among the different techniques.

LIMITATIONS: Different techniques were described and data were reported in a nonhomogeneous way, possibly representing a bias in the present study.

CONCLUSIONS: This study suggests that endovascular treatment of blister aneurysms is associated with good long-term occlusion rates and reasonable complication and mortality rates. There is no consensus on the best endovascular techniques in blister aneurysm management.

ABBREVIATION: HH = Hunt and Hess

B lister aneurysms are uncommon vascular anomalies, responsible for 0.5%–2% of all SAH caused by ruptured intracranial aneurysms.[1,2] Their etiology has not been completely clarified yet, though wall stress or shear stress of vessels has been proposed as having a role in their pathogenesis.[3,4]

Due to their angioarchitectural characteristics, such as a fragile wall and poorly defined neck, blister aneurysm treatment is challenging with either surgical or endovascular approaches. Surgery has been associated with controversial results in terms of surgical and clinical outcomes, demonstrating a high rate of aneurysmal recurrence, subsequent hemorrhages, and complications.[5-7] On the other hand, endovascular treatment, which has been progressively validated as effective for saccular aneurysm management, could represent a valid therapeutic alternative for blister aneurysms. Endovascular treatment options include simple coiling, stent or balloon-assisted coiling, flow-diversion stent placement, liquid embolization, and parent vessel sacrifice. However, there are scarce data on blister aneurysm management using endovascular techniques.

This study aimed to systematically review the pertinent literature investigating clinical-radiologic outcomes and complications of the different endovascular treatments for blister aneurysms.

MATERIALS AND METHODS

Study Design

This is a systematic review of the literature, designed and conducted according to the Preferred Reporting Items for Systematic Review and Meta-Analyses (PRISMA) statement. The review question was formulated according to the PICO criteria, as follows: (P, patients) In the management of blister aneurysms, (I, intervention) what is the endovascular treatment, (C, comparison) that has reported the best results, (O, outcomes) in terms of clinical-radiologic outcomes?

Study Selection

PubMed, Ovid MEDLINE, Ovid EMBASE, Scopus, and the Web of Science were selected as online medical databases to conduct the present systematic review. The search terms were the following: "intracranial," "brain," "cerebral," "blister," "blood-blister," "blisterlike," "aneurysm," "coiling," "coils," "stent," "stent placement," "endovascular," "flow diverters" (Medical Subject Headings), combined using the Boolean operators.

Studies reporting data on patients treated with endovascular techniques for intracranial blister aneurysms were searched. Inclusion criteria were articles written in English and the availability of clinical and radiologic data for single patients. We excluded clinical series reporting data on <5 patients, guidelines, reviews, commentaries, and letters to the editor.

The first-round search was conducted by 2 reviewers (J.V. and A.S.) who independently screened titles and abstracts for eligibility. The selected full texts and their reference lists (forward search) were screened and evaluated for inclusion in the second round.

In the third round, articles were screened for demographics, aneurysm location and size, aneurysm rupture status, treatment modalities, occlusion rates, procedural failure, procedure-related morbidity and mortality, procedure-related complications, and clinical outcome. The article was then excluded in case of data unavailability, incomplete data, improper data reporting, or unavailability of single-patient data (exclusion with a reason). In the fourth round, data were retrieved and added to a database for pooling and statistical analysis (inclusion). Any discordance was solved by consensus with the senior author (C.L.S.).

Outcomes Measurement

For every patient we collected, we recorded blister location, morphology, rupture status, endovascular treatment technique, postoperative and last follow-up angiographic outcome (occlusion rate, rebleeding), perioperative complications (intraoperative rupture, parent artery occlusion, transient ischemic attack, vasospasm, stroke), perioperative morbidity and mortality, and last follow-up functional status. We defined treatment failure as the inability to secure the aneurysm and/or the need for a second therapeutic attempt due to rebleeding or regrowth of the aneurysm.

Clinical outcome was scored according to the mRS.

Statistical Analysis

We performed meta-analyses of proportions to estimate the pooled rates of each outcome. Proportion meta-analyses were not used when the frequency of an outcome was reported in <1% of the sample (raw proportions and 95% confidence intervals were reported in such cases), and a random effects model was adopted to account for the interstudy heterogeneity.

RESULTS

Study Selection and Characteristics

According to our search strategy, 178 articles in English were retrieved through the electronic literature search.

After 178 read the abstracts, 103 articles were primarily excluded, while 75 were assessed for eligibility and analyzed in detail because they met our inclusion criteria.

After full-text reading and a forward search from the bibliography of the selected articles, 43 articles were excluded for the following reasons: Twenty were series of <5 patients, 8 reported incomplete follow-up, 4 did not include blister aneurysms, and in 11 studies, endovascular treatment was not performed. Thirty-two articles[8-39] (31 retrospective and 1 prospective) published between 2010 and 2019 reporting patients who underwent endovascular treatment for blister aneurysms were finally included in this review (Figure).

The last search was launched in January 2020.

Demographic Characteristics

We collected 684 patients with 707 aneurysms. Sex was reported in 674 patients: 228 men (33.8%) and 446 women (66.2%). The mean age was 50.4 years (the SD was reported in a minority of series).

Blister Characteristics

We collected data about a total of 707 blister aneurysms: Six hundred eighty-seven (98.7%) originated from the ICA; 9, from the basilar artery; 3 (0.4%), from the MCA; 3 (0.4%), from the posterior cerebral artery; 2 (0.3%), from the vertebral artery; 2 (0.3%) from the anterior communicating artery; and 1 (0.1%), from the anterior communicating artery.

Mean size was available for 119 of 707 aneurysms (16.8%): One hundred ten aneurysms were large, up to 5 mm; and 9 were between 6 and 10 mm.

All aneurysms were ruptured. Fisher grading at the onset was available for 255 of 268 (95.1%) patients: 21 (4.8%) grade 1; 54 (17.3%) grade 2; 123 (40.1%) grade 3; 57 (19.0%) grade 4.

The Hunt and Hess (HH) grade was reported in 631 of 684 (92.3%) patients: Eighty-seven (10.7%) were HH 1; 248 (24.8%) were HH 2; 184 (20.3%) were HH 3; 88 (9.5%) were HH 4; and 24 (1.0%) were HH 5 (Online Supplemental Data).

Type of Endovascular Procedure

The type of procedure was reported in 705 of 707 blister aneurysms (99.7%). A simple coiling was used in 6 cases. A traditional stand-alone stent placement was performed in 282 procedures, whereas stent-assisted coiling was preferred in 256 procedures. Stand-alone flow diversion was the treatment of choice in 145 cases, while in 16 patients, coiling combined with flow diversion
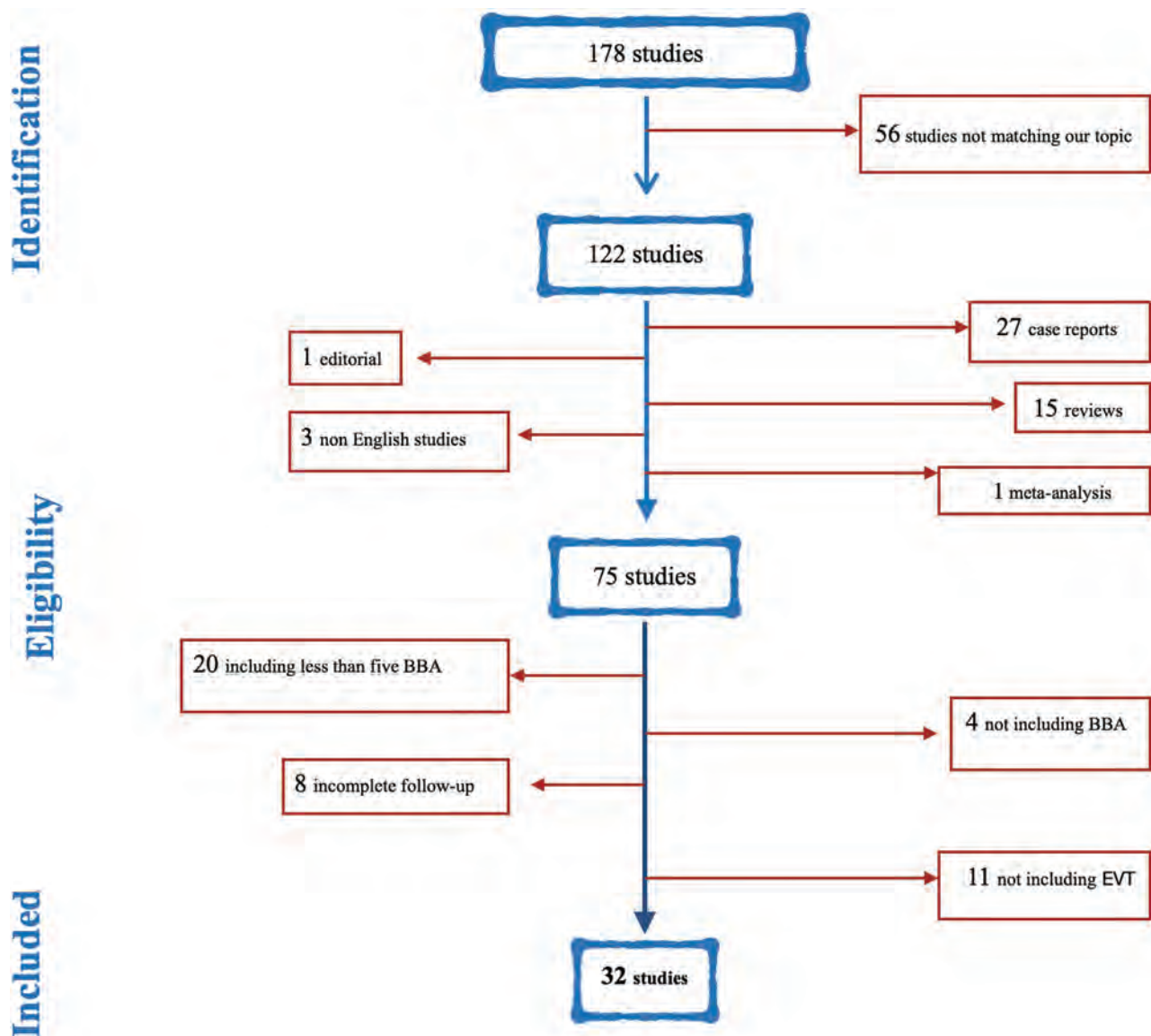
FIGURE. Search strategy. BBA indicates Blister aneurysms; EVT, endovascular treatment.

or an occlusion with glue or parent artery occlusion was performed (Online Supplemental Data).

Radiologic Outcome

Immediate radiologic outcome was reported in 498 of 684 (72.8%) patients: The complete occlusion rate was 50.6% (95% CI, 38.2%–62.9%); near-complete was 11.6% (95% CI, 5.7%–18.7%); partial was 24.4% (95% CI, 14.8%,–35.2%); and failure was reported in 7 patients (0%; 95% CI, 0.0%–1.05).

Radiologic outcome at follow-up was reported in 345 of 684 (50.4%) patients: The complete occlusion rate was 76.9% (95% CI, 69.2%–83.9%); near-complete was 1.6% (95% CI, 0.17%–3.89%); partial occlusion was 1.1% (95% CI, 0.03%–2.97%); and failure was reported in 2.3% (95% CI, 0.41%–5.22%) of patients (Online Supplemental Data).

In 23 studies, the evaluation of the occlusion rate was empirically based on the author's own description on DSA.[8,10,12-18,20,22-24,27-32,34,35,37-39] In 6 studies, authors used the Roy-Raymond scale,[16,19,25,26,33,36] and in 2 studies, they used the simplified Roy-Raymond scale.[9,21] Only 1 study used the O'Kelly-Marotta and the Roy-Raymond scales.[11]

Clinical Outcome and Complications

Details are reported in the Online Supplemental Data: Clinical outcome at discharge was reported in a minority of patients and expressed as the Glasgow Outcome Scale score. Clinical outcome at follow-up was, instead, reported in 674 of 684 (98.5%) patients: 76.6% (95% CI, 68.2%–84.2%) of patients had an mRS of less than 2; and 7.6% (95% CI, 3.09%–13.3%) of patients had an mRS > 2.

The mean follow-up time was reported in 25 of 32 included articles (406 patients) and was about 12.4 months.

Concerning complications, an intraoperative hemorrhage occurred in 27/684 procedures (1.3%; 95% CI, 0.31%–2.85%); vasospasm, in 45/684 (2.7%; 95% CI, 0.14%–7.33%); and thrombosis, in 20/684 (0.7%; 95% CI, 0.00%–2.63%), while

perioperative stroke occurred in 29/684 (1.4%; 95% CI, 0.33%–2.90%). Perioperative death occurred in 40/684 patients (2.8%; 95% CI, 0.93%–5.24%). The overall mortality rate at final follow-up was 50/684 patients (4.8%; 95% CI, 2.30%–7.80%).

Outcome Comparison among the Different Endovascular Treatments

We compared patients' clinical and radiologic outcomes according to the main different modalities of endovascular management (Online Supplemental Data). Because only a minority of cases were treated with simple coiling (0.8%) or parent artery occlusion (0.14%), we decided to compare 3 groups: stand-alone stent placement, stent-assisted coiling, and flow diversion (associated or not with coiling).

The ICA was confirmed as the most common location for blister aneurysm origin (687/707 aneurysms). Blister aneurysms were preferably treated with stand-alone stent placement in 249 cases, followed by a stent-assisted coiling in 179 and flow diverters in 135. Nevertheless, blister aneurysms originating from the anterior cerebral artery, anterior communicating artery, middle cerebral artery, and posterior cerebral artery were exclusively treated with flow diversion. In basilar artery blister aneurysms, 4 cases were treated with flow diversion, and 1, with stent-assisted coiling.

Hunt and Hess grading was not discriminating for the choice of the treatment technique, except for the flow-diverter positioning, which was more often preferred in patients with better clinical conditions on admission (26.2% of HH 1) compared with stent placement (4% of HH 1) and stent-assisted coiling (3.9% of HH 1).

Patients treated with stand-alone stent placement presented with a higher rate of good outcome (mRS 0–2) at follow-up (94.8%) compared with those treated with stent-assisted coiling (85%) and flow diverters (76.5%), as well as a lower mortality rate (1.6% versus 3.7% versus 4.4%).

Regarding the complications, vasospasm was most frequently reported with stent-assisted coiling (10.6%) compared with stent placement and flow diversion (0% and 0.1% of cases, respectively). The hemorrhage rate was, instead, very low in all groups (between 0% and 0.6%). The 3 cases of intraoperative bleeding occurred in only cases of flow-diverter positioning without associated coiling.

The perioperative death rate was >2 times higher in the flow-diverter group (5.2%) compared with stand-alone stent placement (2.1%) and stent-assisted coiling (0%) groups. Stent-assisted coiling was reported as having a higher rate of immediate complete occlusion (63.4%) compared with stand-alone stent placement (42%) and flow diverters (53.7%).

The same trend was confirmed at radiologic follow-up when stent-assisted coiling reached a rate of complete occlusion of 80.3; stand-alone stent placement, 77.1; and flow diverters, 75.6. Noticeably, the rate of complete occlusion at radiologic follow-up appeared to be significantly increased in the stent placement and flow-diverter groups if compared with the immediate outcome.

Finally, the quality of each study was evaluated by the Newcastle-Ottawa grading scale (Table).

Newcastle-Ottawa grading scale for the quality of the study evaluation

Article	Selection	Comparability	Outcome
Kaschner et al[8]	***		*
Fang et al[9]		*	*
Kim MJ et al[10]	***		**
Capocci et al[11]	***		**
Hellstern et al[12]	***		*
Parthasarathy et al[13]	***		***
Mokin et al[14]	***		*
Hao et al[15]	***		***
Xu et al[16]	***	*	**
Ren et al[17]	***	*	**
Cerejo et al[18]	***		**
Yang et al[19]	***		***
Ryan et al[20]	***		***
Zhu et al[21]	****	**	***
Brown et al[22]	***		**
Fang et al[23]	***		**
Linfante et al[24]	***		**
Yu et al[25]	***		**
Song et al[26]	***		*
Ashour et al[27]	***		*
Chinchure et al[28]	***		*
Yoon et al[29]	***		*
Chalouhi et al[30]	***		*
Gonzales et al[31]	***		*
Lim et al[32]	***		**
Walsh et al[33]	***		*
Cinar et al[34]	***		*
Lee et al[35]	***		**
Aydin et al[36]	***		***
Ihn et al[37]	**		**
Fang et al[38]	**		**
Fang et al[39]	***		*

Note:—A study can be awarded a maximum of one star for each numbered item within the Selection and Exposure categories. A maximum of two stars can be given for Comparability.

DISCUSSION

In this study, we systematically reviewed clinical and radiologic data regarding the endovascular treatment of intracranial blister aneurysms. Most of the patients reported in literature were women, and the more common clinical presentation was Hunt and Hess grade 2 or 3.

Blister aneurysms appeared in >85% of cases with small aneurysms (up to 5 mm) and in almost 99% of patients when the aneurysm originated from the internal carotid artery.

Seven different procedures are reported for treatment of blister aneurysms, highlighting the continuing technical evolution and the increasing number of new devices available for endovascular management of these challenging vascular pathologies (or lesions or anomalies). In fact, neither the pathophysiologic mechanisms at the base of blister aneurysm formation nor their optimal treatment has been established yet.

Because blister aneurysms are presumed to be a type of vascular dissection or pseudoaneurysm, their treatment should not focus solely on the aneurysm sac but should also address the reconstruction of the wall of the affected vessel.

Endovascular procedures were initially faced with skepticism because of the reported risk of incomplete aneurysm occlusion in the acute phase and rupture during traditional coiling and

rebleeding at a distance.[40] However, the endovascular treatment of blister aneurysms was completely revolutionized by the introduction of stents and, in particular, with the advent of flow diversion.

In agreement, our data showed that endovascular treatment of blister aneurysms is relatively effective and safe. The rate of immediate aneurysm occlusion/near-complete occlusion is about 62%, and the overall rate of complications is about 9%, with a perioperative mortality rate of <3%. In particular, the risk of perioperative bleeding appeared as significantly lower than after surgical techniques (1.3% vs 29%).[41] At radiologic follow-up, the rate of effective occlusion was >78%, and the overall mortality rate remained below 5% (Online Supplemental Data).

The improvement of the radiologic outcome can be explained considering that most patients were treated with stent placement or a stand-alone flow diverter, which usually guarantees a long-term effect but not always immediate complete occlusion due to the specific hemodynamic modification induced.

However, the risk of prolonged use of antithrombotic medications required in stent-placement procedures needs to be carefully considered. Indeed, concerns about the use of dual-antiplatelet therapy are common.[42,43]

A systematic review by Skukalek et al[44] suggested high-dose aspirin for >6 months to minimize permanent thrombotic complications as well as permanent and transient hemorrhagic complications and loading doses of aspirin and clopidogrel preprocedurally to potentially decrease the incidence of hemorrhagic events.

However, despite the specific type of endovascular approach, our data showed a good clinical outcome (mRS <2) at final follow-up in more than three-fourths of patients (77%). Although an overall mortality rate of 4.8% is not negligible, it mainly reflects the severity of the clinical status at admission rather than a complication of the treatment.

Coiling and Stent-Assisted Coiling
In our review, 262 patients (32.8%) underwent coiling (6 patients) or stent-assisted coiling (256 patients). The largest series have been described by Ren et al,[17] Xu et al,[16] Zhu et al,[21] and Lim et al,[32] who reported 58, 44, 39, and 31 patients, respectively. Major concerns about coiling included the high rate of aneurysm regrowth and of intraprocedural rupture.[37,45-49] Indeed, the frequent lack of a real neck and the small size of the blister aneurysm often rapidly led to the use of adjuvants such as stents by most of the authors, as reported in most of the subsequent literature. However, in our study, small series for coiling alone reported a good rate of occlusion.[17,22]

Indeed, our data showed that stent-assisted coiling was considered by most of the authors as the first-line treatment (about 32% of all cases), with 83% of complete/near-complete occlusion at final follow-up and a clinical outcome comparable with that for the other treatments. The rate of complications was also comparable except for the incidence of vasospasm, which was reported in a significantly higher percentage of cases (about 11%), though these data were not corrected for clinical status at admission. This could be partially explained by the adjunctive mechanical stimulus due to the vessel manipulation for stent and coil release.

In conclusion, pros of coiling/stent-assisted coiling are a good rate of immediate occlusion and a lower cost; the con is the higher risk of vasospasm.

Stand-alone Stent Placement
Single or multiple stand-alone stent placements were the second most common procedure performed, representing the 15.9% of the included cases. Overlapping stents were sometimes anecdotally reported with the rationale of increasing strut density and the thickness of the stent, thus remodeling and reinforcing the arterial wall.[32,35] The larger series was described by Fang et al,[9] including 213 patients, who reported no difference in perioperative ischemic and mortality rates among different numbers of stents delivered.

Our data showed the absence of differences in terms of the number of thrombotic or stroke events in comparison with the other types of treatment (Online Supplemental Data). Similarly, the rate of intraoperative hemorrhage was lower compared with stent-assisted coiling and flow-diverter procedures despite the need for introducing antithrombotic therapy and the delayed occlusive effect compared with procedures including coiling.

In conclusion, the advantage of stand-alone stent placement is a lower risk of intraoperative bleeding, while the disadvantages are the delayed occlusive effect and the need for long-term antithrombotic therapy for the patient.

Flow Diversion
Flow diversion was reported in 155 (27%) patients, but in only 10 patients was it associated with coiling.

Flow diverters are gaining increased attention because of the possibility of parent vessel reconstruction. They represent new effective devices for the management of complex aneurysms, but evidence of their effects on blister aneurysms has not been completely elucidated. Flow-diverter technology is, in fact, controversial for certain aspects related to its architecture and its hemodynamic effect, which expose the patient to potential complications due to the delayed occlusive effect not seen with traditional coiling. Mokin et al[14] described the largest series of patients treated with flow diverters, supporting their use especially for treatment of carotid blister aneurysms.

Our data showed a good rate of occlusion at final follow-up (75.6%), but with a higher rate of perioperative death (5.2%) (Online Supplemental Data).

Overlapping flow diverters were overall reported in a limited number of cases (19 cases of 156). Cerejo et al[18] reported the higher number (n = 7) of patients treated with overlapping stents, described in 4 cases of complete occlusion and in 3 cases of incomplete occlusion. Mokin et al,[14] Ryan et al,[20] Yoon et al,[29] and Chalouhi et al[30] reported, instead, mixed series of patients treated with single or overlapped flow diverters without significant differences in the clinical results. On the contrary, other authors such as Parthasarathy et al,[13] Linfante et al,[24] and Aydin et al[36] specifically preferred single-device procedures for blister aneurysm treatment.

The advantages of placing overlapping flow diverters are the minimization of the risk of postdiversion rerupture and the speed of the parent vessel endothelialization with definitive exclusion of

the lesion (Ryan et al[20]). However, a significant reduction in post-treatment bleeding has not been demonstrated to date by placing multiple stents. On the other hand, some risks should be considered, such as cerebral ischemia due to jailing of perforating vessels, an increased risk of device thrombosis, and procedural complications related to the additional steps required for placement of multiple devices.[29,36]

In conclusion, the advantage of flow diversion is a good final occlusion rate, with the possibility of complete vessel wall healing; the disadvantages are the higher cost of the devices, the delayed occlusion, the higher risk of perioperative death, and the need for a long-term antithrombotic therapy.

Parent Artery Occlusion

Parent artery occlusion with balloons and/or coils as rescue strategy was reported in 3 cases (0.4%) of ruptured blister aneurysms with SAH, and no complications were reported. However, ischemic complications due to important internal carotid artery side-branch occlusion (ophthalmic artery, anterior choroidal artery, and fetal presentation of the posterior communicating artery) have to be considered, even if the patient passes the balloon test occlusion.

In conclusion, the advantage of parent artery occlusion is the immediate aneurysm obliteration and the low cost; the disadvantages are the ischemic complications.

Comparison between Treatments

Our treatment subgroup analyses showed that the higher rate of immediate occlusion is obtained with the stent-assisted coiling technique (pooled percentage of 63.4%). However, at final follow-up, the different endovascular techniques show comparable results in terms of complete occlusion (Online Supplemental Data). Stand-alone stent placement presents the higher rate of good clinical outcome with 94.8% of mRS < 2 and the lower rate of complications in general.

Care must be taken for the incidence of vasospasm after stent-assisted procedures and for the non-negligible rate of perioperative death during flow diverter releasing.

Anticoagulation/Antiplatelet Treatment

Our data did not show particular complications from anticoagulation/antiplatelet therapy (hemorrhage was reported in 1.34% of patients, 0.63% in the flow-diverter group), with no statistically significant differences between groups of treatments.

In flow-diversion procedures, the timing of treatment and the antiplatelet regimen is still a dilemma; a number of differing protocols are currently available and reported.

There is uncertainty about not only the type of drug but also the timing of administration. In the study of Yoon et al,[29] thromboembolic complications occurred in 27% of patients despite preprocedural aspirin and clopidogrel loading (timing not specified) and monitoring of platelet inhibition. No rebleeding was reported. Lin et al[50] administered the antiplatelet loading 12 hours before the procedure. In their series of 26 patients treated with a Pipeline Embolization Device (Medtronic) for a ruptured blister aneurysm, they reported a lower number of in-stent thromboses (7.6%) and brain stem ischemia (3.8%). Still, no rebleeding was reported. Favorable outcome with no incidence of thrombo-embolism or

rebleeding was reported by Chalouhi et al[30] and Aydin et al[36] when treatment was deferred (>5 days). Antiplatelet loading was performed, respectively, 8 and 12 hours before the procedure.

Therefore, although an increased risk for bleeding theoretically exists with antiplatelet administration, from our data and the data in literature, antiplatelet drugs seem not to significantly affect the risk of intra-/postprocedural bleeding. On the other hand, the thromboembolic risk seems to be of more concern (1.81% versus 0.63% risk of hemorrhage in the flow-diverter group; Online Supplemental Data), even when preprocedural antiplatelet loading is performed.

Comparison with Previous Systematic Reviews

Compared with previous systematic reviews on this topic,[41,51,52] our meta-analysis included a larger number of articles and patients, pooled data from different endovascular treatments, and both radiologic and clinical outcome for data analysis. Furthermore, even newer and more advanced techniques and devices involved in the endovascular treatment of blister aneurysms have been reported, fostering a current critical update of their clinical and radiologic outcomes.

Limitations

Our study has several limitations. Clinical and radiologic follow-up times were variable (6–32 months); thus, data are limited by the heterogeneity of follow-up. Most of the selected articles were observational, nonrandomized, and noncomparative studies, and data were collected retrospectively, often lacking in several details. Moreover, in patients with SAH due to blister aneurysm rupture, it is difficult to differentiate procedure-related morbidity from morbidity secondary to complications of SAH.

Also, even though aneurysm topography was reported in all cases, for a minority of patients, it was not possible to associate the location with the specific endovascular technique during the subgroup analysis.

Finally, our results could be influenced by publication bias. In fact, we could have missed some studies with worse outcomes that were performed and not published, distorting the evidence base.

However, this study provides useful data to consider when assessing the effects and risks of endovascular treatment in blister aneurysms and could represent a stepping stone for future comparative or randomized studies in this group of patients.

CONCLUSIONS

Blister aneurysms are complex vascular lesions representing a treatment challenge for cerebrovascular specialists. Currently, the endovascular approach represents a valid treatment option due to its safety and efficacy profile, reaching, at follow-up, a rate of effective occlusion of about 78%, with a relatively low incidence of complications, and an overall mortality below 5%.

REFERENCES

1. Abe M, Tabuchi K, Yokoyama H, et al. **Blood blisterlike aneurysms of the internal carotid artery.** *J Neurosurg* 1998;89:419–24 CrossRef Medline

2. Ogawa A, Suzuki M, Ogasawara K. **Aneurysms at nonbranching sites in the surpaclinoid portion of the internal carotid artery: internal carotid artery trunk aneurysms.** *Neurosurgery* 2000;47:578–83; discussion 583–86 CrossRef Medline

3. Ishikawa T, Nakamura N, Houkin K, et al. **Pathological consideration of a "blister-like" aneurysm at the superior wall of the internal carotid artery: case report.** *Neurosurgery* 1997;40:403–05; discussion 405–06 CrossRef Medline

4. Mizutani T, Miki Y, Kojima H, et al. **Proposed classification of nonatherosclerotic cerebral fusiform and dissecting aneurysms.** *Neurosurgery* 1999;45:253–59; discussion 259–60 CrossRef Medline

5. Meling TR, Sorteberg A, Bakke SJ, et al. **Blood blister-like aneurysms of the internal carotid artery trunk causing subarachnoid hemorrhage: treatment and outcome.** *J Neurosurg* 2008;108:662–71 CrossRef Medline

6. Sim SY, Shin YS, Cho KG, et al. **Blood blister-like aneurysms at nonbranching sites of the internal carotid artery.** *J Neurosurg* 2006;105:400–05 CrossRef Medline

7. Lee JW, Choi HG, Jung JY, et al. **Surgical strategies for ruptured blister-like aneurysms arising from the internal carotid artery: a clinical analysis of 18 consecutive patients.** *Acta Neurochir (Wien)* 2009;151:125–30 CrossRef Medline

8. Kaschner MG, Kraus B, Petridis A, et al. **Endovascular treatment of intracranial 'blister' and dissecting aneurysms.** *Neuroradiol J* 2019;32:353–65. CrossRef Medline

9. Fang Y, Zhu D, Peng Y, et al. **Treatment of blood blister-like aneurysms with stent-assisted coiling: a retrospective multicenter study.** *World Neurosurg* 2019;126:e486–91 CrossRef Medline

10. Kim MJ, Chung J, Shin YS, et al. **Forward deployed coil embolization with multiple overlapping stents for ruptured blood blister-like aneurysms: technical considerations and outcomes.** *Neurol Res* 2019;41:562–68 CrossRef Medline

11. Capocci R, Shotar E, Di Maria F, et al. **Delayed treatment (≥5 days) by flow diversion of ruptured blister-like cerebral aneurysms: case series of 8 consecutive patients.** *Clin Neuroradiol* 2020;30:287–96 CrossRef Medline

12. Hellstern V, Aguilar-Perez M, AlMatter M, et al. **Microsurgical clipping and endovascular flow diversion of ruptured anterior circulation blood blister-like aneurysms.** *Interv Neuroradiol* 2018;24:615–23 CrossRef Medline

13. Parthasarathy R, Gupta V, Gupta A. **Safety of prasugrel loading in ruptured blister like aneurysm treated with a Pipeline device.** *Br J Radiol* 2018;91:20170476 CrossRef Medline

14. Mokin M, Chinea A, Primiani CT, et al. **Treatment of blood blister aneurysms of the internal carotid artery with flow diversion.** *J Neurointerv Surg* 2018;10:1074–78 CrossRef Medline

15. Hao X, Li G, Ren J, et al. **Endovascular patch embolization for blood blister-like aneurysms in dorsal segment of internal carotid artery.** *World Neurosurg* 2018;113:26–32 CrossRef Medline

16. Xu D, Zhang C, Wang T, et al. **Evaluation of Enterprise stent-assisted coiling and telescoping stent technique as treatment of supraclinoid blister aneurysms of the internal carotid artery.** *World Neurosurg* 2018;110:e890–96 CrossRef Medline

17. Ren Y, Liu L, Sun H, et al. **Microsurgical versus endovascular treatments for blood-blister aneurysms of the internal carotid artery: a retrospective study of 83 patients in a single center.** *World Neurosurg* 2018;109:e615–24 CrossRef Medline

18. Cerejo R, Bain M, John S, et al. **Flow diverter treatment of cerebral blister aneurysms.** *Neuroradiology* 2017;59:1285–90 CrossRef Medline

19. Yang C, Vadasz A, Szikora I. **Treatment of ruptured blood blister aneurysms using primary flow-diverter stenting with considerations for adjunctive coiling: a single-centre experience and literature review.** *Interv Neuroradiol* 2017;23:465–76 CrossRef Medline

20. Ryan RW, Khan AS, Barco R, et al. **Pipeline flow diversion of ruptured blister aneurysms of the supraclinoid carotid artery using a single-device strategy.** *Neurosurg Focus* 2017;42:E11 CrossRef Medline

21. Zhu D, Fang Y, Yang P, et al. **Overlapped stenting combined with coiling for blood blister-like aneurysms: comparison of low-profile visualized intraluminal support (LVIS) stent and non-LVIS stent.** *World Neurosurg* 2017;104:729–35 CrossRef Medline

22. Brown MA, Guandique CF, Parish J, et al. **Long-term follow-up analysis of microsurgical clip ligation and endovascular coil embolization for dorsal wall blister aneurysms of the internal carotid artery.** *J Clin Neurosci* 2017;39:72–77 CrossRef Medline

23. Fang C, Tan HQ, Han HJ, et al. **Endovascular isolation of intracranial blood blister-like aneurysms with Willis covered stent.** *J Neurointerv Surg* 2017;9:963–68 CrossRef Medline

24. Linfante I, Mayich M, Sonig A, et al. **Flow diversion with Pipeline embolic device as treatment of subarachnoid hemorrhage secondary to blister aneurysms: dual-center experience and review of the literature.** *J Neurointerv Surg* 2017;9:29–33 CrossRef Medline

25. Yu B, Zheng J, Hong Y, et al. **Stent-assisted coil embolization of ruptured supraclinoid blood blister-like aneurysm of internal carotid artery.** *Turk Neurosurg* 2016;26:219–22 CrossRef Medline

26. Song J, Oh S, Kim MJ, et al. **Endovascular treatment of ruptured blood blister-like aneurysms with multiple (≥3) overlapping Enterprise stents and coiling.** *Acta Neurochir (Wien)* 2016;158:803–09 CrossRef Medline

27. Ashour R, Dodson S, Aziz-Sultan MA. **Endovascular management of intracranial blister aneurysms: spectrum and limitations of contemporary techniques.** *J Neurointerv Surg* 2016;8:30–37 CrossRef Medline

28. Chinchure SD, Gupta V, Goel G, et al. **Subarachnoid hemorrhage with blister aneurysms: endovascular management.** *Neurol India* 2014;62:393–99 CrossRef Medline

29. Yoon JW, Siddiqui AH, Dumont TM, et al; Endovascular Neurosurgery Research Group. **Feasibility and safety of Pipeline Embolization Device in patients with ruptured carotid blister aneurysms.** *Neurosurgery* 2014;75:419–29; discussion 429 CrossRef Medline

30. Chalouhi N, Zanaty M, Tjoumakaris S, et al. **Treatment of blister-like aneurysms with the Pipeline embolization device.** *Neurosurgery* 2014;74:527–32; discussion 532 CrossRef Medline

31. Gonzalez AM, Narata AP, Yilmaz H, et al. **Blood blister-like aneurysms: single-center experience and systematic literature review.** *Eur J Radiol* 2014;83:197–205 CrossRef Medline

32. Lim YC, Kim BM, Suh SH, et al. **Reconstructive treatment of ruptured blood blister-like aneurysms with stent and coil.** *Neurosurgery* 2013;73:480–88 CrossRef Medline

33. Walsh KM, Moskowitz SI, Hui FK, et al. **Multiple overlapping stents as monotherapy in the treatment of 'blister' pseudoaneurysms arising from the supraclinoid internal carotid artery: a single institution series and review of the literature.** *J Neurointerv Surg* 2014;6:184–94 CrossRef Medline

34. Cinar C, Oran I, Bozkaya H, et al. **Endovascular treatment of ruptured blister-like aneurysms with special reference to the flow-diverting strategy.** *Neuroradiology* 2013;55:441–47 CrossRef Medline

35. Lee BH, Kim BM, Park MS, et al. **Reconstructive endovascular treatment of ruptured blood blister-like aneurysms of the internal carotid artery.** *J Neurosurg* 2009;110:431–36 CrossRef Medline

36. Aydin K, Arat A, Sencer S, et al. **Treatment of ruptured blood blister-like aneurysms with flow diverter SILK stents.** *J Neurointerv Surg* 2015;7:202–09 CrossRef Medline

37. Ihn YK, Kim SH, Sung JH, et al. **The efficacy of endovascular treatment of ruptured blood blister-like aneurysms using stent-assisted coil embolization.** *Interv Neuroradiol* 2012;18:432–41 CrossRef Medline

38. Fang YB, Li Q, Wu YN, et al. **Overlapping stents for blood blister-like aneurysms of the internal carotid artery.** *Clin Neurol Neurosurg* 2014;123:34–39 CrossRef Medline

39. Fang YB, Li Q, Yang PF, et al. **Treatment of blood blister-like aneurysms of the internal carotid artery with stent-assisted coil embolization.** *Clin Neurol Neurosurg* 2013;115:920–25 CrossRef Medline

40. Kalani MY, Zabramski JM, Kim LJ, et al. **Long-term follow-up of blister aneurysms of the internal carotid artery.** *Neurosurgery* 2013;73:1026–33; discussion 1033 CrossRef Medline

41. Shah SS, Gersey ZC, Nuh M, et al. **Microsurgical versus endovascular interventions for blood-blister aneurysms of the internal carotid artery: systematic review of literature and meta-analysis on safety and efficacy.** *J Neurosurg* 2017;127:1361–73 CrossRef Medline

42. Chung J, Kim BM, Lim YC. **Five overlapping Enterprise stents in the internal carotid artery-to-middle cerebral artery to treat a ruptured blood blister-like aneurysm.** *Neurol Sci* 2013;34:1485–87 CrossRef Medline

43. Peitz GW, Sy CA, Grandhi R. **Endovascular treatment of blister aneurysms.** *Neurosurg Focus* 2017;42:E12 CrossRef Medline

44. Skukalek SL, Winkler AM, Kang J, et al. **Effect of antiplatelet therapy and platelet function testing on hemorrhagic and thrombotic complications in patients with cerebral aneurysms treated with the Pipeline embolization device: a review and meta-analysis.** *J Neurointerv Surg* 2016;8:58–65 CrossRef Medline

45. Ahn JY, Cho JH, Jung JY, et al. **Blister-like aneurysms of the supraclinoid internal carotid artery: challenging endovascular treatment with stent-assisted coiling.** *J Clin Neurosci* 2008;15:1058–61 CrossRef Medline

46. Kim BM, Chung EC, Park SI, et al. **Treatment of blood blister-like aneurysm of the internal carotid artery with stent-assisted coil embolization followed by stent-within-a-stent technique. case report.** *J Neurosurg* 2007;107:1211–13 CrossRef Medline

47. Park JH, Park IS, Han DH, et al. **Endovascular treatment of blood blister-like aneurysms of the internal carotid artery.** *J Neurosurg* 2007;106:812–19 CrossRef Medline

48. Tanoue S, Kiyosue H, Matsumoto S, et al. **Ruptured "blisterlike" aneurysm with a pseudoaneurysm formation requiring delayed intervention with endovascular coil embolization. case report.** *J Neurosurg* 2004;101:159–62 CrossRef Medline

49. Islam MS, Manabe H, Hasegawa S, et al. **Successful staged treatment for ruptured blister-like dissecting aneurysm of the intracranial internal carotid artery: acute GDC embolization for the blister-like aneurysm followed by proximal occlusion with extracranial-intracranial bypass in the chronic stage.** *Minim Invasive Neurosurg* 2004;47:165–68 CrossRef Medline

50. Lin N, Brouillard AM, Keigher KM, et al. **Utilization of Pipeline embolization device for treatment of ruptured intracranial aneurysms: US multicenter experience.** *J Neurointerv Surg* 2015;7:808–15 CrossRef Medline

51. Peschillo S, Cannizzaro D, Caporlingua A, et al. **A systematic review and meta-analysis of treatment and outcome of blister-like aneurysms.** *AJNR Am J Neuroradiol* 2016;37:856–61 CrossRef Medline

52. Rouchaud A, Brinjikji W, Cloft HJ, et al. **Endovascular treatment of ruptured blister-like aneurysms: a systematic review and meta-analysis with focus on deconstructive versus reconstructive and flow-diverter treatments.** *AJNR Am J Neuroradiol* 2015;36:2331–39 CrossRef

Tailored Vessel-Catheter Diameter Ratio in a Direct Aspiration First-Pass Technique: Is It a Matter of Caliber?

E. Pampana, S. Fabiano, G. De Rubeis, L. Bertaccini, A. Stasolla, A. Vallone, A. Pingi, M. Mangiardi, S. Anticoli, C. Gasperini, and E. Cotroneo

ABSTRACT

BACKGROUND AND PURPOSE: The aspiration technique has gained a prominent role in mechanical thrombectomy. The thrombectomy goal is successful revascularization (modified TICI ≥ 2b) and first-pass effect. The purpose of this study was to evaluate the impact of the vessel-catheter ratio on the modified TICI ≥ 2b and first-pass effect.

MATERIALS AND METHODS: This was a retrospective, single-center, cohort study. From January 2018 to April 2020, 111/206 (53.9%) were eligible after applying the exclusion criteria. Culprit vessel diameters were measured by 2 neuroradiologists, and the intraclass correlation coefficient was calculated. The receiver operating characteristic curve was used for assessing the vessel-catheter ratio cutoff for modified TICI ≥ 2b and the first-pass effect. Time to groin puncture and fibrinolysis were weighted using logistic regression. All possible intervals (interval size, 0.1; sliding interval, 0.01) of the vessel-catheter ratio were plotted, and the best and worst intervals were compared using the χ^2 test.

RESULTS: Modified TICI ≥ 2b outcome was achieved in 75/111 (67.5%), and first-pass effect was achieved in 53/75 (70.6%). The MCA diameter was 2.1 mm with an intraclass correlation coefficient of 0.92. The optimal vessel-catheter ratio cutoffs for modified TICI ≥ 2b were ≤1.51 (accuracy = 0.67; 95% CI, 0.58–0.76; $P = 0.001$), and for first-pass effect, they were significant (≤1.33; $P = .31$). The modified TICI ≥ 2b odds ratio and relative risk were 9.2 (95% CI, 2.4–36.2; $P = 0.002$) and 3.2 (95% CI, 1.2–8.7; $P = .024$). The odds ratio remained significant after logistic regression (7.4; 95% CI, 1.7–32.5; $P = .008$). First-pass effect odds ratio and relative risk were not significant (2.1 and 1.5; $P > .05$, respectively). The modified TICI ≥ 2b best and worst vessel-catheter ratio intervals were not significantly different (55.6% versus 85.7%, $P = .12$). The first-pass effect best vessel-catheter ratio interval was significantly higher compared with the worst one (78.6% versus 40.0%, $P = .03$).

CONCLUSIONS: The aspiration catheter should be selected according to culprit vessel diameter. The optimal vessel-catheter ratio cutoffs were ≤1.51 for modified TICI ≥ 2b with an odds ratio of 9.2 and a relative risk of 3.2.

ABBREVIATIONS: ADAPT = a direct aspiration first-pass technique; mTICI = modified TICI

S troke represents the second leading cause of death in the world;[1] however, the case fatality rate has decreased in recent decades due to primary prevention and treatment improvements.[2] After the introduction in various guidelines,[3,4] patients treated with mechanical thrombectomy showed a significant decrease of disability at 90 days compared with controls (OR = 2.49; 95% CI, 1.76–3.53; $P < .0001$)[5] and a reduction of decompressive hemicraniectomy for malignant cerebral edema (range, 11.4%–4.8%; $P < .001$).[6] Recently, a direct aspiration first-pass technique (ADAPT) has gained a level of I B-R for mechanical thrombectomy in the 2019 guidelines for stroke management.[3] An modified TICI (mTICI) of grade 2b/3 is the mechanical thrombectomy goal for increasing good functional outcome;[3,7] in addition, first-pass effects have earned a prominent role in stroke prognosis.[8]

Nikoubashman et al[9] demonstrated, in an experimental animal study, that large-bore catheters should have an inner diameter of >1.016 mm for the MCA and >1.524 mm for the ICA. Moreover, Alawieh et al[10] showed a higher rate of recanalization and first-pass effect using larger diameter catheters versus smaller ones (ACE64/ACE68 [Penumbra] versus 5MAX ACE [Penumbra], 85%/81% versus 61%, $P < .05$, respectively). However, no differences were found

Table 1: Clinical details

	Patients with MCA Stroke (*n* = 111)
Age (median) (95% CI) (yr)	73 (71.0–76.8)
Male (No.) (%)	66 (59.5%)
BMI (median and 95% CI)	24.9 (23.8–25.4)
Family history (No.) (%)	82 (7.5%)
Smoking (No.) (%)	20 (18.0%)
Atrial fibrillation (No.) (%)	39 (35.1%)
Arterial hypertension (No.) (%)	64 (57.7%)
Obesity (No.) (%)	13 (11.7%)
Atrial septal defect (No.) (%)	5 (4.5%)
Total cholesterol level (median) (95% CI)	155 (148.0–168.1)
HDL (median) (95% CI)	42 (41.0–45.0)
LDL (median) (95% CI)	108.0 (94.1–115.0)
HbA1c (median) (95% CI)	6.0 (5.9–6.0)
NIHSS score	16.0 (15.0–18.0)

Note:—BMI indicates body mass index; HDL, high-density lipoprotein; LDL, low-density lipoprotein; HbA1c, glycated hemoglobin.

Table 2: Technical details

	Patients with MCA Stroke (*n* = 111)
Wake-up stroke (No.) (%)	23 (20.7%)
Time to groin puncture (median) (95% CI) (h)	4.3 (4.1–4.5)
Fibrinolysis (No.) (%)	64 (57.7%)
Catheter inner diameter (No.) (%)	
1.09 mm (3MAX)	1 (0.9%)
1.37mm (3MAX)	3 (2.7%)
1.47mm (3MAX)	2 (1.8%)
1.52 mm (3MAX)	29 (26.1%)
1.62.mm (3MAX)	4 (3.6%)
1.63 mm (3MAX)	1 (0.9%)
1.73 mm (3MAX)	71 (64.0%)

in terms of first-pass effect, reperfusion, and clinical outcome among different large-bore catheters selected (Catalyst 6, Stryker; Sofia, MicroVention; Navien, Covidien; ACE68, Penumbra; *P* > .05).[11]

The aim of this study was to evaluate the impact of the vessel-catheter ratio on successful revascularization and first-pass effect in a tertiary center (Azienda Ospedaliera San Camillo/Forlanini for cerebrovascular disease treatment.

MATERIALS AND METHODS

This study was approved by the ethics institutional review board. Informed consent was waived due to the retrospective nature of this study.

The manuscript was drafted according to the Strengthening the Reporting of Observational Studies in Epidemiology (STROBE) guidelines.[12]

This was a retrospective, single-arm, single-center, cohort study. From January 2018 to April 2020, we evaluated all patients admitted to the stroke unit of a tertiary hub center who underwent endovascular thrombectomy according to current guidelines.[3] The exclusion criteria for the study were the following: non-MCA and mechanical thrombectomy technique different from ADAPT. Because there is no definitive indication regarding which endovascular technique should be used for thrombectomy,[3] the choice was left to the interventional neuroradiologist at the time of the procedure. The clinical details of the cohort are given in Table 1.

Technical success was defined with a mTICI 2b or 3.[3,4] The first-pass effect would be mTICI ≥ 2b in 1 passage of the catheter.

The vessel-catheter ratio was calculated as the fraction between the culprit vessel and the inner diameter of the catheter used for aspiration because the inner diameter is the "active" part for aspiration force.[13]

Vessel-Diameter Measurement

The diameter of the occluded vessel was measured by 2 neuroradiologists (S.F. and L.B. with 20 and 8 years of experience, respectively) in the straight tract of the closest vessel before the thrombus on DSA.[14] The simple mean between these

measurements was taken for further analysis, and the intraclass correlation agreement was calculated.

Endovascular Technique

All patients were treated using ADAPT by 5 experienced neurointerventional radiologists (>7 years' experience) in a dedicated angiosuite (biplane Artis zee; Siemens).

All procedures were performed via arterial access with the patient under sedation or general anesthesia according to the present clinical status and stroke severity. ADAPT was performed through femoral access using a 6F long vascular sheath (Neuro MAX 088, Penumbra; or AXS Infinity LS, Stryker Neurovascular) positioned in the ICA of the culprit side. The size of the intermediate aspiration catheters was chosen by the neurointerventional radiologist at the time of the procedure; in 1/111 (0.9%), a distal aspiration catheter was used. The intermediate catheters used were both Stryker and Penumbra systems and were divided according to their inner diameter into the following: 1.37 mm (5MAX ACE), 1.47 mm (AXS Catalyst 5; Stryker), 1.52 mm (AXS Catalyst 6), 1.62 mm (AXS Catalyst 7), 1.63 mm (ACE64), and 1.73 mm (ACE68). The distal aspiration catheter used has an inner distal lumen of 1.09 (3MAX; Penumbra). The ADAPT was always performed without a microguidewire inside the lumen and with an aspiration pump (Pump MAX; Penumbra).[9] See Table 2 for frequency.

Study Outcome

The primary outcome was to evaluate the cutoff value of the vessel-catheter ratio, maximizing the likelihood of obtaining mTICI ≥ 2b. Furthermore, the impact on successful revascularization of the adequate vessel-catheter ratio was weighted with fibrinolysis and time to groin puncture. Subanalysis was performed for first-pass effect versus a control group (non-first-pass effect revascularization + mTICI ≤ 2a). The secondary outcome was to evaluate the impact of different cutoff values on the likelihood of obtaining a successful revascularization and a first-pass effect.

Data Base Preparation

Clinical data were retrospectively derived from a prospective data base drafted by the stroke unit. The radiologic parameters were evaluated through Radiology and Imaging Specialists/PACS systems by 1 neuroradiologist (5 years of experience) not involved in the procedure. The angiographic measurements of culprit vessel
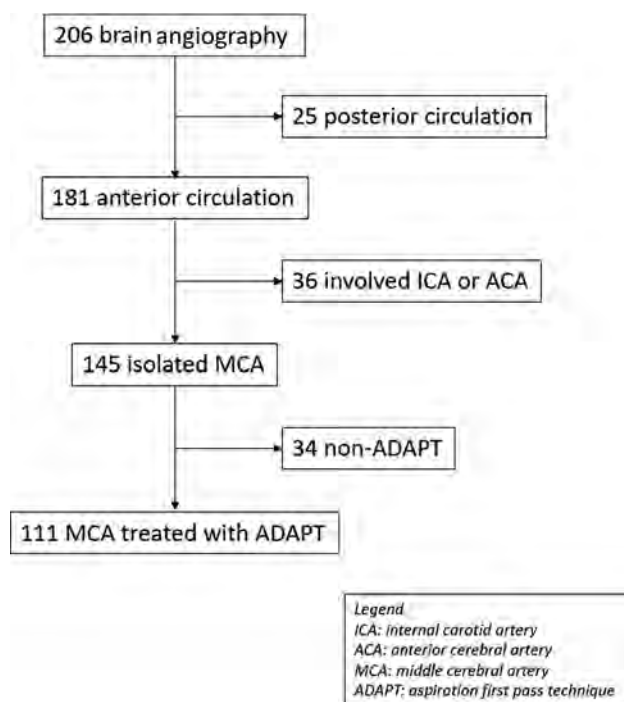
FIG 1. Study flow chart.

diameter were evaluated by 2 neuroradiologists, and the simple mean was taken for the analysis.

Statistical Analysis

Normality was tested using the Kolmogorov-Smirnov Z, and continuous variables were reported accordingly. Ordinal values were reported as percentages. The intraclass correlation coefficient (for vessel diameter) was calculated using the intraclass correlation. mTICI was defined dichotomously in successful (mTICI ≥ 2b) and unsuccessful (mTICI ≤ 2a) revascularization. The receiver operating characteristic curve and Youden index were used for assessing the optimal cutoff values for the vessel-catheter ratio. The odds ratio, the relative risk, and the number of patients to be treated were calculated. Logistic regression was used for analyzing the impact on successful revascularization of the vessel-catheter-ratio, fibrinolysis, and time to groin puncture The impact of different cutoff values of the vessel-catheter ratio was evaluated by calculating the percentage of successful revascularizations and first-pass effects using an interval of 0.1 and an interval increment of 0.01, starting at the lowest value of the vessel-catheter ratio (1.0) to the highest (1.7); subsequently, the percentage was plotted. For both analyses, a subgroup evaluation was performed using first-pass effect as endpoint. Statistical analysis was performed, and the graph was plotted using MedCalc 18.2.1 (MedCalc Software) and Excel (Microsoft). *P* values < .05 were considered statistically significant, and all *P* values were calculated using a 2-tailed significance level.

RESULTS

Two-hundred six consecutive patients underwent brain angiography for mechanical thrombectomy; after applying the exclusion

Table 3: Successful revascularization (mTICI ≥ 2b)[a]

	Non-Wake-Up Stroke		All Patients	
	OR	*P*	OR	*P*
Cutoff ≤1.51	7.3 (1.7–32.1)	.008	9.6 (2.4–38.7)	.0014
Fibrinolysis	1.9 (0.7–5.4)	.22	2.1 (0.9–5.3)	.10
Time to groin (h)	0.9 (0.8–1.1)	.5		

[a] Data are modified treatment in cerebral infarction.

Table 4: First-pass effect

	Non-Wake-Up Stroke		All Patients	
	OR	*P*	OR	*P*
Cutoff ≤1.33	2.1 (0.8–5.6)	.14	1.9 (0.8–4.7)	.14
Fibrinolysis	2.1 (0.8–5.5)	.14	1.7 (0.7–4.0)	.23
Time to groin (h)	1.1 (0.9–1.3)	.5		

criteria, 95/206 (46.1%) were further excluded from the analysis. Thirty-six of 95 (37.9%) of the strokes involved the ICAs, 25/96 (26.3%) had posterior circulation stroke, and in 34/95 (35.8%) ADAPT was not used as the first-line technique. The final population encompassed 111/206 (53.9%) patients with MCA stroke treated with ADAPT; the clinical details are provided in Table 1. Twenty-three of 111 (20.7%) were wake-up strokes. The flow-chart of the study is shown in Fig 1. The rate of mTICI ≥ 2b was 75/111 (67.5%), and the first-pass effect was 53/75 (70.6%). All patients with mTICI ≤ 2a (36/111 [32.5%]) underwent a rescue technique. The median vessel diameter was 2.1 mm (95% CI, 2.0– 2.1; range, 1.3–3.9; mean, 2.1 [SD, 0.4]); the intraclass correlation coefficient was 0.92 (95% CI, 0.84–0.97). Technical parameters are shown in Table 2.

The optimal vessel-catheter ratio cutoff for maximizing the likelihood of obtaining mTICI ≥ 2b was ≤1.51 (accuracy = 0.67; 95% CI, 0.58–0.76; *P* = 0.001). With a vessel-catheter ratio of ≤1.51 as a cutoff, the chances of obtaining mTICI ≥ 2b were significantly higher compared with the vessel-catheter ratio of >1.51 (OR, 9.2; 95% CI, 2.4–36.2; *P* = 0.002; relative risk, 3.2; 95% CI, 1.2–8.7; *P* = 0.02). The number of patients to be treated to observe a benefit with a vessel-catheter ratio of ≤1.51 was 2.0 (95% CI, 1.3–4.0). The likelihood of achieving successful revascularization also remained significant after logistic regression both for all patients and for those with non-wake up stroke (OR = 9.6; 95% CI, 2.4–38.7; *P* = .0014; OR = 7.3; 95% CI, 1.7–32.1; *P* = .008, respectively) (see Tables 3 and 4 for details). No significant cutoff was found for first-pass effect likelihood as outcome, though the highest Youden index was for vessel-catheter ratio of ≤1.33 (accuracy = 0.56; 95% CI, 0.46–0.65; *P* = .31). With the vessel-catheter ratio of ≤1.33, there was a trend toward first-pass effect likelihood, although not statistically significant (OR = 2.1; 95% CI, 0.93–5.0; *P* = .07 with a relative risk of 1.5; 95% CI, 0.93–2.5; *P* = .10, respectively). The ORs of logistic regression analysis were not statistically significant either (Tables 3 and 4).

The percentage of successful revascularizations of the 0.1 interval ranged from 0.0% to 85.7% (median, 66.7%; 95% CI, 64.6%–70.0%). Considering exclusively the interval below 1.51, the percentage ranged from 55.6% to 85.7% (median 68.8%; 95%
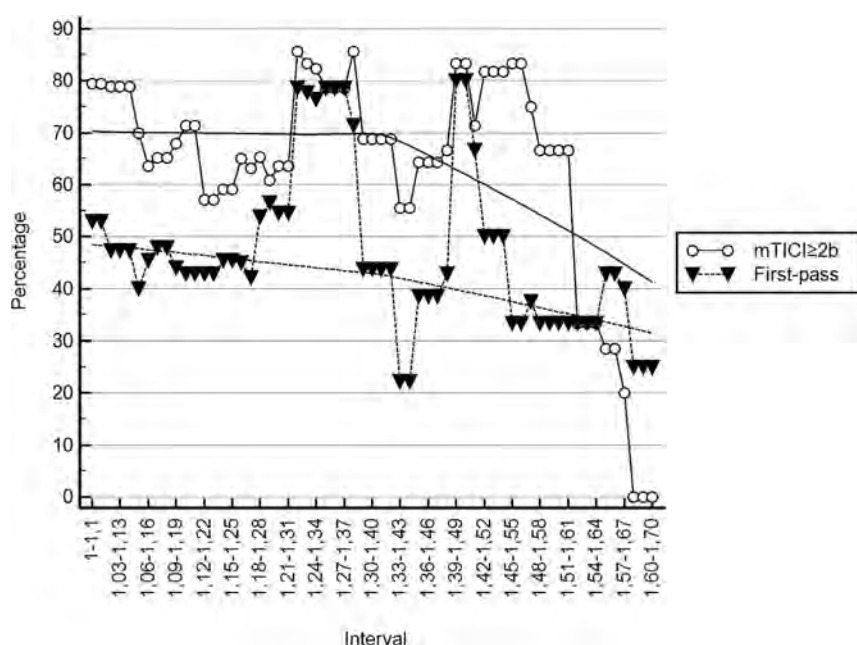
FIG 2. The plot shows the trend of successful revascularization (*line with dot*) and a first-pass effect (*dotted line with triangle*) together with the tendency line among different intervals of vessel-to-catheter ratios. As observed, after the respective cutoff (≤1.51 and ≤1.33) for mTICI ≥ 2b and first-pass effect, the trend remains stable.

CI, 65.0%–71.4%). No statistically significantly differences were found between the percentage of the worst interval (1.34–1.44) and the best one (1.28–1.38; 55.6% versus 85.7%; *P* = .12, respectively) (Fig 2). The percentage for obtaining a successful revascularization in 1 passage ranged from 0.0% to 80.0%; considering the interval below 1.33, the percentage ranged from 40.0% to 78.6% (median, 47.4%; 95% CI, 44.7%–52.9%). The percentage for obtaining first-pass revascularization of the best interval (range, 1.26–1.36) was significantly higher compared with the worst one (range, 1.05–1.15; 78.6% versus 40.0%; *P* = .03, respectively) (Fig 2).

DISCUSSION

The best cutoff of the vessel-catheter ratio to maximize the likelihood for achieving mTICI ≥ 2b was ≤1.51 (accuracy = 0.67, *P* = .0012, OR = 9.2), with a percentage of successful revascularization spanning 55.6% to 85.7% (vessel-catheter ratio interval, 1.0–1.51). For the first pass, the optimal cutoff, though not statistically significant, was 1.33 (accuracy = 0.56, *P* = .31, OR = 2.1), with a range of first-pass effect from 40.0% to 78.6% (vessel-catheter ratio interval, 1.0–1.33).

Different companies tried to increase the diameter of large-bore catheters (from 1.37 to 1.82 mm)[15] for ADAPT, based on the assumption that "the bigger the catheter is, the better the result will be," with the lessening of maneuverability for larger catheters.[9] This paradigm is supported by the concept that a larger inner diameter increases the aspiration flow rate and therefore the likelihood of thrombus aspiration.[13] These results are supported by the present study, which showed a cutoff of the vessel-catheter ratio for reaching mTICI ≥ 2b of ≤1.51 with an OR = 9.2 (95% CI, 2.4–36.2) and a number of patients treated of

2.0 (95% CI, 1.3–4.0). Despite the wide 95% CI, this result remained significant after considering the time to groin puncture and fibrinolysis (Table 3). Most interesting, in the interval of the vessel-catheter ratio between 1.0 and 1.51, the percentage of successful revascularizations ranged from 55.6% to 85.7% without statistically significantly differences (Fig 2). This finding apparently contradicted the above-mentioned axiom; however, probably, once a sufficient aspiration force was achieved,[16] the following increment did not increase the chance of thrombus removal. Thus, the catheter should be selected according to vessel diameter, keeping in mind reaching at least a vessel-catheter ratio of ≤1.51. The ADAPT axiom should move from "the bigger the better" to "the fitter the better."

First-pass effect is a known favorable prediction factor for ischemic stroke recovery (OR = 2.4–3.2).[8,17] Large-bore catheters increased the rate of first-pass effect in an ADAPT series (53% versus 33%, *P* = .04), and the ACE68 was an independent predictor of successful reperfusion and good clinical outcome (OR = 1.67 and 6.2, respectively).[18] Although not significant, a statistical trend for first-pass effect was found with a vessel-catheter ratio of ≤1.33 (accuracy = 0.56; 95% CI, 0.46-0.65; *P* = .31) and an OR = 2.1 (95% CI, 0.93–5.0; *P* = .07). Considering the interval between 1.0 and 1.33, the percentage of first-pass effect ranged from 40.0% to 78.6%, superior to all of cases in the Contact Aspiration vs Stent Retriever for Successful Revascularization (ASTER) trial subanalysis (26.3%),[18] and in line with the results of Delgado Almandoz et al (53%).[19] This discrepancy may be explained by the unknown vessel-catheter ratio in these studies. In fact, a significantly better first-pass effect prevalence was found in the best interval (1.26–1.36) compared with the worst one (1.05–1.15; 78.6% versus 40.0%; *P* = .03) (Fig 2).

The reported mean diameter of the MCA is 2.3 mm, which is similar to our finding of 2.1 (SD, 0.4) mm.[14] Setting a vessel-catheter ratio of ≤1.51 (cutoff for mTICI ≥ 2b) and considering the reported diameter of 2.3 mm, the minimum catheter inner diameter was 1.5 mm.

Our study had several limitations. First, this was a single-center, nonrandomized study with a control group. Second, the large-bore catheters used were mostly Catalyst 6 (26.1%) and ACE68 (64.0%). Third, the sample size was low, especially for a first-pass effect, as shown by the large 95% CI of our findings, though the number of patients (*n* = 111) was in line with those in monocentric stroke studies.

CONCLUSIONS

The catheter selection for ADAPT should be performed keeping in mind the goal of a vessel-catheter ratio of ≤1.51 for increasing

to mTICI ≥ 2b. For achieving mTICI ≥ 2b, considering the average diameter of middle cerebral artery, the inner diameter of the intermediate catheter should be ≥1.5 mm.

REFERENCES

1. World Health Organization. **The top 10 causes of death.** 2020. https://www.who.int/news-room/fact-sheets/detail/the-top-10-causes-of-death. Accessed May 2, 2020
2. Shah R, Wilkins E, Nichols M, et al. **Epidemiology report: trends in sex-specific cerebrovascular disease mortality in Europe based on WHO mortality data.** *Eur Heart J* 2019;40:755–64 CrossRef Medline
3. Powers WJ, Rabinstein AA, Ackerson T, et al. **Guidelines for the Early Management of Patients with Acute Ischemic Stroke: 2019 Update to the 2018 Guidelines for the Early Management of Acute Ischemic Stroke—A Guideline for Healthcare Professionals From the American Heart Association/American Stroke Association.** *Stroke* 2019;50:e344–18 CrossRef Medline
4. Powers WJ, Rabinstein AA, Ackerson T, et al; American Heart Association Stroke Council. **Guidelines for the Early Management of Patients with Acute Ischemic Stroke: A Guideline for Healthcare Professionals From the American Heart Association/American Stroke Association.** *Stroke* 2018;49:e46–110 CrossRef Medline
5. Goyal M, Menon BK, van Zwam WH, et al; HERMES collaborators. **Endovascular thrombectomy after large-vessel ischaemic stroke: a meta-analysis of individual patient data from five randomised trials.** *Lancet* 2016;387:1723–31 CrossRef Medline
6. Rumalla K, Ottenhausen M, Kan P, et al. **Recent nationwide impact of mechanical thrombectomy on decompressive hemicraniectomy for acute ischemic stroke.** *Stroke* 2019;50:2133–39 CrossRef Medline
7. Zhang X, Yuan K, Wang H, et al. **Nomogram to predict mortality of endovascular thrombectomy for ischemic stroke despite successful recanalization.** *J Am Heart Assoc* 2020;9:e014899 CrossRef Medline
8. Zaidat OO, Castonguay AC, Linfante I, et al. **First pass effect: a new measure for stroke thrombectomy devices.** *Stroke* 2018;49:660–66 CrossRef Medline
9. Nikoubashman O, Nikoubashman A, Busen M, et al. **Necessary catheter diameters for mechanical thrombectomy with ADAPT.** *AJNR Am J Neuroradiol* 2017;38:2277–81 CrossRef Medline
10. Alawieh A, Chatterjee AR, Vargas J, et al. **Lessons learned over more than 500 stroke thrombectomies using ADAPT with increasing aspiration catheter size.** *Neurosurgery* 2020;86:61–70 CrossRef Medline
11. Tonetti DA, Desai SM, Casillo S, et al. **Large-bore aspiration catheter selection does not influence reperfusion or outcome after manual aspiration thrombectomy.** *J Neurointerv Surg* 2019;11:637–40 CrossRef Medline
12. von Elm E, Altman DG, Egger M, et al; STROBE Initiative. **The Strengthening the Reporting of Observational Studies in Epidemiology (STROBE) statement: guidelines for reporting observational studies.** *Int J Surg* 2014;12:1495–99 CrossRef Medline
13. Nikoubashman O, Alt JP, Nikoubashman A, et al. **Optimizing endovascular stroke treatment: removing the microcatheter before clot retrieval with stent-retrievers increases aspiration flow.** *J Neurointerv Surg* 2017;9:459–62 CrossRef Medline
14. Abe Y, Yuki I, Otani K, et al. **Agreement of intracranial vessel diameters measured on 2D and 3D digital subtraction angiography using an automatic windowing algorithm.** *J Neuroradiol* 2019 Sep 26 [Epub ahead of print] CrossRef Medline
15. Kang DH, Hwang YH. **Frontline contact aspiration treatment for emergent large vessel occlusion: a review focused on practical techniques.** *J Stroke* 2019;21:10–22 CrossRef Medline
16. Smith M, Pace J, Ju C, et al. **Force and aspiration on catheters utilized in the adapt technique in acute ischemic stroke: a bench top analysis.** *J Neuroradiol* Apr 11 [Epub ahead of print] 2019 CrossRef Medline
17. Nikoubashman O, Dekeyzer S, Riabikin A, et al. **True first-pass effect.** *Stroke* 2019;50:2140–46 CrossRef Medline
18. Ducroux C, Piotin M, Gory B, et al; ASTER Trial investigators. **First pass effect with contact aspiration and stent retrievers in the Aspiration versus Stent Retriever (ASTER) trial.** *J Neurointerv Surg* 2020;12:386–391 CrossRef Medline
19. Delgado Almandoz JE, Kayan Y, Wallace AN, et al. **Larger ACE 68 aspiration catheter increases first-pass efficacy of ADAPT technique.** *J Neurointerv Surg* 2019;11:141–46 CrossRef Medline

Glioma-Induced Disruption of Resting-State Functional Connectivity and Amplitude of Low-Frequency Fluctuations in the Salience Network

J. Yang, S. Gohel, Z. Zhang, V. Hatzoglou, A.I. Holodny, and B.A. Vachha

ABSTRACT

BACKGROUND AND PURPOSE: Cognitive challenges are prevalent in survivors of glioma, but their neurobiology is incompletely understood. The purpose of this study was to investigate the effect of glioma presence and tumor characteristics on resting-state functional connectivity and amplitude of low-frequency fluctuations of the salience network, a key neural network associated with cognition.

MATERIALS AND METHODS: Sixty-nine patients with glioma (mean age, 48.74 [SD, 14.32] years) who underwent resting-state fMRI were compared with 31 healthy controls (mean age, 49.68 [SD, 15.54] years). We identified 4 salience network ROIs: left/right dorsal anterior cingulate cortex and left/right anterior insula. Average salience network resting-state functional connectivity and amplitude of low-frequency fluctuations within the 4 salience network ROIs were computed.

RESULTS: Patients with gliomas showed decreased overall salience network resting-state functional connectivity ($P = .001$) and increased amplitude of low-frequency fluctuations in all salience network ROIs ($P < .01$) except in the left dorsal anterior cingulate cortex. Compared with controls, patients with left-sided gliomas showed increased amplitude of low-frequency fluctuations in the right dorsal anterior cingulate cortex ($P = .002$) and right anterior insula ($P < .001$), and patients with right-sided gliomas showed increased amplitude of low-frequency fluctuations in the left anterior insula ($P = .002$). Anterior tumors were associated with decreased salience network resting-state functional connectivity ($P < .001$) and increased amplitude of low-frequency fluctuations in the right anterior insula, left anterior insula, and right dorsal anterior cingulate cortex. Patients with high-grade gliomas had decreased salience network resting-state functional connectivity compared with healthy controls ($P < .05$). The right anterior insula showed increased amplitude of low-frequency fluctuations in patients with grade II and IV gliomas compared with controls ($P < .01$).

CONCLUSIONS: By demonstrating decreased resting-state functional connectivity and an increased amplitude of low-frequency fluctuations related to the salience network in patients with glioma, this study adds to our understanding of the neurobiology underpinning observable cognitive deficits in these patients. In addition to more conventional functional connectivity, amplitude of low-frequency fluctuations is a promising functional-imaging biomarker of tumor-induced vascular and neural pathology.

ABBREVIATIONS: ALFF = amplitude of low-frequency fluctuations; BOLD = blood oxygen level–dependent; PCG = precentral gyri; RSFC = resting-state functional connectivity; rsfMRI = resting-state fMRI; SN = salience network

Detrimental effects of cancer on cognitive function and, consequently, on the quality of life are emerging as a key focus of cancer survivorship both in research and clinical practice.[1,2]

Brain tumors have been shown to affect memory, processing, and attention in patients; however, their underlying neurobiology is incompletely understood.[3] Using resting-state functional MR imaging (rsfMRI) to evaluate changes in cognitive resting-state

networks may provide a better understanding of the pathology underlying the observable cognitive disruptions in gliomas, the most common primary brain tumor in adults.

A "triple network model" of neurocognitive pathology has been proposed, which encompasses the default mode network, involved in mind wandering; the central executive network, involved in decision-making; and the salience network (SN), implicated in modulating activation of the default mode network and central executive network by detecting the presence of salient stimuli.[4-8] While previous rsfMRI research has largely focused on tumor-induced changes in the default mode network,[9,10] our study examined the less-studied SN, a network rooted in the anterior insula and the dorsal anterior cingulate cortex.[6]

Prior studies evaluating gliomas and SN resting-state functional connectivity (RSFC) provided conflicting results in small patient samples: Maesawa et al[10] found no significant differences in the SN in 12 patients, while Liu et al[11] more recently found decreased SN connectivity in 13 patients. Gliomas impact the integrity of the neurovascular unit to varying degrees, resulting in neurovascular uncoupling that has been reported to confound fMRI interpretations in patients with brain tumors.[12-14] Additionally, research has reported neuronal plasticity manifested by structural reorganization and functional remodeling of neural networks in patients with gliomas with possible alterations in clinically observable cognitive manifestations.[15-17] An rsfMRI metric, the amplitude of low-frequency fluctuations (ALFF), has recently shown promise as a biomarker for brain plasticity and hemodynamic characterization, including neurovascular uncoupling in patients with gliomas.[15-19]

The purpose of this study was to investigate the effect of glioma presence and tumor characteristics on overall RSFC and regional normalized ALFF within the SN in a large patient population. We hypothesized that there would be decreased average SN RSFC and altered ALFF in patients with gliomas compared with healthy controls. Recent studies have acknowledged that gliomas have variable effects on network integrity based on lesion location and proximity to network ROIs,[20-22] and unilateral gliomas can be associated with plasticity in both the ipsilateral and contralateral hemispheres.[11,17] Research also supports differences in resting-state network reorganization in aggressive high-grade gliomas compared with slower-growing low-grade gliomas.[20,23] Therefore, we also hypothesized that there would be differences in average SN RSFC and regional ALFF in patients based on the anterior-versus-posterior location, hemispheric side, and grade of glioma.

MATERIALS AND METHODS
Study Sample
This observational, retrospective case-control study was approved by the Memorial Sloan Kettering Cancer Center institutional review board and was compliant with the Health Insurance Portability and Accountability Act. The re-quirement for written informed consent was waived due to the retrospective nature of the study. Sixty-nine patients with brain tumors referred for presurgical functional mapping by fMRI between January 2016 and April 2018 who met inclusion/exclusion criteria were included in the study. Inclusion criteria were the following: 1) older than

18 years of age, and 2) the presence of supratentorial, unilateral intra-axial gliomas confirmed by pathology after an operation. Patients were excluded from the study for the following reasons: 1) No rsfMRI was performed, or there was incomplete rsfMRI data; 2) histopathology confirmed nonglial tumors; and 3) there were documented pre-existing neuropsychological, neurodegenerative, or psychiatric comorbidities. For comparison, 31 age- and sex-matched healthy controls were selected from the Nathan Kline Institute–Rockland Sample enhanced, open-access data repository.[24]

Image Acquisition
Patients underwent rsfMRI with a 3T imaging unit (750 W; GE Healthcare) and a gradient-echo echo-planar imaging sequence (TR/TE, 2500/30 ms; 64 × 64 matrix; 4-mm section thickness; 80° flip angle; 7-minute acquisitions). Images in control subjects were obtained using a 3T Magnetom Trio, A Tim System imaging unit (Siemens) and an echo-planar imaging sequence (TR/TE, 2500/30 ms; 72 × 72 matrix; 3-mm section thickness; 10-minute acquisitions). T1-weighted anatomic images for patients and control subjects were obtained with spoiled gradient recalled and high-resolution 3D MPRAGE sequences. Similar to control subjects, before each rsfMRI scan, patients were instructed to keep their eyes open and stay awake. Because patients underwent both rsfMRI and task-based fMRI during the same scan sessions as part of presurgical work-up, the order of sequence acquisition was randomized to minimize confounds.

rsfMRI Preprocessing
In the current study, we implemented a data-processing scheme similar to earlier published methods.[21] Analysis was performed using Statistical Parametric Mapping, Version 12 (http://www.fil.ion.ucl.ac.uk/spm/software/spm12) and Analysis of Functional Neuro Images (AFNI, Version 18.0.21; http://afni.nimh.nih.gov/afni).[25] Briefly, we removed the first 5 time points of fMRI data to allow T1-relaxation effects followed by head-motion correction and coregistration. These steps were followed by segmentation of each subject's anatomic images into gray matter, white matter, and CSF images. Deformation fields were derived to transfer functional images into Montreal Neurological Institute standard space using segment procedures in SPM12 software. Finally, we used this subject-specific deformation field to transform the functional images into standard space images. Each of the functional images normalized to standard space was then manually inspected using consensus viewing by a neuroradiologist and a neuroimaging consultant with up to 10 years of fMRI experience to ensure that there were no major distortions due to mass effect from large tumors. A general linear model–based regression approach was implemented using 24 motion regressors (6 motion parameters derived in the motion-correction step, 6 squared of the original motion parameters, 6 one-time-point delayed version of the motion parameters, and finally 6 squared of the delayed-motion parameters) to remove the effects of motion-related noise from the blood oxygen level–dependent (BOLD) fMRI data.[26]

Because most tumors infiltrated the boundaries of gray matter, white matter, and CSF and given the differential locations of tumors, no regressors from the CSF or white matter region were

included in the regression model, to avoid eliminating signals of interest. Following regression, temporal filtering between the frequency bands of 0.01 and 0.1 Hz and spatial smoothing with a 6-mm full width at half maximum Gaussian filter was applied. Using the head-motion parameters, we calculated subject-specific measures of mean frame-wise displacement.[27] Because both patients and healthy controls demonstrated a mean frame-wise displacement of <0.5 mm and no differences in mean frame-wise displacement were observed between the patient and healthy control groups ($P = .28$), data scrubbing was not performed. Only the first 160 time points from the healthy controls were used to match the number of time points in patients with glioma.

rsfMRI Data Analysis

Four spatially distinct ROIs within the SN were identified: left dorsal anterior cingulate cortex (Montreal Neurological Institute coordinates: −5, 26, 31), right dorsal anterior cingulate cortex (Montreal Neurological Institute coordinates: 5, 26, 31), left anterior insula (Montreal Neurological Institute coordinates: −34, 17, −4), and right anterior insula (Montreal Neurological Institute coordinates: 37, 20, −6).[28] For each region, a 6-mm sphere was created, resulting in 4 ROI masks. For each participant, the mean BOLD fMRI for each region was extracted from the preprocessed rsfMRI, and 4 × 4 functional connectivity matrices were derived representing functional integration within the SN. The average value across the different region-specific RSFC values was then computed to derive the average SN RSFC for each subject.

Mean normalized ALFF was calculated for each subject.[29] The ALFF measure at each voxel represented the averaged square root of the power within the frequency window of 0.01–0.1 Hz, normalized by the mean within-brain ALFF value for that subject. The mean normalized ALFF value for each of the 4 SN ROIs (right dorsal anterior cingulate cortex, left dorsal anterior cingulate cortex, right anterior insula, left anterior insula) was extracted. Identical ROIs were used for analysis of the SN RSFC and ALFF maps.

To demonstrate that there were no significant differences in scanner parameters between the patient scans and the Nathan Kline Institute control scans, we compared BOLD fMRI activation between patients and healthy controls using the bilateral precentral gyri (PCG) as a reference region. A subset of 15 patients with no tumor infiltration or mass effect in the bilateral PCG was selected, along with 15 age-matched controls from our healthy control group. A 6-mm spherical ROI mask was created for both PCG regions (left PCG, Montreal Neurological Institute coordinates: −44, −6, 49; right PCG Montreal Neurological Institute coordinates: 44, −11, 38).[30] Mean BOLD fMRI signals were extracted from each of the subject's preprocessed rsfMRI using these ROI masks, and RSFC between the right and left PCG BOLD fMRI signal was calculated. Mean normalized ALFF values were also extracted for the left and right PCG.

Statistical Analysis

Statistical analyses were performed with Matlab 9.4 and the Statistics and Machine Learning Toolbox 11.3 (release 2018a; MathWorks) with statistical significance defined by $P < .05$.

Independent 2-sample t tests were used to evaluate the overall effect of glioma presence on the average SN RSFC and ROI-specific ALFF between patients and healthy controls. ANCOVA with age, sex, and handedness as covariates was used to analyze the effect of glioma location (anterior versus posterior), glioma side (right versus left), and glioma grade on average SN RSFC and ROI-specific ALFF between patients and healthy controls followed by a post hoc Tukey-Kramer test for multiple simultaneous pair-wise comparisons. To correct for multiple comparisons, we calculated the Bonferroni-adjusted significance level of .01 to account for the increased possibility of type I error for the 2-sample t tests and ANCOVA. Two 1-sided tests were used to calculate the equivalence among scanner parameters in a subset of patient and Nathan Kline Institute control scans with the upper and lower equivalence bounds set at a positive or negative difference of $d = 0.5$.[31]

RESULTS

Sample Characteristics

Sixty-nine patients (mean age, 48.74 [SD, 14.32] years; range, 19–77 years; 45 men) and 31 healthy controls (mean age, 49.68 [SD, 15.54] years; range, 22–68 years; 18 men) were included in this study. No differences were observed in age ($P = .7685$), sex ($\chi^2 = 0.47$, $P = .49$), and handedness ($\chi^2 = 0.63$, $P = .43$) between the patient and healthy control groups. The 69 patients were grouped into the following; 1) patients with anterior ($n = 53$) and posterior ($n = 16$) gliomas; 2) patients with left-sided ($n = 41$) and right-sided ($n = 28$) gliomas; and 3) patients with grade II ($n = 25$), III ($n = 17$), and IV ($n = 27$) gliomas. For the purposes of this study, "anterior" gliomas were located in the frontal or anterior temporal lobes and "posterior" gliomas were located in the parietal, occipital, or posterior temporal lobes, as classified by radiology report review and manually confirmed using consensus review by 2 neuroradiologists with up to 20 years of experience. Glioma grade was based on the histopathology of tumor biopsies categorized by the 2016 World Health Organization Classification of Central Nervous System Tumors.[32] Demographic information and tumor characteristics are summarized in Table 1.

Of the 69 patients, 41 (59%) patients had newly diagnosed gliomas (18 with grade II, 8 with grade III, and 15 with grade IV gliomas) and 28 (41%) had recurrent gliomas (7 with grade II, 9 with grade III, and 12 with grade IV gliomas). Although the average SN RSFC was slightly lower in patients with recurrent gliomas (mean ±[SD, 0.55 ± 0.23]) compared with newly diagnosed gliomas (mean ± SD, 0.56 ± 0.27), there were no significant differences between the 2 groups ($P = .89$). Similarly, there were no significant differences in regional ALFF between the newly diagnosed gliomas and the recurrent gliomas (all, $P > .05$). When they were stratified by grade, there were no significant differences in average SN RSFC or ALFF between recurrent gliomas-versus-de novo gliomas (all, $P > .05$).

For the subset of patients with no involvement of the bilateral PCGs by tumor and their age-matched controls, RSFC between the right and left PCG and regional ALFF for each of the right and left PCGs between patient and Nathan Kline Institute control

scans was equivalent, on the basis of equivalence bounds of −0.5 and 0.5.

Overall Effect of Glioma Presence on the RSFC and ROI-Specific ALFF of the SN

Patients with gliomas demonstrated lower average SN RSFC compared with healthy controls ($P = .001$). We observed increased ALFF in patients with gliomas compared with healthy controls in the right dorsal anterior cingulate cortex ($P < .001$), left anterior insula ($P = .001$), and right anterior insula ($P < .001$). Results are reported in Table 2. Maps of RSFC and ALFF for a representative patient and healthy control are illustrated in Fig 1.

Effect of Glioma Anteriority on RSFC and ROI-Specific ALFF of the SN

We observed a significant effect of anterior-versus-posterior tumor location on average SN RSFC ($F[2,94] = 7.09$, $P = .001$). Post hoc Tukey comparison showed lower SN RSFC in patients

with anteriorly located gliomas compared with healthy controls ($P < .001$). No significant difference was found in patients with posteriorly located gliomas ($P = .44$) compared with healthy controls. No significant differences were observed when comparing the patient subgroup with anteriorly located gliomas with those with posteriorly located gliomas ($P = .26$).

There was a significant effect of tumor location on ALFF values for right dorsal anterior cingulate cortex ($F[2,94] = 5.89$, $P = .004$), left anterior insula ($F[2,94] = 5.18$, $P = .0074$), and right anterior insula ($F[2,94] = 10.12$, $P < .001$). Post hoc comparisons showed that compared with healthy controls, patients with anterior tumors demonstrated increased ALFF in the right dorsal anterior cingulate cortex ($P = .009$), left anterior insula ($P = .008$), and right anterior insula ($P = .002$), while patients with posterior tumors demonstrated increased ALFF in the right dorsal anterior cingulate cortex ($P = .016$) and right anterior insula ($P < .001$). There was no significant difference in ALFF between patients in the anterior and posterior tumor groups (Fig 2).

Effect of Glioma Hemispheric Side on RSFC and ROI-Specific ALFF of the SN

An ANCOVA comparing patients with left-sided gliomas, right-sided gliomas, and controls showed significant differences in average SN RSFC ($F[2,94] = 5.70$, $P = .005$). Post hoc comparisons showed patients in both left-sided ($P = .007$) and right-sided ($P = .02$) glioma groups had lower SN RSFC compared with controls. Comparison among the patient subgroups, however, showed no significant effects of glioma sidedness on average SN RSFC ($P = .99$).

ANCOVA analysis showed a significant association between glioma sidedness and ALFF in the right dorsal anterior cingulate cortex ($F[2,94] = 6.37$, $P = .003$), left anterior insula ($F[2,94] = 6.28$, $P = .003$), and right anterior insula ($F[2,94] = 15.09$, $P < .001$). Post hoc comparisons showed that compared with healthy controls, patients with tumors in the left hemisphere demonstrated increased ALFF in the right dorsal anterior cingulate cortex ($P = .002$) and right anterior insula ($P < .001$), while patients with right-sided tumors demonstrated increased ALFF in the left anterior insula ($P = .002$). Within-group comparison showed increased ALFF in right anterior insula in patients with left-sided tumors compared with those with right-sided tumors ($P = .004$). Results are illustrated in Fig 2.

Effect of Tumor Grade on RSFC and ROI-Specific ALFF of the SN

Tumor grade was associated with decreased average SN RSFC ($F[3,93] = 5.03$, $P = .003$). Post hoc comparisons showed decreased average SN RSFC in patients with grade III ($P = .004$) and grade IV tumors ($P = .017$) compared with healthy controls.

Tumor grade was associated with increased ALFF within the left anterior insula ($F[3,93] = 4.48$, $P = .006$) and right anterior insula ($F[3,93] = 5.97$, $P < .001$). Post hoc comparisons showed increased ALFF in the right anterior insula in patients with grade II

Table 1: Study group and tumor characteristics

Sample Characteristics	Patients (n = 69)	Healthy Controls (n = 31)
Sex		
Male	45	18
Female	24	13
Age (yr)		
Mean	48.74 [SD, 14.32]	49.68 [SD, 15.54]
Range	19–77	22–68
Handedness[a]		
Right	61	29
Left	8	2
Glioma location[b]		
Anterior	53	
Posterior	16	
Glioma hemisphere		
Left	41	
Right	28	
Glioma grade (WHO classification)		
Grade II	25	
Grade III	17	
Grade IV	27	
Antiepileptics (yes/no)	55/14	
Steroids (yes/no)	33/36	

Note:—WHO indicates World Health Organization.
[a] Handedness was determined by the Edinburgh Handedness Inventory.
[b] "Anterior" tumors are located in the frontal or anterior temporal lobes. "Posterior" tumors are located in the parietal or posterior temporal lobes, as classified by radiology report review.

Table 2: Effect of glioma presence on SN RSFC and regional ALFF[a]

Analysis	Healthy Controls	Patients with Gliomas	P Values
Average SN RSFC	0.73 [SD, 0.20]	0.56 [SD, 0.25]	.001[b]
ALFF			
L-dACC	0.93 [SD, 0.16]	0.98 [SD, 0.22]	.21
R-dACC	0.93 [SD, 0.16]	1.08 [SD, 0.22]	<.001[b]
L-AINS	0.76 [SD, 0.12]	0.90 [SD, 0.23]	.001[b]
R-AINS	0.87 [SD, 0.13]	1.13 [SD, 0.32]	<.001[b]

Note:—L-dACC indicates left dorsal anterior cingulate cortex; R-dACC, right dorsal anterior cingulate cortex; R-AINS, right anterior insula; L-AINS, left anterior insula.
[a] Data are presented as means.
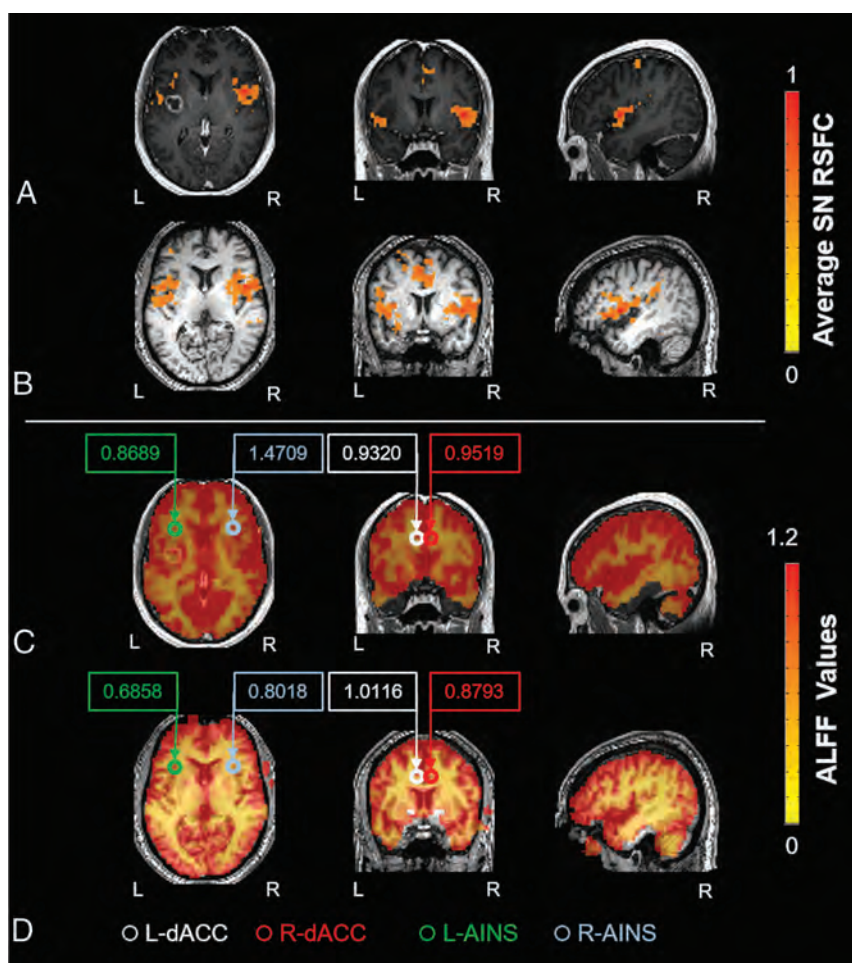[b] $P < .01$ after Bonferroni-correction.

FIG 1. Map of functional connectivity and amplitude of low-frequency fluctuations in the SN. Decreased functional connectivity within the SN was seen by placing a seed in the R-dACC in a representative patient with a left frontal glioblastoma (*A*) and a healthy control (*B*). ALFF map of the same patient (*C*) and a healthy control (*D*). *Circles* represent the 4 SN ROIs. Values in *boxes* represent average ALFF values within the specific ROIs. Increased ALFF values were seen in all 4 SN ROIs in the patient compared with the healthy control. R-dACC indicates right dorsal anterior cingulate cortex; L-dACC, left dorsal anterior cingulate cortex; L-AINS, left anterior insula; R-AINS, right anterior insula; L, left; R, right.

($P = .006$) and IV ($P = .003$) tumors and trend-level differences in patients with grade III tumors ($P = .08$) compared with healthy controls (Fig 3).

DISCUSSION

Our study investigated resting-state fMRI alterations in the SN in a large sample of patients with gliomas and produced 3 main findings: First, the average SN RSFC was decreased in patients with gliomas compared with healthy controls. Second, disruptions in ALFF were found in established SN ROIs. Third, tumor location and grade produced differential effects on SN functional connectivity and ALFF.

The SN functions to select meaningful stimuli from an array of sensory input.[33] At a regional level, patients with gliomas showed disrupted ALFF in 3 of the 4 SN-specific ROIs (right anterior insula, left anterior insula, and right dorsal anterior

cingulate cortex) compared with healthy controls. The most significant change was seen in the right anterior insula, which has specifically been proposed as a "causal outflow hub" driving the switch between the default mode network and central executive network, with anterior insula dysfunction and consequently impaired network switching implicated in other disorders demonstrating impaired executive control.[4,34,35] Our findings of globally decreased SN RSFC and compromised integrity of key SN regions in patients with glioma may explain several of the clinically documented cognitive challenges that these patients experience.[3]

Consistent with previous research, ALFF values in the tumor-contralateral SN ROIs were increased compared with ipsilateral regions in our study.[17,18,36] The relatively increased ALFF in the lesion-contralateral ROIs could be explained not only by truly asymmetric neural activity but also by neurovascular uncoupling in the tumor ipsilateral hemisphere. This tumor-induced loss of neurovascular autoregulation can potentially alter the vascular component of BOLD signal to a degree that confounds measurement of neural activity.[14,18,37,38] The observation of increased ALFF in SN ROIs of patients with tumor compared with controls and in tumor-contralateral compared with tumor-ipsilateral regions could also be explained by functional compensation for injured tissue due to neural plasticity, which may manifest as altered

metabolism or blood flow.[17,39] Future studies should investigate changes in ALFF measured across the whole brain, to study whether there are paradoxic effects on BOLD activation in areas proximal or distal to the tumor produced by a combination of neurovascular uncoupling and functional compensation.

Not unexpectedly, tumors in the frontal or anterior temporal lobes of patients, closer to key SN regions, were associated with lower SN RSFC compared with healthy controls, while posterior tumors showed no significant differences in connectivity. Higher glioma grades were associated with decreased overall SN RSFC compared with controls, possibly due to a combination of factors including true-positive changes due to increased tumor infiltration and disrupted functional reorganization,[9,20] as well as false-negative signals due to tumor-induced neurovascular uncoupling that may have artifactually decreased RSFC due to altered hemodynamics.[22,36] These
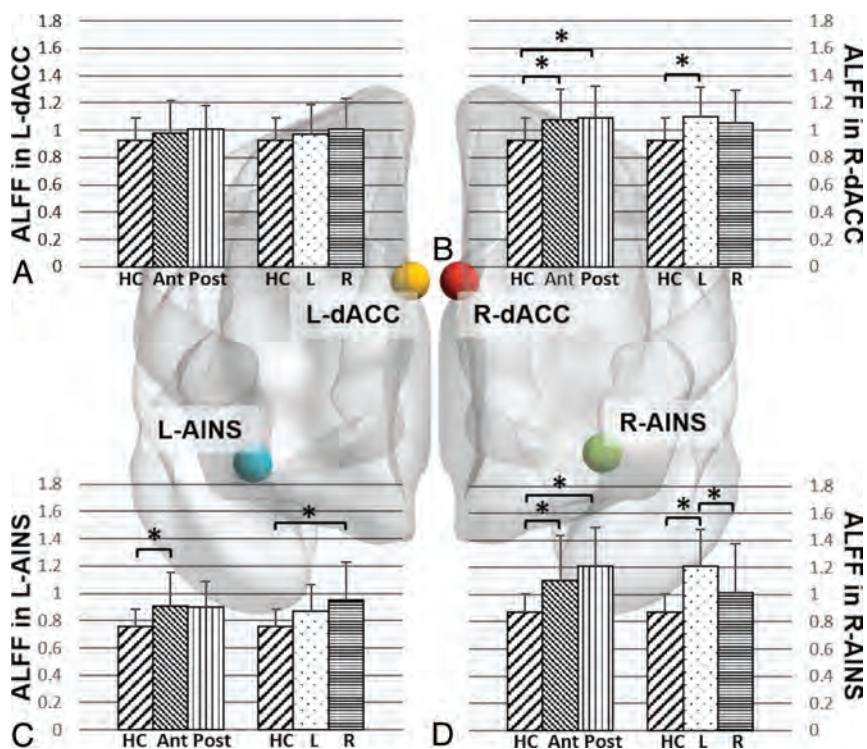
FIG 2. Effect of glioma location on amplitude of low-frequency fluctuations in the SN ROIs. *Bar graphs* for comparison of mean ALFF values in the L-dACC (*A*), R-dACC (*B*), L-AINS (*C*), and R-AINS (*D*) in healthy controls and patients grouped by glioma location. HC indicates healthy controls; L, patients with gliomas in left hemisphere; R, patients with gliomas in right hemisphere; Ant, patients with anteriorly located gliomas; Post, patients with posteriorly located gliomas; L-dACC, left dorsal anterior cingulate cortex; R-dACC, right dorsal anterior cingulate cortex; L-AINS, left anterior insula; R-AINS, right anterior insula. The *asterisk* indicates $P < .05$ post hoc Tukey-Kramer test for multiple comparisons.

differences than fractional ALFF.[42] However, both indexes reflect different aspects of low-frequency oscillation amplitude with complementary strengths and weaknesses in the detection of intrinsic brain activity,[42] and future work that includes both measures of low-frequency oscillations may be useful to characterize the glioma-associated neurophysiologic alterations.

Our study showed no statistically significant differences in average SN RSFC and ALFF between patients with newly diagnosed gliomas and those with recurrent gliomas, even after stratifying for differences in tumor grade, though patients with recurrent gliomas demonstrated slightly decreased average SN RSFC compared with those with newly diagnosed gliomas. Although this countered our expectation of possible decreased functional connectivity in patients with recurrent glioma due to prior operative and chemoradiation treatment, the smaller sample size of the recurrent glioma group may have reduced the power to detect functional differences beyond the findings reported here. In addition, other important factors such as variability in chemotherapeutic regimens, differences in duration and total dosage of radiation therapy, use of concomitant steroids and antiepileptic drugs, as well as differences in genomic mutation would need to be accounted for as well. While beyond the scope of the current study, they merit further exploration in a larger study.

A few limitations to our study warrant further investigation: First, our healthy control group was obtained from an open-access data base that had similar-but-not identical acquisition parameters compared with our patient group. However, previous research has demonstrated that resting-state networks are stable across datasets collected using different scanners and acquisition parameters.[43] Additionally, we demonstrated equivalence in RSFC and ALFF between matched controls and a subset of our patients with no bilateral PCG tumor involvement, suggesting that the differences we observed were largely driven by underlying changes related to tumor presence, while acknowledging that variance related to differences in acquisition parameters may potentially confound interpretation of ALFF regional differences in the tumor group. Future studies using the same scanner to acquire data for patient and control groups will help address potential variances due to differences in acquisition parameters. Second, although our study demonstrated regional alterations in ALFF, these alterations may not be specific to neurovascular uncoupling or functional remodeling and may be indicative

findings warrant cautious clinical interpretation of rsfMRI findings in high-grade gliomas.

In the present study, we observed opposite effects of tumor on measures of resting-state brain function: The RSFC of the SN was significantly reduced, while ALFF measures were significantly increased in patients with tumor compared with healthy controls. While previous research in healthy controls reported a positive correlation between ALFF values and overall functional connectivity of specific brain regions,[40] we suggest the presence of a complex relationship between regional ALFF values and overall RSFC in patients with tumors, likely due to a combination of tumor-induced differences in vascularization, blood flow, and altered neurovascular coupling.[15] These results need further investigation and correlation with perfusion parameters to determine the role of ALFF as a biomarker of tumor vascularity in patients with gliomas.

In addition to ALFF, fractional ALFF is a frequency-normalized index of ALFF that corrects for broad-range frequency variations and suppresses vascular contributions.[41] In the present study, we focused on mean normalized ALFF instead of fractional ALFF because of its reported increased reliability within gray matter regions compared with fractional ALFF and, thus, its potential to be more sensitive to discern group
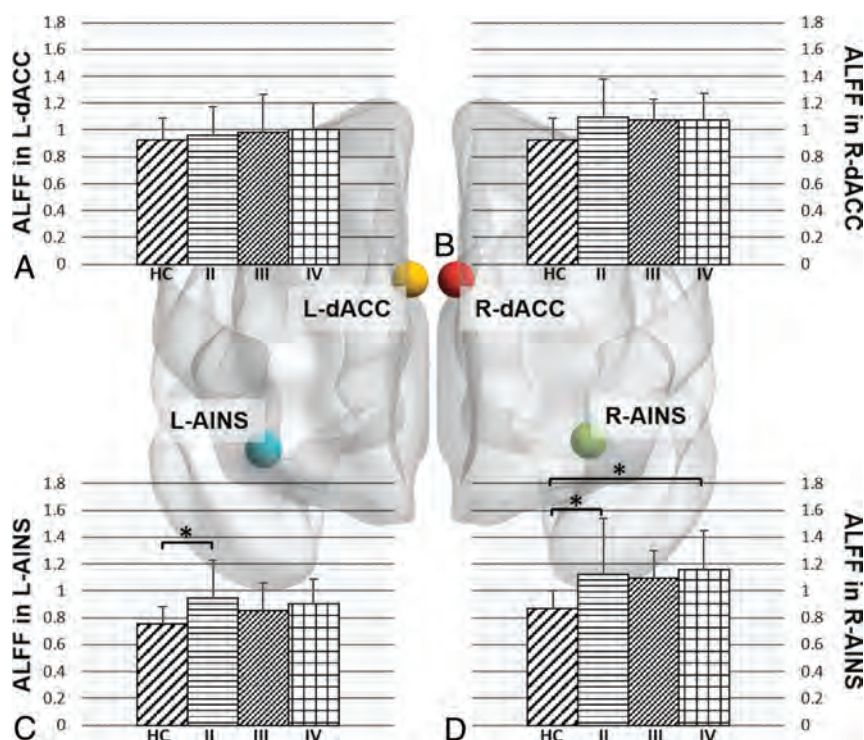
FIG 3. Effect of glioma grade on the amplitude of low-frequency fluctuations in the SN ROIs. *Bar graphs* for comparison of mean ALFF values in the L-dACC (*A*), R-dACC (*B*), L-AINS (*C*), and R-AINS (*D*) in healthy controls and patients grouped by glioma grade. HC indicates healthy controls; II, patients with grade II gliomas; III, patients with grade III gliomas; IV, patients with grade IV gliomas; L-dACC, left dorsal anterior cingulate cortex; R-dACC, right dorsal anterior cingulate cortex; L-AINS, left anterior insula; R-AINS, right anterior insula.. The *asterisk* indicates $P < .05$ post hoc Tukey-Kramer test for multiple comparisons.

patients with gliomas. In addition to more conventional functional connectivity, ALFF is a promising functional imaging biomarker of vascular and neural pathology and provides additional data to enable understanding of tumor-related disturbances of neural networks.

of an inherent property of the tumor itself. Adding a measure of cerebrovascular reactivity with breath-holding or gas-inhalation paradigms could further assess the degree of glioma-associated neurovascular uncoupling,[12,44] and future research is, therefore, warranted on how ALFF and neurovascular uncoupling should be accounted for in measuring rsfMRI results. Third, the clinical significance of these group-level differences at the single-subject level needs validation. Fourth, most of our patients, irrespective of whether they were newly diagnosed or had recurrent gliomas, had received antiepileptic drugs and/or steroids by the time of their rsfMRI scan, which may have contributed to the functional alterations; because only 7 patients were treatment-naïve and due to the variability in dosage and treatment durations among those who received treatment, we did not conduct further analyses on the differential effects of these treatments. Finally, future studies would also benefit from a neurocognitive measure, which could show how changes in SN functional connectivity correlate with cognitive performance.

CONCLUSIONS

By using both functional connectivity and a frequency-domain metric related to the SN, this study adds to the understanding of neurobiologic effects on cognitive function in

REFERENCES

1. Schagen SB, Klein M, Reijneveld JC, et al. **Monitoring and optimising cognitive function in cancer patients: present knowledge and future directions.** *EJC Suppl* 2014;12:29–24 CrossRef Medline

2. Taphoorn MJ, Klein M. **Cognitive deficits in adult patients with brain tumours.** *Lancet Neurol* 2004;3:159–68 CrossRef Medline

3. Bergo E, Lombardi G, Guglieri I, et al. **Neurocognitive functions and health-related quality of life in glioblastoma patients: a concise review of the literature.** *Eur J Cancer Care (Engl)* 2019;28:e12410 CrossRef Medline

4. Uddin LQ. **Salience processing and insular cortical function and dysfunction.** *Nat Rev Neurosci* 2015;16:55–61 CrossRef Medline

5. Goulden N, Khusnulina A, Davis NJ, et al. **The salience network is responsible for switching between the default mode network and the central executive network: replication from DCM.** *Neuroimage* 2014;99:180–90 CrossRef Medline

6. Seeley WW, Menon V, Schatzberg AF, et al. **Dissociable intrinsic connectivity networks for salience processing and executive control.** *J Neurosci* 2007;27:2349–56 CrossRef Medline

7. Menon V. **Large-scale brain networks and psychopathology: a unifying triple network model.** *Trends Cogn Sci* 2011;15:483–506 CrossRef Medline

8. Chand GB, Wu J, Hajjar I, et al. **Interactions of the salience network and its subsystems with the default-mode and the central-executive networks in normal aging and mild cognitive impairment.** *Brain Connect* 2017;7:401–12 CrossRef Medline

9. Esposito R, Mattei PA, Briganti C, et al. **Modifications of default-mode network connectivity in patients with cerebral glioma.** *PLoS One* 2012;7:e40231 CrossRef Medline

10. Maesawa S, Bagarinao E, Fujii M, et al. **Evaluation of resting state networks in patients with gliomas: connectivity changes in the unaffected side and its relation to cognitive function.** *PLoS One* 2015;10:e0118072 CrossRef Medline

11. Liu D, Hu X, Liu Y, et al. **Potential intra- or cross-network functional reorganization of the triple unifying networks in patients with frontal glioma.** *World Neurosurg* 2019;128:e732–43 CrossRef Medline

12. Pillai JJ, Zaca D. **Clinical utility of cerebrovascular reactivity mapping in patients with low grade gliomas.** *World J Clin Oncol* 2011;2:397–403 CrossRef Medline

13. Pak RW, Hadjiabadi DH, Senarathna J, et al. **Implications of neurovascular uncoupling in functional magnetic resonance imaging (fMRI) of brain tumors.** *J Cereb Blood Flow Metab* 2017;37:3475–87 CrossRef Medline

14. Hou BL, Bradbury M, Peck KK, et al. **Effect of brain tumor neovasculature defined by rCBV on BOLD fMRI activation volume in the primary motor cortex.** *Neuroimage* 2006;32:489–97 CrossRef Medline

15. Gupta L, Gupta RK, Postma AA, et al. **Advanced and amplified BOLD fluctuations in high-grade gliomas.** *J Magn Reson Imaging* 2018;47:1616–25 CrossRef Medline

16. Zhang N, Xia M, Qiu T, et al. **Reorganization of cerebro-cerebellar circuit in patients with left hemispheric gliomas involving language network: a combined structural and resting-state functional MRI study.** *Hum Brain Mapp* 2018;39:480219 CrossRef Medline

17. Liu D, Chen J, Hu X, et al. **Contralesional homotopic functional plasticity in patients with temporal glioma.** *J Neurosurg* 2020 Jan 10. [Epub ahead of print]CrossRef Medline

18. Agarwal S, Lu H, Pillai JJ. **Value of frequency domain resting-state functional magnetic resonance imaging metrics amplitude of low-frequency fluctuation and fractional amplitude of low-frequency fluctuation in the assessment of brain tumor-induced neurovascular uncoupling.** *Brain Connect* 2017;7:382–89 CrossRef Medline

19. Agarwal S, Sair HI, Airan R, et al. **Demonstration of brain tumor-induced neurovascular uncoupling in resting-state fMRI at ultrahigh field.** *Brain Connect* 2016;6:267–72 CrossRef Medline

20. Harris RJ, Bookheimer SY, Cloughesy TF, et al. **Altered functional connectivity of the default mode network in diffuse gliomas measured with pseudo-resting state fMRI.** *J Neurooncol* 2014;116:373–79 CrossRef Medline

21. Gohel S, Laino ME, Rajeev-Kumar G, et al. **Resting-state functional connectivity of the middle frontal gyrus can predict language lateralization in patients with brain tumors.** *AJNR Am J Neuroradiol* 2019;40:319–25 CrossRef Medline

22. Sun H, Vachha B, Laino ME, et al. **Decreased hand motor resting-state functional connectivity in patients with glioma: analysis of factors including neurovascular uncoupling.** *Radiology* 2020;294:610–21 CrossRef Medline

23. Zhang H, Shi Y, Yao C, et al. **Alteration of the intra- and cross-hemisphere posterior default mode network in frontal lobe patients with glioma.** *Sci Rep* 2016;6:26972 CrossRef Medline

24. Nooner KB, Colcombe SJ, Tobe RH, et al. **The NKI-Rockland Sample: a model for accelerating the pace of discovery science in psychiatry.** *Front Neurosci* 2012;6:152 CrossRef Medline

25. Cox RW. **AFNI: software for analysis and visualization of functional magnetic resonance neuroimages.** *Comput Biomed Res* 1996;29:162–73 CrossRef Medline

26. Friston KJ, Williams S, Howard R, et al. **Movement-related effects in fMRI time-series.** *Magn Reson Med* 1996;35:346–55 CrossRef Medline

27. Jenkinson M, Bannister P, Brady M, et al. **Improved optimization for the robust and accurate linear registration and motion correction of brain images.** *Neuroimage* 2002;17:825–41 CrossRef Medline

28. Baur V, Hanggi J, Langer N, et al. **Resting-state functional and structural connectivity within an insula-amygdala route specifically index state and trait anxiety.** *Biol Psychiatry* 2013;73:85–92 CrossRef Medline

29. Gohel S, Gallego JA, Robinson DG, et al. **Frequency specific resting state functional abnormalities in psychosis.** *Hum Brain Mapp* 2018;39:4509–18 CrossRef Medline

30. Dosenbach NU, Nardos B, Cohen AL, et al. **Prediction of individual brain maturity using fMRI.** *Science* 2010;329:1358–61 CrossRef Medline

31. Schuirmann DJ. **A comparison of the two one-sided tests procedure and the power approach for assessing the equivalence of average bioavailability.** *J Pharmacokinet Biopharm* 1987;15:657–80 CrossRef Medline

32. Louis DN, Perry A, Reifenberger G, et al. **The 2016 World Health Organization Classification of Tumors of the Central Nervous System: a summary.** *Acta Neuropathol* 2016;131:803–20 CrossRef Medline

33. Menon V, Uddin LQ. **Saliency, switching, attention and control: a network model of insula function.** *Brain Struct Funct* 2010;214:655–67 CrossRef Medline

34. Uddin LQ, Nomi JS, Hebert-Seropian B, et al. **Structure and function of the human insula.** *J Clin Neurophysiol* 2017;34:300–06 CrossRef Medline

35. Sridharan D, Levitin DJ, Menon V. **A critical role for the right fronto-insular cortex in switching between central-executive and default-mode networks.** *Proc Natl Acad Sci U S A* 2008;105:12569–74 CrossRef Medline

36. Agarwal S, Sair HI, Yahyavi-Firouz-Abadi N, et al. **Neurovascular uncoupling in resting state fMRI demonstrated in patients with primary brain gliomas.** *J Magn Reson Imaging* 2016;43:620–26 CrossRef Medline

37. Hadjiabadi DH, Pung L, Zhang J, et al. **Brain tumors disrupt the resting-state connectome.** *Neuroimage Clin* 2018;18:279–89 CrossRef Medline

38. Holodny AI, Schulder M, Liu WC, et al. **Decreased BOLD functional MR activation of the motor and sensory cortices adjacent to a glioblastoma multiforme: implications for image-guided neurosurgery.** *AJNR Am J Neuroradiol* 1999;20:609–12 Medline

39. Cheng X, Gao PY. **Abnormal neural activity in children with diffuse intrinsic pontine glioma had manifested deficit in behavioral inhibition: a resting-state functional MRI study.** *J Comput Assist Tomogr* 2019;43:547–52 CrossRef Medline

40. Di X, Kim EH, Huang CC, et al. **The influence of the amplitude of low-frequency fluctuations on resting-state functional connectivity.** *Front Hum Neurosci* 2013;7:118 CrossRef Medline

41. Zou QH, Zhu CZ, Yang Y, et al. **An improved approach to detection of amplitude of low-frequency fluctuation (ALFF) for resting-state fMRI: fractional ALFF.** *J Neurosci Methods* 2008;172:137141 CrossRef Medline

42. Zuo XN, Di Martino A, Kelly C, et al. **The oscillating brain: complex and reliable.** *Neuroimage* 2010;49:1432–45 CrossRef Medline

43. Biswal BB, Mennes M, Zuo XN, et al. **Toward discovery science of human brain function.** *Proc Natl Acad Sci U S A* 2010;107:4734–39 CrossRef Medline

44. Liu P, Welch BG, Li Y, et al. **Multiparametric imaging of brain hemodynamics and function using gas-inhalation MRI.** *Neuroimage* 2017;146:715–23 CrossRef Medline

Computer-Aided Diagnostic System for Thyroid Nodules on Ultrasonography: Diagnostic Performance Based on the Thyroid Imaging Reporting and Data System Classification and Dichotomous Outcomes

M. Han, E.J. Ha, and J.H. Park

ABSTRACT

BACKGROUND AND PURPOSE: Artificial intelligence-based computer-aided diagnostic systems have been introduced for thyroid cancer diagnosis. Our aim was to compare the diagnostic performance of a commercially available computer-aided diagnostic system and radiologist-based assessment for the detection of thyroid cancer based on the Thyroid Imaging Reporting and Data Systems (TIRADS) and dichotomous outcomes.

MATERIALS AND METHODS: In total, 372 consecutive patients with 454 thyroid nodules were enrolled. The computer-aided diagnostic system was set up to render a possible diagnosis in 2 formats, the Korean Society of Thyroid Radiology (K)-TIRADS and the American Thyroid Association (ATA)-TIRADS-classifications, and dichotomous outcomes (possibly benign or possibly malignant).

RESULTS: The diagnostic sensitivity, specificity, positive predictive value, negative predictive value, and accuracy of the computer-aided diagnostic system for thyroid cancer were, respectively, 97.6%, 21.6%, 42.0%, 93.9%, and 49.6% for K-TIRADS; 94.6%, 29.6%, 43.9%, 90.4%, and 53.5% for ATA-TIRADS; and 81.4%, 81.9%, 72.3%, 88.3%, and 81.7% for dichotomous outcomes. The sensitivities of the computer-aided diagnostic system did not differ significantly from those of the radiologist (all $P > .05$); the specificities and accuracies were significantly lower than those of the radiologist (all $P < .001$). Unnecessary fine-needle aspiration rates were lower for the dichotomous outcome characterizations, particularly for those performed by the radiologist. The interobserver agreement for the description of K-TIRADS and ATA-TIRADS classifications was fair-to-moderate, but the dichotomous outcomes were in substantial agreement.

CONCLUSIONS: The diagnostic performance of the computer-aided diagnostic system varies in terms of TIRADS classification and dichotomous outcomes and relative to radiologist-based assessments. Clinicians should know about the strengths and weaknesses associated with the diagnosis of thyroid cancer using computer-aided diagnostic systems.

ABBREVIATIONS: AI = artificial intelligence; ATA = American Thyroid Association; CAD = computer-aided diagnosis; FNA = fine-needle aspiration; K = Korean; TIRADS = Thyroid Imaging Reporting and Data System; US = ultrasonography

Artificial intelligence (AI)-based computer-aided diagnostic (CAD) systems are projected to substantially influence the field of diagnostic imaging.[1,2] In recent years, the application of AI, particularly deep-learning techniques using convolutional neural networks, has shown promising results in radiology. However, because AI technologic innovation does not guarantee

Indicates open access to non-subscribers at www.ajnr.org

Indicates article with online supplemental data.

http://dx.doi.org/10.3174/ajnr.A6922

its usefulness in real-world medical practice, rigorous external clinical validation is necessary to determine its utility.[1-3]

Several AI-based CAD systems have shown potential in the field of thyroid imaging.[4-7] However, most reports describe proof-of-concept technical feasibility studies and lack robust validation.[8] One AI-based CAD system has recently been integrated into a commercially available ultrasonography (US) platform for thyroid imaging: the S-Detect CAD system (Samsung Medison). The system generates 2 outputs: Thyroid Imaging Reporting and Data System (TIRADS)-based scoring and dichotomous predictions. The dichotomous prediction is a completely independent diagnosis based on convolutional neural network deep learning techniques. However, commercialized CAD systems have not yet undergone rigorous validation, and few articles have described the diagnostic performance using dichotomous outcomes or compared the sensitivity relative to radiologist-based assessments.[9-12] TIRADS classification has been widely
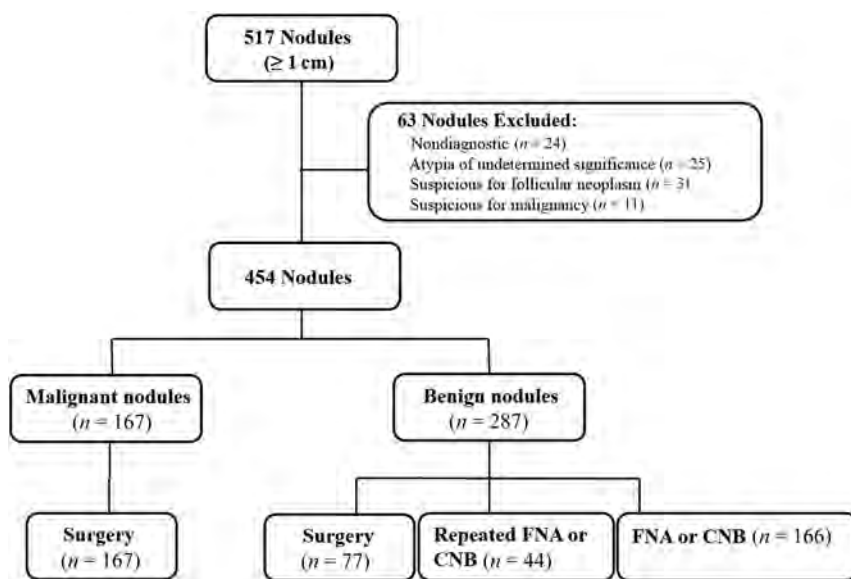
FIG 1. Flowchart shows the study participants. CNB indicates core-needle biopsy.

used for management of thyroid nodules since 2009;[13-15] therefore, evaluations are also needed to assess whether CAD systems can identify TIRADS categories and the risk of malignancy for each category. Two types of TIRADS have been used to manage thyroid nodules: pattern-based and point-based systems. Of these, the S-Detect CAD system takes a pattern-based TIRADS approach including the Korean Society of Thyroid Radiology-TIRADS (K-TIRADS) and the American Thyroid Association-TIRADS (ATA-TIRADS). A point-based TIRADS approach including the American College of Radiology–TIRADS is not yet available.

Therefore, we evaluated the diagnostic performance of the CAD US system in terms of detecting thyroid cancer based on pattern-based TIRADS (the K-TIRADS and ATA-TIRADS) and dichotomous outcome classification methods and compared its performance with that of an experienced radiologist.

MATERIALS AND METHODS
Patients
After obtaining institutional review board approval, written informed consent was obtained before US examinations from all patients. Between October 2018 and April 2019, four hundred fifty-three consecutive patients with 517 thyroid nodules (≥10 mm in diameter) who were referred to the department of radiology of our tertiary hospital for US-guided fine-needle aspiration (FNA) or US examination before a scheduled operation were initially enrolled. US-guided FNA was usually performed on a thyroid nodule exhibiting suspicious US features or on the largest nodule if no suspicious US feature was detected.[14] Data for 63 nodules were excluded because no final diagnoses were obtained (nondiagnostic, atypia of undetermined significance, and suspicions for follicular neoplasm and malignancy raised by FNA cytology but without surgical confirmation). Therefore, 372 patients with 454 thyroid nodules were finally included (83 males and 289 females; mean age, 49.5 years; range, 8–81 years; Fig 1).

Final diagnoses were determined from the cytopathologic results based on the Bethesda system and/or an operation. All malignant cases underwent thyroidectomy and were finally diagnosed by evaluation of surgical specimens. Benign nodules were diagnosed surgically or via benign core needle biopsy histology or cytologically benign FNA.

US Image Acquisition and Analyses
All thyroid US examinations were performed using a 3- to 12-MHz linear probe and a real-time US system (RS85A; Samsung Medison). Two experienced radiologists (E.J.H. and M.H.) with 14 and 10 years of clinical experience, respectively, performed all US examinations and US-guided biopsies.

The S-Detect 2 CAD system integrated into a commercially available US system was used to collect CAD data by the same radiologists. On the transverse image plane, an ROI was manually drawn around the target nodule.[10,11,16] The CAD system automatically outlined the contours of the mass and assessed the US features: composition (solid, partially cystic, or cystic); echogenicity (hyperechoic/isoechoic or hypoechoic); orientation (parallel or nonparallel); margins (well-defined, ill-defined, or microlobulated/spiculated); spongiform status; shape (ovoid to round or irregular); and calcifications (none, microcalcification, macrocalcification, or rim calcification). Finally, the CAD system provided a possible diagnosis using the TIRADS classification (based on the K-TIRADS and the ATA-TIRADS) or a dichotomous outcome classification (possibly benign/possibly malignant) (Fig 2).[13,14]

Gray-scale US images were retrospectively evaluated by the radiologist (E.J.H.) in terms of size, internal content, echogenicity, shape, orientation, margin, and the presence of calcification after at least 6 months, and the radiologist was blinded to all other data including the final histologic diagnoses.[14] The size, internal content, echogenicity, shape, orientation, margin, and calcifications were classified as described in previous reports.[13,14] On the basis of the US images, the nodules were classified according to the categories defined by the K-TIRADS and ATA-TIRADS, and a possible diagnosis was made by the radiologist.[13,14]

Statistical Analyses
Patient demographics, gray-scale US features, and dichotomous outcomes by the CAD system and radiologist were compared using the χ^2 or Fisher exact test. The Student t test was used to compare quantitative variables. The frequency and risk of malignancy according to each category of TIRADS were calculated as percentages. The associations between the categories of TIRADS and the final diagnoses were evaluated using the linear-by-linear association test.

The diagnostic abilities of the CAD system and the radiologist were assessed by calculating the sensitivities, specificities, positive
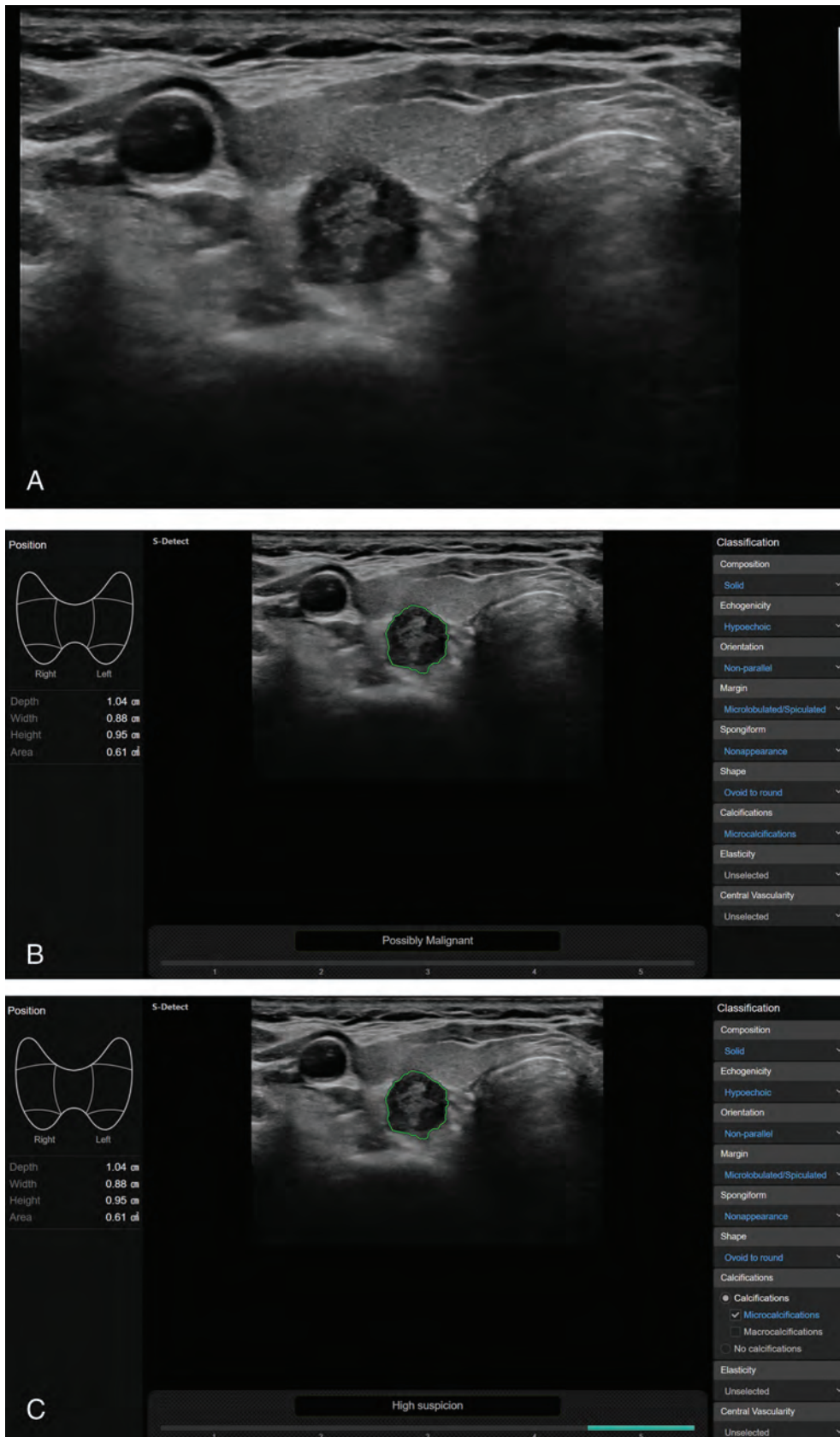
FIG 2. A US image of a thyroid nodule acquired with the S-Detect 2 CAD system. *A*, A solid hypoechoic nodule with suspicious US features is evident in the right thyroid gland. *B* and *C*, The CAD software automatically calculates the mass contours (*green contour*) and presents the US features on the right of the screen and a diagnosis based on the dichotomous outcome and TIRADS classification on the bottom.

Table 1: Sonographic features of thyroid nodules included in this study[a]

Characteristic	Benign Nodules (n = 287)	Malignant Nodules (n = 167)	Total (n = 454)	P Value
Diameter (mm)				.011
Mean [SD]	18.6 [SD, 10.7]	16.4 [SD, 7.5]	17.8 [SD, 9.7]	
Range	10.0–73.0	10.0–48.0	10.0–73.0	
Internal content				<.001
Solid	166 (57.8)	151 (90.4)	317 (69.8)	
Partially cystic	121 (42.2)	16 (9.6)	137 (30.2)	
Cystic	0	0	0	
Echogenicity				<.001
Hypoechogenicity	67 (23.3)	142 (85.0)	209 (46.0)	
Iso-/hyperechogenicity	220 (76.7)	25 (15.0)	245 (54.0)	
Shape				.143
Round-to-oval	278 (96.9)	157 (94.0)	435 (95.8)	
Irregular	9 (3.1)	10 (6.0)	19 (4.2)	
Orientation				<.001
Parallel	267 (93.0)	80 (47.9)	347 (76.4)	
Nonparallel	20 (7.0)	87 (52.1)	107 (23.6)	
Margin				<.001
Smooth	220 (76.7)	56 (33.5)	276 (60.8)	
Spiculated/microlobulated	5 (1.7)	85 (50.9)	90 (19.8)	
Ill-defined	62 (21.6)	26 (15.6)	88 (19.4)	
Calcification				<.001
None	256 (89.2)	49 (29.3)	305 (67.2)	
Microcalcification	8 (2.8)	102 (61.1)	110 (24.2)	
Macrocalcification	23 (8.0)	16 (9.6)	39 (8.6)	
Spongiform				0.534
Absence	285 (99.3)	167 (100.0)	452 (99.6)	
Presence	2 (0.7)	0	2 (0.4)	
CAD diagnosis				<.001
Possibly benign	235 (81.9)	31 (18.6)	266 (58.6)	
Possibly malignant	52 (18.1)	136 (81.4)	188 (41.4)	
Radiologist diagnosis				<.001
Possibly benign	275 (95.8)	30 (18.0)	305 (67.2)	
Possibly malignant	12 (4.2)	137 (82.0)	149 (32.8)	

[a] The numbers in parentheses are percentages.

Table 2: Risk of malignancy in each category based on different TIRADS using CAD and radiologist-based diagnosis[a]

TIRADS Classification	Category 1	Category 2	Category 3	Category 4	Category 5	P Value
CAD-based on K-TIRADS	0 (0/0)	4.8 (1/21)	12.1 (17/141)	20.9 (23/110)	69.2 (126/182)	<.001
Radiologist on K-TIRADS	0 (0/0)	0 (0/2)	6.0 (14/232)	37.5 (33/88)	90.9 (120/132)	<.001
CAD-based on ATA-TIRADS	7.1 (1/14)	11.4 (9/79)	10.6 (7/66)	25.5 (12/47)	65.7 (134/204)	<.001
Radiologist on ATA-TIRADS	0 (0/0)	7.3 (9/124)	5.5 (6/110)	26.3 (15/57)	90.6 (125/138)	<.001

[a] The numbers are percentages unless otherwise specified ; 9.6% (44 of 454) of nodules did not meet the criteria for any pattern using the ATA guidelines (isoechoic nodules with suspicious US features) and were classified as "not specified" by the CAD system, while the malignancy risk was calculated to be 9.1% (4 of 44).

predictive values, negative predictive values, and accuracy rates, and were compared using the McNemar test. Thyroid nodules requiring FNA as indicated by both sets of TIRADS recommendations were considered to indicate thyroid cancer (Online Supplemental Data).[13,14] We performed subgroup analyses of nodules at high and intermediate suspicion of cancer (as indicated by the FNA criteria). The unnecessary FNA rate was defined as the number of benign nodules among the FNA-required nodules (454 in total). Interobserver agreement between the CAD system and the radiologist in terms of the TIRADS and dichotomous outcome classifications was estimated using the κ coefficient. The κ level was defined as follows: <0.20, poor agreement; 0.21–0.40, fair agreement; 0.41–0.60, moderate agreement; 0.61–0.80, substantial agreement; and >0.80, good agreement.

All statistical analyses were performed using SPSS for Windows (Version 25.0; IBM). The significance level was set at .05.

RESULTS

Clinical and Sonographic Features of Benign and Malignant Thyroid Nodules

The mean nodule diameter was 17.8 [SD, 9.7] mm (range, 10.0–73.0 mm). Of the 454 nodules, 287 (63.2%) were benign and 167 (36.8%) were malignant. Malignant nodules included 149 classic papillary thyroid carcinomas, 12 follicular-variant papillary thyroid carcinomas, 4 follicular carcinomas, and 2 medullary carcinomas.

Table 1 lists the US features of included nodules. The mean diameter of benign nodules was 18.6 [SD, 10.7] mm, which was statistically larger than that of malignant nodules (16.4 [SD, 7.5] mm; $P = .011$). Solid component, hypoechogenicity, nonparallel orientation, spiculated/microlobulated margins, and microcalcification were all significantly associated with thyroid cancer (all, $P < .001$). Diagnoses of "possibly malignant" by the CAD system and radiologist were significant in terms of detecting thyroid cancers (both, $P < .001$).

Table 3: Comparison of unnecessary FNA rates for thyroid cancer diagnosis in all nodules[a]

	No. of FNAs	No. of Malignant Nodules among FNA Nodules	No. of Benign Nodules among FNA Nodules	Unnecessary FNA Rate
CAD based on K-TIRADS (categories 3, 4, and 5)	85.5 (388/454)	42.0 (163/388)	58.0 (225/388)	49.6 (225/454)
CAD based on K-TIRADS (categories 4 and 5)	64.3 (292/454)	51.0 (149/292)	49.0 (143/292)	31.5 (143/454)
CAD based on ATA-TIRADS (categories 3, 4, and 5)	79.3 (360/454)	43.9 (158/360)	56.1 (202/360)	44.5 (202/454)
CAD based on ATA-TIRADS (categories 4 and 5)	55.3 (251/454)	57.5 (146/254)	42.5 (108/254)	23.8 (108/454)
CAD based on possible diagnosis	41.4 (188/454)	72.3 (136/188)	27.7 (52/188)	11.5 (52/454)
Radiologist K-TIRADS (categories 3, 4, and 5)	76.2 (346/454)	47.1 (163/346)	52.9 (183/346)	40.3 (183/454)
Radiologist K-TIRADS (categories 4 and 5)	48.5 (220/454)	69.5 (153/220)	30.5 (67/220)	14.8 (67/454)
Radiologist ATA-TIRADS (categories 3, 4, and 5)	68.3 (310/454)	48.4 (150/310)	51.6 (160/310)	35.2 (160/454)
Radiologist ATA-TIRADS (categories 4 and 5)	43.0 (195/454)	71.8 (140/195)	28.2 (55/195)	12.1 (55/454)
Radiologist based on possible diagnosis	32.8 (149/454)	91.9 (137/149)	8.1 (12/149)	2.6 (12/454)

[a] The numbers are percentages. Categories 5, 4, and 3 refer to high-, intermediate-, and low-suspicion nodules in each guideline.

Malignancy Risk according to CAD System and Radiologist and TIRADS Category Classifications

Table 2 lists the malignancy risk for each TIRADS category, classified by the CAD system and the radiologist. The malignancy risk for each K-TIRADS and ATA-TIRADS category determined by the radiologist matched the suggested malignancy risk, with the exception of a slightly higher risk of malignancy for the "very low suspicion" category of the ATA-TIRADS (7.3% [9 of 124] versus <3%). With the CAD system, the predicted probability of malignancy increased with the risk category ($P < .001$). However, when the CAD diagnosis was based on the ATA-TIRADS, the risk of malignancy did not match the suggested risk: It was higher for nodules that were benign and at very low, low, and intermediate suspicion but lower for nodules in the high-suspicion category. Overall, 9.6% (44 of 454) of nodules did not meet the criteria for any pattern using the ATA guidelines (isoechoic nodules with suspicious US features) and were classified as "not specified" by the CAD system. The malignancy risk was 9.1% (4 of 44).

Diagnostic Performance of the CAD System and Radiologist Based on TIRADS Classifications and Dichotomous Outcomes

The Online Supplemental Data summarize thyroid cancer diagnostic performance by the CAD system and the radiologist based on the TIRADS and dichotomous outcome classifications. The sensitivity and negative predictive values were highest for radiologist K-TIRADS and CAD K-TIRADS, followed by CAD ATA-TIRADS, radiologist ATA-TIRADS, radiologist's diagnosis, and CAD diagnosis. The specificity and positive predictive values were highest for the radiologist's diagnosis, followed by the CAD diagnosis, radiologist ATA-TIRADS, radiologist K-TIRADS, CAD ATA-TIRADS, and CAD K-TIRADS.

The TIRADS classifications had significantly higher diagnostic sensitivities but lower specificities compared with dichotomous outcome classifications, while the latter had higher specificities (all, $P < .001$). The diagnostic sensitivities of the CAD systems using the TIRADS classification and dichotomous outcomes did not differ between the CAD systems and radiologist (97.6% versus 97.6%, $P > .999$, for the K-TIRADS; 94.6% versus 89.8%, $P = .077$, for the ATA-TIRADS; and 81.4% versus 82.0%, $P > .999$, for the possible diagnosis, respectively), while the specificity and accuracy were significantly lower for the CAD systems compared with the radiologist (21.6% versus 36.2%; 29.6% versus 44.3%; and 81.9% versus 95.8%, all $P < .001$, respectively, and 49.6% versus 58.8%; 53.5% versus 61.0%; and 81.7% versus 90.7%, respectively; all, $P < .001$).

When we used the FNA criterion to evaluate nodules at high and intermediate suspicion of malignancy, the diagnostic specificity and accuracy of the CAD system increased; however, the diagnostic performance of the TIRADS classifications (compared with the dichotomous outcome classification) was similar to that of the overall diagnostic performance.

Comparison of Unnecessary FNA Rates

The unnecessary FNA rate was the lowest for the radiologist's diagnosis, followed by the CAD diagnosis, radiologist ATA-TIRADS, radiologist K-TIRADS, CAD ATA-TIRADS, and CAD K-TIRADS (Table 3). The dichotomous outcome classification yielded a lower unnecessary FNA rate than the TIRADS classification, particularly by the radiologist.

Interobserver Agreement between the CAD System and the Radiologist

The dichotomous outcome agreement for the CAD system and the radiologist was 83.0% (377/454). The extent of interobserver agreement was substantial ($\kappa = 0.640$) for the dichotomous outcomes and fair-to-moderate to the K-TIRADS and the ATA-TIRADS classifications ($\kappa = 0.356$ and 0.402, respectively, Table 4).

DISCUSSION

Our results revealed that the diagnostic performance of the CAD system varies with the TIRADS and dichotomous outcome classifications. Dichotomous outcomes revealed significantly higher specificity, positive predictive values, and accuracy for detecting

Table 4: Interobserver variability of US characteristics between radiologist and CAD systems[a]

	κ Value
K-TIRADS (CAD vs radiologist)	0.356
ATA-TIRADS (CAD vs radiologist)	0.402
Possible diagnosis (CAD vs radiologist)	0.640

[a] The extent of interobserver agreement between the CAD system and the radiologist was calculated using the Cohen κ value.

thyroid cancer, an outcome associated with a reduction in the unnecessary FNA rates. However, the TIRADS classification achieved higher sensitivity and negative predictive values, which increased unnecessary FNA rates. Clinicians should be aware of these particular strengths and weaknesses of the CAD system in the management of thyroid nodules.

The use of high-resolution US, combined with increased medical surveillance and access to health care services, has markedly increased the detection of thyroid nodules and the number of FNAs.[15,16] Therefore, radiologists who frequently interpret thyroid US images are concerned about how to report nodules and on which nodules to perform FNA. Since 2009, the use of the TIRADS classification system has been recommended to improve consistency across practices and institutions and to decrease unnecessary FNAs.[13-15] Several professional groups, including the American Thyroid Association and the Korean Society of Thyroid Radiology, have proposed the ATA-TIRADS and K-TIRADS, respectively, and have recommended FNA criteria in conjunction with the nodule size and TIRADS category.[13,14] In keeping with this international trend, the currently available CAD system provides both TIRADS classifications and dichotomous outcomes. This CAD system is based on training of a deep learning algorithm using 4916 nodules from 3 different institutions.[12] We found that the risk of malignancy significantly increased with the higher risk categories when the TIRADS category was assigned by the CAD system; however, the calculated prevalence and risk in each category differed depending on whether the CAD-based or radiologist-based method was used. The CAD system overestimated the number of TIRADS category 5 (highly suspicious) nodules and underestimated the risk of malignancy in TIRADS category 5 compared with the radiologist. Therefore, CAD users should be aware that the risk of malignancy differs by category between the CAD- and radiologist-based methods.

In terms of system diagnostic performance, similar sensitivity scores have been reported for CAD- and radiologist-based assessments.[9-11,16] However, reduced specificity and accuracy have been reported for the CAD-based system.[9-11,16] In agreement with these findings, we observed lower specificity and accuracy for the CAD system compared with the radiologist (81.9% versus 95.8% and 81.7% versus 90.7%, respectively) and similar sensitivity (81.4% versus 82.0%) for the detection of thyroid cancer. Furthermore, we present the first assessment of the diagnostic ability of the TIRADS classification of the CAD system. We found that the TIRADS classification had significantly higher diagnostic sensitivities (94.6%–97.6% versus 81.4%) but lower specificities (21.6%–29.6% versus 81.9%) compared with dichotomous outcomes, which increase unnecessary FNA rates (44.5%–49.6% versus 11.5%). The false-positive rate was higher for the CAD system, while the false-negative rate was not significantly

changed. However, these differences were reduced when the FNA criteria for nodules at high and intermediate suspicion were applied. Our study identified only fair-to-moderate agreement between the CAD system and the radiologist's TIRADS classifications, which highlights a limitation of the current CAD system. The interobserver agreement between the CAD system and the radiologist in terms of the margins and calcifications was the lowest but remained fair-to-moderate (κ = 0.390 and 0.448, respectively), reducing the overall system accuracy. A recent blinded multicenter study similarly reported that the inter- and intraobserver agreement (using a US classification system) were 0.34–0.44 and 0.33–0.54, respectively, among thyroid imaging experts.[16] Therefore, CAD users should be aware of the strengths and weaknesses associated with thyroid cancer diagnosis using commercially available CAD systems.

Our study revealed important design issues for an AI-based thyroid cancer CAD system. Previous studies have relied on a simple classification model (benign/malignant) without the inclusion of US features.[4–7] However, several US features are strongly associated with thyroid cancer, and a simple classification system cannot incorporate the influence of these US features on the final diagnosis in convolutional neural network deep learning models.[17,18] Therefore, the currently available CAD system was designed to report information about US features in addition to the possible diagnosis to help inform convolutional neural network deep learning models and infer a conclusion. Such a system could offer great advantages. Less experienced operators find it difficult to accurately recognize and consistently interpret US features, so an AI-based CAD system would improve standardization and ultimately reduce unnecessary FNAs.[11] However, on the contrary, the dichotomous AI prediction showed relatively high specificity and positive predictive values that, in fact, match or exceed nearly all permutations of testing performed in this study with the exception of expert radiologist-based diagnosis. This finding implies that even if a radiologist were able to perfectly score a lesion based on the TIRADS classification, the dichotomous AI prediction may help reduce false-positive FNAs compared with TIRADS-based triage. Further improvements and validations are required on this issue.

Our study had certain limitations. First, we included nodules that had been referred to US-guided FNA or US examination before a scheduled operation. Therefore, the proportion of malignancies was high, and the diagnostic performance of the system might differ in a general population. Second, the radiologist's diagnoses were based on personal experience, so a less experienced radiologist might have reported differently. This feature may influence the generalizability of this study. Third, the CAD data were obtained by the same radiologist who performed US. However, the CAD data were semiautomatically obtained and the radiologist retrospectively assessed the US findings after at least 6 months while blinded to other data, so this process minimized bias. Fourth, the clinical impact of the CAD system might differ slightly in real-world practice. Further research using a prospective study design is required in a general population.

CONCLUSIONS
The diagnostic performance of the CAD system differs depending on the TIRADS and dichotomous outcome classifications and

compared with radiologist-based assessments. Clinicians should be aware of the strengths and weaknesses of the CAD system.

REFERENCES

1. Park SH, Kressel HY. **Connecting technological innovation in artificial intelligence to real-world medical practice through rigorous clinical validation: what peer-reviewed medical journals could do.** *J Korean Med Sci* 2018;33:e152 CrossRef Medline
2. Park SH, Han K. **Methodologic guide for evaluating clinical performance and effect of artificial intelligence technology for medical diagnosis and prediction.** *Radiology* 2018;286:800–09 CrossRef Medline
3. Park SH. **Regulatory approval versus clinical validation of artificial intelligence diagnostic tools.** *Radiology* 2018;288:910–11 CrossRef Medline
4. Li X, Zhang S, Zhang Q, et al. **Diagnosis of thyroid cancer using deep convolutional neural network models applied to sonographic images: a retrospective, multicohort, diagnostic study.** *Lancet Oncol* 2019;20:193–201 CrossRef Medline
5. Chi J, Walia E, Babyn P, et al. **Thyroid nodule classification in ultrasound images by fine-tuning deep convolutional neural network.** *J Digit Imaging* 2017;30:477–86 CrossRef Medline
6. Buda M, Wildman-Tobriner B, Castor K, et al. **Deep learning-based segmentation of nodules in thyroid ultrasound: improving performance by utilizing markers present in the images.** *Ultrasound Med Biol* 2020;46:415–21 CrossRef Medline
7. Song J, Chai YJ, Masuoka H, et al. **Ultrasound image analysis using deep learning algorithm for the diagnosis of thyroid nodules.** *Medicine (Baltimore)* 2019;98:e15133 CrossRef Medline
8. Kim DW, Jang HY, Kim KW, et al. **Design characteristics of studies reporting the performance of artificial intelligence algorithms for diagnostic analysis of medical images: results from recently published papers.** *Korean J Radiol* 2019;20:405–10 CrossRef Medline
9. Choi YJ, Baek JH, Park HS, et al. **A computer-aided diagnostic system using artificial intelligence for the diagnosis and characterization of thyroid nodules on ultrasound: initial clinical assessment.** *Thyroid* 2017;27:546–52 CrossRef Medline
10. Yoo YJ, Ha EJ, Cho YJ, et al. **A computer-aided diagnostic system for thyroid nodules on ultrasonography: initial clinical experience.** *Korean J Radiol* 2018;28:1532–37 CrossRef Medline
11. Jeong EY, Kim HL, Ha EJ, et al. **Computer-aided diagnostic system for thyroid nodules on ultrasonography: diagnostic performance and reproducibility based on the experience level of operators.** *Eur Radiol* 2019;29:1978–85 CrossRef Medline
12. Park VY, Han K, Seong YK, et al. **Diagnosis of thyroid nodules: performance of a deep learning convolutional neural network model vs radiologists.** *Sci Rep* 2019;9:17843 CrossRef Medline
13. Haugen BR. **2015 American Thyroid Association Management Guidelines for Adult Patients with Thyroid Nodules and Differentiated Thyroid Cancer: what is new and what has changed?** *Cancer* 2017;123:372–81 CrossRef Medline
14. Shin JH, Baek JH, Chung J, et al; Korean Society of Thyroid Radiology (KSThR) and Korean Society of Radiology. **Ultrasonography Diagnosis and Imaging-Based Management of Thyroid Nodules: Revised Korean Society of Thyroid Radiology Consensus Statement and Recommendations.** *Korean J Radiol* 2016;17:370–95 CrossRef Medline
15. Ha EJ, Baek JH, Na DG. **Risk stratification of thyroid nodules on ultrasonography: current status and perspectives.** *Thyroid* 2017;27:1463–68 CrossRef Medline
16. Kim HL, Ha EJ, Han M. **Real-world performance of computer-aided diagnostic system for thyroid nodules using ultrasonography.** *Ultrasound Med Biol* 2019;45:2672–78 CrossRef Medline
17. Persichetti A, Stasio E, Coccaro C, et al. **Inter- and intraobserver agreement in the assessment of thyroid nodule ultrasound features and classification systems: a blinded multicenter study.** *Thyroid* 2020;30:237–42 CrossRef Medline
18. Ha EJ, Baek JH, Na DG. **Deep convolutional neural network models for the diagnosis of thyroid cancer.** *Lancet Oncol* 2019;20:e130 CrossRef Medline

Real-Time Ultrasound Image Fusion with FDG-PET/CT to Perform Fused Image-Guided Fine-Needle Aspiration in Neck Nodes: Feasibility and Diagnostic Value

P.K. de Koekkoek-Doll, M. Maas, W. Vogel, J. Castelijns, L. Smit, I. Zavrakidis, R. Beets-Tan, and M. van den Brekel

ABSTRACT

BACKGROUND AND PURPOSE: New imaging techniques such as hybrid imaging of ultrasound and FDG-PET/CT are available but not yet investigated for node staging. The aim of the study was to evaluate the feasibility and added diagnostic value of real-time image-fused ultrasound-guided fine-needle aspiration with FDG-PET/CT data for node staging.

MATERIALS AND METHODS: Ninety-six patients who were referred for cervical lymph node staging with FDG-PET/CT before ultrasound were prospectively included. After routine ultrasound-guided fine-needle aspiration, all FDG-PET-positive nodes were marked on FDG-PET/CT, and real-time image fusing of ultrasound and FDG-PET/CT was performed using the electromagnetic navigation system PercuNav. Already-punctured nodes were confirmed to be PET-positive, and additional fused-ultrasound-guided fine-needle aspiration was performed in previously missed PET-positive nodes.

RESULTS: Of 96 patients, 87 (91%) patients had suspicious nodes requiring fine-needle aspiration cytology. Ultrasound-guided fine-needle aspiration was performed in 175 nodes. Cytology was inconclusive in 9/175 (5%) nodes, and 85/166 (51%) nodes were malignant. Target planning was performed in 201 PET-positive nodes; 195/201 (97%) of those nodes were fused successfully. Twenty of 175 ultrasound-guided fine-needle aspiration nodes turned out to be FDG-PET-negative, and 149/175 (85%) of the fused ultrasound-guided fine-needle aspiration nodes were confirmed to be FDG-PET-positive. Of 201 PET-positive nodes, 46 (23%) were additionally identified, and fused ultrasound-guided fine-needle aspiration was performed. Cytology was inconclusive in 4/46 nodes (9%), and 13/42 (31%) nodes were malignant.

CONCLUSIONS: Real-time ultrasound image fusion with FDG-PET-positive nodes is feasible in cervical lymph nodes, and fused ultrasound-guided fine-needle aspiration increases the number of malignant nodes detected.

ABBREVIATIONS: cN0 = clinically node-negative neck; FNAC = fine-needle aspiration cytology; HNC = head and neck cancer; ND = neck dissection; TNM = Tumor, Node, Metastasis; US = ultrasound; USgFNAC = ultrasound-guided fine-needle aspiration cytology

The Tumor, Node, Metastasis (TNM) stage in head and neck cancer (HNC) is important for prediction of prognosis and stratification of treatment. Besides physical examination, imaging plays a crucial role in defining the TNM stage, assessing tumor volume and nodal involvement.[1,2] Nodal staging with CT and MR imaging is limited with a per-patient sensitivity ranging from 73% to 87% for CT and 70% to 74% for MR imaging.[3] In the

clinically node-negative neck (cN0), the sensitivity ranges from 14% to 80% for CT and from 29% to 85% for MR imaging; on average, the sensitivity is in the range of 40%–60%.[4] Molecular imaging of glucose metabolism with FDG-PET/CT has a higher per-neck-level sensitivity for detection of regional nodal metastases in patients with primary head and neck squamous cell carcinoma, with a sensitivity of up to 84% and a specificity up to 96%.[5,6] However, for cN0, an overall sensitivity of 21.4% and specificity of 98.4% have been reported.[7] In comparison with sentinel node biopsy in cN0 head and neck cancer, MR imaging and CT are not effective in predicting whether prophylactic neck dissection (ND) can be safely avoided, and the sensitivity of FDG-PET/CT may still not be adequate.[8] In clinical practice, ultrasound-guided fine-needle aspiration cytology (USgFNAC) plays an important role, not only as an upfront imaging technique for the neck but also to determine the diagnosis in equivocal lymph nodes on CT, MR imaging, or FDG-PET/CT.[9] The sensitivity of

Table 1: Diagnosis of all patients[a]

Diagnosis	No.	Percentage
Adeno ca parotid gland	1	1%
Angiosarcoma	1	1%
B-cell lymphoma	1	1%
Lung carcinoma	2	2%
Melanoma	6	6%
Merkel cell carcinoma	2	2%
Rhabdomyosarcoma	1	1%
SCC hypopharyngeal	7	7%
SCC laryngeal	16	17%
SCC nasal cavity sinus	4	4%
SCC nasopharyngeal	1	1%
SCC oral cavity	19	20%
SCC oropharyngeal	25	26%
SCC skin	1	1%
SCC unknown primary	6	6%
Second branchial cleft	1	1%
Tuberculosis	1	1%
Unknown primary	1	1%
Total	96	100%

Note:—Aneno ca indicates adenocarcinoma; SCC, squamous cell carcinoma.
[a] In total, 82% of all patients had SCC.

Table 2: Combination of treatments of all 96 patients

Treatment		RT	CRT	BRT	PDT	Chemo
Surgery, no ND	11	5	1	0	0	0
SND/SNB	20	8	1	0	0	0
No surgery	63	31	21	6	1	4
No[a] treatment	2	0	0	0	0	0
Total	96	44	23	6	1	4

Note:—RT indicates radiation therapy; CRT, radiochemotherapy; BRT, bioradiation therapy; PDT, photodynamic therapy; Chemo, chemotherapy; SND, selective neck dissection; SNB, sentinel node biopsy.
[a] Two patients did not have treatment because of benign lesions: second branchial cleft cyst and tuberculosis.

USgFNAC in patients with clinically suspicious nodes has been reported to be 88%,[10] but the sensitivity drops significantly to 39% in patients with a cN0.[11] Apart from minimizing the chance of sampling errors, selection of the most suspicious nodes that need aspiration is a major challenge.[12] Selection of nodes by FDG-PET/CT standard uptake value might improve selection of the most suspicious nodes for fine-needle aspiration cytology (FNAC).

Due to technical improvements, it is possible to fuse real-time ultrasound (US) with cross-sectional imaging techniques such as with PET/CT, CT, or MR imaging.[13] Fusion of US with FDG-PET/CT to guide FNAC of nodes can potentially improve the identification and detection of malignant nodes. The aim of our study was first to evaluate the feasibility of US real-time fusion with FDG-PET/CT data for fused image guidance of fine-needle aspiration in suspicious neck nodes and second to evaluate whether it leads to a more accurate detection of malignant nodes.

MATERIALS AND METHODS
Patient Population
We prospectively included 96 patients (Table 1) who were referred for USgFNAC with prior FDG-PET/CT and met one of the following criteria: histopathologically proved HNC and histologically proved lymph node metastasis with an unknown primary or suspicious head and neck lesion, not yet proved to be malignant. All data were analyzed retrospectively. After routine ultrasound and USgFNAC, real-time fusion of ultrasound and FDG-PET/CT took place to confirm USgFNAC nodes to be PET-positive and to perform additional fused-USgFNAC of missed FDG-PET-positive nodes that would change the N stage. This study was approved by the Netherlands Cancer Institute institutional medical ethics committee (METC16.0745) and the Netherlands Cancer Institute institutional review board (IRBd20-126). All retrospective medical data/biospecimen studies at the Netherlands Cancer Institute have been executed pursuant to Dutch legislation and international standards. Before May 25,

2018, national legislation on data protection applied, as well as the International Guideline on Good Clinical Practice. From May 25, 2019, we also adhered to the General Data Protection Regulation. Within this framework, patients are informed and have always had the opportunity to object or actively consent to the (continued) use of their personal data and biospecimens in research. Hence, the procedures comply with both national and international legislative and ethical standards.

Table 1 shows the diagnosis in number and percentages of all included patients and the number and percentages of patients with head and neck squamous cell carcinoma. Table 2 shows an overview of the treatment.

FDG-PET/CT Imaging
For FDG-PET/CT, images were acquired using a Gemini TF scanner (Philips Healthcare). Patients fasted for 6 hours and were hydrated before administration of FDG. Diabetes mellitus needed to be regulated adequately. The plasma glucose level was required to be below 10 mmol/L. A dose of 190–240 MBq was administered depending on body mass index. FDG-PET images of the head and neck area were acquired for 3 bed positions of 3 minutes each. They were reconstructed to 2-mm isotropic voxels. Low-dose CT was acquired for attenuation correction and anatomic orientation with 40 mAs and 2-mm slices. In addition, images of the neck were acquired. All FDG-PET/CT images were interpreted by an experienced nuclear physician for clinical staging, and this report was available for interpretation of involved nodes in this study.

Ultrasound and FNAC
The FDG-PET/CT data were imported into the US device (EPIQ 7 G; Philips Healthcare) before the routine procedures. First, routine US evaluation and routine USgFNAC with a 21-ga needle without use of FDG-PET/CT data were performed. All USgFNACs were performed by 1 radiologist (P.K.d.K.-D.) who has 10 years of USgFNAC experience in HNC. She was aware of the clinical information and available imaging data, including FDG-PET/CT, before performing US. FNAC was performed in 1 or 2 neck levels ipsilateral and sometimes contralateral in suspicious nodes in the levels at most risk, corresponding to the site of the primary tumor, as well as in suspicious nodes at the lowest neck level of each side. Nodes were aspirated at a short-axis diameter of >1 cm or <1 cm and showed loss of a fatty hilum or showed a thickened or asymmetric cortex or round shape. Also, nodes described in the MR imaging or FDG-PET/CT to be borderline or suspicious were aspirated when identified.
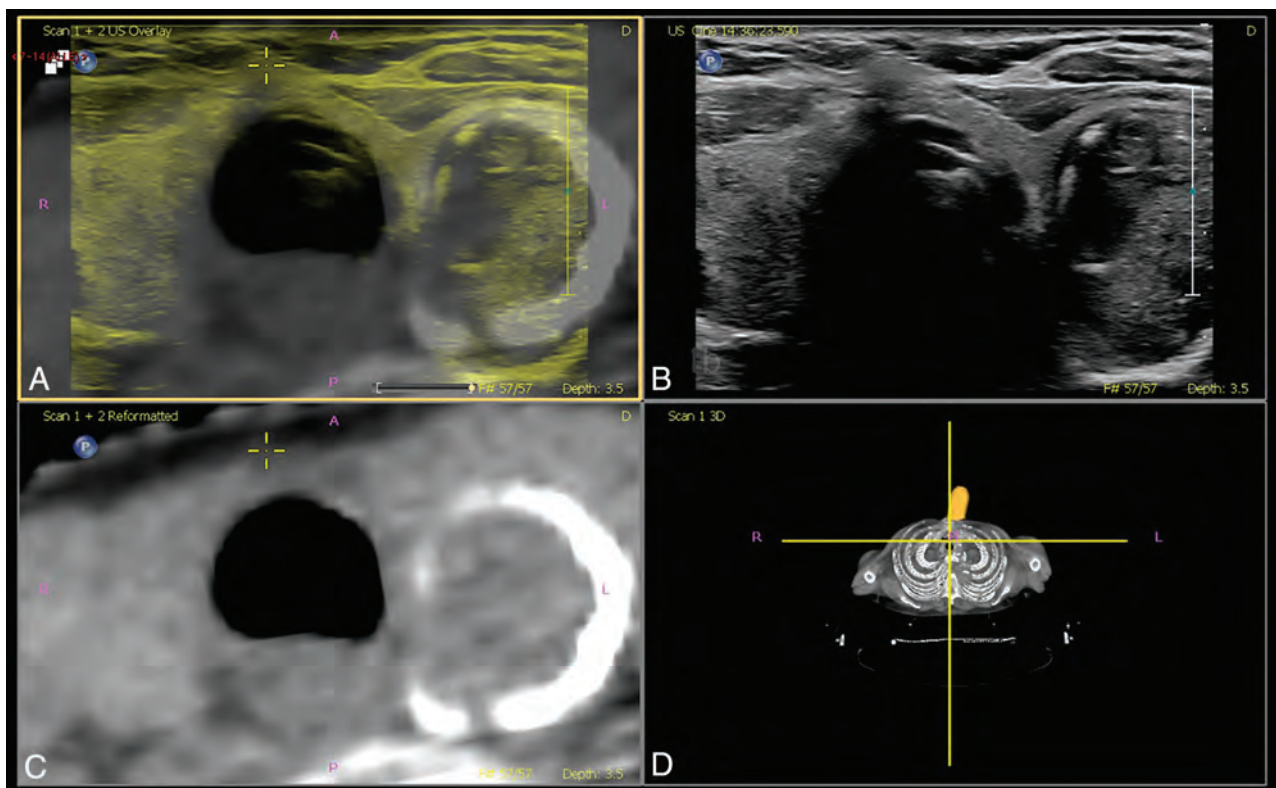
FIG 1. Matched plane fusion, manual correction. *A*, Overlay US (yellow) and CT (gray). *B*, US image. *C*, Reformatted CT image. *D*, Volume representation of CT image and probe location.

Immediately after the routine US and USgFNAC procedures, real-time image fusion of US and FDG-PET/CT using the electromagnetic navigation system PercuNav (Philips Healthcare; FDA- and Conformité Européenne–approved and available worldwide), installed on the same US diagnostic system, took place by the same reader (P.K.d.K.-D.). US was performed using either a L12-5 or an eL18-4 probe with an integrated electromagnetic tracker (both from Philips Healthcare). During the image-fusion steps, a bracket and the respective electromagnetic tracker were added to the L12-5 probe so it could be used with the PercuNav system. The PercuNav setup was used according to the manufacturer's manual. The patient reference tracker was placed on the forehead of the patient and held in place with tape. The field generator was positioned above the patient's neck using a metallic arm. The initial fusion between real-time US and FDG-PET/CT was performed by identifying the thyroid on both modalities and using the "matched plane" function on the system (Fig 1).

Additional manual corrections to the fusion were made by identification of known anatomic structures such as the hyoid bone, submandibular gland, and carotid artery bifurcation. Then a target was created for each FDG-PET/CT–positive lymph node using the target planning function (including nodes with a low risk of malignancy and low standard uptake values) (Fig 2). At this time, the radiologist identified the PET-positive nodes targeted on FDG-PET/CT and verified whether USgFNAC had already been performed (Fig 2). In patients with multiple FDG-PET–positive nodes, a selection was made on the basis of level, size, and standard uptake value for fused aspiration. In case the node had not been previously aspirated, fused-USgFNAC was performed.

Reference Standard

The surrogate reference standard was the pathologic result of FNAC. Because only 19/96 patients underwent ND and 1/96 patients underwent sentinel node biopsy, this series was too small to reliably estimate the sensitivity and specificity of USgFNAC, fused-USgFNAC, or FDG-PET/CT. If available, histopathology of the ND specimen was used as a reference standard and the pN stage was compared with the pN stage of USgFNAC and fused-USgFNAC (Online Supplemental Data).

Statistical Analysis

A 2-sample t test was used to compare the mean size of nodes between USgFNAC and fused-USgFNAC. By means of the Mantel-Haenszel test, the detection rate of malignant nodes in USgFNAC and fused-USGFNAC was compared. The χ^2 test was used to compare the accuracy of the N stage found with USgFNAC and fused-USgFNAC in relation to the cytology results.

RESULTS

Nine of 96 patients (9%) who were selected for the study did not have any FDG-PET–positive nodes or suspicious nodes on US. In the remaining 87/96 (91%) patients, a total of 221 lymph nodes were aspirated. The median number of aspirated nodes per patient was 2 (range, 1–5).

USgFNAC

One hundred seventy-five of 221 lymph nodes were aspirated during routine US; the smallest nodes were 4 mm, and the mean minimal axial diameter was 11.7 mm. At USgFNAC, 9 of 175
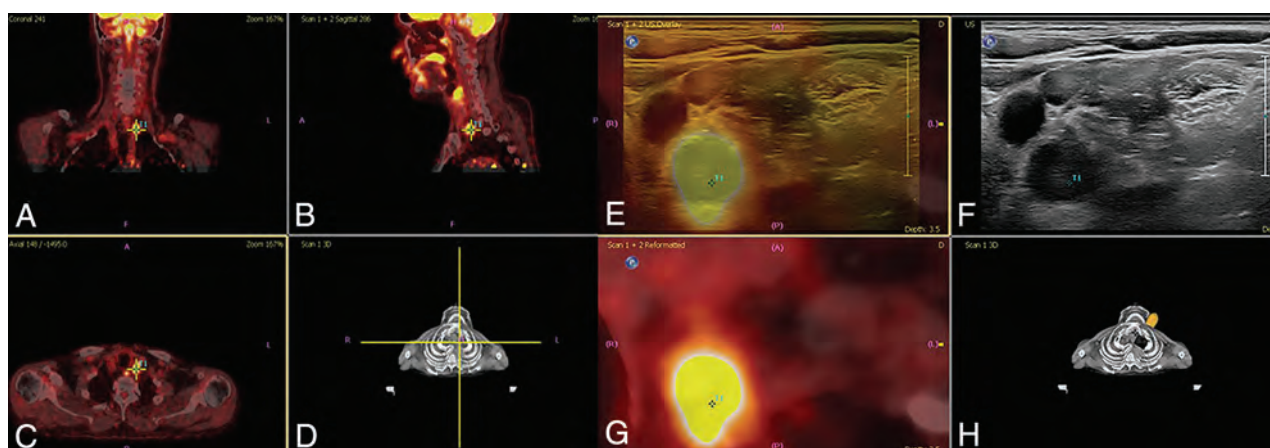
FIG 2. Target planning and real-time fusion of FDG-PET-positive lymph nodes to identify PET-positive nodes. *A*, Coronal view. *B*, Sagittal view. *C*, Axial view. *D*, Volume representation of FDG-PET/CT image and probe location, PET-positive nodes where targeted, and real-time image fused with ultrasound. *E*, Overlay US (yellow) and PET/CT (gray). *F*, US image. *G*, Reformatted PET/CT image. *H*, Volume representation of the CT image and probe location. Fusion of PET and CT and target planning took place using the electromagnetic navigation system PercuNav. First, routine ultrasound and routine USgFNAC were performed. Second, ultrasound and FDG-PET-positive nodes were real-time fused. USgFNAC in PET-positive nodes was confirmed, and additional fused-USgFNAC of missed PET-positive nodes was performed.

Table 3: Size and location of additional fused-USgFNAC nodes

	Total	Malignant		Benign		Insufficient	
Level	No.	No.	Sizes (mm)	No.	Sizes (mm)	No.	Sizes (mm)
1	2	0		1	3	1	8
1a	1	0		1	4	0	
1b	4	1	9	3	4, 3, 6	0	
2	12	3	7, 4, 6	8	9, 6, 11, 8, 5, 6, 8, 5	1	8
2b	1	1	6	0		0	
3	13	4	9, 8, 6, 6	8	5, 4, 3, 5, 4, 4, 6	1	5
4	7	2	6, 12	4		1	4
5	3	1	9	2	5, 6	0	
Parot.gl.	2	0		2	5, 6	0	
Cheek	1	1	6	0		0	
Total	46	13		29		4	

Note:—1 to 5 indicates the neck levels; Parot.gl., parotid gland.

nodes (5%) were inconclusive at cytology, and 85 of 166 (51%) nodes were malignant.

Fused-USgFNAC

Target planning was performed in 201 PET-positive nodes. Fusion was technically successful in 195/201 (97%) FDG-PET-positive nodes.

One hundred forty-nine of 175 (85%) USgFNAC nodes were confirmed to be FDG-PET-positive. Cytology was inconclusive in 9/175 (5%). Of the remaining 140 confirmed PET-positive nodes, 83 (59%) nodes proved to be malignant. At fusion, 20 of the USgFNAC nodes proved to be FDG-PET-negative, and only 1 of those nodes was malignant.

On the basis of fusion, 46/201 (23%) FDG-PET-positive nodes were additionally identified and fused-USgFNAC was performed; the smallest nodes were 3 mm, and the mean minimal axial diameter was 6.3 mm (range, 3–16 mm), which was significantly smaller than in routine USgFNAC (*P* value < .001) (Table 3).

At cytology, 4/46 nodes (9%) were inconclusive and 13 of 42 (31%) nodes proved to be malignant. Added fused-USgFNAC

increased the number of proved malignant nodes from 85 to 98 (15%). Due to additional fused-USgFNAC, the percentage of proved PET-positive malignant nodes changed from 83/166 (50%) to 96/182 (53%) (statistically insignificant *P* value < .29; flow chart, Fig 3).

With fused-USgFNAC, the pN-stage was upgraded in 8/87 (9%); in 2/8, from node-negative neck stage to N1 stage; and in 1/8, from N1 to N3 stage (Fig 4).

N staging with USgFNAC and fused-USgFNAC was not significantly different (*P* value < 0.1).

ND was performed in 19/96 (20%) patients, and sentinel node biopsy, in 1/96 (1%). A total of 610 nodes were removed, and in 11 of these 20 patients, 52 metastases were present. With USgFNAC, the pathologic result was pN0 stage in 2 of these patients, while it was pN2b stage and pN2c stage in the ND. With fused-USgFNAC, it was pN1 in both of those patients.

DISCUSSION

Our study shows that real-time US image fusion with FDG-PET/CT is feasible and allows accurate US identification of the FDG-PET-positive nodes. In our routine FNAC procedure, clinical information and imaging data including FDG-PET/CT are also available but not fused. In this study, we sought to demonstrate the additional effect of using fused USgFNAC, and this was demonstrated by an increase of pathologically confirmed malignant nodes from 85 without fusion to 98 with additional fusion. Accurate nodal staging is a major determinant for treatment decisions in head and neck squamous cell carcinoma.[14]

When we comparing fused-USgFNAC pN-stage with USgFNAC, 8/87 (9%) patients with pN stage were upgraded
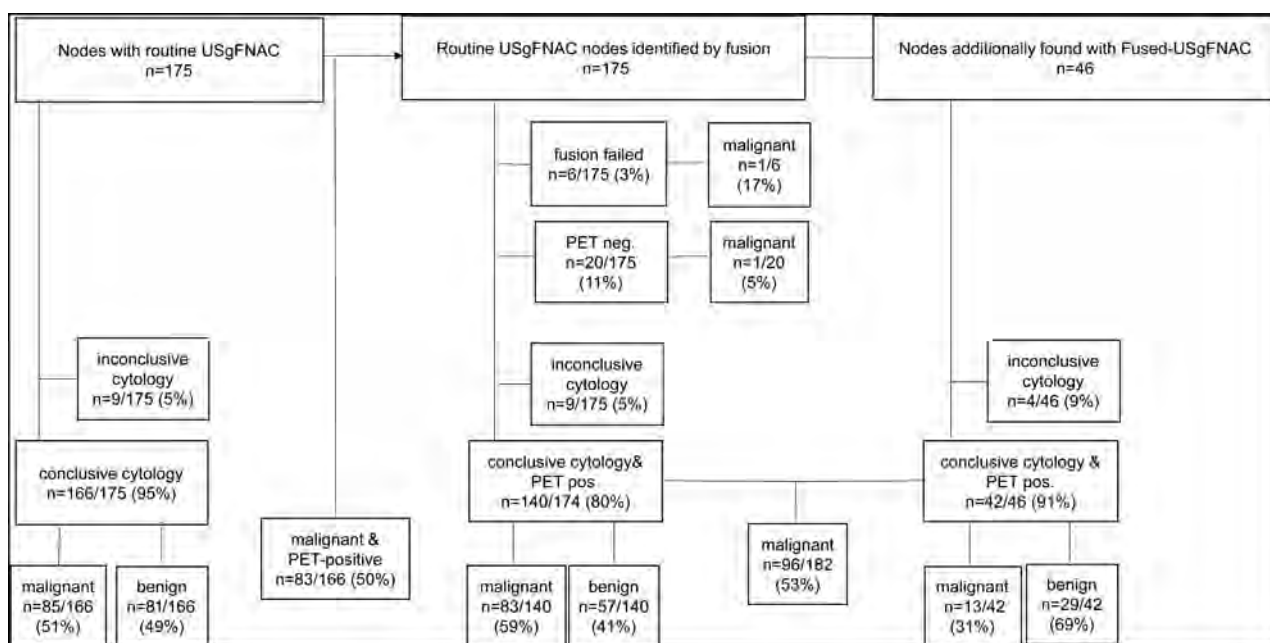
FIG 3. Flow chart results of routine USgFNAC and fused-USgFNAC. Pos. Indicates positive.

though N staging with USgFNAC and fused-USgFNAC was not significantly different.

Currently, the neck is staged by clinical palpation, CT, MR imaging, FDG-PET/CT, and/or USgFNAC in the case of suspicious nodes. For most imaging modalities, apart from irregularities and shape, the minimal axial diameter is one of the most important criteria for suspicious nodes to be selected for aspiration.[15] For FDG-PET/CT, the standard uptake value is a criterion for metastasis. All these imaging techniques fail to accurately detect very small metastases, leading to a sensitivity in the clinically node-negative neck on the order of 40%–60%[8] due to the higher frequency of small-sized nodes. Furthermore, FDG-PET/CT is limited in resolution and glucose uptake in small nodal metastases.[16] The main reason for this feature is that 25% of the metastases in clinically node-negative necks are <3 mm and, thus, will not be easily detected by any individual imaging technique.[11]

Treatment decision-making in HNC relies on imaging, emphasizing the need for high sensitivity to depict nodal disease.[17,18] Not only the extent of neck dissection but also the fields and doses of radiation therapy are guided by imaging results. As with FDG-PET/CT, subtle metabolically active lymph nodes are very difficult to characterize, and a subsequent USgFNAC is performed to make the final verdict. USgFNAC of the wrong lymph node or wrong part of the lymph node will lead to false-negative USgFNAC results, with undertreatment as a result.[18] We were able to show that real-time US image fusion with FDG-PET/CT is feasible. Within the 201 FDG-PET-positive nodes, fusion failed in only 6 nodes (8%), and this was mainly at the starting period when we were still in the midst of our learning curve. Real-time US image fusion with FDG-PET/CT is an excellent method to increase the reliability of the FDG-PET/CT results. Especially in borderline, small FDG-PET/CT-positive lymph nodes, fusion with US can increase the yield of fused-USgFNAC and diminish sampling errors. Particularly for small nodes, real-time US image

fusion with FDG-PET/CT can improve the sensitivity of ultrasound and the specificity of FDG-PET/CT and lead to a higher detection rate of malignant nodes. Although in both fused-USgFNAC and USgFNAC, the smallest FDG-PET-positive malignant lymph nodes were 4 mm, the mean minimal axial diameter of the tumor-positive nodes of fused-USgFNAC (7.8 mm) was significantly smaller than that of USgFNAC (13.4 mm).

Although additional fused-USgFNAC increased the number of confirmed malignant nodes from 85 to 98, the detection rate of malignant PET-positive nodes increased only from 51% to 53%, which was not significant. This can largely be explained by the smaller size of the additional fused-USgFNAC nodes, indicating an increase in sensitivity in small nodes. The N stage was upgraded in 8/87 (9%) patients.

Because we do not have definitive pathology of all aspirated lymph nodes, we cannot determine whether the FDG-PET/CT was false-positive or the aspiration was false-negative for the cases with negative aspirates. In addition, in 3/21(14%) patients with insufficient FNAC results, malignant nodes in elective neck dissection were present, which suggests that every FNAC with an insufficient result should be repeated. On FDG-PET/CT, smaller nodes are more often borderline FDG-positive nodes, which can lead to a problem in diagnosis. A visible slightly higher metabolism can be caused by a metastasis as well as by inflammation. Consequently, the specificity of a maximum standard uptake value between 2 and 3 at FDG-PET/CT is quite low and can be increased by adding fused-USgFNAC. On the other hand, the specificity of USgFNAC is almost 100%, so a combination of using FDG-PET/CT with a lower threshold and fused-USgFNAC might improve the sensitivity of the USgFNAC.

The selection of nodes for aspiration in HNC is a difficult issue. Size and location are the most important selection criteria. This study was meant to see whether image fusion with FDG-PET/CT is a helpful tool for node selection to provide FNAC.
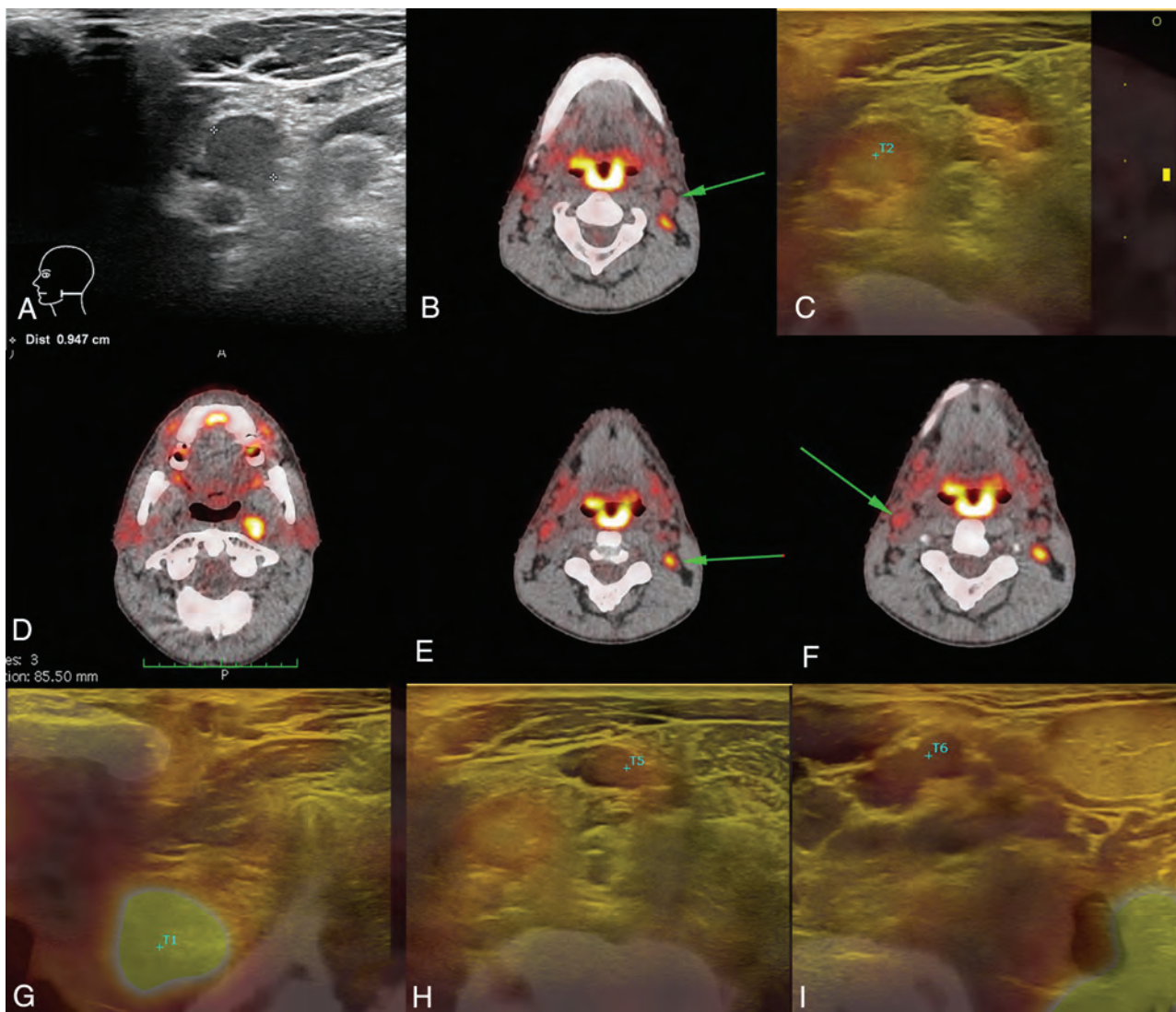
FIG 4. Change of N stage after additional fused-USgFNAC. The patient presented with cT3N0 oropharyngeal squamous cell carcinoma. *A,* Results of routine USgFNAC N1. *B* and C, PET/CT of the same node, controlled by image fusion. *D–F,* Additional nodes on PET/CT; all nodes have been fused, and fused-USgFNAC was performed. *G,* The deep parapharyngeal node was missed at routine ultrasound and only recognized after fusion. *H,* A PET-positive node with a normal appearance on routine ultrasound. *I,* Fused-USgFNAC-proved benign PET-positive contralateral node. Cytologically proved pN stage after fused-USgFNAC was pN2b, while it was N1 with USgFNAC and N2c on PET/CT. The *green arrows* point to the PET-positive nodes.

Especially in small lymph nodes with limited uptake, this technique could be added to USgFNAC. Only 1 patient with negative FDG-PET/CT findings had a suspicious node on ultrasound, which proved to be malignant. In all other patients, after fusion, all the nodes that underwent routine USgFNAC were, to some extent, FDG-PET-positive, so the current criteria for aspiration largely overlap with the glucose uptake at FDG-PET/CT. One could argue whether aspirating from more and smaller nodes without PET guidance would increase the sensitivity irrespective of adding FDG-PET/CT, but selection criteria only guided by size and shape are not very accurate, and borderline glucose uptake may well be more reliable.

Although in the prostate and liver, real-time fused image-guided biopsies are already used clinically,[19,20] the technique has its limitations in head and neck imaging. The mobility of the neck makes fusion much more difficult. Autofusion is not successful. Manual fusion and fusion corrections on the different levels of the neck must been done. To get a reliable accurate fusion, the radiologist must be well-trained. Because fused image-guided FNAC is time-consuming, with an additional 10–15 minutes of examination time, it should be used as a problem-solving tool in small, borderline FDG-PET-positive nodes, which are difficult to identify on routine USgFNAC. As far as we know, this is the first larger study of fused USgFNAC in HNC; therefore, the reproducibility is not known; and because there was only 1 observer, the interobserver variability is also not known. No reliable estimation of the sensitivity and specificity could be made due to the small number of patients who underwent neck dissection and sentinel node biopsy.

CONCLUSIONS

Real-time US image fusion with FDG-PET/CT and fused-USgFNAC is feasible in head and neck cancer. It can improve the

detection and image-guided aspiration of suspicious nodes as visualized on FDG-PET/CT and might increase the sensitivity of USgFNAC by selecting smaller FDG-PET-positive borderline nodes for fused-USgFNAC. Because fused-USgFNAC is time-consuming, it should be used as a problem-solving tool in small, borderline FDG-PET-positive nodes, which are difficult to identify on routine USgFNAC.

REFERENCES

1. Lodder WL, Pameijer FA, Rasch CR, et al. **Prognostic significance of radiologically determined neck node volume: a systematic review.** *Oral Oncol* 2012;48:298–302 CrossRef Medline
2. Gődény M. **Prognostic factors in advanced pharyngeal and oral cavity cancer; significance of multimodality imaging in terms of 7th edition of TNM.** *Cancer Imaging* 2014;14:15 CrossRef Medline
3. Sun J, Li B, Li CJ, et al. **Computed tomography versus magnetic resonance imaging for diagnosing cervical lymph node metastasis of head and neck cancer: a systematic review and meta-analysis.** *Onco Targets Ther* 2015;8:1291–313 CrossRef Medline
4. Castelijns JA, van den Breckel MW. **Imaging of lymphadenopathy in the neck.** *Eur Radiol* 2002;12:727–38 CrossRef Medline
5. Sun R, Tang X, Yang Y, et al. **(18)FDG-PET/CT for the detection of regional nodal metastasis in patients with head and neck cancer: a meta-analysis.** *Oral Oncol* 2015;51:314–20 CrossRef Medline
6. Yongkui L, Jian L, Wanghan, et al. **18FDG-PET/CT for the detection of regional nodal metastasis in patients with primary head and neck cancer before treatment: a meta-analysis.** *Surg Oncol* 2013;22: e11–16 CrossRef Medline
7. Zhang H, Seikaly H, Biron VL, et al. **Utility of PET-CT in detecting nodal metastasis in cN0 early stage oral cavity squamous cell carcinoma.** *Oral Oncol* 2018;80:89–92 CrossRef Medline
8. Liao LJ, Hsu WL, Wang CT, et al. **Analysis of sentinel node biopsy combined with other diagnostic tools in staging cN0 head and neck cancer: a diagnostic meta-analysis.** *Head Neck* 2016;38:628–34 CrossRef Medline
9. Akhavan-Moghadam J, Afaaghi M, Maleki AR, et al. **Fine-needle aspiration: an atraumatic method to diagnose head and neck masses.** *Trauma Mon* 2013;18:117–21 CrossRef Medline
10. Ostermann K, Asanau A, Lang FJ. **Cervical staging by head and neck surgeon-performed ultrasound and FNAC in N + head and neck cancer.** *B-ENT* 2018;14:7–15
11. Borgemeester MC, van den Brekel MW, van Tinteren H, et al. **Ultrasound-guided aspiration cytology for the assessment of the clinically N0 neck: factors influencing its accuracy.** *Head Neck* 2008;30:1505–13 CrossRef Medline
12. Colnot DR, Nieuwenhuis EJ, Van den Brekel MW, et al. **Head and neck squamous cell carcinoma: US-guided fine-needle aspiration of sentinel lymph nodes for improved staging—initial experience.** *Radiology* 2001;218:289–93 CrossRef Medline
13. Wang SY. **Real-time fusion imaging of liver ultrasound background and principles of ultrasound fusion imaging.** *J Med Ultrasound* 2017;25:9–11 CrossRef Medline
14. Edge SB, Compton CC. **The American Joint Committee on Cancer: the 7th edition of the AJCC cancer staging manual and the future of TNM.** *Ann Surg Oncol* 2010;17:1471–4 CrossRef Medline
15. van den Brekel MW, Stel HV, Castelijns JA, et al. **Cervical lymph node metastasis: assessment of radiologic criteria.** *Radiology* 1990;177:379–84 CrossRef Medline
16. Nakamura T, Sumi M, Kimura Y, et al. **Whole-neck imaging for the screening of metastatic nodes.** *Jpn Dent Sci Rev* 2010;46:73–77 CrossRef
17. de Veij Mestdagh PD, Jonker MC, Vogel WV, et al. **SPECT/CT-guided lymph drainage mapping for the planning of unilateral elective nodal irradiation in head and neck squamous cell carcinoma.** *Eur Arch Otorhinolaryngol* 2018;275:2135–44 CrossRef Medline
18. van den Brekel MW, Castelijns JA. **What the clinician wants to know: surgical perspective and ultrasound for lymph node imaging of the neck.** *Cancer Imaging* 2005;5(Spec No A):S41–49 CrossRef Medline
19. Shoji S. **Magnetic resonance imaging-transrectal ultrasound fusion image-guided prostate biopsy: current status of the cancer detection and the prospects of tailor-made medicine of the prostate cancer.** *Investig Clin Urol* 2019;60:4–13 CrossRef Medline
20. European Society of Radiology (ESR). **Abdominal applications of ultrasound fusion imaging technique: liver, kidney, and pancreas.** *Insights Imaging* 2019;10:6 CrossRef Medline

Non-EPI versus Multishot EPI DWI in Cholesteatoma Detection: Correlation with Operative Findings

J.C. Benson, M.L. Carlson, and J.I. Lane

ABSTRACT

BACKGROUND AND PURPOSE: Although multishot EPI (readout-segmented EPI) has been touted as a robust DWI sequence for cholesteatoma evaluation, its efficacy in disease detection compared with a non-EPI (eg, HASTE) technique is unknown. This study sought to compare the accuracy of readout-segmented EPI with that of HASTE DWI in cholesteatoma detection.

MATERIALS AND METHODS: A retrospective review was completed of consecutive patients who underwent MR imaging for the evaluation of suspected primary or recurrent/residual cholesteatomas. Included patients had MR imaging examinations that included both HASTE and readout-segmented EPI sequences and confirmed cholesteatomas on a subsequent operation. Two neuroradiologist reviewers assessed all images, with discrepancies resolved by consensus. The ratio of signal intensity between the cerebellum and any observed lesion was noted.

RESULTS: Of 23 included patients, 12 (52.2%) were women (average age, 47.8 [SD, 25.2] years). All patients had surgically confirmed cholesteatomas: Six (26.1%) were primary and 17 (73.9%) were recidivistic. HASTE images correctly identified cholesteatomas in 100.0% of patients. On readout-segmented EPI sequences, 16 (69.6%) were positive, 5 (21.7%) were equivocal, and 2 (8.7%) were falsely negative. Excellent interobserver agreement was noted between reviews on both HASTE ($\kappa = 1.0$) and readout-segmented EPI ($\kappa = 0.9$) sequences. The average signal intensity ratio was significantly higher on HASTE than in readout-segmented EPI, facilitating enhanced detection (mean difference 0.5; 95% CI, 0.3–0.8; $P = .003$).

CONCLUSIONS: HASTE outperforms readout-segmented EPI in the detection of primary cholesteatoma and disease recidivism.

ABBREVIATIONS: MS = multishot; RESOLVE = readout-segmented EPI

Middle ear cholesteatomas are ectopic, keratinizing squamous epithelium, which may be acquired or, much less commonly, congenital.[1,2] Although not considered a true neoplasm, cholesteatomas are locally destructive and have a high propensity for recurrence following surgical removal. As they gradually expand, cholesteatomas erode the osseous structures within and adjacent to the middle ear cavity, including the ossicles, labyrinth, fallopian canal, and middle fossa bone plate.[3] Current mainstay therapy includes microsurgical extirpation, with the chief goal of complete disease removal and prevention of intratemporal and intracranial complications.[4] The most common microsurgical approach for cholesteatoma is an canal wall up tympanomastoidectomy, in which the posterior bony ear canal is left intact and the tympanic membrane is reconstructed.

Depending on the extent of disease at surgery, a planned second-look procedure may be performed approximately 1 year after the initial operation to evaluate residual disease and potentially reconstruct the ossicular chain when indicated. Nevertheless, residual and/or recurrent (ie, recidivism) disease occurs in up to 30% of cases. Imaging is crucial in cholesteatoma management; it aids in the initial diagnosis and may obviate the need for second-look surgery.[5,6]

During the past decade, DWI has emerged as a powerful diagnostic tool for detection of both primary and residual or recurrent cholesteatomas.[7-9] Cholesteatomas demonstrate marked hyperintensity on DWI , likely related to either T2 shinethrough or intralesional restricted diffusion related to keratin debris.[10] Across the years, there have been many iterations of DWI optimization for cholesteatoma identification. The EPI trajectory used by conventional DWI makes such sequences prone to substantial susceptibility artifacts, and single-shot EPI sequences were found to be poor at identifying lesions of <4–5 mm.[11-13] Consequently, non-EPI DWI techniques began to be favored; such algorithms minimize

susceptibility artifacts and geometric distortion related to the skull base and are able to detect lesions as small as 2 mm.[14,15] BLADE (Siemens) and other such PROPELLER sequences are subtypes of non-EPI techniques that minimize susceptibility artifacts and geometric distortions by sampling k-space in a rotating fashion.[16,17]

More recently, HASTE DWI (Siemens) has emerged as a particularly effective sequence, which is relatively insensitive to motion and has been shown in prior studies to detect cholesteatomas with promising accuracy.[18,19] Although traditional EPI techniques have been largely abandoned in the setting of cholesteatoma detection, readout-segmented EPI (RESOLVE; Siemens) DWI is a relatively new technique that has been promoted as a possible alternative diffusion sequence. RESOLVE is a multishot (MS) EPI sequence that is able to reduce geometric distortions at the expense of longer imaging time. Recent reports have indicated that RESOLVE may be a useful sequence in cases of suspected cholesteatoma.[7,20]

Despite its proposed efficacy in cholesteatoma imaging, the diagnostic utility of RESOLVE sequences has yet to be robustly evaluated against non-EPI DWI, the current criterion standard. Thus, this study was conceived with the chief goal of assessing the accuracy of RESOLVE in the detection of cholesteatomas and comparing the ability of RESOLVE with that of HASTE sequences in this context.

MATERIALS AND METHODS
Patient Selection and Electronic Medical Record Review
Institutional review board approval (approval No. 19–008120) was obtained before study commencement. A retrospective review was completed of consecutive patients who underwent high-resolution MR imaging of the temporal bone between September 20, 2011, and March 9, 2020; patients were identified using an institutional electronic medical record search engine. Inclusion criteria encompassed patients who had preoperative MR imaging including dedicated HASTE and RESOLVE sequences for the evaluation of cholesteatoma (both sequences were routinely performed for cholesteatoma work-ups since 2011) and a subsequent operation in which the diagnosis of cholesteatoma was confirmed. Patients were excluded if images were substantially degraded by artifacts (eg, motion) rendering the imaging nondiagnostic.

MR Imaging Protocol
MR imaging was performed on a 1.5T MR imaging scanner (Magnetom Espree; Siemens) using a 32-channel head coil. HASTE (TR/TE = 800/108 ms, flip angle = 180°, section thickness = 2.0 mm, interslice gap = 2.2 mm, matrix = 128 × 90, acquisition time = 4 minutes 17 seconds) and RESOLVE sequences (TR/TE = 3500/76 ms, flip angle = 180°, section thickness = 2.0 mm, interslice gap = 2.6 mm, matrix = 160 × 128, acquisition time = 3 minutes 44 seconds) were performed in all cases per inclusion criteria.

Imaging Analysis
Two board-certified neuroradiologists (J.I.L. and J.C.B.) reviewed all MR imaging examinations. All discrepancies were resolved by consensus. Each sequence was analyzed for the subjective presence or absence of cholesteatoma (presumed on the basis of a

focus of hyperintensity) on both HASTE and RESOLVE sequences. Images were noted as being "positive," "negative," or "equivocal" for the presence of a lesion. Identified lesions were measured in the longest axial dimensions; measurements were used to calculate the presumed ellipse axial area of all cholesteatomas. Average signal intensities of the presumed cholesteatoma and adjacent cerebellar parenchyma were measured to establish a signal intensity ratio for each diffusion sequence.

Statistical Analysis
Means and SDs for continuous variables were calculated in Excel (Microsoft). A paired t test was used to compare both average signal intensity ratios and measured lesion size on HASTE and RESOLVE. Interobserver agreement was calculated using a Cohen κ statistical test. Statistical analyses were performed with the SAS-based statistical software package (JMP 13.0; SAS Institute). The threshold for significance was set at $P < .05$.

RESULTS
Patient Characteristics
Twenty-five patients met the inclusion criteria, of whom 2 were excluded (one because the incorrect MR imaging protocol was used and one because DWI did not include the entire temporal bone). Hence, the final cohort comprised 23 patients; 12/23 (52.2%) were women, and the average age was 47.8 [SD, 25.2] years. Six patients (26.1%) were diagnosed with a primary cholesteatoma; the remainder (73.9%) represented disease recidivism diagnosed on follow-up MR imaging after prior cholesteatoma resection. Of the patients who had previously undergone surgical resection, the average time interval between the initial surgery and the second-look MR imaging was 104.6 [SD, 162.9] months (median, 60.5 months). For all patients, the average time between MR imaging and surgical confirmation of cholesteatoma was 1.6 [SD, 2.4] months.

Imaging Analysis
Every patient in the cohort had cholesteatoma confirmed at surgery. All (100.0%) lesions were detected on preoperative HASTE imaging. On RESOLVE sequences, 16 (69.6%) were positive (Fig 1), 5 (21.8%) were equivocal (Fig 2), and 2 (8.7%) were falsely negative (Fig 3). Excellent interobserver agreement was noted between reviews of both HASTE ($\kappa = 1.0$) and RESOLVE ($\kappa = 0.9$) sequences. The sole disagreement was regarding a RESOLVE sequence in which the 2 reviewers regarded the examination as either equivocal or negative.

The average axial area of cholesteatoma on HASTE images was 3.7 [SD, 4.2] cm^2 measured in the maximum diameter (range = 0.5–15.6 cm^2); the average size on RESOLVE images was 2.9 [SD, 3.8] cm^2 (range, 0.4–15.6 cm^2). The measured size on HASTE images was significantly larger than that measured on RESOLVE images (mean difference, 1.0 cm^2; 95% CI, 0.6–1.5 cm^2; $P < .001$). Both of the lesions not identified on RESOLVE images were among the smallest cholesteatomas in the cohort, each measuring 0.6 cm^2. Two other similarly sized lesions (0.5 and 0.6 cm^2) were each regarded as "equivocal" on RESOLVE images. Lesions <1.0 cm^2 measured on HASTE were more likely
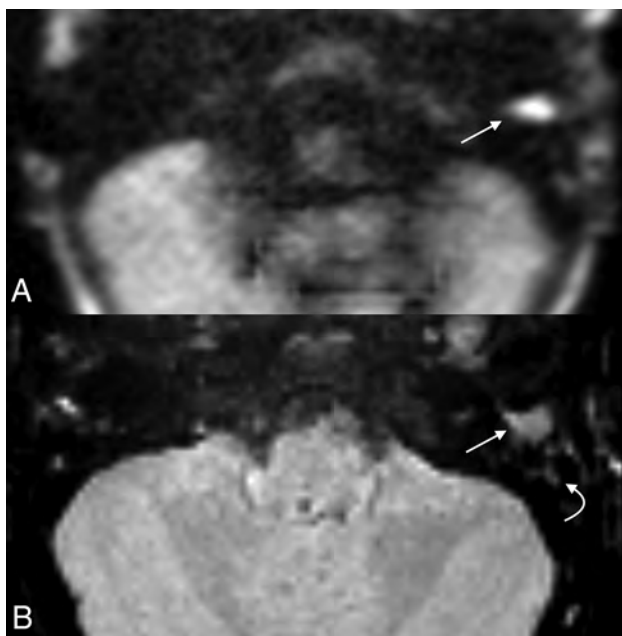
FIG 1. Cholesteatoma with positive findings on both HASTE and RESOLVE in a 4-year-old girl with delayed speech. Both axial HASTE (*A*) and RESOLVE (*B*) demonstrate a region of restricted diffusion in the left external auditory canal (*arrow*). Note greater signal hyperintensity of HASTE compared with the RESOLVE image. Adjacent opacified mastoid air cells demonstrate relatively faint signal (*curved arrow*).

to be equivocal or falsely negative on RESOLVE than those of ≥ 1.0 cm^2 ($P = .02$).

The average ratio between cholesteatoma and cerebellar signal intensities was 1.8 [SD, 0.8] on HASTE and 1.3 [SD, 0.7] on RESOLVE. The average signal intensity ratio was significantly higher on HASTE than on RESOLVE (mean difference, 0.5; 95% CI, 0.3–0.8; $P = .003$).

DISCUSSION

The results of this study indicate that HASTE outperforms RESOLVE in the detection of primary and recidivistic cholesteatoma. HASTE imaging correctly identified lesions in all cases, while RESOLVE results were equivocal in more than one-fifth of cases and falsely negative in 2 patients. These findings have immediate implications in terms of how MR cholesteatoma imaging is approached. Specifically, the results indicated that RESOLVE images are more likely to be equivocal or falsely negative in cases of surgically confirmed cholesteatomas, particularly in the case of small lesions.

The most likely contributor to the superior performance of HASTE imaging is the greater relative intensity of lesions compared with the adjacent cerebellar parenchyma. Cholesteatomas were both subjectively positive and objectively brighter on the HASTE sequence. This observed appearance is similar to that described by Dhepnorrarat et al,[21] in which cholesteatomas were distinctly apparent, even in the setting of postoperative changes with adjacent scar tissue. Cholesteatomas on RESOLVE images, conversely, frequently had signal more similar to that of the adjacent parenchyma, thereby accounting for the equivocal results
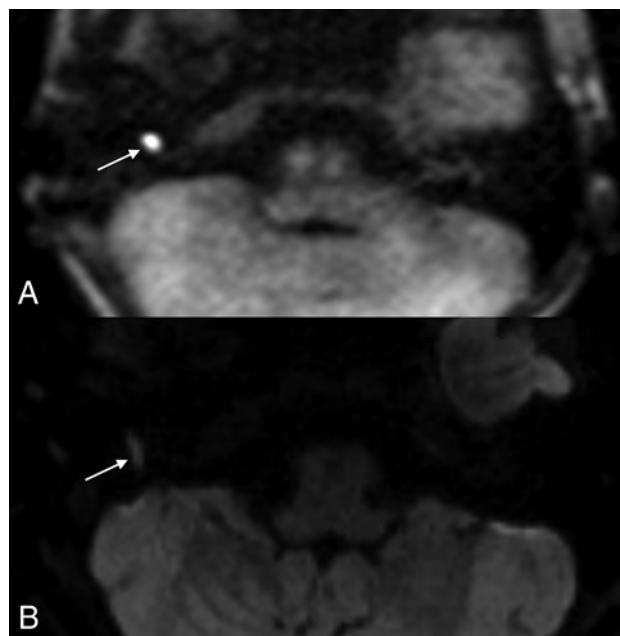
FIG 2. Example of a cholesteatoma seen on HASTE imaging with equivocal findings on RESOLVE. The patient is a 13-year-old boy with a history of bilateral cholesteatomas status post multiple prior surgeries who presented with recurrent hearing loss in his right ear. Axial HASTE (*A*) image clearly depicts a 0.6-cm focus of restricted diffusion in the right hypotympanum (*arrow*). Although faint signal is seen in this region on corresponding axial RESOLVE (*B*) image (*arrow*), the intralesional signal is insufficiently intense to warrant a certain diagnosis.
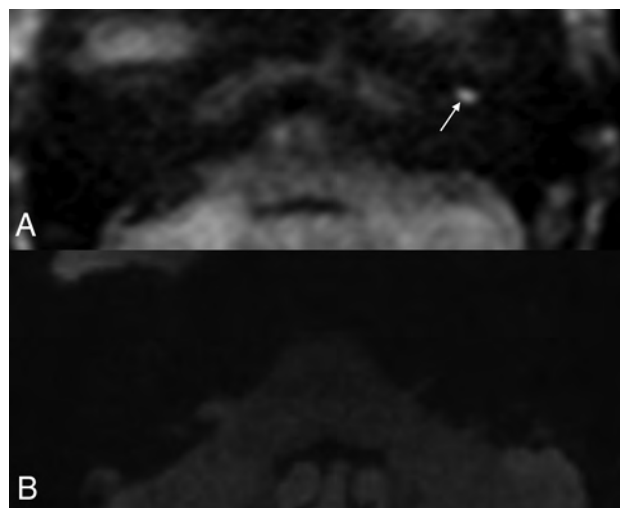
FIG 3. Cholesteatoma visible on HASTE but not on RESOLVE in a 69-year-old woman who had undergone a left tympanomastoidectomy approximately 15 months prior for resection of a cholesteatoma. MR imaging was performed to assess residual or recurrent disease. Axial (*A*) HASTE image demonstrates a well-demarcated 0.6-cm focus of restricted diffusion in the left anterior mesotympanum (*arrow*). No abnormal signal was seen on corresponding RESOLVE image (*B*).

garnered from RESOLVE images. Size, too, appeared to be an important factor: Smaller lesions were more likely to be missed or called equivocal on RESOLVE sequences, and the axial dimensions of lesions were greater when measured on HASTE

compared with RESOLVE. Because many studies have demonstrated a size threshold of about 2 mm for adequate detection, this would favor HASTE over RESOLVE to improve cholesteatoma detection.

The results of this study are in agreement with prior analyses that have found non-EPI (eg, HASTE) sequences to be both sensitive and specific for cholesteatoma detection.[10,22] A systematic review by Jindal et al[23] found the sensitivity, specificity, and positive predictive value of non-EPI DWI to be 91%, 96%, and 97%, respectively. Among postoperative patients, Bakaj et al[24] found that non-EPI DWI had a 100% sensitivity after a canal wall down mastoidectomy. Nevertheless, false-positives have been reported, related to abscess, wax/debris, and encephaloceles.[25] False-negatives, too, occur, particularly in small (<3–5 mm) lesions.[26-28] Horn et al,[27] for example, concluded that non-EPI DWI does not eliminate the need for second-look surgery due to the rate of false-negative examinations. Because the cohort of the current study was made up exclusively of patients with known cholesteatomas, the results should be specifically interpreted as being related to the superiority of HASTE over RESOLVE; any comments regarding the false-negative rate or negative predictive value of either sequence are beyond the scope of this study.

MS EPI sequences such as RESOLVE, conversely, have not been extensively investigated in cholesteatoma imaging. A study by Yamashita et al[20] found the sensitivity (76.7%) and accuracy (87.9%) of MS EPI superior to that of single-shot EPI; the specificity of both was 100%. Henninger and Kremser[7] reported, in 2017, that MS EPI sequences were subjectively reliable for cholesteatoma imaging but did not provide supportive quantitative data. The only prior study that directly compared MS EPI with non-EPI DWI was by Dudau et al.[11] Although the authors found good ($\kappa = 0.75$) agreement between the techniques, non-EPI was better able to predict the presence of cholesteatoma in cases of disagreement. Nevertheless, the authors concluded that MS EPI could be used in conjunction with non-EPI for cholesteatoma detection. The results of the current study, in contrast, indicate that RESOLVE sequences are prone to false-negative or equivocal results in the setting of surgically confirmed cholesteatomas.

Nevertheless, MR cholesteatoma imaging remains a dynamic field. Recently, an optimized BLADE DWI sequence using 2D turbo gradient- and spin-echo imaging was shown to significantly reduce distortion, blurring, and magnetic-sensitive artifacts.[29] A subsequent study demonstrated that turbo gradient- and spin-echo BLADE had fewer ghosting artifacts and higher image quality than REOSLVE and was superior to RESOLVE in identifying particularly small cholesteatomas.[30] To date, however, no studies have sought to compare turbo gradient- and spin-echo imaging with HASTE sequences. Such a comparison could be the focus of future research studies and is a poignant example of the still-evolving landscape of MR imaging used for cholesteatoma detection.

Finally, the effect of MR imaging field strength on cholesteatoma imaging deserves mention. Although the superior signal-to-noise ratio of a 3T scanner could theoretically provide better detection of smaller lesions, the lower field strength of a 1.5T scanner is less susceptible to magnetic field inhomogeneities that often arise near the temporal bone. A recent study by Lips et al[6] found that non-EPI DWI had superior sensitivity and specificity for cholesteatoma detection if imaged on a 1.5T scanner rather than 3T. These results stood in contrast to a prior report by Lincot et al[31] in which the authors found near-equal diagnostic capabilities on 3T and 1.5T scanners. Like most prior studies, the current study was performed using a 1.5T scanner. However, this issue may be of further interest to future investigations.

This study has limitations shared by all retrospective analyses. In addition, the number of included patients is relatively small ($n = 23$). Also, because both imaging sequences were completed as part of the same examination, the neuroradiologists reviewing the cases were not blinded to the results of other corresponding images. Both reviewers were also aware that the cohort consisted of only patients with surgically confirmed cholesteatomas, thereby potentially introducing bias to the results. Similarly, because all patients in the cohort had surgery-proved primary or recurrent/residual cholesteatomas and the decision to operate was influenced by the results of the second-look MR imaging, it is possible that a selection bias influenced the results. Furthermore, the lack of patients without cholesteatoma prevents calculation of test specificity and negative predictive value. Finally, both DWI sequences used in this study were vendor-specific, which may reduce the applicability of the results of this study to the capabilities of all non-EPI and MS EPI DWI techniques.

CONCLUSIONS

HASTE is superior to RESOLVE in the detection of both primary and residual/recurrent cholesteatomas. The discrepancy between sequences may be related to the greater relative intralesional signal intensity and size on HASTE images. Because cholesteatomas appear smaller and less hyperintense on RESOLVE images, such sequences are more likely to provide equivocal and sometimes falsely negative results.

REFERENCES

1. Gilberto N, Custódio S, Colaço T, et al. **Middle ear congenital cholesteatoma: systematic review, meta-analysis and insights on its pathogenesis.** *Eur Arch Otorhinolaryngol Head Neck Dis* 2020;277:987–98 CrossRef Medline
2. Nevoux J, Lenoir M, Roger G, et al. **Childhood cholesteatoma.** *Eur Ann Otorhinolaryngol Head Neck Dis* 2010;127:143–50 CrossRef Medline
3. Olszewska E, Wagner M, Bernal-Sprekelsen M, et al. **Etiopathogenesis of cholesteatoma.** *Eur Arch Otorhinolaryngo l*2004;261:6–24 CrossRef Medline
4. Hu Y, Teh BM, Hurtado G, et al. **Can endoscopic ear surgery replace microscopic surgery in the treatment of acquired cholesteatoma? A contemporary review.** *Int J Pediatr Otorhinolaryngol* 2020;131:109872 CrossRef Medline
5. Choi DL, Gupta MK, Rebello R, et al. **Cost-comparison analysis of diffusion weighted magnetic resonance imaging (DWMRI) versus second look surgery for the detection of residual and recurrent cholesteatoma.** *J Otolaryngol Head Neck Surg* 2019;48:58 CrossRef Medline
6. Lips LM, Nelemans PJ, Theunissen FM, et al. **The diagnostic accuracy of 1.5 T versus 3 T non-echo-planar diffusion-weighted imaging in the detection of residual or recurrent cholesteatoma in the**

middle ear and mastoid. *J Neuroradiol* 2020;47:433–40 CrossRef Medline

7. Henninger B, Kremser C. **Diffusion weighted imaging for the detection and evaluation of cholesteatoma.** *World J Radiol* 2017;9:217–22 CrossRef Medline

8. Ide S, Ganaha A, Tono T, et al. **Value of DW-MRI in the preoperative evaluation of congenital cholesteatoma.** *Int J Pediatr Otorhinolaryngol* 2019;124:34–38 CrossRef Medline

9. Kavanagh RG, Liddy S, Carroll AG, et al. **Rapid diffusion-weighted MRI for the investigation of recurrent temporal bone cholesteatoma.** *Neuroradiol J* 2020;33:210–15 CrossRef Medline

10. van Egmond SL, Stegeman I, Grolman W, et al. **A systematic review of non-echo planar diffusion-weighted magnetic resonance imaging for detection of primary and postoperative cholesteatoma.** *Otolaryngol Head Neck Surg* 2016;154:233–40 CrossRef Medline

11. Dudau C, Draper A, Gkagkanasiou M, et al. **Cholesteatoma: multishot echo-planar vs non echo-planar diffusion-weighted MRI for the prediction of middle ear and mastoid cholesteatoma.** *BJR Open* 2019;1:20180015 CrossRef Medline

12. Vercruysse JP, De Foer B, Pouillon M, et al. **The value of diffusion-weighted MR imaging in the diagnosis of primary acquired and residual cholesteatoma: a surgical verified study of 100 patients.** *Eur Radiol* 2006;16:1461–67 CrossRef Medline

13. Lingam RK, Connor SE, Casselman JW, et al. **MRI in otology: applications in cholesteatoma and Ménière's disease.** *Clin Radiol* 2018;73:35–44 CrossRef Medline

14. Aarts MCJ Rovers MM, van der Veen EL, et al. **The diagnostic value of diffusion-weighted magnetic resonance imaging in detecting a residual cholesteatoma.** *Otolaryngol Head Neck Surg* 2010;143:12–16 CrossRef Medline

15. Cavaliere M, Di Lullo AM, Cantone E, et al. **Cholesteatoma vs granulation tissue: a differential diagnosis by DWI-MRI apparent diffusion coefficient.** *Eur Arch Otorhinolaryngol* 2018;275:2237–43 CrossRef Medline

16. McJunkin J, Chole R. **Clinical utility of MRI for cholesteatoma recurrence.** *Curr Surg Rep* 2014;2:63 CrossRef

17. Kim TH, Baek MY, Park JE, et al. **Comparison of DWI methods in the pediatric brain: PROPELLER turbo spin-echo imaging versus readout-segmented echo-planar imaging versus single-shot echo-planar imaging.** *AJR Am J Roentgenol* 2018;210:1352–58 CrossRef Medline

18. Más-Estellés F, Mateos-Fernández M, Carrascosa-Bisquert B, et al. **Contemporary non–echo-planar diffusion-weighted imaging of middle ear cholesteatomas.** *Radiographics* 2012;32:1197–13 CrossRef Medline

19. Schwartz KM, Lane JI, Bolster BD, et al. **The utility of diffusion-weighted imaging for cholesteatoma evaluation.** *AJNR Am J Neuroradiol* 2011;32:430–36 CrossRef Medline

20. Yamashita K, Yoshiura T, Hiwatashi A, et al. **Detection of middle ear cholesteatoma by diffusion-weighted MR imaging: multishot echo-planar imaging compared with single-shot echo-planar imaging.** *AJNR Am J Neuroradiol* 2011;32:1915–18 CrossRef Medline

21. Dhepnorrarat RC, Wood B, Rajan GP. **Postoperative non-echo-planar diffusion-weighted magnetic resonance imaging changes after cholesteatoma surgery: implications for cholesteatoma screening.** *Otol Neurotol* 2009;30:54–58 CrossRef Medline

22. Romano A, Covelli E, Confaloni V, et al. **Role of non-echo-planar diffusion-weighted images in the identification of recurrent cholesteatoma of the temporal bone.** *Radiol Med* 2020;125:75–79 CrossRef Medline

23. Jindal M, Riskalla A, Jiang D, et al. **A systematic review of diffusion-weighted magnetic resonance imaging in the assessment of postoperative cholesteatoma.** *Otol Neurotol* 2011;32:1243–49 CrossRef Medline

24. Bakaj T, Zbrozkova LB, Salzman R, et al. **Recidivous cholesteatoma: DWI MR after canal wall up and canal wall down mastoidectomy.** *Bratisl Lek Listy* 2016;117:515–20 CrossRef Medline

25. Muhonen EG, Mahboubi H, Moshtaghi O, et al. **False-positive cholesteatomas on non-echoplanar diffusion-weighted magnetic resonance imaging.** *Otol Neurotol* 2020;41:e588–92 CrossRef Medline

26. Geoffray A, Guesmi M, Nebbia JF, et al. **MRI for the diagnosis of recurrent middle ear cholesteatoma in children: can we optimize the technique? Preliminary study.** *Pediatr Radiol* 2013;43:464–73 CrossRef Medline

27. Horn RJ, Gratama JW, van der Zaag-Loonen HJ, et al. **Negative predictive value of non-echo-planar diffusion weighted MR imaging for the detection of residual cholesteatoma done at 9 months after primary surgery is not high enough to omit second look surgery.** *Otol Neurotol* 2019;40:911–19 CrossRef Medline

28. Velthuis S, van Everdingen KJ, Quak JJ, et al. **The value of non echo planar, diffusion-weighted magnetic resonance imaging for the detection of residual or recurrent middle-ear cholesteatoma.** *J Laryngol Otol* 2014;128:599–603 CrossRef Medline

29. Hu HH, McAllister AS, Jin N, et al. **Comparison of 2D BLADE turbo gradient- and spin-echo and 2D spin-echo echo-planar diffusion-weighted brain MRI at 3T: preliminary experience in children.** *Acad Radiol* 2019;26:1597–1604 CrossRef Medline

30. Sheng Y, Hong R, Sha Y, et al. **Performance of TGSE BLADE DWI compared with RESOLVE DWI in the diagnosis of cholesteatoma.** *BMC Med Imaging* 2020;20:40 CrossRef Medline

31. Lincot J, Veillon F, Riehm S, et al. **Middle ear cholesteatoma: compared diagnostic performances of two incremental MRI protocols including non-echo planar diffusion-weighted imaging acquired on 3T and 1.5T scanners.** *J Neuroradiol* 2015;42:193–201 CrossRef Medline

3D Cranial Nerve Imaging, a Novel MR Neurography Technique Using Black-Blood STIR TSE with a Pseudo Steady-State Sweep and Motion-Sensitized Driven Equilibrium Pulse for the Visualization of the Extraforaminal Cranial Nerve Branches

F. Van der Cruyssen, T.-M. Croonenborghs, R. Hermans, R. Jacobs, and J. Casselman

ABSTRACT

SUMMARY: This study investigated the feasibility of a 3D black-blood STIR TSE sequence with a pseudo steady-state sweep and motion-sensitized driven equilibrium pulse for extraforaminal cranial nerve imaging on a 3T system. Assessments of healthy volunteers showed near-perfect agreement in nerve visualization with excellent to good visualization of the extraforaminal trigeminal, greater occipital, and facial nerves. Suppression of surrounding tissues was excellent to good. 3D cranial nerve imaging can produce nerve selective imaging of extraforaminal cranial and spinal nerve branches.

ABBREVIATIONS: 3D CRANI = 3D cranial nerve imaging; PSS = pseudo steady-state; MDSE = motion-sensitized driven equilibrium

Being the largest cranial nerve, the trigeminal nerve—more specifically, its inferior alveolar and lingual branches—is frequently damaged during dental, oral, and maxillofacial surgical procedures.[1] Moreover, it can be subject to myriad disease entities such as inflammatory, infectious, neoplastic, and congenital pathology. MR imaging has been widely applied to the visualization of cranial nerves.[2] Intracranial trajectories such as nuclear and supranuclear, as well as cisternal segments, can be well depicted on routine MR imaging sequences. The cisternal segment is typically visualized using constructive interference in steady state and 3D heavily T2WI.[3] However, visualization of the extracranial peripheral branches on 3D T2WI remains a challenge because of their small diameters, tortuous courses, movement and susceptibility artifacts, and the presence of blood vessels in close proximity, which can all confound nerve visualization.[4] B1 and B0 inhomogeneities further lead to poor fat suppression and low SNR, and the use of multiple echoes

to improve water and fat separation increases acquisition times considerably, making patient compliance difficult. To address these problems, we developed a novel black-blood 3D STIR TSE sequence for extraforaminal cranial nerve imaging (3D CRANI) on a 3T system and here describe its assessment.

Description of Technique

The 3D CRANI is a 3D TSE STIR black-blood sequence that uses a pseudo steady-state (PSS) sweep in combination with a motion-sensitized driven equilibrium (MDSE) pulse. We used STIR in combination with MSDE to ensure that signals from fat, muscle, and blood are suppressed uniformly across the field of view. The PSS sweep is designed such that the signal is smoothly varying during a long TSE shot to keep the signal strength approximately constant. This means that the flip angle sweep is not calculated based on specific tissue parameters (T1, T2). In this manner, it helps us to reduce the T2 decay for a range of tissues, which makes the sequence less sensitive to tissue dependencies. For the PSS functionality, minimum, middle, and maximum angles need to be defined, and 4 intermediate flip angles are used to asymptotically approach the minimum flip angle defined within the sequence (Online Supplemental Data). After reaching the minimum angle, nonlinear interpolation is used to calculate an optimum sweep according to the PSS principle while trying to keep the signal constant.[5] The middle angle is defined at the specified effective TE. After definition of the middle angle, the refocusing angles are increased linearly to the maximum defined angle.

Finally, compressed sensing is added to reduce the acquisition time. The sequence was optimized by comparing it with existing nerve-selective sequences until satisfactory and robust results were obtained, with particular attention being paid to artifact reduction (Online Supplemental Data).

MR Imaging Procedure

After optimization, 6 healthy volunteers (3 women and 3 men; average age, 32 years; range, 23–48 years) were included in this study. Imaging was performed on a 3T MR imaging system (Ingenia; Philips Healthcare) equipped with a 32-channel head coil (Invivo) without the use of any contrast agent. After acquisition of standard T1WI, T2WI, and gradient-echo sequences, the CRANI sequence was acquired using the following parameters: TR = 2300 ms, TE = 150 ms, FOV = $200 \times 200 \times 100$ mm, section thickness = 0.5 mm, act section gap = -0.45 mm, matrix = 224×222, acquired voxel size = $0.9 \times 0.9 \times 0.9$ mm, reconstructed voxel size = $0.5 \times 0.5 \times 0.45$ mm, section oversampling = 1.5, compressed sense reduction = 5, and number of slices = 200. TSE nerve STIR included TSE factor = 45 (startup echoes 2), number of acquisitions = 1, black-blood pulse = MSDE (mode: nerve), and acquisition time = 5:17 min.

Imaging Analysis

Three orthogonal planes, as well as a plane following the course of the nerve trajectory using MPR and MIP, were reconstructed using the Volume postprocessing package (Philips Healthcare). MIP images with a thickness of 5 mm and gap of -0.5 mm (4.5-mm overlap) allowed for the best demonstration of the selected nerve trajectory. The images were analyzed by 2 fixed and independent observers with expertise in cranial nerve imaging. First, a training session was held to familiarize the observers with the grading scales. Then, for the subsequent evaluations, the observers were blinded to each other's scoring. Arterial, venous, and fat suppression were graded on a 3-point Likert scale (0 = unsuppressed and nondiagnostic; 1 = moderately suppressed but diagnostic; 2 = excellent suppression). A nerve scoring system using a 5-point Likert scale (4 = excellent; 3 = good; 2 = fair; 1 = poor; 0 = none) was adopted from Fujii et al[6] to evaluate the signal continuity of the following nerves over a predetermined trajectory. The evaluated trajectory of the inferior alveolar (V3) and lingual (V3) nerves starts at the oval foramen and stops at the mental foramen and the submandibular duct, respectively. The facial nerve (VII) trajectory starts in the labyrinthine portion in the temporal bone and stops at the anterior edge of the parotid. The greater occipital nerve (C2–C3) trajectory starts posterior to the axis and stops before piercing the trapezius muscle.[6]

Weighted kappa scores, confidence intervals, and *P* values for the interobserver agreement for the observed variables

Parameter	Weighted Kappa Score	95% Confidence Interval	*P* Value
Arterial suppression	1	1–1	.014
Venous suppression	1	1–1	.014
Fat suppression	1	1–1	.014
Overall nerve visualization	1	1–1	.014
Inferior alveolar nerve	1	1–1	.014
Lingual nerve	1	1–1	.014
Facial nerve	0.933	0.79–1.10	.020
Greater occipital nerve	1	1–1	.014
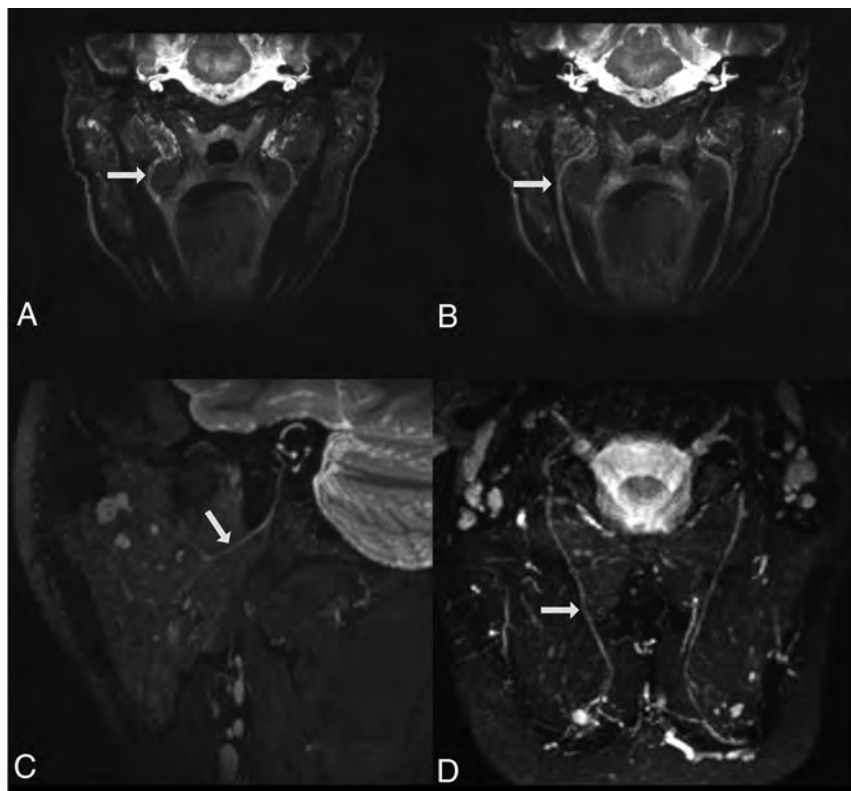
FIGURE. The evaluated cranial and spinal nerve branches acquired using the 3D CRANI sequence. *A*, Lingual nerve (*arrow*) on MIP after MPR. *B*, Inferior alveolar nerve (*arrow*) after MIP MPR on a coronal oblique reconstruction. *C*, Extraforaminal facial nerve (*arrow*) after sagittal oblique MIP MPR, illustrating the intraparotid nerve course. *D*, Greater occipital nerve (*arrow*) extending between the semispinalis muscles on MIP MPR.

Statistical Analysis

All statistical analyses were performed using SPSS version 26.0 (IBM). Interobserver agreement on the Likert scales was tested using weighted kappa statistics with quadratic weights. A *P* value less than .05 was considered statistically significant.

RESULTS

There was a statistically significant near-perfect agreement between the 2 observers, except in the visualization of the extracranial portion of the facial nerve, for which the agreement was still

considered to be very good (independent observer scores are illustrated in the Online Supplemental Data). The strength of agreement ranged from very good to excellent for all parameters (Table). Venous suppression was evaluated as excellent except in 2 cases in which it was considered "moderately suppressed." These 2 cases also had the lowest scores for the other variables observed. When the independent nerve scoring results were evaluated, the facial nerve had the lowest scores. The visualizations of the trigeminal and greater occipital nerve branches were rated as good to excellent. The Figure illustrates the nerve-selective sequence with examples of the evaluated structures.

DISCUSSION

This technical note successfully demonstrates the use of 3D CRANI, a modified black-blood STIR TSE sequence for nerve-selective imaging of peripheral cranial and spinal nerve branches. Diffusion-weighted prepulsing by MSDE for MR neurography purposes was first described by Yoneyama et al[7] and further demonstrated for brachial plexus imaging by Klupp et al.[8] This study is innovative in the sense that an MSDE pulse was applied in combination with a PSS sweep to further optimize nerve-enhanced imaging within clinically feasible acquisition times. The results from our study indicate excellent interobserver agreement. Moreover, the scoring of the images indicates moderate to excellent suppression of surrounding tissues. Chhabra et al[9,10] published several papers on cranial nerve imaging and advocate several sequences for clinical evaluations, including a STIR TSE sequence when magnetic field inhomogeneities are expected.[11,12] However, their main imaging method for MR neurography involves diffusion-weighted reversed fast imaging with steady-state free precession, which is applied using gradient-echo imaging. In the past, gradient-echo imaging was preferred because of its short acquisition times. However, with new techniques such as those illustrated in this study, STIR sequences with reasonable acquisition times, low artifact susceptibility, and excellent fat suppression have become possible. The current limitations appear to be similar signal intensities for nerve and (intraparotid) lymphoid tissue, unpredictable visualization of nerves with a diameter less than 0.9 mm, and imperfect venous suppression of the pterygoid plexus. A future large prospective study will be designed to validate this sequence in both healthy and patient populations, comparing 3D CRANI with existing protocols.

CONCLUSIONS

3D CRANI can produce nerve-selective imaging of the trigeminal, facial, and greater occipital extraforaminal nerve branches, with excellent interobserver agreement and within clinically feasible acquisition times. Prospective studies are needed to further evaluate and validate its clinical use.

REFERENCES

1. Renton T, Van der Cruyssen F. **Diagnosis, pathophysiology, management and future issues of trigeminal surgical nerve injuries.** *Oral Surg* 2019;13:389–403 CrossRef

2. Romano N, Federici M, Castaldi A. **Imaging of cranial nerves: a pictorial overview.** *Insights Imaging* 2019;10:33 CrossRef Medline

3. Casselman J, Mermuys K, Delanote J, et al. **MRI of the cranial nerves—more than meets the eye: technical considerations and advanced anatomy.** *Neuroimaging Clin N Am* 2008;18:197–231 CrossRef Medline

4. Chhabra A, Madhuranthakam AJ, Andreisek G. **Magnetic resonance neurography: current perspectives and literature review.** *Eur Radiol* 2018;28:698–707 CrossRef Medline

5. Busse RF, Brau ACS, Vu A, et al. **Effects of refocusing flip angle modulation and view ordering in 3D fast spin echo.** *Magn Reson Med* 2008;60:640–49 CrossRef Medline

6. Fujii H, Fujita A, Yang A, et al. **Visualization of the peripheral branches of the mandibular division of the trigeminal nerve on 3D double-echo steady-state with water excitation sequence.** *AJNR Am J Neuroradiol* 2015;36:1333–37 CrossRef Medline

7. Yoneyama M, Takahara T, Kwee TC, et al. **Rapid high resolution MR neurography with a diffusion-weighted pre-pulse.** *Magn Reson Med Sci* 2013;12:111–19 CrossRef Medline

8. Klupp E, Cervantes B, Sollmann N, et al. **Improved brachial plexus visualization using an adiabatic iMSDE-prepared STIR 3D TSE.** *Clin Neuroradiol* 2019;29:631–38 CrossRef Medline

9. Chhabra A, Andreisek G, Soldatos T, et al. **MR neurography: past, present, and future.** *AJR Am J Roentgenol* 2011;197:583–91 CrossRef Medline

10. Chhabra A, Padua A Jr, Flammang A, et al. **Magnetic resonance neurography—techniques and interpretation.** *Magnetom Flash-Clin Neurol* 2012;2:4–8

11. Zuniga JR, Mistry C, Tikhonov I, et al. **Magnetic resonance neurography of traumatic and nontraumatic peripheral trigeminal neuropathies.** *J Oral Maxillofac Surg* 2018;76:725–36 CrossRef Medline

12. Cox B, Zuniga JR, Panchal N, et al. **Magnetic resonance neurography in the management of peripheral trigeminal neuropathy: experience in a tertiary care centre.** *Eur Radiol* 2016;26:3392–400 CrossRef Medline

Impact of Prematurity on the Tissue Properties of the Neonatal Brain Stem: A Quantitative MR Approach

V. Schmidbauer, G. Dovjak, G. Geisl, M. Weber, M.C. Diogo, M.S. Yildirim, K. Goeral, K. Klebermass-Schrehof, A. Berger, D. Prayer, and G. Kasprian

ABSTRACT

BACKGROUND AND PURPOSE: Preterm birth interferes with regular brain development. The aim of this study was to investigate the impact of prematurity on the physical tissue properties of the neonatal brain stem using a quantitative MR imaging approach.

MATERIALS AND METHODS: A total of 55 neonates (extremely preterm [$n = 30$]: $<28 + 0$ weeks gestational age; preterm [$n = 10$]: $28 + 0$–$36 + 6$ weeks gestational age; term [$n = 15$]: $\geq37 + 0$ weeks gestational age) were included in this retrospective study. In most cases, imaging was performed at approximately term-equivalent age using a standard MR protocol. MR data postprocessing software SyMRI was used to perform multidynamic multiecho sequence (acquisition time: 5 minutes, 24 seconds)–based MR postprocessing to determine T1 relaxation time, T2 relaxation time, and proton density. Mixed-model ANCOVA (covariate: gestational age at MR imaging) and the post hoc Bonferroni test were used to compare the groups.

RESULTS: There were significant differences between premature and term infants for T1 relaxation time (midbrain: $P < .001$; pons: $P < .001$; basis pontis: $P = .005$; tegmentum pontis: $P < .001$; medulla oblongata: $P < .001$), T2 relaxation time (midbrain: $P < .001$; tegmentum pontis: $P < .001$), and proton density (tegmentum pontis: $P = .004$). The post hoc Bonferroni test revealed that T1 relaxation time/T2 relaxation time in the midbrain differed significantly between extremely preterm and preterm (T1 relaxation time: $P < .001$/T2 relaxation time: $P = .02$), extremely preterm and term (T1 relaxation time/T2 relaxation time: $P < .001$), and preterm and term infants (T1 relaxation time: $P < .001$/T2 relaxation time: $P = .006$).

CONCLUSIONS: Quantitative MR parameters allow preterm and term neonates to be differentiated. T1 and T2 relaxation time metrics of the midbrain allow differentiation between the different stages of prematurity. SyMRI allows for a quantitative assessment of incomplete brain maturation by providing tissue-specific properties while not exceeding a clinically acceptable imaging time.

ABBREVIATIONS: GA = gestational age; PD = proton density; T1R = T1 relaxation time; T2R = T2 relaxation time; MDME = multidynamic multiecho; ICC = intraclass correlation coefficient

The myelination process begins in the fetal period and proceeds in a stepwise manner.[1,2] Brain maturation progresses caudally to rostrally following a characteristic pattern.[3] Hence, histologically, the maximum myelin deposition is detectable in the spinal cord and the brain stem at the time of birth.[1,3]

Based on the biochecture of the myelin sheath, neonatal brain development can be evaluated by MR imaging.[4,5] Thus,

myelination visualized on conventional T1-weighted and T2-weighted MR contrasts serves as an imaging biomarker for the assessment of brain maturation in neonates.[6]

Prematurity is associated with delayed myelination, which is considered a risk factor for impaired neurologic and cognitive development.[7,8] Furthermore, there is a correlation between gestational age (GA) at birth and developmental outcome, with lower GA associated with a higher risk for more severe cognitive impairment.[9,10] Therefore, the assessment of myelination is paramount, primarily in preterm born neonates, to predict potential mental and neurologic impairment. Despite being a highly sensitive tool for the detection of subtle cerebral pathologies in premature infants, the evaluation of myelination by brain MR imaging in this group of patients remains challenging in pediatric neuroimaging.[11-13]

Quantitative MR techniques enable the characterization of cerebral development and brain maturation based on tissue-specific relaxation parameters and proton density (PD).[14-16]

Table 1: Clinical characteristics and demographics

	Neonates: $n = 55$		
	Extremely Preterm Birth (<28 + 0 weeks GA): $n = 30$	Preterm Birth (28 + 0–36 + 6 weeks GA): $n = 10$	Term Born (≥37 + 0 weeks GA): $n = 15$
Clinical characteristics			
Male/female	10/20	5/5	6/9
GA at birth[a]	M = 25 + 5, SD = 1 + 4; R = 23 + 0–27 + 6	M = 32 + 4, SD = 3 + 1; R = 28 + 0–36 + 3	M = 39 + 5, SD = 0 + 6; R = 37 + 6–40 + 5
GA at MR imaging[a]	M = 38 + 2, SD = 2 + 0; R = 35 + 1–43 + 4	M = 39 + 0, SD = 6 + 1; R = 33 + 4–54 + 5	M = 41 + 5, SD = 2 + 1; R = 39 + 0–45 + 3
Clinical diagnosis			
Without pathologic findings[b]	$n = 15$	$n = 4$	$n = 5$
Hemorrhage[b,c]	$n = 10$[d]	$n = 3$[e]	$n = 3$[f]
Cystic PVL[b]	$n = 2$		
Expired infarction[b]	$n = 1$	$n = 1$	$n = 1$
Blake pouch[b]	$n = 1$		
Venous vessel malformation[b]	$n = 1$	$n = 1$	
Intraventricular arachnoid cyst[b]		$n = 1$	
HIE[b]			$n = 4$
Cephalohematoma[b]			$n = 1$
Hygroma[b]			$n = 1$

Note:—HIE indicates hypoxic-ischemic encephalopathy; PVL, periventricular leukomalacia.
[a] Data represented as mean (M), standard deviation (SD), and range (R).
[b] Data represented as total number.
[c] Including hyperacute, acute, subacute, and chronic intraventricular, cortical, subcortical, parenchymal, subarachnoid, and subdural hemorrhage.
[d] Grade III/IV intracranial hemorrhage (according to Deeg et al[43]) in 1 of 10.
[e] Grade III/IV intracranial hemorrhage (according to Deeg et al[43]) in 2 of 3.
[f] Grade III/IV intracranial hemorrhage (according to Deeg et al[43]) in 1 of 3.

Quantitative T1 and T2 mapping have proved beneficial when assessing neonatal brain myelination qualitatively.[6,17] However, quantitative MR data acquisition is a highly time-consuming process, even with modern methods and therefore is not applicable in the clinical routine.[15,17]

By acquiring a single multidynamic multiecho (MDME) sequence (acquisition time: 5 minutes, 24 seconds), the MR data postprocessing software SyMRI (Synthetic MR; version 11.1.5) generates a variety of conventional MR contrasts and quantitative MR maps.[18-20] Based on a single sequence, intrinsic physical parameters of the examined tissue, such as T1 relaxation time (T1R), T2 relaxation time (T2R), and PD, can be determined.[20] The software allows definition of TR, TE, and TI after data acquisition to generate and to modulate the preferred MR contrasts. Because the image postprocessing is performed in less than 1 minute, SyMRI provides qualitative as well as quantitative MR data in a clinically acceptable time.[21-23]

In neonates, the process of myelination leads to subtle MR signal changes because of alterations in relaxation parameters and spin density, detectable by quantitative MR techniques. The aim of this study was to investigate the impact of different stages of prematurity on the maturational characteristics of the neonatal brain stem, as measured by SyMRI-based T1, T2, and PD mapping. The study was designed to prove that certain stages of prematurity are linked to specific quantitative MR metrics.

MATERIALS AND METHODS
Ethical Approval
The protocol of this study was approved by the local ethics commission and performed in accordance with the Declaration of Helsinki.

Study Cohort
Between June 2017 and August 2019, a total of 90 preterm and term-born neonates were examined at the neuroradiology department of a tertiary care hospital. All participants included in this study were referred for neonatal brain MR imaging by the Departments of Pediatrics and Adolescent Medicine, Neonatology, Pediatric Intensive Care, and Neuropediatrics. Indications for MR imaging included extremely preterm birth (GA: <28 + 0 weeks), clinical diagnosis of hypoxic-ischemic encephalopathy, intraventricular hemorrhage, and suspicion of cerebral infarction. Whereas premature infants were studied at approximately term-equivalent age in most cases, term-born neonates were examined between 2 and 48 days postpartum. Table 1 gives an overview of the clinical characteristics and demographic information of included neonates. All infants with proved or suspected pathology of the brain stem were excluded from the study.

Data Acquisition, MDME Sequence, and Postprocessing
To prevent motion artifacts, neonates were either fed or slightly sedated (chloral hydrate [30–50 mg/kg] or chloral hydrate [30 mg/kg] combined with midazolam [0.1 mg/kg]) 30 minutes before MR imaging and positioned on a vacuum mattress. All neonates included in this study were subjected to a standard neonatal MR protocol (T1 spin-echo sequence [axial plane], T2 TSE sequence [3 orthogonal planes], DWI sequence, SWI sequence, T1 3D sequence) on an Ingenia 1.5 T MR system (Philips Healthcare). To obtain quantitative MR data, an MDME sequence (axial plane) was acquired using 2 repeated acquisition phases.[21,24] One slice was saturated by the application of a slice-selective saturation pulse (flip angle: 120°) (first phase). A series of spin echoes was generated for another slice by the application of slice-selective excitation

pulses (flip angle: 90°) and slice-selective refocusing pulses (flip angle: 180°) (second phase).[20,21,24] A matrix with a variety of effects of T1 and T2 relaxation rates was acquired based on the mismatch between the image slice and the saturated slice.[21,24] Transverse and longitudinal relaxation parameters were estimated using echo trains, characterized by different saturation delays.[20,21,24] The local radiofrequency field (B1) was calculated based on the ascertained T1 relaxation constants.[21] T1 and T2 relaxation parameters, as well as B1, allowed the PD to be estimated.[20] SyMRI was used to perform MDME sequence-based image data postprocessing to generate quantitative MR maps (axial plane). Technical features of the individual sequences are shown in the Online Supplementary Data.

Determination of Physical Properties

Five ROIs were defined to quantify T1R (ms), T2R (ms), and PD (%) of the neonatal brain stem: midbrain, pons (basis pontis and tegmentum pontis included), basis pontis (tegmentum pontis excluded), tegmentum pontis (basis pontis excluded), and medulla oblongata. Details regarding ROI placement are shown in Fig 1. The software calculates the average values of all relevant physical parameters based on relaxation time and PD detected in each voxel within the corresponding ROI. ROI placement was performed manually by 2 independent raters with at least 2 years of experience with neonatal MR imaging. Both investigators were blinded to GA at birth and age at MR imaging. During ROI placement, rater 1 performed a visual review of the MR image data. Participants were excluded from the study if incorrect measurements of the physical parameters had to be assumed on the basis of the visual assessment, for instance, because of the presence of distinct motion artifacts. Thus, data exclusion was performed before ROI placement in all excluded cases.

Statistical Analyses

Participants were divided into 3 groups for comparison: extremely preterm (GA: <28 + 0 weeks), preterm (GA: 28 + 0–36 + 6 weeks), and term infants (GA: ≥37 + 0 weeks).[9] Statistical analyses were performed using SPSS Statistics for Macintosh, version 25.0 (IBM, 2017) at a significance level of $\alpha = 5\%$ ($P < .05$). Graphs were created using the statistics software R, version 3.6.3 (https://www.r-project.org). An intraclass correlation coefficient (ICC) was calculated for each ROI to detect concordances of the measurements of both raters. ICC values ≥0.75 were considered to represent a strong correlation.[25] A Pearson correlation analysis was performed to assess correlations between GA at birth and the physical parameters determined in each ROI. ANCOVA (covariate: GA at MR imaging) and the post hoc Bonferroni test were applied to detect statistical differences in T1R, T2R, and PD between the groups. The reported results are based on data determined by rater 1.

RESULTS

Applicability of SyMRI for the Determination of the Physical Tissue Properties

A total of 55/90 (61.1%) neonates were enrolled in this retrospective study, including 30 extremely preterm (mean GA at birth: 25 + 5 weeks [SD = 1 + 4]), 10 preterm (mean GA at birth:
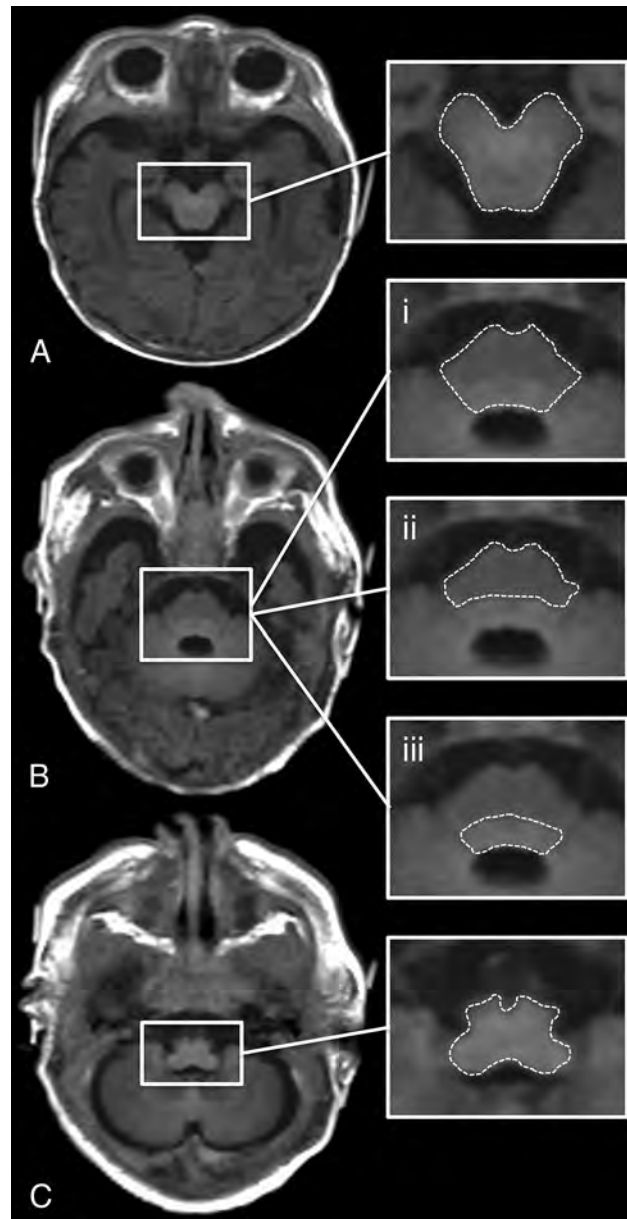
FIG 1. ROI placement is shown on an SyMRI-generated T1-weighted MR image (TR/TE = 650/10 ms) of a term-born neonate (GA: 40 + 1 weeks). *A,* Midbrain. *B.i,* Pons (basis pontis and tegmentum pontis included). *B.ii,* Basis pontis (tegmentum pontis excluded). *B.iii,* Tegmentum pontis (basis pontis excluded). *C,* Medulla oblongata.

32 + 4 weeks [SD = 3 + 1]), and 15 term infants (mean GA at birth: 39 + 5 weeks [SD = 0 + 6]). In 35/90 (38.9%) cases, the applicability of SyMRI for the determination of T1R, T2R, and PD was not possible. In 23/35 participants, image quality was highly degraded because of motion artifacts; 6/35 neonates were excluded because of abnormal findings of the brain stem (superficial siderosis [$n = 1$], hypoxic tissue alterations of the pons [$n = 1$], dysplasia of the brain stem [$n = 2$], suspected AVM of the midbrain [$n = 1$], aqueductal stenosis [$n = 1$]); 1/35 participants was excluded because of neonatal hyperbilirubinemia, which is thought to interfere with brain stem functions and cognitive development[26,27]; and 5/35 infants were excluded because of lack of clinical information.

Interrater Statistics

The ICC analysis revealed a high degree of concordance between the T1R, T2R, and PD determined by both raters. For T1R: midbrain, 0.954 (CI: 0.921–0.973, $P<.001$); pons, 0.909 (CI: 0.585–0.966, $P<.001$); basis pontis, 0.965 (CI: 0.936–0.980, $P<.001$); tegmentum pontis, 0.895 (CI: 0.761–0.947, $P<.001$); and medulla oblongata, 0.975 (CI: 0.740–0.992, $P<.001$).

For T2R: midbrain, 0.925 (CI: 0.871–0.956, $P<.001$); pons, 0.848 (CI: 0.389–0.941, $P<.001$); basis pontis, 0.883 (CI: 0.743–0.940, $P<.001$); tegmentum pontis, 0.836 (CI: 0.666–0.913, $P<.001$); and medulla oblongata, 0.954 (CI: 0.760–0.983, $P<.001$).

For PD: midbrain, 0.832 (CI: 0.712–0.902, $P<.001$); pons, 0.908 (CI: 0.839–0.947, $P<.001$); basis pontis, 0.847 (CI: 0.563–0.931, $P<.001$); tegmentum pontis, 0.817 (CI: 0.686–0.893, $P<.001$); and medulla oblongata, 0.850 (CI: 0.743–0.912, $P<.001$).

Pearson Correlation Analysis

Negative correlations were observed between GA at birth and the T1R (determined in the midbrain [$r=-0.852$, $P<.001$], pons [$r=-0.669$, $P<.001$], basis pontis [$r=-0.550$, $P<.001$], tegmentum pontis [$r=-0.790$, $P<.001$], and medulla oblongata [$r=-0.742$, $P<.001$]), T2R (determined in the midbrain [$r=-0.718$, $P<.001$], pons [$r=-0.366$, $P=.006$], basis pontis [$r=-0.277$, $P=.041$], tegmentum pontis [$r=-0.568$, $P<.001$], and medulla oblongata [$r=-0.414$, $P=.002$]), and PD (determined in the pons [$r=-0.275$, $P=.042$] and the tegmentum pontis [$r=-0.457$, $P<.001$]) (Fig 2).

No correlations were found between GA at birth and the PD determined in the midbrain ($r=0.062$, $P=.651$), basis pontis ($r=-0.255$, $P=.06$), and medulla oblongata ($r=-0.163$, $P=.233$) (Fig 2).

Differences in the Physical Tissue Properties Between the Groups

ANCOVA revealed significant differences in T1R/T2R for the midbrain (T1R/T2R: $P<.001$), pons (T1R: $P<.001$), basis pontis (T1R: $P=.005$), tegmentum pontis (T1R/T2R: $P<.001$), and medulla oblongata (T1R: $P<.001$) between the groups. There were also significant differences in PD for the tegmentum pontis ($P=.004$) between the groups (Fig 3).

Although ANCOVA revealed significant results ($P=.044$), the post-hoc Bonferroni test did not detect significant differences in T2R for the medulla oblongata between the groups ($P>.05$). Based on T2R of the pons ($P=.293$) and basis pontis ($P=.584$), according to the corrections above and PD of the midbrain ($P=.431$), pons ($P=.442$), basis pontis ($P=.472$), and medulla oblongata ($P=.384$), no significant differences were found between the groups (Fig 3). Post hoc results are shown in Table 2.

DISCUSSION

In this study, the impact of prematurity on the tissue properties of the neonatal brain stem, determined at term-equivalent age, was investigated using the MR data postprocessing software SyMRI. Considerable correlations were observed between GA at birth and T1R/T2R, characterized by lower GA, which was associated with longer T1R/T2R and vice versa. In most cases, the physical properties of premature (GA: <37 + 0 weeks) and term infants differed significantly. Moreover, T1R/T2R determined in the midbrain enabled a reliable differentiation between extremely preterm, preterm, and term neonates. Overall, PD values showed the lowest correlations with GA at birth. Based on the data presented here, SyMRI, using quantitative MR parameters, can enable the characterization of cerebral development in different stages of prematurity and in term-born infants.

According to descriptions in the literature, myelination processes primarily lead to changes in T1R, T2R, and PD.[14,15] These alterations affect the appearance of white matter on MR contrasts and allow brain maturation to be assessed qualitatively.[1,5] However, based on the visual evaluation of conventional sequences, myelin-induced MR signal differences in preterm and term infants may be subtle and remain undetected in many cases.[6] In addition, currently, techniques for the quantification of incomplete myelination are scarce. As described by Yakovlev and Lecours,[28] the human brain stem already contains a multitude of myelinated fibers at the time of birth compared with other brain areas. Hence, the physical properties of this region best reflect the current stage of brain maturity.

In this study, the strongest correlations were observed between T1R and GA at birth. It is hypothesized that T1 shortening already occurs at stages of "premyelination" due to interactions between water molecules and isolated myelin components, such as cholesterol and glycolipids.[29-31] This might explain the fact that T1R of the midbrain enabled a reliable discrimination between different stages of prematurity. Nonetheless, T1 shortening of other areas of the brain stem did not reveal similar results, though significant differences between premature and term infants were observed. As described in previous studies, iron deposition also affects the T1R and leads to specific MR signal changes during cerebral development.[32,33] Thus, more pronounced T1 shortening in the mesencephalon, caused by the initial accumulation of iron components in the red nucleus, seems credible and could explain these findings.[32] In addition, melanin shows biochemical interactions with ferric iron.[32,33] However, it has been suggested that iron bound to the substantia nigra and other brain stem nuclei that contain melanin do not affect relaxation parameters before the 10th month of life.[33]

Furthermore, T2R of the midbrain revealed significant differences between extremely preterm, preterm, and term neonates. T2 shortening is initiated by tightening of fully developed myelin sheaths, which becomes most evident in advanced states of brain maturation.[29-31] In extremely preterm infants, myelination is already detectable in the midbrain.[1] Predominantly, the superior cerebellar peduncles and their decussation show an advanced maturation at this stage.[1,28] Between 30 + 0–36 + 0 weeks GA, the myelin amount increases, which is detectable histologically.[1] However, myelin-related changes are hardly detected during this period using a qualitative MR imaging approach.[1] Our data indicate that quantitative MR metrics allow for the discrimination between different stages of prematurity on the basis of T2 shortening, whereas these subtle changes may not be detected visually.[1] Based on T2R of the pontine tegmentum, differences between preterm and term neonates were observed. In contrast
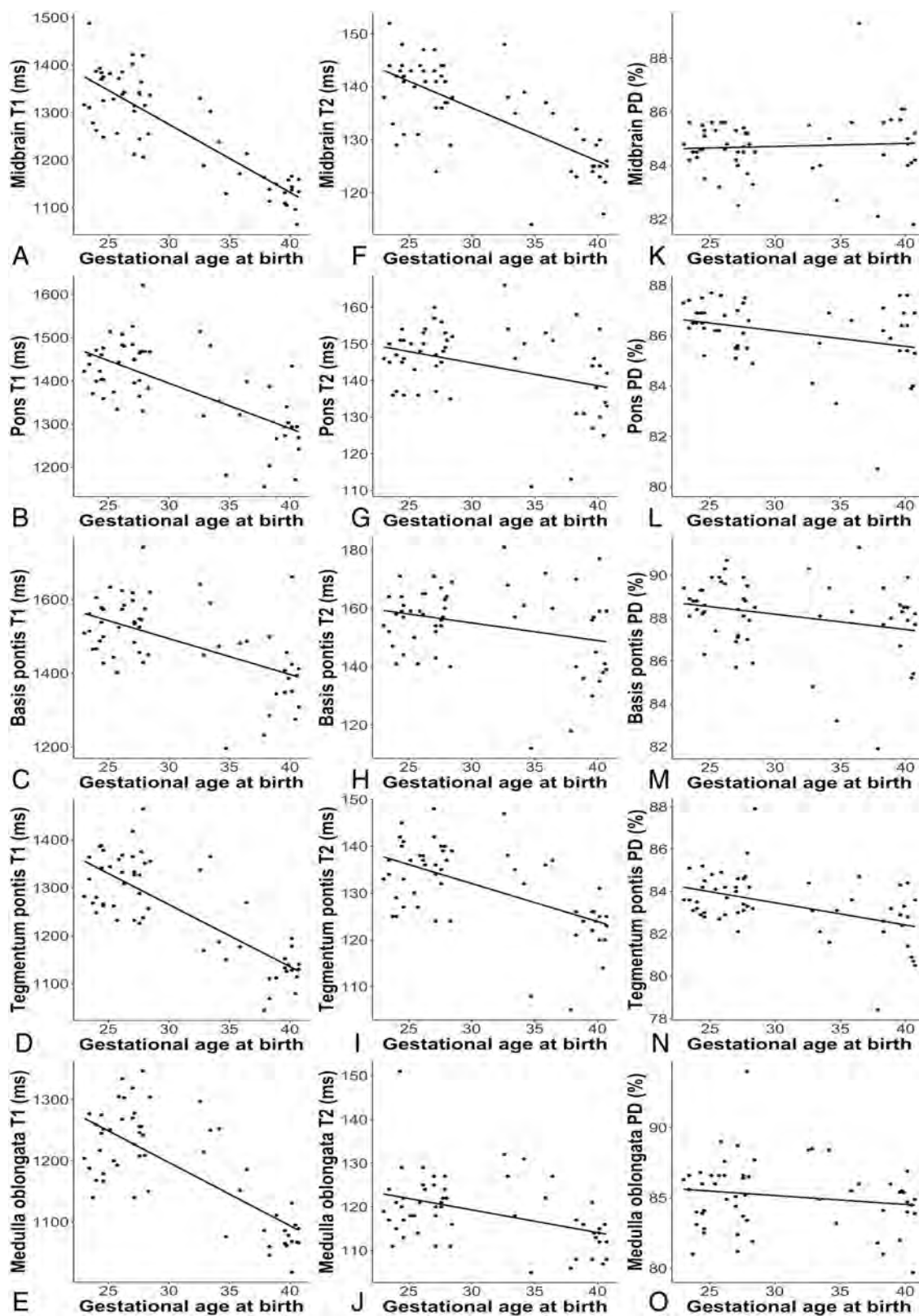
FIG 2. Pearson correlation between GA (weeks) at birth (x-axis) and physical MR parameters (y-axis) determined at term-equivalent age by rater 1. Left column: T1R (A–E). Middle column: T2R (F–J). Right column: PD (K–O).

to other regions of the developing brain, myelin deposition is not detectable before 32 weeks GA in this part of the brain stem.[1,28] Myelination progresses rapidly in this region and corroborates

that T2 shortening is related to advanced states of brain maturity.[1,29-31] However, no significant differences were found on the basis of T2R of the medulla oblongata. This region shows
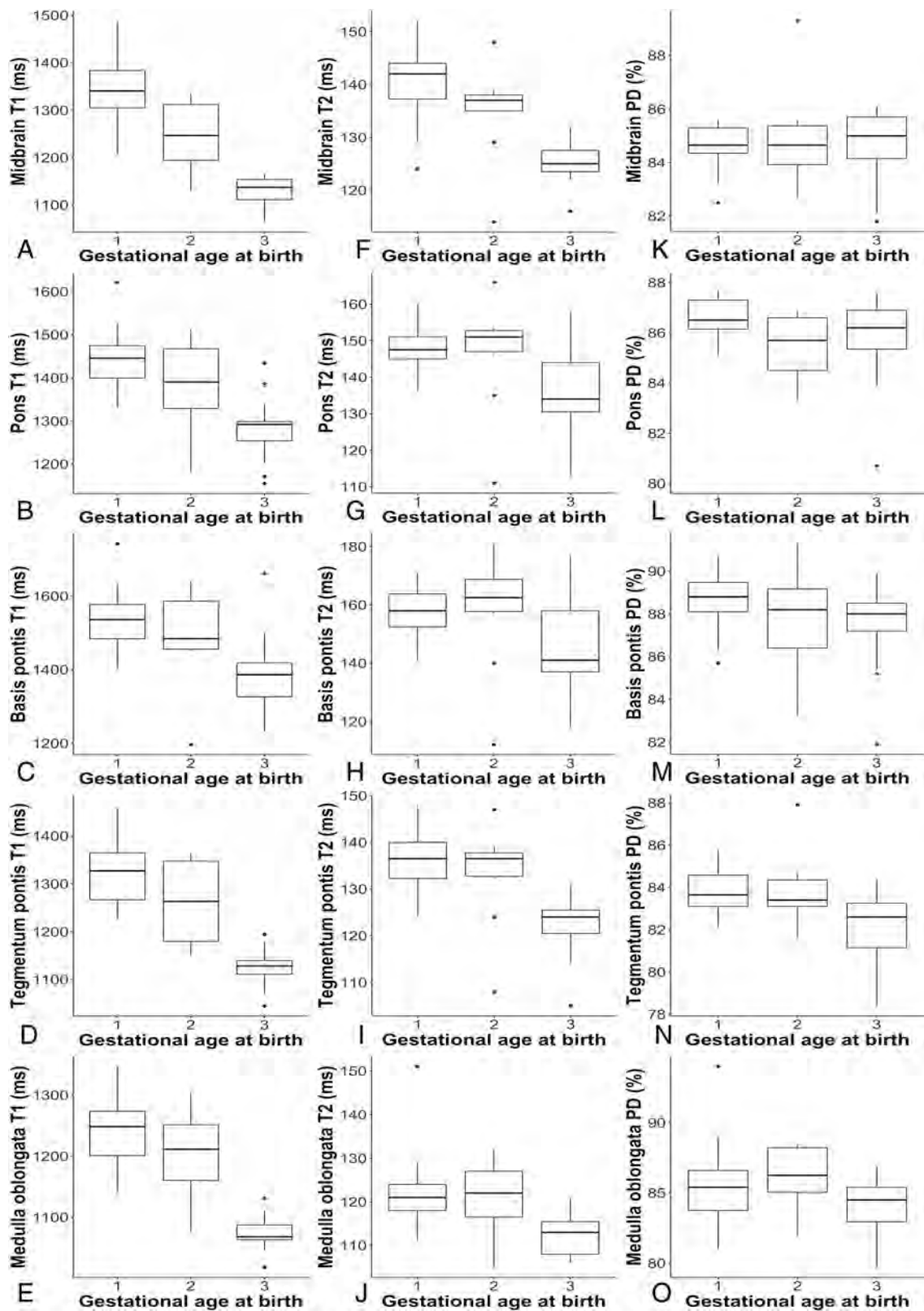
FIG 3. The boxplots show descriptive data for quantitative MR parameters (*y*-axis) of (1) neonates born <28 + 0 weeks GA, (2) neonates born between 28 + 0–36 + 6 weeks GA, and (3) neonates born ≥37 + 0 weeks GA (*x*-axis) determined at term-equivalent age by rater 1. Left column: T1R (*A–E*). Middle column: T2R (*F–J*). Right column: PD (*K–O*).

Table 2: Bonferroni post hoc test results

ROI	Group vs Group		Significance	Differences: Mean vs Mean[a]	
				Absolute[b]	Relative (%)[c]
Midbrain T1 relaxation time (ms)	Extremely preterm	Preterm	$P < .001$	84.4	6.3
		Term born	$P < .001$	182.1	13.7
	Preterm	Term born	$P < .001$	97.7	7.8
Pons T1 relaxation time (ms)	Extremely preterm	Preterm	$P = .241$	43.7	3
		Term born	$P < .001$	124.1	8.7
	Preterm	Term born	$P = .02$	80.4	5.8
Basis pontis T1 relaxation time (ms)	Extremely preterm	Preterm	$P = 1$	27.9	1.8
		Term born	$P = .004$	97.9	6.5
	Preterm	Term born	$P = .147$	70	4.7
Tegmentum pontis T1 relaxation time (ms)	Extremely preterm	Preterm	$P = .051$	54.7	4.2
		Term born	$P < .001$	181.4	13.8
	Preterm	Term born	$P < .001$	126.7	10.1
Medulla oblongata T1 relaxation time (ms)	Extremely preterm	Preterm	$P = .334$	24.5	2
		Term born	$P < .001$	130.9	10.6
	Preterm	Term born	$P < .001$	106.4	8.8
Midbrain T2 relaxation time (ms)	Extremely preterm	Preterm	$P = .02$	4.3	3.1
		Term born	$P < .001$	10.2	7.3
	Preterm	Term born	$P = .006$	5.9	4.4
Tegmentum pontis T2 relaxation time (ms)	Extremely preterm	Preterm	$P = 1$	1.1	0.8
		Term born	$P < .001$	8.4	6.3
	Preterm	Term born	$P = .009$	7.3	5.5
Tegmentum pontis PD (%)	Extremely preterm	Preterm	$P = 1$	0.1	0.1
		Term born	$P = .004$	1	1.2
	Preterm	Term born	$P = .026$	0.9	1

[a] Difference in means between the compared groups.
[b] Absolute difference in means.
[c] Relative difference in means.

considerable myelination even before 30 weeks GA.[1] Hence, the effect of T2 shortening on the differences between the groups may be limited. Compared with T2R, T1R indicated maturation differences more clearly. These results are consistent with the literature and may be attributed to the immediate response of T1 parameters to subtle maturation processes.[4,29-31]

Compared with T1R and T2R, PD indicated neonatal brain maturity less clearly. PD values refer to the concentration of water protons and may indicate the content of water in the investigated tissue.[34] There is evidence that immature or demyelinated brain tissue contains higher proportions of water, which leads to increased PD values.[14,21,35] As demonstrated by Lee et al,[14] PD decreases in most brain areas during regular development. However, as opposed to T1 and T2 shortening, changes in PD occur considerably later and more slowly.[14] This could explain the fact that no correlations between PD and GA at birth were observed in most areas of the neonatal brain stem. Nonetheless, significant results were found in the pons, particularly in the pontine tegmentum. PD determined in the tegmentum pontis revealed significant differences between preterm and term neonates. These data might confirm that maturity-related PD changes appear in a similar manner as T1R/T2R but more slowly.[14] Interestingly, compared with preterm neonates, higher PD values were detected in the midbrains of term infants. These nonsignificant observations may be attributed to the impact of the cerebral aqueduct on PD determined in the mesencephalon. There is evidence that the size of the aqueductus mesencephali increases in the course of development, which might lead to higher PD values because of higher H_2O components.[36] However, descriptions are rare with regard to the proportions of the ventricular system in mature and former premature infants.

As demonstrated in a previous study, delayed myelination is detectable in preterm neonates at the regular, expected due date.[6] The data presented in this study are in line with descriptions in the literature.[6] The specific novelty presented in this study is the fact that distinct maturational differences between different stages of prematurity can be identified noninvasively by novel MR acquisition strategies.

Prematurity leads to structural alterations of infratentorial regions.[37] Furthermore, extremely preterm delivery is associated with disturbances in brain stem functions.[38] As described by Antinmaa et al,[39] impairment of the auditory pathway is highly associated with poor future verbal abilities in former preterm infants. Thus, preterm birth interferes with regular brain stem development and plays an important role in the pathogenesis of neurologic and psychiatric disorders.[37,39,40] SyMRI enables brain maturation to be quantified and therefore allows for a more precise assessment of the neonatal brain stem at early stages of development. Quantitative MR metrics represent novel, clinically feasible diagnostic tools, enabling a more differentiated assessment of functionally important maturational stages in neonatal brain development. This opens further perspectives in pediatric brain imaging and may help physicians to predict neurodevelopmental disabilities in later life. However, this was outside the scope of the present study and should be the subject of future investigations.

This study has several limitations. The sample size was small and included pathologic cases that made the data provided inappropriate as reference data. Nonetheless, this technique bears the

potential to make quantitative MR baseline data available for the assessment of brain maturity in preterm and term neonates. At the date of the MR imaging examination, term-born infants were relatively older than those born prematurely. Hence, statistical methods were used that allow for correction of the effect of GA at MR imaging on the data presented. The physical properties of supratentorial regions, such as the posterior limb of the internal capsule, which is considered highly myelinated by the regular due date, were not determined.[28] This is attributed to the possibility of incorrect determination of T1R, T2R, and PD in participants with telencephalic brain damage. To determine brain maturity–related physical tissue properties unadulterated, participants without abnormal supratentorial findings should be investigated, which was not the case in the presented study cohort. However, the quantifiability of supratentorial brain maturity is an important topic and should be investigated in future studies. Finally, DWI and DTI have been demonstrated to be MR techniques that are sensitive enough to quantify the process of "premyelination."[41,42] An assessment of the relationship between DTI metrics and the mapping technique presented here was outside the scope of this work and should be further addressed in the future.

CONCLUSIONS

In summary, our data indicate that quantitative MR parameters determined at term-equivalent age enable the differentiation of preterm and term neonates. In addition, the method enables the distinction of different stages of prematurity. It can be concluded that SyMRI allows for a quantitative assessment of neonatal brain maturation by providing tissue-specific properties while not exceeding a clinically acceptable imaging time.

REFERENCES

1. van der Knaap MS, Valk J. *Magnetic Resonance of Myelination and Myelin Disorders.* 3rd ed. Springer-Verlag; 2005
2. Flechsig P. **Developmental (myelogenetic) localisation of the cerebral cortex in the human subject.** *Lancet* 1901;158:1027–30
3. Kinney HC. **Human myelination and perinatal white matter disorders.** *J Neurol Sci* 2005;228:190–92 CrossRef Medline
4. Barkovich AJ, Kjos BO, Jackson DE, et al. **Normal maturation of the neonatal and infant brain: MR imaging at 1.5 T.** *Radiology* 1988;166:173–80 CrossRef Medline
5. van der Knaap MS, Valk J. **MR imaging of the various stages of normal myelination during the first year of life.** *Neuroradiology* 1990;31:459–70 CrossRef Medline
6. Schmidbauer V, Geisl G, Diogo M, et al. **SyMRI detects delayed myelination in preterm neonates.** *Eur Radiol* 2019;29:7063–72 CrossRef Medline
7. Ibrahim J, Mir I, Chalak L. **Brain imaging in preterm infants <32 weeks gestation: a clinical review and algorithm for the use of cranial ultrasound and qualitative brain MRI.** *Pediatr Res* 2018;84:799–806 CrossRef Medline
8. Parikh NA. **Advanced neuroimaging and its role in predicting neurodevelopmental outcomes in very preterm infants.** *Semin Perinatol* 2016;40:530–41 CrossRef Medline
9. Glass HC, Costarino AT, Stayer SA, et al. **Outcomes for extremely premature infants.** *Anesth Analg* 2015;120:1337–51 CrossRef Medline
10. Marlow N, Wolke D, Bracewell MA, et al. **Neurologic and developmental disability at six years of age after extremely preterm birth.** *N Engl J Med* 2005;352:9–19 CrossRef Medline
11. Rutherford M, Pennock J, Schwieso J, et al. **Hypoxic-ischaemic encephalopathy: early and late magnetic resonance imaging findings in relation to outcome.** *Arch Dis Child Fetal Neonatal Ed* 1996;75: F145–51 CrossRef Medline
12. Benders MJ, Kersbergen KJ, de Vries LS. **Neuroimaging of white matter injury, intraventricular and cerebellar hemorrhage.** *Clin Perinatol* 2014;41:69–82 CrossRef Medline
13. de Vries LS, Benders MJ, Groenendaal F. **Progress in neonatal neurology with a focus on neuroimaging in the preterm infant.** *Neuropediatrics* 2015;46:234–41 CrossRef Medline
14. Lee SM, Choi YH, You SK, et al. **Age-related changes in tissue value properties in children: simultaneous quantification of relaxation times and proton density using synthetic magnetic resonance imaging.** *Invest Radiol* 2018;53:236–45 CrossRef Medline
15. Ding XQ, Kucinski T, Wittkugel O, et al. **Normal brain maturation characterized with age-related T2 relaxation times: an attempt to develop a quantitative imaging measure for clinical use.** *Invest Radiol* 2004;39:740–46 CrossRef Medline
16. Ferrie JC, Barantin L, Saliba E, et al. **MR assessment of the brain maturation during the perinatal period: quantitative T2 MR study in premature newborns.** *Magn Reson Imaging* 1999;17:1275–88 CrossRef Medline
17. Deoni SC, Mercure E, Blasi A, et al. **Mapping infant brain myelination with magnetic resonance imaging.** *J Neurosci* 2011;31:784–91 CrossRef Medline
18. McAllister A, Leach J, West H, et al. **Quantitative synthetic MRI in children: normative intracranial tissue segmentation values during development.** *AJNR Am J Neuroradiol* 2017;38:2364–72 CrossRef Medline
19. Tanenbaum LN, Tsiouris AJ, Johnson AN, et al. **Synthetic MRI for clinical neuroimaging: results of the magnetic resonance image compilation (MAGiC) prospective, multicenter, multireader trial.** *AJNR Am J Neuroradiol* 2017;38:1103–10 CrossRef Medline
20. Warntjes JB, Leinhard OD, West J, et al. **Rapid magnetic resonance quantification on the brain: optimization for clinical usage.** *Magn Reson Med* 2008;60:320–29 CrossRef Medline
21. Hagiwara A, Warntjes M, Hori M, et al. **SyMRI of the brain: rapid quantification of relaxation rates and proton density, with synthetic MRI, automatic brain segmentation, and myelin measurement.** *Invest Radiol* 2017;52:647–57 CrossRef Medline
22. Schmidbauer V, Geisl G, Cardoso Diogo M, et al. **Validity of SyMRI for assessment of the neonatal brain.** *Clin Neuroradiol* 2020 March 11. [Epub ahead of print] CrossRef Medline
23. Vanderhasselt T, Naeyaert M, Watte N, et al. **Synthetic MRI of preterm infants at term-equivalent age: evaluation of diagnostic image quality and automated brain volume segmentation.** *AJNR Am J Neuroradiol* 2020;41:882–88 CrossRef Medline
24. Kang KM, Choi SH, Kim H, et al. **The effect of varying slice thickness and interslice gap on T1 and T2 measured with the multidynamic multiecho sequence.** *Magn Reson Med Sci* 2019;18:126–33 CrossRef
25. Cicchetti D. **Guidelines, criteria, and rules of thumb for evaluating normed and standardized assessment instruments in psychology.** *Psychol Assess* 1994;6:284–90 CrossRef Medline

26. Sari S, Yavuz A, Batur A, et al. **Brain magnetic resonance imaging and magnetic resonance spectroscopy findings of children with kernicterus.** *Pol J Radiol* 2015;80:72–80 CrossRef Medline

27. Karabulut B, Surmeli M, Bozdag S, et al. **Effect of hyperbilirubinemia on medial olivocochlear system in newborns.** *Int Adv Otol* 2019;15:272–76 CrossRef Medline

28. Yakovlev P, Lecours A. The myelogenetic cycles of regional maturation of the brain. In: Minkowski A, ed. *Regional Development of the Brain in Early Life.* Blackwell; 1967:3–70

29. Wang S, Ledig C, Hajnal JV, et al. **Quantitative assessment of myelination patterns in preterm neonates using T2W MRI.** *Sci Rep* 2019;9:12938 CrossRef Medline

30. Barkovich AJ, Lyon G, Evrard P. **Formation, maturation, and disorders of white matter.** *AJNR Am J Neuroradiol* 1992;13:447–61 Medline

31. Dubois J, Dehaene-Lambertz G, Kulikova S, et al. **The early development of brain white matter: a review of imaging studies in fetuses, newborns and infants.** *Neuroscience* 2014;276:48–71 CrossRef Medline

32. Martin E, Krassnitzer S, Kaelin P, et al. **MR imaging of the brainstem: normal postnatal development.** *Neuroradiology* 1991;33:391–95 CrossRef Medline

33. Drayer B, Burger P, Darwin R, et al. **Magnetic resonance imaging of brain iron.** *AJNR Am J Neuroradiol* 1986;7:373–80

34. Mezer A, Rokem A, Berman S, et al. **Evaluating quantitative proton-density-mapping methods.** *Hum Brain Mapp* 2016;37:3623–35 CrossRef Medline

35. Laule C, Vavasour IM, Moore GR, et al. **Water content and myelin water fraction in multiple sclerosis.** *J Neurol* 2004;251:284–93 CrossRef Medline

36. Viñals F, Ruiz P, Quiroz G, et al. **Two-dimensional ultrasound evaluation of the fetal cerebral aqueduct: improving the antenatal diagnosis and counseling of aqueductal stenosis.** *Fetal Diagn Ther* 2017;42:278–84 CrossRef Medline

37. Wu Y, Stoodley C, Brossard-Racine M, et al. **Altered local cerebellar and brainstem development in preterm infants.** *Neuroimage* 2020;213:116702 CrossRef Medline

38. Jiang ZD, Wang C, Ping LL. **Brainstem auditory pathway function at four months of corrected postnatal age in preterm infants born below 30 week gestation.** *Brain Dev* 2020;42:496–502 CrossRef Medline

39. Antinmaa J, Lapinleimu H, Salonen J, et al. **Neonatal brainstem auditory function associates with early receptive language development in preterm children.** *Acta Paediatr* 2020;109:1387–93 CrossRef Medline

40. Fitzgerald E, Boardman JP, Drake AJ. **Preterm birth and the risk of neurodevelopmental disorders—is there a role for epigenetic dysregulation?** *Curr Genomics* 2018;19:507–21 CrossRef Medline

41. Wimberger DM, Roberts TP, Barkovich AJ, et al. **Identification of "premyelination" by diffusion-weighted MRI.** *J Comput Assist Tomogr* 1995;19:28–33 CrossRef Medline

42. Qiu A, Mori S, Miller MI. **Diffusion tensor imaging for understanding brain development in early life.** *Annu Rev Psychol* 2015;66:853–76 CrossRef Medline

43. Deeg KH, Staudt F, von Rohden L. **Classification of intracranial hemorrhage in premature infants.** *Ultraschall Med* 1999;20:165–70 CrossRef Medline

Neuroradiologic Phenotyping of Galactosemia: From the Neonatal Form to the Chronic Stage

M.C. Rossi-Espagnet, S. Sudhakar, E. Fontana, D. Longo, J. Davison, A.L. Petengill, E. Bevivino, F.T. Pacheco, A.J. da Rocha, P. Hanagandi, M. Soldatelli, K. Mankad, and L.L.F. do Amaral

ABSTRACT

SUMMARY: Galactosemia is a rare genetic condition caused by mutation of enzymes involved in galactose and glucose metabolism. The varying clinical spectrum reflects the genetic complexity of this entity manifesting as acute neonatal toxicity syndrome, requiring prompt diagnosis and treatment, to more insidious clinical scenarios as observed in the subacute and chronic presentations. The current literature predominantly focuses on the long-standing sequelae of this disease. The purpose of this multicenter clinical report comprising 17 patients with galactosemia is to highlight the MR imaging patterns encompassing the whole spectrum of galactosemia, emphasizing the 3 main clinical subtypes: 1) acute neonatal presentation, with predominant white matter edema; 2) subacute clinical onset with a new finding called the "double cap sign"; and 3) a chronic phase of the disease with heterogeneous imaging findings. The knowledge of these different patterns together with MR spectroscopy and the clinical presentation may help in prioritizing galactosemia over other neonatal metabolic diseases and prevent possible complications.

Lactose is the primary source of carbohydrates in neonates. The metabolism and sustaining energy supplementation are pivotal and are channeled through the Leloir pathway. Lactose is catabolized to galactose and glucose and eventually into uridine diphosphate galactose–galactose and uridine diphosphate galactose–glucose. Reduction of enzymatic activity results in an inborn error of metabolism manifesting as galactosemia. Deficiency of galactose-1-phosphate uridyltransferase is associated with the classic galactosemia phenotype or type I galactosemia (Online Mendelian Inheritance in Man, No. 230400; omim.org), an inherited autosomal recessive disorder caused by mutation of the galactose-1-phosphate uridyltransferase–encoding GALT gene on chromosome 9p13.3, with an estimated incidence of 1/30,000.[1] Genetic mutations in the Leloir pathway involving galactokinase and uridine diphosphate galactose 4-epimerase cause type II and III galactosemia, respectively. The latter variants are rarer than classic galactosemia and manifest with insidious onset and a mild clinical course.[2]

The variable clinical outcome in type I galactosemia and disease severity is attributable to the polymorphic nature and molecular heterogeneity of galactose-1-phosphate uridyltransferase.[3] Estimating erythrocyte activity of galactose-1-phosphate uridyltransferase remains the criterion standard technique in diagnosing classic galactosemia (type I), whereas galactokinase (type II) or the uridine diphosphate galactose 4-epimerase mutation (type III) enzymatic activity are measured in white blood cells.[4,5]

Galactosemia is an extremely complex disorder whose clinical spectrum depends on the interaction between genetic (ie, the residual activity of the affected enzyme) and environmental factors. Therefore, symptoms may vary from an acute and lethal presentation, frequently observed in the neonatal period, to more subacute or chronic forms whose pathogenesis has not been well-elucidated.[3] Similarly, the diversity is also reflected in imaging features.

The chronic stage of the disease has been well-cited in the literature, whereas the data on acute neonatal presentation are limited to case reports.[6,7] We intend to present a case series of 17 patients showcasing the divergent imaging patterns, ranging from the emergent neonatal toxicity syndrome, including its complications and sequelae, to the subacute presentations in young children and the more subtle alterations encountered in the chronic juvenile stage.
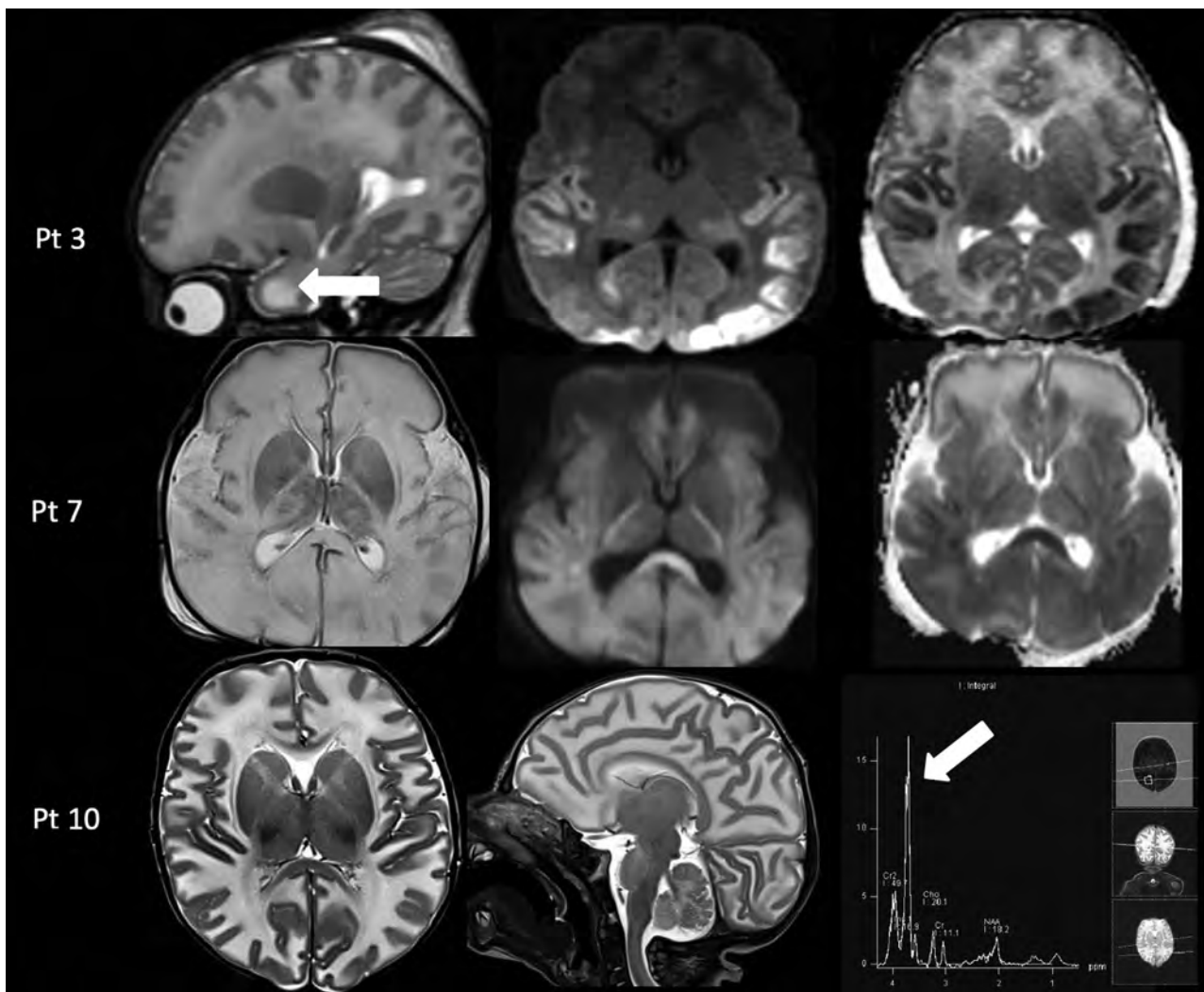
FIG 1. Acute toxicity syndrome in 3 cases of galactosemia. *Upper row*: MR imaging in a 13-day-old male infant (patient 3) with acute liver failure demonstrates diffuse white matter edema with the cystic appearance of the anterior temporal poles on a sagittal T2-weighted image (*left column, arrow*) and cytotoxic edema in the temporo-occipital cortex and thalami on the axial DWI and ADC maps (*middle and right columns*). *Middle row*: MR imaging in a 17-day-old male infant (patient 7) with profound hypotonia and sepsis showing diffuse white matter edema on T2-weighted image (*left column*) and diffuse cytotoxic edema on DWI and ADC maps (*middle and right column*). *Lower row*: MR imaging in a 25-day-old male infant (patient 10) with lethargy and vomiting shows diffuse white matter edema on axial and sagittal T2-weighted images (*left and middle column*) and an abnormal galactitol peak at 3.7 ppm on MR spectroscopy with a short TE of 35 ms (*right column, arrow*). Pt indicates patient.

Case Series

Local institutional review board approval was obtained to analyze the clinical and laboratory records and imaging information of confirmed cases (Great Ormond Street Hospital, London, UK; Bambino Gesù Children's Hospital, Rome, Italy; Hospital de Santa Casa de Misericórdia de São Paulo, São Paulo, Brazil). Clinical medical records from 17 patients (15 males and 2 girls; age range, 13 days to 14 years) from 3 pediatric hospitals were retrospectively reviewed.

All MR images were obtained on a 1.5 or a 3T scanner, which included sagittal and axial T1 spin-echo, axial and coronal T2-weighted, axial DWI, and axial or coronal FLAIR sequences. MR spectroscopy was also acquired in 7 patients with a single-voxel technique (TE = 35 ms).

Clinical and MR Imaging Findings at Presentation

Demographic, clinical, and imaging findings of the 17 patients are summarized in the Online Supplemental Data.

Acute Presentation. Three patients (patients 3, 7, 10) initially presented at 13–25 days of life with macrocephaly and acute symptoms like vomiting, hypotonia, lethargy, jaundice, and variable severity of liver dysfunction. Patient 7 at day 12 of life developed septic shock with disseminated intravascular coagulation, and blood cultures were positive for *Escherichia coli* infection.

MR imaging demonstrated diffuse brain edema. Diffusion-restriction abnormality involving the temporo-occipital cortex (patient 3) and diffuse involvement of the deep white matter and corpus callosum (patient 7) were noted on the DWI sequence. Single-voxel MR spectroscopy was performed (patients 3 and 10) in the ROI and demonstrated the presence of an abnormal doublet peak at 3.67–3.74 ppm, representing galactitol (Fig 1).[7]

Subacute Presentation. Five patients (patients 1, 2, 15, 16, 17) presented between 7 and 18 months of age with a subacute
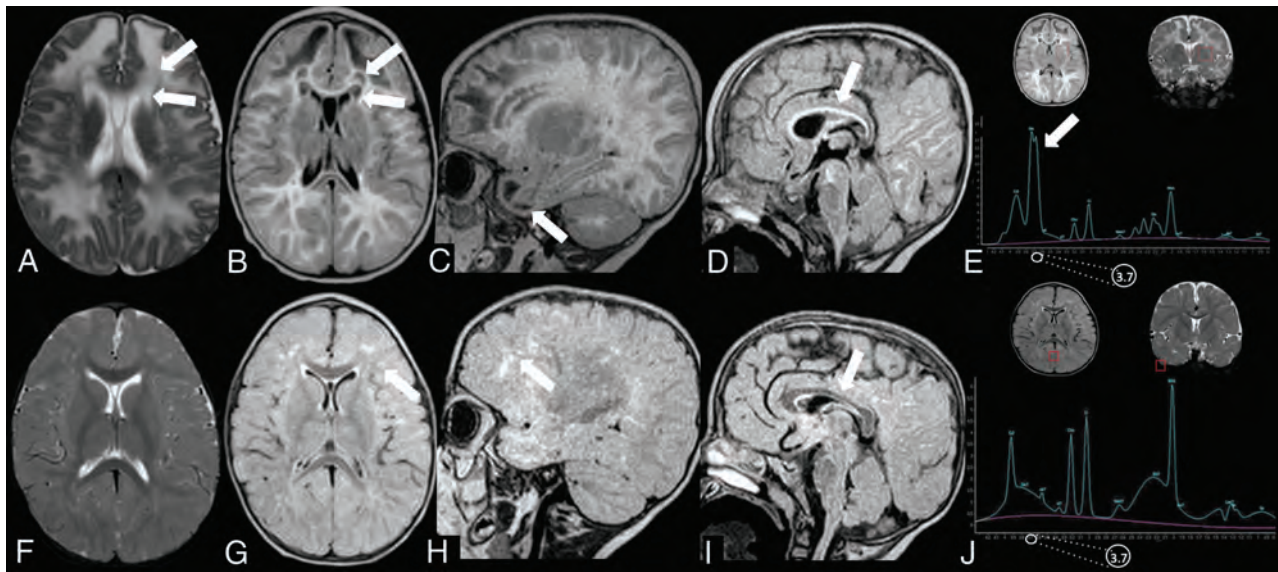
FIG 2. Subacute presentation. MR imaging of patient 15 at 8 months of age (*A–E*) demonstrates the presence of diffuse white matter edema on an axial T2-weighted image (*A*) associated with the double cap sign, best appreciated on T2 and axial FLAIR images (*A* and *B, arrows*). Sagittal T1-weighted image shows the presence of cystlike lesions of the temporal poles (*C, arrow*) and thinning of the corpus callosum (*D, arrow*). Single-voxel MR spectroscopy with a short TE of 35 ms demonstrates the presence of a doublet peak at 3.6–3.74 ppm, corresponding to galactitol (*E, arrow*). Follow-up MR imaging performed at 2 years of age (*F–J*) shows complete resolution of white matter edema on axial T2-weighted sequences (*F*); the double cap sign and temporal lobe cysts, respectively, on axial (*G*) and sagittal FLAIR (*H*), with the presence of patchy alterations in the periventricular white matter, especially in the frontal lobes (*G* and *H, arrows*); and thinning of the corpus callosum on sagittal T1-weighted image (*I, arrow*). MR spectroscopy demonstrates the disappearance of the previously noted galactitol peak (*J*).

clinical onset characterized by psychomotor retardation, developmental delay, cataracts, macrocephaly, hepatosplenomegaly, renal tubulopathy (patients 1 and 2), and seizures (patient 17).

In these patients, MR imaging showed diffuse white matter edema associated with thinning of the corpus callosum (according to the biometric values proposed by Garel et al[8]). A bean-shaped dark line was clearly observed on T2-weighted images with a central area of hyperintensity around the frontal horns of the lateral ventricles demonstrating a "double cap sign" appearance. This was better appreciated on FLAIR sequences in which the central area showed a hypointense signal. Additionally, cystlike lesions in the bilateral anterior temporal poles were observed. Single-voxel MR spectroscopy in the abnormal white matter was performed in 4/5 patients and revealed an abnormal doublet peak at 3.67–3.74 ppm, confirming the accumulation of galactitol (Fig 2). The thalami and anterior portions of the striatum were also symmetrically involved in patients 1 and 2 (Fig 3).

Chronic Presentation. In the remaining 9 patients, MR imaging was performed later in life (between 2.11 and 14 years) during a galactose-free diet, and the clinical condition was characterized by varying degrees of intellectual disability associated with autism spectrum disorder (patient 6), dystonia (patient 5), and acute symptoms, including vomiting and seizures (patient 4). MR imaging demonstrated variable findings including the following: 1) in patients 4 and 13, the presence of multiple patchy areas of T2 hyperintensity in the supratentorial white matter; 2) delayed myelination with variable thinning of corpus

callosum (patients 8, 9, 11, and 14); and 3) the absence of relevant imaging findings (patients 6 and 12). Patient 5, with severe dystonia, demonstrated symmetric T2 hyperintensity in the globus pallidus without significant alterations in the rest of the brain.

Clinical/Imaging Follow-Up
Clinical follow-up was available in 6 patients (patients 3, 4, 5, 7, 8, 15) at different ages (Online Supplemental Data). All of them demonstrated cognitive impairment. MR imaging was available at clinical follow-up in 5 patients with variable findings.

Patient 3 was reassessed at 2 years of age and had a language delay. Patient 4 at 13 years of age had mild cognitive impairment (learning difficulties), left-side weakness, ovarian failure, osteopenia, and epilepsy. MR imaging demonstrated persistence of a peritrigonal and subcortical white matter signal abnormality associated with mild cerebellar atrophy (Fig 4*A, -B*).

In patient 5, there was progressive worsening of dystonia, and male infant died at 11 years of age following severe respiratory failure due to bronchopneumonia.

Patient 7 at 5 years of age had microcephaly, motor stereotypies, self-injury behavior, spastic tetraparesis, and language paucity. MR imaging demonstrated the presence of cystic encephalomalacic changes in the bilateral parieto-occipital regions, significant reduction of white matter bulk resulting in thinning of the corpus callosum, and cystic changes in the periventricular frontal white matter (Fig 4*C, -D*).

Patient 8 at 7 years of age had a mild global developmental delay, and MR imaging confirmed persistent delayed myelination (Fig 4*E, -F*).
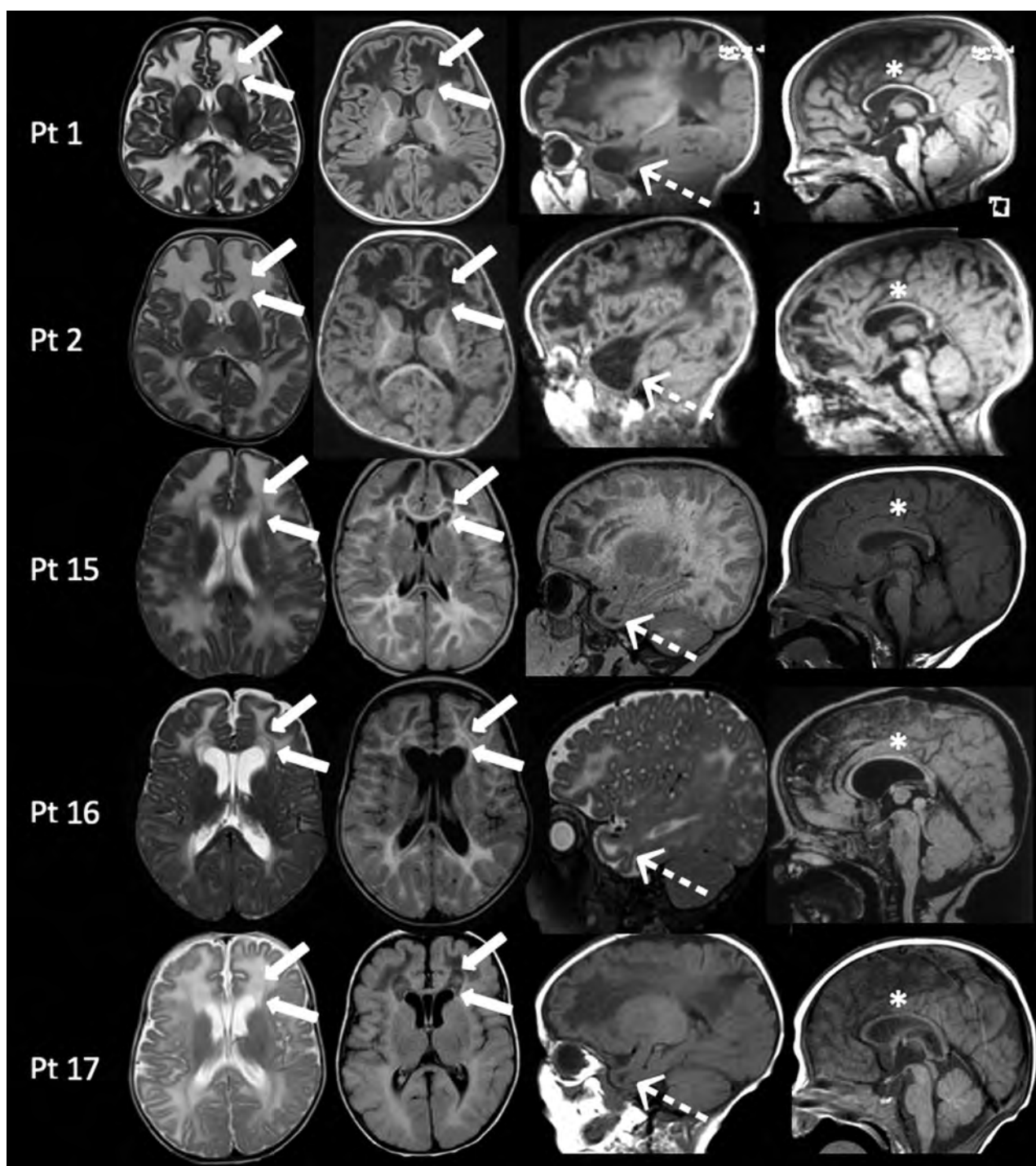
FIG 3. MR imaging findings in patients with galactosemia with subacute clinical presentations between 7 and 18 months of age. In all patients, axial images (*left columns*) show diffuse white matter edema associated with the presence of the double cap sign adjacent to the frontal horns of the lateral ventricles (*arrows*). On sagittal images (*right columns*), MR imaging demonstrates, in all patients, the presence of cystlike lesions of the temporal poles (*dotted arrows*) and thinning of the corpus callosum (*asterisks*). Pt indicates patient.

Patient 15 underwent follow-up MR imaging after dietary restrictions at 2 years of age, which demonstrated complete resolution of brain edema including the double cap sign and cystlike lesions in the temporal poles with patchy periventricular supratentorial white matter abnormalities. In addition, MR spectroscopy demonstrated posttreatment changes, with disappearance of the abnormal galactitol doublet (Fig 2).

DISCUSSION

Since the initial description of galactosemia in 1908, several pathogenic genetic mutations have been identified, and the awareness of the possible clinical presentation has significantly increased with time.[1]

Nelson et al,[9] in 1992, reported the first systematic description of imaging findings highlighting the abnormal T2-hyperintense
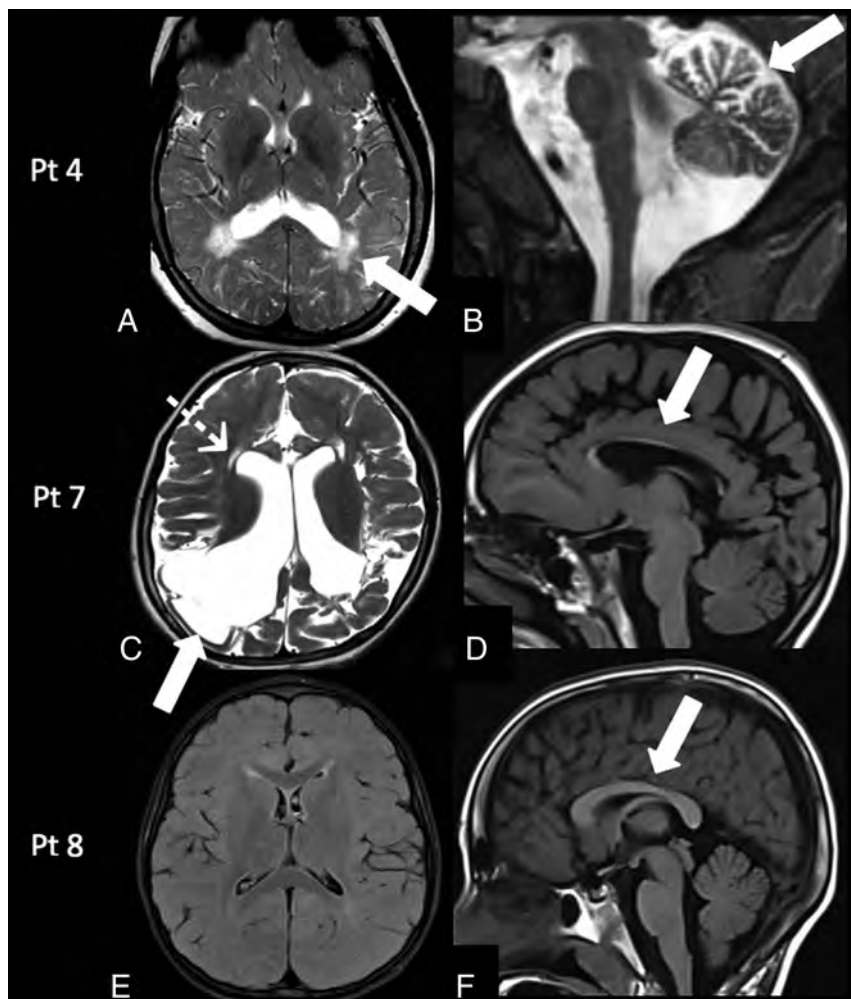
FIG 4. Follow-up MR imaging findings in galactosemia. Patient 4: MR imaging at 13 years of age shows the persistence of the peritrigonal white matter abnormalities on axial T2-weighted image (*A, arrow*) associated with the presence of mild cerebellar atrophy on sagittal T2-weighted image (*B, arrow*). Patient 7: MR imaging at 5 years of age demonstrates encephalomalacic changes in the bilateral cortical and subcortical parieto-occipital regions on axial T2-weighted image (*C, arrow*), with ventricular dilation, cystic changes in the periventricular white matter (*C, dotted arrow*), and corpus callosum thinning on a sagittal T1-weighted image (*D, arrow*). Patient 8: MR imaging at 7 years of age demonstrates persistently delayed myelination on an axial FLAIR image (*E*) and a normal corpus callosum (*F, arrow*). Pt indicates patient.

signal in the peripheral white matter, suggesting delayed myelination. Since then, only a few case reports have been published, mainly focusing on the acute presentation of the disorder.[6,7]

However, it is now evident that all forms of galactosemia present as a continuum disorder in which clinical symptoms depend on the interaction between genetic mutations and environmental factors.[10] Due to lack of a precise pathophysiologic mechanism, galactosemia remains poorly understood, and several multifactorial hypotheses contribute to explaining the disorder, including accumulation of toxic metabolites, defects in galactosylation of glycolipids and glycoproteins, and myo-inositol depletion.[11]

In our series of 17 patients, 3 presented with neonatal toxicity syndrome, a medical emergency characterized by poor feeding, vomiting, bulging of the anterior fontanelle, lethargy, and hypotonia. Impaired activity of the galactose-1-phosphate uridyltransferase enzyme results in accumulation of toxic metabolites,

namely galactitol, galactose-1-phosphate, galactonate, and galactose. Galactitol is an end product of the aldose reductase activity induced by elevated galactose levels.[3] Galactitol is poorly diffusible and highly osmotic, and its intracellular accumulation contributes to cell swelling. This specifically occurs in vulnerable tissues like the lens, predisposing to cataract formation, and in the brain parenchyma, inducing cerebral edema with high mortality in untreated or undiagnosed cases.[12]

During the acute phase of the disease, MR imaging demonstrates diffuse brain edema with increased T2 signal in the white matter and areas of restricted diffusion involving the cortex and deep gray matter nuclei, consistent with cytotoxic edema. MR spectroscopy facilitates the identification of the galactitol doublet at 3.67 and 3.74 ppm, with reduction of myo-inositol-, choline-, and N-acetylaspartate-containing compounds (Fig 1).[7] The increase in morbidity and mortality in the acute clinical setting can be further complicated by *E coli* sepsis, as seen in patient 7 of our study.[13] Prompt initiation of a lactose-free diet along with effective measures to prevent sepsis and coagulopathy are crucial in the clinical outcome of neonatal toxicity syndrome.

In 5 patients of our series, the disease manifested later in life (between 7 and 18 months of age) with subtle presentation, mainly characterized by macrocephaly, hepatomegaly, and psychomotor developmental delay. MR imaging revealed diffuse brain edema, with a peculiar imaging finding, the double cap sign, observed in the frontal lobes (Figs 2 and 3). To our knowledge, these findings have not been described in the imaging literature. They are typically better appreciated on FLAIR images as a darker central zone attributable to accumulation of free water without diffusion restriction on DWI and suggests vasogenic edema within the fibers of the forceps minor. Reversibility of these changes on follow-up imaging was demonstrated, thereby reinforcing and supporting our assumption of vasogenic edema (Fig 2). In addition, cystlike lesions were also noted in the anterior temporal poles (Fig 3). Anterior temporal lobe cysts have been well-described as a hallmark of some congenital diseases and genetic leukoencephalopathies.[14]

We hypothesize that the observed findings may represent the effect of significant vasogenic edema within structures that are normally characterized by an increased free-water content (the

deep white matter) and a more delayed myelination compared with other lobes.[15] This hypothesis could also possibly explain why the FLAIR sequence, which is sensitive to both T1- and T2-relaxation times, may be particularly sensitive to demonstrate the double cap sign by inverting the CSF-like signal within edematous myelinating regions, with higher free-water content in the frontal lobes with partial sparing of myelinated fibers of the forceps minor and the periventricular bright line, normally described on FLAIR images before complete myelination.[15] This finding may serve as a relevant imaging clue to prioritize galactosemia among the list of differential diagnoses. MR spectroscopy was not only pivotal in identifying the galactitol peak, but follow-up imaging also demonstrated resolution of the abnormal spectral pattern and thereby correlates well with initiation and maintenance of an appropriate dietary regimen in our patient (patient 15) (Fig 2).

Despite being on a galactose-free diet, patients may also experience delayed neurologic symptoms, which are believed to be the result of the endogenous production of galactose from glucose and the accumulation of secondary toxic products such as galactitol and galactose-1-phosphate.[16] It is evident that early detection and avoiding complications of acute neonatal toxicity syndrome may prevent cataracts, but it does not alter the overall long-term neurologic morbidity.[3] It is not well-understood whether these complications result from developmental abnormalities that are initiated in utero, long-term exposure to endogenously produced galactose, poor dietary control, or a combination of both and other undetermined factors.[3,4] A prompt diagnosis with early treatment based on galactose dietary restriction is associated with considerable symptom improvement, though some degree of cognitive developmental delay persists, particularly in the language and executive function domains.[17]

In our case series, conventional MR imaging findings in a galactose-free dietary regimen demonstrated a lack of significant signal abnormalities (patients 6 and 12), patchy white matter signal alterations (patients 4, 13, and 15), and delayed myelination (patients 8, 9, 11, and 14). Ventricular enlargement and cerebellar atrophy were also noted, and our observations match those in the existing imaging literature.[9] Although the exact mechanism of injury remains unclear, pathologic studies in the past have suggested the deficiency of galactocerebrosides as a possible cause of myelin breakdown.[18] Impaired myelination has also been postulated from the results of a recent study investigating in vivo microstructural alteration in patients with galactosemia with advanced imaging techniques such as neurite orientation dispersion and density imaging.[19]

In our series, 1 patient (patient 5) presented with severe dystonia, and MR imaging findings at 7 years of age revealed bilateral globus pallidus abnormalities. These findings are atypical for classic galactosemia and may represent a sequela of neonatal kernicterus as reported by the clinical history of the patient. This case highlights the importance of possible comorbidities while evaluating patients affected by galactosemia.

The only efficacious treatment of classic galactosemia is a dietary galactose restriction, though the necessity to maintain a life-long restriction remains a matter of debate and is not sufficient to prevent long-term sequelae.[2,20]

In conclusion, galactosemia is a rare genetic disorder with a continuum spectrum of varying imaging and clinical profiles ranging from a life-threatening acute medical emergency to delayed cognitive effects. Conventional MR imaging features in the delayed phase are often nonspecific and overlap other pathologies. The double cap sign observed in our case series may help in prioritizing galactosemia over other neonatal metabolic diseases, with the added benefit that performing MR spectroscopy to detect a galactitol peak can prevent the complications of the acute neonatal toxicity presentation of galactosemia.

REFERENCES

1. Timson DJ. **The molecular basis of galactosemia: past, present and future.** *Gene* 2016;589:133–41 CrossRef Medline
2. Bosch AM, Maurice-Stam H, Wijburg FA, et al. **Remarkable differences: the course of life of young adults with galactosaemia and PKU.** *J Inherit Metab Dis* 2009;32:706–12 CrossRef Medline
3. Leslie ND. **Insights into the pathogenesis of galactosemia.** *Annu Rev Nutr* 2003;23:59–80 CrossRef Medline
4. Bosch AM. **Classical galactosaemia revisited.** *J Inherit Metab Dis* 2006;29:516–25 CrossRef Medline
5. Coelho AI, Rubio-Gozalbo ME, Vicente JB, et al. **Sweet and sour: an update on classic galactosemia.** *J Inherit Metab Dis* 2017;40:325–42 CrossRef Medline
6. Oliveira TG, Soares-Fernandes JP. **Brain MRI in a patient with classical galactosemia: acute event of unilateral hemispheric cerebral edema.** *Childs Nerv Syst* 2017;33:1879–80 CrossRef Medline
7. Otaduy MC, Leite CC, Lacerda MT, et al. **Proton MT spectroscopy and imaging of a galactosemic patient before and after dietary treatment.** *AJNR Am J Neuroradiol* 2006;27:204–07 Medline
8. Garel C, Cont I, Alberti C, et al. **Biometry of the corpus callosum in children: MR imaging reference data.** *AJNR Am J Neuroradiol* 2011;32:1436–43 CrossRef Medline
9. Nelson MD, Wolff JA, Cross CA, et al. **Galactosemia: evaluation with MR imaging.** *Radiology* 1992;184:255–61 CrossRef Medline
10. Openo KK, Schulz JM, Vargas CA, et al. **Epimerase-deficiency galactosemia is not a binary condition.** *Am J Hum Genet* 2006;78:89–102 CrossRef Medline
11. van der Knaap MS, Valk J. *Magnetic Resonance of Myelination and Myelin Disorders.* New York: Springer-Verlag; 2005
12. Quan-Ma R, Wells HJ, Wells WW, et al. **Galactitol in the tissues of a galactosemic child.** *Am J Dis Child* 1966;112:477–78 CrossRef Medline
13. Rathi N, Rathi A. **Galactosemia presenting as recurrent sepsis.** *J Trop Pediatr* 2011;57:487–89 CrossRef Medline
14. Nunes RH, Pacheco FT, Rocha AD. **Magnetic resonance imaging of anterior temporal lobe cysts in children: discriminating special imaging features in a particular group of diseases.** *Neuroradiology* 2014;56:569–77 CrossRef Medline
15. Murakami JW, Weinberger E, Shaw DW. **Normal myelination of the pediatric brain imaged with fluid-attenuated inversion-recovery (FLAIR) MRI.** *AJNR Am J Neuroradiol* 1999;20:1406–11 Medline
16. Van Der Knaap MS, Van Wezel-Meijler G, Barth PG, et al. **Normal gyration and sulcation in preterm and term neonates:**

appearance on MR images. *Radiology* 1996;200:389–96 CrossRef Medline

17. Doyle CM, Channon S, Orlowska D, et al. **The neuropsychological profile of galactosaemia.** *J Inherit Metab Dis* 2010;33:603–09 CrossRef Medline

18. Haberland C, Perou M, Brunngraber EG, et al. **The neuropathology of galactosemia.** *J Neuropathol Exp Neurol* 1971;30:431–47 CrossRef Medline

19. Timmers I, Zhang H, Bastiani M, et al. **White matter microstructure pathology in classic galactosemia revealed by neurite orientation dispersion and density imaging.** *J Inherit Metab Dis* 2015;38:295–304 CrossRef Medline

20. Broomfield A, Brain C, Grunewald S. **Galactosaemia: diagnosis, management and long-term outcome.** *Paediatr Child Health* 2015;25:113–18 CrossRef

The Restless Spinal Cord in Degenerative Cervical Myelopathy

M. Hupp, N. Pfender, K. Vallotton, J. Rosner, S. Friedl, C.M. Zipser, R. Sutter, M. Klarhöfer, J.M. Spirig, M. Betz, M. Schubert, P. Freund, M. Farshad, and A. Curt

ABSTRACT

BACKGROUND AND PURPOSE: The spinal cord is subject to a periodic, cardiac-related movement, which is increased at the level of a cervical stenosis. Increased oscillations may exert mechanical stress on spinal cord tissue causing intramedullary damage. Motion analysis thus holds promise as a biomarker related to disease progression in degenerative cervical myelopathy. Our aim was characterization of the cervical spinal cord motion in patients with degenerative cervical myelopathy.

MATERIALS AND METHODS: Phase-contrast MR imaging data were analyzed in 55 patients (37 men; mean age, 56.2 [SD,12.0] years; 36 multisegmental stenoses) and 18 controls (9 men, $P = .368$; mean age, 62.2 [SD, 6.5] years; $P = .024$). Parameters of interest included the displacement and motion pattern. Motion data were pooled on the segmental level for comparison between groups.

RESULTS: In patients, mean craniocaudal oscillations were increased manifold at any level of a cervical stenosis (eg, C5 displacement: controls [$n = 18$], 0.54 [SD, 0.16] mm; patients [$n = 29$], monosegmental stenosis [$n = 10$], 1.86 [SD, 0.92] mm; $P < .001$) and even in segments remote from the level of the stenosis (eg, C2 displacement: controls [$n = 18$], 0.36 [SD, 0.09] mm; patients [$n = 52$]; stenosis: C3, $n = 21$; C4, $n = 11$; C5, $n = 18$; C6, $n = 2$; 0.85 [SD, 0.46] mm; $P < .001$). Motion at C2 differed with the distance to the next stenotic segment and the number of stenotic segments. The motion pattern in most patients showed continuous spinal cord motion throughout the cardiac cycle.

CONCLUSIONS: Patients with degenerative cervical myelopathy show altered spinal cord motion with increased and ongoing oscillations at and also beyond the focal level of stenosis. Phase-contrast MR imaging has promise as a biomarker to reveal mechanical stress to the cord and may be applicable to predict disease progression and the impact of surgical interventions.

ABBREVIATIONS: DCM = degenerative cervical myelopathy; ECG = electrocardiography; PCMR = phase-contrast MR imaging; RR = R wave-to-R wave interval in the ECG

D egenerative changes of the cervical spine lead to cervical spinal stenosis, with consecutive spinal cord compression and degenerative cervical myelopathy (DCM), a common health burden in the elderly population.[1] The pathophysiology of DCM is attributed to immediate (ie, direct or static) cord compression, spinal malalignment leading to altered cord tension, impaired vascular supply, and repeat dynamic injury.[2-5] Dynamic spinal cord injury is often narrowed to segmental hypermobility; however, cardiac-related periodic cord motion may play a by far underestimated role in this pathophysiologic consideration. The cervical spinal cord is subject to physiologic craniocaudal motion supposedly due to cardiac pulse wave dynamics, which can be readily assessed by phase-contrast MR imaging (PCMR).[6,7] In a person with 70 heartbeats per minute, the spinal cord oscillates >100,000 times per day. In patients with DCM, increased spinal cord motion at the level of the cervical stenosis has been independently reported.[8-11] However, due to differences in analysis techniques applied,[8,10,11] results are not sufficiently comparable. Most interesting, increased spinal cord motion was associated with sensory deficits,[8,10] impaired electrophysiologic readouts,[10] and decreased functional scores in patients with DCM.[11] While measurements of CSF flow have been shown to be less reliable and rather complex (ie, not easy to implement and run for clinical application) at the level of stenosis,[11] spinal cord motion appears to be a more feasible alternative.

In summary, altered spinal cord motion provides a potential surrogate of spinal cord tissue distress, contributing to intramedullary damage even before it becomes clinically evident; therefore, it warrants further research to reveal mechanisms of cord damage in cervical spinal cord stenosis.

We hypothesisized the following: 1) The cord motion pattern during the cardiac cycle is altered in patients with DCM, and 2) due to elastic properties of the spinal cord and its surroundings, increased cord motion will extend to segments remote from the spinal stenosis.

In axial PCMR, craniocaudal spinal cord motion within the cardiac cycle was tracked with an evaluation method established in healthy controls.[6] In summary, cord displacement was measured 20 times during the cardiac cycle using a predefined ROI and corrected for the phase drift.

MATERIALS AND METHODS
Population
A consecutive series of 55 patients, prospectively recruited in the outpatient clinic of the University Spine Center, University Hospital Balgrist, Zurich, from October 2016 to August 2019, was used for analysis. Inclusion criteria for patients were a cervical spinal stenosis on MR imaging and clinical symptoms consistent with degenerative cervical myelopathy. Clinical symptoms of DCM comprised pain, sensory or motor deterioration in the upper or lower limbs, gait problems, or bladder dysfunction. Patients with any other neurologic disorder (identified by medical history and neurologic examination) were excluded. In patients with suspicion of any other neurologic disease (eg, radiculopathy at the lower limbs, polyneuropathy, CNS disorders), further examinations (eg, cranial MR imaging, electrophysiologic examinations) were conducted before study inclusion. Eighteen healthy subjects were randomly recruited (randomly chosen from a list) from a research data base of the University Hospital Balgrist, Zurich. Controls had neither neurologic symptoms nor a stenosis on MR imaging. The age for inclusion was 18–80 years. Exclusion criteria consisted of general MR imaging contraindications, epileptic seizures, mental illness, severe medical illness, and pregnancy.

Standard Protocol Approvals, Registrations, and Patient Consents
This prospective study was approved by the local ethics committee (Kantonale Ethikkommission Zurich, KEK-ZH 2012–0343, BASEC Nr. PB_2016-00623) and registered with clinicaltrials.gov (www.clinicaltrials.gov; NCT 02170155). All methods were in accordance with the relevant guidelines and regulations. Informed consent was obtained from all participants before study enrolment. Study data were collected and managed using REDCap electronic data capture tools (https://projectredcap.org/software/) hosted at Balgrist University Hospital, Zurich, Switzerland.[12]

Imaging
All subjects underwent a 3T MR imaging (Magnetom Skyra fit and Magnetom Prisma; Siemens), including axial T2-weighted (TE = 93 ms; TR = 3600 ms; section thickness = 3 mm; flip angle = 150°; FOV = 160 mm; bandwidth = 284 Hz/Px; base resolution = 320; phase resolution = 80%; spatial resolution = 0.5 × 0.5 × 3.0 mm; parallel acquisition techniques mode: generalized autocalibrating partially parallel acquisition 2) and axial 2D phase-contrast imaging encoding craniocaudal spinal cord motion (TE = 12.36 ms; TR = 60.84 ms; section thickness = 5 mm; flip angle = 10°; FOV = 140 mm; bandwidth = 355 Hz/Px; base resolution = 256; phase resolution = 50%; spatial resolution = 0.3 × 0.3 × 5.0 mm; parallel acquisition techniques mode: none; retrospectively cardiac gated using a finger clip). The velocity encoding value of the phase-contrast sequence was set to 2 cm/s based on previous findings of cord motion.[6,8-11,13] During the cardiac cycle, the velocity signal was assessed within 20 time points, and 128 cardiac cycles were averaged per segment. Section orientation in phase-contrast imaging was adjusted perpendicular to the spinal cord. Axial T2-weighted imaging covered segments C2–C6 in all patients and segment C7 in 32 of 55 patients. In controls, axial T2-weighted imaging covered all cervical segments. Section orientation in axial T2-weighted imaging was adjusted to cover most of the spinal cord within the FOV perpendicularly. Breathing was not monitored in any participant. Total scanning time of the whole protocol was approximately 23 minutes.

In all patients, the C2 segment and the stenotic segment (loss of CSF signal in axial T2-weighted imaging ventral and dorsal to the spinal cord) (monosegmental stenosis), respectively, the most stenotic segment (defined as maximum spinal canal narrowing in patients with a multisegmental stenosis) were measured. The stenotic and most stenotic segment, respectively, were judged visually in T2-weighted imaging by 2 investigators (N.P., M.H.; consultant neurologists) well-experienced in neuroradiologic imaging with a focus on spinal cord disorders for several years. In all patients, depending on the available scanning time within the clinical setting, additional measurements in as many as possible other stenotic (multisegmental stenosis) and nonstenotic (monosegmental and multisegmental stenoses) cervical segments were obtained (randomly selected by the investigator [N.P., M.H., Table 1; on average, 2.8 segments per patient). In controls, all cervical segments were recorded.

Imaging Analysis
Image analyses were performed using the Osirix free DICOM viewer (www.osirix-viewer.com) and the Horos free DICOM viewer (www.horosproject.org) by 2 investigators (N.P., M.H.). Imaging analyses were supported by a radiologist (R.S.) and a physicist (M.K.). Cervical segments were classified as "stenotic" or "nonstenotic" for analysis. A stenotic segment was defined as a loss of the CSF signal on axial T2-weighted imaging ventral and dorsal to the spinal cord. Segments with visible CSF signal in axial T2-weighted imaging ventral and/or dorsal to the spinal cord were defined as nonstenotic. Additional nonstenotic segments (in patients with monosegmental and multisegmental stenoses, respectively) were measured 1–4 segments apart and stenotic segments (in patients with a multisegmental stenosis) 1–2 segments apart from the next cervical stenosis. Phase-contrast images were visually controlled for artifacts before further analysis. In 55 patients, a total of 154 segmental PCMR measurements were obtained. Due to artifacts, 13 (8.4%) measurements (C2, 2/5 [3.6%]; C3, 1/17 [5.8%]; C4, 0/25; C5, 4/39 [10.3%]; C6, 6/16 [37.5%]; C7, 0/2) could not be used for analysis (Table 1). In 18 controls, no artifacts were observed.

Table 1: Number of stenotic segments and number of sufficient phase-contrast measurements in patients

Segment	No. Stenotic Segments	No. Sufficient Measurements			
		Monosegmental Stenosis, Stenotic Segment	Multisegmental Stenosis, Stenotic Segment	Monosegmental Stenosis, Nonstenotic Segment	Multisegmental Stenosis, Nonstenotic Segment
C2	1	0	1	18	34
C3	22	1	14	0	1
C4	23	4	14	4	3
C5	41	10	19	4	2
C6	22	0	5	4	1
C7	1	0	1	0	1
Total	110	15	54	30	42

Data Calculations and Parameters of Interest

In phase-contrast measurements, craniocaudal spinal cord motion was analyzed by a predefined ellipsoid ROI ($30.52\,mm^2$ in the Osirix Viewer; $30.56\,mm^2$ in the Horos Viewer) midcentered into the spinal cord (Online Supplemental Data). In a subgroup of 10 consecutive patients (22 measurements; C2, ten measurements; C3, four measurements; C4, two measurements; C5, five measurements; C6, one measurement), motion was analyzed in the ventral, dorsal, and right and left aspects of the spinal cord (round ROI, $5.60\,mm^2$; comparison between different regions within the spinal cord over all measurements; Online Supplemental Data). The predefined velocity encoding (2 cm/s) encoded in gray-scale values from -4096 to 4096 in the Osirix and Horos Viewers, respectively. The mean of the measured gray-scale values within the ROI in each of 20 time points during 1 cardiac cycle was used for calculation of the velocity. Velocity data were corrected for phase drift before further statistical analysis. Because phase-contrast imaging is a relative measure of motion, phase drift[14] leads to an offset error of the raw data ending in misleading velocity values. Therefore, phase drift will result in over- or underestimation of the velocity measurements, so a correction for phase drift is needed. Phase drift correction was conducted analogous to healthy subjects previously.[6] Corrected values were obtained by subtraction of the mean of all 20 velocity measurements within 1 cardiac cycle from the raw velocity value at each time point. Net motion of the spinal cord over 1 cardiac cycle is assumed to be zero (the start and end locations of the spinal cord are expected to be at the same position, assuming that the mean velocity has to be zero). Other approaches to velocity correction (ie, subtraction of velocity values of static tissue surrounding the spinal cord) were dropped due to low reliability previously.

Parameters of interest included the area under the curve (displacement) of the velocity signal over the whole cardiac cycle, within the first (time points 1–10) and second (time points 11–20) half of the cardiac cycle, and the spinal cord motion pattern. The area under the curve was calculated by stepwise summation of calculated squared areas (1/20 RR time multiplied by the mean of 2 consecutive velocity values). Negative velocity values were transformed to a positive value for calculation of the area under the curve. For the spinal cord motion pattern analysis, the velocity value in all 20 time points during 1 cardiac cycle was plotted for single values and the mean of all values per segment. The time point of the motion onset (first negative deflection) and the time point of the subsequent negative and positive motion peak, respectively, within the cardiac cycle (time points 1–20) were manually (visually) identified and analyzed.

Anatomic Measurements

In axial T2-weighted images, the spinal canal and spinal cord cross-sectional areas at the disc level were manually measured in all cervical segments. CSF space was calculated by the spinal canal cross-sectional area minus the spinal cord cross-sectional area.

Statistical Analysis

Statistical analysis was performed using SPSS (Versions 23 and 25; IBM). Measurements were pooled by the cervical segment because previous work showed differences in spinal cord motion among the cervical segments.[6] Measurements in segments classified as stenotic and nonstenotic, respectively (pooled by the cervical segment; entire patient group, monosegmental and multisegmental stenoses; patients with monosegmental stenosis only; patients with multisegmental stenosis only), were compared with measurements in controls and between the patient groups. Additional analyses investigated the influence of the number of stenotic segments and how measures of cord motion changed in relation to the distance from the stenotic segment (pooled by the distance to the next stenotic segment or the number of stenotic segments; comparison between patient groups and controls). Metrics are reported as group mean [SD]. Between-group differences were calculated using the Mann-Whitney U test (anatomic measurements, motion measurements, body size, body weight, age, RR time/heart rate, motion onset and peaks) and the χ^2 test (sex) if the number of measurements was at least 2 per group. For comparison of >2 groups, the Kruskal-Wallis test with the Bonferroni correction for multiple comparisons was used (distance to next stenosis, number of stenoses, motion in different spinal cord areas). Significance level of α was set to $<.05$.

Interrater Reliability

Interrater reliability in healthy volunteers has been reported in a previous study.[6] Interrater reliability in patients was assessed by calculating intraclass correlation coefficients (2-way mixed model, absolute agreement, average measures). Two independent raters evaluated 34 consecutive patients using 2 different programs (rater 1, Osirix Viewer; rater 2, Horos Viewer) with manually configured ROIs with ellipsoid shapes of nearly the same size ($30.52\,mm^2$, Osirix Viewer; $30.56\,mm^2$, Horos Viewer). Additionally, the intraclass correlation coefficients of anatomic measurements and the spinal cord pattern analyses were calculated.

Data Availability

The datasets generated and analyzed during the current study are available from the corresponding author on reasonable request.

Table 2: Basic demographics of the control and patient group

	Controls (n = 18)	Patients (n = 55)	P
Sex (male)	9 (50%)	37 (67.3%)	.368
Age (yr)	62.2 [SD, 6.5]	56.2 [SD, 12.0]	.024
Body size (m)	1.70 [SD, 0.06]	1.70 [SD, 0.08]	.947
Body weight (kg)	67.2 [SD, 12.3]	77.9 [SD, 13.6]	.007
Monosegmental stenosis		19 (34.5%)	
Multisegmental stenosis		36 (65.5%)	

RESULTS

Population

Fifty-five patients (37 men; 67.3%) and 18 healthy controls (9 men; 50%) were recruited. No differences between the groups were found for sex ($P = .368$), body size ($P = .947$), or RR time/ heart rate ($P = .263–.961$), but patients were younger ($P = .024$) and had a higher body weight ($P = .007$) (Table 2). In the patient group, 19 (34.5%) had a single stenosis and 36 (65.5%) had multiple stenotic segments (Tables 1 and 2). CSF spaces in patients' segments classified as stenotic were significantly smaller compared with segments classified as nonstenotic ($P < .001$, Fig 1).

Reliability of Anatomic and Spinal Cord Motion Measurements

The excellent interrater reliability of spinal cord motion measurements shown in controls previously[6] could be confirmed in patients (intraclass correlation coefficient, 0.838–1.000; $P \leq .020$; Online Supplemental Data). At C7, no calculation was possible due to the small number of measurements. Reliability was also good for anatomic measurements (intraclass correlation coefficient, 0.806–0.938; $P < .001$; Online Supplemental Data).

Altered Spinal Cord Motion Pattern in Patients

In the entire patient group (monosegmental and multisegmental stenoses), the craniocaudal and afterward caudocranial oscillation pattern was comparable with that in controls (stenotic segments: Fig 2; nonstenotic segments: Online Supplemental Data), but the magnitude of the oscillation was increased, corresponding to manifold higher mean displacement values at stenotic (C3 [$n = 15$]: 1.882 [SD, 1.278] mm versus 0.420 [SD, 0.113] mm; C4 [$n = 18$]: 2.149 [SD, 1.343] mm versus 0.484 [SD, 0.128] mm; C5 [$n = 29$]: 1.863 [SD, 0.915] mm versus 0.543 [SD, 0.159] mm; C6 [$n = 5$]: 2.021 [SD, 0.934] mm versus 0.491 [SD, 0.098] mm; $P < .001$; number of controls [$n = 18$] in all segments) but also nonstenotic (C2 [$n = 52$]: 0.852 [SD, 0.464] mm versus 0.362 [SD, 0.094] mm; C4 [$n = 7$]: 1.677 [SD, 0.956] mm versus 0.484 [SD, 0.128] mm; C5 [$n = 6$]: 1.725 [SD, 0.912] mm versus 0.543 [SD, 0.159] mm; C6 [$n = 5$]: 1.712 [SD, 0.640] mm versus 0.491 [SD, 0.098] mm; $P \leq .025$; number of controls [$n = 18$] in all segments) segments (Fig 3 and Online Supplemental Data).

The same was true in subgroup analysis in patients with monosegmental ([$n = 19$]; stenotic segments: C4 [$n = 4$]: 2.015 [SD, 1.361] mm versus 0.484 [SD, 0.128] mm; C5 [$n = 10$]: 2.036 [SD, 1.271] mm versus 0.491 [SD, 0.098] mm; $P < .001$;

nonstenotic segments: C2 [$n = 18$]: 0.719 [SD, 0.222] mm versus 0.362 [SD, 0.094] mm; C4 [$n = 4$]: 1.281 [SD, 0.790] mm versus 0.484 [SD, 0.128] mm; C5 [$n = 4$]: 1.818 [SD, 0.547] mm versus 0.543 [SD, 0.159] mm; C6 [$n = 4$]: 1.455 [SD, 0.326] mm versus 0.491 [SD, 0.098] mm; $P < .001$; number of controls [$n = 18$] in all segments) and, respectively, multisegmental ([$n = 36$]; stenotic segments: C3 [$n = 14$]: 1.924 [SD, 1.316] mm versus 0.420 [SD, 0.113] mm; C4 [$n = 14$]: 2.187 [SD, 1.388] mm versus 0.484 [SD, 0.128] mm; C5 [$n = 19$]: 1.772 [SD, 0.685] mm versus 0.491 [SD, 0.098] mm; C6 [$n = 5$]: 2.021 [SD, 0.934] mm versus 0.491 [SD, 0.098] mm; $P < .001$; nonstenotic segments: C2 [$n = 34$]: 0.922 [SD, 0.540] mm versus 0.362 [SD, 0.094] mm; C4 [$n = 3$]: 2.205 [SD, 1.035] mm versus 0.484 [SD, 0.128] mm; $P \leq .002$; C5 [$n = 2$]: 1.540 [SD, 1.776] mm versus 0.543 [SD, 0.159] mm; $P = 1.000$; number of controls [$n = 18$] in all segments) stenoses in subgroups with >2 measurements (Online Supplemental Data).

The detailed analysis of the velocity pattern did not show a difference in the timing of the motion onset (first negative deflection; stenotic segments: $P \geq .424$; nonstenotic segments: $P \geq .326$) and the subsequent negative velocity peak (stenotic segments: $P \geq .161$; nonstenotic segments: $P \geq .074$) between all patients (monosegmental and multisegmental stenoses) and controls in stenotic and nonstenotic segments (Online Supplemental Data). Most interesting, the mean positive velocity peak in the second half of the cardiac cycle in stenotic segments C3–C6 (time points: patients [entire patient group] versus controls ($n = 18$): C3 [$n = 15$]: 18.13 [SD, 1.13] versus 16.61 [SD, 1.85]; C4 [$n = 18$]: 18.33 [SD, 1.09] versus 16.11 [SD, 2.06]; C5 [$n = 23$]: 17.93 [SD, 1.13] versus 16.56 [SD, 1.85]; C6 [$n = 5$]: 18.60 [SD, 1.52] versus 16.17 [SD, 2.01]; $P \leq .018$) and in the nonstenotic segment, C4 (patients, entire patient group [$n = 7$] versus controls [$n = 18$]: 18.14 [SD, 1.07] versus 16.11 [SD, 2.0]; $P = .021$) was prolonged in patients (Fig 4 and Online Supplemental Data).

Subgroup analysis in patients with monosegmental and multisegmental stenoses, respectively confirmed a delay of the mean positive motion peak in patients with a multisegmental stenosis (time points, patients versus controls [$n = 18$]: stenotic segments: C3 ($n = 14$): 18.14 [SD, 1.17] versus 16.61 [SD, 1.85]; C4 [$n = 14$]: 18.43 [SD, 1.16] versus 16.11 [SD, 2.06]; C5 [$n = 19$]: 18.26 [SD, 0.99] versus 16.56 [SD, 1.85]; C6 [$n = 5$]: 18.60 [SD, 1.52] versus 16.17 [SD, 2.01]; $P \leq .015$; nonstenotic segment: C4 [$n = 3$]: 18.67 [SD, 0.58] versus 16.11 [SD, 2.06]; $P = .035$; Online Supplemental Data).

Additionally, the mean negative motion peak in patients with multisegmental stenoses was delayed at C4 in nonstenotic segments compared with controls ($n = 3$; 13.67 [SD, 0.58] versus 12.28 [SD, 0.96]; $P = .024$). In patients with a monosegmental stenosis, a trend for a delay of the mean positive velocity peak could be found at C4 in stenotic ($n = 4$; 18.00 [SD, 0.82] versus 16.11 [SD, 2.06]; $P = .141$) and nonstenotic ($n = 4$; 17.75 [SD, 1.26] versus 16.11 [SD, 2.06]; $P = .166$) segments compared with controls. While hardly any motion could be observed within the first half (time points 1–10) of the cardiac cycle in healthy controls (reflecting a "resting phase"), spinal cords in most patients showed continuous upward motion during this part of the cycle. This was observed at the stenosis (Fig 2) and also at nonstenotic segments (Online Supplemental Data). Displacement separately calculated for the first (time points 1–10) and the
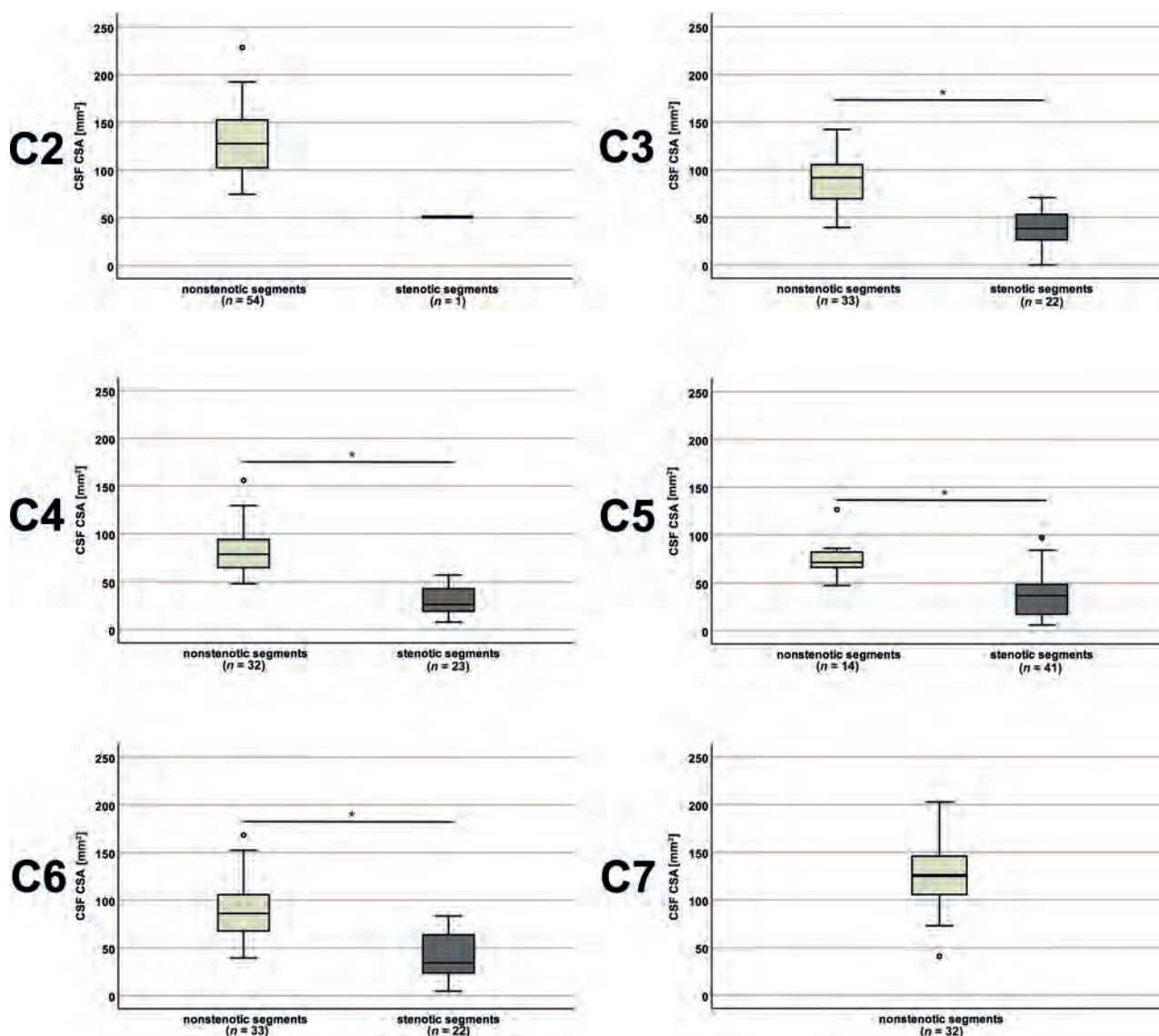
FIG 1. CSF space in controls and patients The CSF cross-sectional area (CSA) was smaller in patients with segments classified as stenotic (*dark gray plots*) compared with segments classified as nonstenotic (*light gray plots*). At C7 in 32 patients, the CSA was available, but no segment was classified as stenotic. The *asterisk* indicates $P < .001$.

second half of the cardiac cycle (time points 11–20) also revealed highly increased values between patients (monosegmental and multisegmental stenoses) and controls in both parts in stenotic and nonstenotic segments ($P \leq .015$; Online Supplemental Data). The same was true in subgroup analysis in patients with monosegmental ($P \leq .003$; Online Supplemental Data) and multisegmental ($P \leq .002$; Online Supplemental Data) stenoses, respectively, in patient groups with >2 measurements.

Motion Differences between Segments Classified as Stenotic and Nonstenotic

No differences of the displacement or the timing of the spinal cord motion pattern could be found between measurements in stenotic and nonstenotic segments in the entire patient group (monosegmental and multisegmental stenoses) and the

subgroups with monosegmental and multisegmental stenoses, respectively.

Motion Differences between Patients with Mono- and Multisegmental Stenoses

At C2 in patients with a multisegmental cervical stenosis ($n = 34$; distance to next stenosis: 1 segment/stenosis, C3, $n = 20$; two segments/stenosis, C4, $n = 6$; three segments/stenosis, C5, $n = 8$), displacement in the first half of the cardiac cycle was increased compared with patients with a monosegmental stenosis ($n = 18$; distance to next stenosis: 1 segment/stenosis, C3, $n = 1$; two segments/stenosis, C4, $n = 5$; three segments/stenosis, C5, $n = 10$; four segments/stenosis, C6, $n = 2$) in nonstenotic segments (mean, 0.289 [SD, 0.210] mm versus 0.189 [SD, 0.085] mm; $P = .048$). This difference was lost in subgroup analysis with regard to the distance to the next stenosis (distance to next stenosis: 1 segment/stenosis, C3:

healthy controls **patients**

C3 (n = 18) | (n = 15)

C4 (n = 18) | (n = 18)

C5 (n = 18) | (n = 29)

C6 (n = 18) | (n = 5)
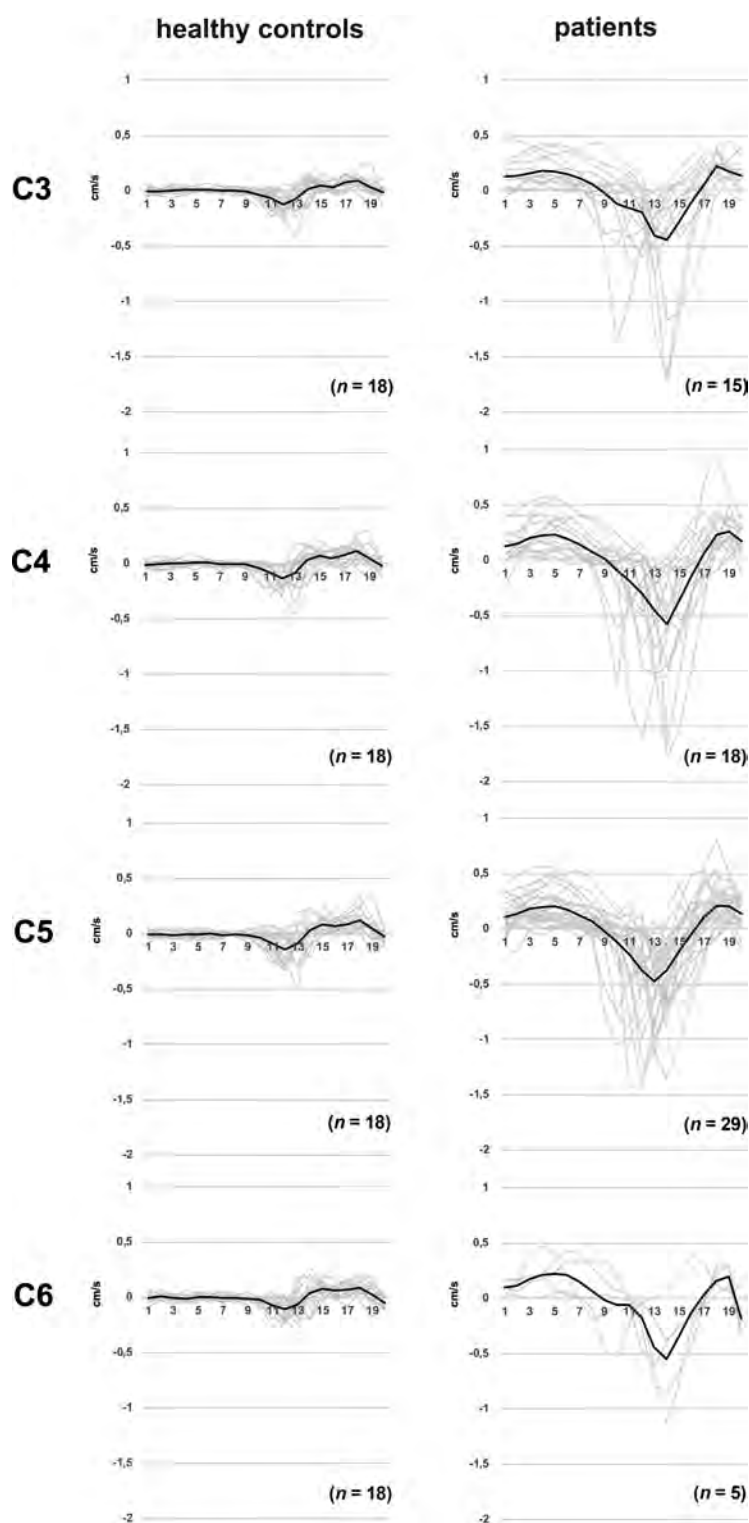
FIG 2. Spinal cord motion pattern in healthy controls and patients (stenotic segments). Spinal cord velocity values are displayed within 20 time points during the cardiac cycle in healthy controls (*left column*) and stenotic segments in patients (monosegmental and multisegmental stenoses, *right column*). Velocity values are pooled per cervical segment. Single measures are displayed in light gray; the *black line* represents the group mean.

stenosis, C5: monosegmental, $n = 10$; multisegmental, $n = 8$; $P = .460$; Online Supplemental Data).

In the analysis of the motion velocity pattern, a trend toward a delayed positive motion peak in patients with a multisegmental stenosis could be found at C2 in segments classified as nonstenotic (multisegmental [$n = 34$]; distance to next stenosis: 1 segment/stenosis, C3 [$n = 20$]; two segments/stenosis, C4, [$n = 6$]; three segments/stenosis, C5 [$n = 8$]: mean, 18.06 [SD, 1.09] versus monosegmental [$n = 18$]; distance to next stenosis: 1 segment/stenosis, C3, [$n = 1$]; two segments/stenosis, C4, [$n = 5$]; three segments/stenosis, C5, [$n = 10$]; four segments/stenosis, C6, [$n = 2$]: mean, 17.44 [SD, 1.10]; $P = .063$). In subgroup analysis with regard to the distance to the next stenosis, this trend could be seen at C2 in measurements 3 segments apart from the next stenosis (distance to next stenosis: 2 segments/stenosis, C4; monosegmental [$n = 5$] mean, 17.80 [SD, 0.84]; multisegmental [$n = 6$] mean, 18.17 [SD, 0.7]; $P = .537$; three segments/stenosis, C5; monosegmental [$n = 10$] mean, 17.30 [SD, 1.34]; multisegmental [$n = 8$] mean, 18.50 [SD, 0.93]; $P = .068$).

Motion Differences Regarding the Distance to the Next Stenosis and the Number of Stenotic Segments

Displacement at C2 in the entire patient group (monosegmental and multisegmental stenoses) in nonstenotic segments was increased with the proximity to the next stenotic segment (distance to next stenosis: 1 segment/stenosis, C3 [$n = 21$]: mean, 1.074 [SD, 0.622] mm; 2 segments/stenosis, C4 [$n = 11$]: mean, 0.769 [SD, 0.285] mm; 3 segments/stenosis, C5 [$n = 18$]: mean, 0.691 [SD, 0.166] mm; 4 segments/stenosis, C6 [$n = 2$]: mean, 0.420 [SD, 0.025] mm; $P = .039$, Fig 5A). Subgroup analysis in patients with a monosegmental and multisegmental stenoses, respectively, showed a corresponding trend (displacement in the entire cardiac cycle: monosegmental: [$n = 18$]; distance to next stenosis: 1 segment/stenosis, C3 [$n = 1$] 0.900 mm; 2 segments/stenosis, C4 [$n = 5$] mean, 0.819 [SD, 0.247]; mm; 3 segments/stenosis, C5 [$n = 10$] mean, 0.710 [SD, 0.247] mm; 4 segments/stenosis, C6 [$n = 2$] mean, 0.420 [SD, 0.024] mm; $P = .113$; multisegmental: [$n = 34$]; distance to next stenosis: 1 segment/stenosis, C3 [$n = 20$] mean, 1.082 [SD, 0.637] mm; 2 segments/stenosis C4 [$n = 6$] mean, 0.728 [SD, 0.330] mm; 3 segments/stenosis C5 [$n = 8$] mean, 0.667 [SD, 0.136] mm; $P = .173$; displacement at second half of the cardiac cycle: monosegmental: [$n = 18$]; $P = .069$; multisegmental: [$n = 34$]; $P = .108$, Online Supplemental Data).
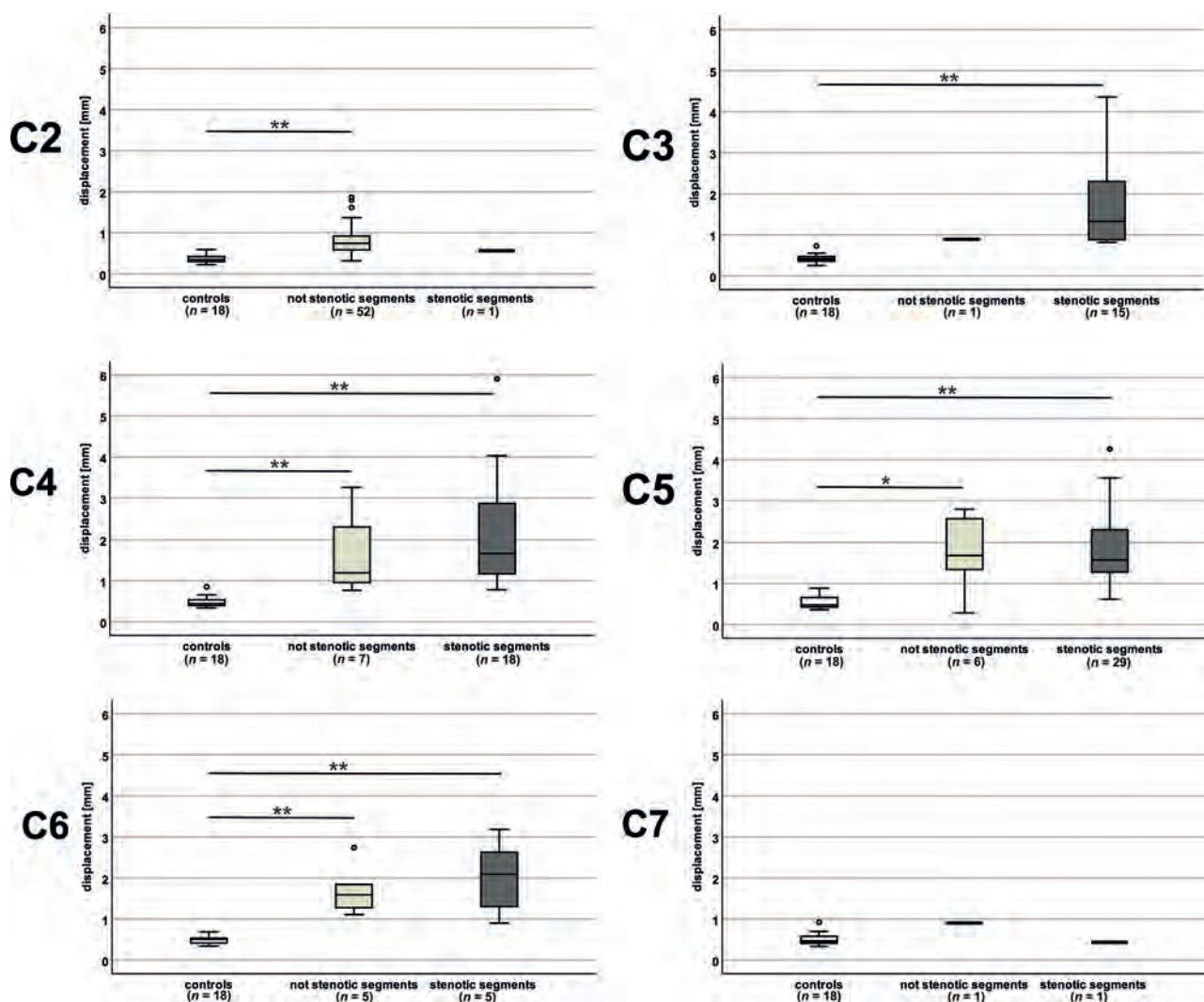
monosegmental, $n = 1$; multisegmental, $n = 20$; no analysis due to low monosegmental group size; 2 segments/stenosis, C4: monosegmental, $n = 5$; multisegmental, $n = 6$; $P = .429$; three segments/

FIG 3. Displacement values in controls and patients. Displacement values (entire cardiac cycle) are increased manifold in patients (monosegmental and multisegmental stenoses) in segments classified as stenotic (*dark gray plots*) and nonstenotic (*light gray plots*) compared with controls (*white plots*). In groups with only 1 measurement, no analysis was possible. *Double asterisks* indicate $P < .001$; *asterisk*, $P = .015$.

Compared with controls, motion values in patients at the nonstenotic segment C2 were increased up to 3 segments apart from the next cervical stenosis (distance to next stenosis: 1 segment/stenosis, C3: multisegmental [$n = 20$]; $P < .001$; two segments/stenosis, C4: monosegmental [$n = 5$]; $P \leq .001$; multisegmental [$n = 6$]; $P \leq .015$, [$P = .066$ for displacement in the second half of the cardiac cycle]; 3 segments/stenosis, C5: monosegmental [$n = 10$]; $P < .001$; multisegmental [$n = 8$]; $P < .001$; Online Supplemental Data). The same was true in patients with a monosegmental stenosis in nonstenotic segments, C4 ($n = 4$; $P < .001$), C5 ($n = 4$; $P < .001$), and C6 ($n = 4$; $P = .002$) 1 segment apart from the next stenosis. In patients with a multisegmental stenoses in stenotic segments, C3 (distance to the next stenosis: 1 segment: [$n = 9$]; $P < .001$; 2 segments: [$n = 4$]; $P < .001$), and C5 (distance to next stenosis: 1 segment: [$n = 14$]; $P < .001$; 2 segments: [$n = 5$]; $P < .001$) up to 2 segments apart and in nonstenotic ($n = 3$, $P = .002$) and stenotic segments, C4 ($n = 13$; $P < .001$) and stenotic segments C6 ($n = 4$; $P < .001$) 1 segment apart from the

next cervical stenosis motion was increased compared to controls. Additionally, displacement at C2 in nonstenotic segments was different according to the number of stenotic segments in the entire (monosegmental and multisegmental) patient group (number of stenotic segments: 1 [$n = 18$]: mean, 0.719 [SD, 0.222] mm; 2 [$n = 20$]: mean, 0.880 [SD, 0.415] mm; 3 [$n = 10$]: mean, 1.173 [SD, 0.743] mm; 4 [$n = 4$]: mean, 0.504 [SD, 0.097] mm; $P = .036$; Fig 5B). The same was true for the displacement within the first half of the cardiac cycle (number of stenotic segments: 1 [$n = 18$]: mean, 0.189 [SD, 0.085] mm; 2 [$n = 20$]: mean, 0.267 [SD, 0.168] mm; 3 [$n = 10$]: mean, 0.383 [SD, 0.287] mm; 4 [$n = 4$]: mean, 0.162 [SD, 0.080] mm; $P = .036$; $P = .047$). A subgroup analysis in the patient group with a multisegmental stenosis showed analogous results ($n = 34$; number of stenotic segments: 2 [$n = 20$]: mean, 0.880 [SD, 0.415] mm; 3 [$n = 10$]: mean, 1.173 [SD, 0.743] mm; 4 ($n = 4$): mean, 0.504 [SD, 0.097] mm; $P = .029$). While a trend toward higher motion values could be assumed with an increasing number of 1–3 stenotic segments, lower values could be observed in patients with 4 stenotic segments.
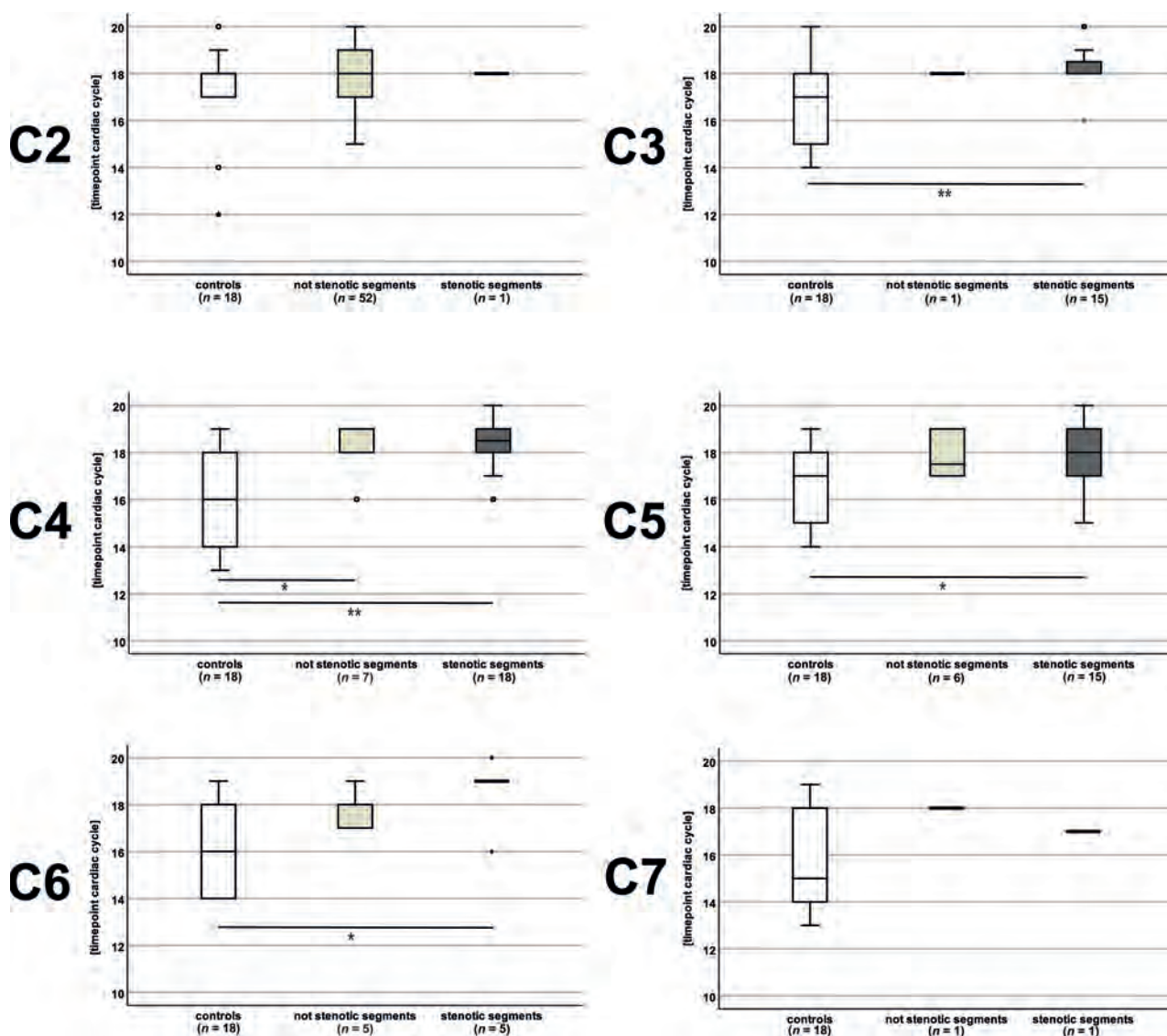
FIG 4. Timing of the positive motion peaks in controls and patients. The positive motion peak was delayed in patients (monosegmental and multisegmental stenoses) in segments classified as stenotic (*dark gray plots*) at C3, C4, C5, and C6 and in segments classified as nonstenotic (*light gray plots*) at C4 compared with controls (*white plots*). In groups with only 1 measurement, no analysis was possible. *Double asterisks* indicate $P < .01$; *asterisk*, $P \le .021$.

Motion Differences between Different Regions of the Spinal Cord

No motion differences could be found comparing the ventral, dorsal, and right and left aspects of the spinal cord (10 consecutive patients; 22 measurements; C2: 10 measurements; C3: four measurements; C4: two measurements; C5: five measurements; C6: one measurement; Online Supplemental Data).

DISCUSSION

This is the first study analyzing spinal cord motion in patients with a cervical spinal stenosis also remote from the stenotic segment, focusing on the motion pattern throughout the cardiac cycle and the impact of the distance to the next stenotic segment and the number of cervical stenotic segments. In addition to a previously reported increase of cord movement

in cervical stenosis,[7-11,15] our findings revealed a propagation of increased motion to the adjacent cervical segments up to 3 segments apart from the next cervical stenosis and continuous ("restless") spinal cord movement throughout the whole cardiac cycle in patients, reflecting an emerging pathophysiologic pattern. A resting phase without motion during the first half of the cardiac cycle, which could be observed in healthy controls, was lost in patients irrespective of and remote from the cervical level of stenosis. This finding suggests continuous and increased mechanical stress to the spinal cord tissue as a prominent and potentially contributing dynamic factor in DCM pathophysiology.[1,3,16-19]

Feasibility-Reliability

For feasibility, high interrater and test-retest reliability of the method was reported previously in healthy controls[6] and could
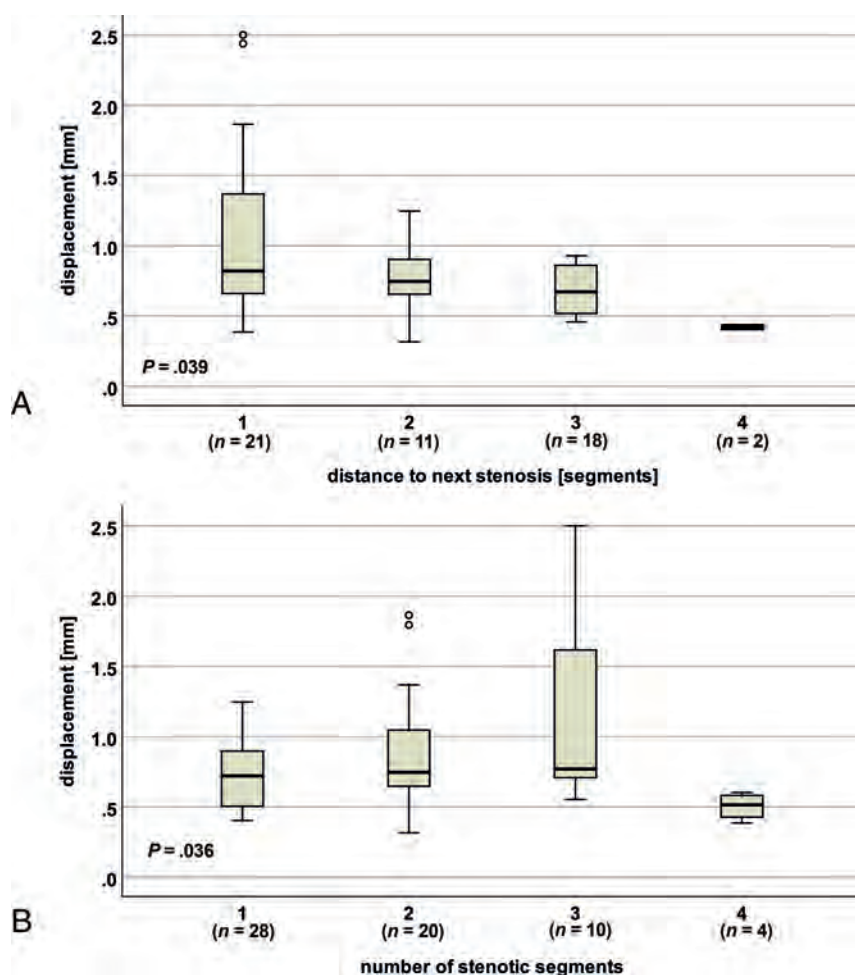
FIG 5. Spinal cord motion at C2 regarding the distance to the next stenosis and the number of stenotic segments. In patients (monosegmental and multisegmental stenoses), displacement (entire cardiac cycle) differs with the distance to the next stenosis (*A*) and the number of stenotic segments (*B*).

be confirmed in patients. Reliability across different scanners should be shown in future measurements.

Spinal Cord Motion Readouts

Increased segmental cord motion readouts at the level of stenosis are in line with previous work.[8-11] However, the comparability of this work is limited due to different readouts (half amplitude,[8] total displacement,[10,11] maximum displacement,[10] peak velocities,[7,15] mean velocity,[10] and velocity difference between cervical segments[9]) and different evaluation techniques (magnetic field strength,[7-11,13,15] ROIs,[7-11] velocity encoding,[6-9,11,13] no correction for offset error/phase drift[11]), underlining the need for a standardized evaluation.

Motion Differences in Regard to the Distance to the Next Stenosis and the Number of Stenotic Segments

Patients with a multisegmental stenosis showed a higher displacement within the first half of the cardiac cycle at C2 compared with patients with a monosegmental stenosis, but this difference

was lost in subgroup analysis in regard to the distance to the next stenosis and might, therefore, be mostly attributable to the high number of measurements with a proximate stenosis at C3 in the patient group with multisegmental stenoses. Motion at C2 was increased in regard to a higher number of stenotic segments (entire patient group and subgroup multisegmental stenoses) and the distance to the next stenosis (with a trend in subgroup analysis in patients with monosegmental and multisegmental stenoses, respectively). Due to the elastic properties of the spinal cord and its surroundings,[20-22] increased motion in the stenotic segment might, therefore, propagate to adjacent segments, ending in a further increased oscillation. Increased motion values compared with controls in nonstenotic segments at C2 up to 3 segments apart from the next stenosis support this hypothesis. However, it remains open why motion in patients with 4 stenotic segments was less compared with motion in those with a lower number of stenotic segments. Potentially, there might be a threshold of obstruction of the spinal canal, where spinal cord motion decreases.

Origin of Spinal Cord Motion

The origin of spinal cord motion was attributed to intracranial CNS and CSF pulsation related to the cardiac cycle,[9,11,23-27] breathing,[28] and local factors, eg, arterial pulsation. Breathing only causes slower frequency spinal cord movements[29,30] and was shown to have minor effects on CSF measurements within steady breathing conditions using cardiac-gated PCMR.[31] Because patients and healthy controls in our study underwent no defined breathing protocol, breathing was not monitored systematically but is expected to have only minor effects. Increased spinal cord motion can be attributed to narrowed anatomic conditions inducing changes of fluid dynamics because correlations of higher motion with less CSF space and smaller spinal canal measures could be found in healthy controls[6] and patients.[8] These findings are comparable with CSF dynamics reported before,[32,33] following the law of Hagen-Poiseuille.[34] Previous studies also revealed a close interaction between CSF dynamics and spinal cord motion.[11] However, CSF measurements at the level of cervical stenosis[11] were considered less reliable. Local mechanisms (ie, arterial pulsation) are also affected in spinal stenosis due to the loss of the CSF buffer zone around the spinal cord. When we compared our measurements with those in other studies on spinal cord and cardiovascular motion using electrocardiography (ECG) triggering,[7,9,35] a major influence on spinal cord motion
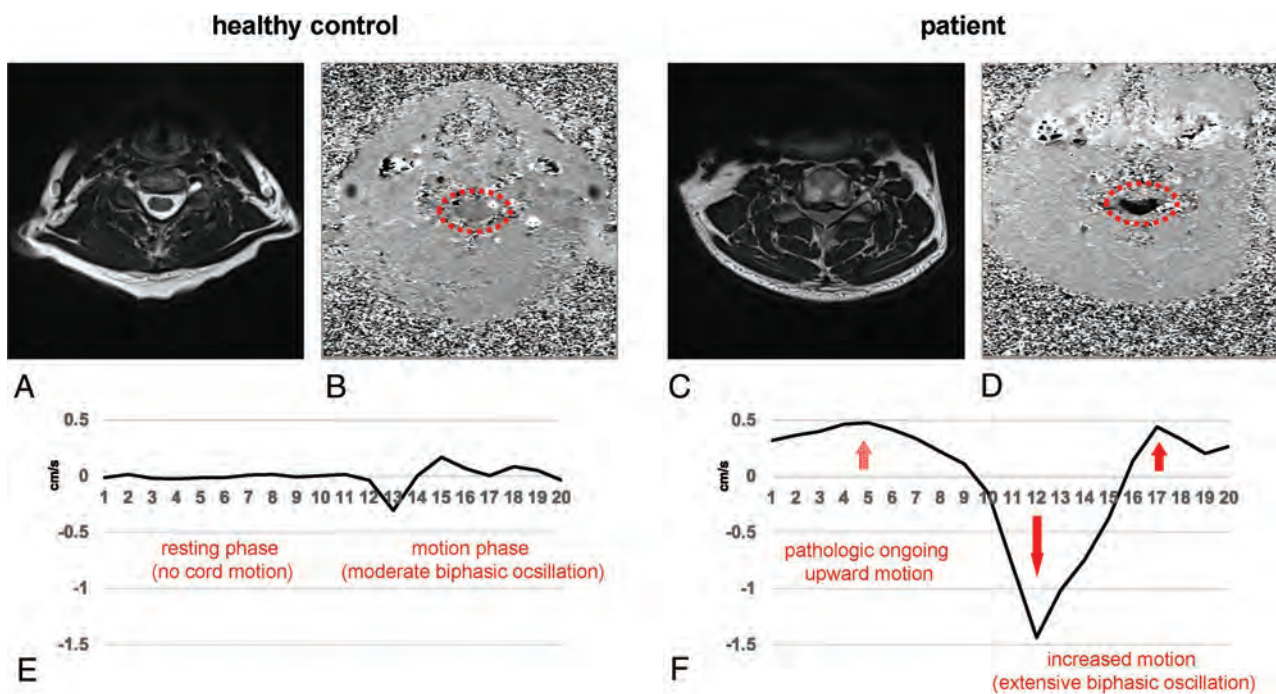
FIG 6. Comparison of physiologic and pathologic spinal cord motion. At C5 in a nonstenotic segment in a healthy control (*A*, axial T2-weighted), only moderate velocities can be observed in phase-contrast imaging with *light gray shading* of the cord (*B*, axial PCMR, *red dotted circle*). In contrast, in a patient's stenotic segment (*C*, axial T2-weighted), extensively increased spinal cord motion velocity can be identified by *black shading* of the spinal cord (*D*; axial PCMR; *red dotted circle*). While the phase-contrast images (*B*, healthy control; *D*, patient) show the maximum caudal velocity, the velocity graphs (*E*, healthy control; *F*, patient) display the velocity at 20 time points during 1 cardiac cycle. While in physiologic conditions, only a moderate biphasic oscillation in the second half of the cardiac cycle (*E*, time points 11–20) and no motion during the first half (*E*, time points 1–10) can be observed; in cervical stenosis, the spinal cord shows an extensively increased oscillation in the second half (*F*, time points 11–20; *red arrows*) and ongoing upward motion in the first half (*F*, time points 1–10; *red dotted arrow*).

could be attributed to the cardiac function,[7] causing a strong craniocaudal oscillation shortly after the RR peak in the ECG. Motion readouts were correlated to the heart rate in healthy volunteers,[6] underlining a relation to the cardiac action and local vascular pulsation. Most interesting, in a canine model, spinal cord oscillations diminished after transection of the local vascular support,[36] speaking to the importance of local arterial pulsation for spinal cord motion. That spinal cord oscillations in conditions with stenosis occur with increased movement throughout the entire cardiac cycle suggests other influences, ie, altered CSF dynamics or elastic properties of the spinal cord and its surrounding structures.

Spinal Cord Motion Pattern
Spinal cord motion in healthy volunteers was shown to start with a strong craniocaudal oscillation shortly after the RR peak in the ECG.[7] This caudal motion was followed by a cranial oscillation and subsequent caudal/cranial oscillations of different extents, with no motion at the end of the diastole.[7] In line with these reports, hardly any motion was observed in our control group during the first half (time points 1–10) of the cardiac cycle (measured by peripheral pulse triggering), followed by a biphasic craniocaudal oscillation (Fig 6 and Online Video 1). In summary, in line with previous[7] work, our findings show craniocaudal oscillations, with an onset shortly after the cardiac systole, extending into the cardiac diastole, but with zero motion at the end of the diastole under physiologic conditions. In cardiovascular MR imaging measurements simultaneously comparing 3 triggering methods (ECG,

peripheral pulse, sonography), a temporal right shift of the velocity curve was reported when using a peripheral pulse trigger (about 60% of the RR interval) compared with the ECG trigger.[35] These findings correspond well to the shifted spinal cord motion curve in our analysis, using a peripheral pulse trigger, with a motion onset at approximately 50%–55% of the cardiac cycle compared with earlier spinal cord motion studies using the ECG trigger.[7,9] Analogous results across studies using various triggering criteria underline the technical robustness of measuring spinal cord motion with PCMR.

Altered Motion Pattern in Patients: The Restless Spinal Cord
Systolic motion in patients showed a craniocaudal followed by a caudocranial oscillation similar to findings in physiologic conditions,[6,7] but with manifold higher velocity values (Fig 6 and Online Video 2). While the onset of the oscillation did not differ in patients compared with controls, the subsequent negative velocity peak and the positive velocity peak were significantly delayed. Additionally, while physiologic conditions are present almost without cord motion during the first half of the cardiac cycle (time points 1–10), providing a resting phase for the spinal cord, patients presented with a continuous motion that was seen throughout the whole cardiac cycle, reflecting ongoing upward motion (Fig 6). These findings suggest a timely onset but increased caudal motion driven by arterial pulsation and CSF flow. Downward motion was extended in 1 subgroup, while a delayed and prolonged upward oscillation in cervical stenosis was evident in most patients. The origin of the upward motion might be mostly attributed to a passive

recoil, caused by elastic structures like the dental ligaments and the pia mater and the elastic properties of the spinal cord itself.[20-22] Additionally, in physiologic conditions, CSF flow shows a sinusoidal pattern with diastolic upward flow,[37,38] which is restricted in the stenotic segments. Due to the obstruction of the spinal canal in cervical stenosis, the spinal cord might be subject to diastolic upward motion also driven by CSF backward flow.

In summary, the increased downward motion and the entrapment of the spinal cord at the stenotic segment might cause the delayed and ongoing upward motion. Therefore, in pathologic conditions, the physiologic diastolic resting phase vanished, resulting in a restless oscillation of the spinal cord. Considering >100,000 heartbeats with consecutively increased spinal cord oscillations per day, this ongoing mechanical stress to the spinal cord provides an important dynamic factor in the pathophysiology of DCM beyond static compression, potentially contributing to tissue damage, myelopathy, and its clinical conditions. Associations of increased spinal cord motion with sensory deficits,[8,10] impaired electrophysiologic readouts,[10] and decreased functional scores[11] in patients with DCM are in line with this hypothesis. Additionally, each arterial pulsation acts on the spinal cord tissue with a magnitude corresponding to the blood pressure in patients missing the CSF buffer to absorb each pulsation. Most interesting, the mechanosensitivity of central nervous system tissue to low-level magnitude strains was shown.[39-41]

Various other pathologic conditions are reported with altered spinal cord motion, underlining its clinical importance. In symptomatic patients with a tethered cord, limited cord motion was revealed, and a markedly decreased cord motion suggested a poor outcome for surgery.[42,43] Analogous to our findings, changes with increased spinal cord motion and an impaired passive recoil have been reported in Chiari malformation,[44-46] associated with Chiari-associated syringomyelia.[45,47] Obstruction of the foramen magnum in Chiari malformations, therefore, shows analogous findings to the obstructed spinal canal in patients with DCM.

In summary, assessing spinal cord motion may help to improve diagnostics and monitoring of disease progression because it reflects mechanical stress to the spinal cord not revealed by standard static MR imaging. Especially in patients with mild DCM, treatment decisions are challenging.[48] Increased spinal cord motion in this population may provide a complementary aspect for decision-making. Also, postoperative measurements of spinal cord motion might provide a tool to identify sufficient decompression because normalization of preoperatively increased cord motion has been reported before.[8] In contrast to other techniques (ie, multimodal MR imaging protocols[49-52]) requiring extensive postprocessing, spinal cord motion measurements can be easily implemented in routine MR imaging protocols.

Limitations
Because controls were not matched for age and sex, a possible bias of these characteristics could not be excluded. Due to limited time for MR imaging measurements, not all cervical segments could be evaluated in the individual patients. However, the group findings could show changes of the pattern of cord motion range across the whole cervical spinal segments. The temporal resolution of our motion measurements was limited by the high spatial in-plane resolution and the low velocity encoding value, both leading to a long TR. Due to limited scanning time per patient, a further extension of the phase-contrast acquisition time unfortunately was not possible. However, the approach used here might provide a reasonable compromise for clinical application.

CONCLUSIONS
This study revealed ongoing (restless) spinal cord motion over the whole cardiac cycle and provides further insight into the pathophysiology of degenerative cervical myelopathy contributing to tissue damage beyond static compression. Measuring spinal cord motion provides an interesting surrogate to potentially reveal conditions of spinal cord distress, even before it is clinically evident. This might enable advanced evaluation of patients thought to have DCM and provide a means for a timely surgical intervention at an early stage.

ACKNOWLEDGMENTS

REFERENCES
1. Kalsi-Ryan S, Karadimas SK, Fehlings MG. **Cervical spondylotic myelopathy: the clinical phenomenon and the current pathobiology of an increasingly prevalent and devastating disorder.** *Neuroscientist* 2013;19:409–21 CrossRef Medline
2. Karadimas SK, Moon ES, Yu WR, et al. **A novel experimental model of cervical spondylotic myelopathy (CSM) to facilitate translational research.** *Neurobiol Dis* 2013;54:43–58 CrossRef Medline
3. Karadimas SK, Gatzounis G, Fehlings MG. **Pathobiology of cervical spondylotic myelopathy.** *Eur Spine J* 2015;24(Suppl 2):132–38 CrossRef Medline
4. Karadimas SK, Klironomos G, Papachristou DJ, et al. **Immunohistochemical profile of NF-kappaB/p50: NF-kappaB/p65, MMP-9, MMP-2, and u-PA in experimental cervical spondylotic myelopathy.** *Spine (Phila Pa 1976)* 2013;38:4–10 CrossRef Medline
5. Beattie MS, Manley GT. **Tight squeeze, slow burn: inflammation and the aetiology of cervical myelopathy.** *Brain* 2011;134:1259–61 CrossRef Medline
6. Hupp M, Vallotton K, Brockmann C, et al. **Segmental differences of cervical spinal cord motion: advancing from confounders to a diagnostic tool.** *Sci Rep* 2019;9:7415 CrossRef Medline
7. Mikulis DJ, Wood ML, Zerdoner OA, et al. **Oscillatory motion of the normal cervical spinal cord.** *Radiology* 1994;192:117–21 CrossRef Medline

8. Chang HS, Nejo T, Yoshida S, et al. **Increased flow signal in compressed segments of the spinal cord in patients with cervical spondylotic myelopathy.** *Spine (Phila Pa 1976)* 2014;39:2136–42 CrossRef Medline

9. Tanaka H, Sakurai K, Iwasaki M, et al. **Craniocaudal motion velocity in the cervical spinal cord in degenerative disease as shown by MR imaging.** *Acta Radiol* 1997;38:803–09 CrossRef Medline

10. Vavasour IM, Meyers SM, MacMillan EL, et al. **Increased spinal cord movements in cervical spondylotic myelopathy.** *Spine J* 2014;14:2344–54 CrossRef Medline

11. Wolf K, Hupp M, Friedl S, et al. **In cervical spondylotic myelopathy spinal cord motion is focally increased at the level of stenosis: a controlled cross-sectional study.** *Spinal Cord* 2018;56:769–76 CrossRef Medline

12. Harris PA, Taylor R, Thielke R, et al. **Research electronic data capture (REDCap): a metadata-driven methodology and workflow process for providing translational research informatics support.** *J Biomed Inform* 2009;42:377–81 CrossRef Medline

13. Tanaka H, Sakurai K, Kashiwagi N, et al. **Transition of the craniocaudal velocity of the spinal cord: from cervical segment to lumbar enlargement.** *Invest Radiol* 1998;33:141–45 CrossRef Medline

14. Gatehouse PD, Rolf MP, Bloch KM, et al. **A multi-center inter-manufacturer study of the temporal stability of phase-contrast velocity mapping background offset errors.** *J Cardiovasc Magn Reson* 2012;14:72 CrossRef Medline

15. Levy LM, Di Chiro G, McCullough DC, et al. **Fixed spinal cord: diagnosis with MR imaging.** *Radiology* 1988;169:773–78 CrossRef Medline

16. David G, Mohammadi S, Martin AR, et al. **Traumatic and nontraumatic spinal cord injury: pathological insights from neuroimaging.** *Nat Rev Neurol* 2019;15:718–31 CrossRef Medline

17. Grabher P, Mohammadi S, Trachsler A, et al. **Voxel-based analysis of grey and white matter degeneration in cervical spondylotic myelopathy.** *Sci Rep* 2016;6:24636 CrossRef Medline

18. Grabher P, Mohammadi S, David G, et al. **Neurodegeneration in the spinal ventral horn prior to motor impairment in cervical spondylotic myelopathy.** *J Neurotrauma* 2017;34:2329–34 CrossRef Medline

19. Nouri A, Tetreault L, Singh A, et al. **Degenerative cervical myelopathy: epidemiology, genetics, and pathogenesis.** *Spine (Phila Pa 1976)* 2015;40:E675–93 CrossRef Medline

20. Tunturi AR. **Elasticity of the spinal cord, pia, and denticulate ligament in the dog.** *J Neurosurg* 1978;48:975–79 CrossRef Medline

21. Tubbs RS, Salter G, Grabb PA, et al. **The denticulate ligament: anatomy and functional significance.** *J Neurosurg* 2001;94:271–75 Medline

22. Ceylan D, Tatarli N, Abdullaev T, et al. **The denticulate ligament: anatomical properties, functional and clinical significance.** *Acta Neurochir (Wien)* 2012;154:1229–34 CrossRef Medline

23. Jokich PM, Rubin JM, Dohrmann GJ. **Intraoperative ultrasonic evaluation of spinal cord motion.** *J Neurosurg* 1984;60:707–11 CrossRef Medline

24. Baron EM, Young WF. **Cervical spondylotic myelopathy: a brief review of its pathophysiology: clinical course, and diagnosis.** *J Neurosurg* 2007;60(1 Suppl 1):S35–41 CrossRef Medline

25. Schaller B, Graf R. **Different compartments of intracranial pressure and its relationship to cerebral blood flow.** *J Trauma* 2005;59:1521–31 CrossRef Medline

26. Greitz DW, Franck A, Nordell B, et al. **Pulsatile brain movement and associated hydrondynamics studies by magnetic resonance phase imaging: the Monro-Kellie doctrine revisited.** *Neuroradiology* 1992;34:370–80 CrossRef Medline

27. Schroth G, Klose U. **Cerebrospinal fluid flow, I: physiology of cardiac-related pulsation.** *Neuroradiology* 1992;35:1–9 CrossRef Medline

28. Winklhofer S, Schoth F, Stolzmann P, et al. **Spinal cord motion: influence of respiration and cardiac cycle.** *Rofo* 2014;186:1016–21 CrossRef Medline

29. Tseng CL, Sussman MS, Atenafu EG, et al. **Magnetic resonance imaging assessment of spinal cord and cauda equina motion in supine patients with spinal metastases planned for spine stereotactic body radiation therapy.** *Int J Radiat Oncol Biol Phys* 2015;91:995–1002 CrossRef Medline

30. Cai J, Sheng K, Sheehan JP, et al. **Evaluation of thoracic spinal cord motion using dynamic MRI.** *Radiother Oncol* 2007;84:279–82 CrossRef Medline

31. Yildiz S, Thyagaraj S, Jin N, et al. **Quantifying the influence of respiration and cardiac pulsations on cerebrospinal fluid dynamics using real-time phase-contrast MRI.** *J Magn Reson Imaging* 2017;46:431–39 CrossRef Medline

32. Bunck AC, Kroger JR, Juttner A, et al. **Magnetic resonance 4D flow characteristics of cerebrospinal fluid at the craniocervical junction and the cervical spinal canal.** *Eur Radiol* 2011;21:1788–96 CrossRef Medline

33. Mardal KA, Rutkowska G, Linge S, et al. **Estimation of CSF flow resistance in the upper cervical spine.** *Neuroradiol J* 2013;26:106–10 CrossRef Medline

34. Douglas JF. *Fluid Mechanics.* Harlow, England ; New York: Prentice Hall; 2011

35. Kording F, Yamamura J, Lund G, et al. **Doppler ultrasound triggering for cardiovascular MRI at 3T in a healthy volunteer study.** *Magn Reson Med Sci* 2017;16:98–108 CrossRef Medline

36. Matsuzaki H, Wakabayashi K, Ishihara K, et al. **The origin and significance of spinal cord pulsation.** *Spinal Cord* 1996;34:422–26 CrossRef Medline

37. Armonda RA, Citrin CM, Foley KT, et al. **Quantitative cine-mode magnetic resonance imaging of Chiari I malformations: an analysis of cerebrospinal fluid dynamics.** *Neurosurgery* 1994;35:214–23; discussion 223–34 CrossRef Medline

38. Levy LM, Di Chiro G. **MR phase imaging and cerebrospinal fluid flow in the head and spine.** *Neuroradiology* 1990;32:399–406 CrossRef Medline

39. Franze K, Janmey PA, Guck J. **Mechanics in neuronal development and repair.** *Annu Rev Biomed Eng* 2013;15:227–51 CrossRef Medline

40. Goriely A, Geers MG, Holzapfel GA, et al. **Mechanics of the brain: perspectives, challenges, and opportunities.** *Biomech Model Mechanobiol* 2015;14:931–65 CrossRef Medline

41. Lee L. **Riding the wave of ependymal cilia: genetic susceptibility to hydrocephalus in primary ciliary dyskinesia.** *J Neurosci Res* 2013;91:1117–32 CrossRef Medline

42. McCullough DC, Levy LM, DiChiro G, et al. **Toward the prediction of neurological injury from tethered spinal cord: investigation of cord motion with magnetic resonance.** *Pediatr Neurosurg* 1990;16:3–7; discussion 7 CrossRef Medline

43. Johnson DL, Levy LM. **Predicting outcome in the tethered cord syndrome: a study of cord motion.** *Pediatr Neurosurg* 1995;22:115–19 CrossRef Medline

44. Wolpert SM, Bhadelia RA, Bogdan AR, et al. **Chiari I malformations: assessment with phase-contrast velocity MR.** *AJNR Am J Neuroradiol* 1994;15:1299–1308 Medline

45. Terae S, Miyasaka K, Abe S, et al. **Increased pulsatile movement of the hindbrain in syringomyelia associated with the Chiari malformation: cine-MRI with presaturation bolus tracking.** *Neuroradiology* 1994;36:125–29 CrossRef Medline

46. Pujol J, Roig C, Capdevila A, et al. **Motion of the cerebellar tonsils in Chiari type I malformation studied by cine phase-contrast MRI.** *Neurology* 1995;45:1746–53 CrossRef Medline

47. Hofmann E, Warmuth-Metz M, Bendszus M, et al. **Phase-contrast MR imaging of the cervical CSF and spinal cord: volumetric motion analysis in patients with Chiari I malformation.** *AJNR Am J Neuroradiol* 2000;21:151–58 Medline

48. Badhiwala JH, Ahuja CS, Akbar MA, et al. **Degenerative cervical myelopathy: update and future directions.** *Nat Rev Neurol* 2020;16:108–24 CrossRef Medline

49. Martin AR, De Leener B, Cohen-Adad J, et al. **A novel MRI biomarker of spinal cord white matter injury: T2*-weighted white**

matter to gray matter signal intensity ratio. *AJNR Am J Neuroradiol* 2017;38:1266–73 CrossRef Medline

50. Martin AR, De Leener B, Cohen-Adad J, et al. **Clinically feasible microstructural MRI to quantify cervical spinal cord tissue injury using DTI, MT, and T2*-weighted imaging: assessment of normative data and reliability.** *AJNR Am J Neuroradiol* 2017;38:1257–65 CrossRef Medline

51. Martin AR, De Leener B, Cohen-Adad J, et al. **Can microstructural MRI detect subclinical tissue injury in subjects with asymptomatic cervical spinal cord compression? A prospective cohort study.** *BMJ Open* 2018;8:e019809 CrossRef Medline

52. Martin AR, De Leener B, Cohen-Adad J, et al. **Monitoring for myelopathic progression with multiparametric quantitative MRI.** *PLoS One* 2018;13:e0195733 CrossRef Medline

Spinal Cord Gray and White Matter Damage in Different Hereditary Spastic Paraplegia Subtypes

K.R. Servelhere, R.F. Casseb, F.D. de Lima, T.J.R. Rezende, L.P. Ramalho, and M.C. França Jr

ABSTRACT

BACKGROUND AND PURPOSE: Spinal cord damage is a hallmark of hereditary spastic paraplegias, but it is still not clear whether specific subtypes of the disease have distinctive patterns of spinal cord gray (GM) and white (WM) matter involvement. We compared cervical cross-sectional GM and WM areas in patients with distinct hereditary spastic paraplegia subtypes. We also assessed whether these metrics correlated with clinical parameters.

MATERIALS AND METHODS: We analyzed 37 patients (17 men; mean age, 47.3 [SD, 16.5] years) and 21 healthy controls (7 men; mean age, 42.3 [SD, 13.2] years). There were 7 patients with spastic paraplegia type 3A (SPG3A), 12 with SPG4, 10 with SPG7, and 8 with SPG11. Image acquisition was performed on a 3T MR imaging scanner, and T2*-weighted 2D images were assessed by the Spinal Cord Toolbox. Statistical analyses were performed in SPSS using nonparametric tests and false discovery rate–corrected P values $<$ .05.

RESULTS: The mean disease duration for the hereditary spastic paraplegia group was 22.4 [SD, 13.8] years and the mean Spastic Paraplegia Rating Scale score was 22.8 [SD, 11.0]. We failed to identify spinal cord atrophy in SPG3A and SPG7. In contrast, we found abnormalities in patients with SPG4 and SPG11. Both subtypes had spinal cord GM and WM atrophy. SPG4 showed a strong inverse correlation between GM area and disease duration ($\rho = -0.903$, $P <$ .001).

CONCLUSIONS: Cervical spinal cord atrophy is found in some but not all hereditary spastic paraplegia subtypes. Spinal cord damage in SPG4 and 11 involves both GM and WM.

ABBREVIATIONS: CSA = cross sectional area; HSP = hereditary spastic paraplegia; SC = spinal cord; SCT = Spinal Cord Toolbox; SPG = spastic paraplegia; SPRS-BR = Brazilian version of the Spastic Paraplegia Rating Scale

Hereditary spastic paraplegia (HSP) consists of a heterogeneous group of inherited neurodegenerative disorders in which the longest descending fibers of the spinal cord (SC) are the main target of damage.[1-3] Clinically, patients present with spastic gait that can be associated with variable degrees of lower limb weakness as well as sensory deficits and bladder or bowel dysfunction. HSP can be inherited in every possible way, but autosomal dominant and recessive are the most common patterns of inheritance.[4]

So far, >70 loci and 60 genes are linked to HSP, and the different genetic subtypes of the disease are spastic paraplegia (SPG)1 to SPG80, corresponding to the chronologic order of gene description.[4]

Since the first postmortem descriptions in subjects with HSP,[5-7] the corticospinal tract and the SC have been indicated as the key targets of damage in the disease.[8,9] Studies using MR imaging have already shown atrophy of the SC in these patients.[9-11] However, these studies had some important limitations. First, the sample sizes were small; thus, the authors lumped different HSP subtypes into a single group to compare with healthy controls.[9-11] Second, MR imaging analyses failed to separate SC white (WM) and gray (GM) matter for individualized analyses.[9-11]

In this scenario, novel MR imaging acquisition protocols that allow quantifying GM and WM separately have been developed in the past decade.[12] The Spinal Cord Toolbox (SCT; https://spinalcordtoolbox.com/en/stable/), a robust tool capable of isolating GM and WM automatically, is a comprehensive and open-source software specifically designed to process SC MR imaging data and perform cord-specific quantification of cross-

sectional areas across vertebral levels.[13] This pipeline has high segmentation accuracy and acceptable intra- and inter-scanner reliability.[13,14] The measurement of these segmented structures can contribute to identifying potential biomarkers for HSPs through understanding the pattern of SC damage. This might be helpful for diagnostic purposes and also to assess disease progression.

As far as we know, no studies approaching GM and WM separately in HSP have been performed. Therefore, this study used the SCT in a representative sample of genotype-specific HSP subtypes, aiming to compare cross-sectional cervical SC, GM, and WM areas. Furthermore, we verified whether these metrics correlated with clinical aspects such as age at onset, disease, and disease severity.

MATERIALS AND METHODS

Subject Selection

We initially recruited and scanned 55 patients and 23 healthy controls from 2018 to 2019. We excluded 13 patients (4 with SPG15, 1 with SPG6, 3 with SPG72, 3 with SPG8, and 2 with SPG33) because these genotypes did not have large-enough sample sizes to enable comparisons. Furthermore, we excluded images from 5 patients (3 with SPG4, 1 with SPG11, and 1 with SPG3A) and 2 controls due to motion artifacts and poor segmentation. In the end, 37 patients with HSP (7 with SPG3A, 12 with SPG4, 10 with SPG7, and 8 with SPG11) with a mean age of 47.3 [SD, 16.5] years and 21 healthy controls with a mean age of 42.3 [SD, 13.2] years took part in the study. None of these remaining subjects had relevant disc disease or cord compression. All patients were followed at our neurogenetics outpatient clinic.

All patients were older than 18 years of age and had genotypes confirmed by molecular testing. This study was approved by the ethics committee of UNICAMP (CAAE 83241318.3.1001.5404) and have been performed in accordance with the ethical standards laid down in the 1964 Declaration of Helsinki and its later amendments. All subjects agreed to participate and signed an informed consent form before any study-related procedure.

Clinical Parameters

We recorded the age at onset of the first symptom and disease duration for all patients. Phenotypes were classified into pure and complicated. We used 3 clinical scales to quantify disease severity: the Brazilian version of the Spastic Paraplegia Rating Scale (SPRS-BR), the Ashworth scale, and the Medical Research Council Scale for Muscle Strength.[15-17] The last 2 scales were applied only to the lower limb muscles. Clinical evaluations were performed by a specialized researcher on the same day that MR images were obtained.

MRI Acquisition

All images were acquired in an Achieva 3T scanner (Philips Healthcare) using a standard 16-channel neurovascular head coil. We obtained sagittal and axial standard T1 and T2 scans of the cervical SC to rule out incidental findings (eg, degenerative disc disease, cord compression). Routine brain MR images were also obtained to rule out incidental findings.

To locate the ROI within the cervical SC, we obtained sagittal T2-weighted images with the following parameters: FOV = 220 × 220 × 36 mm^3; voxel size = 0.7 × 0.7 × 3 mm^3; 11 slices; gap = 0.3 mm; flip angle = 90°; TR/TE = 1075/120 ms.

For quantitative analyses, we used the T2*-weighted 3D slab-selective fast-field echo images acquired in the axial plane from C2 to C4 with an acquisition time of 4 minutes 30 seconds (FOV = 200 × 153 × 49 mm^3; voxel size = 0.8 × 0.8 × 3 mm^3; matrix = 252 × 191; 15 slices; gap = 0.3 mm; 4 echoes; flip angle = 28°; TR/TE = 700/6.7 ms).

MRI Analysis

We used the SCT pipeline, Version 4.0.1, to obtain SC metrics.[13] In brief, we followed some processing steps. Initially, we obtained the automatic segmentation of the cross-sectional total SC and GM areas using deep learning algorithms, followed by manual correction of the segmentation if necessary. This initial step enabled the generation of the WM area as the difference between cross sectional area (CSA)–GM areas. Next, the vertebral levels C2, C3, and C4 were automatically identified. Afterward, we proceeded to the registering of the T2* images to the PAM50 Template (https://spinalcordtoolbox.com/en/stable/overview/concepts/pam50.html) by means of linear and/or nonlinear algorithms. Last, this template was warped to match the subject imaging, so that the mean total CSA and GM area for C2, C3, and C4 vertebrae can be computed. These measures are corrected for the curvature of the spine using the angle of the section with the SC centerline. Fifteen slices for each SC level were considered, and a mean value was estimated. Figure 1 shows examples of SC segmentation obtained using the SCT.

Statistical Analysis

We compared the entire HSP group as well as the subgroups defined according to the genetic test (SPG3A, SPG4, SPG7, and SPG11) against the entire control group ($n = 21$). Considering the relatively small sample size of each HSP subgroup, we used a nonparametric test (Mann-Whitney) to perform between-group comparisons of the CSA, GM, and WM areas at each spinal level. We applied the Benjamini-Hochberg correction to control for the false discovery rate in these analyses.

Correlation analyses were assessed separately within each HSP subtype using Spearman coefficients (ρ). Again, we investigated whether CSA, GM, and WM measures correlated with clinical parameters, such as age at onset, disease severity, and disease duration. Because this investigation was exploratory, we decided not to correct for multiple correlations. Although we have an apriori hypotheses for each correlation, we accepted a more conservative 2-tailed P value. We set $P < .05$ for all analyses.

RESULTS

There were 17 men in the patient group (45.9%) and 7 men (33.3%) in the control group. There was no significant difference regarding age between groups (patients versus healthy controls). Patients had a mean disease duration of 22.4 [SD, 13.8] years, and the mean SPRS-BR score was 22.8 [SD, 11.0]. There were 17 patients with complicated HSP (8 with SPG11 and 9 with SPG7) and 20 with pure HSP (7 with SPG3A, 12 with SPG4, and 1 with

SPG7). When we considered those with complicated phenotypes, all subjects with SPG11 had neurophysiologic signs of chronic lower motor neuron involvement (including the arms), and all except one had cognitive decline. The 9 patients with SPG7 had cerebellar ataxia. The patients with pure HSP only had lower-limb pyramidal and sensory manifestations. Ten patients were wheelchair-bound, 12 used canes, and 3 needed some assistance to walk. Demographic data of each HSP subtype are presented in the Table.
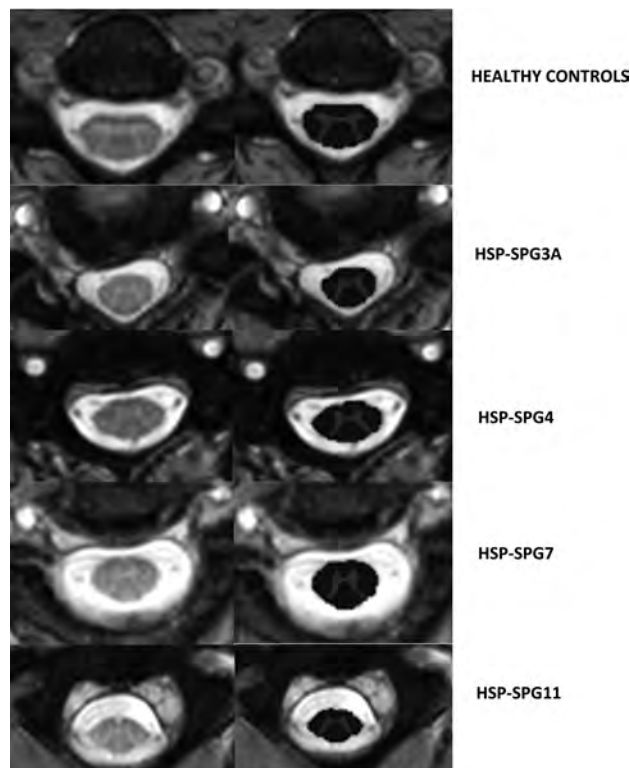

FIG 1. Axial T2* slices of the cervical spinal cord in a healthy control (*upper row*) and patients with HSP-SPG3A, HSP-SPG4, HSP-SPG7, and HSP-SPG11 (*lower rows*). In each case, the original image is shown in the left column, whereas the segmented white (dark gray) as well as the gray matter (light gray) cross-sectional areas are shown in the *right column*.

Demographic and clinical data from genotype-specific patients with HSP included in this study[a]

Parameter	SPG3A	SPG4	SPG7	SPG11
Sample (No.)	7	12	10	8
Sex (M/F)	2:5	6:6	5:5	4:4
Age (yr)	37.0 (12.0)	57.0 (12.5)	63.0 (10.0)	29.0 (6.0)
Age at onset (yr)	0 (3.5)	37.5 (8.5)	35.0 (10.0)	17.5 (3.5)
Disease duration (yr)	33.0 (10.2)	21.0 (13.0)	27.0 (24.0)	10.0 (6.0)
SPRS-BR	21.0 (18.0)	18.5 (9.0)	22.5 (23.0)	24.0 (9.5)
Leg spasticity	1 (0–2)	1 (0–2)	1 (0–2)	1 (0–2)
Leg muscle strength	4 (3–5)	4 (4–5)	5 (4–5)	4 (4–5)

[a] Parameters are expressed using median (interquartile range). Muscle spasticity and strength were assessed in the following lower limb muscles: thigh adductors and abductors, quadriceps, hamstrings, ankle plantar flexors and dorsal flexors using the Ashworth scale and the Medical Research Council Scale for Muscle Strength, respectively. Results shown in the table represent an average value from all muscles tested in each patient.

MRI Group Comparison (Patients versus Healthy Controls)

Considering the entire HSP group, all measures (CSA, GM, and WM) at all levels were significantly smaller than in the control group (Online Supplemental Data). There was a significant difference in terms of CSA only for HSP-SPG4 and HSP-SPG11 (Online Supplemental Data and Fig 2). All 3 evaluated slices presented significant area reduction for both genetic subtypes. The pattern of GM and WM damage was also similar in HSP-SPG4 and HSP-SPG11 (Online Supplemental Data and Fig 2). In both groups, we found GM as well as WM area reduction in comparison with healthy controls.

CSA, GM, and WM areas were not different between controls and the HSP-SPG3A and SPG7 groups at any spinal level.

Correlations (Clinical Parameters versus SC Areas)

We assessed correlations using the Spearman rank correlation coefficient. Considering that only HSP-SPG4 and SPG11 had significant SC morphometric changes, we decided to explore potential clinical correlates (age at onset, disease duration, and disease severity) for only those 2 subgroups. None of these parameters correlated with imaging findings in the HSP-SPG11 group. In contrast, we found significant correlations in the HSP-SPG4 group: 1) CSA at C4 had a direct correlation with the age at onset ($\rho = 0.753$, $P = .005$); 2) the GM area at C3 had a direct correlation with age at onset ($\rho = 0.706$, $P = .01$) and a negative correlation with disease severity, expressed by SPRS-BR scores ($\rho = -0.630$, $P = .03$); and 3) GM area at C4 had a positive correlation with age at onset ($\rho = 0.754$, $P = .01$), but a negative correlation with disease duration ($\rho = -0.903$, $P < .001$) and disease severity ($\rho = -0.866$, $P = .001$).

As a second step, for each HSP group, we performed correlation analyses of SC areas and disease severity, controlling for age, sex, and disease duration as covariates, but none of the results reached the significance threshold ($P < .05$).

DISCUSSION

This study focused on the comparison of cervical SC, GM, and WM areas in 4 genotype-specific HSP groups and healthy controls. Currently, there are some pipelines available for SC segmentation,[18,19] but we chose the SCT because it is highly reproducible and less affected by artifacts.[12-14] Then, we were able to show, for the first time, that cervical SC atrophy is found in some but not all HSP subtypes. Moreover, SC morphometric changes in HSP-SPG4 and SPG11 extend to both GM and WM. SC WM involvement in HSP-SPG4 and SPG11 is expected because of the involvement of the corticospinal tract, which has been shown in previous pathologic reports in both diseases.[20,21] It is rather probable that corticospinal tract axonal loss and gliosis are the pathologic correlates of the atrophy we found using MR imaging. In addition to upper motor neuron damage, HSP-SPG11 is also characterized by lower motor neuron dysfunction.
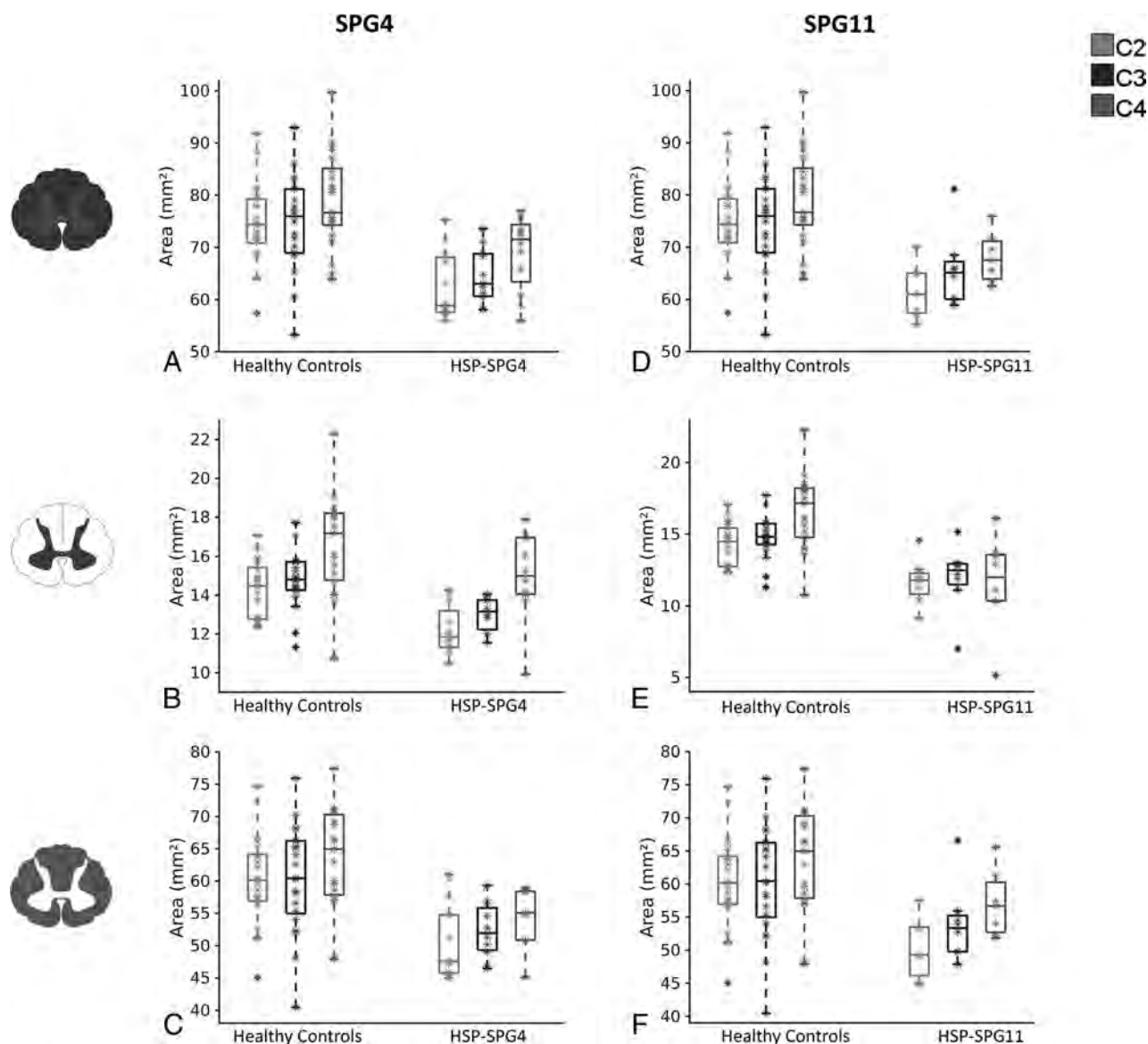
FIG 2. Box-and-whisker plots showing the distribution of the SC (*upper row*), GM (*middle row*), and WM (*lower row*) areas of patients with HSP-SPG4 versus healthy controls (*left side*) and patients with HSP-SPG11 versus healthy controls (*right side*) along cervical levels C2, C3, and C4.

Some patients actually present with a phenotype resembling juvenile amyotrophic lateral sclerosis.[21,22] Faber et al,[22] found almost universal lower motor neuron disease in a cohort of 25 subjects with HSP-SPG11. All patients with SPG11 herein included indeed had signs of anterior horn damage (including the arms). In this scenario, we hypothesize that reduced GM area in this genetic subtype could be related to the loss of motor neurons in the ventral horns of the SC.[21] The explanation for SC GM atrophy in subjects with HSP-SPG4 must not be the same because these patients do not have lower motor neuron disease in general.[23] In our cohort of HSP-SPG4, none of the subjects had clinical lower motor neuron signs, but only a few of them underwent nerve conduction studies and electromyography. Then, it is possible that we may have missed subclinical lower motoneuronal involvement. Nevertheless, we believe that loss of other neuronal populations within SC GM, such as those located in the sensory lamina of Rexed, is a more reasonable explanation for GM

atrophy. This last hypothesis deserves further investigation in pathologic studies.

Another interesting finding in this study was the striking correlation between SC metrics and clinical disability in SPG4. In this subgroup, SC GM but not WM area at C4 had an extremely high and statistically significant association with both disease duration and severity. This was somewhat unexpected but indicates that damage to neuronal circuits within the SC GM is relevant to the disease. In the face of these findings, one should no longer consider this HSP subtype as a "pure" distal motor axonopathy. In addition, our results highlight the importance of pursuing SC segmentation into GM and WM in the context of HSPs. Separate analyses of GM and WM, rather than just looking at the entire SC area, might provide more interesting insights, not only into the biology of these diseases but also into potential biomarkers for clinical use. Some previous studies indeed failed to identify the clinical correlates of SC damage, possibly because they used

this whole SC measurement approach.[9,10] In the near future with technical MR imaging advancements, it is possible that deeper segmentation of the SC, for instance, determining the area of the anterior and posterior horns as well the dorsal columns, will help us even more in the understanding of HSP.[24,25] Other metabolic and genetic SC disorders may also benefit from a similar approach using quantitative GM and WM evaluation.[26]

We failed to show the same relevant associations for subtypes HSP-SPG7 and SPG11. This could be due to a ceiling effect of SPRS-BR for these 2 subtypes. Indeed, patients with SPG7 and SPG11 were the most disabled (many of them already wheelchair-bound). In late disease stages, the scale fails to capture clinical deterioration (even though neurodegeneration was still taking place), and this may have interfered with the correlation analyses.[27] The assessment of cohorts in the early stages of SPG7 and SPG11 would help to clarify this point.

We were not able to find SC atrophy in the HSP-SPG3A and SPG7 groups. This may indicate that SC involvement in these subtypes does not lead to macroscopic abnormalities. Only microstructural abnormalities would be present and could only be uncovered with other imaging techniques, such as DTI.[25] An alternative explanation is that SC volumetric reduction actually takes place but is mild. In this scenario, our sample size could have been underpowered to detect such small differences. This is sometimes an issue in single-center studies dealing with rare diseases such as HSP. To overcome these limitations, multicentric studies using a multimodal SC MR imaging approach in a longitudinal setting would be important to enable the recruitment of more patients, including HSP subtypes not explored here. Additional levels of the SC, such as the thoracic region, were not evaluated in our study and should be assessed in these future studies as well.

CONCLUSIONS

We were able to show that HSP types 4 and 11 have SC atrophy involving both GM and WM. GM SC morphometry correlated with clinical parameters in HSP-SPG4 and might be a useful biomarker to track disease progression in this condition, but longitudinal studies should now be performed to validate these findings.

ACKNOWLEDGMENTS

This study was approved by the ethics committee of University of Campinas (CAAE 83241318.3.1001.5404) and has been performed in accordance with the ethical standards laid down in the 1964 Declaration of Helsinki and its later amendments.

REFERENCES

1. Parodi L, Fenu S, Stevanin G, et al. **Hereditary spastic paraplegia: more than an upper motor neuron disease.** *Rev Neurol (Paris)* 2017;173:352–60 CrossRef Medline

2. Faber I, Pereira ER, Martinez AR, et al. **Hereditary spastic paraplegia from 1880 to 2017: an historical review.** *Arq Neuropsiquiatr* 2017;75:813–18 CrossRef Medline

3. Parodi L, Coarelli G, Stevanin G, et al. **Hereditary ataxias and paraparesis: clinical and genetic update.** *Curr Opin Neurol* 2018;31:462–71 CrossRef Medline

4. Shribman S, Reid E, Crosby AH, et al. **Hereditary spastic paraplegia: from diagnosis to emerging therapeutic approaches.** *Lancet Neurol* 2019;18:1136–46 CrossRef

5. Strümpell A. **Ueber eine bestimmte Form der primaren combinirten Systemerkrankung des Rückenmarks.** *Archiv für Psychiatrie und Nervenkrankheiten* 1886;17:217–38 CrossRef

6. Strümpell A. **Die primare Seitenstrangsklerose (spastische Spinalparalyse).** *Deutsche Zeitschrift für Nervenheilkunde* 1904;27:291–339 CrossRef

7. DeLuca GC, Ebers GC, Esiri MM. **The extent of axonal loss in the long tracts in hereditary spastic paraplegia.** *Neuropathol Appl Neurobiol* 2004;30:576–84 CrossRef Medline

8. List J, Kohl Z, Winkler J, et al. **Ascending axonal degeneration of the corticospinal tract in pure hereditary spastic paraplegia: a cross-sectional DTI study.** *Brain Sci* 2019;9:268 CrossRef Medline

9. Hedera P, Eldevik OP, Maly P, et al. **Spinal cord magnetic resonance imaging in autosomal dominant hereditary spastic paraplegia.** *Neuroradiol* 2005;47:730–34 CrossRef Medline

10. Sperfeld AD, Baumgartner A, Kassubek J. **Magnetic resonance investigation of the upper spinal cord in pure and complicated hereditary spastic paraparesis.** *Eur Neurol* 2005;54:181–85 CrossRef Medline

11. Agosta F, Scarlato M, Spinelli EG, et al. **Hereditary spastic paraplegia: beyond clinical phenotypes toward a unified pattern of central nervous system damage.** *Radiology* 2015;276:207–18 CrossRef Medline

12. Prados F, Ashburner J, Blaiotta C, et al. **Spinal cord grey matter segmentation challenge.** *Neuroimage* 2017;152:312–29 CrossRef Medline

13. De Leener B, Lévy S, Dupont SM, et al. **SCT: Spinal Cord Toolbox, an open-source software for processing spinal cord MRI data.** *Neuroimage* 2017;145:24–43 CrossRef Medline

14. Papinutto N, Henry RG. **Evaluation of intra- and interscanner reliability of MRI protocols for spinal cord gray matter and total cross-sectional area measurements.** *J Magn Reson Imaging* 2019;49:1078–90 CrossRef

15. Servelhere KR, Faber I, Coan AC, et al. **Translation and validation into Brazilian Portuguese of the Spastic Paraplegia Rating Scale (SPRS).** *Arq Neuropsiquiatr* 2016;74:489–94 CrossRef Medline

16. Bohannon RW, Smith MB. **Interrater reliability of a modified Ashworth scale of muscle spasticity.** *Phys Ther* 1987;67:206–07 CrossRef Medline

17. Compston A. **Aids to the investigation of peripheral nerve injuries. Medical Research Council: Nerve Injuries Research Committee. His Majesty's Stationery Office: 1942; pp. 48 (iii) and 74 figures and 7 diagrams; with aids to the examination of the peripheral nervous system. By Michael O'Brien for the Guarantors of Brain. Saunders Elsevier: 2010; pp. [8] 64 and 94 Figures.** *Brain* 2010;133:2838–44 CrossRef Medline

18. Datta E, Papinutto N, Schlaeger R, et al. **Gray matter segmentation of the spinal cord with active contours in MR images.** *Neuroimage* 2017;147:788–99 CrossRef Medline

19. Papinutto N, Schlaeger R, Panara V, et al. **2D phase-sensitive inversion recovery imaging to measure in vivo spinal cord gray and**

white matter areas in clinically feasible acquisition times. *J Magn Reson Imaging* 2015;42:698–708 CrossRef Medline

20. White KD, Ince PG, Lusher M, et al. **Clinical and pathologic findings in hereditary spastic paraparesis with spastin mutation.** *Neurology* 2000;55:89–94 CrossRef Medline

21. Denora PS, Smets K, Zolfanelli F, et al. **Motor neuron degeneration in spastic paraplegia 11 mimics amyotrophic lateral sclerosis lesions.** *Brain* 2016;139:1723–34 CrossRef Medline

22. Faber I, Martinez AR, de Rezende TJR, et al. *SPG11* **mutations cause widespread white matter and basal ganglia abnormalities, but restricted cortical damage.** *Neuroimage Clin* 2018;19:848–57 CrossRef Medline

23. Parodi L, Rydning SL, Tallaksen C, et al. **Spastic paraplegia 4.** *GeneReviews [Internet]* 2003 April 17. [Updated 2019 Jun 13]

24. Paquin ME, EL Mendili MM, Gros C, et al. **Spinal cord gray matter atrophy in amyotrophic lateral sclerosis.** *AJNR Am J Neuroradiol* 2018;39:184–92 CrossRef Medline

25. Samson RS, Lévy S, Schneider T, et al. **Zoom or Non-Zoom? Assessing spinal cord diffusion tensor imaging protocols for multi-centre studies.** *PLoS One* 2016;11:e0155557 CrossRef Medline

26. Marelli C, Salsano E, Politi LS, et al. **Spinal cord involvement in adult-onset metabolic and genetic diseases.** *J Neurol Neurosurg Psychiatry* 2019;90:211–18 CrossRef Medline

27. Schüle R, Holland-Letz T, Klimpe S, et al. **The Spastic Paraplegia Rating Scale (SPRS): a reliable and valid measure of disease severity.** *Neurology* 2006;67:430–34 CrossRef Medline

Celebrating 35 Years of the AJNR
March 1986 edition

MR Imaging of Angiographically Occult Vascular Malformations

Luis Lemme-Plaghos[1,2]
Walter Kucharczyk[1,3]
Michael Brant-Zawadzki[1]
Antoine Uske[1]
Michael Edwards[1]
David Norman[1]
T. Hans Newton[1]

Eleven patients with 15 angiographically occult arteriovenous malformations were studied by magnetic resonance (MR) imaging and computed tomography (CT). Five patients had biopsy proof; six were clinically diagnosed from the long-term clinical follow-up (more than 3 years) and imaging features. Of the 15 lesions, 11 were recognized by both CT and MR. Each method was falsely negative for two lesions. The most useful contribution of MR in the characterization of angiographically occult arteriovenous malformations was the depiction of hemorrhagic foci in 12 of 13 lesions seen on MR. High-attenuation foci indicative of hematomas were seen in only five lesions on CT; the rest were iso- or hypoattenuating. CT detected two very small lesions, in one case as punctate foci of enhancement and in the other as punctate calcification, that were not seen with MR. MR complements CT in characterizing angiographically occult arteriovenous malformations and in distinguishing them from similar-appearing lesions, in particular, small neoplasms. However, when such lesions are seen with only focal calcification and subtle enhancement on CT, routine MR may miss them.

The detection and accurate diagnosis of angiographically occult arteriovenous vascular malformations (AVMs) of the brain on the basis of clinical or radiologic manifestations was uncommon until the introduction of computed tomography (CT). Although CT criteria have now been well established and serve to improve detection of these lesions [1–3], preoperative discrimination from tumors remains problematic. The relative sensitivity and specificity of magnetic resonance (MR) imaging in these lesions is as yet unreported. However, this modality does have promising capabilities in depicting vascular structures with great anatomic detail and in identifying hemorrhagic lesions [4]. The purpose of our present study was to establish in a preliminary fashion the relative value of MR in the diagnosis and characterization of AVMs.
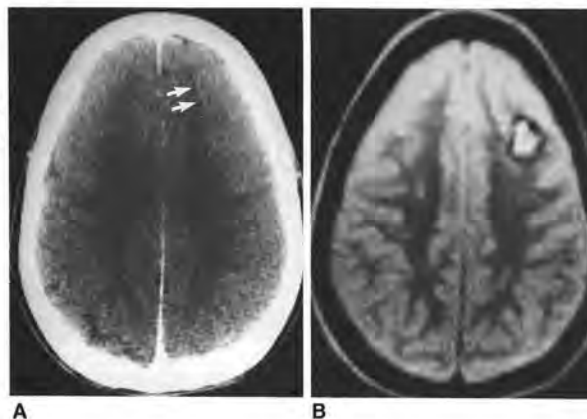
MRI of Optic Chiasm and Optic Pathways

Ana Albert[1]
Benjamin C. P. Lee[1,2]
Leslie Saint-Louis[1]
Michael D. F. Deck[1]

Eight verified lesions of the optic chiasm were examined on 0.5 T magnetic resonance (MR) and GE 9800, 8800 computed tomographic (CT) scanners. Enlargement of the optic chiasm was demonstrated in all cases. There was some change of MR signal compared with brain in all but one case, which had no resemblance to contrast enhancement on CT scans. The signal was specific for hematoma in one case. Abnormal signal, probably signifying tumor spread into the optic radiation, was detected on T2-weighted images in one case. The resolution of MR scans is similar or superior to CT, and sagittal views are most useful in evaluating lesions in this location.

Abnormalities of the optic chiasm are difficult to detect on CT scans because of the poor contrast difference between this structure and the subarachnoid space and the frequent occurrence of streak artifacts in this region [1–4]. Primary lesions are seldom distinguishable from secondary involvement by adjacent pathology. Metrizamide CT is usually performed for detailed delineation of lesions in this location [5]. High-resolution MR scanning is reported to be helpful in evaluating the normal optic chiasm and nerves, but documentation of pathologic lesions is limited [6]. Our study was aimed at comparing MR with plain CT and metrizamide CT in the evaluation of lesions of the optic chiasm, tracts, and radiation.

Subjects and Methods

Eight patients with lesions of the optic chiasm were examined. Three had primary optic chiasm tumors, two had extensions of optic nerve gliomas posteriorly into the optic chiasm and tract, one had a hematoma (probably secondary to a glioma), one had infiltration by an incompletely excised craniopharyngioma, and one had intracranial extension of retinoblastoma. Spin-echo (SE) MR scanning was performed on a 0.5 T superconducting scanner. Single- or multisection scans in the axial and sagittal planes were obtained in all cases using echo times (TEs) of 30 msec, repetition times (TRs) of 500 msec (SE 30/500), T1-weighted technique, and TE 90, TR 1500 (SE 90/1500), T2-weighted technique, in all cases. Supplementary coronal sections and SE imaging using multiecho (SE 30–120/2000) and inversion-recovery techniques were used in selected cases. Multisection scans were 8 mm; single sections were 10 mm thick. Two signal averages were used in all scanning sequences. Spatial resolution was 1.2–1.5 mm.

CT was performed using GE 8800, 9800, or equivalent third- or fourth-generation scanners. 1.5–3-mm-thick axial or coronal sections were obtained after a single dose of intravenous contrast material in all cases. Metrizamide CT using 1.5 mm axial sections with multiple-plane reconstruction was performed in two cases.

Results

The optic chiasms were enlarged in all five cases of glioma: symmetric in three and asymmetric in two (figs. 1 and 2). There was extension into the optic tract in two, with compression of the ambient cistern, and displacement of the midbrain in
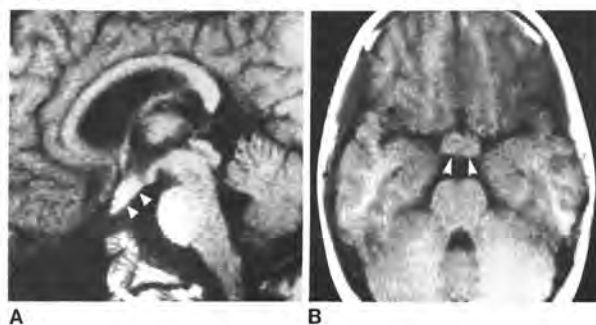
Recommendations for Neuroradiology Training during Radiology Residency by the American Society of Neuroradiology Section Chiefs Leadership Group

M. Wintermark, J. Anderson, V. Gupta, T.A. Kennedy, L.A. Loevner, R.F. Riascos, C. Robson, G. Saigal, and C. Glastonbury

The American Society of Neuroradiology [ASNR] Section Chiefs Leadership Group strongly feels that residency education in neuroradiology should become more standardized and wishes to make recommendations and facilitate the ability of residency programs to educate and train their residents in neuroradiology.

Background

Various changes to Accreditation Council for Graduate Medical Education (ACGME) radiology residency programs have resulted in a highly variable amount and type of exposure to neuroradiology cases and education. These include, but are not limited to, the advent of the IR residency and ESIR training, potentially limiting the number of rotations by the IR residents to neuroradiology, increased reliance on overnight and float rotations that may have significant neuroimaging exposure but are staffed by non-neuroradiologists, and specialized curricula or mini-fellowships in non-neuroradiology areas in the R4/PGY5 year that may limit the exposure to the expertise of neuroradiologists and neuroimaging. Additionally, the structure of the current ABR certification process, though allowing testing for routine competency with the Core Examination, does not necessarily ensure that there is continued learning and growth, because the individual can opt out of the neuroradiology modules.

From the Department of Radiology (M.W.), Neuroradiology Section, Stanford University and Healthcare, Stanford, California; Department of Radiology (J.A.), Neuroradiology Section, Oregon Health and Science University, Portland, Oregon; Department of Radiology (V.G.), Division of Neuroradiology, Mayo Clinic, Jacksonville, Florida; Department of Radiology, Division of Neuroradiology (T.A.K.), University of Wisconsin School of Medicine and Public Health, Madison, Wisconsin; Department of Radiology (L.A.L.), Division of Neuroradiology, University of Pennsylvania Health System, Philadelphia, Pennsylvania; Department of Diagnostic and Interventional Imaging (R.F.R.), Division of Neuroradiology, University of Texas Health Houston, Houston, Texas; Department of Radiology (C.R.), Neuroradiology Division, Boston Children's Hospital, Harvard Medical School, Boston, Massachusetts; Department of Radiology (G.S.), Neuroradiology Section, University of Miami Miller School of Medicine, Miami, Florida; and Department of Radiology and Biomedical Imaging (C.G.), Neuroradiology Section, University of California, San Francisco, San Francisco, California.

Please address correspondence to Max Wintermark, MD, Stanford University, Department of Radiology, Neuroradiology Division, 300 Pasteur Dr, Room S047, Stanford, CA 94305-5105; e-mail: max.wintermark@gmail.com

○╍ Indicates open access to non-subscribers at www.ajnr.org

http://dx.doi.org/10.3174/ajnr.A6968

Thus, the ASNR Section Chiefs Leadership Group has made the following recommendations:

Exposure

- It is strongly recommended that radiology trainees have at least 16–24 weeks of training in neuroradiology under the direction of a neuroradiologist. Additionally, it is recommended that at least 8–12 of those weeks occur during the last 3 years of their training before they start practicing independently.

- Continued exposure and education in neuroimaging is needed to maintain skills developed during the early years of residency. The neuroradiology training during residency should be modeled on the neuroradiology curriculum developed by ASNR (https://www.asnr.org/education/neuroradiology-curricula-for-trainees/).

- It is strongly recommended that radiology trainees have at least 60 hours of dedicated instruction in neuroimaging. Additionally, it is recommended that at least 30 of those hours occur during the last 3 years of their training before they start practicing independently.

- It is strongly recommended that residents be exposed to educational activities including lectures and other didactic education by faculty at the institution/program. In addition, it is recommended that online resources such as (but not limited to) those made available by ASNR (https://www.asnr.org/education/fellowship-portal/educational-resources) be used during residency training.

Experience

- It is strongly recommended that radiology trainees interpret a variety of neuroimaging studies throughout their training.

- Continued interpretation and education in brain, spine, head & neck, and neurovascular imaging should occur throughout the residency. Although specific numbers of cases are not an indication of competency, a guideline for consideration is that a radiology trainee interpret at least 300 neuroimaging CT scans, 150 Neuroimaging MRI scans, and 50 neurovascular imaging studies (neuro CTAs and neuro MRAs) under the guidance and direction of a neuroradiologist during the last 3 years of their training, before he or she starts practicing independently.

- It is important to read a significant number and variety of neuroimaging cases and although we understand the value of float and call type experiences for neuroimaging, the fundamental aspects of routine neuroimaging are felt to be best done under the direction and guidance of dedicated neuroradiologists, even if the feedback from the neuroradiologists may not be in real-time.

Competency
- It is strongly recommended that competency in Neuroimaging be tested.
- Resources for evaluation could include competency tests established in the home institution, performance on RadExam (https://www.acr.org/Lifelong-Learning-and-CME/Learning-Activities/RadExam), or similar testing formats. Ideally, competency testing should occur at each level of residency either defined by year in residency or number of rotations completed.
- The ASNR has developed milestone recommendations for each level of residency defined either by the year in residency or number of rotations completed (https://www.acgme.org/Portals/0/PDFs/Milestones/NeuroradiologyMilestones.pdf?ver=2015-11-06-120525-910).

Resources
As mentioned above, the ASNR is committed to supporting the education of radiology trainees and provides educational and evaluation resources to help optimize resident education and competency in neuroradiology.

CONCLUSIONS
From a patient safety perspective, radiology trainees graduating on or after June 2021 and joining practice who have not met the recommendations listed above should seriously consider *not* interpreting even *routine* neuroradiology studies.

For the independent practice and interpretation of *advanced* neuroradiology (including pediatric neuroradiology, head and neck radiology, and advanced neuroimaging), a formal, ACGME-approved neuroradiology fellowship is *strongly recommended*. A neuroradiology fellowship will ensure exposure, experience, and competency for both *routine* and *advanced* neuroradiology. The ACGME requirements for a neuroradiology fellow include the interpretation of 3000 cross-sectional neuro examinations including CTs of the head, neck, and spine; at least 1500 MRIs of the brain, neck, and spine; and at least 250 neurovascular imaging examinations (CTAs and MRAs) (https://www.acgme.org/Portals/0/PFAssets/ProgramRequirements/423_Neuroradiology_2020.pdf?ver=2020-06-29-164131-690). These numbers are significantly higher than the number of imaging studies required for radiology residents as listed above and are justified for the safe practice of *advanced* neuroradiology as opposed to *routine* neuroradiology The Neuroradiology Subspecialty Examination administered by the American Board of Radiology (ABR) allows direct testing of the competencies acquired during a neuroradiology fellowship (https://www.theabr.org/diagnostic-radiology/subspecialties/neuroradiology).

Hemert, MD, University of Arkansas for Medical Sciences, *Katie D. Vo, MD, Washington University School of Medicine, Mallinckrodt Institute of Radiology, *Matthew White, MD, University of Nebraska, *Christopher T. Whitlow, MD, PhD, Wake Forest University, *Max Wintermark, MD, Stanford University, *Carlos Zamora, MD, University of North Carolina, *Michael Zeineh, MD, PhD, Stanford University, *William B. Zucconi, MD, Yale University School of Medicine.

American Society of Neuroradiology (ASNR) Section Chiefs Leadership Group.*

MR Imaging of the Olfactory Bulbs in Patients with COVID-19 and Anosmia: How to Avoid Misinterpretation

We recently read the article entitled "Brain Imaging of Patients with COVID-19: Findings at an Academic Institution during the Height of the Outbreak in New York City," a retrospective neuroimaging cohort by Lin et al.[1] The authors reported T2-FLAIR postgadolinium olfactory bulb (OB) signal abnormalities in 4 patients positive for coronavirus disease 2019 (COVID-19) with only 1 having documented anosmia. This finding was subsequently interpreted as olfactive neuritis and a correlate of the anosmia.

Anosmia has been identified as one of the first or only recognizable symptoms of the Severe Acute Respiratory Syndrome coronavirus 2 (SARS-CoV-2) infection, accounting for >50% of Western patients.[2] It is now known that post-SARS-CoV-1 anosmia could persist for as long as 2 years. It, thus, becomes relevant to identify MR imaging biomarkers of OB involvement, including signal and volume changes, that might be predictive of the olfactory disorder outcome. We, thus, find it important to draw the attention to the OB signal and volume analysis.

The OB signal intensity can vary according to the field strength applied, the MR imaging manufacturer, and the acquisition parameters of T2-FLAIR sequences. Furthermore, it has previously been reported that OBs could appear hyperintense on T2-FLAIR in healthy subjects.[3] Lin et al[1] reported that they recruited patients who had undergone brain MR imaging from 3 different machines (1.5T and 3T), increasing the risk of signal variation in tiny structures and thus making the results more questionable.

Age- and sex-matched healthy controls scanned on the same MR imaging scanner need to be analyzed to overcome these technical issues and avoid an incorrect OB edema/gadolinium-enhancement description. In our institution, a blind, independent comparison by 2 experienced neuroradiologists of 10 patients with COVID-19–associated anosmia and 10 age- and sex-matched subjects negative for COVID-19 without olfactory dysfunction was performed. It showed that visual analysis of OB high-resolution T2-FLAIR signal could not distinguish the 2 groups because all the subjects presented with the same T2-FLAIR high signal intensity (Fig 1).
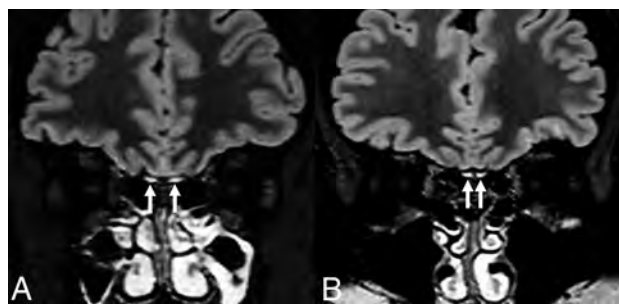

FIG 1. 3T brain MR imaging in a healthy subject (*A*) and a patient with COVID-19–related anosmia (*B*). Coronal reformatted 3D FLAIR images show OB hyperintensity (*arrows*) compared with the cortex in both subjects.

Thus, the OBs described by Lin et al[1] as being abnormally "hyperintense" can probably correspond to a normal signal intensity.

It has been shown that the OB volume decreased in postinfectious anosmia.[4] Because the OBs are tiny structures surrounded by CSF, sequences with high resolution such as CISS should be used for volume segmentation. As for the signal on an individual scale, the signal intensity evolution of the OB could be compared with the surrounding structures, such as the cortex or the optic nerves. Subjective appreciation, especially for such a small structure, could lead to misinterpretation.

In summary, OB imaging is challenging, and one should be careful while interpreting its signal and volume, especially in the context of COVID-19.

REFERENCES

1. Lin E, Lantos JE, Strauss SB, et al. **Brain imaging of patients with COVID-19: findings at an academic institution during the height of the outbreak in New York City.** *AJNR Am J Neuroradiol* 2020 Aug 20. [Epub ahead of print] CrossRef Medline
2. Lechien JR, Chiesa-Estomba CM, Hans S, et al. **Loss of smell and taste in 2013 European patients with mild to moderate COVID-19.** *Ann Intern Med* 2020 May 26. [Epub ahead of print] CrossRef Medline

Indicates open access to non-subscribers at www.ajnr.org

http://dx.doi.org/10.3174/ajnr.A6921

3. Chung MS, Choi WR, Jeong HY, et al. **MR imaging–based evaluations of olfactory bulb atrophy in patients with olfactory dysfunction.** *AJNR Am J Neuroradiol* 2018;39:532–37 CrossRef Medline

4. Yao L, Yi X, Pinto JM, et al. **Olfactory cortex and olfactory bulb volume alterations in patients with post-infectious olfactory loss.** *Brain Imaging Behav* 2018;12:1355–62 CrossRef Medline

N. Shor
Service de Neuroradiologie
Assistance Publique Hôpitaux de Paris, Hôpital Pitié-Salpêtrière
Paris, France

L. Chougar
N. Pyatigorskaya
Service de Neuroradiologie
Assistance Publique Hôpitaux de Paris, Hôpital Pitié-Salpêtrière
Paris, France

Paris Brain Institute
Sorbonne Université
Paris, France

"Movement Investigations and Therapeutics" Team
Centre de NeuroImagerie de Recherche
Institut du Cerveau
Paris, France

REPLY:

⚷

We read the letter written by Shor et al with great interest, and we appreciate the data that they shared from their institution. We concur that subjective perception of olfactory bulb (OB) hyperintensity in isolation should not be interpreted as definitive evidence of coronavirus disease 2019 (COVID-19) infection but wish to note that quantitative assessment of OB signal intensity was additionally performed in the patient sample reported in Lin et al,[1] as detailed in a subsequently published article by Strauss et al.[2] Normalized OB T2 FLAIR signal intensity values were computed to account for technical differences in scan acquisitions among patients. There was a significant difference in a normalized OB T2 FLAIR signal intensity between the patients with COVID-19 (mean normalized signal intensity, 1.85; range, 0.74–1.85) and the controls with anosmia (mean normalized signal intensity, 1.27; range, 0.99–3.13) ($P = .003$). These preliminary findings have important implications for our understanding of potential neurotropism or, at the very least, neuroinflammatory changes associated with Severe Acute Respiratory Syndrome coronavirus 2 infection and pose an avenue for future prospective investigation.

⚷ Indicates open access to non-subscribers at www.ajnr.org

http://dx.doi.org/10.3174/ajnr.A6932

REFERENCES

1. Lin E, Lantos JE, Strauss SB, et al. **Brain imaging of patients with COVID-19: findings at an academic institution during the height of the outbreak in New York City.** *AJNR Am J Neuroradiol* 2020 Aug 20. [Epub ahead of print] CrossRef Medline

2. Strauss SB, Lantos JE, Heier LA, et al. **Olfactory bulb signal abnormality in patients with COVID-19 who present with neurologic symptoms.** *AJNR Am J Neuroradiol* 2020;41:1882–87 CrossRef Medline

ⓘ**S.B. Strauss**
ⓘ**J.E. Lantos**
ⓘ**C.D. Phillips**
Department of Radiology
Weill Cornell Medicine
New York, New York
ⓘ**A. Gupta**
Department of Radiology
Weill Cornell Medicine
New York, New York
Clinical and Translational Neuroscience Unit
Feil Family Brain and Mind Research Institute and Department of Neurology
Weill Cornell Medicine
New York, New York
ⓘ**E. Lin**
Department of Radiology
Weill Cornell Medicine
New York, New York

A Comparison of Chest Radiograph and CTA Apical Pulmonary Findings in Patients Presenting with Suspected Acute Stroke during the COVID-19 Pandemic

In conjunction with our recently published article entitled "COVID-19 Stroke Apical Lung Examination Study: A Diagnostic and Prognostic Imaging Biomarker in Suspected Acute Stroke,"[1] the authors are pleased to also report our supplementary findings related to chest radiographs.

In our search for relevant diagnostic biomarkers within the lung apices on CTA performed in patients presenting with acute stroke, we also determined whether the chest radiograph is a reliable diagnostic imaging biomarker and how it compared with CTA-derived reliable diagnostic imaging biomarkers.

Chest radiographs are routine investigations for patients admitted with both suspected stroke and suspected coronavirus disease 2019 (COVID-19). The investigation is often available to a neuroradiologist when reviewing the CTA. In the setting of a neuroradiology department, we wished to determine whether the chest radiograph is a reliable diagnostic imaging biomarker (using the British Society of Thoracic Imaging COVID-19 Radiology Guidance; https://www.bsti.org.uk/standards-clinical-guidelines/clinical-guidelines/covid-19-bsti-statement-and-guidance/) and how it compares with CTA-derived reliable diagnostic imaging biomarkers.

Anterior-posterior or posterior-anterior chest radiographs, if obtained within 6 hours of the CTA, were evaluated at the 3 sites included in our multicenter study in adult patients also undergoing CT of the head and craniocervical CTA as acute stroke investigations. Radiographs were acquired with standard techniques using digital radiography machines GC80 (Samsung), Discovery 656 (GE Healthcare), Multix Select (Siemens Healthineers), and Diagnost (Philips Healthcare).

Eighty-seven patients had a chest radiograph within 6 hours of the CTA; 55.2% (48/87) had normal findings; 13.8% (12/87) were COVID-19-typical; 26.4% (23/87) had indeterminate findings; and 4.6% (4/87) were non-COVID-19. By means of a descriptive COVID-19 chest radiograph grading system, the interrater reliability among the 4 neuroradiologist raters was "substantial" across the study (Fleiss κ = 0.73; 95% CI, 0.62–0.84). Shown to be reliable, we then determined the diagnostic accuracy of this chest radiograph imaging biomarker for Severe Acute Respiratory Syndrome coronavirus 2 (SARS-CoV-2) using the reverse transcriptase polymerase chain reaction (RT-PCR) test as the reference standard (Table). Fifty-nine patients had both SARS-CoV-2 RT-PCR results and a chest radiograph. All measures of diagnostic accuracy of the chest radiograph were inferior to our selected CTA-derived reliable diagnostic imaging biomarkers.

Chest radiographs are routine investigations for those admitted with suspected stroke and those admitted with suspected COVID-19. In the setting of a neuroradiology department, while a descriptive chest radiograph grading system proved reliable, it was not an accurate COVID-19 diagnostic biomarker in the cohort of patients undergoing immediate CTA for suspected stroke, in contrast to the reliable diagnostic biomarkers identified in the CTA apical assessment.

Chest radiographs had a much lower diagnostic performance than all CTA biomarkers with a sensitivity of 50% (95% CI, 29–71) and a specificity of 61% (95% CI, 46–74) for COVID-19 (Table). We showed that chest radiograph assessment should not, therefore, replace a simple assessment of the presence of ground glass opacification on CTA for COVID-19.

Given the high frequency of chest radiographs as a screening investigation, particularly in the current era, with the additional prothrombotic sequalae of COVID-19, the findings are highly relevant to both emergency radiologists and neuroradiologists reporting acute stroke studies. Data pertaining to chest radiographs and COVID-19 in the acute stroke population have not been previously reported.

REFERENCE

1. Siddiqui J, Bala F, Sciacca S, et al. **COVID-19 stroke apical lung examination study: a diagnostic and prognostic imaging biomarker in suspected acute stroke.** *AJNR Am J Neuroradiol* 2020 Sept 17. [Epub ahead of print] CrossRef Medline

Diagnostic accuracy of chest radiograph and CTA features in patients who had undergone both a chest radiograph and a SARS-CoV-2 RT-PCR test (_n_ = 59)

	Sensitivity (95% CI)	Specificity (95% CI)	PPV (95% CI)	NPV (95% CI)
COVID-typical/indeterminate (chest radiograph)[a]	50% (29–71)	61% (46–74)	36% (24–51)	74% (62–82)
Presence of GGO (CTA)	83% (58–96)	80% (65–91)	65% (43–83)	92% (76–98)
Focal GGO (CTA)	56% (31–78)	85% (70–94)	62% (36–84)	81% (66–91)
Bilateral GGO (CTA)	56% (31–78)	83% (67–92)	59% (33–81)	80% (65–91)
Peripheral GGO (CTA)	78% (52–93)	85% (70–94)	70% (46–87)	90% (75–97)
COVID-typical/indeterminate (CTA)	72% (46–89)	90% (76–97)	76% (50–92)	88% (74–95)

Note:—PPV indicates positive predictive value; NPV, negative predictive value; GGO, ground glass opacification.
[a] COVID-typical alone gave a low sensitivity (44%) and was excluded from further analysis.

J. Siddiqui
F. Bala
Department of Neuroradiology
King's College Hospital NHS Foundation Trust
London, UK

S. Sciacca
A.M. Falzon
Lysholm Department of Neuroradiology
National Hospital for Neurology and Neurosurgery
University College London Hospitals NHS Foundation Trust
London, UK

M. Benger
Department of Neurology
King's College Hospital NHS Foundation Trust
London, UK

S.A. Matloob
Department of Neurosurgery
National Hospital for Neurology and Neurosurgery
University College London Hospitals NHS Foundation Trust
London, UK

F.N.A.C. Miller
Department of Radiology
King's College Hospital NHS Foundation Trust
London, UK

R.J. Simister
Comprehensive Stroke Service
University College London Hospitals NHS Foundation Trust
London, UK
Stroke Research Centre
University College London Queen Square Institute of Neurology
London, UK

I. Chatterjee
Comprehensive Stroke Service
University College London Hospitals NHS Foundation Trust
London, UK

L.K. Sztriha
Department of Neurology
King's College Hospital NHS Foundation Trust
London, UK

I. Davagnanam
Lysholm Department of Neuroradiology
National Hospital for Neurology and Neurosurgery
University College London Hospitals NHS Foundation Trust
London, UK
Brain Repair & Rehabilitation Unit
University College London Queen Square Institute of Neurology
London, UK

T.C. Booth
Department of Neuroradiology
King's College Hospital NHS Foundation Trust
London, UK
School of Biomedical Engineering and Imaging Sciences
King's College London
London, UK

Diagnostic Value of "Mushroom" Morphology in Vertebral Chordoma

We read with great interest the recently published article "Exophytic Lumbar Vertebral Body Mass in an Adult with Back Pain." We thank John C. Benson et al[1] for their lucid description of imaging features of chordoma presenting as an exophytic lumbar vertebral mass. We recently encountered a similar case and would like to add few points related to this pathology.

Our patient, 68 years old male, presented with a history of low back pain for the previous 3 years. The initial spine MR imaging done 3 years earlier showed a small L4 lesion (Figure *A*, *B*) confined to the vertebral body itself without any extraosseous component. He was provisionally diagnosed with vertebral hemangioma and managed conservatively with intermittent analgesics. A recent aggravation of his low back pain and new-onset paresthesia of bilateral lower limbs made him seek medical attention at our institute, and he underwent repeat imaging.

The MR imaging (Figure *C*, *D*) revealed an exophytic L4 vertebral body lesion with an extraosseous soft tissue component remarkably similar to the mass described in the Benson et al[1] article. The appearance on the noncontrast imaging mimicked an aggressive hemangioma with expansile extraosseous soft tissue component and preserved vertically oriented bony trabeculae. However, the dynamic time-resolved imaging of contrast kinetics (TRICKS) MR image did not show any arterial phase early enhancement or any prominent artery supplying the lesion, which was against the diagnosis of vertebral hemangioma (Figure *E*, *F*). An imaging differential of chordoma was considered,[2] and it was decided to proceed with CT-guided Tru-Cut (Merit Medical) biopsy. On histopathology, the lesion was proved to be chordoma.

Regarding the imaging, we would like to add a couple of inputs that we have learned from this case to differentiate chordoma from other differential diagnoses.

First, the noncontrast CT and MR images in vertebral chordoma may be confused with aggressive vertebral hemangioma. A dynamic TRICKS MR image may prove helpful in differentiating this condition by showing lack of early arterial enhancement and lack of a prominent feeding vessel[3] (Figure *E*, *F*).

Second, as mentioned in the article, chordoma typically spares the adjoining intervertebral discs, but in our case, it showed few focal areas of involvement of adjoining IV discs (Figure *C*, *D*), suggestive of its locally aggressive nature.

Third, our case demonstrates the natural history of vertebral chordoma over a 3-year duration. It originated from the mid L4 vertebral body, had slow growth, and later progressed to a large vertebral mass with a dumbbell- or mushroom-shaped exophytic paravertebral extension.

Finally, a biopsy from a suspected vertebral chordoma is not encouraged because of the risk of recurrence along the biopsy tract. In our case, to prevent such an event, embolization of the biopsy tract with doxorubicin beads was done.

In conclusion, despite being an exceedingly rare entity, chordoma should be considered as a differential for exophytic vertebral body lesion with extraosseous soft tissue component along with other differential diagnoses as mentioned by Benson et al.[1]

REFERENCES

1. Benson JC, Vizcaino MA, Kim DK, et al. **Exophytic lumbar vertebral body mass in an adult with back pain.** *AJNR Am J Neuroradiol* 2020;41:1786–90 CrossRef Medline
2. Smolders D, Wang X, Drevelengas A, et al. **Value of MRI in the diagnosis of non-clival, non-sacral chordoma.** *Skeletal Radiol* 2003;32:343–50 CrossRef Medline
3. Hurley MC, Gross BA, Surdell D, et al. **Preoperative Onyx embolization of aggressive vertebral hemangiomas.** *AJNR Am J Neuroradiol* 2008;29:1095–97 CrossRef Medline

T.S. Ghosh
S. Tiwari
P.K. Garg
P.S. Khera
Department of Diagnostic and Interventional Radiology
All India Institute of Medical Sciences, Jodhpur
Rajasthan, India

P. Elhence
Department of Pathology
All India Institute of Medical Sciences, Jodhpur
Rajasthan, India

FIGURE. The T2 sagittal (*A*) and axial (*B*) MR images done in December 2017 show a nonexophytic and centrally located T2 hyperintense lesion, confined to the L4 vertebral body outline without any extraosseous soft tissue. Repeat T2 sagittal (*C*) and coronal (*D*) MR imaging in August 2020 shows increase in the size of mass. The mass is centered within the body of vertebra with an exophytic component extending to the left lateral aspect causing smooth displacement of the psoas major muscle. Note the focal areas of infiltration of adjoining intervertebral disc (*white arrows*) by the tumor. The sagittal dynamic TRICKS MR image arterial phase (*E*) shows no early enhancement or any dominant feeder to the mass. The venous phase of angiogram (*F*) shows mild diffuse tumoral enhancement of the lesion.

REPLY:

We thank Drs. Ghosh, Tiwari, Garg, Khera, and Elhence for their interest in our recent manuscript titled "Exophytic Lumbar Vertebral Body Mass in an Adult with Back Pain." We appreciate their valuable insight on this subject and thank them for sharing a case of a spinal chordoma that exemplifies many of the imaging characteristics we described.

First, we agree that the intervertebral disk may be invaded by chordomas; Firooznia et al[1] described occasional disk involvement, and other previously published case reports[2,3] have similarly shown disk invasion. Although chordomas classically spare the intervertebral disks, all types of pathologies can have atypical findings. Disk involvement should therefore not dissuade radiologists from raising the possibility of a chordoma.

Next, we believe that it is an oversimplification to state that biopsy of suspected chordomas is not encouraged. True, chordomas are prone to dissemination along a biopsy tract. However, in the setting of an uncertain diagnosis, tissue is often still needed for pathologic confirmation of imaging findings, particularly given the complexity and morbidity of potential surgeries such as sacrectomy. In such cases, a biopsy may still be performed as long as the percutaneous biopsy tract is known so that it can be resected at the time of surgery.

Finally, Ghosh et al are correct in saying that atypical hemangiomas can share imaging features with more sinister skeletal lesions, such as metastases, multiple myeloma, and chordomas.[4] To our knowledge, however, time-resolved imaging of contrast kinetics (TRICKS) has not been shown to confidently distinguish between hemangiomas and chordomas. TRICKS is a recently introduced MR technique that allows for dynamic MR imaging during the arterial, capillary, and venous phases.[5] Dynamic enhancement curves have been offered as a method to distinguish atypical hemangiomas (typically with minimal and delayed enhancement) from metastases (often demonstrating a sharp rise in enhancement with a high peak followed by quick washout).[6] However, literature on this subject remains extremely sparse. Even the Hurley et al[7] article referenced by the authors does not mention marked early arterial enhancement or specific prominence of the feeding vessels in hemangiomas. Instead, much of our current understanding of the contrast dynamics of vertebral hemangiomas comes from angiography. On DSA, hemangiomas have been described as having a diffuse blush of enhancement that persists into the capillary phase.[1] However, their appearance is not specific and can vary based on the aggressiveness of the lesions. For now, we believe that more evidence is needed before dynamic MR can be labeled a useful tool for differentiating aggressive hemangiomas from chordomas.

REFERENCES

1. Firooznia H, Pinto RS, Lin JP, et al. **Chordoma: radiologic evaluation of 20 cases.** *AJR Am J Roentgenol* 1976;127:797–805 CrossRef Medline
2. Kivrak AS, Koc O, Emlik D, et al. **Differential diagnosis of dumbbell lesions associated with spinal neural foraminal widening: imaging features.** *Eur J Radiol* 2009;71:29–41 CrossRef Medline
3. Breen N, Eames N. **Chordoma of the lumbar spine—a potential diagnosis not to be forgotten.** *J Surg Case Rep* 2012;2012:4 CrossRef Medline
4. Gaudino S, Martucci M, Colantonio R, et al. **A systematic approach to vertebral hemangioma.** *Skeletal Radiol* 2015;44:25–36 CrossRef Medline
5. Romano A, Tavanti F, Rossi Espagnet MC, et al. **The role of time-resolved imaging of contrast kinetics (TRICKS) magnetic resonance angiography (MRA) in the evaluation of head–neck vascular anomalies: a preliminary experience.** *Dentomaxillofac Radiol* 2015;44:20140302 CrossRef Medline
6. Morales KA, Arevalo-Perez J, Peck KK, et al. **Differentiating atypical hemangiomas and metastatic vertebral lesions: the role of T1-weighted dynamic contrast-enhanced MRI.** *AJNR Am J Neuroradiol* 2018;39:968–73 CrossRef Medline
7. Hurley MC, Gross BA, Surdell D, et al. **Preoperative Onyx embolization of aggressive vertebral hemangiomas.** *AJNR Am J Neuroradiol* 2008;29:1095–97 CrossRef Medline

J.C. Benson
J.M. Morris
Mayo Clinic
Department of Neuroradiology
Rochester, Minnesota